

MAY 2021

AJNR

VOLUME 42 • PP 807-993

AJNR

AMERICAN JOURNAL OF NEURORADIOLOGY

MAY 2021
VOLUME 42
NUMBER 5
WWW.AJNR.ORG

THE JOURNAL OF DIAGNOSTIC AND
INTERVENTIONAL NEURORADIOLOGY

Endovascular treatment of CSF-venous fistulas
Trends in neuroradiology fellow performance
Ultrashort TE MRI in multiple sclerosis
Algorithm for childhood posterior fossa tumors

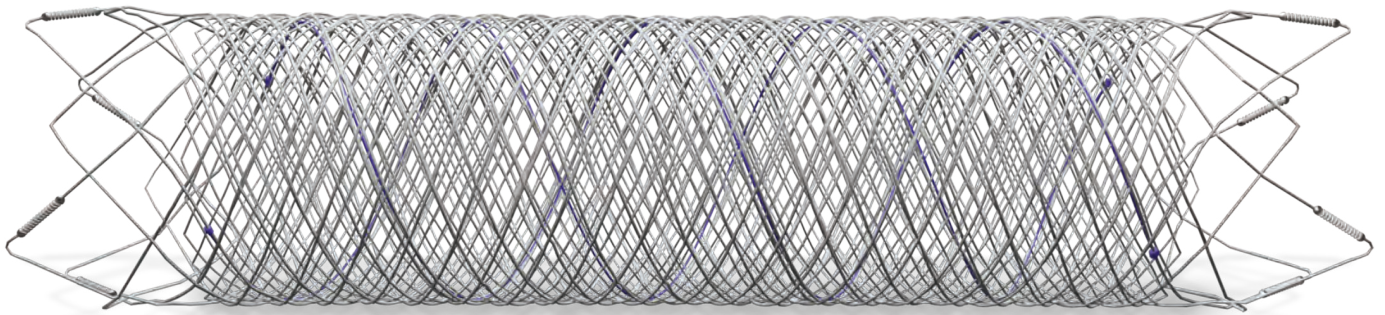
Official Journal ASNR • ASFNR • ASHNR • ASPNR • ASSR



FRED™

Flow Re-Direction
Endoluminal Device

FLOW DIVERSION.



SIMPLIFIED.

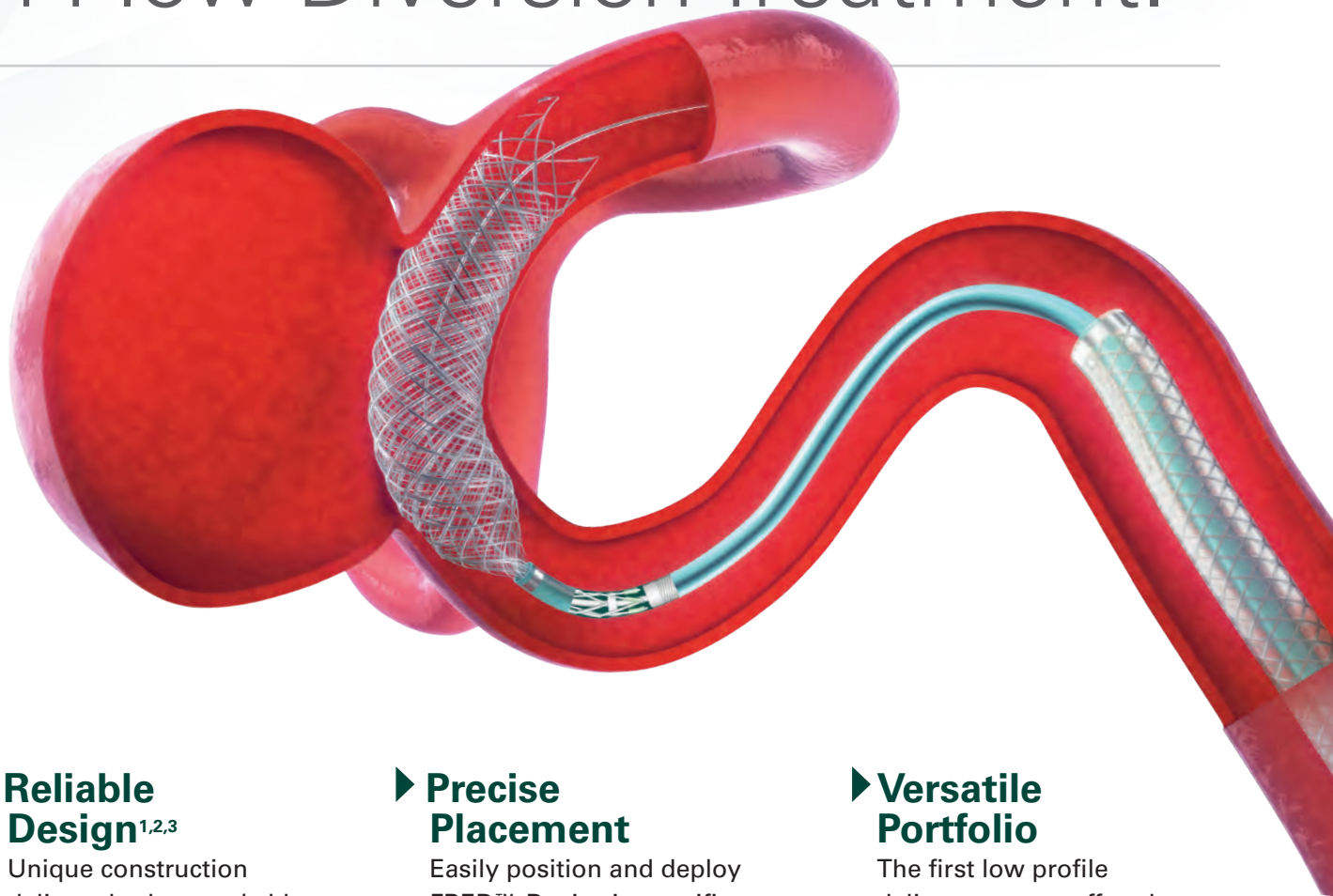


MicroVention Worldwide
Innovation Center
35 Enterprise
Aliso Viejo, CA 92656 USA
MicroVention UK Limited
MicroVention Europe S.A.R.L.
MicroVention Deutschland GmbH
Web

PH +1 714.247.8000

PH +1 44 (0) 191 258 6777
PH +33 (1) 39 21 77 46
PH +49 211 210 798-0
microvention.com

The New Standard of **Ease and Simplicity** in Flow Diversion Treatment.



► **Reliable Design**^{1,2,3}

Unique construction delivers both remarkable ease of use and excellent flow diversion^{1,2,3}

► **Precise Placement**

Easily position and deploy FRED™ Device in specific, targeted locations^{4,5,6}

► **Versatile Portfolio**

The first low profile delivery system offered in combination with large diameter and long length options

References:

1. TR11-211 2. TR13-171 3. TR15-055 4. TR13-192 5. TR15-072 6. TR19-145

The Flow Re-Direction Endoluminal Device (FRED™) System is indicated for use in the internal carotid artery from the petrous segment to the terminus for the endovascular treatment of adult patients (22 years of age or older) with wide-necked (neck width ≥ 4 mm or dome-to-neck ratio < 2) saccular or fusiform intracranial aneurysms arising from a parent vessel with a diameter ≥ 2.0 mm and ≤ 5.0 mm.

Use of the FRED™ System is contraindicated under these circumstances: Patients in whom anticoagulant, anti-platelet therapy, or thrombolytic drugs are contraindicated. Patients with known hypersensitivity to metal such as nickel-titanium and metal jewelry. Patients with anatomy that does not permit passage or deployment of the FRED™ System. Patients with an active bacterial infection. Patients with a pre-existing stent in place at the target aneurysm. Patients in whom the parent vessel size does not fall within the indicated range. Patients who have not received dual anti-platelet agents prior to the procedure. For complete indications, contraindications, potential complications, warnings, precautions, and instructions, see instructions for use (IFU provided in the device).

RX Only: Federal (United States) law restricts this device to sale by or on the order of a physician.

MICROVENTION™ and FRED™ are registered trademarks of MicroVention, Inc. in the United States and other jurisdictions. © 2020 MicroVention, Inc. 04/2020.

Explore the New ASNR Career Center



Your Premier Resource for Professional Development

- Access to jobs in the National Healthcare Career Network
- Confidential resume posting
- One-time free resume review
- Professional online profile
- Saved jobs capability

Start here: careers.asnr.org

ASNR
American Society of Neuroradiology

AJNR

AMERICAN JOURNAL OF NEURORADIOLOGY

MAY 2021
VOLUME 42
NUMBER 5
WWW.AJNR.ORG

Publication Preview at www.ajnr.org features articles released in advance of print. Visit www.ajnrblog.org to comment on AJNR content and chat with colleagues and AJNR's News Digest at <http://ajnrndigest.org> to read the stories behind the latest research in neuroimaging.

807 **PERSPECTIVES** L.A. Grajauskas

REVIEW ARTICLE

 808 **A Review of Robotic Interventional Neuroradiology** C.B. Beaman, et al.

INTERVENTIONAL

PRACTICE PERSPECTIVES

 815 **Am I Ready to Be an Independent Neuroradiologist? Objective Trends in Neuroradiology Fellows' Performance during the Fellowship Year** J.H. Masur, et al.



PATIENT SAFETY

824 **Impact of Kidney Function on CNS Gadolinium Deposition in Patients Receiving Repeated Doses of Gadobutrol** S. Dogra, et al.

GENERAL CONTENTS

 831 **Severity of Chest Imaging is Correlated with Risk of Acute Neuroimaging Findings among Patients with COVID-19** M. Lang, et al.

ADULT BRAIN

  838 **Development and Validation of a Deep Learning–Based Model to Distinguish Glioblastoma from Solitary Brain Metastasis Using Conventional MR Images** I. Shin, et al.


**ADULT BRAIN
FUNCTIONAL**

 845 **MRI-Based Deep-Learning Method for Determining Glioma MGMT Promoter Methylation Status** C.G.B. Yogananda, et al.

**ADULT BRAIN
FUNCTIONAL**

 853 **MGMT Promoter Methylation Status in Initial and Recurrent Glioblastoma: Correlation Study with DWI and DSC PWI Features** H.J. Choi, et al.

**ADULT BRAIN
FUNCTIONAL**

 861 **Traumatic Cerebral Microbleeds in the Subacute Phase Are Practical and Early Predictors of Abnormality of the Normal-Appearing White Matter in the Chronic Phase** A.W. van der Eerden, et al.

**ADULT BRAIN
FUNCTIONAL**

  868 **Inversion Recovery Ultrashort TE MR Imaging of Myelin is Significantly Correlated with Disability in Patients with Multiple Sclerosis** H. Jang, et al.

**ADULT BRAIN
FUNCTIONAL**

 875 **Peak Width of Skeletonized Mean Diffusivity as Neuroimaging Biomarker in Cerebral Amyloid Angiopathy** N. Raposo, et al.

**ADULT BRAIN
FUNCTIONAL**

AJNR (Am J Neuroradiol ISSN 0195–6108) is a journal published monthly, owned and published by the American Society of Neuroradiology (ASNR), 800 Enterprise Drive, Suite 205, Oak Brook, IL 60523. Annual dues for the ASNR include approximately 21% for a journal subscription. The journal is printed by Intellicor Communications, 330 Eden Road, Lancaster, PA 17601; Periodicals postage paid at Oak Brook, IL and additional mailing offices. Printed in the U.S.A. POSTMASTER: Please send address changes to American Journal of Neuroradiology, P.O. Box 3000, Denville, NJ 07834, U.S.A. Subscription rates: nonmember \$410 (\$480 foreign) print and online, \$320 online only; institutions \$470 (\$540 foreign) print and basic online, \$935 (\$1000 foreign) print and extended online, \$380 online only (basic), \$825 online only (extended); single copies are \$35 each (\$40 foreign). Indexed by PubMed/MEDLINE, BIOSIS Previews, Current Contents (Clinical Medicine and Life Sciences), EMBASE, Google Scholar, HighWire Press, Q-Sensei, RefSeek, Science Citation Index, SCI Expanded, Meta/CZI, ReadCube, and Semantic Scholar. Copyright © American Society of Neuroradiology.



MIDRC

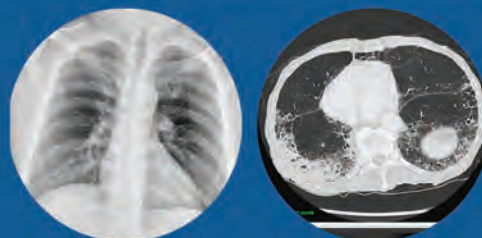
MEDICAL IMAGING AND DATA RESOURCE CENTER.

Medical Imaging in the Fight against COVID-19 Call for Contributions

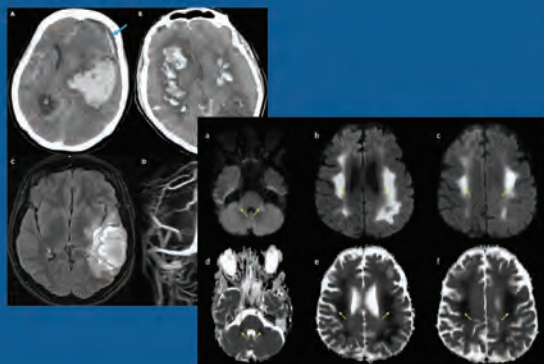
The Medical Imaging and Data Resource Center (MIDRC) is a multi-organizational initiative in the fight against the ongoing worldwide pandemic co-led by the ACR®, the RSNA, and the AAPM and is hosted at the University of Chicago.



The primary goal is to accelerate machine learning research by creating a high quality COVID-19 image commons linked to relevant clinical data made available as a public resource.



ASNR has teamed up with MIDRC to advance the understanding of the neuroimaging manifestations of COVID-19 and to enhance the MIDRC image commons.



- To ensure success, MIDRC encourages all institutions and hospitals, both small and large, to donate their COVID-19 medical images and data to the cause.
- MIDRC provides a HIPAA-compliant mechanism to securely submit medical images and clinical metadata, and is committed to helping institutions throughout the submission process.

Visit midrc.org for more information



AMERICAN ASSOCIATION
of PHYSICISTS IN MEDICINE



THE UNIVERSITY OF
CHICAGO



National Institute of Biomedical Imaging and Bioengineering
Creating Biomedical Technologies to Improve Health

	882	A Novel Endovascular Therapy for CSF Hypotension Secondary to CSF-Venous Fistulas <i>W. Brinjikji, et al.</i>	INTERVENTIONAL SPINE
	888	Distal Transradial Access for Diagnostic Cerebral Angiography and Neurointervention: Systematic Review and Meta-analysis <i>H. Hoffman, et al.</i>	INTERVENTIONAL
	896	Posterior Circulation Endovascular Thrombectomy for Large-Vessel Occlusion: Predictors of Favorable Clinical Outcome and Analysis of First-Pass Effect <i>A.M. Alexandre, et al.</i>	INTERVENTIONAL
	904	Early Postmarket Results with EmboTrap II Stent Retriever for Mechanical Thrombectomy: A Multicenter Experience <i>A. Srivatsan, et al.</i>	INTERVENTIONAL
	910	Do Outcomes between Women and Men Differ after Endovascular Thrombectomy? A Meta-analysis <i>A.A. Dmytriw, et al.</i>	INTERVENTIONAL
	916	Middle Meningeal Artery Embolization Using Combined Particle Embolization and <i>n</i> -BCA with the Dextrose 5% in Water Push Technique for Chronic Subdural Hematomas: A Prospective Safety and Feasibility Study <i>F. Al-Mufti, et al.</i>	INTERVENTIONAL
	921	Postprocedural Antiplatelet Treatment after Emergent Carotid Stenting in Tandem Lesions Stroke: Impact on Stent Patency beyond Day 1 <i>R. Pop, et al.</i>	INTERVENTIONAL
	926	Commentary The Challenge of an Acute Antithrombotic Regimen for Treatment of Tandem Lesions Stroke <i>P. Papanagiotou, et al.</i>	
	927	Diagnosing Carotid Near-Occlusion with Phase-Contrast MRI <i>E. Johansson, et al.</i>	EXTRACRANIAL VASCULAR
	930	Altered Processing of Complex Visual Stimuli in Patients with Postconcussive Visual Motion Sensitivity <i>J.W. Allen, et al.</i>	FUNCTIONAL
	938	The Pharyngolaryngeal Venous Plexus: A Potential Pitfall in Surveillance Imaging of the Neck <i>P.M. Bunch, et al.</i>	HEAD & NECK
	945	Improved Lesion Conspicuity with Contrast-Enhanced 3D T1 TSE Black-Blood Imaging in Cranial Neuritis: A Comparative Study of Contrast-Enhanced 3D T1 TSE, 3D T1 Fast-Spoiled Gradient Echo, and 3D T2 FLAIR <i>T.-W. Baek, et al.</i>	HEAD & NECK
	951	Neuroimaging Offers Low Yield in Children Positive for SARS-CoV-2 <i>G. Orman, et al.</i>	PEDIATRICS
	955	Transient Hyperintensity of the Infant Thyroid Gland on T1-Weighted MR Imaging: Correlation with Postnatal Age, Gestational Age, and Signal Intensity of the Pituitary Gland <i>H. Maki, et al.</i>	PEDIATRICS
	961	A Diagnostic Algorithm for Posterior Fossa Tumors in Children: A Validation Study <i>C.A.P.F. Alves, et al.</i>	PEDIATRICS
	969	Interobserver Reliability of an MR Imaging Scoring System in Infants with Hypoxic-Ischemic Encephalopathy <i>E. Szakmar, et al.</i>	PEDIATRICS
	975	Widening the Neuroimaging Features of Adenosine Deaminase 2 Deficiency <i>A.F. Geraldo, et al.</i>	PEDIATRICS
	980	A Systematic Review of Procedural Complications from Transforaminal Lumbar Puncture for Intrathecal Nusinersen Administration in Patients with Spinal Muscular Atrophy <i>A. Grayev, et al.</i>	SPINE
	986	Spinal Compliance Curves: Preliminary Experience with a New Tool for Evaluating Suspected CSF Venous Fistulas on CT Myelography in Patients with Spontaneous Intracranial Hypotension <i>M.T. Caton Jr, et al.</i>	SPINE

AJNR *go green*

***AJNR* urges American Society of Neuroradiology members to reduce their environmental footprint by voluntarily suspending their print subscription.**

The savings in paper, printing, transportation, and postage directly fund new electronic enhancements and expanded content.

The digital edition of *AJNR* presents the print version in its entirety, along with extra features including:

- Publication Preview
- Case Collection
- Podcasts
- The *AJNR* News Digest
- The *AJNR* Blog

It also reaches subscribers much faster than print. An electronic table of contents will be sent directly to your mailbox to notify you as soon as it publishes.

Readers can search, reference, and bookmark current and archived content 24 hours a day on www.ajnr.org.

ASNR members who wish to opt out of print can do so by using the *AJNR* Go Green link on the *AJNR* Website (<http://www.ajnr.org/content/subscriber-help-and-services>). Just type your name in the email form to stop print and spare our ecosystem.

BOOK REVIEWS *R.M. Quencer, Section Editor*

Please visit www.ajnrblog.org to read and comment on Book Reviews.



Brinjikji, et al. in this issue: Steps involved in CSF-venous fistula embolization.



Indicates Editor's Choices selection



Indicates Fellows' Journal Club selection



Indicates open access to non-subscribers at www.ajnr.org



Indicates article with supplemental online data



Indicates article with supplemental online video



Evidence-Based Medicine Level 1



Evidence-Based Medicine Level 2

EDITOR-IN-CHIEF

Jeffrey S. Ross, MD

Professor of Radiology, Department of Radiology,
Mayo Clinic College of Medicine, Phoenix, AZ

SENIOR EDITORS

Harry J. Cloft, MD, PhD

Professor of Radiology and Neurosurgery,
Department of Radiology, Mayo Clinic College of
Medicine, Rochester, MN

Christopher G. Filippi, MD

Professor and Alice Ettinger-Jack R. Dreyfuss
Chair of Radiology,
Tufts University School of Medicine,
Radiologist-in-Chief
Tufts University Medical Center, Boston, MA

Thierry A.G.M. Huisman, MD

Radiologist-in-Chief, Texas Children's Hospital,
Houston, TX

Yvonne W. Lui, MD

Associate Professor of Radiology,
Chief of Neuroradiology,
New York University School of Medicine,
New York, NY

C.D. Phillips, MD, FACR

Professor of Radiology, Weill Cornell Medical
College, Director of Head and Neck Imaging,
New York-Presbyterian Hospital, New York, NY

Lubdhra M. Shah, MD, MS

Professor of Radiology and Director of Spine
Imaging, University of Utah Department of
Radiology and Imaging Sciences, Salt Lake City, UT

STATISTICAL SENIOR EDITOR

Bryan A. Comstock, MS

Senior Biostatistician,
Department of Biostatistics,
University of Washington, Seattle, WA

ARTIFICIAL INTELLIGENCE DEPUTY EDITOR

Peter D. Chang, MD

Assistant Professor-in-Residence,
Departments of Radiological Sciences,
Computer Sciences, and Pathology,
Director, Center for Artificial Intelligence in
Diagnostic Medicine (CAIDM),
University of California, Irvine, Irvine, CA

EDITORIAL BOARD

Ashley H. Aiken, Atlanta, GA

Lea M. Alhilali, Phoenix, AZ

Mohammed A. Almekhlafi, Calgary, Alberta,
Canada

Joachim Berkefeld, Frankfurt, Germany

Aashim Bhatia, Pittsburgh, PA

Waleed Brinjikji, Rochester, MN

Judah Burns, New York, NY

Danielle Byrne, Dublin, Ireland

Federico Cagnazzo, Montpellier, France

J. Levi Chazen, New York, NY

James Y. Chen, San Diego, CA

Gloria C. Chiang, New York, NY

Daniel Chow, Irvine, CA

Kars C.J. Compagne, Rotterdam, The Netherlands

Arturo Consoli, Suresnes, France

Seena Dehkharghani, New York, NY

Nilesh K. Desai, Houston, TX

Yonghong Ding, Rochester, MN

Birgit Ertl-Wagner, Toronto, Ontario, Canada

Clifford J. Eskey, Hanover, NH

Massimo Filippi, Milan, Italy

Nils D. Forkert, Calgary, Alberta, Canada

Ana M. Franceschi, New York, NY

Frank Gaillard, Melbourne, Australia

Joseph J. Gemmete, Ann Arbor, Michigan

Wende N. Gibbs, Phoenix, AZ

Philipp Göltz, Erlangen, Germany

Brent Griffith, Detroit, MI

Joseph M. Hoxworth, Phoenix, Arizona

Raymond Y. Huang, Boston, MA

Gábor Janiga, Magdeburg, Germany

Christof Karmonik, Houston, TX

Timothy J. Kaufmann, Rochester, MN

Hillary R. Kelly, Boston, MA

Toshitomi Kinoshita, Akita, Japan

Alexander W. Korutz, Chicago, IL

Stephen F. Kralik, Houston, TX

Alexander Lerner, Los Angeles, CA

Yinsheng Li, Madison, WI

Franklin A. Marden, Chicago, IL

Markus A. Möhlenbruch, Heidelberg, Germany

Kambiz Nael, Los Angeles, CA

Renato Hoffmann Nunes, Sao Paulo, Brazil

Sasan Partovi, Cleveland, OH

Johannes A.R. Pfaff, Salzburg, Austria

Laurent Pierot, Reims, France

Alireza Radmanesh, New York, NY

Prashant Raghavan, Baltimore, MD

Eytan Raz, New York, NY

Paul M. Ruggieri, Cleveland, OH

Sebastian Schafer, Madison, WI

Maksim Shapiro, New York, NY

Timothy Shepherd, New York, NY

James Shin, New York, NY

Mark S. Shiroishi, Los Angeles, CA

Bruno P. Soares, Baltimore, MD

Jason F. Talbot, San Francisco, CA

Ruth Thiex, Everett, Washington

Vincent Thijs, Melbourne, Victoria, Australia

Anderanik Tomasian, Los Angeles, CA

Fabio Triulzi, Milan, Italy

Anja G. van der Kolk, Utrecht, the Netherlands

Arastoo Vossough, Philadelphia, PA

Elysa Widjaja, Toronto, Ontario, Canada

Leonard Yeo, Singapore

Woong Yoon, Gwangju, South Korea

David M. Yousem, Evergreen, CO

Carlos Zamora, Chapel Hill, NC

Chengcheng Zhu, Seattle, WA

EDITORIAL FELLOW

Matthew D. Alvin, Baltimore, MD

SPECIAL CONSULTANTS TO THE EDITOR

AJNR Blog Editor

Neil Lall, Denver, CO

Case of the Month Editor

Nicholas Stence, Aurora, CO

Case of the Week Editors

Matylda Machnowska, Toronto, Ontario, Canada

Anvita Pauranik, Calgary, Alberta, Canada

Sapna Rawal, Toronto, Ontario, Canada

Classic Case Editor

Sandy Cheng-Yu Chen, Taipei, Taiwan

Health Care and Socioeconomics Editor

Pina C. Sanelli, New York, NY

Physics Editor

Greg Zaharchuk, Stanford, CA

Podcast Editor

Courtney Tomblinson, Nashville, TN

Deputy Podcast Editor

Kevin Hiatt, Winston-Salem, NC

Twitter Editor

Roger Jordan, Houston, TX

Official Journal:

American Society of Neuroradiology

American Society of Functional Neuroradiology

American Society of Head and Neck Radiology

American Society of Pediatric Neuroradiology

American Society of Spine Radiology

Founding Editor

Juan M. Taveras

Editors Emeriti

Mauricio Castillo, Robert I. Grossman,

Michael S. Huckabee, Robert M. Quencer

Managing Editor

Karen Halm

Assistant Managing Editor

Laura Wilhelm

Editorial Assistant

Margaret B. Sabato

Executive Director, ASNR

Mary Beth Hepp

Dotarem®

(gadoterate meglumine) Injection

REAL-WORLD TESTED. REAL-WORLD PROVEN.

The Dotarem® safety profile has been tested and proven in both clinical studies and more than 30 years of global clinical use.*



1 Dotarem®
The first macrocyclic
and ionic GBCA molecule.¹

A low incidence of adverse events can help your patient focus on what matters most in their life.²

0.007%

Spontaneously Reported Worldwide
Adverse Events. (>50 million doses)²

Dotarem remains an industry
standard for contrast imaging with
a low incidence of immediate adverse
events for patients of all ages.²⁻⁵

Guerbet | 



IMPORTANT SAFETY INFORMATION¹

WARNING: NEPHROGENIC SYSTEMIC FIBROSIS (NSF)

Gadolinium-based contrast agents (GBCAs) increase the risk for NSF among patients with impaired elimination of the drugs. Avoid use of GBCAs in these patients unless the diagnostic information is essential and not available with non-contrast MRI or other modalities. NSF may result in fatal or debilitating fibrosis affecting the skin, muscle and internal organs.

- The risk for NSF appears highest among patients with:
 - Chronic, severe kidney disease (GFR < 30 mL/min/1.73m²), or
 - Acute kidney injury.
- Screen patients for acute kidney injury and other conditions that may reduce renal function. For patients at risk for chronically reduced renal function (e.g. age > 60 years, hypertension, diabetes), estimate the glomerular filtration rate (GFR) through laboratory testing.
- For patients at highest risk for NSF, do not exceed the recommended DOTAREM dose and allow a sufficient period of time for elimination of the drug from the body prior to any re-administration.



Indications and Usage

DOTAREM[®] (gadoterate meglumine) injection is a prescription gadolinium-based contrast agent indicated for intravenous use with magnetic resonance imaging (MRI) in brain (intracranial), spine and associated tissues in adult and pediatric patients (including term neonates) to detect and visualize areas with disruption of the blood brain barrier (BBB) and/or abnormal vascularity.

Contraindications

History of clinically important hypersensitivity reactions to DOTAREM.

Warnings and Precautions

- **Hypersensitivity Reactions:** Anaphylactic and anaphylactoid reactions have been reported with DOTAREM, involving cardiovascular, respiratory, and/or cutaneous manifestations. Some patients experienced circulatory collapse and died. In most cases, initial symptoms occurred within minutes of DOTAREM administration and resolved with prompt emergency treatment.
- Before DOTAREM administration, assess all patients for any history of a reaction to contrast media, bronchial asthma and/or allergic disorders. These patients may have an increased risk for a hypersensitivity reaction to DOTAREM.
- Administer DOTAREM only in situations where trained personnel and therapies are promptly available for the treatment of hypersensitivity reactions, including personnel trained in resuscitation.
- **Gadolinium Retention:** Gadolinium is retained for months or years in several organs. The highest concentrations have been identified in the bone, followed by brain, skin, kidney, liver and spleen. The duration of retention also varies by tissue, and is longest in bone. Linear GBCAs cause more retention than macrocyclic GBCAs.
- Consequences of gadolinium retention in the brain have not been established. Adverse events involving multiple organ systems have been reported in patients with normal renal function without an established causal link to gadolinium retention.
- **Acute Kidney Injury:** In patients with chronically reduced renal function, acute kidney injury requiring dialysis has occurred with the use of GBCAs. The risk of acute kidney injury may increase with increasing dose of the contrast agent; administer the lowest dose necessary for adequate imaging.
- **Extravasation and Injection Site Reactions:** Ensure catheter and venous patency before the injection of DOTAREM. Extravasation into tissues during DOTAREM administration may result in tissue irritation.

Adverse Reactions

- The most common adverse reactions associated with DOTAREM in clinical trials were nausea, headache, injection site pain, injection site coldness and rash.
- Serious adverse reactions in the Postmarketing experience have been reported with DOTAREM. These serious adverse reactions include but are not limited to: arrhythmia, cardiac arrest, respiratory arrest, pharyngeal edema, laryngospasm, bronchospasm, coma and convulsion.

Use in Specific Populations

- **Pregnancy:** GBCAs cross the human placenta and result in fetal exposure and gadolinium retention. Use only if imaging is essential during pregnancy and cannot be delayed.
- **Lactation:** There are no data on the presence of gadoterate in human milk, the effects on the breastfed infant, or the effects on milk production. However, published lactation data on other GBCAs indicate that 0.01 to 0.04% of the maternal gadolinium dose is present in breast milk.
- **Pediatric Use:** The safety and efficacy of DOTAREM at a single dose of 0.1 mmol/kg has been established in pediatric patients from birth (term neonates ≥ 37 weeks gestational age) to 17 years of age based on clinical data. The safety of DOTAREM has not been established in preterm neonates. No cases of NSF associated with DOTAREM or any other GBCA have been identified in pediatric patients age 6 years and younger.

You are encouraged to report negative side effects of prescription drugs to the FDA. Visit www.fda.gov/medwatch or call 1-800-FDA-1088.

Please see the full Prescribing Information, including the patient Medication Guide, for additional important safety information.

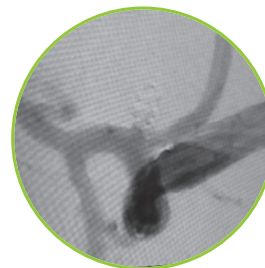
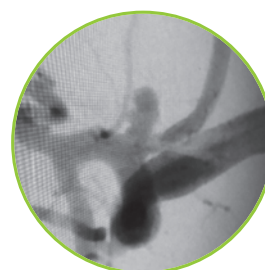
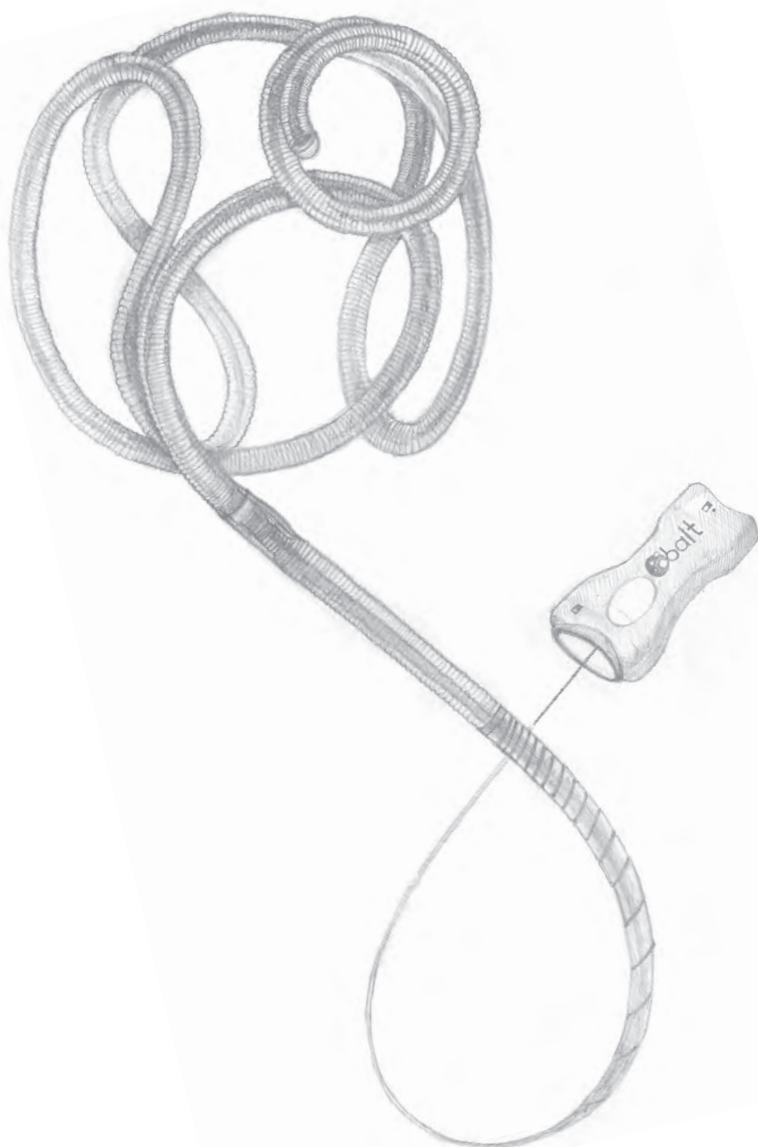
*Dotarem was launched globally in 1989 and approved by the FDA for use in the US in 2013.

References:

1. Dotarem [package insert]. Princeton, NJ: Guerbet LLC; Oct 2019. 2. de Kerviler E et al. Adverse reactions to gadoterate meglumine: review of over 25 years of clinical use and more than 50 million doses. *Invest Radiol.* 2016 Sep;51(9):544-51. 3. Briand Y. Daily Paediatric Use of MRI Contrast Agents: Results of a Multi-Centre Survey. *Proceedings of the 29th Congress of the European Society of Pediatric Radiology.* 1992. 4. Soyer et al. Observational Study on the Safety Profile of Gadoterate Meglumine in 35,499 Patients: The SECURE Study. *J. Magn. Reson. Imag.* 2017; 45, 988-997. 5. Behzadi AH, Zhao Y, Farooq Z, Prince MR. Immediate allergic reactions to gadolinium-based contrast agents: a systematic review and meta-analysis. *Radiology.* 2018;286(2):471-482.

OPTIMAX

**FEEL THE DIFFERENCE:
VOLUME, SOFTNESS AND STABILITY**



Complete and Unique Offerings:

The only large volume coil
available in a **Super Soft**
configuration in 1mm to 3.5mm
diameters, including half sizes.

Visit our products page at www.Balt-USA.com to learn more.

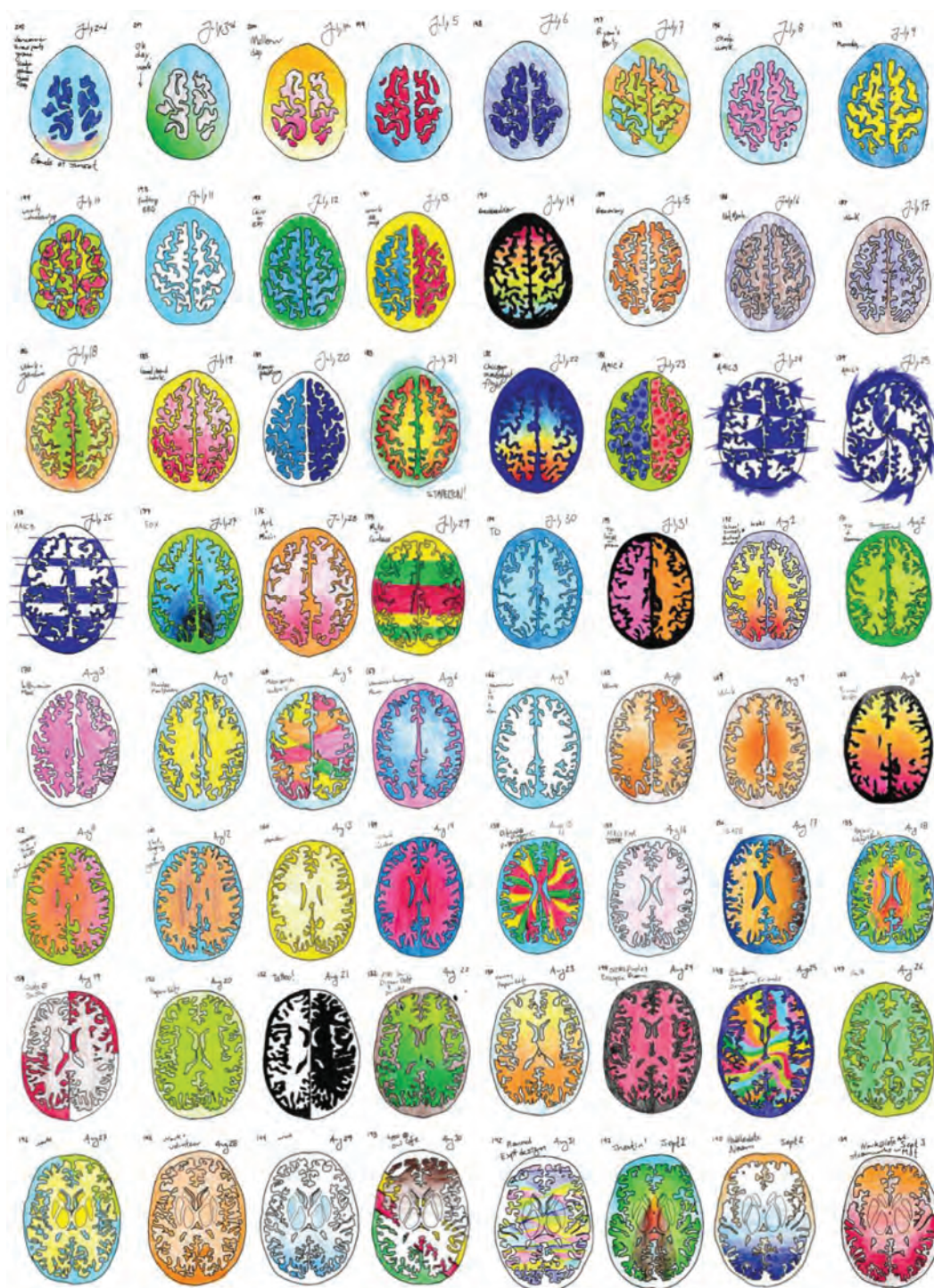
Balt USA

29 Parker, Irvine, CA 92618
tel 949.788.1443 fax 949.788.1444

balt-usa.com

©2021 BALT USA MKTG-250 Rev. A





Title: Looking In. This is a series of 64 mixed media drawings consolidated into a single work. Over the course of my MSc research, I assessed over 1000 MR images in the validation of a rating scale to be used for the evaluation of age-related neurodegeneration. During this process, I found the work was very disengaging in contrast to my clinical work with elderly individuals. When viewing the MR images I was "looking in" the brains of real humans with rich histories and stories, but I felt so separated from them as human beings. This inspired the creation of this art piece. Taking 64 slices from an MR image of my own brain, I created a daily journal of my experiences and emotions, tracing and coloring in each subsequent slice to create artistic works representing my internal world. This served as a reminder that each MR image I looked at involved a real person and had real human impacts. This work has also been impactful as I begin my medical training, where empathy is vital, but where it is also so easy to forget the human impact of your work when you are looking at an MRI scan of a patient's brain, or an incision into a body hidden by surgical drapes. Hopefully this work will serve to strengthen the empathy that readers have for their patients and research subjects, and be a reminder of the real human impact of their work.

Lukas A. Grajauskas, MSc, MD Student, Class of 2022, Cumming School of Medicine, University of Calgary, Calgary, Alberta, Canada

A Review of Robotic Interventional Neuroradiology

 C.B. Beaman,  N. Kaneko,  P.M. Meyers, and  S. Tateshima



ABSTRACT

SUMMARY: Robotic interventional neuroradiology is an emerging field with the potential to enhance patient safety, reduce occupational hazards, and expand systems of care. Endovascular robots allow the operator to precisely control guidewires and catheters from a lead-shielded cockpit located several feet (or potentially hundreds of miles) from the patient. This has opened up the possibility of expanding telestroke networks to patients without access to life-saving procedures such as stroke thrombectomy and cerebral aneurysm occlusion by highly-experienced physicians. The prototype machines, first developed in the early 2000s, have evolved into machines capable of a broad range of techniques, while incorporating newly automated maneuvers and safety algorithms. In recent years, preliminary clinical research has been published demonstrating the safety and feasibility of the technology in cerebral angiography and intracranial intervention. The next step is to conduct larger, multisite, prospective studies to assess generalizability and, ultimately, improve patient outcomes in neurovascular disease.

ABBREVIATION: COVID-19 = coronavirus disease 2019

In 1927, Moniz¹ first used radiopaque dye and x-rays to visualize cerebral vessels *in vivo*. In the past 100 years, major advances have been made in the field of endovascular neurointervention, including treatment of aneurysms, arteriovenous malformations, subdural hematomas, and ischemic strokes. Despite this progress, these procedures still require an operator who stands next to the patient and manually injects contrast, manipulates wires and catheters, and operates x-ray imaging, all while being exposed to ionizing radiation. In the 1980s, robotic systems were first introduced in a variety of disciplines to enhance precision and reproducibility in minimally-invasive surgical procedures.²⁻⁴ Early endovascular innovators adapted this technology and developed new remote-controlled catheter systems with the hopes of improving navigation and procedural precision.^{5,6} In recent years, interventional cardiologists have made tremendous progress with robotic technology. Large multicenter trials have demonstrated the safety and efficacy of robotics both in simple and in complex percutaneous coronary interventions.^{7,8} These successes paved


the way for investigations into the feasibility of robotic systems for endovascular neurointervention, including the implementation of automated maneuvers, machine learning, and remote operation.

As the indications for neuroendovascular intervention grow, operators spend more and more time in the angiography suite. Robotic systems have the potential to alleviate the occupational hazards associated with ionizing radiation.⁹ A concerning observational study was published in 2012, noting a predominance of left-sided brain tumors in interventional cardiologists.^{10,11} A much larger nationwide prospective cohort of 90,957 radiology technologists found a 2-fold increase in the risk of brain cancer mortality and increased incidences of breast cancer and melanoma compared with controls.¹² Even a single procedure has been shown to create radiation-induced DNA damage in circulating lymphocytes in operators.¹³ The concern is exacerbated by the growth of radial access, which exposes operators to higher doses of ionizing radiation compared with femoral access.¹⁴ As well as cancer-related risks, radiation increases the rates of cataracts and atherosclerosis during a long career.^{15,16} Interventionalists also have higher rates of orthopedic injuries, attributed to long hours standing in lead aprons.¹⁷ In addition, decreased occupational hazards may help improve distinct sex inequality in the field of neurointervention. Fewer than 10% of interventional radiologists are women, and this disparity may be partly attributed to fears related to radiation and orthopedic stress during pregnancy.^{18,19} Preliminary studies demonstrate that robotic

Received September 29, 2020; accepted after revision October 26.

From the Departments of Neurology (C.B.B.) and Radiology and Neurological Surgery (P.M.M.), Columbia University Irving Medical Center, New York, New York; and Department of Radiological Sciences (N.K., S.T.), David Geffen School of Medicine, University of California Los Angeles, Los Angeles, California.

Please address correspondence to Charles B. Beaman, MD, PhD, Columbia University Irving Medical Center, 710 W 168th St, New York, NY 10032; e-mail: cb3333@cumc.columbia.edu; @charlesbeaman

 Indicates open access to non-subscribers at www.ajnr.org

<http://dx.doi.org/10.3174/ajnr.A6976>



FIG 1. A, Sterile Corpath GRX patient-side robotic system during setup. B, Lead-shielded remote Corpath GRX control station during cerebral angiography procedure.

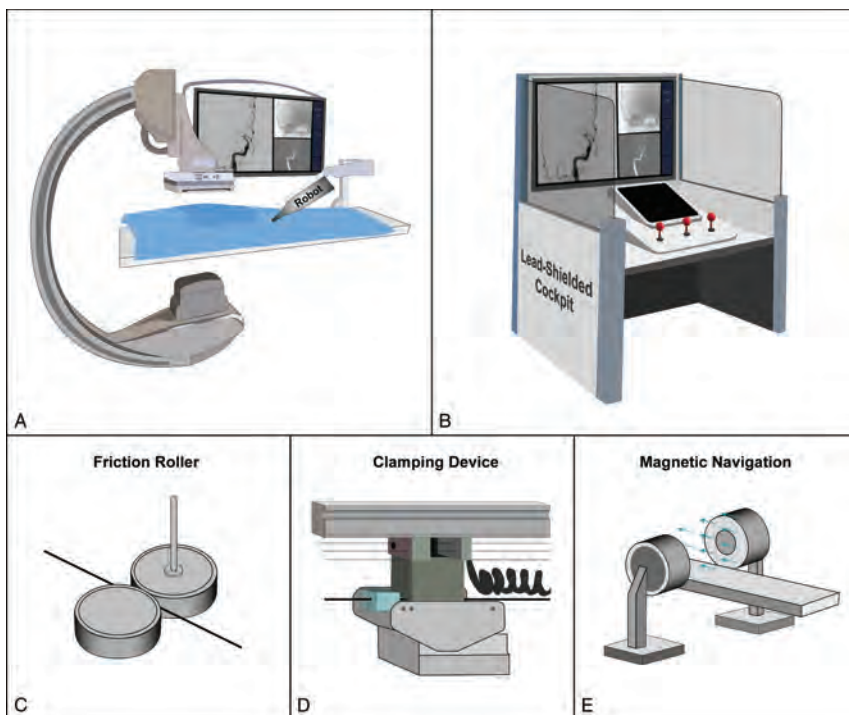


FIG 2. Robotic systems. A, Patient-side robot with articulating arm. B, Lead-shielded cockpit with monitors and controls. C, Friction roller drive mechanism. D, Clamping device mechanism. E, Magnetic navigation system.

endovascular systems can greatly mitigate these occupational risks. In the prospective Percutaneous Robotically Enhanced Coronary Intervention (PRECISE) study, the median radiation exposure to operators was reduced by 95.2% (0.98 versus 20.6 μGy , $P < .001$),⁷ and a recent study demonstrated that robotic systems also significantly decreased radiation doses to the patient (884 versus 1110 mGy, $P = .002$).²⁰ Furthermore, robotic systems may reduce the occupational spread of infection, such as coronavirus disease 2019

(COVID-19), by limiting staff exposure to the patient during procedures.²¹ Clearly, the opportunity for improved procedural safety is promising; however, it is of paramount importance to fully understand the technical strengths and limitations of current robotic systems to fully realize these ideals.

Overview of Robotics Specifications

Current endovascular robotic systems consist chiefly of 2 components: the patient-side mechanical robot and the operator control station (Fig 1). The control station, originally designed to remain in the procedure room, is a radiation-shielded cockpit outfitted with computer monitors, various sensors, and joysticks to control the guidewire and catheters with millimeter-scale resolution. The robot is typically connected to an articulating arm next to the patient (Fig 2A, -B). It receives instructions (either through cables or wireless telecommunication) from the control station and physically manipulates the wires and catheters using linear and rotational drive motors. There are 3 principal drive mechanisms in use for axial motion of the guidewire and catheters. The first mechanism implements a friction or pinch roller to press the wire against a capstan and drive it forward and backward (Fig 2C).^{22,23} The second mechanism consists of a clamping device that grasps the wire and uses a linear motor to drive it axially along a shaft (Fig 2D).²⁴⁻²⁶ The third mechanism uses large externally generated magnetic fields for traction on a passive ferromagnetic catheter (Fig 2E).^{27,28}

The pinch roller and clamping mechanisms are more well-studied, but the magnetic system does have the benefit of distal tip navigation, which can theoretically allow omnidirectional

distal tip control and in vivo wire reshaping.²⁹

The first robotic system in general use, the CorPath 200 (launched in 2012 by Corindus, a Siemens Healthineers Company), implements pinch roller propulsion. It is an open-architecture machine, compatible with 0.014-inch guidewires, rapid exchange catheters, and stent-delivery systems. With any new technology, it is critical to analyze potential failure modes and their causes and effects. Indeed, failure modes during robotic percutaneous coronary intervention were investigated by Harrison et

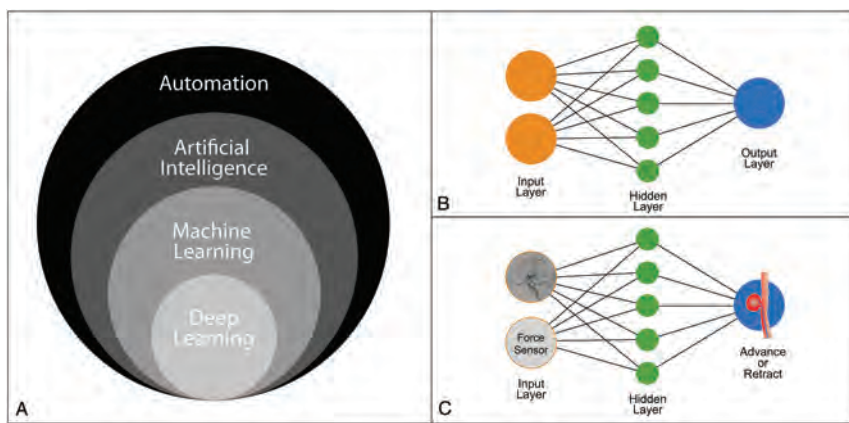


FIG 3. Automation in robotic neurointervention. A, Subfields of automation in computer science. B, Illustrated neural network with input layer, hidden layer, and output layer. C, Sample neural network with cerebral angiography and force sensor as inputs and the decision to advance or retract the catheter as the output.

al,³⁰ who found that conversion to manual operation was required in 20 of 108 patients (18.5%). Of these 20 cases, 12 required only partial manual assistance, defined as planned or unplanned temporary disengagement of the robotic drive for manual operation and then a return to full robotic operation. The other 8 cases required full conversion to manual operation for the duration of the procedure. The most common failure mode was related to lack of wire and catheter support and manipulation, which occurred in 9 cases. The remaining causes of failure were mostly due to known limitations of the system such as the need to use incompatible intracoronary imaging devices. Only 3 cases required manual intervention for adverse events such as vessel closure or dissection.

The second-generation CorPath GRX was cleared by the FDA for percutaneous coronary interventions in 2016 and for peripheral vascular interventions in 2018. It includes the ability to robotically control the guide catheter to enhance support, an essential feature for tortuous neurovasculature. The current working length is 20 cm, or more precisely, ± 10 cm from a neutral starting position that can be manually changed. Britz et al²² conducted a neurovascular in vitro and porcine feasibility study and found that microcatheters occasionally herniated from the guide track. The herniation is similar to a line of train cars pushed from the back by a locomotive rather than pulled from the front by the same locomotive. Frictional forces prevent linear translation of force due to lateral instability of the line, or microcatheter in this case. In addition, they found that smaller-diameter devices, such as coils and stents, were too short to use in the guidewire track. This led the company to improve the machine by adding a Y-connector cover and adapter to prevent device herniation and a new driving gear to facilitate smaller-diameter devices. Corindus is now conducting a prospective, multicenter, clinical study to determine the effectiveness and safety of the robotic system in embolization of cerebral aneurysms compared with historical controls.³¹

Automated Maneuvers and Machine Learning

A principal advantage of endovascular robotics is the ability to automate maneuvers to reduce procedural time and decrease

variability of repeat manual maneuvers. Currently available algorithms are sparse, but machine learning has the potential to augment the neurointerventionalist's tool kit. Rotate-on-Retract was the first FDA-approved automated feature of the CorPath GRX Robotic System. With the feature activated, the robot will automatically rotate the guidewire during retraction to facilitate vessel selection. Preclinical work presented at the Transcatheter Cardiovascular Therapeutics Conference in 2017 demonstrated a significant reduction in mean wiring time (20 [SD, 8] versus 48 [SD, 8] seconds) when the feature was enabled.³² In addition, Al Nooryani and Aboushokka³³ published a case report describing its suc-

cessful use in robot-assisted percutaneous coronary intervention to the left anterior descending coronary artery.

There is, however, a paucity of data regarding automated maneuvers in neuroendovascular cases. The cerebral vasculature has relatively small-diameter vessels that are structurally delicate with complex 3D branching arborization.³⁴ In their in vitro and porcine feasibility study, Britz et al²² found inadvertent forward movement of the wire when delivering the microcatheter, risking perforation. This work led to the development of "Active Device Fixation," an open-loop control algorithm to counteract unexpected movements of the guidewire made in response to microcatheter actuation.³⁵ This feature allows the operator to maintain the guidewire in a consistent position relative to the patient's anatomy and was recently implemented for the stent-coiling case report published by Mendes Pereira et al.³⁶ Other automated features are currently in the development stage, including "Spin," a lesion-crossing algorithm that rotates the guidewire in an oscillating motion during advancement; "Wiggle," a navigation algorithm that automatically rotates the guidewire in a reciprocating motion during advancement; "Dotter," a lesion-crossing algorithm that advances and retracts in a stepwise fashion during advancement; and "Constant Speed," a measurement algorithm that allows the operator to select a constant drive speed. In the future, artificial intelligence and its subsets, machine learning and deep learning, may be fully integrated into robotic systems (Fig 3A). This integration entails collecting large datasets of procedural techniques, using statistical methods, and implementing multilayer neural networks to allow robotic systems to "learn" and ultimately improve their performance (Fig 3B, -C). The hope is that automating certain interventional techniques may reduce procedural variability and treatment time, leading to improved patient safety and outcomes.

One major limitation of current robotic endovascular systems is the loss of tactile feedback during manual procedures. Tactile feedback is additional sensory input that increases the operating physician's situational awareness beyond that provided by 2D or 3D visual imaging. Interventionalists can use this critical

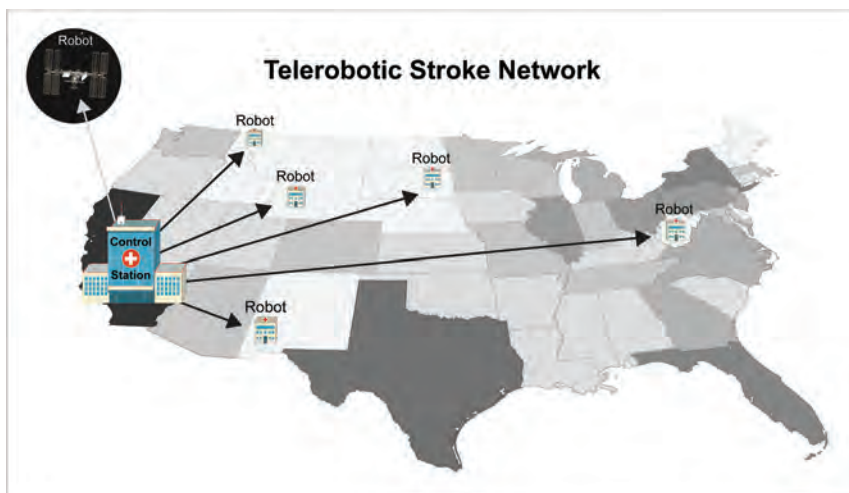


FIG 4. Telerobotic stroke network. A neurointerventionalist at the control station can operate multiple interventional robots to expand networks of care. “Robot” indicates potential sites of patient-side, interventional robots. Gray-scale indicates relative population size of each state.

information to anticipate the release of potential energy in catheter systems to prevent wire advancement, vessel dissection, or perforation. Force-sensing capabilities were built into 1 early robotic catheter system by Negoro et al.⁵ The diameter of their force sensor was 1.2 mm (0.047 inches), with a resolution of <0.5 mN, and a frequency response up to 2 kHz. Guo et al.³⁷ also developed a force-sensing catheter with a fiber pressure sensor (OPP-M40; OpSens). Their probe diameter was 0.25 mm (0.010 inches), a size more compatible with neuroendovascular procedures. They also developed an early safety warning system with a pressure threshold function that can be changed in real-time to adapt to different patients and their vascular characteristics. Future research may also allow interventionalists to physically sense the pressure in the guidewire or catheter, a technology known as haptics. For example, haptic technology is incorporated into many commercially available game controllers. The additions of force-sensing and haptic technology to robotic endovascular systems will likely be key areas of future research.

Telerobotics

Inequality in the geographic distribution of subspecialty health care limits medical access to a significant proportion of people. Only one-fifth of the US population has direct access to a thrombectomy-capable center within 15 minutes of travel time, and relying on interhospital transfer has unfortunately been associated with a treatment delay of up to 95 minutes.^{38,39} Recent research has shown that even a 15-minute delay in treatment is associated with a 10% decrease in the likelihood of good functional outcome.^{40,41} In the past 2 decades, telestroke has become one of the most effective telemedicine applications by showing increased rates of tPA administration, reduced door-to-needle times, and decreased patient death and dependency.^{42,43}

Telerobotics refers to transmission of data through telecommunication systems to allow the active control of instruments by a remote physician located at a distance from the interventional suite. The principal goal of telerobotics is to build on the

telestroke model to dramatically expand coverage for acute vascular procedures and further decrease time to treatment (Fig 4). Telementoring is another potential variant involving a remote physician who provides real-time observation and evaluation of the local physician's performance and may even be able to take control of the local tools to assist in the procedure. This may help provide low-volume operators with high-volume skills, allowing safer acute neurointerventional procedures.⁴⁴ Telementoring can also offer a solution to the issue of proctor availability under travel restrictions during a pandemic such as COVID-19.⁴⁵

Early clinical examples of telesurgery date back to the 1990s, but remote cerebral angiography was not attempted until 2011 when Lu et al.⁴⁶ completed the procedure in an animal model in Beijing, China, from a control center in Kagawa, Japan. In 2017, Madder et al.⁴⁷ first conducted telestenting of coronary arteries in 20 patients from approximately 55 feet away over Wi-Fi. Technical success (without conversion to manual operation) was achieved in 86.4% of lesions, and procedural success (<30% residual stenosis) was achieved in 95% of patients. The first-in-human, long-distance, telerobotic coronary stent was recently placed by Patel et al.⁴⁸ in India in 2019. They successfully telestented 5 patients with single, type A coronary artery lesions from a distance of 20 miles. The mean time delay between the remote console and the in-lab robotic system was only 53 ms, well below perceptible limits. Further clinical research steps will be to conduct multicenter evaluations of teleoperation of both simple and complex lesions without in-lab operators as backup. Neurointerventional procedures have yet to be completed from a remote distance, but this will likely be attempted in the coming years.

Preliminary investigations into network performance and its impact on telerobotics are also underway. Several groups have demonstrated that network latencies of ≤ 250 ms are not noticeable to the operator and do not impact performance.⁴⁹⁻⁵¹ However, the impact of other network features such as jitter, redundancy, and bandwidth have yet to be fully explored.⁵¹ In a world rife with data security breaches, end-to-end encryption to ensure patient confidentiality and safety will be necessary. Commodity internet is widely available, and its use would greatly increase telerobotic adaptation, but special-purpose restricted networks may be more reliable. Further technical investigation of network performance is essential to the widespread expansion of telerobotics.

Clinical Applications of Robotic Neurointervention

The early clinical work in robotic endovascular intervention was primarily completed in cardiac and peripheral vascular studies. In 2007, Dabus et al.²⁷ began to conduct neuroendovascular procedures and published a series of 10 cases using magnetic

navigation. Yet, during the next decade, little clinical progress was made in neurovascular robotics. In 2016, Lu et al²³ published 15 cases of robot-assisted cerebral angiography using the vascular interventional robot (VIR-2; Navy General Hospital of People's Liberation Army, Beijing University) without complications. In 2017, Vuong et al⁵² used the Magellan Robotic Catheter System (Hansen Medical) and shared their experience with 9 robot-assisted cerebral angiograms and 18 robot-assisted intracranial interventions. The details of the interventional cases were not published; yet they compared robot-assisted angiography with matched angiographic controls and found no significant differences in procedural time, fluoroscopy times, and contrast volumes. In 2020, Sajja et al⁵³ published their experience using the CorPath GRX Robotic System to complete 7 transradial cerebral angiograms and 3 cases of carotid artery angioplasty and stent placement. 3 of the 7 angiography cases were converted to manual operation after discovery of a bovine arch that necessitated catheter exchange.

A similar research group conducted a retrospective comparison of transradial robot-assisted carotid stent placement with manual stent placement and found that the mean procedural duration was significantly longer while using the robot (85.0 [SD, 14.3] versus 61.2 [SD, 17.5] minutes), but there was no significant difference in other procedural characteristics such as fluoroscopy time, contrast dose, radiation exposure, catheter exchanges, technical success, transfemoral conversion, and complications.⁵⁴ Nogueira et al⁵⁵ also recently treated 4 patients with severe symptomatic carotid stenosis and achieved technical and procedural success. All steps of the procedure were completed by the robotic system except for navigation and deployment of the stent, which is currently incompatible. The first true intracranial robotic neurointervention was recently conducted by Mendes Pereira et al³⁶ in Toronto, Ontario, Canada. They conducted a stent-assisted coiling procedure to treat a 12-mm basilar trunk aneurysm. Other than the placement of the guide-sheath and coaxial catheter that was performed manually, all manipulations of the microcatheter, microguidewire, intracranial stent, and aneurysm coils were performed under robotic control.

Limitations

The field of robotic interventional neuroradiology is still in its infancy. Prototype systems were initially developed to conduct robotic percutaneous coronary intervention; thus, current machines are not perfectly adapted to neurovascular procedures. The CorPath GRX, for example, is not capable of implementing the triaxial approach (guiding catheter, distal access catheter, and microcatheter) necessary for many neurovascular cases; it cannot manipulate over-the-wire equipment, precluding most modern devices; and it cannot robotically deploy some devices without manual assistance. Any catheter with a side port, such as balloon guide, cannot fit into the disposable cassette of the CorPath GRX. In addition, the current working length is 20 cm, but 40 cm would be more appropriate for neurovascular cases. Moreover, the range of motion of the CorPath GRX robotic arm is limited and should be more versatile in future systems.

One of the major goals of robotic endovascular systems is to increase efficiency and decrease procedural time; yet, early

research indicates prolonged procedural time when using the robot.⁵⁴ It is unclear whether this issue is entirely due to inherent deficiencies of current robots or more related to limited operator experience. Clearly, a standardized training curriculum is needed to optimize physician interaction with robotic systems. Future devices should also measure and optimize physician performance and help trainees learn new procedures in an immersive simulated environment.⁵⁶ A third-generation robotic system is currently under development and will undoubtedly address some of these deficiencies. Yet, given the open-architecture nature of current technology, ongoing development of new microwires, catheters, and advanced intravascular imaging tools will necessitate frequent updates of robotic systems to facilitate them. In the future, angiography, robotics, and device companies should work synergistically to create a streamlined workflow to guarantee compatibility and decrease procedural time.

Acute stroke care fundamentally changed following the publication of landmark endovascular thrombectomy trials in 2015. Despite this paradigm shift, limited access to care remains a tremendous impediment to improving patient outcomes. The pinnacle of robotic neurointervention may be completing an acute thrombectomy in a remote geographic location. To achieve this goal, several critical roles need to be defined. A physician must be on-site to obtain manual vascular access, place the sheath, and guide the catheter into the arch; support staff must be present in the room to operate the table; and personnel must be trained to efficiently set up the robotic system to decrease lead time in emergency cases. Published literature has not demonstrated an increase in case complications with robot-assisted interventions; yet, no one has actually shown the ability of the robot to assist in the resolution of endovascular complications. During a fully remote procedure, there may be no on-site physician capable of converting to manual operation to avert a serious adverse event. Other large-scale logistical concerns remain, such as the following: which hospitals would most benefit from the installation of robotic systems for neurointervention, how much training is needed for physicians and staff to safely perform robotic procedures, would medical licensing boards allow interstate teleoperation, and who is held liable if the robot or telecommunications system makes an error?

CONCLUSIONS

Sociopolitical issues often provide a catalyst for the dissemination of new technology. Indeed, social distancing required during the COVID-19 pandemic has ushered in the rise of telemedicine. The field of endovascular robotics can leverage this growth to eliminate legal and geographic barriers to expand stroke networks worldwide. Future autonomous robotic systems may also provide care in combat zones, spacecraft, and other areas where access to health care is greatly restricted.⁵⁷ Other impending upgrades include improved sensors, tactile feedback, machine learning algorithms, and autonomous functions to enhance precision and reduce (or remove) human error. The initial goal of robotic neurointervention is to replicate the safety and success of traditional, manual approaches. However, in the coming years, basic and clinical research will determine whether robotic systems can truly

improve technologic capabilities, offer remote teleoperation, and improve patient outcomes.

Disclosures: Satoshi Tateshima—UNRELATED: Consultancy: Corindus Vascular Robotics, Medtronic, Stryker, Cerenovus, Balt USA; Grants/Grants Pending: MicroVention, Biomedical Solutions Inc; Payment for Lectures Including Service on Speakers Bureaus: Kaneka Medix, Century Medical Inc, Terumo; Stock/Stock Options: Corindus Vascular Robotics.

REFERENCES

- Moniz E. **Arterial encephalography, its importance in the location of cerebral tumors.** <https://thejns.org/view/journals/j-neurosurg/21/2/article-p145.xml>. Accessed August 1, 2020
- Kwoh YS, Hou J, Jonckheere EA, et al. **A robot with improved absolute positioning accuracy for CT guided stereotactic brain surgery.** *IEEE Trans Biomed Eng* 1988;35:153–60 CrossRef Medline
- Davies BL, Hibberd RD, Ng WS, et al. **The development of a surgeon robot for prostatectomies.** *Proc Inst Mech Eng H* 1991;205:35–38 CrossRef Medline
- Sung GT, Gill IS. **Robotic laparoscopic surgery: a comparison of the DA Vinci and Zeus systems.** *Urology* 2001;58:893–98 CrossRef Medline
- Negoro M, Tanimoto M, Arai F, et al. **An intelligent catheter system robotic controlled catheter system.** *Interv Neuroradiol* 2001;7:111–13 CrossRef Medline
- Beyar R, Wenderow T, Lindner D, et al. **Concept, design and pre-clinical studies for remote control percutaneous coronary interventions.** *EuroIntervention* 2005;1:340–45 Medline
- Weisz G, Metzger DC, Caputo RP, et al. **Safety and feasibility of robotic percutaneous coronary intervention: PRECISE (Percutaneous Robotically-Enhanced Coronary Intervention) study.** *J Am Coll Cardiol* 2013;61:1596–1600 CrossRef Medline
- Mahmud E, Naghi J, Ang L, et al. **Demonstration of the safety and feasibility of robotically assisted percutaneous coronary intervention in complex coronary lesions: results of the CORA-PCI Study (Complex Robotically Assisted Percutaneous Coronary Intervention).** *JACC Cardiovasc Interv* 2017;10:1320–27 CrossRef Medline
- Kim KP, Miller DL, Balter S, et al. **Occupational radiation doses to operators performing cardiac catheterization procedures.** *Health Phys* 2008;94:211–27 CrossRef Medline
- Roguin A, Goldstein J, Bar O. **Brain tumours among interventional cardiologists: a cause for alarm: report of four new cases from two cities and a review of the literature.** *EuroIntervention* 2012;7:1081–86 [Database] CrossRef Medline
- Roguin A, Goldstein J, Bar O, et al. **Brain and neck tumors among physicians performing interventional procedures.** *Am J Cardiol* 2013;111:1368–72 CrossRef Medline
- Rajaraman P, Doody MM, Yu CL, et al. **Cancer Risks in U.S.: radiologic technologists working with fluoroscopically guided interventional procedures, 1994–2008.** *AJR Am J Roentgenol* 2016;206:1101–08; quiz 1109 CrossRef Medline
- El-Sayed T, Patel AS, Cho JS, et al. **Radiation-induced DNA damage in operators performing endovascular aortic repair.** *Circulation* 2017;136:2406–16 CrossRef Medline
- Plourde G, Pancholy SB, Nolan J, et al. **Radiation exposure in relation to the arterial access site used for diagnostic coronary angiography and percutaneous coronary intervention: a systematic review and meta-analysis.** *Lancet* 2015;386:2192–2203 CrossRef Medline
- Smilowitz NR, Balter S, Weisz G. **Occupational hazards of interventional cardiology.** *Cardiovasc Revasc Med* 2013;14:223–28 CrossRef Medline
- Andreassi MG, Piccaluga E, Gargani L, et al. **Subclinical carotid atherosclerosis and early vascular aging from long-term low-dose ionizing radiation exposure: a genetic, telomere, and vascular ultrasound study in cardiac catheterization laboratory staff.** *JACC Cardiovasc Interv* 2015;8:616–67 CrossRef Medline
- Goldstein JA, Balter S, Cowley M, et al; Interventional Committee of the Society of Cardiovascular Interventions. **Occupational hazards of interventional cardiologists: prevalence of orthopedic health problems in contemporary practice.** *Catheter Cardiovasc Interv* 2004;63:407–11 CrossRef Medline
- Parra-Farinas C. **How to fight the fear under the x-ray beam: interventional neuroradiology fellow mom to be.** *Stroke* 2020;51:e121–23 CrossRef Medline
- Vu CT, Elder DH. **Pregnancy and the working interventional radiologist.** *Semin Intervent Radiology* 2013;30:403–07 CrossRef Medline
- Patel TM, Shah SC, Soni YY, et al. **Comparison of robotic percutaneous coronary intervention with traditional percutaneous coronary intervention: a propensity score-matched analysis of a large cohort.** *Circ Cardiovasc Interv* 2020;13:e008888 CrossRef Medline
- Tabaza L, Virk HU, Janzer S, et al. **Robotic-assisted percutaneous coronary intervention in a COVID-19 patient.** *Catheter Cardiovasc Interv* 2020 May 20. [Epub ahead of print] CrossRef Medline
- Britz GW, Tomas J, Lumsden A. **Feasibility of robotic-assisted neurovascular interventions: initial experience in flow model and porcine model.** *Neurosurgery* 2020;86:309–14 CrossRef Medline
- Lu WS, Xu WY, Pan F, et al. **Clinical application of a vascular interventional robot in cerebral angiography.** *Int J Med Robot* 2016;12:132–36 CrossRef Medline
- Guo J, Guo S, Xiao N, et al. **A novel robotic catheter system with force and visual feedback for vascular interventional surgery.** *International Journal of Mechatronics and Automation* 2012;2:15–24 CrossRef
- Wang K, Chen B, Lu Q, et al. **Design and performance evaluation of real-time endovascular interventional surgical robotic system with high accuracy.** *Int J Med Robot* 2018;14:e1915 CrossRef Medline
- Arai F, Fujimura R, Fukuda T, et al. **New catheter driving method using linear stepping mechanism for intravascular neurosurgery.** In: *Proceedings 2002 IEEE International Conference on Robotics and Automation* (Cat No 02CH37292), Washington, DC. May 11–15, 2002:2944–49
- Dabus G, Gerstle RJ, Cross DT, et al. **Neuroendovascular magnetic navigation: clinical experience in ten patients.** *Neuroradiology* 2007;49:351–55 CrossRef Medline
- Jin QI, Pehrson S, Jacobsen PK, et al. **Efficacy and safety of atrial fibrillation ablation using remote magnetic navigation: experience from 1,006 procedures.** *J Cardiovasc Electrophysiol* 2016;27:S23–28 CrossRef Medline
- Krings T, Finney J, Niggemann P, et al. **Magnetic versus manual guidewire manipulation in neuroradiology: in vitro results.** *Neuroradiology* 2006;48:394–401 CrossRef Medline
- Harrison J, Ang L, Naghi J, et al. **Robotically-assisted percutaneous coronary intervention: reasons for partial manual assistance or manual conversion.** *Cardiovasc Revasc Med* 2018;19:526–31 CrossRef Medline
- CorPath® GRX Neuro Study. <https://ClinicalTrials.gov/show/NCT04236856>. Accessed August 15, 2020
- Ryan Madder, William Lombardi, Manish Parikh, et al. **TCT-539 impact of a novel advanced robotic wiring algorithm on time to wire a coronary artery bifurcation in a porcine model.** *J Am Coll Cardiol* 2017;70:B223 CrossRef
- Al Nooryani A, Aboushokka W. **Rotate-on-retract procedural automation for robotic-assisted percutaneous coronary intervention: first clinical experience.** *Case Rep Cardiol* 2018;2018:6086034 CrossRef Medline
- Meyers PM, Schumacher HC, Tanji K, et al. **Use of stents to treat intracranial cerebrovascular disease.** *Annu Rev Med* 2007;58:107–22 CrossRef Medline
- Britz GW, Panesar SS, Falb P, et al. **Neuroendovascular-specific engineering modifications to the CorPath GRX Robotic System.** *J Neurosurg* 2019 Nov 29. [Epub ahead of print] CrossRef Medline

36. Mendes Pereira V, Cancelliere NM, Nicholson P, et al. **First-in-human, robotic-assisted neuroendovascular intervention.** *J Neurointerv Surg* 2020;12:338–40 CrossRef Medline
37. Guo J, Jin X, Guo S. **Study of the operational safety of a vascular interventional surgical robotic system.** *Micromachines (Basel)* 2018;9:119 CrossRef Medline
38. Saver JL, Goyal M, van der Lugt A, et al; HERMES Collaborators. **Time to treatment with endovascular thrombectomy and outcomes from ischemic stroke: a meta-analysis.** *JAMA* 2016;316:1279–88 CrossRef Medline
39. Sarraj A, Savitz S, Pujara D, et al. **Endovascular thrombectomy for acute ischemic strokes: current US access paradigms and optimization methodology.** *Stroke* 2020;51:1207–17 CrossRef Medline
40. He AH, Churilov L, Mitchell PJ, et al. **Every 15-min delay in recanalization by intra-arterial therapy in acute ischemic stroke increases risk of poor outcome.** *Int J Stroke* 2015;10:1062–67 CrossRef Medline
41. Snyder T, Agarwal S, Huang J, et al. **Stroke treatment delay limits outcome after mechanical thrombectomy: stratification by arrival time and ASPECTS.** *J Neuroimaging* 2020;30:625–30 CrossRef Medline
42. Muller-Barna P, Hubert GJ, Boy S, et al. **TeleStroke units serving as a model of care in rural areas: 10-year experience of the TeleMedical Project for Integrative Stroke Care.** *Stroke* 2014;45:2739–44 CrossRef Medline
43. Audebert HJ, Schultes K, Tietz V, et al; Telemedical Project for Integrative Stroke Care (TEMPiS). **Long-term effects of specialized stroke care with telemedicine support in community hospitals on behalf of the Telemedical Project for Integrative Stroke Care (TEMPiS).** *Stroke* 2009;40:902–08 CrossRef Medline
44. El Nawar R, Lapergue B, Piotin M, et al; ETIS Investigators. **Higher annual operator volume is associated with better reperfusion rates in stroke patients treated by mechanical thrombectomy: the ETIS Registry.** *JACC Cardiovasc Interv* 2019;12:385–91 CrossRef Medline
45. Bechstein M, Elsheikh S, Wodarg F, et al. **Interhospital teleproctoring of endovascular intracranial aneurysm treatment using a dedicated live-streaming technology: first experiences during the COVID-19 pandemic.** *BMJ Case Rep* 2020;13:e016722 CrossRef Medline
46. Lu WS, Wang DM, Liu D, et al. **Regarding “Application of robotic telemanipulation system in vascular interventional surgery”.** *J Vasc Surg* 2013;57:1452–53 CrossRef Medline
47. Madder RD, VanOosterhout SM, Jacoby ME, et al. **Percutaneous coronary intervention using a combination of robotics and telecommunications by an operator in a separate physical location from the patient: an early exploration into the feasibility of telestenting (the REMOTE-PCI study).** *EuroIntervention* 2017;12:1569–76 CrossRef Medline
48. Patel TM, Shah SC, Pancholy SB. **Long distance tele-robotic-assisted percutaneous coronary intervention: a report of first-in-human experience.** *EClinicalMedicine* 2019;14:53–58 CrossRef Medline
49. Rayman R, Croome K, Galbraith N, et al. **Long-distance robotic tele-surgery: a feasibility study for care in remote environments.** *Int J Med Robot* 2006;2:216–24 CrossRef Medline
50. Xu S, Perez M, Yang K, et al. **Determination of the latency effects on surgical performance and the acceptable latency levels in telesurgery using the dV-Trainer® simulator.** *Surg Endosc* 2014;28:2569–76 CrossRef Medline
51. Madder RD, VanOosterhout S, Mulder A, et al. **Network latency and long-distance robotic telestenting: exploring the potential impact of network delays on telestenting performance.** *Catheter Cardiovasc Interv* 2020;95:914–19 CrossRef Medline
52. Vuong SM, Carroll CP, Tackla RD, et al. **Application of emerging technologies to improve access to ischemic stroke care.** *Neurosurg Focus* 2017;42:E8 CrossRef Medline
53. Sajja KC, Sweid A, Al Saiegh F, et al. **Endovascular robotic: feasibility and proof of principle for diagnostic cerebral angiography and carotid artery stenting.** *J Neurointerv Surg* 2020;12:345–49 CrossRef Medline
54. Weinberg JH, Sweid A, Sajja K, et al. **Comparison of robotic-assisted carotid stenting and manual carotid stenting through the transradial approach.** *J Neurosurg* 2020 Aug 28. [Epub ahead of print] CrossRef Medline
55. Nogueira RG, Sachdeva R, Al-Bayati AR, et al. **Robotic assisted carotid artery stenting for the treatment of symptomatic carotid disease: technical feasibility and preliminary results.** *J Neurointerv Surg* 2020;12:341–44 CrossRef Medline
56. Kreiser K, Strober L, Gehling KG, et al. **Simulation training in neuroangiography-validation and effectiveness.** *Clin Neuroradiol* 2020 Apr 17. [Epub ahead of print] CrossRef Medline
57. Panesar SS, Ashkan K. **Surgery in space.** *Br J Surg* 2018;105:1234–43 CrossRef Medline

Am I Ready to Be an Independent Neuroradiologist? Objective Trends in Neuroradiology Fellows' Performance during the Fellowship Year

J.H. Masur, J.E. Schmitt, D. Lalevic, T.S. Cook, L.J. Bagley, S. Mohan, and A.P. Nayate



ABSTRACT

BACKGROUND AND PURPOSE: Aside from basic Accreditation Council for Graduate Medical Education guidelines, few metrics are in place to monitor fellows' progress. The purpose of this study was to determine objective trends in neuroradiology fellowship training on-call performance during an academic year.

MATERIALS AND METHODS: We retrospectively reviewed the number of cross-sectional neuroimaging studies dictated with complete reports by neuroradiology fellows during independent call. Monthly trends in total call cases, report turnaround times, relationships between volume and report turnaround times, and words added to preliminary reports by attending neuroradiologists were evaluated with regression models. Monthly variation in frequencies of call-discrepancy macros were assessed via χ^2 tests. Changes in frequencies of specific macro use between fellowship semesters were assessed via serial 2-sample tests of proportions.

RESULTS: From 2012 to 2017, for 29 fellows, monthly median report turnaround times significantly decreased during the academic year: July (first month) = 79 minutes (95% CI, 71–86 minutes) and June (12th month) = 55 minutes (95% CI, 52–60 minutes; P value = .023). Monthly report turnaround times were inversely correlated with total volumes for CT ($r = -0.70$, $F = 9.639$, P value = .011) but not MR imaging. Words added to preliminary reports, a surrogate measurement of report clarity, slightly improved and discrepancy rates decreased during the last 6 months of fellowship. A nadir for report turnaround times, discrepancy errors, and words added to reports was seen in December and January.

CONCLUSIONS: Progress through fellowship correlates with a decline in report turnaround times and discrepancy rates for cross-sectional neuroimaging call studies and slight improvement in indirect quantitative measurement of report clarity. These metrics can be tracked throughout the academic year, and the midyear would be a logical time point for programs to assess objective progress of fellows and address any deficiencies.

ABBREVIATIONS: CSNI = cross-sectional neuroimaging studies; RIS = radiology information system; RTAT = report turnaround time

A fellow's progress in an academic year is primarily assessed using qualitative, thus subjective, criteria, including achievement of Accreditation Council for Graduate Medical Education-prescribed milestones and faculty evaluations. While the Accreditation Council for Graduate Medical Education provides requirements for total yearly cases read¹ and individual

programs may have internal metrics for fellows' progress, there are no concrete external objective measurements for documenting fellows' progress within the academic year. Often, fellows are unsure whether their efficiency in generating reports, report turnaround times (RTATs) for on-call examinations, or quality of on-call reports is satisfactory.

The total number of studies dictated by the fellow and the RTATs of on-call studies may be reviewed by the attendings and program director with the fellows, but more meaningful interpretation of these numbers is lacking because there are no comparison benchmarks or quantitative checkpoints within the fellowship year. Knowledge of these factors is critical in a fellowship program so that program directors and fellows are jointly aware of progress throughout the year and remediation or additional focused training can be implemented, as necessary. More data on neuroradiology fellowship training are especially needed because a survey in 2016

Received May 31, 2020; accepted after revision November 19.

From the Department of Radiology (J.H.M., J.E.S., D.L., T.S.C., L.J.B., S.M.), Hospital of the University of Pennsylvania, Philadelphia, Pennsylvania; and Department of Radiology (A.P.N.), University Hospitals Cleveland Medical Center, Cleveland, Ohio.

J.H. Masur and J.E. Schmitt are co-first authors.

Paper previously presented, in part, at: Annual Meeting of the American Society of Neuroradiology, May 18–23, 2019; Boston, Massachusetts.

Please address correspondence to Ameya P. Nayate, MD, Department of Radiology, University Hospitals Cleveland Medical Center, 11100 Euclid Ave, BSH 5056, Cleveland, OH 44106; e-mail: Ameya.Nayate@UHhospitals.org

<http://dx.doi.org/10.3174/ajnr.A7030>

demonstrated that 25% of practicing neuroradiologists in the United States believe that fellows' abilities have declined.² Prior studies have analyzed various other factors related to radiology residency training, including total cases read, turnaround time, and on-call accuracy,^{3,4} but to our knowledge, no studies have analyzed the quantitative trends in fellowship training during an academic year.

We hypothesized that within an academic year, the RTAT for on-call studies dictated by fellows will decrease (ie, improve). Meanwhile, the discrepancy rates will decrease, and clarity of reports will improve. We also hypothesized that participating in independent call will have residual short-term effects on increasing clinical productivity during a subsequent regular work week.

MATERIALS AND METHODS

This study was approved by Hospital of University of Pennsylvania institutional review board.

Fellowship Structure

Each fellowship class consists of approximately 6 first-year fellows. During the 12-month academic year, approximately 7.5 months consisted of fellows interpreting and dictating cross-sectional neuroimaging (CSNI) studies on adult patients from the 3 major hospitals (affiliated with our tertiary care academic institution) during regular workdays, under the supervision of ~18 neuroradiology attendings, with interspersed evening and weekend call. For the remaining 4.5 months, fellows rotated through neurointerventional radiology, pediatric neuroradiology at an affiliated children's hospital, or were off service.

Typical Call Duties

The fellows participated in 3 types of call at our program: weekday neuroradiology evening and overnight call, weekend neuroradiology call, and 1 week of general call.

Primary weekday neuroradiology call duties (Monday–Friday) for fellows at our institution included the interpretation and dictation of emergent and inpatient CT and MR imaging CSNI studies from the 3 major hospitals from 5–11:00 PM. After 11:00 PM, diagnostic radiology residents and overnight radiology fellows dictated all CT studies, while emergent and inpatient MR imaging and CTA studies were dictated by the neuroradiology fellow until 7:00 AM. Most fellows stayed in the hospital until 7:00 AM, though the option was available for fellows to return home and use a “take-home laptop” after 11:00 PM for home pager call (once all work lists for which the fellow was responsible were empty). The take-home laptop contained the same PACS and dictation software as the regular workstations at the hospital and reports were generated in the same manner. Although not explicitly measured, we estimate that >90% of the on-call studies were dictated in-house. Most preliminary reports contained a full dictation, including a clinical history, technique, findings, and impression. One hundred percent of 200 cases randomly audited had full reports. We do not use structured or standardized reporting.

Primary weekend neuroradiology call duties (Saturday and Sunday) for fellows included working with a neuroradiology attending from approximately 7:00 AM to 5:00 PM, during which time the workflow resembled a regular workday (ie, the attending would review studies with the fellow and then finalize the reports with an

attestation). From 5:00 PM to 7:00 AM, the fellow would be on independent call and dictate emergent neuroradiology MR imaging and CTA studies in the same manner as in the weekday call.

Coverage of neuroradiology weekday and weekend call was equally split among the fellows throughout the academic year. Each fellow was typically on weekday and/or weekend call once every 1–2 months. An on-call attending neuroradiologist was available as needed but was rarely consulted. Our institution does not use an in-house overnight neuroradiologist.

During the 1 week of overnight general call, the fellow would primarily interpret both neuroradiology and non-neuroradiology CT studies and occasionally plain films and other cross-sectional imaging.

Review of Preliminary Call Reports by Neuroradiology Attendings

Preliminary neuroradiology call reports were reviewed by neuroradiology attendings the following morning and evaluated using a standardized template to assign a degree of discrepancy based on our internally designed system for attending review of preliminary reports:⁵

1. Agree: The attending fully agrees with the report and no words are added.
2. Addition: The attending agrees with the report and adds minor information such as description of a mucosal retention cyst in a paranasal sinus.
3. Minor change: The attending mostly agrees with the report but adds information to clarify the report or correct a mistake, which will not have immediate clinical impact, for example, describing a lesion in the wrong lobe in the cerebral hemisphere or an old orbital blowout fracture.
4. Major change: The fellow missed or misinterpreted a finding that could have immediate clinical impact such as a missed arterial occlusion or acute intracranial hemorrhage.
5. Great call: The fellow detected a subtle finding that could have immediate clinical impact such as detection of a subtle acute infarct on a CT head.

Multiple examinations linked by a single report (eg, CT head and CT cervical spine studies performed concurrently generate 2 separate accession numbers but are dictated as 1 combined report) were assigned the template that captured the highest desired degree of discrepancy (ie, if there was a major miss on the CT head study but not on the CT cervical spine study, the 1 report would be categorized as a “Major change”). All attendings were educated about this scoring system and the templates before finalizing these studies. On average, attendings were in practice 10+ years after completion of their fellowship.

Of note, the attending was not able to edit any portion of the preliminary report dictated by the neuroradiology fellow, including the clinical history, technique, findings, and impression. Additional information and corrections were added by the attending below the preliminary fellow-dictated report.

Call and Noncall Studies

Using our electronic medical record and radiology information system (RIS), we queried all neuroradiology call and noncall

reports generated by neuroradiology fellows on adult patients between July 1, 2012, and June 30, 2017 (60 consecutive months, 29 fellows).

Inclusion criteria for call studies consisted of CSNI reports in which attendings used 1 of the 5 “discrepancy” templates to finalize the study. By contrast, attendings are required to use an “attestation” template during the workday (ie, for noncall studies) to explicitly confirm their participation in the case; such cases were included in the noncall studies pool. Pediatric neuroradiology studies were interpreted at another hospital with a different neuroradiology staff, electronic medical record, and RIS and were excluded. Examinations with RTATs of >1400 minutes (>24 hours) and <0 minutes were excluded because these data entries are nearly uniformly due to errors in “crossover” between various systems (eg, between the dictation software and the RIS).

Determination of RTAT on Call Studies

Our RIS records several workflow-related timestamps for each imaging study in the system. RTAT was defined as the time between verification of images arriving in the PACS to the time of issuance of a full preliminary report by the fellow. RTAT was analyzed separately for CT and MR imaging studies. Of note, the fellow was not responsible for interventional procedures during call shifts. We did not include other factors such as answering phone calls when determining RTAT.

Effects of Taking a Week of Independent Call on Subsequent Clinical Productivity

To measure the effect on the number of studies dictated by a fellow during a regular work week after taking a week of independent call, we analyzed the number of CSNI studies dictated per day by fellows during a regular work week before and after taking a week of independent evening call.

Statistical Analysis

Raw data from the RIS were imported into the R statistical environment for (<https://www.r-project.org/>) data wrangling and analysis.⁶ Each record represented a single imaging study. Available fields in the dataset included provider names (both the fellows and attendings), study (Current Procedural Terminology) codes, multiple procedural timestamps, and the entire radiologic report. Non-neuroradiologic studies were filtered on the basis of the Current Procedural Terminology codes. Minor errors in data entry (eg, misspelling of provider names) were corrected. RTATs were defined as the difference (in minutes) between study completion and the generation of a preliminary report. Using natural language processing, we identified studies performed on call using the text of the discrepancy and attestation templates. These templates also enabled tabulation of the severity of discrepancies between the attending and fellow for call cases (eg, major-versus-minor changes). Finally, we used the position of this attending-inserted template to define the boundary between fellow-generated (above) and attending-generated (below) report text. This feature allowed word and character counts for attending-inserted text for each call case.

Several additional, simple, derived variables were generated on the basis of the raw data, including imaging technique (CT versus

MR imaging), day the fellowship study was performed, and the month that a study was completed. Basic statistics were calculated, including total CSNI frequencies, RTATs, and frequencies of report discrepancies. Monthly trends in total call cases, RTATs, and relationships between volume and RTATs were evaluated via regression. We also investigated RTATs for specific imaging studies via general linear regression models that simultaneously accounted for the effects of the day of fellowship, imaging technique (CT versus MR), and interactions. To fully account for the longitudinal nature of the data, we also analyzed RTATs using linear mixed-models treating fellow identification and the day of fellowship as random effects, looking at both linear and nonlinear trends in RTAT with time, ie, allowing each fellow to have a unique nonlinear trajectory in RTAT during the fellow year. Results with both approaches were similar, resulting in identical statistical inferences. Thus, parameter estimates from the more traditional linear regression models are reported here. Multivariable linear regression analysis was used to compare RTAT, word count, and discrepancy rate with the day of fellowship, technique (CT versus MR imaging), daily case load, and RTAT while controlling for individual fellow performance. Similar models were used to compare RTATs between the 11 fellows who completed the diagnostic radiology residency program at our institution versus at other institutions; data from both the first and last 60 days of fellowship were analyzed.

Variables with nonlinear monthly trends were also evaluated with the ANOVA and post hoc Tukey-Kramer tests. Monthly variation in frequencies of call-discrepancy templates were assessed via χ^2 tests. Changes in frequencies of specific template use between fellowship semesters were assessed via serial 2-sample tests of proportions.

Finally, we attempted to determine whether the presence of a week of call influences case volumes during subsequent day shifts. We constructed a crude measure comparing the total number of cases for the week before and after each week-long call shift. Given their non-normal distribution, differences in the number of cases read before and after call were assessed via the Wilcoxon test. For testing our hypotheses, statistical significance was defined as $P < .05$.

RESULTS

During 5 academic years, data from 12,072 CSNI call studies dictated by fellows were analyzed. One hundred forty-six studies (1.2%) were excluded due to 0 minutes < RTAT > 1400 minutes. Twenty-nine fellows dictated 11,926 CSNI call studies with a mean annual call volume of 411.2 [SD, 306] per fellow. Fellows participated in 53 median annual call shifts that covered adult CSNI: mean total call studies = 18.29 [SD, 8.12]; mean MR imaging call studies = 7.03 [SD, 4.14]; and mean CT call studies = 10.28 [SD, 6.39].

Call Cases per Month

Trends in call volumes per month are summarized in Fig 1. The number of call cases dictated per month increased significantly throughout the academic year ($F_{10}^1 = 37.61$, P value = .001, reaching a maximum of 1448 total cases in June (48.3 cases/day; MR imaging = 504 [16.8 cases/day] and CT = 944 [31.5 cases/day]). When they were measured separately, there were

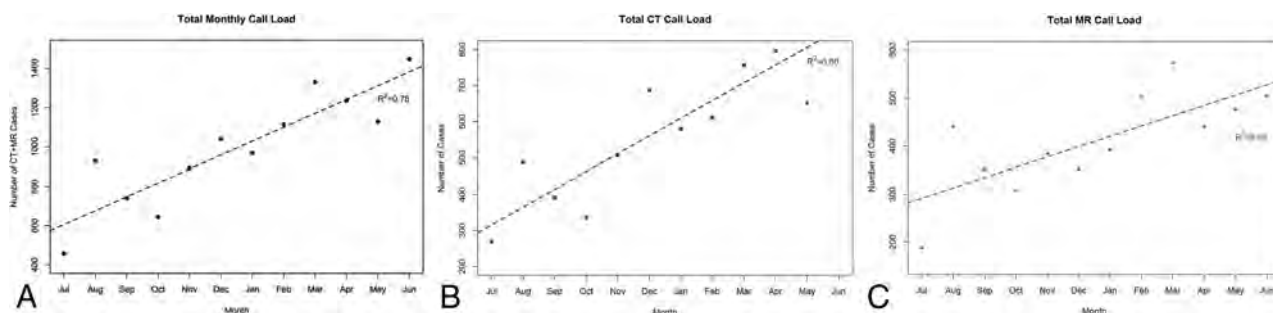


FIG 1. A, Mean total (CT + MR imaging) call cases per month aggregated over 5 fellowship classes with R^2 values. B, Mean total (CT) call cases per month aggregated over 5 fellowship classes with R^2 values. C, Mean total (MR imaging) call cases per month aggregated over 5 fellowship classes with R^2 values.

statistically significant increases in both monthly MR imaging ($F_{10}^1 = 12.71$, P value = .005) and CT volumes ($F_{10}^1 = 38.81$, $P < .0001$). The rate of CT studies dictated during the year increased significantly faster than that of MR imaging ($F = 7.734$, P value = .011). Fellows interpreted a mean of 72 call MR imaging studies during their first 6 months [SD, 60] and 100 MR imaging studies [SD, 70] during the last 6 months of fellowship, and a mean of 96 call CT studies during the first 6 months [SD, 102] and 150 studies [SD, 121] during their final 6 months.

Report Turnaround Times

Most preliminary reports were generated by fellows within 3 hours of study completion (RTAT mean = 136 minutes; 95% CI, 132–139 minutes; median = 72 minutes; 95% CI, 70–74 minutes), though the mean was skewed upward by (relatively infrequent) studies with very long RTATs. In general, MR imaging studies required significantly more time to complete than CT ($\chi^2 = 901.0$, $df = 1$, P value = .0001); during the study interval, the mean time to generate a preliminary MR imaging report was 183 minutes (95% CI, 177.1–188.8 minutes; median, 111 minutes; 95% CI, 107–116 minutes), while for CT, the mean RTAT was 104 minutes (95% CI, 100.9–107.1 minutes; median, 55 minutes; 95% CI, 54–57 minutes). Days since beginning fellowship were significantly associated with faster mean RTAT ($F_{11924}^1 = 136.2$, P value < .0001; $\beta = -0.19$, P value < .0001), with each day of fellowship estimated to improve RTATs by 0.18 minutes in our regression models. Hierarchic linear mixed-models (Fig 2D) found significant variability of RTAT trajectories among fellows during the academic year, with some fellows demonstrating minimal improvement or even increases with time. However, most fellows improved with increased training, as did the group mean. There was a statistically significant interaction between imaging technique and day of fellowship ($\beta = -0.07$, $t = -2.39$, $P = .01$), with RTATs for MR imaging decreasing faster than for CT (-0.15 min/day for CT and -0.22 min/day for MR imaging). RTAT was 67.7 minutes slower for MR imaging compared with CT (P value $\leq .0001$).

When data were aggregated by month, there were small-but-statistically significant decreases in both mean ($F_{10}^1 = 7.25$, P value = .023) and median ($F_{10}^1 = 12.16$, P value = .006) monthly RTATs during the fellowship year (Fig 2A). The pattern was not entirely monotonic, however, with the RTAT nadir seen in mid-fellowship around December (median RTAT = 58 minutes). When month

was treated as a categorical rather than continuous variable, ANOVA suggested significant monthly variation ($F_{11816}^{11} = 34.04$, P value < .0001). Post hoc tests found that RTATs were significantly faster in December relative to all other months, with the exception of May and June. From July (first month of fellowship) to June (12th and last month of fellowship), the mean report turnaround time for all CSNI studies decreased from 144.4 to 99.4 minutes (-45 minutes, -31%) and median report turnaround time decreased from 79 to 55 minutes (-24 minutes, -30%).

We hypothesized that average RTAT would be associated with call volumes, with busier months associated with slower rates of reporting. However, we observed that call volumes were inversely related to RTATs (Fig 2C). Specifically, RTATs for CT studies significantly decreased with increasing case volumes ($r = -0.70$, $F_{10}^1 = 9.639$, P value = .011), while the RTATs for MR imaging cases decreased slightly but were not statistically significant ($r = -0.13$, $F_{10}^1 = 0.1782$, P value = .682). Linear regression demonstrated that RTATs decreased by 0.44 minutes for each extra case dictated that day (P value = .004).

Finally, we compared the RTAT for fellows who completed a diagnostic radiology residency at our institution ($n = 11$) with fellows who completed it at another institution ($n = 18$). Linear regression analysis demonstrated that fellows who completed a radiology residency at our institution had significantly lower RTATs during the first 60 days of fellowship (P value $\leq .0001$); however, the effect persisted during the year, with a similar group difference in the last 60 days of fellowship (P value < .0001).

Discrepancies in CSNI Interpretation between Fellows and Attending

The monthly proportion of “Great call,” “Agree,” “Addition,” “Minor change,” and “Major change” template use varied significantly during the academic year ($\chi^2 = 517.07$, $df = 44$, P value < .0001). In general, the frequencies of less discrepant codes increased during the year, with corresponding decreases in templates associated with more substantial discrepancies. The lowest percentages of Major and Minor changes were seen during the seventh month of fellowship (January, 0% and 4.5%, respectively). When data were aggregated by semester, significant changes were seen between the first 6 months of training compared with the last 6 months for most categories (Tables 1 and 2). Multivariable linear regression demonstrated that the call discrepancies slightly decreased with each day of fellowship ($P \leq$

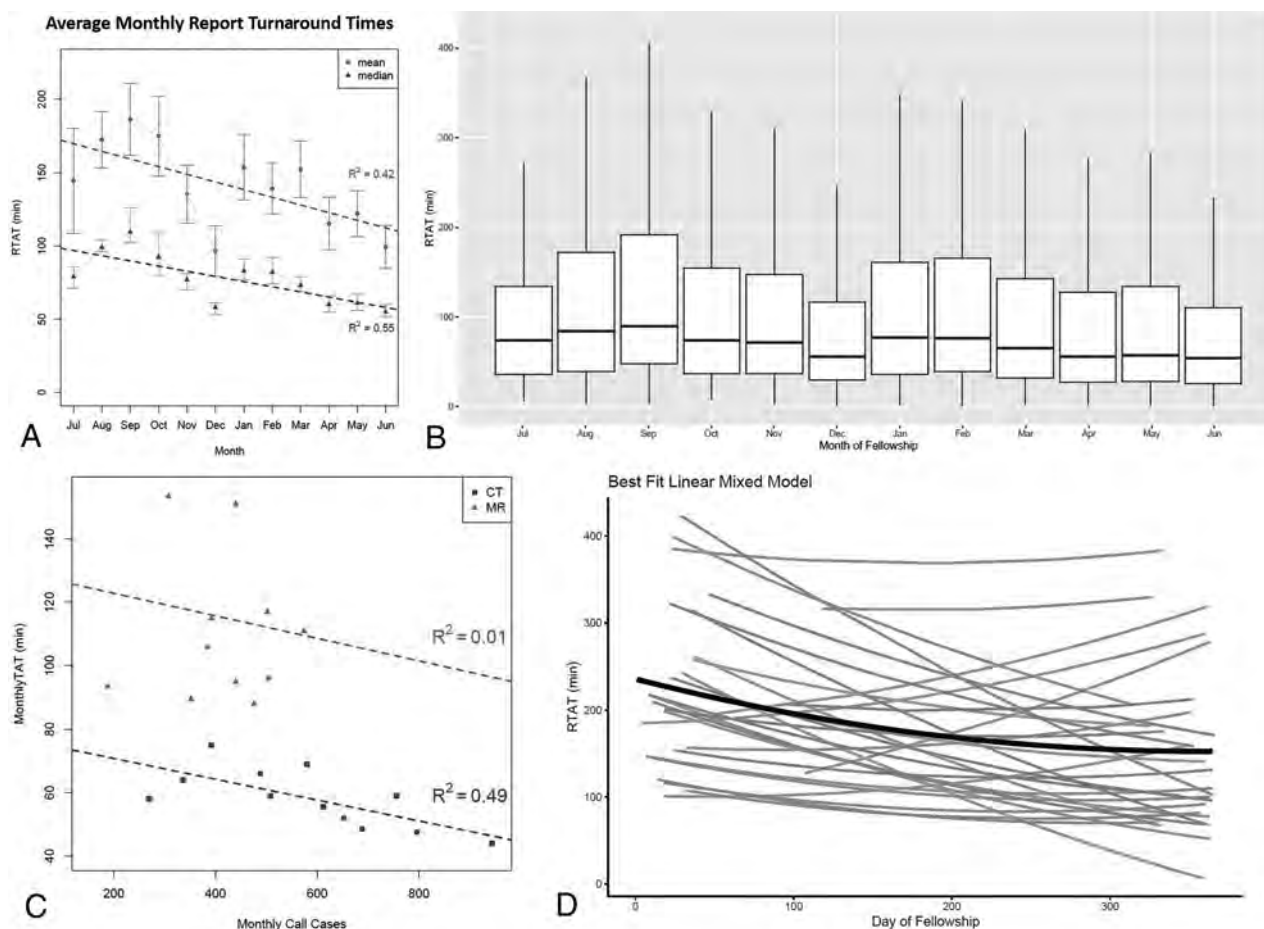


FIG 2. A, Average monthly turnaround times for CT and MR studies during fellows' call. Mean (circle) and median (triangle) values are both shown. Dashed lines represent best-fit regression lines during the academic year, while month-to-month changes are shown by the dotted lines. R^2 values are provided. B, Box-and-whisker plot demonstrates the RTAT for each month. C, Relationships between monthly call volume and monthly median RTATs for CT (square) and MRI (triangle) separately. R^2 values are provided. D, Lines depict individual trajectories in RTAT during the fellowship year for each fellow based on a linear mixed-model. The bold line shows the curve for the aggregated data.

Table 1: Median RTATs by quarters of the academic year

Quarter	RTAT (Min)
1st (July-September)	97 (95% CI, 91–102)
2nd (October-December)	68 (95% CI, 65–73)
3rd (January-March)	79 (95% CI, 75–83)
4th (April-June)	59 (95% CI, 56–62)

Table 2: Median RTAT and CI for December and January

Month	RTAT (Min)
December	58 (95% CI, 53–61)
January	83 (95% CI, 77–91)

.001). With an increasing daily case load, the number of discrepancies slightly increased ($P \leq .0001$). Technique (eg, CT versus MR imaging) and RTAT had no statistically significant effect on call discrepancies. We did an ordered logistic regression for graduation years 2015–2017 and looked at the day of fellowship, imaging technique (CT versus MR imaging), and daily case load as predictors of the severity of call discrepancy. There was a significant effect of graduation year (logistic regression, 39; P value

$< .0001$). We looked at the discrepancy data for each year and saw a generalized decline in the proportion of Minor changes, an increase in Agree + Addition, and no significant change in the proportion of Major changes or Great calls. We looked at 131 major misses, 100% of the total major misses, 53% CT and 47% MR imaging. Most (75%) were perception errors, while 25% were misinterpretation errors and overcalls. Of the misses, there were 14% missed thrombus/occlusion, 9% missed infarcts, 9% missed intracranial hemorrhages, 6% missed fractures, and 6% missed aneurysms. The remaining 56% of cases had a variety of perceptually missed or misinterpreted findings.

Quantitation of Attending Additions to Final Reports

On average, neuroradiology attendings added 141 words (95% CI, 137–145) and 1015 (95% CI, 987–1044) characters to reports coded "Addition," 184 (95% CI, 173–195) words and 1305 (95% CI, 1227–1383) characters to those with Minor changes and 188 (95% CI, 165–211) words and 1304 (95% CI, 1142–1469) characters to those with Major changes. There were significant changes in monthly rates of both words ($F_{12060}^{11} = 8.05$, P value $< .001$) and characters ($F_{12060}^{11} = 9.44$, P value $< .001$) added to preliminary reports, with the lowest number of additions seen during the sixth

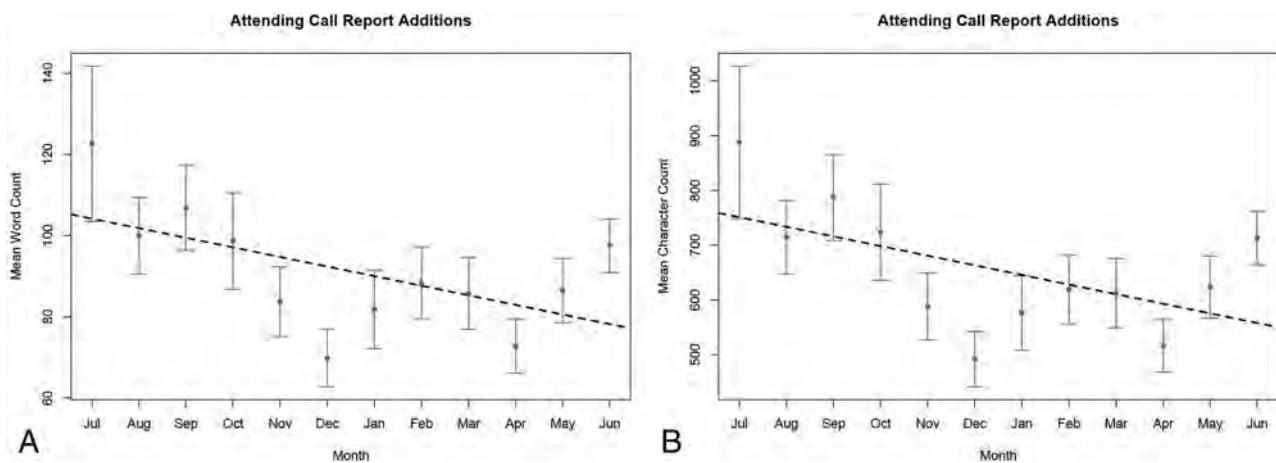


FIG 3. A, Mean word count added to call reports per month of fellowship of training. Confidence intervals are shown with bars. B, The mean character count added to call reports per month of fellowship training. Confidence intervals are shown with bars.

month (December; Fig 3). When data were aggregated into semesters, the second 6 months of the fellowship year had significantly fewer mean additions of both words, 93.5 (95% CI, 89–98) versus 86.2 (95% CI, 83–89; $F_{1,12070}^1 = 7.28$, P value = .007) and characters, 672 (95% CI, 641–702) versus 616 (95% CI, 593–640; $F_{1,12060}^1 = 9.44$, P value < .001) compared with the first 6 months of fellowship. Linear regression demonstrated that for each day of fellowship, the number of words added to preliminary reports decreased by 0.154 (P value \leq .0001). The number of words added to MR imaging reports was greater by 39.4 compared with CT reports (P value \leq .0001). Daily case load and RTAT did not significantly affect the number of words added.

Effect of Taking Week-Long Call on the Number of Studies Dictated during the Subsequent Week

There was a slight but not statistically significant decrease in number of studies dictated per day (8 studies/day) a week (7 days) after taking a week of call (5 days) compared with the prior week (9 studies/day for 7 days) (Wilcoxon test $W = 1295598$, P value = .06).

DISCUSSION

The results of this study demonstrate that progress through a 1-year neuroradiology fellowship at a large academic institution with participation in independent call correlates with the following: 1) a decrease in RTAT for independent call studies, 2) a decrease in discrepant findings and an increase in agreement with the attendings' final interpretation of independent call studies, and 3) a decrease in words added to correct or clarify descriptions of pertinent findings in independent call reports despite an increase in call volume throughout the academic year. While we are aware that neuroradiology fellowship programs are variable in their education and call structures, we believe that all programs have some type of call component as well as attendings with varying reporting styles and levels of interest in fellows' education; thus, our findings are generalizable to objectively monitoring fellowship progress.

Reducing RTAT for radiology studies has become an essential goal for both academic and nonacademic radiology practices in

the past 2 decades.⁷ Studies have analyzed RTATs for radiology residents;^{3,8} however, our findings are unique because they investigate RTAT during 1 academic year in a postresidency fellowship. Most fellows are employed radiologists in radiology practices on graduation, and their duties often center on interpretation of CSNI studies,⁹ with reimbursement and advancement potentially tied to RTATs.⁷ Hence, it is important that knowledge of trends in RTAT for call studies be available to fellows and hiring radiology practices. Our findings demonstrate a gradual decline in RTATs for both MR imaging (−0.22 min/day) and CT (−0.15 min/day) reports during the academic year, with a nadir in December (midpoint of the academic year, median RTAT of 58 minutes), and a 30% decrease in RTAT for all CSNI studies from the first (July) to the last month (June) of the academic year, indicative of growing proficiency in interpreting CSNI studies. Our results are consistent with a prior study that demonstrated decreased RTATs after changing from general to subspecialty reporting,¹⁰ noting that the decrease in our study was nonlinear, as shown in Fig 2B and -D. The RTATs for CSNI MR imaging studies remained higher than for CTs throughout the academic year, a finding we attribute to the increased number of images per study and their overall complexity. This finding is congruent with a prior study that demonstrated that neuroradiology fellows interpret and dictate MR imaging brain reports in an average of 18 minutes, which is significantly higher than for CTs.¹¹ The RTAT for fellows who completed diagnostic radiology residency at our institution remained significantly lower for the first 60 and last 60 days of the fellowship compared to fellows who did not complete a diagnostic radiology residency at our institution. The reason is probably multifactorial and related to familiarity with the dictation, PACS, and hospital electronic medical record systems and the attendings.

We hypothesized that increasing volumes on call would cause an increase in RTAT. However, our findings demonstrate an inverse relationship, with a statistically significant decline in RTATs for CT studies and a trend toward a decline for MRIs. Radiology residents are typically exposed to higher numbers of CT studies during residency compared with MRIs; therefore, new fellows start with a relative proficiency in this technique. This

Table 3: Semiannual change in proportions of call discrepancies between fellows and attendings

Template	July-December (p_A)	January-June (p_B)	Difference	Hypothesis Tests ($H_0: p_A = p_B$)
Great call	0.7%	0.9%	+0.2%	$\chi^2 = 1.26$, P value < .262
Agree	33.4%	42.8%	+9.4%	$\chi^2 = 106.17$, P value < .0001
Addition	52.2%	46.7%	-5.4%	$\chi^2 = 33.57$, P value < .0001
Minor change	12.3%	8.2%	-3.7%	$\chi^2 = 42.27$, P value < .0001
Major change	1.4%	0.9%	-0.5%	$\chi^2 = 6.61$, P value = .010

Note:— p_A indicates proportions of call discrepancy during the first half of the academic year; p_B , proportions of call discrepancy during the second half of the academic year; H_0 , null hypothesis.

“experience differential” between modalities may be particularly pertinent in the call setting because many residents have minimal experience in interpreting MR imaging studies independently, and MR imaging studies typically contain more images and are often more complex. On high-volume call nights, fellows may more easily adapt to expanding CT worklists due to a greater experience with this technique, while their relative inexperience in MR imaging attenuates the ability to reduce RTAT with increasing case volumes. We also believe that RTAT decreased as case volumes increased due to necessity: If not busy, then fellows can spend more time reviewing and dictating cases. Of note, our fellowship program does not actively track or emphasize RTAT; therefore, fellows did not have pressure to rapidly interpret studies and generate reports on the basis of productivity benchmarks. Anecdotal, some fellowship programs track RTAT, and our data can help these programs assess the progress of their fellows by following the data shown in Tables 1 and 2 and Fig 2, noting that large variabilities in RTAT trends can be seen among fellows. Care must be taken because overemphasis on RTAT can be detrimental and might encourage the fellow to work out of their comfort zone to quickly interpret and generate a report, potentially leading to more interpretive errors. A prior study demonstrated that required RTAT negatively affected a radiologist’s ability to teach and the quality of resident education.¹²

In many radiology residency and fellowship programs, radiology trainee performance on call is objectively evaluated with discrepancy rates. The major discrepancy rate for our fellows was 1.1%, which is overall lower than for residents^{3,8} and lower than rates for neuroradiology fellows reported by another institution (4.8%).¹³ Our findings demonstrate decreases in major and minor changes during the academic year per day, with the nadir during January (around the midpoint of the fellowship year). To our knowledge, no prior study has analyzed the discrepancy rate trends in fellows, but declines in discrepancy rates were reported in a prior study for radiology residents assessed for 5 years.⁴ Our findings also demonstrate that the percentage of the Addition template usage decreased and the percentage of Agree template usage increased, all while the monthly call load increased. This finding suggests that fellows’ skills overall improved in identifying the pertinent findings and making accurate diagnoses during the course the academic year so that attendings did not need to add any extra wording to the report. Overall usage of the Great call template was low but increased slightly during the last 6 months of training. A study published in 2017 demonstrated that 25%, 62%, and 13% of surveyed neuroradiologists who trained fellows in the United States believed that fellows were less capable, equally capable, or more capable, respectively, compared with prior years.² We analyzed data from 2015 to 2017 (ie, close

to the time of the survey) and saw a generalized slight decline in the proportion of Minor changes, an increase in Agree and Addition templates, and no change in Major change and Great call templates, suggesting no increase in discrepancy rates in our fellows. Caution must be used when comparing our findings with those in the prior survey because we looked only at discrepancy rates at 1 institution, while the survey asked a global question about overall capabilities of fellows.

The data in Table 3 can be used by fellowship programs to assess progress at the end of December, at which time, on average, during 6 months, approximately 86% of reports would have agreement or the addition of relatively minor information, approximately 12% of reports would have minor changes, and approximately 1% of studies would have major changes. The percentages in each category can be combined as needed because some programs might not differentiate between major or minor discrepancies or between reports with words added by the attending and general agreement.

We sought to determine whether other variables associated with call could affect the discrepancy rate. The discrepancy rate slightly increased with an increasing daily case work load (ie, more cases on call results in a higher discrepancy rate) and is congruent with a prior study that demonstrated that higher daily case volumes are associated with higher discrepancy rates for neuroradiologists.¹⁴ Fatigue from a busy clinical day is a likely contributory factor as well. RTAT and imaging technique (CT versus MR imaging) had no effect on the discrepancy rate. We analyzed 100% of the reports with a major discrepancy and found that 75% of cases had a perception error and 25% had a misinterpretation or overcall error. Most interesting, our findings are very similar to those in a prior study that demonstrated that for discrepant neuroradiology attending reports, 74.8% were perception errors and 25.2% interpretation errors.¹⁵

The quality and clarity of neuroradiology reports are important factors that clinicians use to judge the value a neuroradiologist provides in clinical practice.¹⁵ Our study indirectly evaluated the clarity of preliminary call study reports quantitatively by determining the number of words and characters added to the end of reports. Our neuroradiology attendings regularly edit fellow reports during regular workdays to correct or emphasize relevant findings and/or for style. However, for call studies, attendings cannot change, add, or delete words in the preliminary report and are instructed and expected to only add words to the end of the fellow’s report to clarify, change, or emphasize pertinent findings regardless of the report style or the fellow’s level of training. Therefore, we believe that the number of words and characters added to call reports is a surrogate marker for the

clarity of a report. Because fellows generally did not review the findings with an attending before dictation, a study with no or minimal addition of words reflects an independently well-constructed, accurate, and coherent report, an objective metric for progression in fellowship. Our method is a variation of analysis of percentage change characters used by a prior study¹⁶ to measure the quality of reports by trainees and has been shown to be a meaningful measure of trainee progress in residency.¹⁷ On these prior studies, a distinction between when trainees had discussed the findings with the attending before generating a report compared with a solo interpretation and report generation was not always made. In contrast, in our study, for nearly all studies, the fellow interpreted the study and generated a report without prior input from an attending.

Our study demonstrates that ~29% more characters were added to reports with major and minor changes (ie, missed important findings) compared with reports with the Addition templates, while an earlier study demonstrated a 41.6% character change for studies with missed critical findings.¹⁶ Although we cannot directly compare the data, we find it interesting that both studies demonstrated an increase in words and characters used to denote a missed finding. Studies with critical misses often have complex and multiple findings requiring more verbiage to effectively describe them. The number of words and characters added at the end of the preliminary call reports reached a nadir during December and decreased by approximately 8% in the second semester, despite an overall increase in call volume and a decrease in RTAT. From July to December, a mean of approximately 94 words and 672 characters was added to reports. These data could be used by programs to assess whether fellows are within a range of the norm at the end of December or might require additional training to increase the quality and clarity of their reports.

The etiology of this nadir in December is likely multifactorial and probably related to holiday workflow (though the number of studies dictated during December and January did not decline) as well as the fellow's increasing skill level, comfort level with attendings, and confidence in interpreting studies and generating reports. During the second half of the fellowship, many fellows have already procured a postfellowship job, which, therefore, possibly reduced the motivation to impress the attendings (ie, generating the "perfect" call report) and could be a contributing factor. We do not believe attending clinical duties would impact the number of words added because each regular work day has a dedicated attending assigned to finalize fellow preliminary reports without pressure of interpreting mounting cases on that day (ie, there is no real incentive to minimize time spent on each case).

We sought to determine whether other variables associated with call might affect the number of words added to the preliminary report. MR imaging reports had significantly more words added compared with CT; and this feature is likely due to the more complex information obtained from MR imaging compared with CT, requiring longer and often more detailed reports. Most interesting, the daily case load and RTAT had no effect on the number of words added.

Finally, we wanted to determine whether participating in weekly independent call had any residual effect on the

number of studies dictated during a regular subsequent work week. We hypothesized that due to the autonomy practiced during call, the fellows would become more efficient in interpreting and dictating CSNI studies and this outcome would lead to higher clinical productivity, eg, more cases dictated. However, our data demonstrate no significant difference in the number of cases dictated during a regular work week before and after taking a week of call. The reason for this finding is probably multifactorial but is likely, in part, because fellows function differently during the regular workday (honing skills) rather than on call (applying skills). Postcall fatigue may also be a contributory factor.

Overall increases in CSNI call volumes seen at our institution fit with recent national trends.¹⁸ The monthly increase in call volume is probably multifactorial and attributable to inclusion of new criteria for stroke imaging and the addition of overnight MR imaging technologists, among others. Analysis of these factors is beyond the scope of our article.

Our study has limitations that must be considered when interpreting our results. First, this study uses a retrospective cohort design, which could be affected by confounding factors including incomplete retrieval of data due to technical factors. Given the large sample of >10,000 cases, we could not easily assess data integrity for all data points. Additionally, we believe the possible exclusion of some studies would likely not substantially affect the trends shown in our article because we could not identify a systematic bias in patterns of missing data. Second, we did not differentiate the type of CT and MR imaging studies or discrepancies on the basis of technique; however, the complexity of cases can be highly variable irrespective of technique. Third, we did not determine the reasons for the discrepancies in call reports (ie, perceptual-versus-cognitive errors) or the clinical impact of the words added by the attendings at the end of the preliminary report. Fourth, we did not look at RTAT, discrepancy rates, or words added for noncall reports. Although some of these data from another institution were addressed in a prior study.¹⁷ Fifth, there are no criterion standards with which to compare our data with regard to ideal RTAT, discrepancy rate, or words added to reports. Sixth, we could not correlate the discrepancy rates or number of words added to the report with individual attendings. Due to technical factors related to storing preliminary fellow reports in our RIS software, 89% of call reports did not have the name of the attending who finalized the report. However, given that our section had a relatively stable cohort of attendings, their clinical duties were relatively equally distributed, and they were instructed specifically on when and how to add reports, we believe this variability is largely diminished.

CONCLUSIONS

Progression through neuroradiology fellowship and independent call correlates with decreased discrepancies and improvement in indirect quantitative measurements of the clarity of call reports, significant decreases in RTAT for CT studies, and some decrease in RTAT for MR imaging studies, despite increases in call volumes during the academic year. These metrics can be tracked throughout the academic year, and the midyear would be a

logical time point for programs to assess objective progress of fellows and address any deficiencies.

Disclosures: J. Eric Schmitt—UNRELATED: Travel/Accommodations/Meeting Expenses Unrelated to Activities Listed: Radiological Society of North America, Comments: waived registration for teaching a statistical computing course. Tessa S. Cook—UNRELATED: Board Membership: Society for Imaging Informatics in Medicine, Association of University Radiologists, Pennsylvania Radiological Society, Philadelphia Roentgen Ray Society, Comments: travel reimbursement for meetings; Grants/Grants Pending: Radiological Society of North America, American College of Radiology, Society for Imaging Informatics in Medicine, American College of Radiology Imaging Network*; Royalties: Osler Institute, Comments: royalties for lectures originally given and recorded in 2012 on cardiac imaging. Suyash Mohan—UNRELATED: Consultancy: Northwest Biotherapeutics; Grants/Grants Pending: Novocure, Galileo.* *Money paid to the institution.

REFERENCES

- ACGME Program Requirements for Graduate Medical Education in Neuroradiology. July 1, 2020. https://www.acgme.org/Portals/0/PFAssets/ProgramRequirements/423_Neuroradiology_2020.pdf?ver=2020-06-29-164131-690. Accessed July 15, 2020
- Chen JY, Lexa FJ. Baseline survey of the neuroradiology work environment in the United States with reported trends in clinical work, nonclinical work, perceptions of trainees, and burnout metrics. *AJNR Am J Neuroradiol* 2017;38:1284–91 CrossRef Medline
- Shah NA, Hoch M, Willis A, et al. Correlation among on-call resident study volume, discrepancy rate, and turnaround time. *Acad Radiol* 2010;17:1190–94 CrossRef Medline
- Sistrom C, Deitte L. Factors affecting attending agreement with resident early readings of computed tomography and magnetic resonance imaging of the head, neck, and spine. *Acad Radiology* 2008;15:934–41 CrossRef Medline
- Chen PH, Chen YJ, Cook TS. Capricorn: a Web-based automatic case log and volume analytics for diagnostic radiology residents. *Acad Radiol* 2015;22:1242–51 CrossRef Medline
- Core Team R. R: A language and environment for statistical computing. R Foundation for Statistical Computing. <https://www.R-project.org/>. Accessed August 1, 2020
- Giles WL, Boland EF, Halpern G. Radiologist report turnaround time: impact of pay-for-performance measures. *AJR Am J Roentgenol* 2010;195:707–11 CrossRef
- Ruutinen AT, Scanlon MH, Itri JN. Identifying benchmarks for discrepancy rates in preliminary interpretations provided by radiology trainees at an academic institution. *J Am Coll Radiol* 2011;8:644–48 CrossRef Medline
- Rosenkrantz AB, Wang W, Hughes DR, et al. Generalist versus subspecialist characteristics of the U.S. radiologist workforce. *Radiology* 2018;286:929–37 CrossRef Medline
- Stern C, Boehm T, Burkhardt S, et al. Subspecialized radiological reporting expedites turnaround time of radiology reports and increases productivity. *Rofo* 2018;190:623–29 CrossRef Medline
- Al Yassin A, Sadaghiani MS, Mohan S, et al. It is about “time”: academic neuroradiologist time distribution for interpreting brain MRIs. *Acad Radiol* 2018;25:1521–25 CrossRef Medline
- England E, Collins J, White RD, et al. Radiology report turnaround time: effect on resident education. *Acad Radiol* 2015;22:662–67 CrossRef Medline
- Huntley JH, Carone M, Yousem DM, et al. Opportunities for targeted education: critical neuroradiologic findings missed or misinterpreted by residents and fellows. *AJR Am J Roentgenol* 2015;205:1155–59 CrossRef Medline
- Patel SH, Stanton CL, Miller SG, et al. Risk factors for perceptual-versus-interpretative errors in diagnostic neuroradiology. *AJNR Am J Neuroradiol* 2019;40:1252–56 CrossRef Medline
- Olthof AW, De Groot JC, Zorgdrager AN, et al. Perception of radiology reporting efficacy by neurologists in general and university hospitals. *Clin Radiol* 2018;73:675.e1–e7 CrossRef Medline
- Stankiewicz K, Cohen M, Carone M, et al. Comparing preliminary and final neuroradiology reports: what factors determine the differences? *AJNR Am J Neuroradiol* 2016;37:1977–82 CrossRef Medline
- Surrey D, Sharpe RE Jr, Gorniak RJ, et al. QRSE: a novel metric for the evaluation of trainee radiologist reporting skills. *J Digit Imaging* 2013;26:678–82 CrossRef Medline
- Verdoorn JT, Hunt CH, Luetmer MT, et al. Increasing neuroradiology exam volumes on-call do not result in increased major discrepancies in primary reads performed by residents. *Open Neuroimag J* 2014;8:11–15 CrossRef Medline

Impact of Kidney Function on CNS Gadolinium Deposition in Patients Receiving Repeated Doses of Gadobutrol

S. Dogra, M.J. Borja, and Y.W. Lui

ABSTRACT

BACKGROUND AND PURPOSE: Studies associate repeat gadolinium-based contrast agent administration with T1 shortening in the dentate nucleus and globus pallidus, indicating CNS gadolinium deposition, most strongly with linear agents but also reportedly with macrocyclics. Renal impairment effects on long-term CNS gadolinium deposition remain underexplored. We investigated the relationship between signal intensity changes and renal function in patients who received ≥ 10 administrations of the macrocyclic agent gadobutrol.

MATERIALS AND METHODS: Patients who underwent ≥ 10 brain MR imaging examinations with administration of intravenous gadobutrol between February 1, 2014, and January 1, 2018, were included in this retrospective study. Dentate nucleus-to-pons and globus pallidus-to-thalamus signal intensity ratios were calculated, and correlations were calculated between the estimated glomerular filtration rate (minimum and mean) and the percentage change in signal intensity ratios from the first to last scan. Partial correlations were calculated to control for potential confounders.

RESULTS: One hundred thirty-one patients (73 women; mean age at last scan, 55.9 years) showed a mean percentage change of the dentate nucleus-to-pons of 0.31%, a mean percentage change of the globus pallidus-to-thalamus of 0.15%, a mean minimum estimated glomerular filtration rate of 69.65 (range, 10.16–132.26), and a mean average estimated glomerular filtration rate at 89.48 (range, 38.24–145.93). No significant association was found between the estimated glomerular filtration rate and percentage change of the dentate nucleus-to-pons (minimum estimated glomerular filtration rate, $r = -0.09$, $P = .28$; average estimated glomerular filtration rate, $r = -0.09$, $P = .30$) or percentage change of the globus pallidus-to-thalamus ($r = 0.07$, $P = .43$; $r = 0.07$, $P = .40$). When we controlled for age, sex, number of scans, and total dose, there were no significant associations between the estimated glomerular filtration rate and the percentage change of the dentate nucleus-to-pons ($r = 0.16$, $P = .07$; $r = 0.15$, $P = .08$) or percentage change of the globus pallidus-to-thalamus ($r = -0.14$, $P = .12$; $r = -0.15$, $P = .09$).

CONCLUSIONS: In patients receiving an average of 12 intravenous gadobutrol administrations, no correlation was found between renal function and signal intensity ratio changes, even in those with mild or moderate renal impairment.

ABBREVIATIONS: DN/P = dentate nucleus-to-pons; eGFR = estimated glomerular filtration rate; GBCA = gadolinium-based contrast agent; GP/T = globus pallidus-to-thalamus; SI = signal intensity

Gadolinium-based contrast agents (GBCAs) are commonly used in imaging to increase conspicuity and reveal enhancement characteristics of lesions. GBCAs can have either a macrocyclic or a linear molecular structure. Recent studies investigating CNS gadolinium deposition following repeat GBCA administrations showed measurable T1 shortening in the dentate nucleus and

globus pallidus in patients who received GBCAs with a linear molecular structure.^{1–12} Postmortem studies in patients who received linear agents have documented gadolinium deposition in the CNS, again most prominently in the dentate nucleus and globus pallidus, lending further credibility to imaging findings.^{13–15}

The underlying mechanism of gadolinium retention remains unknown, as does the chemical formulation of the accumulated gadolinium. Despite these unknown mechanisms, gadolinium deposition is thought to involve dissociation of gadolinium from its chelating ligand, so macrocyclic agents are thought to be more stable than linear GBCAs due to their lower dissociation constants.¹⁶ Although the CNS deposition of linear GBCAs has been demonstrated previously, most studies failed to show increased signal

Received August 18, 2020; accepted after revision November 24.

From the Department of Radiology, New York University Langone Health, New York, New York.

Please address correspondence to Yvonne W. Lui, MD, Department of Radiology, NYU School of Medicine/NYU Langone Health, 660 First Ave, 3rd Floor, New York, NY 10016; e-mail: Yvonne.lui@nyulangone.org
<http://dx.doi.org/10.3174/ajnr.A7031>

intensity in the dentate nucleus and globus pallidus^{2-10,17-27} after the use of macrocyclic GBCAs. Nevertheless, a few studies do report increased signal in the brain,^{20,27-29} including a postmortem study that detected brain gadolinium, even in the setting of macrocyclic GBCA use.³⁰ On the other hand, two studies using highly sensitive inductively coupled plasma mass spectrometry to measure gadolinium in the brain in animal models did not find significant deposition with macrocyclic agents in the parenchyma, so the picture remains mixed.^{31,32}

GBCAs undergo primary renal clearance;³³ hence, determining whether renal impairment could predispose a patient to gadolinium deposition is important. Patients on hemodialysis receiving a linear GBCA have a greater increase in dentate nucleus signal intensity (SI) compared with controls not on dialysis.¹¹ In 2017, Lee et al²⁰ showed that in a subgroup of 28 patients, there was a significant change in SI ratios in patients with estimated glomerular filtration rates (eGFR) between 45 and 60 mL/min/m² who received the macrocyclic agent gadoterate meglumine. Although much has been discussed regarding nephrogenic systemic fibrosis in the context of renal impairment, there is surprisingly little known regarding the potential effects of abnormal renal function on long-term CNS gadolinium deposition.

The purpose of this study was to specifically investigate whether a relationship exists between SI and renal function in patients receiving a large number (≥ 10) of administrations of the macrocyclic GBCA gadobutrol.

MATERIALS AND METHODS

This single-institution retrospective study was approved by the institutional review board. A waiver of consent was obtained due to the anonymized and retrospective nature of the study.

Subject Selection

MR images and electronic health records of all patients who underwent ≥ 10 brain MR imaging studies with intravenous gadobutrol contrast at our institution between February 1, 2014, and January 1, 2018, were included. Exclusion criteria were a history of contrast-enhanced MR imaging at an outside facility during the study period, a lack of precontrast axial T1-weighted images in either the first or last study, no creatinine measurements in the electronic health record during the study period, and the presence of masses or lesions that precluded the ability to interrogate any of the following regions of interest (ROIs): dentate nucleus, globus pallidus, pons, and thalamus.

Clinical Data

Demographic and clinical data were obtained, including indications for imaging. The number of gadobutrol MR imaging scans and gadobutrol doses for each scan were recorded, from which the total gadobutrol administration was calculated. The time between the first and last MR imaging examinations during the study period was also calculated. Peak and average creatinine during the study period was collected for each patient. As per standard clinical practice, the Chronic Kidney Disease Epidemiology Collaboration equation was used to calculate the minimum and average eGFR

for adult patients, while the Bedside Schwartz equation was used for this purpose in patients younger than 18 years of age.^{34,35}

MR Imaging and Analysis

MR imaging examinations were performed using clinical 1.5T or 3T MR imaging units at our institution (1.5T Magnetom Aera, 1.5T Magnetom Avanto, 3T Magnetom Trio, 3T Biograph mMR, 3T Magnetom Skyra, 3T Magnetom Prisma; Siemens). Axial unenhanced T1-weighted images were obtained using standard product pulse sequence clinical scanning parameters for 2D T1-weighted turbo spin-echo imaging, though the exact parameters varied on the basis of the scanner. Section thickness ranged from 3 to 5 mm.

All MR imaging examinations were performed before and after the administration of the intravenous agent Gadavist (gadobutrol; Bayer Schering Pharma), using a standard, weight-based target dose of 0.1 mL/kg (0.1 mmol/kg) to obtain contrast-unenhanced and contrast-enhanced images.

Unenhanced axial T1-weighted turbo spin-echo images were analyzed using previously described techniques by Kanda et al.³⁶ Circular ROIs were placed on the dentate nucleus, globus pallidus, pons, and thalamus for the first and last imaging study in each patient. ROIs were placed on left-sided anatomic structures, unless a mass or lesion precluded proper ROI placement on the left, in which case the right-sided structure was used if suitable. These ROIs were used to measure the mean SI in each structure and to calculate the SI ratios of the dentate nucleus-to-pons (DN/P) and the globus pallidus-to-thalamus (GP/T) for first and last scans as per previously described methodology.³⁶ ROIs were placed in consensus by 2 observers blinded to the number of scans.

Statistical Analysis

Statistical analyses were performed using GraphPad Prism (Version 8; GraphPad Software) and Matlab (2018a; MathWorks). Normality of data was determined using the Shapiro-Wilk test, and parametric or nonparametric statistical tests were applied correspondingly.

Variables of interest were age at last scan, sex, total gadobutrol dose, total number of scans, percentage changes in DN/P and GP/T SIs from first to last scan (Δ DN/P, Δ GP/T), and the minimum and mean eGFR. The null hypothesis that Δ DN/P and Δ GP/T were equal to zero was first tested using a 1-sample *t* test or Wilcoxon signed rank test. Pearson and Spearman correlations were performed to check for associations between the Δ DN/P and Δ GP/T with each of age, sex, total dose, number of scans, and minimum and mean eGFR. Partial correlations were then calculated between Δ DN/P and Δ GP/T and minimum and mean eGFR while controlling for the other variables. Subjects were batched into groups based on minimum eGFR, using standard cutoffs for stages of chronic kidney disease (>90 , 60–90, 45–60, <45) and average eGFR (>90 , 60–90, <60), and differences in Δ DN/P and Δ GP/T between the groups were assessed using the ANOVA test. Two-sided *P* values $\leq .05$ were considered statistically significant. All correlations were performed in Matlab (MathWorks), while the other statistical tests were performed via GraphPad Prism (GraphPad Software).

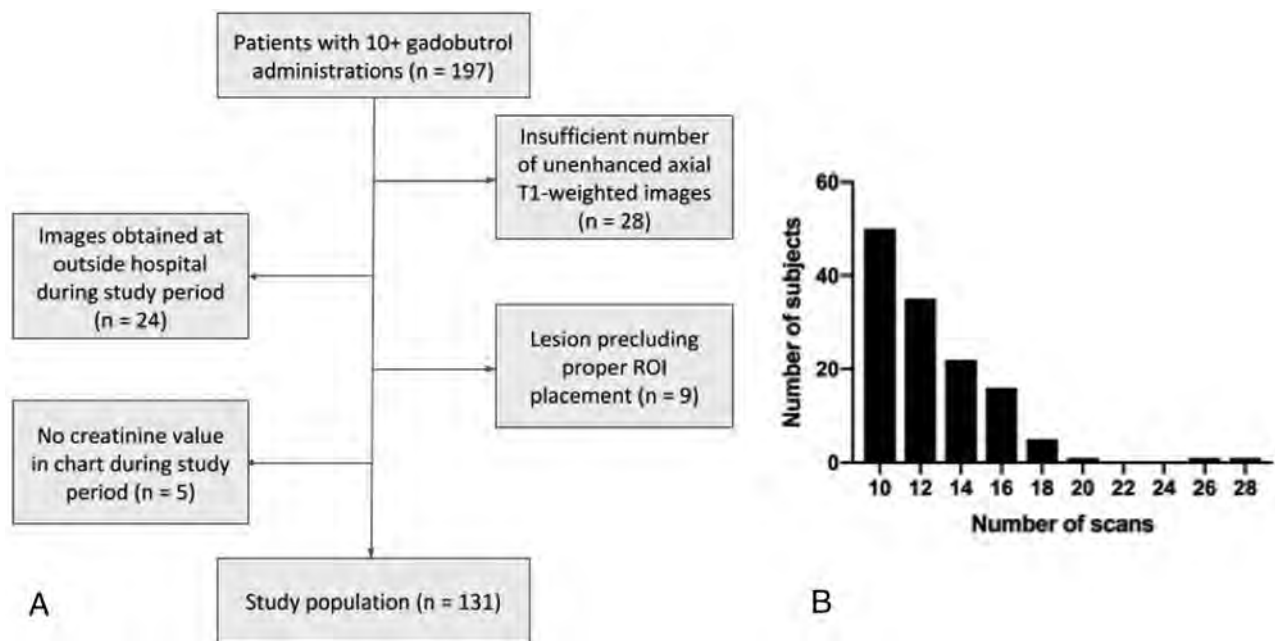


FIG 1. Flow chart detailing patient selection (A) along with a histogram detailing how many subjects had a specific number of scans performed (B).

Table 1: Patient demographics and clinical characteristics^a

Parameter	Result (Total n = 131)
Age at last scan (mean) (range) (yr)	55.95 (3–86)
Sex	
Male (No.)	58
Female (No.)	73
Indication for imaging	
Current or prior tumor (No.)	127
Cerebral amyloid angiopathy (No.)	1
Neurosarcoidosis (No.)	1
Progressive multifocal leukoencephalopathy (No.)	1
Recurrent abscesses (No.)	1
Total gadobutrol dose (mean) [SD] (mL)	85.43 [29.20]
No. of scans (mean) (range)	12.31 (10–28)
Time between first and last scan (median) (range) (mo)	32.4 (2.1–47.2)
Lowest eGFR (mL/min/m ²)	
>90 (No.) (range)	22 (90.51–132.26)
60–90 (No.) (range)	59 (60.06–89.75)
45–60 (No.) (range)	34 (45.82–59.83)
<45 (No.) (range)	16 (10.16–44.24)
Average eGFR (mL/min/m ²)	
>90 (No.) (range)	61 (90.77–145.93)
60–90 (No.) (range)	61 (61.00–89.88)
<60 (No.) (range)	9 (38.24–57.26)

^aNo. of scans refers to scans performed with gadolinium contrast.

RESULTS

197 patients underwent ≥ 10 contrast-enhanced MR imaging examinations with gadobutrol at our institution between February 1, 2014, and January 1, 2018. Of these, 28 were excluded due to lack of unenhanced precontrast axial T1-weighted images in the needed studies, 24 were excluded due to contrast imaging at an outside hospital during the study period, 9 were excluded due to the presence of brain lesions precluding ROI placement, and 5 were excluded on the basis of the lack of documented

creatinine during the study period (Fig 1A). 131 patients were ultimately included in the study, with a range of 10–28 total number of scans per patient (Fig 1B). Demographics and clinical characteristics are summarized in Table 1. 127 of 131 patients were imaged for prior or active tumors, and 101 patients (77.1%) received radiation therapy during the study period.

The Shapiro-Wilk test showed that eGFR, mean eGFR, and Δ GP/T between first and last scans were normally distributed ($P > .05$), while age at last scan, sex, total gadobutrol dose, number of scans, and Δ DN/P between the first and last scans were not. These results dictated whether parametric or nonparametric tests would be used for statistical analyses.

When we compared the first and last scans among all patients, the average Δ DN/P was 0.31%, while the average Δ GP/T was 0.15% (Fig 2). A 1-sample t test with the null hypothesis

that the average Δ GP/T was equal to zero was statistically insignificant (95% confidence interval, 0.57–0.87; $P = .68$). A Wilcoxon signed rank test with the null hypothesis that the median Δ DN/P was equal to zero also failed to show a statistically significant change (data median = 0.24, sum of positive ranks = 4629, sum of negative ranks = –4018, $P = .48$).

Figure 3 shows scatterplots of Δ DN/P and Δ GP/T versus the minimum and mean eGFR. The results of correlational analyses are shown in Table 2. Pearson correlations were calculated for

Δ GP/T versus the minimum and mean eGFR, while Spearman correlations were calculated for every other comparison. We found no association between eGFR and Δ DN/P ($r = -0.09$, $P = .28$; $r = -0.09$, $P = .30$ for minimum and mean eGFR,

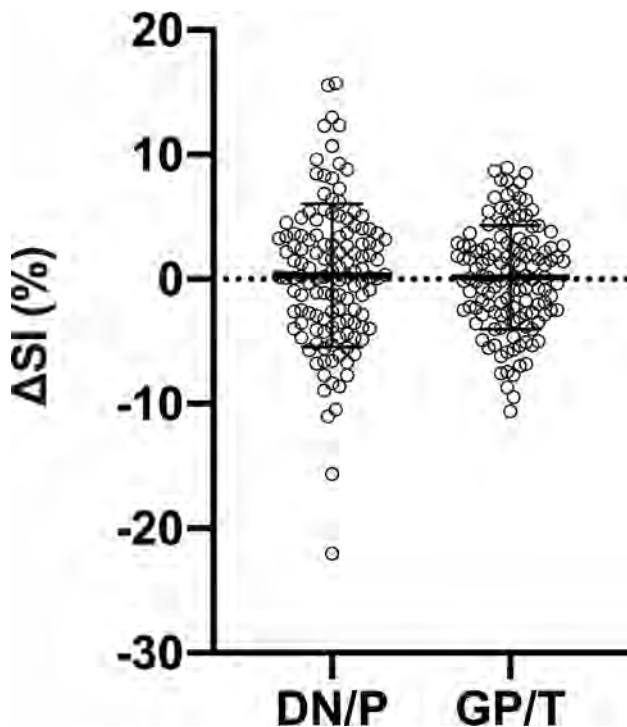


FIG 2. Plot of the percentage change from the first to last scan of the signal intensity ratios of both DN/P and GP/T. Circles represent each of the 131 individual subjects. Error bars indicate the SD from the mean.

respectively) or Δ GP/T ($r = 0.07$, $P = .43$; $r = 0.07$, $P = .40$). There was also no association of Δ GP/T with age at last scan ($r = -0.05$, $P = .54$), sex ($r = -0.04$, $P = .65$), total gadobutrol dose ($r = 0.12$, $P = .18$), and number of scans ($r = 0.09$, $P = .33$). Furthermore, no significant associations were present between Δ DN/P and age at last scan ($r = 0.11$, $P = .21$), sex ($r = 0.05$, $P = .54$), total gadobutrol dose ($r = -0.07$, $P = .43$), or number of scans ($r = 0.12$, $P = .18$).

Table 2 shows the results of partial correlations performed to assess the relationships of both Δ GP/T and Δ DN/P with minimum eGFR and average eGFR, controlling for the other variables. Again, no statistically significant correlations were present ($r = 0.16$, $P = .07$; $r = 0.15$, $P = .08$ for Δ DN/P; $r = -0.14$, $P = .12$; $r = -0.15$, $P = .09$ for Δ GP/T).

Patients were batched into groups based on their minimum eGFR and mean eGFR (Fig 4). Groups for minimum eGFR were the following: >90 ($n = 22$, average Δ GP/T = 0.18, average Δ DN/P = 2.13), 60–90 ($n = 59$, Δ GP/T = -0.41 , Δ DN/P = -0.57), 45–60 ($n = 34$, Δ GP/T = 0.28, Δ DN/P = 1.06), and <45 ($n = 16$, Δ GP/T = 1.91, Δ DN/P = -0.51). Because only four patients had a minimum eGFR below 30, we did not create a group with eGFR < 30 . Groups for average eGFR were >90 ($n = 61$, Δ GP/T = -0.08 , Δ DN/P = .68), 60–90 ($n = 61$, Δ GP/T = 0.17, Δ DN/P = .02), and <60 ($n = 9$, Δ GP/T = 1.60, Δ DN/P = -0.18). Because only three patients had an average eGFR of <45 , we did not create a group with eGFR < 45 . ANOVA was performed to check whether there were differences in the mean Δ GP/T and Δ DN/P between groups. ANOVA in the minimum eGFR group did not find a significant difference in either mean Δ GP/T ($F = 1.34$, $P = .26$) or mean Δ DN/P ($F = 1.52$, $P = .21$). ANOVA in the average eGFR group also did not find a significant difference in either mean Δ GP/T ($F = 0.63$, $P = .53$) or mean Δ DN/P ($F = 0.23$, $P = .79$).

DISCUSSION

In this study of 131 clinical patients with variable renal function and high gadobutrol exposure during a 4-year period, we found no clear relationship between gadobutrol exposure (either total dosage or number of administrations) and SI change in anatomic brain regions implicated in previous reports of GBCA CNS deposition, including in patients with mild or moderate renal impairment.

GBCAs undergo renal clearance, and renal insufficiency is associated with nephrogenic systemic fibrosis. Peripheral tissue fibrosis has been correlated with the amount of deposited gadolinium.³⁷ By prolonging GBCA circulation, renal impairment may effectively increase gadolinium exposure and potentially increase the risk of gadolinium deposition. Previous studies have documented increased DN/P or GP/T SI associated with intravenous

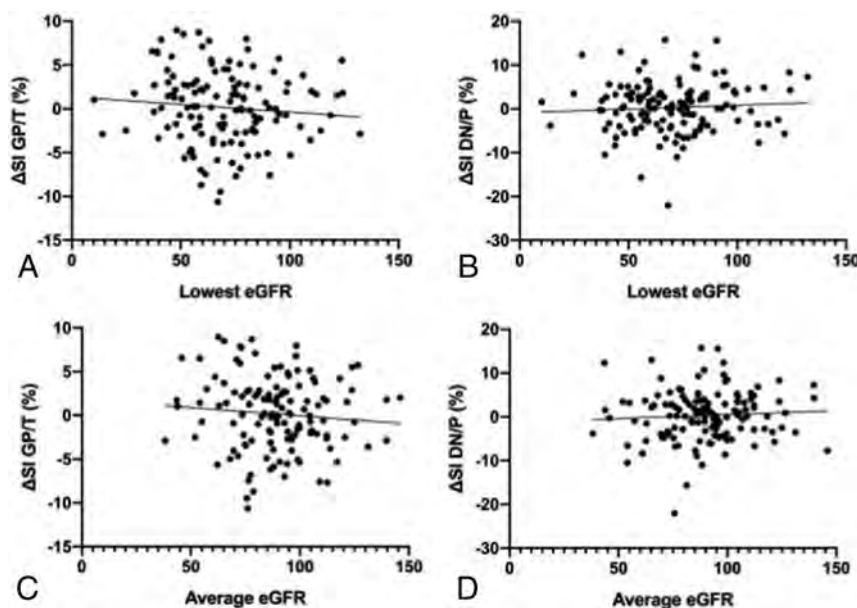


FIG 3. Scatterplot of the lowest and average eGFR versus percentage change in signal intensity ratios of GP/T, shown in A and C, respectively, and DN/P, shown in B and D, respectively, from first to last scan. Lines of best fit are also shown on each graph.

gadolinium administration, particularly with linear agents. Macrocytic agents have been shown to be markedly less frequently associated with such long-term CNS gadolinium effects. Nevertheless, pathology reports show that even macrocytic agents can be associated with small amounts of CNS gadolinium deposition, though it remains unclear why corresponding MR imaging signal changes are not frequently detected.³⁰

Table 2: Correlation coefficients and *P* values for relationships between either Δ GP/T or Δ DN/P and age at last scan, sex, total gadobutrol dose, number of scans performed with gadolinium contrast, lowest eGFR, and average eGFR^a

	Δ GP/T		Δ DN/P	
	<i>r</i>	<i>P</i>	<i>r</i>	<i>P</i>
Age at last scan	−0.05	.54	0.11	.21
Sex	−0.04	.65	0.05	.54
Total gadobutrol dose	0.12	.18	−0.07	.43
No. of scans	0.09	.33	0.12	.18
Lowest eGFR	0.07	0.43	−0.09	0.28
Partial correlation	−0.14	.12	0.16	.07
Average eGFR	0.07	0.40	−0.09	0.30
Partial correlation	−0.15	.09	0.15	.08

^aPearson coefficients were used for Δ GP/T with lowest and average eGFR. Spearman coefficients were used for every other calculation. Partial correlations were obtained only for Δ GP/T and Δ DN/P versus lowest and average eGFR, while controlling for the other variables.

Limited studies explored the effect of renal function on the deep gray nuclei T1 after gadolinium exposure. Lee et al²⁰ have previously reported a significant DN/P SI ratio increase from the first to last examinations in a subgroup of 28 patients with moderate renal insufficiency (eGFR = 45–60) who received gadoterate meglumine. Differences in our results may reflect differences in the contrast agent; although gadoterate meglumine and gadobutrol are both macrocyclic agents, there are differences in the relaxivity profile and formulation.³⁸

Saake et al³⁹ evaluated SI ratio changes and T1 relaxation times in patients with normal and abnormal renal function. In concordance with our study, no differences in the SI ratio were seen in subjects with either normal or impaired renal function who had a gadobutrol injection. However, changes in T1 relaxation time were demonstrated in the globus pallidus in subjects with gadolinium studies, indicating that T1 relaxation time changes may be more sensitive to gadolinium retention than SI ratios. Given the limitations of obtaining pathologic tissue samples, MR imaging remains a practical in vivo alternative, and overall, the use of SI ratios remains a practical approach to assessing clinical scans, though it has more limited sensitivity for the detection of low levels of gadolinium deposition in the brain compared with pathologic assessments and possibly the use of absolute relaxation times.

Limitations of the study include its retrospective nature. There were difficulties in globally capturing renal function throughout

the study period, and because of the possibility of fluctuations in renal function, the granularity of renal function may be incompletely captured. However, we included two measures (minimum and mean eGFR) to develop a reasonable estimate of renal function throughout the study period, and, in fact, the results are similar using both metrics. The low number of patients with severe renal impairment (eGFR < 30) suggests that our results are most applicable to patients with mild or moderate renal impairment. Other limitations are the variability of scanner type, field strength, and pulse sequence parameters among subjects as well as scans; however, some of this variability should be mitigated via normalization of parenchymal values against internal structures, as has been used previously. As in similar studies, it is possible that age-related CNS changes during the course of the study period may have partially masked gadolinium deposition.

CONCLUSIONS

In 131 subjects who underwent an average of 12.3 MR imaging scans with intravenous administration of the macrocyclic GBCA gadobutrol,

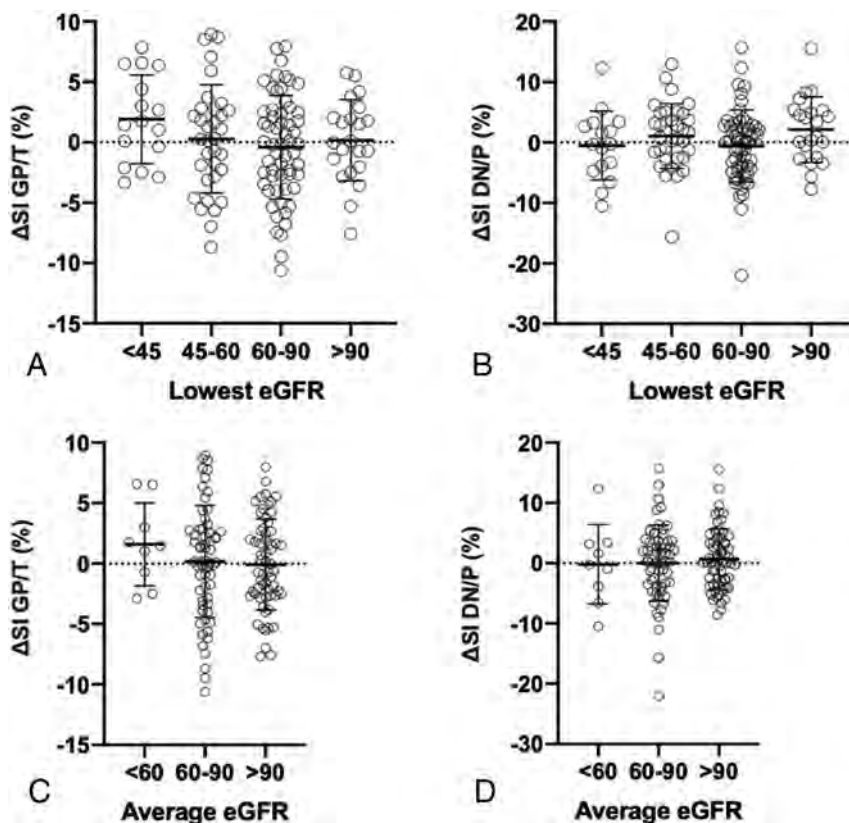


FIG 4. Plot of the lowest and average eGFR versus percentage change in signal intensity ratios of GP/T, shown in A and C, respectively, and DN/P, shown in B and D, respectively, from first to last scan, broken down by eGFR groupings. eGFR batches were >90, 60–90, 45–60, <45 for the lowest eGFR, and >90, 60–90, <60 for the average eGFR. Circles represent each of the 131 individual subjects. Error bars indicate the SD from the mean.

no clear relationship was observed between kidney impairment and detectable changes in DN/P or GP/T SI ratios.

















Disclosures: Maria J. Borja—UNRELATED: Employment: NYU Langone Health; Stock/Stock Options: Teachers Insurance and Annuity Association of America-College Retirement Equities Fund; Travel/Accommodations/Meeting Expenses Unrelated to Activities Listed: reimbursement from NYU for Continuing Medical Education meetings. Yvonne W. Lui—RELATED: Grant: Leon Lowenstein Foundation.* *Money paid to the institution.

REFERENCES

- Rossi Espagnet MC, Bernardi B, Pasquini L, et al. Signal intensity at unenhanced T1-weighted magnetic resonance in the globus pallidus and dentate nucleus after serial administrations of a macrocyclic gadolinium-based contrast agent in children. *Pediatr Radiol* 2017;47:1345–52 CrossRef Medline
- Cao Y, Huang DQ, Shih G, et al. Signal change in the dentate nucleus on T1-weighted MR images after multiple administrations of gadopentetate dimeglumine versus gadobutrol. *AJR Am J Roentgenol* 2016;206:414–19 CrossRef Medline
- Kanda T, Osawa M, Oba H, et al. High signal intensity in dentate nucleus on unenhanced T1-weighted MR images: association with linear versus macrocyclic gadolinium chelate administration. *Radiology* 2015;275:803–09 CrossRef Medline
- Radbruch A, Weberling LD, Kieslich PJ, et al. Gadolinium retention in the dentate nucleus and globus pallidus is dependent on the class of contrast agent. *Radiology* 2015;275:783–91 CrossRef Medline
- Radbruch A, Weberling LD, Kieslich PJ, et al. Intraindividual analysis of signal intensity changes in the dentate nucleus after consecutive serial applications of linear and macrocyclic gadolinium-based contrast agents. *Invest Radiol* 2016;51:683–90 CrossRef Medline
- Schlemm L, Chien C, Bellmann-Strobl J, et al. Gadopentetate but not gadobutrol accumulates in the dentate nucleus of multiple sclerosis patients. *Mult Scler* 2017;23:963–72 CrossRef Medline
- Rowe SK, Rodriguez D, Cohen E, et al. Switching from linear to macrocyclic gadolinium-based contrast agents halts the relative T1-weighted signal increase in deep gray matter of children with brain tumors: a retrospective study. *J Magn Reson Imaging* 2020;51:288–95 CrossRef Medline
- Young JR, Qiao J, Orosz I, et al. Gadolinium deposition within the paediatric brain: no increased intrinsic T1-weighted signal intensity within the dentate nucleus following the administration of a minimum of four doses of the macrocyclic agent gadobutrol. *Eur Radiol* 2018;28:4882–89 CrossRef Medline
- Young JR, Pope WB, Bobinski M. Gadolinium deposition within the pediatric brain: no increased intrinsic T1-weighted signal intensity within the dentate nucleus following the administration of a minimum of 4 doses of the macrocyclic agent gadoteridol. *AJNR Am J Neuroradiol* 2018;39:1604–08 CrossRef Medline
- Ryu YJ, Choi YH, Cheon JE, et al. Pediatric brain: gadolinium deposition in dentate nucleus and globus pallidus on unenhanced T1-weighted images is dependent on the type of contrast agent. *Invest Radiol* 2018;53:246–55 CrossRef Medline
- Cao Y, Zhang Y, Shih G, et al. Effect of renal function on gadolinium-related signal increases on unenhanced T1-weighted brain magnetic resonance imaging. *Invest Radiol* 2016;51:677–82 CrossRef Medline
- Roberts DR, Chatterjee AR, Yazdani M, et al. Pediatric patients demonstrate progressive T1-weighted hyperintensity in the dentate nucleus following multiple doses of gadolinium-based contrast agent. *AJNR Am J Neuroradiol* 2016;37:2340–47 CrossRef Medline
- Kanda T, Fukusato T, Matsuda M, et al. Gadolinium-based contrast agent accumulates in the brain even in subjects without severe renal dysfunction: evaluation of autopsy brain specimens with inductively coupled plasma mass spectroscopy. *Radiology* 2015;276:228–32 CrossRef Medline
- McDonald RJ, McDonald JS, Kallmes DF, et al. Intracranial gadolinium deposition after contrast-enhanced MR imaging. *Radiology* 2015;275:772–82 CrossRef Medline
- McDonald RJ, McDonald JS, Kallmes DF, et al. Gadolinium deposition in human brain tissues after contrast-enhanced MR imaging in adult patients without intracranial abnormalities. *Radiology* 2017;285:546–54 CrossRef Medline
- Rogosnitzky M, Branch S. Gadolinium-based contrast agent toxicity: a review of known and proposed mechanisms. *Biomaterials* 2016;29:365–76 CrossRef Medline
- Radbruch A, Weberling LD, Kieslich PJ, et al. High-signal intensity in the dentate nucleus and globus pallidus on unenhanced T1-weighted images: evaluation of the macrocyclic gadolinium-based contrast agent gadobutrol. *Invest Radiol* 2015;50:805–10 CrossRef Medline
- Radbruch A, Haase R, Kieslich PJ, et al. No signal intensity increase in the dentate nucleus on unenhanced T1-weighted MR images after more than 20 serial injections of macrocyclic gadolinium-based contrast agents. *Radiology* 2017;282:699–707 CrossRef Medline
- Eisele P, Alonso A, Szabo K, et al. Lack of increased signal intensity in the dentate nucleus after repeated administration of a macrocyclic contrast agent in multiple sclerosis: an observational study. *Medicine (Baltimore)* 2016;95:e4624 CrossRef Medline
- Lee JY, Park JE, Kim HS, et al. Up to 52 administrations of macrocyclic ionic MR contrast agent are not associated with intracranial gadolinium deposition: multifactorial analysis in 385 patients. *PLoS One* 2017;12:e0183916 CrossRef Medline
- Radbruch A, Haase R, Kickingereder P, et al. Pediatric brain: no increased signal intensity in the dentate nucleus on unenhanced T1-weighted MR images after consecutive exposure to a macrocyclic gadolinium-based contrast agent. *Radiology* 2017;283:828–36 CrossRef Medline
- Pozeg P, Forget J, Meuli RA, et al. Age, but not repeated exposure to gadoterate meglumine, is associated with T1- and T2-weighted signal intensity changes in the deep brain nuclei of pediatric patients. *Invest Radiol* 2019;54:537–48 CrossRef Medline
- Olchowcy C, Maciaõg EJ, Sanchez-Montanez A, et al. Measurements of signal intensity of globus pallidus and dentate nucleus suggest different deposition characteristics of macrocyclic GBCAs in children. *PLoS One* 2018;13:e0208589 CrossRef Medline
- Jalent P, Hannoun S, Koccevar G, et al. Weekly enhanced T1-weighted MRI with gadobutrol injections in MS patients: is there a signal intensity increase in the dentate nucleus and the globus pallidus? *Eur J Radiol* 2018;105:204–08 CrossRef Medline
- Tibussek D, Rademacher C, Caspers J, et al. Gadolinium brain deposition after macrocyclic gadolinium administration: a pediatric case-control study. *Radiology* 2017;285:223–30 CrossRef Medline
- Bhargava R, Persad AR, Bhargava NK, et al. Multiple administrations of gadobutrol in the pediatric brain; no change in T1 signal at MRI. *Radiology* 2018;289:204–09 CrossRef Medline
- Björnerud A, Vatnehol SA, Larsson C, et al. Signal enhancement of the dentate nucleus at unenhanced MR imaging after very high cumulative doses of the macrocyclic gadolinium-based contrast agent gadobutrol: an observational study. *Radiology* 2017;285:434–44 CrossRef
- Stojanov DA, Aracki-Trenkic A, Vojinovic S, et al. Increasing signal intensity within the dentate nucleus and globus pallidus on unenhanced T1W magnetic resonance images in patients with relapsing-remitting multiple sclerosis: correlation with cumulative dose of a macrocyclic gadolinium-based contrast agent, gadobutrol. *Eur Radiol* 2016;26:807–15 CrossRef Medline
- Topcuoglu ED, Topcuoglu OM, Semiz Oysu A, et al. Does gadoterate meglumine cause gadolinium retention in the brain of children? A case-control study. *J Magn Reson Imaging* 2020;51:1471–77 CrossRef Medline
- Murata N, Gonzalez-Cuyar LF, Murata K, et al. Macrocyclic and other non-group 1 gadolinium contrast agents deposit low levels of gadolinium in brain and bone tissue: preliminary results from 9 patients with normal renal function. *Invest Radiol* 2016;51:447–53 CrossRef Medline

31. Jost G, Frenzel T, Boyken J, et al. **Long-term excretion of gadolinium-based contrast agents: linear versus macrocyclic agents in an experimental rat model.** *Radiology* 2019;290:340–48 CrossRef Medline
32. Radbruch A, Richter H, Fingerhut S, et al. **Gadolinium deposition in the brain in a large animal model: comparison of linear and macrocyclic gadolinium-based contrast agents.** *Invest Radiology* 2019;54:531–36 CrossRef Medline
33. Morcos SK. **Extracellular gadolinium contrast agents: differences in stability.** *Eur J Radiol* 2008;66:175–79 CrossRef Medline
34. Levey AS, Stevens LA, Schmid CH, et al. for the CKD-EPI (Chronic Kidney Disease Epidemiology Collaboration). **A new equation to estimate glomerular filtration rate.** *Ann Intern Med* 2009;150:604–12 CrossRef Medline
35. Schwartz GJ, Munoz A, Schneider MF, et al. **New equations to estimate GFR in children with CKD.** *J Am Soc Nephrol* 2009;20:629–37 CrossRef Medline
36. Kanda T, Ishii K, Kawaguchi H, et al. **High signal intensity in the dentate nucleus and globus pallidus on unenhanced T1-weighted MR images: relationship with increasing cumulative dose of a gadolinium-based contrast material.** *Radiology* 2014;270:834–41 CrossRef Medline
37. High WA, Ranville JF, Brown M, et al. **Gadolinium deposition in nephrogenic systemic fibrosis: an examination of tissue using synchrotron x-ray fluorescence spectroscopy.** *J Am Acad Dermatol* 2010;62:38–44 CrossRef Medline
38. Maravilla KR, San-Juan D, Kim SJ, et al. **Comparison of gadoterate meglumine and gadobutrol in the MRI diagnosis of primary brain tumors: a double-blind randomized controlled intraindividual crossover study (the REMIND Study).** *AJNR Am J Neuroradiol* 2017;38:1681–88 CrossRef Medline
39. Saake M, Schmidle A, Kopp M, et al. **MRI brain signal intensity and relaxation times in individuals with prior exposure to gadobutrol.** *Radiology* 2019;290:659–68 CrossRef Medline

Severity of Chest Imaging is Correlated with Risk of Acute Neuroimaging Findings among Patients with COVID-19

 M. Lang,  M.D. Li,  K.Z. Jiang,  B.C. Yoon,  D.P. Mendoza,  E.J. Flores,  S.P. Rincon,  W.A. Mehan Jr,  J. Conklin,  S.Y. Huang,  A.L. Lang,  D.M. Gao,  T.M. Leslie-Mazwi,  J. Kalpathy-Cramer,  B.P. Little, and  K. Buch



ABSTRACT

BACKGROUND AND PURPOSE: Severe respiratory distress in patients with COVID-19 has been associated with higher rate of neurologic manifestations. Our aim was to investigate whether the severity of chest imaging findings among patients with coronavirus disease 2019 (COVID-19) correlates with the risk of acute neuroimaging findings.

MATERIALS AND METHODS: This retrospective study included all patients with COVID-19 who received care at our hospital between March 3, 2020, and May 6, 2020, and underwent chest imaging within 10 days of neuroimaging. Chest radiographs were assessed using a previously validated automated neural network algorithm for COVID-19 (Pulmonary X-ray Severity score). Chest CTs were graded using a Chest CT Severity scoring system based on involvement of each lobe. Associations between chest imaging severity scores and acute neuroimaging findings were assessed using multivariable logistic regression.

RESULTS: Twenty-four of 93 patients (26%) included in the study had positive acute neuroimaging findings, including intracranial hemorrhage ($n = 7$), infarction ($n = 7$), leukoencephalopathy ($n = 6$), or a combination of findings ($n = 4$). The average length of hospitalization, prevalence of intensive care unit admission, and proportion of patients requiring intubation were significantly greater in patients with acute neuroimaging findings than in patients without them ($P < .05$ for all). Compared with patients without acute neuroimaging findings, patients with acute neuroimaging findings had significantly higher mean Pulmonary X-ray Severity scores (5.0 [SD, 2.9] versus 9.2 [SD, 3.4], $P < .001$) and mean Chest CT Severity scores (9.0 [SD, 5.1] versus 12.1 [SD, 5.0], $P = .041$). The pulmonary x-ray severity score was a significant predictor of acute neuroimaging findings in patients with COVID-19.

CONCLUSIONS: Patients with COVID-19 and acute neuroimaging findings had more severe findings on chest imaging on both radiographs and CT compared with patients with COVID-19 without acute neuroimaging findings. The severity of findings on chest radiography was a strong predictor of acute neuroimaging findings in patients with COVID-19.

ABBREVIATIONS: CCS = Chest CT Severity; COVID-19 = coronavirus disease 2019; ICU = intensive care unit; PXS = Pulmonary X-ray Severity; ROC = receiver operating characteristic; SARS-CoV-2 = Severe Acute Respiratory Syndrome coronavirus 2

The Severe Acute Respiratory Syndrome coronavirus 2 (SARS-CoV-2), which causes coronavirus disease 2019 (COVID-19), has now infected >40 million people worldwide, with >1 million deaths reported by the end of October 2020.¹

Received November 8, 2020; accepted after revision December 11.


From the Departments of Radiology (M.L., M.D.L., B.C.Y., D.P.M., E.J.F., S.P.R., W.A.M., J.C., S.Y.H., J.K.-C., B.P.L., K.B.), Anesthesia, Critical Care, and Pain Medicine (A.L.L.), Neurosurgery and Neurology (T.M.L.-M.), and Athinoula A. Martinos Center for Biomedical Imaging (J.C., S.Y.H., J.K.-C.), Massachusetts General Hospital, Harvard Medical School, Boston, Massachusetts; School of Medicine (K.Z.J.), Baylor College of Medicine, Houston, Texas; and Harvard Medical School (D.M.G.), Boston, Massachusetts.

B.P. Little and K. Buch are equal co-senior authors.

This study was supported by sundry funds to J. Kalpathy-Cramer. This research was carried out, in whole or in part, at the Athinoula A. Martinos Center for Biomedical Imaging at the Massachusetts General Hospital, using resources provided by the Center for Functional Neuroimaging Technologies, P41EB015896, a P41 Biotechnology Resource Grant supported by the National Institute of Biomedical Imaging and Bioengineering, National Institutes of Health. GPU computing resources were provided by the MGH and BWH Center for Clinical Data Science.

While COVID-19 is well-known for its pulmonary manifestations, it has been shown to involve other organs, including the heart, kidneys, liver, and central nervous system.²⁻⁵ This involvement is consistent with viral entry through the angiotensin-converting enzyme 2 receptor, which is abundantly expressed on vascular endothelial cells of the lungs but also in other organs, including the central nervous system, heart, kidneys, intestines, and muscles.⁶ Reported neurologic manifestations of COVID-19 infection include ischemic and hemorrhage stroke, encephalitis, and leukoencephalopathy.⁷⁻¹²

Please address correspondence to Min Lang, MD, MSc, Department of Radiology, Massachusetts General Hospital, 55 Fruit St, Boston, MA 02114; e-mail: mlang@mgh.harvard.edu

 Indicates open access to non-subscribers at www.ajnr.org

<http://dx.doi.org/10.3174/ajnr.A7032>

Table 1: Summary of patient characteristics, clinical data, and indication for neuroimaging

Demographics	With Neuroimaging Findings (n = 24)	Without Neuroimaging Findings (n = 69)	P Value
Age (mean) [SD] (yr)	63 [SD, 16]	66 [SD, 16]	.396
Female sex (No.) (%)	8 (33)	23 (33)	1.000
Clinical data			
Length of stay (mean) [SD] (day)	31 [SD, 12]	23 [SD, 15]	.021
ICU admission (No.) (%)	22 (92)	46 (67)	.035
Intubation (No.) (%)	21 (88)	36 (52)	.005
Death (No.) (%)	5 (21)	12 (17)	.945
Indication for neuroimaging			.089
Altered mental status	13 (54)	42 (61)	
Concern for stroke	10 (42)	14 (20)	
Trauma	0 (0)	10 (15)	
Seizure	1 (4)	1 (3)	
Headache	0 (0)	2 (3)	

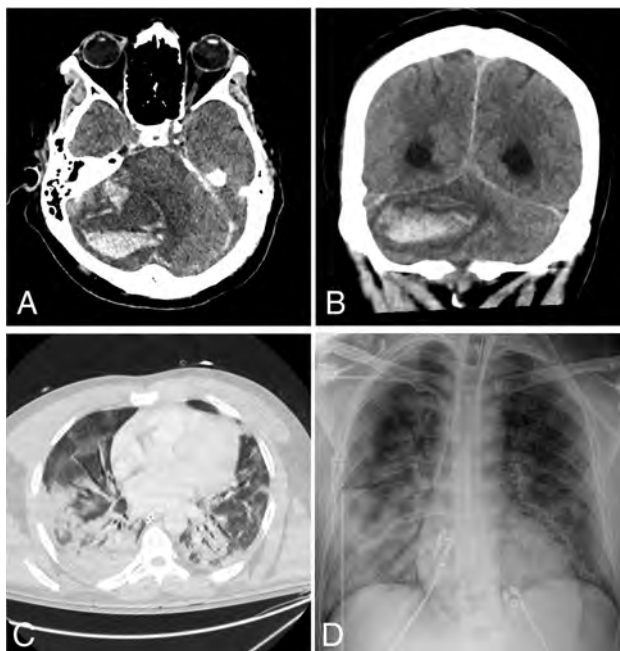


FIG 1. A 42-year-old man presented with hypoxemic respiratory failure. Non-contrast-enhanced axial (A) and coronal (B) CT head images demonstrate a new, large, right cerebellar intraparenchymal mixed-attenuation hematoma suggestive of hyperacute or active hemorrhage. C, Chest CT of the patient demonstrates bilateral consolidation and ground-glass opacities involving all lobes, with a CCS score of 18. D, Portable chest radiograph demonstrates bilateral patchy air space opacities with a PXS score of 10.3.

It has been previously reported that patients with COVID-19 and severe respiratory distress have a relatively high rate of neurologic involvement.¹³ Furthermore, patients with COVID-19 and neurologic symptoms have been shown to have poorer outcomes than those without them.¹⁴ Thus, it would be important to identify clinical or imaging features in patients with COVID-19 that may help predict an increased risk of neurologic injury. Severity of disease on chest imaging is a strong predictor of clinical outcome and risk of complications.¹⁵⁻¹⁷ The objective of our study was to identify whether the severity of chest imaging

findings is correlated with the risk of positive neuroimaging findings in patients admitted for COVID-19 infection.

MATERIALS AND METHODS

Study Cohort

This retrospective study was approved by Massachusetts General Hospital institutional review board of our institution with a waiver of informed consent, and patient privacy was ensured in compliance with the Health Insurance Portability and Accountability Act. Between March 3, 2020, and May 6, 2020, a total of 641 patients received medical care at our quaternary care academic medical center for COVID-19. Patients were included if they

tested positive for SARS-CoV-2 infection diagnosed via real-time polymerase chain reaction, underwent CT and/or MR imaging for the evaluation of neurologic symptoms, and underwent chest radiography and/or CT within 10 days of neuroimaging for pulmonary symptoms. Patients were excluded if their neuroimaging was affected by substantial artifacts that precluded diagnostic assessment.

Clinical Data

Basic demographic information, including age and sex, as well as indications for neuroimaging were obtained from the electronic medical record for each patient. Clinical data, including length of hospital stay, admission to intensive care unit, intubation status, and death, were obtained for each patient.

Imaging Technique

All neuroimaging CT examinations were obtained on 64-section multidetector row CT scanners, either a Revolution CT (GE Healthcare) or a Somatom Force CT (Siemens) scanner. For non-contrast-enhanced head CTs, the studies were axially acquired (120 kV/auto-milliampere-seconds) at 5- and 1.25-mm-thick slices, from the level of the skull base to the vertex. For MR brain imaging, sequences performed included axial DWI, axial T2 FLAIR, axial T2WI, axial SWI, and sagittal T1WI. Intravenous contrast was used in a subset of studies.

All patients included in the study underwent portable chest radiography within 10 days before neuroimaging. The chest radiograph with the highest severity (highest Pulmonary X-ray Severity [PXS] score) within 10 days before neuroimaging was used for analysis (a mean of 3.3 [SD, 3.3] days for patients with acute neuroimaging findings versus a mean of 1.8 [SD, 3.7] days for patients without acute neuroimaging findings, $P = .18$).

Chest CT was performed in a subset of patients during admission and within 10 days before neuroimaging (a mean of 2.2 [SD, 2.9] days for patients with acute neuroimaging findings versus a mean of 1.5 [SD, 2.6] days for patients without acute neuroimaging findings, $P = .40$). The images were obtained with the patient in the supine position using one of the following CT scanners: Discovery CT750 HD (GE Healthcare), Revolution Frontier (GE

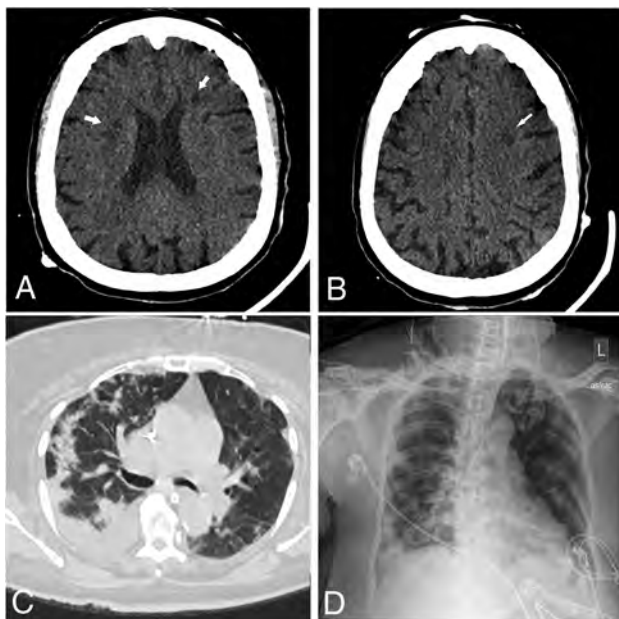


FIG 2. An 85-year-old man presented with increasing shortness of breath. Non-contrast-enhanced axial CT of the head demonstrates multiple new foci of hypodensity within the bilateral frontal corona radiata (arrows on A) and left centrum semiovale (arrow on B), in keeping with acute infarcts. C, Chest CT of the patient shows diffuse bilateral, right greater-than-left, predominantly consolidation and ground-glass opacities as well as bilateral pleural effusions. The CCS score was calculated as 13. D, Portable chest radiograph demonstrates bilateral patchy opacities with a PXS score of 10.6.

Healthcare), Somatom Definition Flash (Siemens), Somatom Definition AS (Siemens), Somatom Force (Siemens), and Aquilion ONE (Toshiba). The scanning parameters were the following: tube voltage = 140 kV(peak) (plus 80 kVp for dual energy), matrix = 512×512 , section thickness = 1.25 mm, FOV = 440×440 mm.

Image Evaluation

All neuroimaging examinations included in this study were reviewed by 2 fellowship-trained neuroradiologists, and the presence of intracranial hemorrhage, acute or subacute infarction, and/or leukoencephalopathy was recorded.

Portable chest radiographs for each patient were assessed using a previously validated convolutional Siamese neural network-based approach for automated assessment of COVID-19 lung disease severity, called the PXS score.^{16,18} Briefly, this machine learning model takes pixel-level image data from frontal chest radiographs as input and outputs a quantitative score for parenchymal lung disease severity. This score has previously been shown to correlate with manual radiologic assessments of COVID-19 radiographic severity as well as clinical outcome. A PXS score of ≤ 2.5 indicates no or minimal disease; > 2.5 and ≤ 5.0 , mild disease; > 5.0 and ≤ 9.0 , moderate disease; and > 9.0 , severe disease.^{16,18}

Chest CT severity was assessed by 3 fellowship-trained thoracic radiologists on the basis of a previously published grading system, the Chest CT Severity (CCS) score.¹⁹ Briefly, the 5 lung lobes were assessed individually for the degree of involvement by

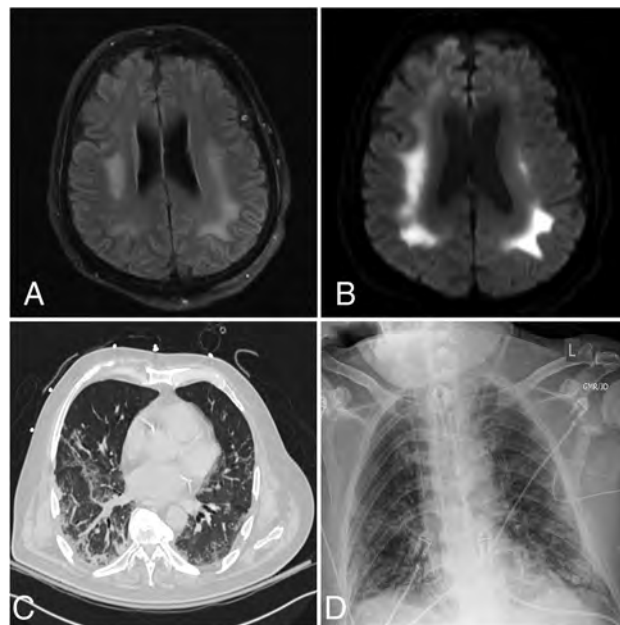


FIG 3. A 64-year-old man presented with fever and shortness of breath. Axial FLAIR (A) and diffusion-weighted (B) images demonstrate extensive symmetric confluent T2/FLAIR signal abnormality and restricted diffusion involving the corona radiata bilaterally. C, Chest CT shows bilateral peripheral ground-glass opacities and a small amount of consolidation involving all lobes, with a CCS score of 15. D, Portable chest radiograph demonstrates bilateral lower-zone-predominant peripheral opacities with a PXS score of 8.8.

Table 2: Distribution of neuroimaging findings and RSNA categories

	With Neuroimaging Findings (n = 24)	Without Neuroimaging Findings
Acute neuroimaging findings		
Infarction	7 (29)	NA
Hemorrhage	7 (29)	NA
Leukoencephalopathy	6 (25)	NA
Combination	4 (17)	NA
Chest CT RSNA category	n = 14	n = 66
Typical	9 (64)	34 (52)
Indeterminate	1 (7)	18 (27)
Atypical	4 (29)	10 (15)
Negative	0 (0)	4 (6)

Note:—NA indicates not applicable; RSNA, Radiological Society of North America.

ground-glass opacities and consolidation. A score of 0 indicates no involvement; 1, minimal involvement (1%–25%); 2, mild involvement (26%–50%); 3, moderate involvement (51%–75%); and 4, severe involvement (76%–100%). The summation of the individual lobe scores yields the total CCS score.

Statistical Analysis

Statistical analysis was performed using GraphPad Prism software (GraphPad Software) and R Studio (<http://rstudio.org/download/desktop>). Continuous data were presented as means

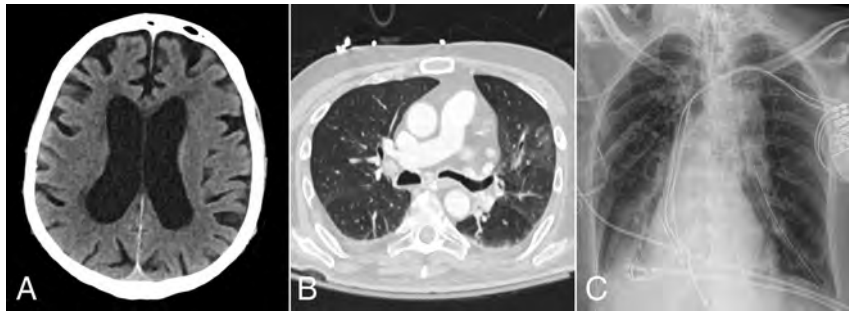


FIG 4. A 67-year-old woman presented with hypoxemic respiratory failure. Axial non-contrast-enhanced head CT image (A) shows no acute findings. B, Chest CT image of the patient demonstrates bilateral peripherally distributed ground-glass opacities involving 4 of the 5 lobes with a CCS score of 8. D, Portable chest radiograph demonstrates bibasilar patchy opacities with a PXS score of 4.4.

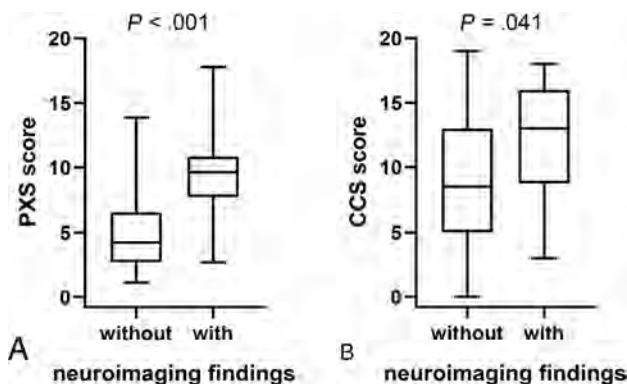


FIG 5. A, Comparison of portable chest radiograph severity (PXS) score between patients with and without acute neuroimaging findings. B, Comparison of the CCS score between patients with and without acute neuroimaging findings.

[SD] and were analyzed by a 2-tailed *t* test; categorical data were presented as frequency (%) and analyzed with a χ^2 test. Associations between the lung disease severity scores (PXS and CCS) and neuroimaging findings were examined using multivariable logistic regression. Models were risk-adjusted for age, sex, the need for intubation, and intensive care unit (ICU) admission. The R Studio package pROC (<https://www.rdocumentation.org/packages/pROC/versions/1.16.2>) was used to generate receiver operating characteristic (ROC) curves and to calculate the area under the ROC curve.²⁰ We computed 95% confidence intervals with 2000 stratified bootstrap replicates. Statistical significance was set at $P < .05$.

RESULTS

A total of 93 patients met the inclusion criteria for the study. Twenty-four (26%) patients had acute neuroimaging findings, whereas 69 (74%) patients did not. The proportion of patients who underwent MR imaging or CT was not significantly different between patients without acute neuroimaging findings (58 underwent head CT and 11 underwent brain MR imaging) and patients with acute neuroimaging findings (18 underwent head CT and 6 underwent brain MR imaging; $P = .36$). The mean age of patients

without acute neuroimaging findings was 66 [SD, 16] years of age, 33% of whom were women. The mean age for patients with acute neuroimaging findings was 63 [SD, 16] years, 33% of whom were women as well. The most common indication for neuroimaging was altered mental status and concern for stroke for patients with and without neuroimaging findings (Table 1).

The average length of hospital stay was significantly longer in patients with acute neuroimaging findings (31 [SD, 12] days versus 23 [SD, 15] days, $P = .021$; Table 1). In addition, the prevalence of ICU admission and intubation was significantly higher for

patients with acute neuroimaging findings than for patients without acute neuroimaging findings (92% versus 67%, $P = .04\%$, and 88% versus 52%, $P = .005$, respectively; Table 1). The mortality rate, however, was not significantly different between patients without acute neuroimaging findings (17%) and patients with acute neuroimaging findings (21%, $P = .945$).

Of the 24 patients with acute neuroimaging findings, 7 patients were found to have intracranial hemorrhage (Fig 1), 7 patients were found to have acute infarction (Fig 2), 6 patients were found to have leukoencephalopathy (Fig 3), 3 patients had intracranial hemorrhage and infarction, and 1 patient had intracranial hemorrhage, infarction, and leukoencephalopathy (Table 2). Sixty-nine patients did not have acute neuroimaging findings (Fig 4). There was no significant difference ($P = .225$) between the distribution of Radiological Society of North America categories of chest CT findings between patients without acute neuroimaging findings ($n = 66$) and those with acute neuroimaging findings ($n = 14$), with the “typical” category being the most prevalent in both groups (Table 2).²¹

The mean PXS score was significantly greater in patients with acute neuroimaging findings ($n = 23$, 9.2 [SD, 3.4]) than in patients without acute neuroimaging findings ($n = 64$, 5.0 [SD, 2.9], $P < .001$; Fig 5A). The PXS score was a significant predictor of positive acute neuroimaging findings in patients with COVID-19 after adjusting for age, sex, ICU admission, and intubation status (odds ratio = 1.45, $P < .001$; Fig 6). The mean CCS score was also significantly greater in patients with acute neuroimaging findings ($n = 14$, 12.1 [SD, 5.0]) than in patients without acute neuroimaging findings ($n = 64$, 9.0 [SD, 5.1], $P = .041$; Fig 5B). However, after we adjusted for age, sex, ICU admission, and intubation status, the CCS score was not a significant predictor of positive acute neuroimaging findings in patients with COVID-19 (odds ratio = 1.08, $P = .308$; Fig 6).

The area under the ROC curve using the PXS score to classify acute neuroimaging findings was 0.83 (95% CI, 0.72–0.93; Fig 7A). The optimal threshold PXS score was 7.55, which corresponded to a sensitivity of 83%, specificity of 81%, positive likelihood ratio of 4.7, and negative likelihood ratio of 0.2. By means of this threshold, meaning scores of ≥ 7.6 were labeled as positive

for acute neuroimaging findings and scores of ≤ 7.5 were labeled as negative for acute neuroimaging findings, 77% of cases in our study would be correctly classified.

The area under the curve using the CCS score to classify acute neuroimaging findings was 0.67 (95% CI, 0.50–0.84; Fig 7B). The optimal threshold CCS score was 12.5. This threshold corresponded to a sensitivity of 64%, specificity of 73%, positive likelihood ratio of 2.4, and negative likelihood ratio of 0.5. By means of this threshold, meaning scores of ≥ 13 were labeled as positive for acute neuroimaging findings and scores of ≤ 12 were labeled as negative for acute neuroimaging findings, 61% of cases in our study would be correctly classified.

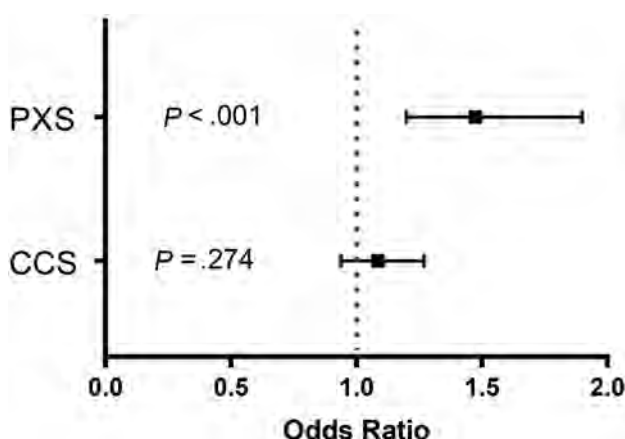


FIG 6. Odds ratio of the PXS score and the CCS score in association with the risk of acute neuroimaging findings. A multivariate logistic regression model was used after adjusting for age, sex, the need for intubation, and ICU admission status.

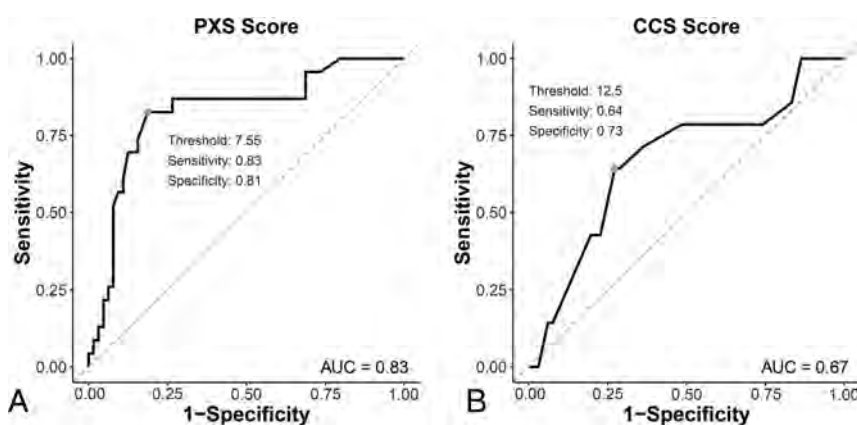


FIG 7. ROC curves of the PXS and CCS scores to classify acute neuroimaging findings in patients with COVID-19. A, The area under the ROC curve using the PXS score to classify acute neuroimaging findings was 0.83 (95% CI, 0.72–0.93). The optimal threshold PXS score was 7.55, which corresponded to a sensitivity of 83%, specificity of 81%, positive likelihood ratio of 4.7, and negative likelihood ratio of 0.2. B, The area under the ROC curve using the CCS score to classify acute neuroimaging findings was 0.67 (95% CI, 0.50–0.84). The optimal threshold CCS score was 12.5, which corresponded to a sensitivity of 64%, specificity of 73%, positive likelihood ratio of 2.4, and negative likelihood ratio of 0.5.

DISCUSSION

A variety of neuroimaging findings have been reported in patients with COVID-19, including infarction, intracranial hemorrhage, leukoencephalopathy, and hemorrhagic encephalitis.^{8–11,14,22} The presence of acute-to-subacute neuroimaging findings in patients with COVID-19 is associated with a higher risk of ICU admission, intubation, and mortality.¹⁴ However, the risk factors for developing neurologic deficits in patients with COVID-19 are unclear. The results of this retrospective study showed that the severity of disease on chest radiographs and chest CT images was significantly greater among patients with COVID-19 with acute neuroimaging findings than in patients without acute neuroimaging findings, suggesting that more severe pulmonary manifestations are associated with a higher likelihood of neurologic injury.

Similar to prior reports, the presence of acute neuroimaging findings in our study was associated with an increased length of hospital stay, increased risk of requiring ICU admission, and risk of intubation.^{14,23} Acute ischemic and hemorrhagic strokes, the most common neuroimaging manifestation, have been reported to be a strong prognostic marker for poor clinical outcome in patients with COVID-19.¹⁴ While ischemic and hemorrhagic strokes were also the most common neuroimaging findings in our study population, mortality was not significantly different between patients with acute neuroimaging findings and those without them. The small number of patients with acute neuroimaging findings may be underpowered to detect a statistically significant difference.

Respiratory symptoms are the most common manifestations of COVID-19, and extensive research has been performed on chest imaging features of the disease, including using chest radiograph and chest CT severity as a prognostic tool for clinical outcome.^{16,19,24–29} A study by Mao et al¹³ has also demonstrated high rates of neurologic symptoms in patients with COVID-19 and severe respiratory disease. This outcome may be due to

shared mechanisms, including cytokine-related abnormal inflammatory response, coagulopathy, and micro- and macroangiopathy, which contribute to both chest and neuroimaging findings in patients with COVID-19.^{28–34} Both chest and neuroimaging manifestations, however, are unlikely due to a single etiology but rather a combination of interconnected pathophysiologic processes. The greater severity of chest imaging findings may therefore indicate more severe system-wide pathology, in which case-heightened suspicion for acute neurologic injury is warranted. Consistent with this theory, PXS scores of patients with COVID-19 were found to be significantly associated with an increased risk of acute neuroimaging findings in our study. While a higher CCS score was associated with an increased risk

of acute neuroimaging findings in the current study, this did not reach statistical significance. This may be related to the small number of patients who underwent chest CT relative to the number of patients who underwent chest radiographic assessment. Future investigation with a larger patient cohort is needed.

Three patients in the current study who had minimal-to-mild chest radiographic findings were found to have either infarction or intracranial hemorrhage. Similarly, 3 patients with mild disease on chest CT were found to have infarction, hemorrhage, and leukoencephalopathy on neuroimaging. The cause of neurologic injury in these patients may be better explained by direct neurotropism of the SARS-CoV-2 virus, which may occur through retrograde transmission through peripheral nerve terminals including the olfactory nerves, rather than widespread cytokine storm.^{35,36} Other proposed mechanisms of neurologic injury without severe chest imaging manifestations include silent hypoxia, metabolic disturbances, neuroinflammation, angiopathy, embolic phenomenon, or an autoimmune-mediated process.³⁷⁻⁴⁰ While neurologic injury can occur in patients with mild pulmonary disease and with less evident chest imaging findings, the relative proportion of these patients is much smaller than those with more severe pulmonary findings.

Limitations of the current study include its retrospective nature and relatively small sample size from a single institution. The small number of patients also precluded further analysis of the risk of developing different types of neurologic injury, such as infarction, hemorrhage, or leukoencephalopathy. Furthermore, additional patient information including laboratory values and comorbidities was incomplete and therefore was not included in the study. Finally, most of these patients did not have additional imaging of other body parts, including the abdomen and pelvis, limiting correlation of findings in other organ systems.

CONCLUSIONS

Patients with COVID-19 and acute neuroimaging findings had greater disease severity on both chest radiography and CT than patients without acute neuroimaging findings. In our adjusted regression models, chest radiograph severity was a strong predictor of acute neuroimaging findings in patients with COVID-19, while the small number of patients may have underpowered the study to detect a significant correlation with chest CT. Therefore, a high severity of disease on chest imaging should raise suspicion for neurologic injury in patients with COVID-19. Early use of neuroimaging in these patients should be considered.

Disclosures: Matthew D. Li—UNRELATED: Grants/Grants Pending: Radiological Society of North America, Comments: M.D.L. reports funding from a Radiological Society of North America Research and Education Presidents Circle Research Resident Grant, outside of the submitted work.* Efren J. Flores—UNRELATED: Grants/Grants Pending: National Cancer Institute Research Diversity Supplement, American College of Radiology Innovation Fund. William A. Mehan, Jr—UNRELATED: Consultancy: Kura Oncology, Comments: independent reviewer of imaging for a head and neck cancer trial; Employment: Massachusetts General Hospital; Expert Testimony: expert opinion for medicolegal cases involving neuroimaging. Susie Y. Huang—UNRELATED: Grants/Grants Pending: Siemens, Comments: research grant for clinical translation of fast brain MRI sequences*; Payment for Lectures Including Service on Speakers Bureaus: Siemens, Comments: payment for speaking on Connectome 2.0 at OHBM 2020. Jayashree Kalpathy-Cramer—UNRELATED: Grants/Grants Pending: GE Healthcare, Genentech

Foundation*; Travel/Accommodations/Meeting Expenses Unrelated to Activities Listed: IBM. Brent P. Little—UNRELATED: Royalties: Elsevier, Comments: textbook royalties, chest radiology textbook, author/associate editor. *Money paid to the institution.

REFERENCES

1. Johns Hopkins University. COVID-19 Dashboard by the Center for Systems Science and Engineering (CSSE) at Johns Hopkins University (JHU). January 7, 2021. <https://coronavirus.jhu.edu/map.html>. Accessed November 4, 2020
2. Bhayana R, Som A, Li MD, et al. Abdominal imaging findings in COVID-19: preliminary observations. *Radiology* 2020;297:E207–15 CrossRef Medline
3. Puelles VG, Lütgehetmann M, Lindenmeyer MT, et al. Multiorgan and renal tropism of SARS-CoV-2. *N Engl J Med* 2020;383:590–92 CrossRef Medline
4. Zaim S, Chong JH, Sankaranarayanan V, et al. COVID-19 and multiorgan response. *Curr Probl Cardiol* 2020;45:100618 CrossRef Medline
5. Wang D, Hu B, Hu C, et al. Clinical characteristics of 138 hospitalized patients with 2019 novel coronavirus-infected pneumonia in Wuhan, China. *JAMA* 2020;323:1061–69 CrossRef Medline
6. Li MY, Li L, Zhang Y, et al. Expression of the SARS-CoV-2 cell receptor gene ACE2 in a wide variety of human tissues. *Infect Dis Poverty* 2020;9:45 CrossRef Medline
7. De Felice FG, Tovar-Moll F, Moll J, et al. Severe acute respiratory syndrome coronavirus 2 (SARS-CoV-2) and the central nervous system. *Trends Neurosci* 2020;43:355–57 CrossRef Medline
8. Poyiadji N, Shahin G, Noujaim D, et al. COVID-19-associated acute hemorrhagic necrotizing encephalopathy: imaging features. *Radiology* 2020;296:E119–20 CrossRef Medline
9. Ye M, Ren Y, Lv T. Encephalitis as a clinical manifestation of COVID-19. *Brain Behav Immun* 2020;88:945–46 CrossRef Medline
10. Moriguchi T, Harii N, Goto J, et al. A first case of meningitis/encephalitis associated with SARS-coronavirus-2. *Int J Infect Dis* 2020;94:55–58 CrossRef Medline
11. Lang M, Li MD, Buch K, et al. Risk of acute cerebrovascular events in patients with COVID-19 infection. *AJNR Am J Neuroradiol* 2020;41:E92–93 CrossRef Medline
12. Josephson SA, Kamel H. Neurology and COVID-19. *JAMA* 2020;324:1139–40 CrossRef Medline
13. Mao L, Jin H, Wang M, et al. Neurologic manifestations of hospitalized patients with coronavirus disease 2019 in Wuhan, China. *JAMA Neurol* 2020;77:683–90 CrossRef Medline
14. Jain R, Young M, Dogra S, et al. COVID-19 related neuroimaging findings: a signal of thromboembolic complications and a strong prognostic marker of poor patient outcome. *J Neurol Sci* 2020;414:116923 CrossRef Medline
15. Feng Z, Yu Q, Yao S, et al. Early prediction of disease progression in COVID-19 pneumonia patients with chest CT and clinical characteristics. *Nat Commun* 2020;11:4968 CrossRef Medline
16. Li MD, Arun NT, Gidwani M, et al. Automated assessment and tracking of COVID-19 pulmonary disease severity on chest radiographs using convolutional Siamese neural networks. *Radiology: Artificial Intelligence* 2020 Jul 22. [Epub ahead of print] CrossRef
17. Toussie D, Voutsinas N, Finkelstein M, et al. Clinical and chest-radiography features determine patient outcomes in young and middle-aged adults with COVID-19. *Radiology* 2020;297:E197–206 CrossRef Medline
18. Li MD, Arun NT, Aggarwal M, et al. Improvement and multi-population generalizability of a deep learning-based chest radiograph severity score for COVID-19. *medRxiv* 2020. CrossRef. Accessed November 5, 2020
19. Steinberger S, Lin B, Bernheim A, et al. CT features of coronavirus disease (COVID-19) in 30 pediatric patients. *AJR Am J Roentgenol* 2020;215:1303–11 CrossRef Medline

20. Robin X, Turck N, Hainard A, et al. **pROC: an open-source package for R and S+ to analyze and compare ROC curves.** *BMC Bioinformatics* 2011;12:77 CrossRef Medline
21. Simpson S, Kay FU, Abbata S, et al. **Radiological Society of North America Expert Consensus Statement on Reporting Chest CT Findings Related to COVID-19: endorsed by the Society of Thoracic Radiology, the American College of Radiology, and Radiological Society of North America—secondary publication.** *J Thorac Imaging* 2020;35:219–27 CrossRef Medline
22. Lang M, Buch K, Li MD, et al. **Leukoencephalopathy associated with severe COVID-19 infection: sequela of hypoxemia?** *AJNR Am J Neuroradiol* 2020;41:1641–45 CrossRef Medline
23. Yoon BC, Buch K, Lang M, et al. **Clinical and neuroimaging correlation in patients with COVID-19.** *AJNR Am J Neuroradiol* 2020; 41:1791–96 CrossRef Medline
24. Huang C, Wang Y, Li X, et al. **Clinical features of patients infected with 2019 novel coronavirus in Wuhan.** *Lancet* 2020;395:497–506 CrossRef Medline
25. Pan Y, Guan H, Zhou S, et al. **Initial CT findings and temporal changes in patients with the novel coronavirus pneumonia (2019-nCoV): a study of 63 patients in Wuhan, China.** *Eur Radiol* 2020; 30:3306–09 CrossRef Medline
26. Shi H, Han X, Jiang N, et al. **Radiological findings from 81 patients with COVID-19 pneumonia in Wuhan, China: a descriptive study.** *Lancet Infect Dis* 2020;20:425–34 CrossRef Medline
27. Chung M, Bernheim A, Mei X, et al. **CT imaging features of 2019 novel coronavirus (2019-nCoV).** *Radiology* 2020;295:202–07 CrossRef Medline
28. Lang M, Som A, Mendoza DP, et al. **Hypoxaemia related to COVID-19: vascular and perfusion abnormalities on dual-energy CT.** *Lancet Infect Dis* 2020;20:1365–66 CrossRef Medline
29. Lang M, Som A, Carey D, et al. **Pulmonary vascular manifestations of COVID-19 pneumonia.** *Radiology: Cardiothoracic Imaging* 2020; 2:e200277 CrossRef
30. Scholkmann F, Nicholls J. **Pulmonary vascular pathology in COVID-19.** *N Engl J Med* 2020;383:887–88 CrossRef Medline
31. Ackermann M, Verleden SE, Kuehnel M, et al. **Pulmonary vascular endotheliitis, thrombosis, and angiogenesis in COVID-19.** *N Engl J Med* 2020;383:120–28 CrossRef Medline
32. Chan NC, Weitz JI. **COVID-19 coagulopathy, thrombosis, and bleeding.** *Blood* 2020;136:381–83 CrossRef Medline
33. Becker RC. **COVID-19 update: COVID-19-associated coagulopathy.** *J Thromb Thrombolysis* 2020;50:54–67 CrossRef Medline
34. McElvaney OJ, McEvoy NL, McElvaney OF, et al. **Characterization of the inflammatory response to severe COVID-19 illness.** *Am J Respir Crit Care Med* 2020;202:812–21 CrossRef Medline
35. Mehraeen E, Behnezhad F, Amin Salehi M, et al. **Olfactory and gustatory dysfunctions due to the coronavirus disease (COVID-19): a review of current evidence.** *Eur Arch Otorhinolaryngol* 2020 Jun 17. [Epub ahead of print] CrossRef Medline
36. Conde Cardona G, Quintana Pajaro LD, Quintero Marzola ID, et al. **Neurotropism of SARS-CoV 2: mechanisms and manifestations.** *J Neurol Sci* 2020;412:116824 CrossRef Medline
37. Delorme C, Paccoud O, Kas A, et al; CoCo-Neurosciences study group and COVID SMIT PSL study group. **Covid-19-related encephalopathy: a case series with brain FDG-positron-emission tomography/computed tomography findings.** *Eur J Neurol* 2020;27: 2651–57 CrossRef Medline
38. Fontana IC, Bongarzone S, Gee A, et al. **PET imaging as a tool for assessing COVID-19 brain changes.** *Trends Neurosci* 2020;43:935–38 CrossRef Medline
39. Wenting A, Gruters A, van Os Y, et al. **COVID-19 neurological manifestations and underlying mechanisms: a scoping review.** *Front Psychiatry* 2020;11:860 CrossRef Medline
40. Kreye J, Reincke SM, Pruss H. **Do cross-reactive antibodies cause neuropathology in COVID-19?** *Nat Rev Immunol* 2020;20:645–46 CrossRef Medline

Development and Validation of a Deep Learning–Based Model to Distinguish Glioblastoma from Solitary Brain Metastasis Using Conventional MR Images

I. Shin, H. Kim, S.S. Ahn, B. Sohn, S. Bae, J.E. Park, H.S. Kim, and S.-K. Lee



ABSTRACT

BACKGROUND AND PURPOSE: Differentiating glioblastoma from solitary brain metastasis preoperatively using conventional MR images is challenging. Deep learning models have shown promise in performing classification tasks. The diagnostic performance of a deep learning–based model in discriminating glioblastoma from solitary brain metastasis using preoperative conventional MR images was evaluated.

MATERIALS AND METHODS: Records of 598 patients with histologically confirmed glioblastoma or solitary brain metastasis at our institution between February 2006 and December 2017 were retrospectively reviewed. Preoperative contrast-enhanced T1WI and T2WI were preprocessed and roughly segmented with rectangular regions of interest. A deep neural network was trained and validated using MR images from 498 patients. The MR images of the remaining 100 were used as an internal test set. An additional 143 patients from another tertiary hospital were used as an external test set. The classifications of ResNet-50 and 2 neuroradiologists were compared for their accuracy, precision, recall, F1 score, and area under the curve.

RESULTS: The areas under the curve of ResNet-50 were 0.889 and 0.835 in the internal and external test sets, respectively. The area under the curve of neuroradiologists 1 and 2 were 0.889 and 0.768 in the internal test set and 0.857 and 0.708 in the external test set, respectively.

CONCLUSIONS: A deep learning–based model may be a supportive tool for preoperative discrimination between glioblastoma and solitary brain metastasis using conventional MR images.

ABBREVIATIONS: CE = contrast enhanced; GBM = glioblastoma; ROC = receiver operating characteristic; AUC = area under the curve

Glioblastoma (GBM) and brain metastases are the most common malignant tumors in adults.¹ These 2 entities have different treatment options, and it is therefore essential to distinguish them promptly to determine the proper treatment strategy. In patients with a history of underlying malignancy and conventional MR imaging findings of multiple enhancing lesions, a diagnosis can be made easily. However, approximately 25%–30% of brain metastases present as single lesions, and in

lung cancer—the most common cancer to metastasize to the brain—approximately 50% of patients are thought to have brain metastases as the initial presentation.^{2,3} In addition, GBM and solitary brain metastasis have overlapping MR imaging features, including rim enhancement with perilesional T2 hyperintensity, and are thus difficult to differentiate preoperatively.⁴ However, GBM has an infiltrative growth pattern; therefore, tumor cells diffusely infiltrate beyond the enhancing portion, manifesting as a perilesional T2 hyperintense region. Brain metastases have similar MR imaging features; however, this perilesional T2 hyperintensity is primarily due to vasogenic edema caused by the leaky capillary vessels of the enhancing tumor.^{5,6} In an effort

Received June 12, 2020; accepted after revision November 13.

From the Department of Radiology, Research Institute of Radiological Science and Center for Clinical Imaging Data Science (I.S., H.K., S.S.A., B.S., S.-K.L.), Yonsei University College of Medicine, Seoul, Korea; Department of Radiology (S.B.), National Health Insurance Corporation Ilsan Hospital, Goyang, Korea; and Department of Radiology and Research Institute of Radiology (J.E.P., H.S.K.), Asan Medical Center, University of Ulsan College of Medicine, Seoul, Korea.

I.Shin and H.Kim are co-first authors and contributed equally to this work.

Funded by Basic Science Research Program through the National Research Foundation of Korea, funded by Ministry of Science, Information, and Communication Technologies & Future Planning (2017R1D1A1B03030440)

Previously presented at: 105th Scientific Assembly and Annual Meeting of the Radiological Society of North America, December 1–6, 2019, Chicago, Illinois.

Please address correspondence to Sung Soo Ahn, MD, PhD, Department of Radiology, Severance Hospital, Research Institute of Radiological Science and Center for Clinical Image Data Science, Yonsei University, College of Medicine, 50 Yonsei-ro, Seodaemun-gu, 03722 Seoul, Korea; e-mail: sungsoo@yuhs.ac

Indicates open access to non-subscribers at www.ajnr.org

Indicates article with online supplemental data.

<http://dx.doi.org/10.3174/ajnr.A7003>

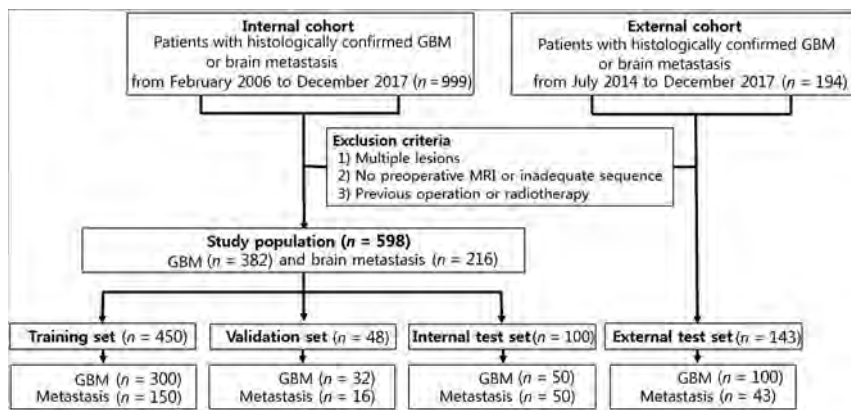


FIG 1. Flow chart showing the patient population in the internal and external cohorts.

to detect these microstructural differences, various advanced MR imaging techniques, such as perfusion MR imaging, MR spectroscopy, and diffusion tensor imaging, have been applied to distinguish GBM from solitary brain metastasis, with particular emphasis on the aforementioned perilesional T2 hyperintense region.⁷⁻¹⁰ Collectively, these studies have shown promising results indicating that the perilesional T2 hyperintense region, along with the enhancing portion itself, carries valuable information that may preoperatively distinguish these 2 entities. However, advanced imaging techniques require additional scanning time, and their quantitative values can vary depending on the imaging parameters, posing difficult challenges for practical application.

Recently, radiomics have been used to analyze various textural and handcrafted features to classify or predict prognosis of disease through medical images that are beyond the perception of human eye.^{11,12} However, radiomics needs careful preprocessing steps, including delicate segmentation. Deep learning—a subfield in machine learning—extracts information directly from the data, omitting the step of manual feature extraction in decision making.¹³ In the field of neuro-oncology, specifically glioma imaging, previous studies have shown the potential of deep learning for classifying gliomas based on genetic mutations or clinical outcomes.¹⁴⁻¹⁶

In this study, we hypothesized that deep learning may differentiate GBM from solitary brain metastasis without extraction of predefined features. Thus, we aimed to develop a deep learning-based model to differentiate GBM from solitary brain metastasis using preoperative T2-weighted and contrast-enhanced (CE) T1-weighted MR images and further validate its diagnostic performance.

MATERIALS AND METHODS

Patient Population

This retrospective study was approved by the institutional review board of our hospital, which waived the requirement to obtain informed patient consent. The records of 999 consecutive patients with histologically confirmed GBM or brain metastasis between February 2006 and December 2017 were retrospectively reviewed. Among these patients, those with preoperative MR images, including T2-weighted and CE T1WI, were included. Exclusion criteria

included 1) multiple enhancing lesions; 2) patients with absent or inadequate MR images; and 3) patients with previous intracranial intervention, such as operation, gamma knife surgery, or radiation therapy. According to these criteria, 598 patients were included (357 men and 241 women; mean age, 57.4 ± 14.7 years). Fig 1 summarizes the study population selection.

From the total study cohort, 450 patients were randomly selected for model training (300 GBM, 150 metastasis), and 48 patients (32 GBM, 16 metastases) were selected for model validation. The remaining 100 patients (50 GBM, 50 metastases) were left out

on the patient level as an internal test dataset. The MR images of 143 patients (100 GBM, 43 metastases) at an outside tertiary referral hospital were used as an external test dataset; patients who satisfied the same inclusion and exclusion criteria as the internal cohort were extracted from their electronic database between January 2014 and December 2017.

MR Acquisition and Image Preprocessing

Preoperative imaging was performed using 1 of 4 3T MR imaging units (Ingenia or Achieva, Philips Healthcare; Discovery MR750, GE Healthcare; Tim Trio, Siemens) using an 8-channel sensitivity-encoding head coil. Details on the MR scanners and imaging parameters are summarized in the Online Supplemental Data. A diagram of the overall workflow is shown in Fig 2. The CE T1WI and T2WI of each patient were preprocessed, conducting intensity normalization by WhiteStripe normalization and N4 bias field correction. Images were resampled to $1 \times 1 \times 1$ mm isotropic voxels. Preprocessed CE T1WI was coregistered to the T2WI. Rectangular-shaped ROIs were manually drawn on T2WI by a radiologist with 8 years of experience (B.S.) in MR imaging analysis using a conventional software package (MIPAV, National Institutes of Health) and confirmed by another radiologist with 13 years of experience (S.S.A.). ROIs were drawn on every section in which the mass was visualized on preoperative T2WI and included the peritumoral T2 hyperintense area, which was defined as a high signal intensity on T2WI beyond the border of the enhancing tumor portion.

Deep Learning Model

A 2D convolutional neural network (specifically the ResNet-50 model) with 50 layers consisting of 3-layer residual blocks¹⁷ pretrained with the ImageNet database was used. Hyperparameters of the fully connected layer of ResNet were fine-tuned using the training set data, and the convoluting and pooling layers were frozen. The batch size was 64, and a drop-out rate of 0.5 was applied with rectifier linear unit as the activation function. The model was trained for 100 epochs with stochastic gradient descent optimized with the Adam optimizer¹⁸ and the initial learning rate set to 0.001. Batch normalization was used in each layer to improve learning stability.¹⁹ Coregistered CE T1WI and

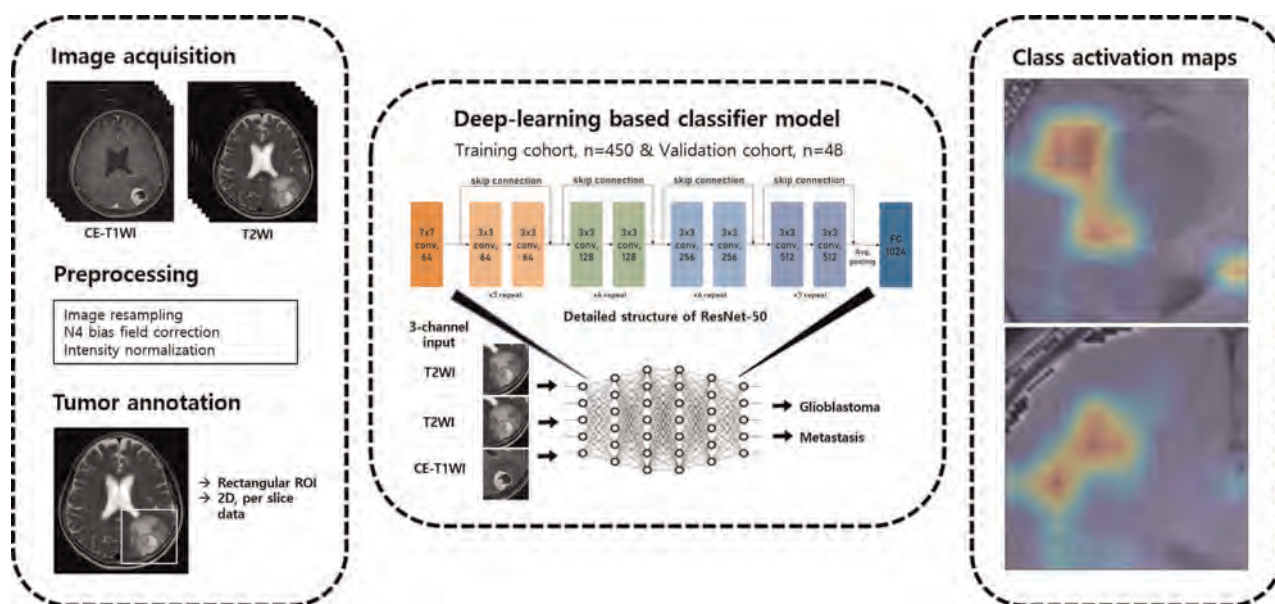


FIG 2. Diagram of overall workflow.

T2WI were used as inputs to 2 of the 3 channels for training of our ResNet model. The same T2WI was inserted again into the last channel of our deep learning. Each section of CE T1WI and corresponding T2WI was treated as an independent image to increase the number of input data even though a group of slices belonged to the same patient. An ensemble learning method based on 5-fold cross-validation was used for model validation with most voting among models for final decision. Data splitting during training of the model was done per patient and not per section image to avoid overlapping bias. Regularization and fine tuning of hyperparameters of our model was done using the validation set ($n = 48$) from our institution. To establish the basis for judgment of our deep learning model, a class activation map was derived from each section of the images. All steps of the methodology were implemented with Python 3.7 and PyTorch v1.2 framework (<https://pytorch.org/>).

The final model was validated in an internal test set. The predictive index was defined as the number of slides classified as GBM by our classification model divided by the total number of slides per patient (ranging from 0 to 1). To determine the optimal cutoff value of the percentage of corrected slides for each patient, receiver operating characteristic (ROC) curves were derived. ROC curves were derived using SPSS version 25 (IBM).

Image Review by Neuroradiologists

The internal and external test datasets were reviewed by both experienced and junior neuroradiologists (S.S.A., neuroradiologist 1) and (I.S., neuroradiologist 2), with 13 and 4 years of experience, respectively. Both neuroradiologists were blinded to the pathologic and clinical information of all patients and were asked to classify each image as either GBM or metastasis, referring to the T2WI and CE T1WI. Subsequently, internal and external test sets were re-evaluated and classified again by both neuroradiologists, this time referring to the classification results of the ResNet-50 model.

Statistical Analysis

Patient demographics were compared between the GBM and metastasis subgroups using the independent 2-sample t test or chi-square test. The classification performance of the classification model and 2 neuroradiologists were evaluated on their accuracy, precision, recall, F1 score, and area under the curve (AUC). The 95% CIs of the precision, recall, and F1 scores were derived using the bootstrapping method with 1000 times 90% random sampling.

All statistical values were derived using SPSS version 25. The bootstrapping method was performed using R version 3.6.2 (<http://www.r-project.org/>). A P value $\leq .05$ was considered statistically significant.

RESULTS

Subjects

A total of 6617 axial slices of tumors from 598 patients with GBM or solitary metastases were included in the analysis. There was no significant difference in age and sex distribution between the GBM and metastasis groups in the internal and external cohorts; however, a higher percentage of patients had infratentorial lesions in the metastasis group (3.4% for the GBM group versus 22.7% for the metastasis group). Patients in the metastasis group included those with various primary tumor subtypes, most of which were lung cancer. The demographics of internal and external test sets are summarized in the Table.

Diagnostic Performance of Deep Learning–Based Model

The optimal cutoff value for the predictive index was 0.55 when the AUC was 0.881 for the ROC curve drawn for the internal test cohort (Fig 3). The accuracy, precision, recall, F1 score, and AUC of the deep learning–based model were 89%, 0.852, 0.939, 0.893, and 0.889 in the internal test cohort and 85.9%, 0.907, 0.889, 0.893, and 0.835 in the external validation, respectively (Online Supplemental Data).

Patient demographics of internal and external cohorts

	Internal Cohort (n = 598)			External Cohort (n = 143)		
	GBM (n = 382)	Metastasis (n = 216)	P Value	GBM (n = 100)	Metastasis (n = 43)	P Value
Age (years) ^a	57.3 ± 15.2	57.5 ± 13.8	.808	57.2 ± 12.8	61.0 ± 10.2	.081
Male sex (%)	223 (58.4)	134 (62.0)	.381	63 (62.4)	25 (56.8)	.633
Supratentorial location (%)	369 (96.9)	167 (77.3)	<.001	98 (97.0)	32 (72.7)	<.001
Primary tumor (%)	—	Lung 91 (42.1) Breast 25 (11.6) GI ^b 46 (21.3) GU ^c 16 (7.4) Others ^d 38 (17.6)	—	—	Lung 20 (45.5) Breast 6 (13.6) GI ^b 7 (15.9) GU ^c 7 (15.9) Others ^d 3 (6.8)	—

^a Mean ± SD.

^b Gastrointestinal (GI) origin includes tumors of colorectal, esophageal, stomach, and hepatic origin.

^c Genitourinary (GU) origin includes tumors of kidney, ovary, and cervix origin.

^d Other origin includes melanoma, head and neck, sarcoma, and unknown primary origin.

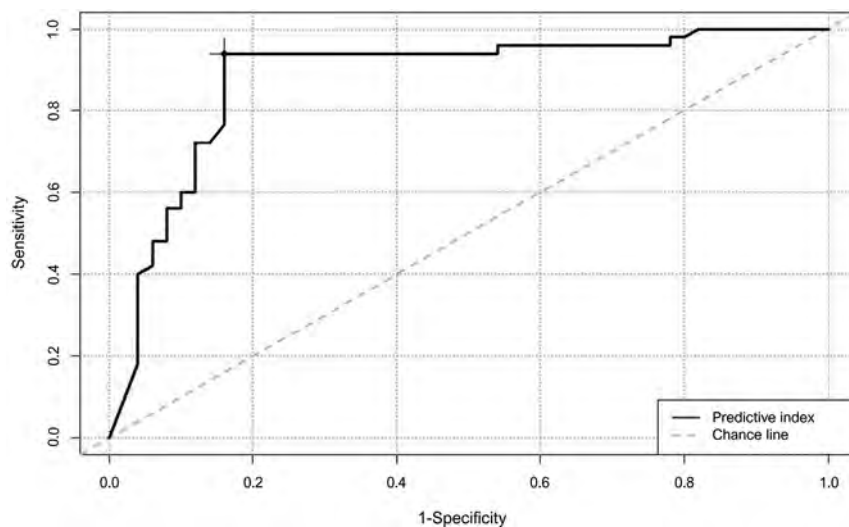


FIG 3. ROC curve for differentiating GBM and metastasis in the internal test set (AUC, 0.881; optimal cutoff for predictive index, 0.55).

In the internal test cohort, 8/50 (16.0%) metastases were misclassified as GBM, and 3/50 (6.0%) GBMs were misclassified as metastases. Similarly, 9/43 (20.9%) metastases were misclassified as GBM, and 12/100 (12.0%) GBMs were misclassified as metastases in the external test cohort. According to tumor location, 83 lesions were located in the supratentorial area, and 17 lesions were located in the infratentorial area in the internal test set. ResNet-50 miscategorized 10.8% (9/83) of the supratentorial lesions and 11.8% (2/17) of the infratentorial lesions. In the external test set, 130 lesions were supratentorial, and 13 lesions were infratentorial. All the infratentorial lesions were correctly categorized by ResNet-50, and all 21 miscategorized lesions were located in the supratentorial area in the external test set.

Because metastases were more prevalent in the cerebellum compared with GBM, our deep learning model seemed to recognize posterior fossa structures included in the ROIs, possibly contributing to the higher classification performance for infratentorial lesions (Figs 4 and 5).

Diagnostic Performance of Neuroradiologists

The accuracy, precision, recall, F1 score, and AUC of neuroradiologist 1 were 88.9%, 0.865, 0.918, 0.891, and 0.889 for the internal test set and 86.6%, 0.926, 0.88, 0.903, and 0.857 for the external test set, respectively. The accuracy, precision, recall, F1 score, and AUC of neuroradiologist 2 were 77%, 0.760, 0.776, 0.768, and 0.768 for the internal test set and 75.3%, 0.828, 0.82, 0.824, and 0.708 for the external test set, respectively (Online Supplemental Data).

Both neuroradiologists showed improved diagnostic performance after referring to the classification results of ResNet-50. The accuracy, precision, recall, F1 score, and AUC of neuroradiologist 1 after referring to ResNet-50 were 92.0%, 0.904, 0.940, 0.922, and 0.920 respectively, for the internal test set and 90.1%, 0.939, 0.920, 0.929, and 0.889 respectively, for the external test set. The accuracy, precision, recall, F1 score, and AUC of neuroradiologist 2 after referring to ResNet-50 were 91.0%, 0.940, 0.887, 0.913, and 0.910, respectively, in the internal test set and 88.0%, 0.895, 0.940, 0.917, and 0.839, respectively, in the external test set (Online Supplemental Data).

DISCUSSION

We proposed a deep learning-based model to differentiate solitary brain metastasis from GBM preoperatively using T2WI and CE T1-weighted conventional MR images. The model was developed using a large study population with varying scan parameters and validated in an external cohort and thus is expected to be robust and reproducible. Also, the classification model showed superior performance to that of the junior neuroradiologist and comparable results with those of the experienced neuroradiologist for both the internal and external test sets. Moreover, the classification model complemented the performance of the neuroradiologists, improving the classification performance of both junior and experienced neuroradiologists referring to the ResNet model.

It was noted that the deep learning-based model more frequently misclassified brain metastasis as GBM than GBM as metastasis. This might be because of the heterogeneity of the metastasis group, which included various primary cancer subtypes. In comparison, the GBM group included a histologically homogeneous group of patients. Although GBMs are known to have unique imaging and radiomics findings depending on their underlying genetic mutation statuses,^{20,21} they are thought to be

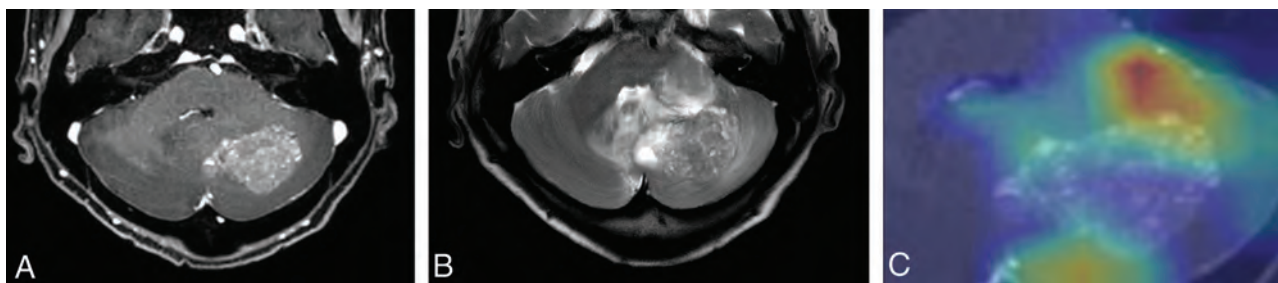


FIG 4. Images of a 65-year-old woman with history of recurrent ovarian cancer and pathologically proved brain metastasis. Contrast-enhanced T1WI (A) shows a heterogeneously enhancing mass in the left cerebellum. B, T2WI shows a perilesional T2 hyperintensity area surrounding the enhancing portion. C, Corresponding class activation maps show that the ResNet-50 model is referring to the mass and perilesional T2 hyperintensity area as well as the surrounding posterior fossa structures. ResNet-50 and both radiologists all correctly classified this lesion as brain metastasis.

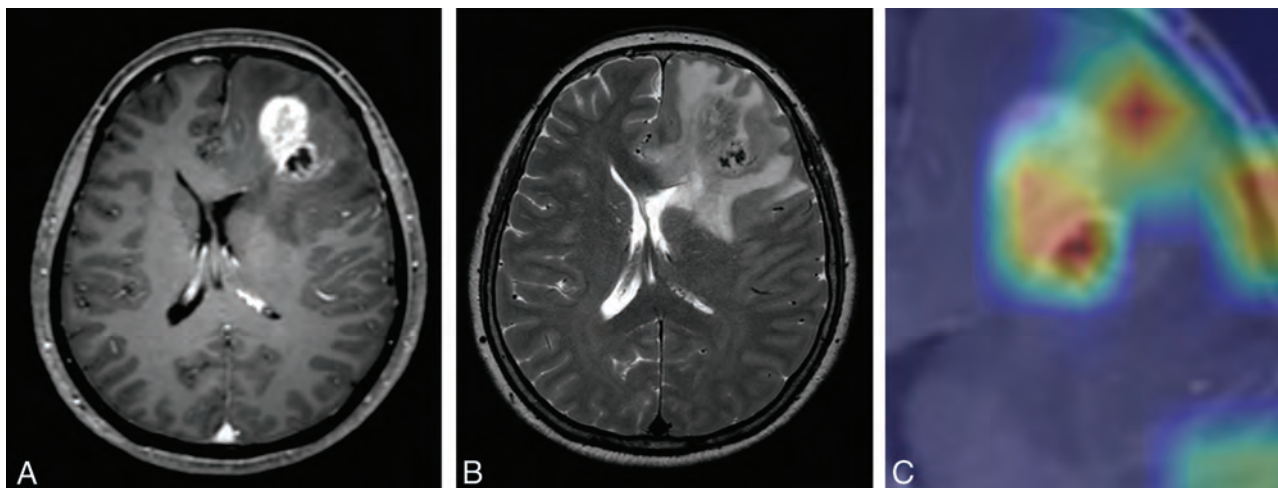


FIG 5. Images of a 62-year-old woman with pathologically proved GBM. CE T1WI (A) and T2WI (B) show an enhancing mass in the left frontal lobe with surrounding perilesional T2 hyperintensity area. Whereas ResNet-50 and radiologist 1 correctly classified this mass as GBM, radiologist 2 misclassified this lesion as metastasis. Corresponding class activation map (C) shows that ResNet-50 is referring to the enhancing portion as well as the surrounding peritumoral T2 hyperintensity areas.

relatively histologically homogeneous compared with metastases, which can have completely different histologic backgrounds.

In conventional deep neural networks, deeper networks are susceptible to the degradation problem, in which the network depth increases and the accuracy subsequently becomes saturated and degrades rapidly. ResNet-50 is a deep learning network that uses a residual learning framework that allows substantially deeper layers for training than that of conventional networks without degradation of performance. This type of deep learning network is capable of extracting more features and thus more accurately analyzing input images compared with conventional deep neural networks. Since its introduction, it has been widely used in various tasks in medical imaging, including detection, classification, and localization,^{22,23} showing comparable or better performance than that of conventional neural networks.^{24,25} Several imaging biomarkers have been studied to distinguish GBM from solitary brain metastasis. In previous studies, the shape of the enhancing portion, the signal intensity, and the extent of the peritumoral T2 hyperintensity were used to differentiate these 2 entities in conventional MR images.^{26,27} In those studies, nonspherical morphology of the enhancing portion and a higher normalized T2 signal intensity of

the peritumoral portion were defining features of GBM. However, these previous studies had limitations in that they were conducted in small study populations.

Recent studies have applied radiomics-based machine learning methods to discriminate between GBM and solitary brain metastasis.^{28–30} Radiomics-based machine learning models were used to preoperatively discriminate between these 2 entities based on CE T1WI. In that study, the best-performing supervised model showed accuracy of 85%.³¹ Another study used radiomics-based machine learning to distinguish between GBM and solitary brain metastasis.³⁰ The researchers collectively investigated the diagnostic performances of 30 diagnostic models, with the 2 best-performing models showing an accuracy of 80%. Although these studies had somewhat promising results, they also had limitations in that the ROIs concentrated solely on the enhancing portions, failing to include data from the peritumoral portion and lacking external validation results. A recent study extracted radiomic features from an enhancing tumor portion and peritumoral T2 hyperintensity area of GBM and solitary brain metastasis and constructed a deep learning model based on these radiomic features.³² The study conducted external validation of the deep

learning model with a high AUC value of 0.956. However, radiomics-based methods have innate limitations in that they include labor-intensive segmentation steps. To date, there is no study using an end-to-end deep learning–based method to discriminate between GBM and solitary brain metastasis. Our method had superior performance compared with those in the aforementioned studies using radiomics-based machine learning methods. Moreover, a strength of our deep learning model was that it could be robustly applied to conventional MR images with roughly drawn rectangular ROIs.

Our study had several limitations. First, instead of a 3D-based analysis, we used a 2D-based deep learning analysis to discriminate between GBM and solitary brain metastasis. However, considering that our training set was rather small ($n = 450$) for deep learning–based algorithm training, we reasoned that training with multiple MR image slices would be more suitable for adequate model training. Moreover, our deep learning model showed good performance in internal as well as external data, showing that our model has been properly trained. Second, because the patients had multiple MR slices, we arbitrarily adopted a new variable termed the “predictive index.” This variable required certain considerations because it was derived from a small internal test set; however, the diagnostic performance after adapting this cutoff in the external validation set demonstrated sustained discrimination performance. Third, in clinical practice, brain masses represent various clinical entities along with GBM and metastasis. These entities, such as lymphoma, demyelinating disease, infarction, and so on, should also be considered and integrated into the classification model in future studies. Finally, our model used only T2WI and CE T1WI, neglecting information from other sequences, such as T2 FLAIR images, and other advanced MR images, such as perfusion- or diffusion-weighted images. In addition, T2 FLAIR images are generally used to evaluate infiltrative nonenhancing glial tissue of GBM from vasogenic edema of brain metastasis. However, the heterogeneity of T2 FLAIR sequences (ie, precontrast versus postcontrast or 2D versus 3D acquisition) in our patient population prevented their use in training our deep learning model. Nevertheless, T2WI and CE T1WI are considered to be the most fundamental MR images and are almost always included in routine MR protocols, thus making our classification model more robust.

CONCLUSIONS

We developed a deep learning–based classification model to discriminate between GBM and solitary brain metastasis using conventional MR images. Our model had a diagnostic performance comparable with that of an experienced radiologist and had a complementary role in discriminating GBM and solitary brain metastasis. Therefore, deep learning may be used as an auxiliary tool for the discrimination of GBM from solitary brain metastasis.

Disclosures: Sung Soo Ahn—RELATED: Grant: Basic Science Research Program through the National Research Foundation of Korea, Comments: 2017RID1A1B03030440*. *Money paid to institution.

REFERENCES

1. Lemke DM. Epidemiology, diagnosis, and treatment of patients with metastatic cancer and high-grade gliomas of the central nervous system. *J Infus Nurs* 2004;27(4):263–9 CrossRef
2. Schiff D. Single brain metastasis. *Curr Treat Options Neurol* 2001;3:89–99 CrossRef Medline
3. Villano JL, Durbin EB, Normandeau C, et al. Incidence of brain metastasis at initial presentation of lung cancer. *Neuro Oncol* 2015;17:122–28 CrossRef Medline
4. Baris MM, Celik AO, Gezer NS, et al. Role of mass effect, tumor volume and peritumoral edema volume in the differential diagnosis of primary brain tumor and metastasis. *Clin Neurol Neurosurg* 2016;148:67–71 CrossRef Medline
5. Wesseling P, Ruiter DJ, Burger PC. Angiogenesis in brain tumors; pathobiological and clinical aspects. *J Neurooncol* 1997;32:253–65 CrossRef Medline
6. Long DM. Capillary ultrastructure in human metastatic brain tumors. *J Neurosurg* 1979;51:53–58 CrossRef Medline
7. Cha S, Lupo JM, Chen MH, et al. Differentiation of glioblastoma multiforme and single brain metastasis by peak height and percentage of signal intensity recovery derived from dynamic susceptibility-weighted contrast-enhanced perfusion MR imaging. *AJNR Am J Neuroradiol* 2007;28:1078–84 CrossRef
8. Skogen K, Schulz A, Helseth E, et al. Texture analysis on diffusion tensor imaging: discriminating glioblastoma from single brain metastasis. *Acta Radiol* 2019;60:356–66 CrossRef Medline
9. Sunwoo L, Yun TJ, You SH, et al. Differentiation of glioblastoma from brain metastasis: qualitative and quantitative analysis using arterial spin labeling MR imaging. *PLoS One* 2016;11:e0166662 CrossRef Medline
10. Law M, Cha S, Knopp EA, et al. High-grade gliomas and solitary metastases: differentiation by using perfusion and proton spectroscopic MR imaging. *Radiology* 2002;222:715–21 CrossRef Medline
11. Chaddad A. Automated feature extraction in brain tumor by magnetic resonance imaging using Gaussian mixture models. *Int J Biomed Imaging* 2015;2015:1–11 CrossRef
12. Chaddad A, Colen R. Statistical feature selection for enhanced detection of brain tumor. *Proc SPIE* 2014;XXXVII:92170V CrossRef
13. Chartrand G, Cheng PM, Vorontsov E, et al. Deep learning: a primer for radiologists. *Radiographics* 2017;37:2113–31 CrossRef Medline
14. Lotan E, Jain R, Razavian N, et al. State of the art: machine learning applications in glioma imaging. *AJR Am J Roentgenol* 2019;212:26–37 CrossRef Medline
15. Chang P, Grinband J, Weinberg BD, et al. Deep-learning convolutional neural networks accurately classify genetic mutations in gliomas. *AJNR Am J Neuroradiol* 2018;39:1201–07 CrossRef
16. Lao J, Chen Y, Li ZC, et al. A deep learning-based radiomics model for prediction of survival in glioblastoma multiforme. *Sci Rep* 2017;7:10353 CrossRef
17. He K, Zhang X, Ren S, et al. Deep residual learning for image recognition. *arXiv* 2016;1512.03385
18. Kingma DP, Ba J. Adam: a method for stochastic optimization. *arXiv* 2014;1412.6980
19. Ioffe S, Szegedy C. Batch normalization: accelerating deep network training by reducing internal covariate shift. *arXiv* 2015;1502.03167
20. Lee MH, Kim J, Kim S-T, et al. Prediction of IDH1 mutation status in glioblastoma using machine learning technique based on quantitative radiomic data. *World Neurosurg* 2019;125:e688–e96 CrossRef Medline
21. Yamashita K, Hiwatashi A, Togao O, et al. MR imaging–based analysis of glioblastoma multiforme: estimation of IDH1 mutation status. *AJNR Am J Neuroradiol* 2016;37:58–65 CrossRef Medline
22. Talo M, Yildirim O, Baloglu UB, et al. Convolutional neural networks for multi-class brain disease detection using MRI images. *Comput Med Imaging Graph* 2019;78:101673 CrossRef
23. Korolev S, Safiullin A, Belyaev M, et al. Residual and plain convolutional neural networks for 3D brain MRI classification. *arXiv* 2017;1701.06643 CrossRef
24. Ardakani AA, Kanafi AR, Acharya UR, et al. Application of deep learning technique to manage COVID-19 in routine clinical practice using CT images: results of 10 convolutional neural networks. *Comput Biol Med* 2020;121:103795 CrossRef Medline

25. Bressen KK, Adams LC, Erxleben C, et al. **Comparing different deep learning architectures for classification of chest radiographs.** *Sci Rep* 2020;10:13590 CrossRef Medline
26. Blanchet L, Krooshof P, Postma G, et al. **Discrimination between metastasis and glioblastoma multiforme based on morphometric analysis of MR images.** *AJNR Am J Neuroradiol* 2011;32:67–73 CrossRef Medline
27. Chen XZ, Yin XM, Ai L, et al. **Differentiation between brain glioblastoma multiforme and solitary metastasis: qualitative and quantitative analysis based on routine MR imaging.** *AJNR Am J Neuroradiol* 2012;33:1907–12 CrossRef Medline
28. Tateishi M, Nakaura T, Kitajima M, et al. **An initial experience of machine learning based on multi-sequence texture parameters in magnetic resonance imaging to differentiate glioblastoma from brain metastases.** *J Neurol Sci* 2020;410:116514 CrossRef Medline
29. Swinburne NC, Schefflein J, Sakai Y, et al. **Machine learning for semi-automated classification of glioblastoma, brain metastasis and central nervous system lymphoma using magnetic resonance advanced imaging.** *Ann Transl Med* 2019;7:232 CrossRef Medline
30. Qian Z, Li Y, Wang Y, et al. **Differentiation of glioblastoma from solitary brain metastases using radiomic machine-learning classifiers.** *Cancer Lett* 2019;451:128–35 CrossRef Medline
31. Artzi M, Bressler I, Ben Bashat D. **Differentiation between glioblastoma, brain metastasis and subtypes using radiomics analysis.** *J Magn Reson Imaging* 2019;50:519–28 CrossRef Medline
32. Bae S, An C, Ahn SS, et al. **Robust performance of deep learning for distinguishing glioblastoma from single brain metastasis using radiomic features: model development and validation.** *Sci Rep* 2020;10:12110 CrossRef Medline

MRI-Based Deep-Learning Method for Determining Glioma *MGMT* Promoter Methylation Status

C.G.B. Yogananda, B.R. Shah, S.S. Nalawade, G.K. Murugesan, F.F. Yu, M.C. Pinho, B.C. Wagner, B. Mickey, T.R. Patel, B. Fei, A.J. Madhuranthakam, and J.A. Maldjian



ABSTRACT

BACKGROUND AND PURPOSE: *O*⁶-Methylguanine-DNA methyltransferase (*MGMT*) promoter methylation confers an improved prognosis and treatment response in gliomas. We developed a deep learning network for determining *MGMT* promoter methylation status using T2 weighted Images (T2WI) only.

MATERIALS AND METHODS: Brain MR imaging and corresponding genomic information were obtained for 247 subjects from The Cancer Imaging Archive and The Cancer Genome Atlas. One hundred sixty-three subjects had a methylated *MGMT* promoter. A T2WI-only network (*MGMT*-net) was developed to determine *MGMT* promoter methylation status and simultaneous single-label tumor segmentation. The network was trained using 3D-dense-UNets. Three-fold cross-validation was performed to generalize the performance of the networks. Dice scores were computed to determine tumor-segmentation accuracy.

RESULTS: The *MGMT*-net demonstrated a mean cross-validation accuracy of 94.73% across the 3 folds (95.12%, 93.98%, and 95.12%, [SD, 0.66%]) in predicting *MGMT* methylation status with a sensitivity and specificity of 96.31% [SD, 0.04%] and 91.66% [SD, 2.06%], respectively, and a mean area under the curve of 0.93 [SD, 0.01]. The whole tumor-segmentation mean Dice score was 0.82 [SD, 0.008].

CONCLUSIONS: We demonstrate high classification accuracy in predicting *MGMT* promoter methylation status using only T2WI. Our network surpasses the sensitivity, specificity, and accuracy of histologic and molecular methods. This result represents an important milestone toward using MR imaging to predict prognosis and treatment response.

ABBREVIATIONS: *IDH* = isocitrate dehydrogenase; *MGMT* = *O*⁶-methylguanine-DNA methyltransferase; PCR = polymerase chain reaction; T2WI = T2 weighted Images; TCGA = The Cancer Genome Atlas; TCIA = The Cancer Imaging Archive

*O*⁶-methylguanine-DNA methyltransferase (*MGMT*) promoter methylation is a molecular biomarker of gliomas that has prognostic and therapeutic implications. Unlike *isocitrate dehydrogenase* (*IDH*) mutations and 1p/19q co-deletions, *MGMT* promoter methylation is an *epigenetic* event. Epigenetic events are functionally relevant but do not involve a change in the nucleotide sequence. Therefore, while *MGMT* promoter methylation is an important prognostic marker, it does not

define a distinct subset of gliomas. *MGMT* is a DNA repair enzyme that protects normal and glioma cells from alkylating chemotherapeutic agents. The methylation of the *MGMT* promoter is an example of *epigenetic silencing*, which results in a loss of function of the *MGMT* enzyme and its protective effect on glioma cells. The survival benefit incurred by *MGMT* promoter methylation in patients treated with temozolomide (TMZ) was determined in 2005.¹ Subsequent work by Stupp et al² has shown that in patients who received both radiation and temozolomide, *MGMT* promoter methylation improved median survival compared with patients with unmethylated gliomas (21.7 versus 12.7 months).² Long-term follow-up from that initial study has further substantiated the survival benefit.^{2,3} As a result, determining *MGMT* promoter methylation status is an important step in predicting survival and determining treatment.

Currently, the only reliable way to determine *MGMT* promoter methylation status requires analysis of glioma tissue obtained either via an invasive brain biopsy or following open surgical resection. Surgical procedures carry the risk of neurologic injury and

Received June 24, 2020; accepted after revision November 21.

From the Advanced Neuroscience Imaging Research Lab (C.G.B.Y., B.R.S., S.S.N., G.K.M., F.F.Y., M.C.P., B.C.W., A.J.M., J.A.M.), Department of Radiology, and Department of Neurological Surgery (B.M., T.R.P.), University of Texas Southwestern Medical Center, Dallas, Texas; and Department of Bioengineering (B.F.), University of Texas at Dallas, Richardson, Texas.

This work was supported by National Institutes of Health/National Cancer Institute U01CA207091 (A.J.M., J.A.M.).

Please address correspondence to Joseph A. Maldjian, MD, Department of Radiology, UT Southwestern Medical Center, 5323 Harry Hines Blvd, Dallas, TX 75390-9178; e-mail: joseph.maldjian@utsouthwestern.edu

Indicates open access to non-subscribers at www.ajnr.org

Indicates article with online supplemental data.

<http://dx.doi.org/10.3174/ajnr.A7029>

Cross-validation results

Fold Description	MGMT-Net		
Fold Number	% Accuracy	AUC	Dice score
Fold 1	95.12	0.9574	0.8140
Fold 2	93.98	0.8978	0.8165
Fold 3	95.12	0.9390	0.8291
Average	94.73	0.93	0.82
	[SD, 0.66]	[SD, 0.03]	[SD, 0.008]

Note:—AUC indicates area under the curve.

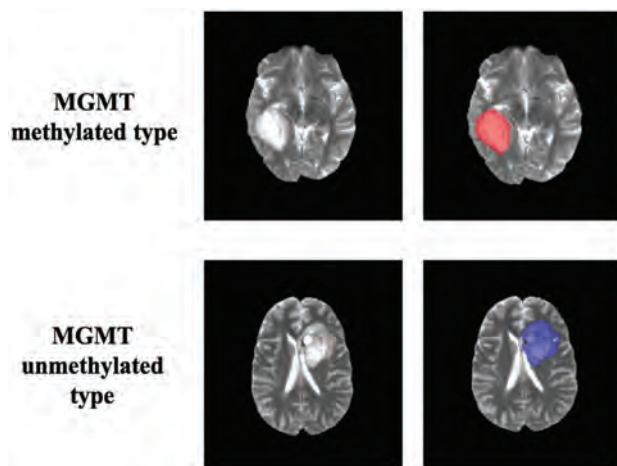


FIG 1. Ground truth whole-tumor masks. Red voxels represent methylated *MGMT* promoter status (values of 1) and blue voxels represent unmethylated *MGMT* promoter status (values of 2). The ground truth labels have the same *MGMT* promoter status for all voxels in each tumor.

complications. Therefore, considerable attention has been dedicated to developing noninvasive, image-based diagnostic methods to determine *MGMT* promoter methylation status. A meta-analysis of MR imaging features demonstrated that glioblastomas with methylated *MGMT* promoters were associated with less edema, high ADC, and low perfusion. However, the summary sensitivity and specificity of these clinical features was only 79% and 78%, respectively.⁴ Although multiple radiomic approaches have also been attempted for *MGMT* prediction, none, to date, have achieved accuracies sufficient for clinical viability.^{5–9} Sasaki et al¹⁰ attempted to establish an MR imaging–based radiomic model for predicting *MGMT* promoter status of the tumor, but it reached a predictive accuracy of only 67%. Wei et al¹¹ extracted radiomic features from the tumor and peritumoral edema using multisequence, postcontrast MR imaging but only achieved an accuracy of 51%–74% in predicting *MGMT* promoter methylation status in astrocytomas. Drabycz et al⁵ performed texture analysis on MR images to predict *MGMT* promoter methylation status in glioblastoma, but it reached an accuracy of only 71%. Korfiatis et al⁹ combined texture features with supervised classification schemes as potential imaging biomarkers for predicting the *MGMT* methylation status of glioblastoma multiforme, but they achieved a sensitivity and specificity of only 0.803 and 0.813, respectively. Ahn et al⁷ used dynamic contrast-enhanced MR imaging and diffusion tensor imaging to predict *MGMT* promoter methylation in glioblastoma, but this method

achieved a sensitivity and specificity of only 56.3% and 85.2%, respectively.

Recent advances in deep learning methods have also been used for noninvasive, image-based molecular profiling. Our group has previously demonstrated highly accurate, MR imaging–based, voxelwise, deep learning networks for determining *IDH* classification and 1p/19q co-deletion status using only T2WI.^{12,13} The benefits of using T2WIs are that they are routinely acquired, they can be obtained quickly, and high quality T2WI can even be obtained in the setting of motion degradation. Because *MGMT* promoter methylation in gliomas is such an important biomarker, we sought to develop a highly accurate, fully automated deep learning 3D network for *MGMT* promoter determination of methylation status using only T2WI.

MATERIALS AND METHODS

Data and Preprocessing

Multiparametric MR images of patients with brain gliomas were obtained from The Cancer Imaging Archive (TCIA) data base.^{14,15} The genomic information was obtained from both The Cancer Genome Atlas (TCGA) and TCIA data bases.^{14,16,17} Subject datasets were screened for the availability of preoperative MR images, T2WI, and known *MGMT* promoter status. The final dataset of 247 subjects included 163 methylated cases and 84 unmethylated cases. TCGA subject identification, *MGMT* status, and tumor grade are listed in Table 1 of the Online Supplemental Data.

Tumor masks for 179 subjects were available through previous expert segmentation.^{18–20} Tumor masks for the remaining 68 subjects were generated by our previously trained 3D-*IDH* network and were reviewed by 2 neuroradiologists for accuracy.²⁰ These tumor masks were used as ground truth for tumor segmentation in the training step. Ground truth whole-tumor masks for methylated and unmethylated *MGMT* promoter type were labeled with 1's and 2's, respectively (Fig 1). Data preprocessing steps included the following: 1) the Advanced Normalization Tools software package (<http://stnava.github.io/ANTs/>) affine coregistration²¹ to the SRI24 T2 template,²² 2) skull stripping using the Brain Extraction Tool (BET; <http://fsl.fmrib.ox.ac.uk/fsl/fslwiki/BET>)²³ from FSL,^{23–26} 3) removing radiofrequency inhomogeneity using N4 Bias Field Correction (https://simpleitk.readthedocs.io/en/master/link_N4BiasFieldCorrection_docs.html),²⁷ and 4) normalizing intensity to zero-mean and unit variance. The preprocessing took <5 minutes per dataset.

Network Details

Transfer learning for determination of *MGMT* promoter status was implemented using our previously trained 3D-*IDH* network.²⁰ The decoder part of the network was fine-tuned for a voxelwise dual-class segmentation of the whole tumor, with 1 and 2 representing methylated and unmethylated *MGMT* promoter types, respectively. The network architecture is shown in Fig 2B. A detailed schematic of the network is provided in the Online Supplemental Data.

Network Implementation and Cross-Validation

To generalize the network's performance, we performed a 3-fold cross-validation. The dataset of 247 subjects was randomly shuffled

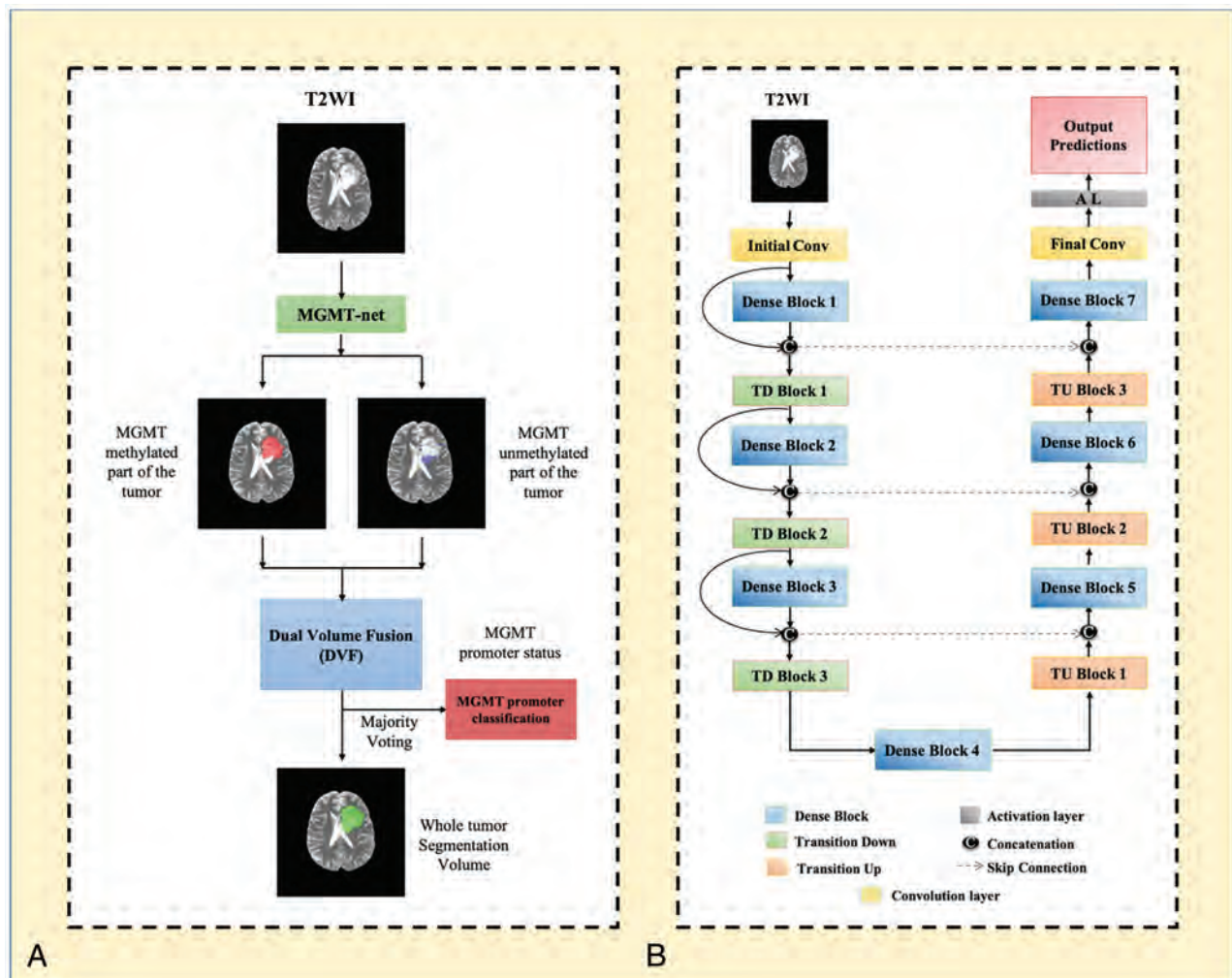


FIG 2. A, MGMT-net overview. Voxelwise classification of MGMT promoter status is performed to create 2 volumes (methylated and unmethylated MGMT promoter). Volumes are combined using Dual Volume Fusion to eliminate false-positives and generate a tumor-segmentation volume. Majority voting across voxels is used to determine the overall MGMT promoter status. B, Network architecture for MGMT-net. 3D-dense-UNets are used with 7 dense blocks, 3 transition-down (TD) blocks, and 3 transition-up (TU) blocks. Conv indicates convolution layer.

and distributed into 3 groups (approximately 82 subjects for each group). Group 1 had 82 subjects (54 methylated, 28 unmethylated), group 2 had 83 subjects (55 methylated, 28 unmethylated), and group 3 had 82 subjects (54 methylated, 28 unmethylated). The 3 groups alternated among training, in-training validation, and held-out testing groups so that each fold of the cross-validation was a new training phase based on a unique combination of the 3 groups. The network uses the in-training validation dataset to evaluate its learning after each training round and updates model parameters to improve performance. However, the network performance is reported only on the held-out testing group for each fold because it is never seen by the network. The group membership for each cross-validation fold is listed in the Online Supplemental Data.

Seventy-five percent overlapping 3D patches (size: $32 \times 32 \times 32$ voxels) were extracted from the training and in-training validation dataset. The patch extraction was performed as a translation in the x-y-z-plane. During training, only patches with at least 1 tumor voxel were included; thus, the number of patches included per training cases varied depending on the size of the

tumor. For testing however, the entire image was sampled, including background masked voxels (of value zero). No patch from the same subject was mixed with the training, in-training validation, or testing datasets to prevent the problem of data leakage.^{28,29} Data augmentation steps included horizontal and vertical flipping, random and translational rotation, the addition of salt and pepper noise, the addition of Gaussian noise, and projective transformation. Additional data augmentation steps included down-sampling images by 50% and 25% (reducing the voxel resolution to 2 and 4 mm³). The data augmentation provided a total of approximately 300,000 patches for training and 300,000 patches for in-training validation for each fold. The networks were implemented using the Tensorflow³⁰ backend engine, the Keras³¹ Python package, and an Adaptive Moment Estimation optimizer (Adam).³² The initial learning rate was set to 10^{-5} with a batch size of 15 and maximal epochs of 100 for each fold.

MGMT-net outputs 2 segmentation volumes (V1 and V2), which are combined to generate the voxelwise prediction of methylated and unmethylated MGMT promoter tumor voxels, respectively. The 2 volumes are fused, and the largest connected

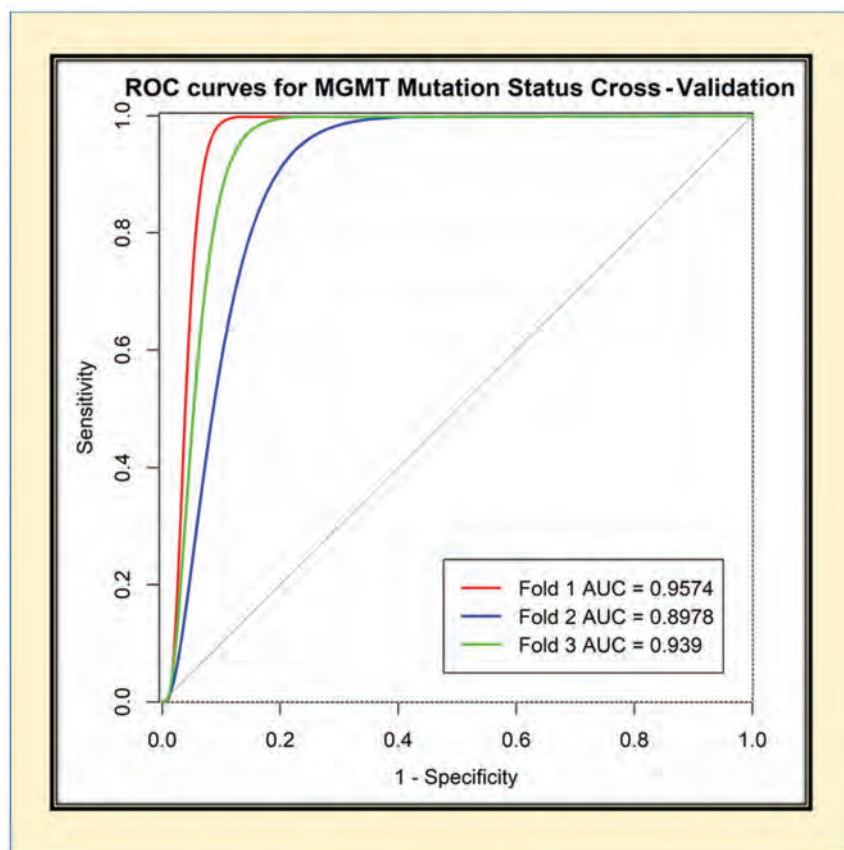


FIG 3. Receiver operating characteristic (ROC) analysis for *MGMT*-net. Separate curves are plotted for each cross-validation fold along with corresponding area under the curve (AUC) value.

component (the 3D-connected component algorithm in Matlab [MathWorks]) is obtained as the single tumor-segmentation map. Majority voting over the voxelwise classes of methylated or unmethylated type provided a single *MGMT* promoter classification for each subject. Tesla V100s, P100, P40, and K80 NVIDIA-GPUs were used to implement the networks. This *MGMT* promoter determination process is fully automated, and a tumor segmentation map is a natural output of the voxelwise classification approach.

Statistical Analysis

Statistical analysis of the network's performance was performed in Matlab and R statistical and computing software (<http://www.r-project.org/>). Network accuracies were evaluated using majority voting (ie, a voxelwise cutoff of 50%). The accuracy, sensitivity, specificity, positive predictive value, and negative predictive value of the model for each fold of the cross-validation procedure were calculated using this threshold. Receiver operating characteristic curves for each fold were generated separately. Dice scores were calculated to evaluate the tumor-segmentation performance of the networks. The Dice score calculates the spatial overlap between the ground truth segmentation and the network segmentation.

RESULTS

The network achieved a mean cross-validation testing accuracy of 94.73% across the 3 folds (95.12%, 93.98%, and 95.12% [SD,

0.66%]). Mean cross-validation sensitivity, specificity, positive predictive value, negative predictive value, and area under the curve for the *MGMT*-net was 96.31% [SD, 0.04%], 91.66% [SD, 2.06%], 95.74% [SD, 0.95%], 92.76% [SD, 0.15%], and 0.93 [SD, 0.03], respectively. The mean cross-validation Dice score for tumor segmentation was 0.82 [SD, 0.008] (Table). The network misclassified 4 cases for fold one, 5 cases for fold 2, and 4 cases for fold three (13 total of 247 subjects). Six subjects were misclassified as unmethylated, and 7, as methylated.

Receiver Operating Characteristic Analysis

The receiver operating characteristic curves for each cross-validation fold for the network are provided in Fig 3. The network demonstrated very good performance with high sensitivities and specificities.

Voxelwise Classification

The network is a voxelwise classifier with the tumor segmentation map being a natural output. Figure 4 shows examples of the voxelwise classification for methylated and unmethylated *MGMT* promoter types, respectively. The volume-fusion procedure was effective in removing false-positives and improving the Dice scores by approximately 6%. We also computed the voxelwise accuracy for the network. The mean voxelwise accuracies were 81.68% [SD, 0.02%] for methylated type and 70.83% [SD, 0.04%] for unmethylated type.

The network is a voxelwise classifier with the tumor segmentation map being a natural output. Figure 4 shows examples of the voxelwise classification for methylated and unmethylated *MGMT* promoter types, respectively. The volume-fusion procedure was effective in removing false-positives and improving the Dice scores by approximately 6%. We also computed the voxelwise accuracy for the network. The mean voxelwise accuracies were 81.68% [SD, 0.02%] for methylated type and 70.83% [SD, 0.04%] for unmethylated type.

Training and Segmentation Times

Fine-tuning the network took approximately 1 week. The trained network took approximately 3 minutes to segment the whole tumor and determine the *MGMT* status for each subject.

DISCUSSION

We developed a fully-automated, highly accurate, deep learning network for determining the methylation status of the *MGMT* promoter that outperforms previously reported algorithms.³³⁻³⁵ Our network is able to determine *MGMT* promoter methylation status from T2WI alone. This eliminates potential failures from image-acquisition artifacts and makes clinical translation straightforward because T2WI is routinely obtained as part of standard clinical brain MR imaging. Previous approaches have required multicontrast input, which can be compromised due to patient motion from lengthier examination times and the need for gadolinium contrast. Obviating the need for intravenous contrast makes our algorithm applicable to patients with contrast allergies and renal failure. Compared with previously published algorithms, our

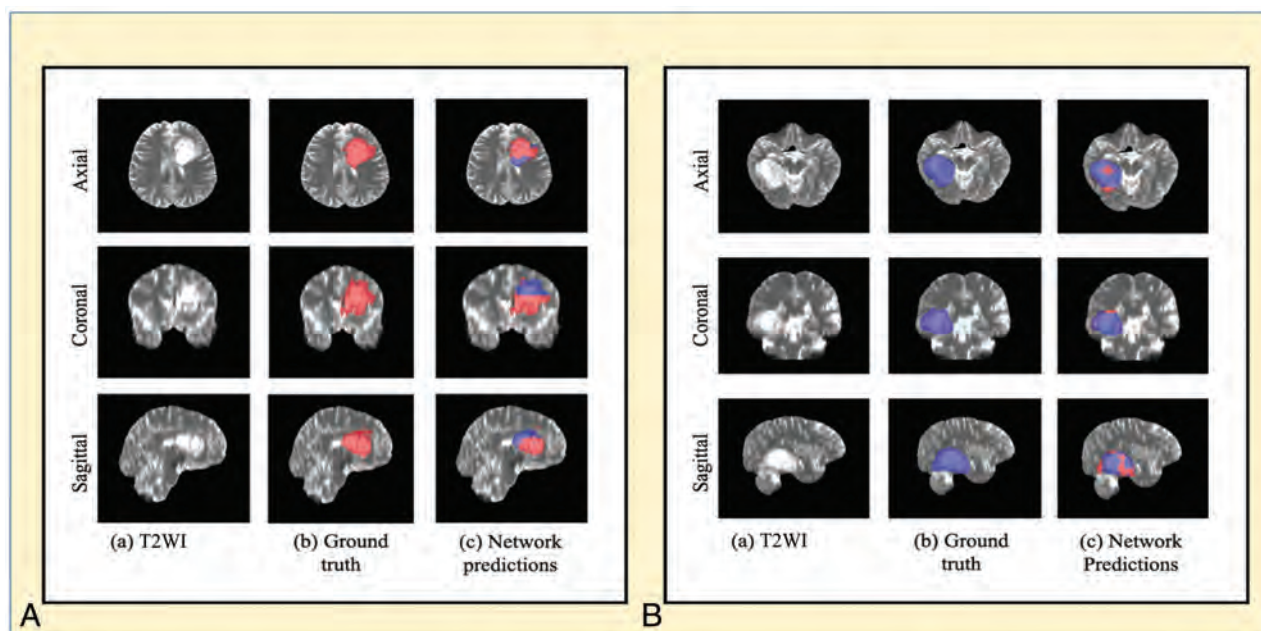


FIG 4. A, An example of voxelwise segmentation for a tumor with a methylated *MGMT* promoter: native T2WI (a), ground truth segmentation (b), and network output after Dual Volume Fusion (c). *Red voxels* correspond to *MGMT* methylated class, and *blue voxels* correspond to *MGMT* unmethylated class. B, An example of voxelwise segmentation for a tumor with an unmethylated *MGMT* promoter. The sharp borders visible between methylated and unmethylated types result from the patch-wise classification approach.

methodology is fully automated and uses minimal preprocessing. The time required for the *MGMT*-net to segment the whole tumor and predict the *MGMT* promoter methylation status for 1 subject is approximately 3 minutes on a K80 or P40 NVIDIA-GPU.

Other groups have also proposed deep learning methods for noninvasive, image-based *MGMT* molecular profiling, but each of these has several limitations. Korfiatis et al⁹ implemented a 2D-based slice-wise network, pre-selecting only cases of glioblastoma multiforme for training and prediction. While they achieved a high slice-wise accuracy, their average subject-wise *MGMT* prediction accuracy was only 90%. Most important, in clinical practice, the tumor grade is unknown a priori. Thus, the approach of Korfiatis et al is a nonviable clinical method from the outset. Our approach of using a mix of low-grade and high-grade gliomas is a better approximation of the real-world clinical workflow in which tissue is not yet available.

Similar to the work of Korfiatis et al, Chang et al³⁵ also implemented a 2D-network, but instead used a case mix like ours (low-grade and high-grade gliomas from the TCIA/TCGA). However, they were only able to achieve an *MGMT* prediction accuracy of 83% (range, 76%–88%), and their network required tumor presegmentation. Our algorithm far outperformed the approach of Chang et al on a similar dataset without the need for presegmentation. Additionally, it is unclear whether 2D algorithms of either Korfiatis et al⁹ or Chang et al³⁵ addressed the issue of “data leakage.”^{28,29} This is a potentially significant limitation for 2D networks that can occur during the slice-wise randomization process if different slices of the same tumor from the same subject are mixed among training, validation, and testing datasets. Unless this is explicitly addressed during the slice-randomization

procedure, the reported accuracies can be upwardly biased. Our approach outperforms all prior reports on noninvasive determination of *MGMT* status and is the first to achieve tissue-level performance, representing a milestone in the clinical viability of MR imaging-based *MGMT* promoter status prediction.

The higher performance achieved by our network compared with previous image-based classification studies can be explained by several factors. The dense connections in our 3D network architecture are easier to train, carry information from the previous layers to the following layers, and can reduce over-fitting.^{36,37} 3D networks also interpolate between slices to maintain interslice information more accurately. The Dual Volume Fusion postprocessing step improved the Dice scores by approximately 6% by eliminating extraneous voxels not connected to the tumor. Our approach also uses voxelwise classifiers and provides a classification for each voxel in the image. These steps provide simultaneous single-label tumor segmentation. The cross-validation single-label whole-tumor segmentation performance for the *MGMT* network provided excellent Dice scores of 0.82 [SD, 0.008].

The ability to determine *MGMT* promoter methylation status on the basis of MR images alone is clinically significant because it helps determine whether the glioma will be susceptible to temozolomide (TMZ). Alkylating agents such as temozolomide damage DNA by methylating the oxygen at position 6 of the guanine nucleotide (O⁶-methylguanine). The process by which many DNA repair enzymes remove O⁶-methylguanine, results in DNA breaks, culminating in cell death. However, *MGMT* works differently by restoring the normal guanine residue and rescuing the glioma cell. Therefore, *MGMT* activity leads to resistance to therapy. Methylation of the *MGMT* promoter leads to inactivation of

MGMT and loss of resistance of glioma cells to alkylating agents. The *MGMT* protein is encoded on the long arm of chromosome 10 at position 26 (10q26). Transcription of the *MGMT* gene is regulated by several promoters.²⁹

Although incompletely understood, at least 9 specific regions within the promoter's gene determine whether a cell will express or not express *MGMT*.²⁹ However, some regions have been shown to be more important for loss of *MGMT* expression.³⁸ In the clinical setting, methods for determining *MGMT* methylation focus on these regions in the promoter gene. The 4 most prevalent methods to detect *MGMT* methylation are the following: immunohistochemistry, pyrosequencing, quantitative methylation-specific polymerase chain reaction (PCR), and methylation-specific PCR. Pyrosequencing is considered the theoretic criterion standard but is not readily available, and although it is quantitative, there is no agreement on what cutoff values to use when determining *MGMT* promoter methylation status.³⁰ Therefore, although it is not quantitative, methylation-specific PCR is the most widely used method.³⁹ Additionally, most centers perform *MGMT* methylation detection on formalin-fixed or paraffin-embedded tissue specimens. These methods have several limitations. Evaluating multiple different methylation sites is technically challenging on a single tissue specimen.³⁹ Tumor heterogeneity poses a substantial limitation of these methods because sampling bias can lead to inaccurate determinations. The presence of hemorrhage, necrosis, or nonmalignant cells contaminates the specimen.³⁹ Therefore, some institutions mandate that at least 50% of the sample to be analyzed contains tumor cells. Prior to PCR, several tissue-processing steps are required. Bisulfite treatment is the most critical step because it will produce the modified DNA that will be used for PCR; however, it also degrades the amount of DNA available, and incomplete treatment can lead to false-positive results.³⁹ The reported sensitivity and specificity of methylation-specific PCR is 91% and 75%, respectively, while the reported sensitivity and specificity of pyrosequencing is 78% and 90%.³²

Our noninvasive, MR imaging-based deep learning algorithm outperformed these methods with a sensitivity and specificity of 96.3% and 91.6%, respectively. The overall determination of *MGMT* promoter methylation status is based on the majority voxels in the tumor. Given the variability in the cutoff values for pyrosequencing-based detection, we performed a Youden statistical index analysis to determine whether the optimal cutoff for our deep learning algorithm was different from majority voting (>50%). The analysis demonstrated that maximum accuracy, sensitivity, specificity, positive predictive value, and negative predictive value were obtained at an optimal cutoff of 50%, the same as majority voting.

Our algorithm was trained on ground truth obtained from the TCGA data base. TCGA uses the Infinium Methylation Assay (<https://www.illumina.com/science/technology/microarray/infinium-methylation-assay.html>) to determine *MGMT* promoter methylation status.^{40–42} Infinium Methylation Assays are an immunofluorescence method that uses next-generation high-throughput microchip arrays and probes. While these methods have been reported to be more sensitive and specific than the most widely available clinical assays, they require pre-existing probes to detect specific methylation sites.⁴² The sensitivity and

specificity values change depending on the probe and analytic model used to interpret the results.⁴² The sensitivities for the best probes range from 87.5% to 90.6%, while the specificity is 94.4%.⁴² The overall accuracy of these probes with an optimized analytic model ranges from 91.24% to 93.6%.³⁴ The accuracy of the commercially available Infinium Methylation Assay with the best analytic model is 92%.³⁴ Our algorithm outperforms this assay with a mean cross-validation testing accuracy of 94.73%. While the algorithm appears to outperform the ground truth, there are additional factors that need to be considered for this dataset. The TCGA data base used very stringent tissue screening before molecular testing, including review of tissue to ensure a minimum of 80% tumor nuclei and a maximum of 50% necrosis with additional quality-control measurements of the extracted DNA and RNA before analyses. Additionally, the *MGMT* determinations made in the TCGA data base were verified by a secondary test.⁴³ Thus, the reported accuracy of the Infinium Methylation Assay is not necessarily comparable with the accuracy in TCIA/TCGA datasets. It is also possible that the algorithm learns features that allow it to perform better than the single-site tissue-biopsy sample ground truth performance because the algorithm “samples” the entire tumor and learns imaging features that are specific to *MGMT* mutation.

Tissue-based methods for determining *MGMT* promoter methylation status remain a complex, multistep process that is susceptible to failure and inaccuracy even after an adequate tissue sample has been obtained. Thus, the ability to determine *MGMT* promoter methylation status on the basis of routine T2WI alone is highly desirable. Additionally, because our algorithm was trained and evaluated on the multi-institutional TCIA database, it is a better representative of algorithm robustness, real-world performance, and potential clinical use than the previously reported methods.²⁵

The algorithm misclassified 13 cases: Six subjects were misclassified as unmethylated, and 7, as methylated. Despite these misclassifications, our network achieved a mean cross-validation testing accuracy of 94.73%, which is higher than that for the methylation-specific PCR, pyrosequencing (PYR), and Infinium Methylation Assays.⁴² While these tissue-based methods require an invasive procedure and subsequent tissue processing for at least 48 hours, our deep learning algorithm can segment the entire glioma and determine *MGMT* promoter methylation status in 3 minutes. The deep learning algorithm can also be fine-tuned to variations in institutional MR imaging scanners, while other tissue-based methods currently lack standardization as mentioned above.

The limitations of our study are that deep learning studies require large amounts of data and the relative number of subjects with *MGMT* promoter methylation is small in the TCGA database. While the number of subjects may seem small, we used a patch-based algorithm with data augmentation, which provided well over 300,000 samples (patches) for training and validation. Additionally, acquisition parameters and imaging vendor platforms vary across imaging centers that contribute data, though this may also be regarded as a desirable aspect for the generalizability of the approach. Our current classification approach uses a largest connected component step to limit false-positives. As a

consequence, multifocal tumors represent a potential limitation. Despite these caveats, our algorithm demonstrated high accuracy in determining *MGMT* promoter methylation status approaching tissue-level performance.

CONCLUSIONS

We demonstrate high accuracy in determining *MGMT* promoter methylation status using only T2WI. This represents an important milestone toward using MR imaging to predict glioma histology, prognosis, and appropriate treatment.

ACKNOWLEDGMENTS

We thank Yin Xi, PhD, a statistician, for help with the receiver operating characteristics and areas under the curve.

Disclosures: Chandan Ganesh Bangalore Yogananda—UNRELATED: Employment: University of Texas Southwestern Medical Center. Baowei Fei—RELATED: Grant: National Institutes of Health. Comments: This research was supported, in part, by the US National Institutes of Health grants (R01CA156775, R01CA204254, R01HL140325, and R21CA231911) and by the Cancer Prevention and Research Institute of Texas grant RP190588.* Ananth J. Madhuranthakam—RELATED: Grant: National Institutes of Health/National Cancer Institute. Comments: U01CA207091.* Joseph A. Maldjian—RELATED: Grant: National Institutes of Health/National Cancer Institute grant*; UNRELATED: Consultancy: BioClinica, Comments: blinded clinical trial reader. *Money paid to the institution.

REFERENCES

- Hegi ME, Diserens AC, Gorlia T, et al. *MGMT* gene silencing and benefit from temozolomide in glioblastoma. *N Engl J Med* 2005;352:997–1003 CrossRef Medline
- Stupp R, Hegi ME, Mason WP, et al. European Organisation for Research and Treatment of Cancer Brain Tumour and Radiation Oncology Groups. Effects of radiotherapy with concomitant and adjuvant temozolomide versus radiotherapy alone on survival in glioblastoma in a randomised phase III study: 5-year analysis of the EORTC-NCIC trial. *Lancet Oncol* 2009;10:459–66 CrossRef Medline
- Chen R, Smith-Cohn M, Cohen AL, et al. Glioma subclassifications and their clinical significance. *Neurotherapeutics* 2017;14:284–97 CrossRef Medline
- Suh CH, Kim HS, Jung SC, et al. Clinically relevant imaging features for *MGMT* promoter methylation in multiple glioblastoma studies: a systematic review and meta-analysis. *AJNR Am J Neuroradiol* 2018;39:1439–45 CrossRef Medline
- Drabycz S, Roldan G, de Robles P, et al. An analysis of image texture, tumor location, and *MGMT* promoter methylation in glioblastoma using magnetic resonance imaging. *Neuroimage* 2010;49:1398–1405 CrossRef Medline
- Moon WJ, Choi JW, Roh HG, et al. Imaging parameters of high grade gliomas in relation to the *MGMT* promoter methylation status: the CT, diffusion tensor imaging, and perfusion MR imaging. *Neuroradiology* 2012;54:555–63 CrossRef Medline
- Ahn SS, Shin NY, Chang JH, et al. Prediction of methylguanine methyltransferase promoter methylation in glioblastoma using dynamic contrast-enhanced magnetic resonance and diffusion tensor imaging. *J Neurosurg* 2014;121:367–73 CrossRef Medline
- Kanas VG, Zacharaki EI, Thomas GA, et al. Learning MRI-based classification models for *MGMT* methylation status prediction in glioblastoma. *Comput Methods Programs Biomed* 2017;140:249–57 CrossRef Medline
- Korfiatis P, Kline TL, Coufalova L, et al. MRI texture features as biomarkers to predict *MGMT* methylation status in glioblastomas. *Med Phys* 2016;43:2835–44 CrossRef Medline
- Sasaki T, Kinoshita M, Fujita K, et al. Radiomics and *MGMT* promoter methylation for prognostication of newly diagnosed glioblastoma. *Sci Rep* 2019;9:14435 CrossRef Medline
- Wei J, Yang G, Hao X, et al. A multi-sequence and habitat-based MRI radiomics signature for preoperative prediction of *MGMT* promoter methylation in astrocytomas with prognostic implication. *Eur Radiol* 2019;29:877–88 CrossRef Medline
- Yogananda CG, Shah BR, Yu FF, et al. A novel fully automated MRI-based deep-learning method for classification of 1p/19q co-deletion status in brain gliomas. *Neurooncol Adv* 2020;2:vdaa066 CrossRef Medline
- Yogananda CG, Shah BR, Vejdani-Jahromi M, et al. A novel fully automated MRI-based deep-learning method for classification of IDH mutation status in brain gliomas. *Neuro Oncol* 2019;22:402–11 CrossRef Medline
- Clark K, Vendt B, Smith K, et al. The Cancer Imaging Archive (TCIA): maintaining and operating a public information repository. *J Digit Imaging* 2013;26:1045–57 CrossRef Medline
- Puchalski RB, Shah N, Miller J, et al. An anatomic transcriptional atlas of human glioblastoma. *Science* 2018;360:660–63 CrossRef Medline
- Erickson B, Akkus Z, Sedlar J, et al. Data From LGG-1p19qDeletion. *The Cancer Imaging Archive*. 2017;76. <https://doi.org/10.7937/K9/TCIA.2017.dwehtz9v>. Accessed November 30, 2017
- Ceccarelli M, Barthel FP, Malta TM, et al. TCGA Research Network. Molecular profiling reveals biologically discrete subsets and pathways of progression in diffuse glioma. *Cell* 2016;164:550–63 CrossRef Medline
- Menze BH, Jakab A, Bauer S, et al. The multimodal Brain Tumor Image Segmentation Benchmark (BRATS). *IEEE Trans Med Imaging* 2015;34:1993–2024 CrossRef Medline
- Bakas S, Akbari H, Sotiras A, et al. Advancing The Cancer Genome Atlas glioma MRI collections with expert segmentation labels and radiomic features. *Sci Data* 2017;4:170117 CrossRef Medline
- Yogananda CG, Shah BR, Vejdani-Jahromi M, et al. A novel fully automated MRI-based deep learning method for classification of IDH mutation status in brain gliomas. *Neuro Oncol* 2020;22:402–11 CrossRef Medline
- Avants BB, Tustison NJ, Song G, et al. A reproducible evaluation of ANTs similarity metric performance in brain image registration. *Neuroimage* 2011;54:2033–44 CrossRef Medline
- Rohlfing T, Zahr NM, Sullivan EV, et al. The SRI24 multichannel atlas of normal adult human brain structure. *Hum Brain Mapp* 2010;31:798–819 CrossRef Medline
- Smith SM. Fast robust automated brain extraction. *Hum Brain Mapp* 2002;17:143–55 CrossRef Medline
- Smith SM, Jenkinson M, Woolrich MW, et al. Advances in functional and structural MR image analysis and implementation as FSL. *Neuroimage* 2004;23(Suppl 1):S208–19 CrossRef Medline
- Woolrich MW, Jbabdi S, Patenaude B, et al. Bayesian analysis of neuroimaging data in FSL. *Neuroimage* 2009;45:S173–86 CrossRef Medline
- Jenkinson M, Beckmann CF, Behrens TE, et al. FSL. *Neuroimage* 2012;62:782–90 CrossRef Medline
- Tustison NJ, Cook PA, Klein A, et al. Large-scale evaluation of ANTs and FreeSurfer cortical thickness measurements. *Neuroimage* 2014;99:166–79 CrossRef Medline
- Wegmayr VA, Aitharajus S, Buhmann J, et al. Classification of brain MRI with big data and deep 3D convolutional neural networks. In: Petrick N, Mori K, eds. *Medical Imaging 2018: Computer-Aided Diagnosis*. SPIE Proceedings 2018;1057501 CrossRef
- Feng X, Yang J, Lipton ZC, et al. Deep learning on MRI affirms the prominence of the hippocampal formation in Alzheimer's disease classification. *bioRxiv* 2018 <https://www.biorxiv.org/content/10.1101/456277v1.full.pdf>. Accessed April 8, 2020
- Abadi M, Barham P, Chen J, et al. Tensorflow: a system for large-scale machine learning. *12th (USENIX) symposium on operating systems design and implementation (OSDI 16)*; 2016:265–283. May 27, 2016. <https://arxiv.org/abs/1605.08695>. Accessed April 24, 2018

31. Chollet F. Keras: **The python deep learning library.** *Astrophysics Source Code Library* 2018. <https://keras.io/>. Accessed February 10, 2018
32. Kingma DP, Ba JL. **Adam: a method for stochastic optimization.** In: *Proceedings of the International Conference on Learning Representations*, San Diego, California. May 7–9, 2015
33. Korfiatis P, Kline TL, Lachance DH, et al. **Residual deep convolutional neural network predicts MGMT methylation status.** *J Digit Imaging* 2017;30:622–28 CrossRef Medline
34. Han L, Kamdar MR. **MRI to MGMT: predicting methylation status in glioblastoma patients using convolutional recurrent neural networks.** *Pac Symp Biocomput* 2018;23:331–42 Medline
35. Chang P, Grinband J, Weinberg BD, et al. **Deep-learning convolutional neural networks accurately classify genetic mutations in gliomas.** *AJNR Am J Neuroradiol* 2018;39:1201–07 CrossRef Medline
36. Jégou S, Drozdal M, Vazquez D, et al. **The one hundred layers tiramisu: fully convolutional densenets for semantic segmentation.** In: *Proceedings of the 2017 IEEE Conference on Computer Vision and Pattern Recognition Workshops*. 2017:11–19. <https://ieeexplore.ieee.org/xpl/conhome/8014302/proceeding>. Accessed March 28, 2018
37. Wang G, Li W, Ourselin S, et al. **Automatic brain tumor segmentation based on cascaded convolutional neural networks with uncertainty estimation.** *Front Comput Neurosci* 2019;13:56 CrossRef Medline
38. Everhard S, Tost J, El Abdalaoui H, et al. **Identification of regions correlating MGMT promoter methylation and gene expression in glioblastomas.** *Neuro Oncol* 2009;11:348–56 CrossRef Medline
39. Cankovic M, Nikiforova MN, Snuderl M, et al. **The role of MGMT testing in clinical practice: a report of the association for molecular pathology.** *J Mol Diagn* 2013;15:539–55 CrossRef Medline
40. Estival A, Sanz C, Ramirez JL, et al. **Pyrosequencing versus methylation-specific PCR for assessment of MGMT methylation in tumor and blood samples of glioblastoma patients.** *Sci Rep* 2019;9:11125 CrossRef
41. Poulin M, Zhou JY, Yan L, et al. **Pyrosequencing methylation analysis.** *Methods Mol Biol* 2018;1856:283–96 CrossRef Medline
42. Bady P, Sciuscio D, Diserens AC, et al. **MGMT methylation analysis of glioblastoma on the Infinium methylation BeadChip identifies two distinct CpG regions associated with gene silencing and outcome, yielding a prediction model for comparisons across datasets, tumor grades, and CIMP-status.** *Acta Neuropathol* 2012;124:547–60 CrossRef Medline
43. Cancer Genome Atlas Research Network. **Comprehensive genomic characterization defines human glioblastoma genes and core pathways.** *Nature* 2008;455:1061–68 CrossRef Medline

MGMT Promoter Methylation Status in Initial and Recurrent Glioblastoma: Correlation Study with DWI and DSC PWI Features

H.J. Choi, S.H. Choi, S.-H. You, R.-E. Yoo, K.M. Kang, T.J. Yun, J.-h. Kim, C.-H. Sohn, C.-K. Park, and S.-H. Park



ABSTRACT

BACKGROUND AND PURPOSE: *O*⁶-methylguanine-DNA methyltransferase (MGMT) promoter methylation status in primary and recurrent glioblastoma may change during treatment. The purpose of this study was to correlate MGMT promoter methylation status changes with DWI and DSC PWI features in patients with recurrent glioblastoma after standard treatment.

MATERIALS AND METHODS: Between January 2008 and November 2016, forty patients with histologically confirmed recurrent glioblastoma were enrolled. Patients were divided into 3 groups according to the MGMT promoter methylation status for the initial and recurrent tumors: 2 groups whose MGMT promoter methylation status remained, group methylated ($n = 13$) or group unmethylated ($n = 18$), and 1 group whose MGMT promoter methylation status changed from methylated to unmethylated ($n = 9$). Normalized ADC and normalized relative CBV values were obtained from both the enhancing and nonenhancing regions, from which histogram parameters were calculated. The ANOVA and the Kruskal-Wallis test followed by post hoc tests were performed to compare histogram parameters among the 3 groups. The t test and Mann-Whitney U test were used to compare parameters between group methylated and group methylated to unmethylated. Receiver operating characteristic curve analysis was used to measure the predictive performance of the normalized relative CBV values between the 2 groups.

RESULTS: Group methylated to unmethylated showed significantly higher means and 90th and 95th percentiles of the cumulative normalized relative CBV values of the nonenhancing region of the initial tumor than group methylated and group unmethylated (all $P < .05$). The mean normalized relative CBV value of the nonenhancing region of the initial tumor was the best predictor of methylation status change ($P < .001$), with a sensitivity of 77.78% and specificity of 92.31% at a cutoff value of 2.594.

CONCLUSIONS: MGMT promoter methylation status might change in recurrent glioblastoma after standard treatment. The normalized relative CBV values of the nonenhancing region at the first preoperative MR imaging were higher in the MGMT promoter methylation change group from methylation to unmethylation in recurrent glioblastoma.

ABBREVIATIONS: CCRT = concurrent chemoradiation therapy; EGFR = epidermal growth factor receptor; GBM = glioblastoma; IDH = isocitrate dehydrogenase; MGMT = *O*⁶-methylguanine-DNA methyltransferase; MM = methylated; MU = methylation to unmethylation; nADC = normalized ADC; NER = non-enhancing region; nrCBV = normalized relative CBV; rCBV = relative CBV; TMZ = temozolomide; UU = unmethylated; VASARI = Visually Accessible Rembrandt Images; WHO = World Health Organization

Glioblastoma (GBM) is the most common malignant brain tumor and has a poor prognosis, with a median survival time of

12–15 months, even after operation followed by concurrent chemoradiation therapy (CCRT) with adjuvant temozolomide (TMZ).¹ Patients with GBM containing a methylated *O*⁶-methylguanine-DNA methyltransferase (MGMT) gene promoter are associated with a favorable outcome after TMZ chemotherapy, whereas patients with an unmethylated MGMT promoter do not have such a benefit.² The MGMT gene encodes a DNA repair protein involved in the

Received July 28, 2020; accepted after revision November 16.

From the Department of Radiology (H.J.C.), Cha Bundang Medical Center, Cha University, Seongnam, Korea; Departments of Radiology (S.H.C., R.-E.Y., K.M.K., T.J.Y., J.-h.K., C.-H.S.), Neurosurgery (C.-K.P.), and Pathology (S.-H.P.), Seoul National University Hospital, Seoul, Korea; and Department of Radiology (S.-H.Y.), Korea University Hospital, Seoul, Korea.

This study was supported by a grant from the Korea Healthcare Technology R&D Projects, Ministry for Health, Welfare & Family Affairs (HI16C111); the Brain Research Program through the National Research Foundation of Korea funded by the Ministry of Science, ICT and Future Planning (NRF-2016M3C7A1914002); National Research Foundation of Korea funded by the Korea government (MSIT) (NRF-2020R1G1A1A01027701); the Basic Science Research Program through the National Research Foundation of Korea funded by the Ministry of Science, ICT and Future Planning (NRF-2020R1A2C2008949 and NRF-2020R1A4A1018714); the Creative-Pioneering Researchers Program through Seoul National University; and the Institute for Basic Science (IBS-R006-A1).

Please address correspondence to Seung Hong Choi, MD, PhD, Department of Radiology, Seoul National University Hospital, 101 Daehak-ro, Jongno-gu, Seoul, 03080, Korea; e-mail: verocay@snuh.org

Indicates open access to non-subscribers at www.ajnr.org

Indicates article with online supplemental data.

<http://dx.doi.org/10.3174/ajnr.A7004>

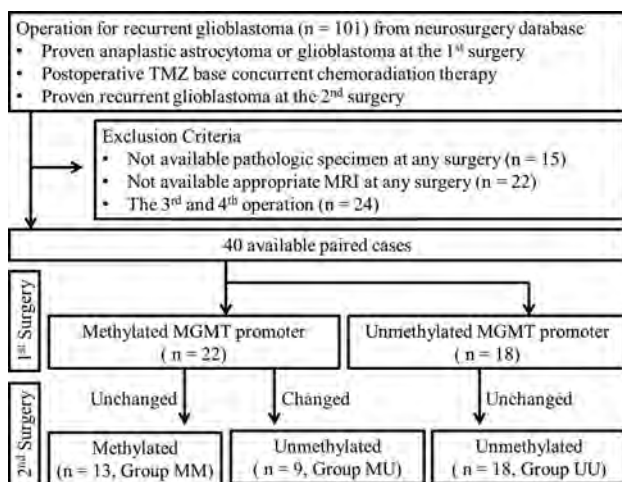


FIG 1. Study design.

removal of TMZ-induced damaged DNA, and epigenetic silencing by methylation of its promoter on the O⁶ position of guanine is correlated with the cytotoxic effect of TMZ.³ *MGMT* promoter methylation is reported to be present in 35%–75% of GBMs.⁴ Pseudoprogression after CCRT is more common in tumors with *MGMT* promoter methylation in GBM, and methylation of the *MGMT* promoter should be considered when interpreting follow-up MR imaging.⁵

MGMT promoter methylation status in primary and recurrent GBM may change during treatment.^{3,6,7} Some authors have suggested that reduced *MGMT* promoter methylation in recurrent GBM after TMZ treatment is one of the mechanisms for the acquisition of therapeutic resistance; however, controversy remains as to whether changes in the methylation status of the *MGMT* promoter may be a prognostic factor for recurrent GBM.^{8,9}

Many authors have reported the relationships of *MGMT* promoter methylation status and imaging features, including CT, DWI, DSC PWI, or DTI, in patients with high-grade glioma or GBM before treatment.^{10–13} However, to our knowledge, there has been no previous report regarding the correlation of DSC PWI and DWI with changes in the *MGMT* promoter methylation status in recurrent GBM. Therefore, the purpose of our study was to correlate changes in the *MGMT* promoter methylation status with DSC PWI and DWI features in patients with recurrent GBM after standard treatment.

MATERIALS AND METHODS

Patients

This retrospective study was approved by the institutional review board of Seoul National University Hospital. The requirement for informed consent was waived. One hundred one patients with anaplastic astrocytoma or GBM who underwent surgical resection and a second operation for suspected recurrence at our hospital between January 2008 and November 2016 were screened for this study from the neurosurgery data base. The inclusion criteria were as follows: 1) histopathologic diagnosis of anaplastic astrocytoma or GBM based on the World Health Organization (WHO) 2016 criteria at the initial operation; 2) histopathologic diagnosis of recurrent GBM based on the WHO 2016 criteria at the second operation; and

3) a CCRT and adjuvant TMZ-based regimen between the operations. Sixty-one patients were excluded because of the following: 1) unavailable pathologic specimen from either operation ($n = 15$); 2) unavailable appropriate MR imaging from either operation ($n = 22$); and 3) a third and fourth operation ($n = 24$).

Finally, 40 consecutive patients (20 men, 20 women; mean age, 49.85 years; range, 21–74 years) were included in the present study. We reviewed the clinical characteristics of each patient, including age, sex, preoperative Karnofsky Performance Status score at the first and second operation, *MGMT* promoter methylation status, *isocitrate dehydrogenase (IDH) 1* or 2 mutation status, epidermal growth factor receptor (*EGFR*) amplification results at each operation, radiation dose, TMZ cycles, and treatment options after the second operation from the electronic medical records of our institution. These patients were divided into 3 groups according to the *MGMT* promoter methylation status of the initial and recurrent tumors: unchanged *MGMT* promoter methylation status, further divided into methylated (group MM, $n = 13$) and unmethylated (group UU, $n = 18$), and changed *MGMT* promoter methylation status from methylation to unmethylation (group MU, $n = 9$) (Fig 1). The extent of resection was defined on the basis of immediate postoperative MR imaging obtained within 24–72 hours after the operation.¹⁴

Imaging Acquisition

A total of 80 MR images were obtained for 40 patients with 1.5T or 3T MR imaging scanners (3T Signa Excite [$n = 11$], 1.5T Signa HDxt [$n = 17$], and 1.5T Signa HDx [$n = 1$], GE Healthcare; 3T Verio [$n = 45$], 3T Magnetom Trio [$n = 3$], 3T Magnetom Skyra [$n = 1$], and 3T Biograph mMR [$n = 1$], Siemens; and 3T Ingenia [$n = 1$], Philips Healthcare) with variable channel head coils (8-, 16-, 32-, and 64-channel). Imaging sequences of the brain included spin-echo or gradient-echo T1WI, FSE T2WI, FLAIR T2WI, SWI, contrast-enhanced spin-echo or gradient-echo T1WI with gadobutrol (Gadovist; Bayer Schering Pharma) and DSC PWI. DWI was performed with a single-shot spin-echo EPI sequence in the axial plane with b-values of 0 and 1000 s/mm². Using these data, we calculated ADC maps on a voxel-by-voxel basis with the software that was incorporated into the MR imaging unit. For DSC PWI, a single-shot gradient-echo EPI sequence was used. Sixty images were obtained in each section at intervals equal to the TR. After 4–5 time points, a bolus of gadobutrol at a dose of 0.1 mmol/kg of body weight and a rate of 4 mL/s was injected with an MR imaging-compatible power injector (Spectris; Medrad). The imaging parameters of the MR imaging scanners are shown in the Online Supplemental Data. Patients generally undergo MR imaging at presurgery, pre-CCRT, immediate post-CCRT, and continued follow-up. The first preoperative MR imaging for the initial tumor at presurgery and the second preoperative MR imaging at recurrence were reviewed (Online Supplemental Data).

Image Postprocessing and Analysis

Postprocessing and histogram analysis were performed with dedicated software, NordicICE and Nordic TumorEX (NordicNeuroLab), using the first preoperative and second preoperative MR images. Relative CBV (rCBV) was obtained with an established tracer kinetic model for the first-pass data.^{15,16}

Realignment for minimizing motion, γ -variate fitting for reducing the recirculation effect, and correction of the dynamic curve for reducing the leakage effect were applied. To minimize variances in the rCBV in an individual patient, we normalized the pixel-based rCBV maps by dividing every rCBV value in a specific section by the value in the unaffected contralateral deep white matter.¹⁷ Normalized ADC (nADC) values were obtained using the same equation. Coreregistrations between the contrast-enhanced T1WI and the rCBV maps and between the contrast-enhanced T1WI and the ADC maps were performed on the basis of geometric information stored in the respective datasets. The differences in section thickness between images were corrected automatically by reslicing and coregistration, which were based on the underlying structural images. Two neuroradiologists (H.J.C. and S.H.C. with 6 and 15 years of experience in neuroradiology, respectively) manually defined the ROIs in consensus. To contain each complete enhancing tumor and avoid macrovessels and cystic, hemorrhagic, or necrotic portions, they drew ROIs on every tumor section on contrast-enhanced T1WI using a semiautomatic method with signal intensity thresholds and seed-growing. To obtain exclusively T2 hyperintense nonenhancing regions (NERs), we determined exclusion ROIs (based on FLAIR and ROIs based on contrast-enhanced T1WI) in the batch process.

After obtaining the total voxel values of the normalized rCBV (nrCBV) and nADC of each enhancing region and the NER of the tumor (Online Supplemental Data), we performed histogram analysis as follows: The mean, 90th percentile, and 95th percentile of nrCBV and the mean, 5th percentile, and 10th percentile of nADC of histogram values were calculated. The ratios of the nrCBV and nADC histogram values of the recurrent and initial tumors were calculated by $(nrCBV_{\text{recurrent}}/nrCBV_{\text{initial}})$ and $(nADC_{\text{recurrent}}/nADC_{\text{initial}})$, respectively.

Selected conventional MR imaging features of the tumors were recorded by a neuroradiologist (H.J.C.) according to the Visually Accessible Rembrandt Images (VASARI) feature scoring system for human glioma.¹⁸ Preoperative tumor volumes based on contrast-enhanced T1WI and FLAIR images were also measured.

Molecular/Genetic Analysis

Immunohistochemical staining was performed using a Bench Mark XT (automated immunohistochemical slide staining system; Roche Diagnostics). Immunohistochemistry was performed on individual whole block sections using antibodies against the *IDH 1* R132H mutant protein (H09; Dianova, 1: 50). Sanger sequencing was used to analyze the frequency of *IDH 1* and 2 mutations. Labeled locus-specific *EGFR* SpectrumOrange/CEP7 SpectrumGreen dual color probes (Abbott Molecular) were used to determine the status of the *EGFR* gene. *MGMT*-specific polymerase chain reaction using a methylation EZ Kit (<https://www.qiagen.com/us/listpages/ez1-kits/>) was used to evaluate the methylation status of the *MGMT* promoter.

Statistical Analysis

Data for each parameter were assessed for normality with the Kolmogorov-Smirnov test or Shapiro-Wilk normality test. The ANOVA and the Kruskal-Wallis test followed by post hoc tests were performed to compare histogram values among the 3

groups. Focusing on the initially methylated *MGMT* groups, we used independent *t* tests and Mann-Whitney *U* tests to compare group MM and group MU. Additionally, to evaluate the diagnostic performance of the imaging parameters, we performed receiver operating characteristic curve analysis, and the area under the curve was calculated to identify the optimal threshold for maximizing sensitivity and specificity. Additionally, multivariable logistic regression analysis was performed with statistically significant variables on univariable analysis. All statistical analyses were performed using R statistical and computing software (<https://www.R-project.org>) and MedCalc for Windows, Version 17.1 (MedCalc Software). A *P* value < .05 was considered statistically significant.

RESULTS

Clinical Characteristics

The clinical characteristics of the patients, including age, sex, *IDH* mutation status, *EGFR* fluorescence in situ hybridization results (on primary and recurrent tumors), histopathology, surgical extent, first and second preoperative Karnofsky Performance Status scores, postoperative treatment, and radiation dose after the first operation were not significantly different among the 3 groups (Table 1).

Histogram Analysis

The mean, 90th percentile, and 95th percentile of the nrCBV values of the NER of the initial tumor were significantly higher in group MU than in group MM and group UU ($P = 0.006$, $P = 0.001$ and $P < .001$, respectively) (Online Supplemental Data and Figs 2 and 3). The mean nADC of the NER of recurrent tumors in group MU was significantly higher than that in group MM and group UU ($P < .001$) (Online Supplemental Data). In addition, the ratio of the mean nADC values of the NER was also significantly higher in group MU than in group MM and group UU ($P < .001$) (Online Supplemental Data). There was no statistically significant difference in the nrCBV or nADC values among the 3 groups in the enhancing region of the initial or recurrent tumors. There was no significant difference in the nADC values in the NER of the initial tumors among the 3 groups.

Imaging feature trends through time for each group are demonstrated in the Online Supplemental Data.

Subgroup Analysis in Groups MM and MU

In the subgroup analysis, focusing on the initially methylated *MGMT* promoter groups (group MM versus group MU), there was no significant difference in the nADC or nrCBV values in the enhancing region of the initial tumors (Online Supplemental Data). In the NER of the initial tumors, the mean 90th percentile and 95th percentile values of the nrCBV were higher in group MM than in group MU ($P = .002$). For recurrent tumors, the nrCBV values in the NER were not significantly different among the 3 groups. In terms of the mean nADC value of the NER of recurrent tumors, group MU showed significantly higher values than group MM ($P < .001$).

Table 2 summarizes the diagnostic performance of the cumulative histogram nrCBV and nADC values for discriminating sustained *MGMT* methylation status (group MM) from changed

Table 1: Clinical characteristics of the patients^a

	Group MM (n = 13)	Group UU (n = 18)	Group MU (n = 9)	P ^b
Age (yr)	49.9 (SD, 14.3)	51.6 (SD, 14.5)	46.3 (SD, 11.1)	.61
Sex				.52
Female	7 (53.8%)	10 (55.6%)	3 (33.3%)	
Male	6 (46.2%)	8 (44.4%)	6 (66.7%)	
IDH 1 or 2 mutation				.06
Negative	9 (90.0%)	14 (100.0%)	6 (66.7%)	
Positive	1 (10.0%)	0 (0.0%)	3 (33.3%)	
EGFR amplification: initial tumor				.85
Negative	7 (53.8%)	10 (55.6%)	4 (44.4%)	
Positive	6 (46.2%)	8 (44.4%)	5 (55.6%)	
EGFR amplification: recurrent tumor				.81
Negative	8 (66.7%)	10 (55.6%)	5 (55.6%)	
Positive	4 (33.3%)	8 (44.4%)	4 (44.4%)	
WHO grade: initial tumor				.12
Grade III anaplastic astrocytoma	1 (7.7%)	0 (0.0%)	2 (22.2%)	
Grade IV glioblastoma	12 (92.3%)	18 (100.0%)	7 (77.8%)	
WHO grade: recurrent tumor				
Grade IV	13 (100.0%)	18 (100.0%)	9 (100.0%)	
Surgical extent				.32
Total resection	11 (84.62%)	11 (61.1%)	7 (77.78%)	
Subtotal resection	2 (15.4%)	0 (0.0%)	0 (0.0%)	
1st preoperative KPS	100.0 (90.0–100.0)	92.5 (80.0–100.0)	100.0 (90.0–100.0)	.41
2nd preoperative KPS	90.0 (80.0–100.0)	90.0 (70.0–100.0)	100.0 (90.0–100.0)	.39
Postoperative treatment after 1st operation				.42
CCRT/TMZ	11 (84.6%)	17 (94.5%)	8 (88.9%)	
Hypo-CCRT/TMZ	2 (15.4%)	0 (0.0%)	0 (0.0%)	
Hypo-CCRT	0 (0.0%)	1 (5.6%)	1 (11.1%)	
Radiation dose (Gy)	61.0 (61.0–61.0)	61.0 (61.0–61.0)	61.0 (61.0–61.0)	.69

Note:—KPS indicates Karnofsky Performance Status.

^aData are number of patients, means [2 SDs] for normally distributed variables, or medians (interquartile ranges) for nonnormally distributed variables.

^bP values were calculated using the Kruskal-Wallis test for nonparametric variables and the 1-way ANOVA for parametric variables.

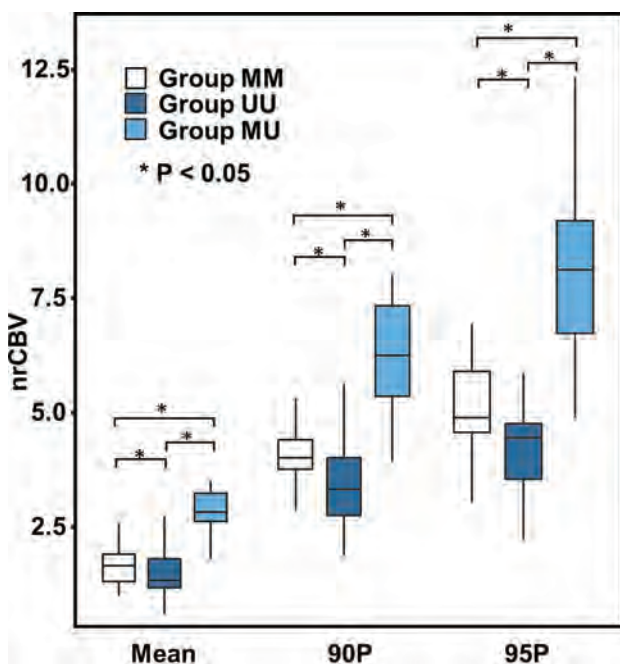


FIG 2. Comparison of nrCBV histogram parameters across each group of NER in the initial tumor. The mean, 90th percentile, and 95th percentile of the nrCBV values of the NER of the initial tumor were significantly higher in group MU than in group MM and group UU. Asterisks represent statistically significant differences among groups. 90P indicates the 90th percentile; 95P, the 95th percentile.

MGMT methylation status (group MU) on the basis of the NER of the initial tumor. The mean histogram value of the nrCBV in the NER of the initial tumors showed the highest area under the curve (0.889, $P < .001$; 95% CI, 0.682–0.982). Multivariable logistic regression was performed with the statistically significant variables (mean, 90th percentile, and 95th percentile values of the nrCBV of the NER of initial tumors and mean value of the nADC of the enhancing region of recurrent tumors) on univariable analysis. Only the mean nrCBV value of the NER of the initial tumors was significant (OR = 9.53, $P = 0.01$; 95% CI, 1.575–57.703) in multiple logistic regression analysis.

Conventional Imaging Features and Volume Measurements among the 3 Groups

Several conventional imaging features based on the selected VASARI scale showed no significant differences among the 3 groups for initial and recurrent tumors (Online Supplemental Data). Only the enhancing volumes of the recurrent tumors of group UU were significantly larger than those of group MU ($P = .03$).

DISCUSSION

The results of the present study demonstrate that among patients with recurrent GBM, the histogram parameters of the nrCBV of the NER of tumors are higher for the group whose MGMT promoter methylation status changed from methylated

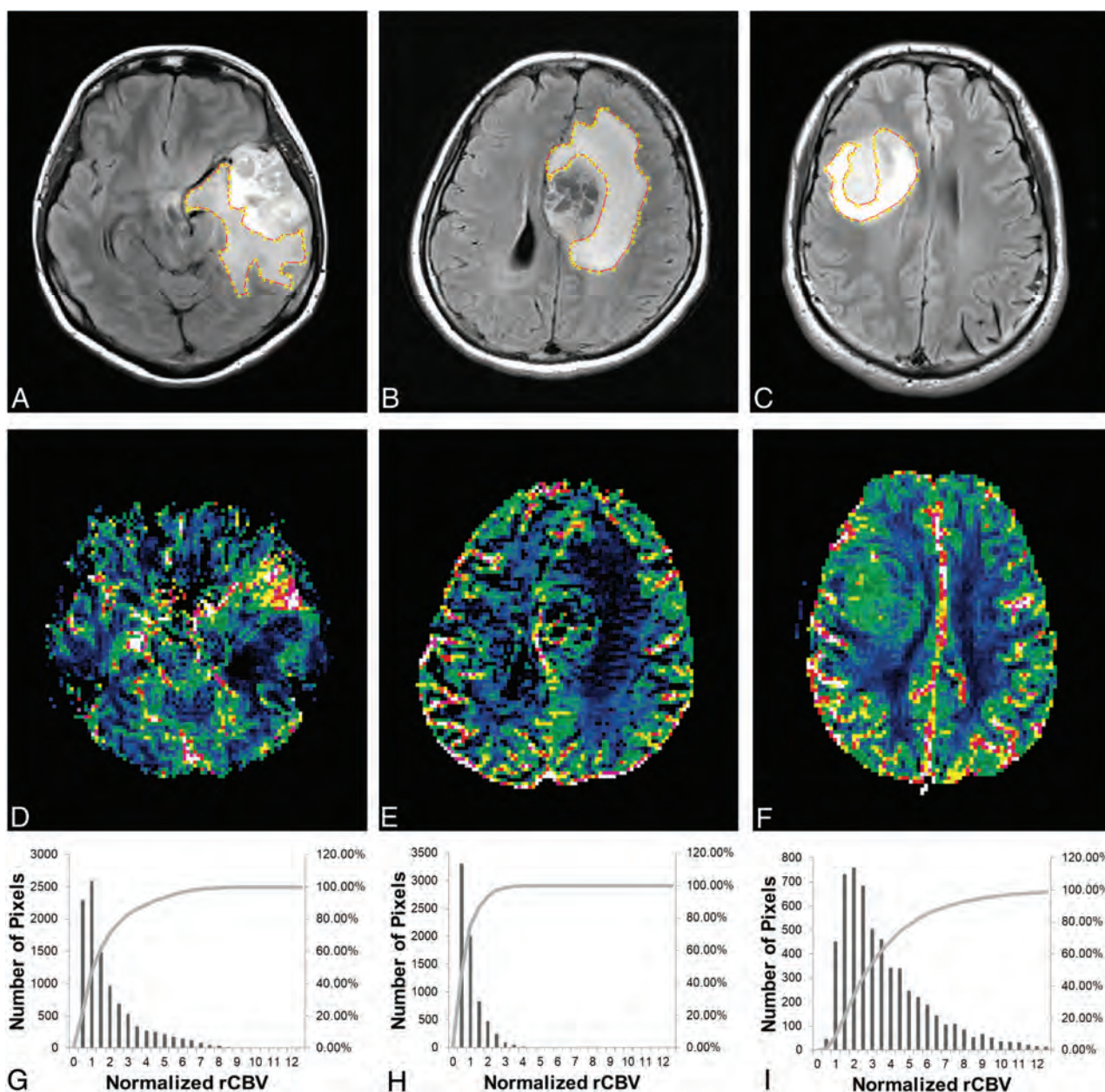


FIG 3. FLAIR images (A–C) and nrCBV maps (D–F) with corresponding cumulative histograms (G–I) for representative patients. A, D, G, A 34-year-old woman in group MM. B, E, H, A 37-year-old woman in group UU. C, F, I, A 32-year-old man in group MU. The histogram values (mean, 90th percentile, and 95th percentile) of the nrCBV in the NER of the tumors in group MU are higher than those in group UU or group MM.

Table 2: Diagnostic performance of the nrCBV values for discriminating unchanged *MGMT* methylation status (group MM) from changed *MGMT* methylation status (group MU) on the basis of the NER of the initial tumor

Variable	AUC	Sensitivity (%)	Specificity (%)	Cutoff	Standard Error	95% CI	P
Initial tumor							
nrCBV mean	0.889	77.78	92.31	>2.594	0.073	0.682–0.982	<.0001
nrCBV 90P	0.846	88.89	76.92	>4.159	0.091	0.630–0.963	.0001
nrCBV 95P	0.855	66.67	92.31	>6.794	0.082	0.640–0.967	<.0001

Note:—90P indicates 90th percentile; 95P, 95th percentile; AUC, area under the curve.

to unmethylated than for the group whose *MGMT* promoter methylation status was unchanged (either methylated or unmethylated).

By repairing DNA damaged by alkylating agents such as TMZ, the *MGMT* protein is thought to provide resistance against the cytotoxic effect of the anticancer drug.¹⁹ In addition, silencing the

MGMT gene by promoter methylation achieves a therapeutic effect by means of increasing sensitivity to alkylating agents.¹⁹ In routine diagnostics, the *MGMT* promoter methylation status has predictive and prognostic value.²⁰ Many investigators have reported that *MGMT* promoter methylation status may change from that of the initial tumor when GBM recurs after treatment.^{3,6,7} This shift was also observed in in vitro experiments with patient-derived GBM cell lines.^{6,21} We found stability of *MGMT* promoter methylation in 31 of 40 patients (77.5%) from the first to the second operation. Nine of 40 (22.5%) patients showed changes in methylation status, which was slightly higher than that reported in the latest meta-analysis (71/476, 14.9%).²² However, the range of changes in *MGMT* promoter methylation is very wide, on the basis of the different methods and cutoff values and the presence of selection bias.²²

Meanwhile, conventional and advanced imaging features in GBM based on *MGMT* promoter methylation have been studied by many researchers. Previous studies revealed that tumors with methylated *MGMT* promoters showed less aggressive imaging features, including less edema, higher ADC, and low CBV values.^{10,23–25} However, conflicting results have also been reported, indicating that the imaging features of tumors with methylated *MGMT* promoters are not clearly distinguished from those with an unmethylated status.^{10,13,26–28} As far as we know, there is no previous work analyzing the imaging features associated with *MGMT* promoter methylation changes after standard treatment.

In the present study, we focused on the imaging features of initial and recurrent tumors after treatment according to the change in the *MGMT* promoter methylation status. There was no significant difference in the nADC or nrCBV values among the groups in the enhancing region of initial or recurrent tumors. However, in the NER of initial tumors, the nrCBV values were higher in group MU than in the other groups. The importance of the NER in GBM is increasing in diagnostics, treatment, and prognosis.^{29–34} In a recent study, the rCBV of the NER was a significant prognostic biomarker, independent of morphologic features in GBM.³⁵ In addition, the volume transfer constant in the NER could be a potential prognostic imaging biomarker in GBM.^{36,37} Blood perfusion in the tumor and surrounding tissue may be related to the chemotherapeutic agent in drug delivery.³⁸ Yoo et al³⁹ reported that an enhancing lesion with a low volume transfer constant and v_e (volume of extravascular extracellular space) was more likely to progress because of its low permeability or leakiness of the BBB, in which the delivery of TMZ to viable tumor cells might be less effective during standard treatment. A recent study about the combination of tumor perfusion and *MGMT* promoter methylation indicated a potential interaction effect in the treatment of recurrent GBM with TMZ.³⁸ The authors hypothesized that GBM contains immature vessels from neoangiogenesis, which may influence drug delivery to the tumor cells. Given that the therapeutic strategy of TMZ involves reduction of *MGMT* activity,⁴⁰ it could be assumed that higher nrCBV in the NER of the tumor could be related to depleting the methylated *MGMT*. Further studies are necessary to evaluate whether epigenetic alterations during the clinical course of the disease are related to the perfusion feature of the remaining tumor burden.

In recurrent GBM, treatment strategies are less established.⁴¹ Systemic chemotherapy is one option for treatment, but no chemotherapeutic agents showed major differences in efficacy.

Nevertheless, TMZ rechallenge in patients with *MGMT* promoter methylation is a reasonable option.³⁸ In patients with an unmethylated *MGMT* promoter, another treatment option can be suggested according to the results from the recurrent tumor.⁴² PWI provides information on nrCBV in a noninvasive manner, and we suggest that it should be considered in deciding the follow-up duration or treatment option for patients with higher mean nrCBVs in the NER of primary tumors with *MGMT* promoter methylation. The clinical impact and imaging features should be further investigated.

This study has some limitations, including its retrospective nature and small cohort size. First, because different scanners were used to acquire MR imaging data, there was inherent heterogeneity in the raw data and postprocessing steps. To overcome this limitation, we used normalized values for the CBV and ADC values to standardize the data and postprocessing leakage correction to obtain the CBV values. Second, the evaluation of *MGMT* promoter methylation with an *MGMT*-specific polymerase chain reaction has some technical issues.⁴³ Furthermore, hemimethylated promoters were not considered in the *MGMT* evaluation.⁴³ Nevertheless, *MGMT*-specific polymerase chain reaction is a widely accepted method with a significant correlation with *MGMT* activity.⁹ Third, the results of *MGMT* promoter methylation status were tested in surgical specimens obtained primarily from enhancing tumors. There have been reports about differences in *MGMT* promoter methylation and expression, depending on the sampling area in the GBM.⁴⁴ However, *MGMT* promoter methylation is usually seen as homogeneous within the tumor.⁴⁵ We did not examine serial sections of the tumor, hypothesizing that *MGMT* promoter methylation in the specimens was homogeneous. Further studies are needed to address the issue of intratumoral heterogeneity in *MGMT* promoter methylation. Fourth, 3 anaplastic astrocytomas were included in the first operation. The inclusion criteria were patients with recurrent glioblastoma who had primarily surgery and TMZ-based CCRT followed by adjuvant TMZ. Therefore, 3 anaplastic astrocytomas were included in the first operation. We re-tested after removal of the 3 cases and found that there was no significant change in the results (Online Supplemental Data).

CONCLUSIONS

MGMT promoter methylation status might change in recurrent GBM after standard treatment. The nrCBV values of the NER at the first preoperative MR imaging were higher in the *MGMT* promoter methylation change group from methylation to unmethylation in recurrent GBM.

Disclosures: Seung Hong Choi—RELATED: Grant: governmental grants.* Chul-Keek Park—UNRELATED: Employment: Seoul National University Hospital. *Money paid to the institution.

REFERENCES

1. Stupp R, Mason WP, van den Bent MJ, et al; European Organisation for Research and Treatment of Cancer Brain Tumor and Radiotherapy Groups; National Cancer Institute of Canada Clinical Trials Group. Radiotherapy plus concomitant and adjuvant temozolomide for glioblastoma. *N Engl J Med* 2005;352:987–96 CrossRef Medline

2. Hegi ME, Diserens AC, Gorlia T, et al. **MGMT gene silencing and benefit from temozolomide in glioblastoma.** *N Engl J Med* 2005;352:997–1003 CrossRef Medline
3. Brandes AA, Franceschi E, Tosoni A, et al. **O(6)-methylguanine DNA-methyltransferase methylation status can change between first surgery for newly diagnosed glioblastoma and second surgery for recurrence: clinical implications.** *Neuro Oncol* 2010;12:283–88 CrossRef Medline
4. Gupta K, Salunke P. **Molecular markers of glioma: an update on recent progress and perspectives.** *J Cancer Res Clin Oncol* 2012;138:1971–81 CrossRef Medline
5. Kong DS, Kim ST, Kim EH, et al. **Diagnostic dilemma of pseudo-progression in the treatment of newly diagnosed glioblastomas: the role of assessing relative cerebral blood flow volume and oxygen-6-methylguanine-DNA methyltransferase promoter methylation status.** *AJNR Am J Neuroradiol* 2011;32:382–87 CrossRef Medline
6. Jung TY, Jung S, Moon KS, et al. **Changes of the O6-methylguanine-DNA methyltransferase promoter methylation and MGMT protein expression after adjuvant treatment in glioblastoma.** *Oncol Rep* 2010;23:1269–76 CrossRef Medline
7. Brandes AA, Franceschi E, Paccapelo A, et al. **Role of MGMT methylation status at time of diagnosis and recurrence for patients with glioblastoma: clinical implications.** *Oncologist*. 2017;22:432–37 CrossRef Medline
8. Johnson BE, Mazar T, Hong C, et al. **Mutational analysis reveals the origin and therapy-driven evolution of recurrent glioma.** *Science* 2014;343:189–93 CrossRef Medline
9. Park CK, Kim JE, Kim JY, et al. **The changes in MGMT promoter methylation status in initial and recurrent glioblastomas.** *Transl Oncol* 2012;5:393–97 CrossRef Medline
10. Moon WJ, Choi JW, Roh HG, et al. **Imaging parameters of high-grade gliomas in relation to the MGMT promoter methylation status: the CT, diffusion tensor imaging, and perfusion MR imaging.** *Neuroradiology* 2012;54:555–63 CrossRef Medline
11. Sunwoo L, Choi SH, Park CK, et al. **Correlation of apparent diffusion coefficient values measured by diffusion MRI and MGMT promoter methylation semiquantitatively analyzed with MS-MLPA in patients with glioblastoma multiforme.** *J Magn Reson Imaging* 2013;37:351–58 CrossRef Medline
12. Choi YS, Ahn SS, Kim DW, et al. **Incremental prognostic value of ADC histogram analysis over MGMT promoter methylation status in patients with glioblastoma.** *Radiology* 2016;281:175–84 CrossRef Medline
13. Ryoo I, Choi SH, Kim JH, et al. **Cerebral blood volume calculated by dynamic susceptibility contrast-enhanced perfusion MR imaging: preliminary correlation study with glioblastoma genetic profiles.** *PLoS One* 2013;8:e71704 CrossRef Medline
14. McGirt MJ, Chaichana KL, Gathinji M, et al. **Independent association of extent of resection with survival in patients with malignant brain astrocytoma.** *J Neurosurg* 2009;110:156–62 CrossRef Medline
15. Rosen BR, Belliveau JW, Vevea JM, et al. **Perfusion imaging with NMR contrast agents.** *Magn Reson Med* 1990;14:249–65 CrossRef Medline
16. Ostergaard L, Sorensen AG, Kwong KK, et al. **High resolution measurement of cerebral blood flow using intravascular tracer bolus passages, Part II: experimental comparison and preliminary results.** *Magn Reson Med* 1996;36:726–36 CrossRef Medline
17. Wetzel SG, Cha S, Johnson G, et al. **Relative cerebral blood volume measurements in intracranial mass lesions: interobserver and intraobserver reproducibility study.** *Radiology* 2002;224:797–803 CrossRef Medline
18. The National Cancer Institute Web site. **Wiki for the VASARI feature set.** Updated May 25, 2015. <https://wiki.cancerimagingarchive.net/display/Public/VASARI+Research+Project>. Accessed June 1, 2016
19. Gerson SL. **MGMT: its role in cancer aetiology and cancer therapeutics.** *Nat Rev Cancer* 2004;4:296–307 CrossRef Medline
20. Preusser M. **MGMT analysis at DNA, RNA and protein levels in glioblastoma tissue.** *Histol Histopathol* 2009;24:511–18 CrossRef Medline
21. Storey K, Leder K, Hawkins-Daarud A, et al. **Glioblastoma recurrence and the role of O(6)-methylguanine-DNA methyltransferase promoter methylation.** *JCO Clin Cancer Inform* 2019;3:1–12 CrossRef Medline
22. Feldheim J, Kessler AF, Monoranu CM, et al. **Changes of O(6)-methylguanine DNA methyltransferase (MGMT) promoter methylation in glioblastoma relapse: a meta-analysis type literature review.** *Cancers (Basel)* 2019;11:1837 CrossRef Medline
23. Ellingson BM, Cloughesy TF, Pope WB, et al. **Anatomic localization of O6-methylguanine DNA methyltransferase (MGMT) promoter methylated and unmethylated tumors: a radiographic study in 358 de novo human glioblastomas.** *Neuroimage* 2012;59:908–16 CrossRef Medline
24. Han Y, Yan LF, Wang XB, et al. **Structural and advanced imaging in predicting MGMT promoter methylation of primary glioblastoma: a region of interest based analysis.** *BMC Cancer* 2018;18:215 CrossRef Medline
25. Suh CH, Kim HS, Jung SC, et al. **Clinically relevant imaging features for MGMT promoter methylation in multiple glioblastoma studies: a systematic review and meta-analysis.** *AJNR Am J Neuroradiol* 2018;39:1439–45 CrossRef Medline
26. Smits M, van den Bent MJ. **Imaging correlates of adult glioma genotypes.** *Radiology* 2017;284:316–31 CrossRef Medline
27. Rundle-Thiele D, Day B, Stringer B, et al. **Using the apparent diffusion coefficient to identifying MGMT promoter methylation status early in glioblastoma: importance of analytical method.** *J Med Radiat Sci* 2015;62:92–98 CrossRef Medline
28. Romano A, Calabria LF, Tavanti F, et al. **Apparent diffusion coefficient obtained by magnetic resonance imaging as a prognostic marker in glioblastomas: correlation with MGMT promoter methylation status.** *Eur Radiol* 2013;23:513–20 CrossRef Medline
29. Kotrotsou A, Elakkad A, Sun J, et al. **Multi-center study finds post-operative residual non-enhancing component of glioblastoma as a new determinant of patient outcome.** *J Neurooncol* 2018;139:125–33 CrossRef Medline
30. Stummer W, Pichlmeier U, Meinel T, et al. **Fluorescence-guided surgery with 5-aminolevulinic acid for resection of malignant glioma: a randomised controlled multicentre Phase III trial.** *Lancet Oncol* 2006;7:392–401 CrossRef Medline
31. Idoate MA, Diez Valle R, Echeveste J, et al. **Pathological characterization of the glioblastoma border as shown during surgery using 5-aminolevulinic acid-induced fluorescence.** *Neuropathology* 2011;31:575–82 CrossRef Medline
32. Aldave G, Tejada S, Pay E, et al. **Prognostic value of residual fluorescent tissue in glioblastoma patients after gross total resection in 5-aminolevulinic acid-guided surgery.** *Neurosurgery* 2013;72:915–920; discussion 920–21 CrossRef Medline
33. Lasocki A, Gaillard F. **Non-contrast-enhancing tumor: a new frontier in glioblastoma research.** *AJNR Am J Neuroradiol* 2019;40:758–65 CrossRef Medline
34. Pope WB, Sayre J, Perlina A, et al. **MR imaging correlates of survival in patients with high-grade gliomas.** *AJNR Am J Neuroradiol* 2005;26:2466–74 Medline
35. Jain R, Poisson LM, Gutman D, et al. **Outcome prediction in patients with glioblastoma by using imaging, clinical, and genomic biomarkers: focus on the nonenhancing component of the tumor.** *Radiology* 2014;272:484–93 CrossRef Medline
36. Kim R, Choi SH, Yun TJ, et al. **Prognosis prediction of non-enhancing T2 high signal intensity lesions in glioblastoma patients after standard treatment: application of dynamic contrast-enhanced MR imaging.** *Eur Radiol* 2017;27:1176–85 CrossRef Medline
37. Hwang I, Choi SH, Park CK, et al. **Dynamic contrast-enhanced MR imaging of nonenhancing T2 high-signal-intensity lesions in baseline and posttreatment glioblastoma: temporal change and**

- prognostic value. *AJNR Am J Neuroradiol* 2020;41:49–56 CrossRef Medline
38. Kim C, Kim HS, Shim WH, et al. **Recurrent glioblastoma: combination of high cerebral blood flow with MGMT promoter methylation is associated with benefit from low-dose temozolomide rechallenge at first recurrence.** *Radiology* 2017;282:212–21 CrossRef Medline
 39. Yoo RE, Choi SH, Kim TM, et al. **Dynamic contrast-enhanced MR imaging in predicting progression of enhancing lesions persisting after standard treatment in glioblastoma patients: a prospective study.** *Eur Radiol* 2017;27:3156–66 CrossRef Medline
 40. Tolcher AW, Gerson SL, Denis L, et al. **Marked inactivation of O6-alkylguanine-DNA alkyltransferase activity with protracted temozolomide schedules.** *Br J Cancer* 2003;88:1004–11 CrossRef Medline
 41. Birk HS, Han SJ, Butowski NA. **Treatment options for recurrent high-grade gliomas.** *CNS Oncol* 2017;6:61–70 CrossRef Medline
 42. Taylor JW, Schiff D. **Treatment considerations for MGMT-unmethylated glioblastoma.** *Curr Neurol Neurosci Rep* 2015;15:507 CrossRef Medline
 43. Christmann M, Nagel G, Horn S, et al. **MGMT activity, promoter methylation and immunohistochemistry of pretreatment and recurrent malignant gliomas: a comparative study on astrocytoma and glioblastoma.** *Int J Cancer* 2010;127:2106–18 CrossRef Medline
 44. Della Puppa A, Persano L, Masi G, et al. **MGMT expression and promoter methylation status may depend on the site of surgical sample collection within glioblastoma: a possible pitfall in stratification of patients?** *J Neurooncol* 2012;106:33–41 CrossRef Medline
 45. Grasbon-Frodl EM, Kreth FW, Ruiter M, et al. **Intratumoral homogeneity of MGMT promoter hypermethylation as demonstrated in serial stereotactic specimens from anaplastic astrocytomas and glioblastomas.** *Int J Cancer* 2007;121:2458–64 CrossRef Medline

Traumatic Cerebral Microbleeds in the Subacute Phase Are Practical and Early Predictors of Abnormality of the Normal-Appearing White Matter in the Chronic Phase

A.W. van der Eerden, T.L. van den Heuvel, V. Perlberg, P. Vart, P.E. Vos, L. Puybasset, D. Galanaud, B. Platel, R. Manniesing, and B.M. Goraj



ABSTRACT

BACKGROUND AND PURPOSE: In the chronic phase after traumatic brain injury, DTI findings reflect WM integrity. DTI interpretation in the subacute phase is less straightforward. Microbleed evaluation with SWI is straightforward in both phases. We evaluated whether the microbleed concentration in the subacute phase is associated with the integrity of normal-appearing WM in the chronic phase.

MATERIALS AND METHODS: Sixty of 211 consecutive patients 18 years of age or older admitted to our emergency department ≤ 24 hours after moderate to severe traumatic brain injury matched the selection criteria. Standardized 3T SWI, DTI, and TIWI were obtained 3 and 26 weeks after traumatic brain injury in 31 patients and 24 healthy volunteers. At baseline, microbleed concentrations were calculated. At follow-up, mean diffusivity (MD) was calculated in the normal-appearing WM in reference to the healthy volunteers (MD_z). Through linear regression, we evaluated the relation between microbleed concentration and MD_z in predefined structures.

RESULTS: In the cerebral hemispheres, MD_z at follow-up was independently associated with the microbleed concentration at baseline (left: $B = 38.4$ [95% CI 7.5–69.3], $P = .017$; right: $B = 26.3$ [95% CI 5.7–47.0], $P = .014$). No such relation was demonstrated in the central brain. MD_z in the corpus callosum was independently associated with the microbleed concentration in the structures connected by WM tracts running through the corpus callosum ($B = 20.0$ [95% CI 24.8–75.2], $P < .000$). MD_z in the central brain was independently associated with the microbleed concentration in the cerebral hemispheres ($B = 25.7$ [95% CI 3.9–47.5], $P = .023$).

CONCLUSIONS: SWI-assessed microbleeds in the subacute phase are associated with DTI-based WM integrity in the chronic phase. These associations are found both within regions and between functionally connected regions.

ABBREVIATIONS: B = linear regression coefficient; B_{cmb-conc} = linear regression coefficient with microbleed concentration as independent variable; B_{cmb-nr} = linear regression coefficient with microbleed number as independent variable; MD = mean diffusivity; MD_z = Z-score of mean diffusivity, normalized to the healthy control participants; t1 = 3 (2–5) weeks after TBI; t2 = 26 (25–28) weeks after TBI; TAI = traumatic axonal injury; TBI = traumatic brain injury; FA = fractional anisotropy; MARS = Microbleed Anatomical Rating Scale; GCS = Glasgow Coma Scale

The yearly incidence of traumatic brain injury (TBI) is around 300 per 100,000 persons.^{1,2} Almost three-quarters of patients with moderate to severe TBI have traumatic axonal injury (TAI).³ TAI is a major predictor of functional outcome,^{4,5} but it is mostly invisible on CT and conventional MR imaging.^{6,7}

DTI provides direct information on WM integrity and axonal injury.^{5,8} However, DTI abnormalities are neither specific for TAI

nor stable over time. Possibly because of the release of mass effect and edema and resorption of blood products, the effects of concomitant (non-TAI) injury on DTI are larger in the subacute than in the chronic phase (>3 months).^{4,9,10} Therefore, DTI findings are expected to reflect TAI more specifically in the chronic than in the subacute phase (1 week–3 months).⁴ Even in regions without concomitant injury, the effects of TAI on DTI are dynamic, possibly

Received September 29, 2020; accepted after revision November 16.

From the Department of Radiology and Nuclear Medicine (A.W.v.d.E., T.L.v.d.H., B.P., R.M., B.M.G.), Radboud University Medical Center, Nijmegen, The Netherlands; Department of Radiology & Nuclear Medicine (A.W.v.d.E.), Erasmus Medical Center, Rotterdam, The Netherlands; Inserm, Sorbonne Université (V.P.), CNRS, Laboratoire d'Imagerie Biomédicale, Paris, France; BrainTale SAS (V.P.), Paris, France; Department of Epidemiology and Biostatistics (P.V.), Radboud University Nijmegen, Nijmegen, The Netherlands; Department of Neurology (P.E.V.), Santiz-Slingeland Hospital, Doetinchem, The Netherlands; Department of Neurosurgical ICU (L.P.) and Department of Neuroradiology (D.G.), Pitié Salpêtrière Hospital, Assistance Publique-Hôpitaux de Paris, Paris, France; and Department of Diagnostic Imaging (B.M.G.), Medical Centre of Postgraduate Education, Warsaw, Poland.

This is an investigator-initiated study supported by Trauma Regio Oost, Radboudumc, Nijmegen, and by Stichting Fonds Catharine van Tussenbroek (travel grant). The funding organizations did not participate in the design and conduct of the study; collection, management, analysis, and interpretation of the data; preparation, review, and approval of the manuscript; and the decision to submit the manuscript for publication.

Please address correspondence to A.W. van der Eerden, MD, Erasmus Medical Center, Department of Radiology & Nuclear Medicine, P.O. Box 2040, 3000 CA Rotterdam, The Netherlands; e-mail: a.vandereerden@erasmusmc.nl

Indicates article with online supplemental data.
<http://dx.doi.org/10.3174/ajnr.A7028>

caused by degeneration and neuroplastic changes.^{6,11,12} These ongoing pathophysiological processes possibly contribute to the emerging evidence that DTI findings in the chronic phase are most closely associated with the eventual functional outcome.^{12,13}

Although DTI provides valuable information, its acquisition, postprocessing, and interpretation in individual patients are demanding. SWI, with which microbleeds can be assessed with high sensitivity, is easier to interpret and implement in clinical practice. In contrast to DTI, SWI-detected traumatic microbleeds are more stable¹ except in the hyperacute^{14,15} and the late chronic phases.¹⁶ Traumatic cerebral microbleeds are commonly interpreted as signs of TAI. However, the relation is not straightforward. On the one hand, nontraumatic microbleeds may be pre-existing. On the other hand, even if traumatic in origin, microbleeds represent traumatic vascular rather than axonal injury.¹⁷ Indeed, TAI is not invariably hemorrhagic.¹⁸ Additionally, microbleeds may secondarily develop after trauma through mechanisms unrelated to axonal injury, such as secondary ischemia.¹⁸

DTI is not only affected by pathophysiological changes but also by susceptibility.¹⁹ The important susceptibility-effect generated by microbleeds renders the interpretation of DTI findings at the location of microbleeds complex. In the chronic phase, mean diffusivity (MD) is the most robust marker of WM integrity.^{4,6} For these reasons, we evaluated MD in the normal-appearing WM.

Much TAI research focuses on the corpus callosum because it is commonly involved in TAI.^{5,18,20} and it can reliably be evaluated with DTI.^{5,21} and TAI in the corpus callosum is related to clinical prognosis.^{6,20} The corpus callosum consists of densely packed WM tracts that structurally and functionally connect left- and right-sided brain structures.²² The integrity of the corpus callosum is associated with the integrity of the brain structures it connects.²³ Therefore, microbleeds in brain structures that are connected through the corpus callosum may affect callosal DTI findings. Analogous to this, microbleeds in the cerebral hemispheres, which exert their function through WM tracts traveling through the deep brain structures and brain stem,^{24,25} may affect DTI findings in the WM of the latter.

Our purpose was to evaluate whether the microbleed concentration in the subacute phase is associated with the integrity of normal-appearing WM in the chronic phase. We investigated this relation within the cerebral hemispheres and the central brain and between regions that are functionally connected by WM tracts.

MATERIALS AND METHODS

We report a retrospective interpretation of prospectively collected data within an observational follow-up cohort study in consecutive patients with moderate to severe TBI and healthy volunteers, approved by Radboud university medical center institutional review board. All healthy volunteers and patients or their next of kin gave written informed consent.

Study Design and Research Questions

We evaluated whether the microbleed concentration (number of microbleeds per cm³) detected with SWI in the subacute phase of TBI is correlated with MD of normal-appearing WM in the chronic phase. MD was measured in the normal-appearing WM after the exclusion of abnormalities based on an SWI-based mask drawn for each patient. The research questions are specified in the Figure.

Patient Selection and MR Acquisition

All 211 consecutive patients 18 years of age or older having sustained a moderate to severe TBI ≤ 24 hours before presenting at our level I trauma center emergency department were prospectively screened for the exclusion criteria specified in the Online Supplemental Data. Details of the patient selection process are described in the Online Supplemental Data. Finally, this yielded SWI, DTI, and T1WI data for 31 patients, obtained median 3 (interquartile range 2–5 [*t1*]) and median 26 (interquartile range 25–28 [*t2*]) weeks after TBI using a standardized trauma protocol on a single 3T MR imaging scanner (Magnetom Trio, Siemens). The Online Supplemental Data summarize the parameters of the relevant MR imaging sequences.

Patient characteristics are summarized in the Online Supplemental Data.

Healthy Volunteers

To increase generalizability and facilitate interpretation, we normalized the patients' MD values to those of 24 healthy volunteers, scanned on the same MR imaging scanner with equal acquisition parameters, and recruited as described in the Online Supplemental Data. The section "DTI Processing" below describes the normalization procedure.

Microbleed Anatomical Rating Scale Atlas

We manually segmented the standard brain in Montreal Neurological Institute space²⁶ into the regions specified in the Microbleed Anatomical Rating Scale (MARS) scoring template.²⁷ We defined the following compound regions: 1) cerebral hemispheres (left, right, and bilateral), 2) central brain region, and 3) structures connected through the corpus callosum. See the Online Supplemental Data for details and definitions of these compound regions.

Microbleed Evaluation


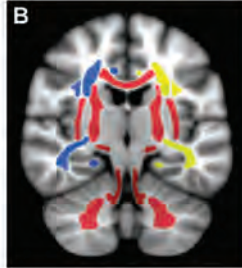
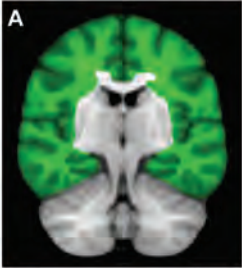
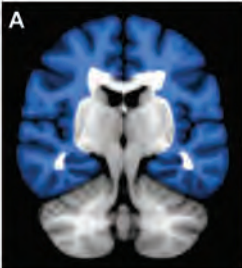
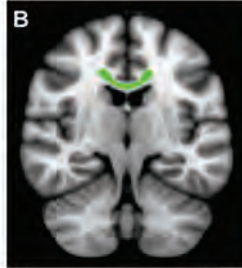
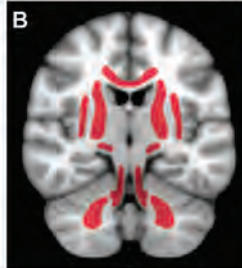
We detected microbleeds and allocated them to MARS regions as described in the Online Supplemental Data. As recommended,²⁷ we performed our analyses on definite microbleeds only. Per patient, we calculated the microbleed concentration (cm⁻³) within each anatomic region as the number of microbleeds divided by the volume of the region under investigation on the T1-weighted scan at *t1* (cm³).


Creation of Susceptibility Mask


To rule out bias caused by the effect of susceptibility on DTI findings,¹⁹ we created individual exclusion masks, eliminating from the DTI measurements any potential source of susceptibility related to trauma and its clinical management. See the Online Supplemental Data for details.


DTI Processing


We extracted MD values from the normal-appearing WM of the following compound regions: 1) cerebral hemispheres, 2) central brain region, and 3) corpus callosum based on the ICBM-DTI-81 WM labels atlas designed by Mori et al.²⁸ Definitions of these compound regions and details of the DTI processing procedure are described in the Online Supplemental Data. Regional MDs were calculated for each patient and healthy volunteer as the

RESEARCH QUESTION	REGION OF CMB-CONCENTRATION ^a <i>t1</i> , MARS atlas	REGION OF MD-MEASUREMENT ^b <i>t2</i> , ICBM-DTI-81 atlas
1. Is the microbleed concentration at <i>t1</i> associated with white matter integrity at <i>t2</i> ? a. within the left and within the right cerebral hemisphere b. within the central brain region		
2.a Is the microbleed concentration in the structures connected through the corpus callosum at <i>t1</i> associated with integrity of the corpus callosum at <i>t2</i> ? 2.b Is the microbleed concentration in the cerebral hemispheres at <i>t1</i> associated with white matter integrity in the central brain region at <i>t2</i> ?	 	 

 right cerebral hemisphere (1), cerebral hemispheres (2.b.A)

 left cerebral hemisphere

 central brain region

 structures connected through the corpus callosum (2.a.A), corpus callosum (2.a.B)

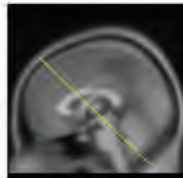


FIGURE. Study design and research questions. Images are oblique coronal sections of the Montreal Neurological Institute brain, illustrating the regions evaluated for each research question (image plane illustrated in the *thumbnail image in the right lower corner*). ^aNumber of microbleeds per cm³ brain tissue. ^bZ-score of mean diffusivity. *t1* indicates Moment of SWI-acquisition, i.e. 3 (2–5) weeks after TBI; *t2*, Moment of DTI-acquisition, i.e. 26 (25–28) weeks after TBI; MARS atlas, Microbleed Anatomical Rating Scale atlas²⁷; ICBM-DTI-81 atlas, the ICBM-DTI-81 white matter labels atlas designed by Mori S et al.²⁸

averaged MD within each region, and the Z score of MD (MD_z) of each region was calculated as:

$$MD_z = \frac{MD_p - [MD_v]}{SD_{MD_v}}$$

in which MD_p is the patient's MD, MD_v is the mean MD of the healthy volunteers, and SD_{MD_v} is the standard deviation of the healthy volunteers' MD.

Blinding

The persons processing (T.v.d.H., B.P.) and interpreting the SWI data (A.v.d.E., B.M.G.) had no access to clinical information nor

DTI results. V.P., who processed the DTI data, had no access to clinical information nor to microbleed counts.

Statistical Analysis

Data were analyzed by P.V. (statistician) and A.v.d.E. using SPSS 25 statistical software (IBM).

We used 2-sample *t*-tests to test differences in MD_z between patients and healthy volunteers.

We used linear regression analyses to examine the relation between the microbleed concentration and MD_z , as specified in the Figure. We adjusted for sex, age at the day of DTI, and time passed from TBI to DTI acquisition (Table, multivariable model). Because the severity of TBI is associated with both microbleeds¹⁷ and MD_z ,³

Association between microbleed concentrations at $t1$ and MD_z at $t2$

Research Question	Region of Microbleed Concentration	White Matter Region of MD Measurement	Univariable		Multivariable ^a	
			$B_{\text{cmb-conc}}$ (95% CI, P)	$B_{\text{cmb-nr}}$ (95% CI)	$B_{\text{cmb-conc}}$ (95% CI, P)	$B_{\text{cmb-nr}}$ (95% CI)
1.a	Cerebral hemispheres:	Cerebral hemispheres:				
	Left	Left	35.2 (8.6–61.8, .011)	0.067 (0.016–0.117)	38.4 (7.5–69.3, .017)	0.073 (0.014–0.131)
	Right	Right	28.3 (11.1–45.5, .002)	0.055 (0.022–0.089)	26.3 (5.7–47.0, .014)	0.051 (0.011–0.091)
1.b	Central brain region	Central brain region	8.2 (–8.5–24.9, .322)	0.024 (–0.025–0.074)	7.8 (–9.9–25.6, .374)	0.023 (–0.029–0.076)
2.a	Structures connected through the corpus callosum	Corpus callosum	44.2 (23.6–64.8, .000)	0.041 (0.022–0.060)	20.0 (24.8–75.2, .000)	0.019 (0.023–0.070)
2.b	Cerebral hemispheres	Central brain region	24.2 (6.8–41.5, .008)	0.024 (0.007–0.040)	25.7 (3.9–47.5, .023)	0.025 (0.004–0.046)

Note:—Results of linear regression analyses. None of the variables other than microbleed concentration is associated with MD_z with $P < .05$ in the multivariable analyses.

^a Multivariable linear regression analyses with the following independent variables: microbleed concentration, sex, age at the day of DTI imaging (years), and time passed from TBI to DTI acquisition (weeks). MD_z indicates Z-score of mean diffusivity; $t1$, 3 (2–5) weeks after trauma; $t2$, 26 (25–28) weeks after trauma; $B_{\text{cmb-conc}}$, linear regression coefficient with microbleed-concentration as independent variable; $B_{\text{cmb-nr}}$, linear regression coefficient with number of microbleeds as independent variable.

it could confound the association between microbleeds and MD. Therefore, we adjusted the analyses for the Glasgow Coma Scale (GCS) score at the injury site (research question 2: Online Supplemental Data; research question 1: results described in the text). Because microbleed concentrations in different regions of the same brain may covary, the associations in research question 2 could be confounded by the microbleed concentration in the region of MD measurement. Therefore, we adjusted the analyses for the microbleed concentration in the region of MD measurement (Online Supplemental Data).

To facilitate clinical implementation of our findings, in addition to the linear regression coefficients for microbleed concentration ($B_{\text{cmb-conc}}$), we also present the linear regression coefficients for microbleed number ($B_{\text{cmb-nr}}$). These 2 coefficients can be interpreted as follows: with each increase of the microbleed concentration by $1/\text{cm}^3$, MD_z increases with $B_{\text{cmb-conc}}$, but with each additional microbleed, MD_z increases with $B_{\text{cmb-nr}}$.

Differences with $P < .05$ were considered significant. Continuous variables are presented as median (interquartile range). Categorical variables are presented as number (%). Regression coefficients are presented as linear regression coefficient (95% CI).

For a detailed description of the statistical procedures, please refer to the Online Supplemental Data.

As discussed earlier, we chose MD as the DTI variable of interest. To facilitate comparison with other papers, we performed the same analyses with the more frequently reported fractional anisotropy (FA). Please refer to the Online Supplemental Data for the results.

RESULTS

At $t1$, the 31 patients had a total of 856 microbleeds (median 24 [interquartile range, 14–35] per patient), anatomically distributed as shown in Supplemental Online Table A4. MD_z at $t2$ was higher in patients than in healthy volunteers (Supplemental Online Table A4).

Associations within Regions (Research Question 1)

Within both of the cerebral hemispheres, MD_z at $t2$ was positively associated with the microbleed concentration at $t1$ (Table and

Online Supplemental Data). This association was independent of sex, age, and time passed from TBI to DTI acquisition (Table). It was also independent of GCS score at the injury site ($B_{\text{cmb-conc}}$ 30.3 [95% CI 11.5–49.1, $P = .003$] and 36.3 [95% CI 8.8–63.7, $P = .011$] for microbleed concentration in the right and left cerebral hemisphere, respectively, in bivariable linear regression corrected for GCS score). Within the central brain region, MD_z was not associated with the microbleed concentration (Table and Online Supplemental Data).

Associations between Connected Regions (Research Question 2)

MD_z in the corpus callosum at $t2$ was positively associated with the microbleed concentration in the structures connected through the corpus callosum at $t1$ (Table and Online Supplemental Data) even after correction for the microbleed concentration in the corpus callosum itself (Online Supplemental Data). The 95% CIs of $B_{\text{cmb-conc}}$ in these 2 regions did not overlap (Online Supplemental Data).

MD_z in the central brain region was positively associated with the microbleed concentration at $t1$ in the cerebral hemispheres (Table and Online Supplemental Data) even after correction for the microbleed concentration in the central brain region itself (Online Supplemental Data).

All of these associations were independent of GCS score, sex, age, and time passed from TBI to DTI acquisition (Table, Online Supplemental Data).

See the Online Supplemental Data for the results of the equivalent analyses with FA.

DISCUSSION

We have shown that as early as the subacute phase of TBI, microbleeds are predictors of the integrity of normal-appearing WM in the chronic phase. Microbleeds are not only predictive of WM integrity in the same region but also of WM integrity in functionally connected regions.

To our knowledge, this is the first study to address the association between microbleeds detected early with SWI and later DTI findings in normal-appearing WM in consecutive patients with moderate to severe TBI.

Our findings are based on more microbleeds than the 3 previous studies on the relation between traumatic microbleeds and DTI. Whereas our patients had a total of 856 microbleeds, occurring in 30 patients (1 patient had no microbleeds), the patients reported previously had only 97–138 microbleeds,^{29,30} occurring in 14 and 29 patients,^{29,30} or an unreported number of microbleeds, occurring in 8 patients.³¹ The relatively large amount of microbleeds allowed us to correct for possible interfering factors such as age, sex, GCS score, and time passed from TBI to DTI acquisition.

The interpretation of our results is facilitated by the use of microbleed concentrations and normalized MD values, which enhance uniformity between regions with different volumes and reference MD values. In contrast, previous groups quantified their microbleed data using dichotomized,³¹ ordinal,²⁹ or absolute microbleed numbers in regions of varying volume³⁰ and used absolute values of the DTI variables.²⁹⁻³¹

The inclusion of DTI findings inside the microbleeds^{29,31} by previous authors may have introduced possible confounding by the effects of susceptibility on DTI findings.¹⁹ Two of the previous studies detected microbleeds with a less sensitive technique.^{29,31} Previous authors evaluated SWI and DTI simultaneously at widely varying time points after TBI³⁰ or defined less clearly the timing of microbleed detection.³¹ They defined their inclusion criteria less clearly^{30,31} or the severity of TBI differed from our patients.³⁰

Relation between Microbleeds and WM Integrity within the Cerebral Hemispheres

Within both of the cerebral hemispheres, WM integrity in the chronic phase is predictive of the microbleed concentration in the subacute phase. This prediction is independent of GCS score, sex, age, and time passed from TBI to DTI acquisition. Although our data do not allow evaluation of the causality of this association, our findings support the assessment of microbleeds in daily practice because microbleeds are easier to evaluate in a clinical setting than DTI, especially in the subacute phase. The relation we found between microbleeds and WM integrity is consistent with autopsy studies showing that MR imaging–detected microbleeds are related to axonal necrosis,³² and anatomopathologic microbleeds are related to axonal injury.³³

Compatible with our findings, the 2 previous longitudinal MR imaging studies found a lower FA in patients with microbleeds³¹ and inside callosal and cerebral hemispheric microbleeds.²⁹ In contrast to the association we found between microbleeds and MD in the cerebral hemispheres, Toth et al³⁰ found no such association within the subcortical WM. On the one hand, this suggests a relation between cortical microbleeds and integrity of the underlying WM. On the other hand, the apparent difference between their and our findings may partly rely on methodologic differences, such as the different and widely varying timing of their scans, the small number of microbleeds and of patients with microbleeds, and the wide range of trauma severity.³⁰

Relation between Microbleeds and WM Integrity in Connected Regions

We have shown that microbleeds are predictive of WM abnormality in functionally connected regions: microbleeds in structures connected by WM tracts running through the corpus callosum are predictive of the integrity of the corpus callosum, and microbleeds in the cerebral hemispheres are predictive of the integrity of the central brain region.

Our findings suggest that the integrity of WM is not only determined by nearby primary traumatic lesions but can also be affected by distant traumatic lesions. Indeed, the distant relation described earlier is independent of the microbleeds in the corpus callosum and the central brain region themselves. The integrity of the corpus callosum is even more strongly predicted by microbleeds in the connected regions than by local microbleeds in the corpus callosum itself. Analogous to this, in the central brain, the size of the regression coefficients suggests a stronger association of abnormality with microbleeds in the cerebral hemispheres than with microbleeds in the central brain, though the difference is not statistically significant. The distant effect of microbleeds could be an expression of degradation within neural networks at distance of the primary injury,¹⁸ such as the thalamocortical and pontothalamocortical deafferentiation observed in patients with TBI.²⁴ It could be mediated by the axons or vessels involved in the primary injury, either by functional deprivation of the corpus callosum and the central brain, respectively or by biochemical changes within the long axons or perivascular spaces.¹⁷

Consistent with our findings, Kumar et al³¹ found a decreased MD in the corpus callosum only in the patients with microbleeds, which were all outside the corpus callosum, and a normal MD in the patients without microbleeds. Like us, Toth et al³⁰ found no local effect of microbleeds within the corpus callosum on callosal integrity. Unlike us, they found no association between microbleeds in the subcortical WM and integrity of the normal-appearing callosal tissue. The methodologic differences discussed earlier may have contributed to this lack of association.³⁰

Limitations

A potential bias results from the manual delineation of the microbleeds and concomitant injury.

The limited number of patients did not allow us to assess the potential prognostic value of microbleed concentration or of MD_z measurements.

Inherent to TBI research, the effects of injury severity and concomitant intracranial injury on MD are difficult to disentangle from the microbleeds' effects. To minimize these effects, we included GCS score in our analyses and measured MD outside any concomitant lesions using the susceptibility mask.

Implications and Future Perspectives

We have shown that as early as the subacute phase of TBI, microbleeds inform us on the expected integrity of normal-appearing WM in the chronic phase and that this relation differs between regions. The evidence of the prognostic value of DTI in the chronic phase is growing,^{6,13} but in the subacute phase, DTI has

less robust prognostic value, possibly because of the more dynamic and heterogeneous pathophysiologic mechanisms influencing DTI findings in that phase.^{6,11} The evidence for the prognostic value of traumatic microbleeds is limited.¹⁷ Our findings encourage a shift in the search for the prognostic value of microbleeds to the use of their regional distribution and their concentration instead of their number and a shift of attention to early prognostication when microbleeds have the clear advantage of stability over DTI.

The different relations we found between microbleeds and MD and FA, respectively, may indicate that not only chronic encephalopathic degeneration³⁴ but also earlier stages of distant effects of traumatic lesions develop in a centripetal way. The timing of DTI-evaluation in our study is at the border between the subacute and the chronic stage. At that transitional stage, the peripheral brain may already be entering the chronic stage, but the central brain is still in the subacute phase. This hypothesis should be tested in further studies.

CONCLUSIONS

Whereas DTI interpretation is complex in the subacute phase of TBI, microbleeds assessed with SWI in the subacute phase proved to be predictive of DTI abnormalities of the normal-appearing WM in the chronic phase. Associations are not only found within regions but also between functionally connected regions. The latter are independent of the local microbleed concentration and GCS score, indicating that microbleeds may exert effects at a distance.

ACKNOWLEDGMENTS

We thank TMJC Andriessen, psychologist at Saffier, Den Haag, for her contribution to the collection of data. We thank D Hasboun, PhD, neurologist and anatomist at Université Pierre et Marie Curie, Paris, for his support in selection and definition of functionally relevant compound regions of interest. We thank SC van de Leemput, data and information scientist at Radboudumc, Nijmegen, for providing the software we used for manual adjustments of the susceptibility mask. We also thank FL van der Panne, medical photographer at Erasmus MC, Rotterdam, and K Koschmieder, PhD, student traumatic imaging analysis at Radboudumc, for their help with figure design. Last, we thank Stichting Fonds Catharine van Tussenbroek for the travel grant that facilitated our international collaboration.

Disclosures: Anke van der Eerden—RELATED: Grant: Trauma Regio Oost, Radboudumc, Nijmegen, The Netherlands, Comments: Investigator-initiated study supported by Trauma Regio Oost, Radboudumc, Nijmegen. The funding organization did not participate in the design and conduct of the study; collection, management, analysis, and interpretation of the data; preparation, review, and approval of the manuscript; and the decision to submit the manuscript for publication*; Support for Travel to Meetings for the Study or Other Purposes: Stichting Fonds Catharine van Tussenbroek, Comments: Partial reimbursement of travel expenses from Nijmegen to Paris to facilitate our collaboration. The funding organization did not participate in the design and conduct of the study; collection, management, analysis, and interpretation of the data; preparation, review, and approval of the manuscript; and the decision to submit the manuscript for publication; UNRELATED: Employment: Erasmus Medical Center, Comments: clinical neuroradiologist and head and neck radiologist. Louis Puybasset—UNRELATED: Stock/Stock Options: BrainTale co-founder. *Money paid to institution.

REFERENCES

1. Nguyen R, Fiest KM, McChesney J, et al. **The international incidence of traumatic brain injury: a systematic review and meta-analysis.** *Can J Neurol Sci* 2016;43:774–85 CrossRef Medline
2. Peeters W, Van den Brande R, Polinder S, et al. **Epidemiology of traumatic brain injury in Europe.** *Acta Neurochir (Wien)* 2015;157:1683–96 CrossRef Medline
3. Skandsen T, Kvistad KA, Solheim O, et al. **Prevalence and impact of diffuse axonal injury in patients with moderate and severe head injury: a cohort study of early magnetic resonance imaging findings and 1-year outcome.** *J Neurosurg* 2010;113:556–63 CrossRef
4. Wallace EJ, Mathias JL, Ward L. **The relationship between diffusion tensor imaging findings and cognitive outcomes following adult traumatic brain injury: a meta-analysis.** *Neurosci Biobehav Rev* 2018;92:93–103 CrossRef Medline
5. Hulkower MB, Poliak DB, Rosenbaum SB, et al. **A decade of DTI in traumatic brain injury: 10 years and 100 articles later.** *AJNR Am J Neuroradiol* 2013;34:2064–74 CrossRef Medline
6. Sidaros A, Engberg AW, Sidaros K, et al. **Diffusion tensor imaging during recovery from severe traumatic brain injury and relation to clinical outcome: a longitudinal study.** *Brain* 2008;131:559–72 CrossRef
7. Haller S, Vernooij MW, Kuijter JPA, et al. **Cerebral microbleeds: imaging and clinical significance.** *Radiology* 2018;287:11–28 CrossRef Medline
8. Shenton ME, Hamoda HM, Schneiderman JS, et al. **A review of magnetic resonance imaging and diffusion tensor imaging findings in mild traumatic brain injury.** *Brain Imaging Behav* 2012;6:137–92 CrossRef Medline
9. Ma C, Liu A, Li Z, et al. **Longitudinal study of diffusion tensor imaging properties of affected cortical spinal tracts in acute and chronic hemorrhagic stroke.** *J Clin Neurosci* 2014;21:1388–92 CrossRef Medline
10. Yokoyama K, Matsuki M, Shimano H, et al. **Diffusion tensor imaging in chronic subdural hematoma: correlation between clinical signs and fractional anisotropy in the pyramidal tract.** *AJNR Am J Neuroradiol* 2008;29:1159–63 CrossRef Medline
11. Mac Donald CL, Dikranian K, Bayly P, et al. **Diffusion tensor imaging reliably detects experimental traumatic axonal injury and indicates approximate time of injury.** *J Neurosci* 2007;27:11869–76 CrossRef Medline
12. Edlow BL, Copen WA, Izzy S, et al. **Diffusion tensor imaging in acute-to-subacute traumatic brain injury: a longitudinal analysis.** *BMC Neurol* 2016;16 CrossRef Medline
13. Perez AM, Adler J, Kulkarni N, et al. **Longitudinal white matter changes after traumatic axonal injury.** *J Neurotrauma* 2014;31:1478–85 CrossRef
14. Einarsen CE, Moen KG, Håberg AK, et al. **Patients with mild traumatic brain injury recruited from both hospital and primary care settings: a controlled longitudinal magnetic resonance imaging study.** *J Neurotrauma* 2019;36:3172–82 CrossRef Medline
15. Toth A, Kovacs N, Tamas V, et al. **Microbleeds may expand acutely after traumatic brain injury.** *Neurosci Lett* 2016;617:207–12 CrossRef Medline
16. Liu W, Soderlund K, Senseney JS, et al. **Imaging cerebral microhemorrhages in military service members with chronic traumatic brain injury.** *Radiology* 2016;278:536–45 CrossRef Medline
17. Griffin AD, Turtzo LC, Parikh GY, et al. **Traumatic microbleeds suggest vascular injury and predict disability in traumatic brain injury.** *Brain* 2019;142:3550–64 CrossRef Medline
18. Benson RR, Gattu R, Sewick B, et al. **Detection of hemorrhagic and axonal pathology in mild traumatic brain injury using advanced MRI: implications for neurorehabilitation.** *NeuroRehabilitation* 2012;31:261–79 CrossRef Medline
19. Zhang J, Tao R, Liu C, et al. **Possible effects of iron deposition on the measurement of DTI metrics in deep gray matter nuclei: an in vitro and in vivo study.** *Neurosci Lett* 2013;551:47–52 CrossRef Medline

20. Cicuendez M, Castaño-León A, Ramos A, et al. **Prognostic value of corpus callosum injuries in severe head trauma.** *Acta Neurochir* 2017;159:25–32 CrossRef
21. Wang JY, Abdi H, Bakhadirov K, et al. **A comprehensive reliability assessment of quantitative diffusion tensor tractography.** *NeuroImage* 2012;60:1127–38 CrossRef Medline
22. Dennis EL, Ellis MU, Marion SD, et al. **Callosal function in pediatric traumatic brain injury linked to disrupted white matter integrity.** *J Neurosci* 2015;35:10202–11 CrossRef Medline
23. Domin M, Lotze M. **Parcellation of motor cortex-associated regions in the human corpus callosum on the basis of Human Connectome Project data.** *Brain Struct Funct* 2019;224:1447–55 CrossRef Medline
24. Laouchedi M, Galanaud D, Delmaire C, et al. **Deafferentation in thalamic and pontine areas in severe traumatic brain injury.** *J Neuroradiol* 2015;42:202–11 CrossRef Medline
25. Chen YJ, Nabavizadeh SA, Vossough A, et al. **Wallerian degeneration beyond the corticospinal tracts: conventional and advanced MRI findings.** *J Neuroimaging* 2017;27:272–80 CrossRef Medline
26. MNI ICBM 152 non-linear 6th Generation Symmetric Average Brain Stereotaxic Registration Model. <http://nist.mni.mcgill.ca/?p=858>. Accessed December 2017
27. Gregoire SM, Chaudhary UJ, Brown MM, et al. **The Microbleed Anatomical Rating Scale (MARS): reliability of a tool to map brain microbleeds.** *Neurology* 2009;73:1759–66 CrossRef
28. Mori S, Oishi K, Jiang H, et al. **Stereotaxic white matter atlas based on diffusion tensor imaging in an ICBM template.** *Neuroimage* 2008;40:570–82 CrossRef Medline
29. Moen KG, Vik A, Olsen A, et al. **Traumatic axonal injury: relationships between lesions in the early phase and diffusion tensor imaging parameters in the chronic phase of traumatic brain injury.** *J Neurosci Res* 2016;94:623–35 CrossRef Medline
30. Toth A, Kornyei B, Kovacs N, et al. **Both hemorrhagic and non-hemorrhagic traumatic MRI lesions are associated with the microstructural damage of the normal appearing white matter.** *Behav Brain Res* 2018;340:106–16 CrossRef Medline
31. Kumar R, Husain M, Gupta RK, et al. **Serial changes in the white matter diffusion tensor imaging metrics in moderate traumatic brain injury and correlation with neuro-cognitive function.** *J Neurotrauma* 2009;26:481–95 CrossRef Medline
32. Keene CD, Latimer CS, Steele LM, et al. **First confirmed case of chronic traumatic encephalopathy in a professional bull rider.** *Acta Neuropathol* 2018;135:303–05 CrossRef Medline
33. Adams JH, Graham DI, Murray LS, et al. **Diffuse axonal injury due to nonmissile head injury in humans: an analysis of 45 cases.** *Ann Neurol* 1982;12:557–63 CrossRef Medline
34. McKee AC, Stein TD, Nowinski CJ, et al. **The spectrum of disease in chronic traumatic encephalopathy.** *Brain* 2013;136:43–64 CrossRef Medline

Inversion Recovery Ultrashort TE MR Imaging of Myelin is Significantly Correlated with Disability in Patients with Multiple Sclerosis

H. Jang, Y.-J. Ma, E.Y. Chang, S. Fazeli, R.R. Lee, A.F. Lombardi, G.M. Bydder, J. Corey-Bloom, and J. Du



ABSTRACT

BACKGROUND AND PURPOSE: MR imaging has been widely used for the noninvasive evaluation of MS. Although clinical MR imaging sequences are highly effective in showing focal macroscopic tissue abnormalities in the brains of patients with MS, they are not specific to myelin and correlate poorly with disability. We investigated direct imaging of myelin using a 2D adiabatic inversion recovery ultrashort TE sequence to determine its value in assessing disability in MS.

MATERIALS AND METHODS: The 2D inversion recovery ultrashort TE sequence was evaluated in 14 healthy volunteers and 31 patients with MS. MPRAGE and T2-FLAIR images were acquired for comparison. Advanced Normalization Tools were used to correlate inversion recovery ultrashort TE, MPRAGE, and T2-FLAIR images with disability assessed by the Expanded Disability Status Scale.

RESULTS: Weak correlations were observed between normal-appearing white matter volume ($R = -0.03$, $P = .88$), lesion load ($R = 0.22$, $P = .24$), and age ($R = 0.14$, $P = .44$), and disability. The MPRAGE signal in normal-appearing white matter showed a weak correlation with age ($R = -0.10$, $P = .49$) and disability ($R = -0.19$, $P = .31$). The T2-FLAIR signal in normal-appearing white matter showed a weak correlation with age ($R = 0.01$, $P = .93$) and disability ($R = 0.13$, $P = .49$). The inversion recovery ultrashort TE signal was significantly negatively correlated with age ($R = -0.38$, $P = .009$) and disability ($R = -0.44$; $P = .01$).

CONCLUSIONS: Direct imaging of myelin correlates with disability in patients with MS better than indirect imaging of long-T2 water in WM using conventional clinical sequences.

ABBREVIATIONS: ANTs = Advanced Normalization Tools; EDSS = Expanded Disability Status Scale; GM_L = long-T2 GM; GM_S = short-T2 GM; IR-UTE = inversion recovery prepared UTE; NAWM = normal-appearing white matter; UTE = ultrashort TE; WM_L = long-T2 WM; WM_S = short-T2 WM

MS is the most common demyelinating disease of the brain.¹ Demyelination affects many aspects of neurologic function, including speech, balance, and cognitive awareness. Across time, this frequently leads to severe and irreversible clinical disability. MR imaging has been widely used for accurate diagnosis of MS, with current techniques focused on imaging the long-T2 water components in WM and GM.²⁻⁴ MS lesions often appear hypointense with T1-weighted gradient recalled-echo sequences² and hyperintense with T2-weighted FSE and T2-weighted FLAIR

sequences.³ Active lesions can be highlighted with gadolinium-enhanced imaging.⁴ The magnetization transfer ratio has been used as an indirect marker of myelin disorder in regions of normal-appearing WM (NAWM).⁵ There are also several other advanced imaging techniques for indirect myelin imaging via assessment of myelin water, such as multicomponent T2 or T2* analysis^{6,7} and direct visualization of components with short transverse relaxation times.^{8,9}

While conventional MR imaging sequences are highly effective in detecting focal macroscopic brain tissue abnormalities, they are not specific for pathologic substrates of MS lesions such as demyelination and remyelination, and they may not correlate well with patients' neurologic deficits. Current MR imaging techniques correlate only modestly with disability assessed by the Expanded Disability Status Scale (EDSS).¹⁰⁻¹⁵ The total lesion load showed statistically significant-but-weak correlations with the EDSS score in several large-scale studies ($R = 0.1-0.3$).¹⁰⁻¹² Composite scores including relaxation times of different tissues and/or volumetric measures generally correlate more strongly with the EDSS score, with a maximum observed correlation of

Received May 17, 2020; accepted after revision November 16.

From the Departments of Radiology (H.J., Y.-J.M., E.Y.C., S.F., R.R.L., A.F.L., G.M.B., J.D.) and Neurosciences (J.C.-B.), University of California San Diego, San Diego, California; and Radiology Service (E.Y.C., R.R.L.), VA San Diego Healthcare System, San Diego, California.

This work was supported by grants from the National Institutes of Health (1R01 NS092650, T32 EB005970-09) and GE Healthcare.

Please address correspondence to Jiang Du, PhD, University of California San Diego, Department of Radiology, 200 West Arbor Drive, San Diego, CA 92103-8226; e-mail: jiangdu@ucsd.edu

Indicates open access to non-subscribers at www.ajnr.org

<http://dx.doi.org/10.3174/ajnr.A7006>

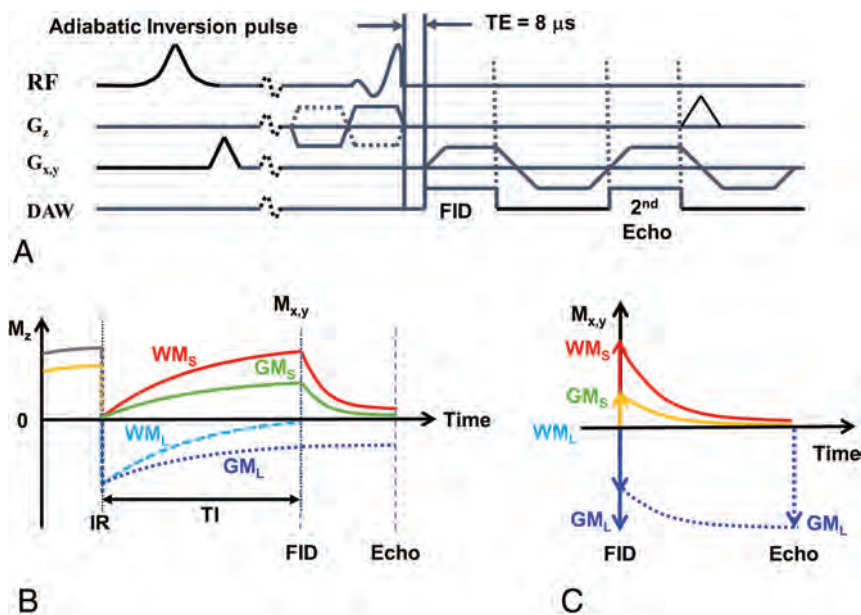


FIG 1. The 2D IR-UTE sequence (A) and contrast mechanism with adiabatic inversion recovery (B) and echo subtraction (C). At TI, WM signal comes only from WM_S. In GM, there is a cancellation between positive GM_S and negative GM_L longitudinal magnetizations at TI, which reduces the net transverse magnetization in GM after the excitation pulse. At the second echo, WM_S and GM_S signals both decay to zero or near zero, but the GM_L transverse magnetization is essentially unchanged. Subtraction of the second echo from the first leads to a positive signal for myelin in WM, but a negative signal for myelin in GM. This result creates very high contrast between the myelin in WM and GM (WM_S = short-T2 WM, WM_L = long-T2 WM, GM_S = short-T2 GM, GM_L = long-T2 GM).

$R = 0.34$ ($P < .001$).¹³ Lesions seen with gadolinium-enhanced imaging are only moderately correlated with disability in the first 6 months and are not predictive of changes in the EDSS score in the subsequent 1 or 2 years.¹⁴ A large-scale multicenter study reported very limited correlation between the EDSS score and normalized brain volume ($R = -0.18$), cross-sectional area ($R = -0.26$), magnetization transfer ratio of whole-brain tissue ($R = -0.16$), and GM ($R = -0.17$).¹⁵

The poor performance of conventional MR imaging sequences in assessing disability highlights the need for novel MR imaging techniques that can directly image myelin lipid and enable direct assessment of both myelin damage and repair. However, myelin has an extremely short transverse relaxation time and is not directly detectable with conventional MR images, which typically have TEs of several milliseconds or longer. Ultrashort TE (UTE) sequences can directly detect signal from myelin with ultrashort T2 (ie, excluding water with longer T2s).¹⁶⁻²¹ In this study, we describe imaging of WM using a 2D adiabatic inversion recovery prepared UTE (IR-UTE) sequence in healthy volunteers and patients with MS and evaluate its performance in assessing disability in patients with MS compared with 2 conventional clinical sequences.

MATERIALS AND METHODS

Imaging Subjects

A total of 31 patients with MS (21 women; 26–75 years of age; mean, age 55.8 years) were recruited. All patients underwent a

complete neurologic examination with an EDSS score at the time of MR imaging by a neurologist with >30 years of experience. Another 14 healthy volunteers (5 women; 24–56 years of age; mean age, 37.3 years) were also recruited for comparison. Institutional review board approval from Human Research Protections Program at University of California, San Diego was obtained, and informed consent was collected from each subject.

Pulse Sequence

A 2D IR-UTE sequence (Fig 1A) was implemented on a 3T clinical MR imaging scanner (MR750; GE Healthcare). The sequence uses half sinc radio-frequency pulses (duration = 472 μ s, bandwidth = 2.7 kHz) for excitation.¹⁹ Two excitations were performed with the gradient polarity reversed on the second occasion. The data from these excitations were added to produce a single radial line of k -space. After re-gridding, we reconstructed the raw data by inverse Fourier transformation. Bipolar slice-selective gradients and readout gradients were used to help reduce eddy currents.¹⁹

While a UTE sequence can detect signal from myelin protons, the major challenge is the much higher signal obtained from water in long-T2 WM and long-T2 GM (WM_L and GM_L in Fig 1).¹⁶ Because myelin represents only a small fraction of the total UTE signal, it is essential to suppress the WM_L signal to generate specific images of myelin in WM. To do this, a relatively long adiabatic fast-passage inversion pulse (Silver-Hoult pulse, duration = 8.64 ms) was used to invert the longitudinal magnetization of WM_L and GM_L.¹⁶⁻²¹ The transverse magnetization of myelin (WM_S and GM_S in Fig 1) has an extremely short T2* and was saturated during the long adiabatic inversion pulse.²² Data acquisition was started at the TI necessary for the inverted longitudinal magnetization of WM_L to reach its null point, leaving signals from myelin and other long-T2 tissues (eg, GM_L) to be detected by a dual-echo UTE acquisition. The second echo acquired signals from non-nulled long-T2 tissues such as GM_L but did not detect signal from myelin because the signal from this tissue decays to zero by the second TE. Subtraction of the second echo image from the first one provided selective imaging of the myelin in WM. Figure 1B describes this contrast mechanism. Note that on the subtracted image using magnitude reconstruction, myelin in WM has a positive signal, while ultrashort T2 components, including myelin in GM, have a negative signal (Fig 1C).

Image Acquisitions

Clinical 3D MPRAGE, 3D T2-FLAIR, and 2D IR-UTE sequences were performed for all 45 subjects. The 3D MPRAGE sequence used the following parameters: FOV = 220 × 220 × 160 mm³,

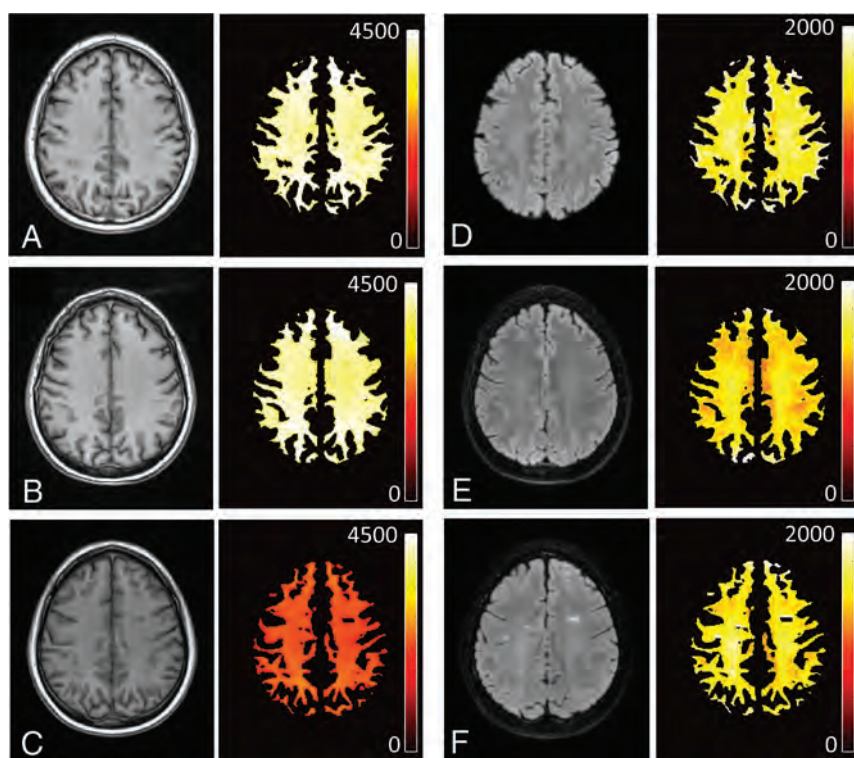


FIG 2. MPRAGE (A, B, and C, first column) and T2-FLAIR (D, E, and F, third column) images with their corresponding NAWM maps shown to the right of them (second and fourth columns, respectively) in a healthy volunteer (a 49-year-old man: A and D, upper row), a patient with MS with an EDSS score of 2 (a 56-year-old man: B and E, middle row), and a patient with MS with an EDSS score of 6 (a 46-year-old woman: C and F, lower row).

bandwidth = 83.4 kHz, flip angle = 12°, matrix = 256 × 256 × 136, TE = 3.2 ms, TR = 8.2 ms, TI = 450 ms, acceleration factor = 4, scan time = 4 minutes 12 seconds. The 3D T2-FLAIR sequence used the following parameters: FOV = 256 × 256 × 256 mm³, bandwidth = 83.4 kHz, flip angle = 90°, matrix = 256 × 256 × 256, TE = 116.5 ms, TR = 7600 ms, TI = 2162 ms, acceleration factor = 4, scan time = 6 minutes 54 seconds. The 2D IR-UTE sequence used the following parameters: FOV = 240 × 240 mm², section thickness = 4 mm, bandwidth = 256 kHz, flip angle = 60°, matrix = 256 × 256, number of projections = 131, sampling points per projection = 192, TR = 1500 ms, TI = 425 ms, dual-echo with TEs of 8 μs and 2.3 ms, scan time = 5 minutes 5 seconds. A 12-channel brain coil was used for signal reception.

Image Analysis

For image analysis, automatic brain segmentation codes were written in R programming language (<http://www.r-project.org/>) with Advanced Normalization Tools (ANTs; <http://stnava.github.io/ANTs/>).²³ The codes processed the 3D MPRAGE, 3D T2-FLAIR, and 2D IR-UTE images for all 45 subjects. The MPRAGE and T2-FLAIR images were processed with an N4 bias correction and then normalized (or registered) to a standard domain provided by the ICBM 152 brain template (<https://www.mcgill.ca/bic/software/tools-data-analysis/anatomical-mri/atlas/icbm152lin>)²⁴ using an affine transform followed by a deformable transform. Next, MPRAGE images of brain tissue were segmented into GM, WM,

and CSF using a multivariate 3-class segmentation.²⁵ For the 2D IR-UTE sequence, the echo-subtracted image was input to a similar-but-simplified framework, with N4 bias correction and 3-class tissue segmentation and without spatial normalization.

The raw segmentation map from ANTs was postprocessed using Matlab 2017b (MathWorks). The initial WM map from MPRAGE and T2-FLAIR was refined by removing regions with T2 lesions on the basis of the upper threshold set by the weighted sum of minimum and maximum signals in WM on T2-FLAIR images (weighting factors of 0.8 and 0.2). A radiologist with >15 years of experience manually refined the initial WM map from 2D IR-UTE by segmenting out the hypointense lesions. This step produced the final NAWM maps. All NAWM maps were manually inspected by a researcher with 9 years of experience in MR imaging research and a radiologist with 15 years of experience.

Statistical Analysis

All statistical analyses were conducted using Matlab 2017b. The mean NAWM signal was calculated for all subjects for

MPRAGE, T2-FLAIR, and 2D IR-UTE. Effects of flip angle, loading, analog-digital conversion, and reconstruction scaling were automatically compensated for by calibrating a transmit gain in prescan and by performing signal rescaling on the basis of receiver gains in image reconstruction to directly compare NAWM signal among different subjects.

The NAWM signal was compared in the 2 groups of healthy controls ($n = 14$) and patients with MS ($n = 31$) using a 2-tailed Mann-Whitney-Wilcoxon test, with a significance level set to .05. The Spearman correlation was calculated between the NAWM signal and age in all subjects ($n = 45$). The correlation between the NAWM signal and the EDSS scores in patients with MS was also calculated. In addition, NAWM volume (relative volume of NAWM to the total brain) and lesion load (relative volume of T2 lesions to WM) were calculated. Correlations between calculated NAWM volume and the EDSS score as well as between lesion load and the EDSS score in patients were calculated.

RESULTS

Figure 2 shows results with MPRAGE (Fig 2A–C) and T2-FLAIR images (Fig 2D–F) in 3 representative subjects, a healthy volunteer (a 49-year-old man: upper row) and 2 patients with MS with an EDSS score of 2 (a 56-year-old man: middle row) and with an EDSS score of 6 (a 46-year-old woman: lower row). The NAWM signal map from MPRAGE shows a marked reduction in signal

in the patient with MS with the higher EDSS score of 6 (lower row).

Figure 3 shows the results with the IR-UTE sequences in 3 representative subjects: a healthy volunteer (a 49-year-old man: Fig 3A), a patient with MS with an EDSS score of 2 (a 56-year-old man: Fig 3B), and a patient with MS with an EDSS of 6 (a 46-year-old woman: Fig 3C). The UTE images at TE = 8 μ s (first column) show myelin signal present in the NAWM region. This decays to zero, or near zero, at the second TE of 2.3 ms due to the short T2* of myelin (second column). The long-T2 components

in WM and GM are suppressed on echo subtraction, producing high-contrast myelin-specific images (third column). The signal on the segmented NAWM maps (fourth column) in the patient with MS with the higher EDSS score of 6 (Fig 3C) is much lower than that of the healthy volunteer (Fig 3A) and the patient with MS with an EDSS score of 2 (Fig 3B).

Figure 4 shows the scatterplots between NAWM volume and the EDSS score (Fig 4A) and between lesion load and the EDSS score (Fig 4B). The NAWM volume and lesion load were calculated from the segmented tissue maps obtained with the clinical sequences. Both the NAWM volume and the lesion load show low correlations with the EDSS score, which did not reach significance ($R = -0.03$, $P = .88$ and $R = 0.22$, $P = .24$, respectively).

The mean NAWM signal in the MPRAGE images was 3602.6 (SD, 498.1) in the control group and 2676.7 (SD, 877.8) in the MS group. The mean NAWM signal on the T2-FLAIR images was 1267.7 (SD, 184.2) in the control group and 1184.8 (SD, 218.4) in the MS group. The mean myelin signal in NAWM obtained with the IR-UTE image was 169.6 (SD, 39.5) in the control group and 136.3 (SD, 39.2) in the MS group. Figure 5 shows boxplots and the Mann-Whitney-Wilcoxon test between healthy controls and patients with MS. Both the MPRAGE (Fig 5A) and the IR-UTE (Fig 5C) NAWM maps show a significant difference in the 2 groups with P values of .003 and .02, respectively, while the T2-FLAIR NAWM maps (Fig 5B) show no significant difference ($P = .23$).

Figure 6 shows scatterplots of NAWM signals and subject age on MPRAGE (Fig 6A), T2-FLAIR (Fig 6B), and IR-UTE (Fig 6C) maps in the healthy controls and patients with MS. The MPRAGE and T2-FLAIR maps show weak correlations, which did not reach significance ($R = -0.10$, $P = .49$ and $R = 0.01$, $P = .93$, respectively). The IR-UTE map shows a moderate negative correlation ($R = -0.38$, $P = .009$).

Figure 7A–C shows scatterplots between the NAWM signal and EDSS score for MPRAGE (Fig 7A), T2-FLAIR (Fig 7B), and IR-UTE (Fig 7C). The MPRAGE data show a weak negative correlation with the EDSS score, which did not reach significance ($R = -0.19$, $P = .31$), and T2-FLAIR shows a weak positive correlation with the EDSS score, which did not reach significance

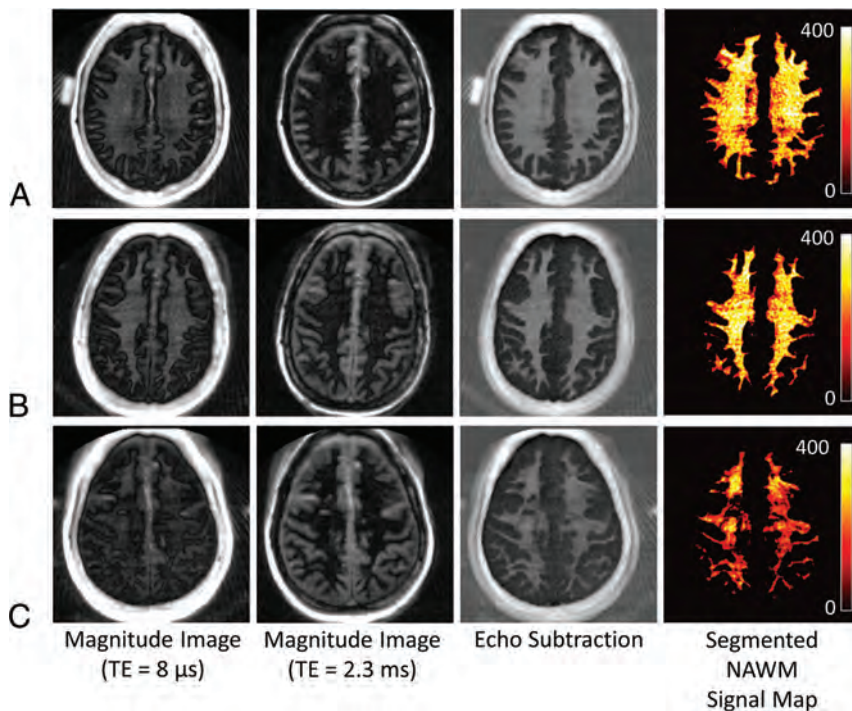


FIG 3. IR-UTE images and NAWM map. These show first-echo IR-UTE images (TE = 8 μ s) in the first column, second-echo images (TE = 2.3 ms) in the second column, and echo-subtraction images in the third column with the corresponding NAWM maps in the fourth column for a healthy volunteer (a 49-year-old man: A, upper row), a patient with MS with an EDSS score of 2 (a 56-year-old man: B, middle row), and a patient with MS with an EDSS score of 6 (a 46-year-old woman: C, lower row). The 2D IR-UTE images are in the native domain, which is different from the MPRAGE and T2-FLAIR images, which are in the normalized template domain.

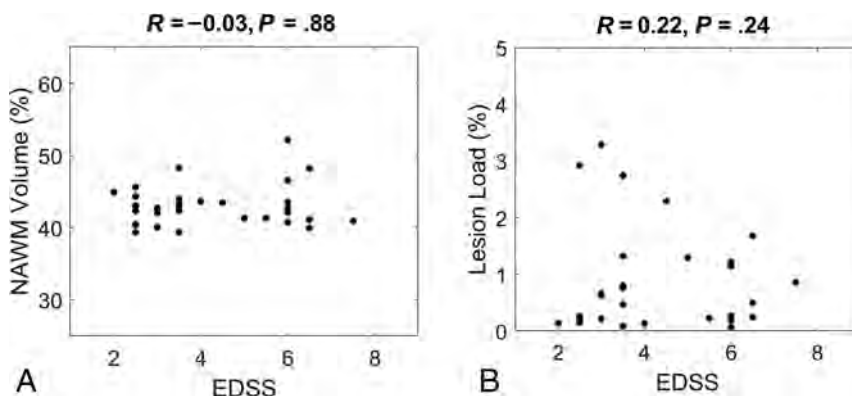


FIG 4. Scatterplots and the corresponding Spearman correlations between NAWM volume and the EDSS score (A), and between lesion load and the EDSS score (B). Both NAWM volume and lesion load show only low correlations with the EDSS score ($R = -0.03$, $P = .88$, and $R = 0.22$, $P = .24$, respectively).

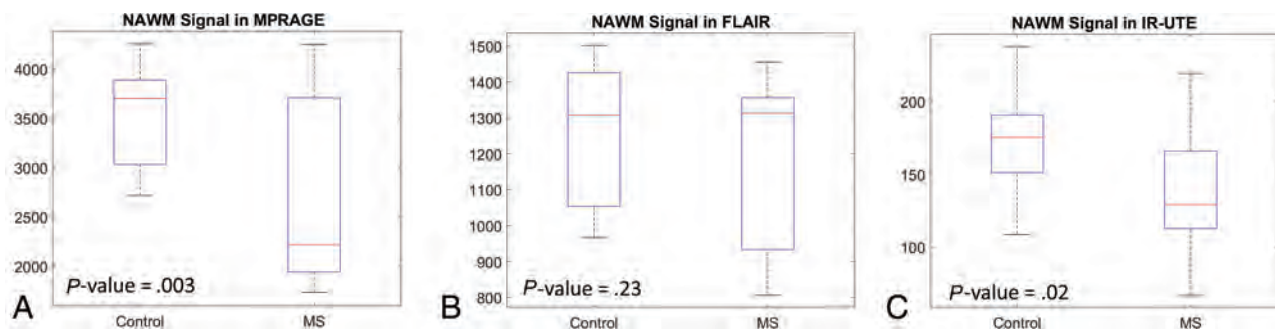


FIG 5. Mann-Whitney-Wilcoxon tests between the control ($n = 14$) and MS groups ($n = 31$) for NAWM signal on MPRAGE (A), T2-FLAIR (B), and IR-UTE (C) maps. The MPRAGE and IR-UTE maps show statistically significant differences between the 2 groups with P values of .003 and .02, respectively. The T2-FLAIR maps show no significant difference between the 2 groups ($P = .23$). In the boxplots, red and black horizontal lines represent median and minimum/maximum values. The upper and lower edges of the blue boxes indicate the 75th and 25th percentiles, respectively.

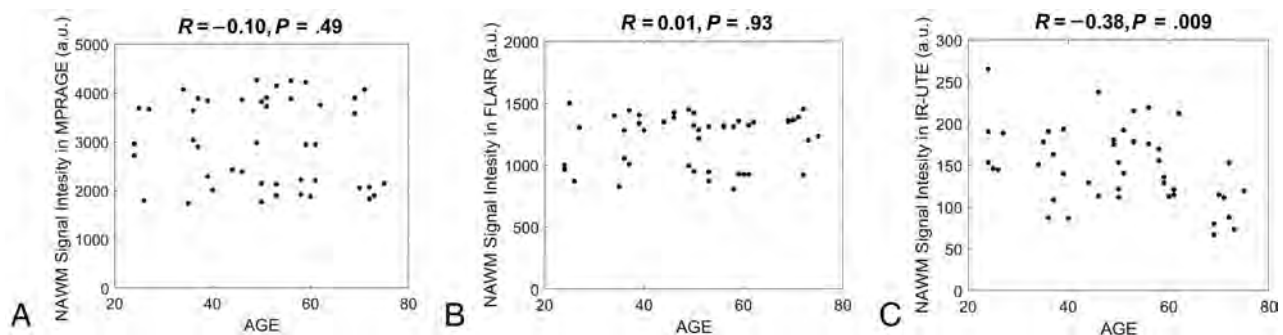


FIG 6. Scatterplots between NAWM signal and age on MPRAGE (A), T2-FLAIR (B), and IR-UTE (C) maps with the all subjects, including both the healthy controls and patients with MS. A weak correlation is seen on the MPRAGE ($R = -0.10$, $P = .49$) and T2-FLAIR ($R = 0.01$, $P = .93$) maps. The IR-UTE maps show a much larger negative correlation with the subject's age ($R = -0.38$, $P = .009$). a.u. indicates arbitrary units.

($R = 0.13$, $P = .49$). The IR-UTE data show a much larger negative correlation with the EDSS score ($R = -0.44$, $P = .01$). Figure 7D shows the scatterplot between the EDSS score and the patient's age. There is a weak positive correlation that did not reach significance ($R = 0.14$, $P = .44$).

DISCUSSION

This is the first study to demonstrate a significant correlation between IR-UTE-based direct MR imaging of myelin and disability in MS assessed by the EDSS score. MPRAGE and T2-FLAIR provided a low correlation with the EDSS score, consistent with the literature.¹⁰⁻¹⁵ NAWM volume and lesion load also correlated poorly with the EDSS score. The novel IR-UTE sequence provided a much higher correlation than the clinical sequences. The IR-UTE signal reduction in NAWM with an increase in the EDSS score is consistent with increasing demyelination in NAWM as patient disability worsens. A moderate negative correlation was observed between the NAWM signal and the patient's age on IR-UTE, which implies that IR-UTE also detects age-related myelin reduction. The overall myelin change correlated with the EDSS score observed with IR-UTE may also include a contribution from age-related myelin reduction. However, a much weaker correlation was observed between the patient's age and the EDSS score, implying that disability related to disease is the dominant factor observed in this study.

Myelination is dynamically regulated throughout life. It is disrupted in a variety of neurologic conditions including MS, which is characterized by the formation of focal or global demyelinating lesions disseminated in time and space. MS likely affects NAWM as well as GM. These are frequently associated with neurologic deficits. It is very difficult or impossible to separate demyelination and remyelination with conventional MR imaging sequences at different phases of MS. With the advent of IR-UTE sequences, it may be possible to separate demyelination from remyelination and dynamically monitor myelin changes with time. However, more validation studies are still needed.

It has been reported in the literature that colocalized iron may also affect MR imaging contrast in a human brain.^{26,27} The proposed IR-UTE method only resolves signal from myelin with ultrashort $T2^*$ decay. $T2^*$ of iron depends on the concentration, but both normal and abnormal brains show iron levels below ~ 0.2 ppm,²⁸ in which $T2^*$ is expected to be much longer than that of myelin. Quantitative susceptibility mapping can be used to assess iron. Combining quantitative susceptibility mapping with UTE may allow higher detection sensitivity to a broader range of iron.^{29,30}

A limitation of this study is that the 2D IR-UTE sequence is based on half-pulse radiofrequency excitations and the use of gradients for section selection, which result in eddy currents causing distortions in the section profile. Some simple calibration methods³¹

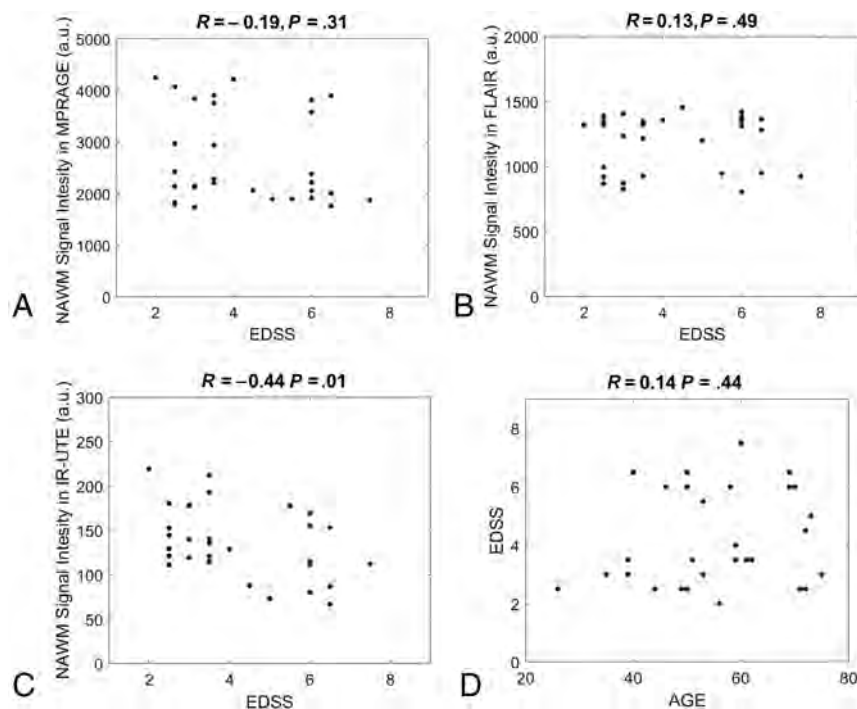


FIG 7. Scatterplots between NAWM signal and the EDSS scores with MPRAGE (A), T2-FLAIR (B), and IR-UTE (C) maps. Weak correlations are observed with the MPRAGE ($R = -0.19$, $P = .31$) and the T2-FLAIR ($R = 0.13$, $P = .49$) maps. The IR-UTE maps provide a larger negative correlation ($R = -0.44$, $P = .01$). A weak positive correlation is observed between the EDSS scores and patients' ages ($R = 0.14$, $P = .44$) (D). a.u. indicates arbitrary units.

are likely to improve the robustness of this technique. The results in this study may be improved by the use of a novel 3D-IR-UTE sequence, which does not require 2D section selection.^{32,33} The 3D technique provides volumetric imaging of myelin with reduced sensitivity to eddy currents.

There are other limitations of this study. First, the number of patients with MS was relatively low, possibly reducing the statistical power in the analyses. Second, T1 variation in NAWM may compromise the adiabatic nulling of WM water signal, which is a major limitation for single IR-based UTE myelin imaging techniques.¹⁶⁻²¹ More advanced techniques, such as the sliding window technique or complex echo subtraction can help suppress residual water signal contamination.^{32,33} Third, myelin in GM was not investigated because it has an even lower myelin proton density than WM, making it more difficult to detect. GM_L has a longer T1 than in WM, making it difficult to suppress both WM_L and GM_L simultaneously using a single TI. More advanced techniques are needed for accurate and quantifiable imaging of myelin in GM.

CONCLUSIONS

The correlation between the EDSS score and direct imaging of myelin in WM demonstrated in this study may provide a link between the pathologic substrate that characterizes MS and patients' clinical statuses. This may lead to more specific monitoring of the degree to which remyelination can be enhanced with treatment and assessment of how much this ameliorates disability.















Disclosures: Soudabeh Fazeli—RELATED: Grant: National Institutes of Health, Comments: As part of my training in a clinician-scientist radiology residency program, I am supported by the National Institutes of Health T32 EB005970-09. Jiang Du—RELATED: Grant: National Institutes of Health, Comments: This work was supported by National Institutes of Health grant IR01NS092650.* *Money paid to the institution.

REFERENCES

1. van der Knaap MS, Valk J. *Magnetic Resonance of Myelination and Myelin Disorders*. Springer-Verlag; 2005: 1-19
2. Nelson F, Poonawalla A, Hou P, et al. **3D MPRAGE improves classification of cortical lesions in multiple sclerosis.** *Mult Scler* 2008;14:1214-19 CrossRef Medline
3. Thompson AJ, Miller DH, MacManus DG, et al. **Patterns of disease activity in multiple sclerosis.** *BMJ* 1990;301:44-45 CrossRef Medline
4. Grossman RI, Braffman BH, Brorson JR, et al. **Multiple sclerosis: serial study of gadolinium-enhanced MR imaging.** *Radiology* 1988;169:117-22 CrossRef Medline
5. Chen JT, Collins DL, Atkins HL, et al; Canadian MS/BMT Study Group. **Magnetization transfer ratio evolution with demyelination and remyelination in multiple sclerosis lesions.** *Ann Neurol* 2008;63:254-62 CrossRef Medline
6. Whittall KP, MacKay AL, Graeb DA, et al. **In vivo measurement of T2 distributions and water contents in normal human brain.** *Magn Reson Med* 1997;37:34-43 CrossRef Medline
7. Hwang D, Kim DH, Du YP. **In vivo multi-slice mapping of myelin water content using T2* decay.** *Neuroimage* 2010;52:198-204 CrossRef Medline
8. Oh SJ, Bilello M, Schindler M, et al. **Direct visualization of short transverse relaxation time component (ViSta).** *Neuroimage* 2013;83:485-92 CrossRef Medline
9. Ouellette R, Mangeat G, Polyak I, et al. **Validation of rapid magnetic resonance myelin imaging in multiple sclerosis.** *Ann Neurol* 2020;87:710-24 CrossRef Medline
10. Miki Y, Grossman RI, Udupa JK, et al. **Relapsing-remitting multiple sclerosis: longitudinal analysis of MR images—lack of correlation between changes in T2 lesion volume and clinical findings.** *Radiology* 1999;213:395-99 CrossRef Medline
11. Li DK, Held U, Petkau J, et al. **Sylvia Lawry Centre for MS Research. MRI T2 lesion burden in multiple sclerosis: a plateauing relationship with clinical disability.** *Neurology* 2006;66:1384-89 CrossRef Medline
12. Charil A, Zijdenbos AP, Taylor J, et al. **Statistical mapping analysis of lesion location and neurological disability in multiple sclerosis: application to 452 patient data sets.** *Neuroimage* 2003;19:532-44 CrossRef Medline
13. Poonawalla AH, Datta S, Juneja V, et al. **Composite MRI scores improve correlation with EDSS in multiple sclerosis.** *Mult Scler* 2010;16:1117-25 CrossRef Medline
14. Kappos L, Moeri D, Radue EW, et al. **Predictive value of gadolinium-enhanced magnetic resonance imaging for relapse rate and changes in disability or impairment in multiple sclerosis: a meta-analysis.** *Lancet* 1999;353:964-69 CrossRef Medline
15. Rovaris M, Judica E, Sastre-Garriga J, et al. **Large-scale, multicenter, quantitative MRI study of brain and cord damage in primary progressive multiple sclerosis.** *Mult Scler* 2008;14:455-64 CrossRef Medline

16. Waldman A, Rees JH, Brock CS, et al. **MRI of the brain with ultrashort echo time pulse sequences.** *Neuroradiology* 2003;45:887–92 CrossRef Medline
17. Horch RA, Gore JC, Does MD. **Origins of the ultrashort T2 1H NMR signals in myelinated nerve: a direct measure of myelin content?** *Magn Reson Med* 2011;66:24–31 CrossRef Medline
18. Wilhelm MJ, Ong HH, Wehrli SL, et al. **Direct magnetic resonance detection of myelin and prospects for quantitative imaging of myelin density.** *Proc Natl Acad Sci U S A* 2012;109:9605–10 CrossRef Medline
19. Du J, Ma G, Li S, et al. **Ultrashort TE echo time (UTE) magnetic resonance imaging of the short T2 components in white matter of the brain using a clinical 3T scanner.** *Neuroimage* 2014;87:32–41 CrossRef Medline
20. Du J, Sheth V, He Q, et al. **Measurement of T1 of the ultrashort T2* components in white matter of the brain at 3T.** *PLoS One* 2014;9:e103296 CrossRef Medline
21. Sheth V, Shao H, Chen J, et al. **Magnetic resonance imaging of myelin using ultrashort echo time (UTE) pulse sequence: phantom, specimen, volunteers and multiple sclerosis patient studies.** *Neuroimage* 2016;136:37–44 CrossRef Medline
22. Larson PE, Conolly SM, Pauly JM, et al. **Using adiabatic inversion pulses for long-T2 suppression in ultrashort echo time (UTE) imaging.** *Magn Reson Med* 2007;58:952–61 CrossRef Medline
23. Tustison NJ, Cook PA, Klein A, et al. **Large-scale evaluation of ANTs and FreeSurfer cortical thickness measurements.** *Neuroimage* 2014;99:166–79 CrossRef Medline
24. Fonov VS, Evans AC, Botteron K, et al. **Brain Development Cooperative Group. Unbiased average age-appropriate atlases for pediatric studies.** *Neuroimage* 2011;54:313–27 CrossRef Medline
25. Avants BB, Tustison NJ, Wu J, et al. **An open source multivariate framework for n-tissue segmentation with evaluation on public data.** *Neuroinformatics* 2011;9:381–400 CrossRef Medline
26. Fukunaga M, Li TQ, Van Gelderen P, et al. **Layer-specific variation of iron content in cerebral cortex as a source of MRI contrast.** *Proc Natl Acad Sci U S A* 2010;107:3834–39 CrossRef Medline
27. Stüber C, Morawski M, Schäfer A, et al. **Myelin and iron concentration in the human brain: a quantitative study of MRI contrast.** *Neuroimage* 2014;93:95–106 CrossRef Medline
28. Acosta-Cabronero J, Betts MJ, Cardenas-Blanco A, et al. **In vivo MRI mapping of brain iron deposition across the adult lifespan.** *J Neurosci* 2016;36:364–74 CrossRef Medline
29. Jang H, Drygalski A, Wong J, et al. **Ultrashort echo time quantitative susceptibility mapping (UTE-QSM) for detection of hemosiderin deposition in hemophilic arthropathy: a feasibility study.** *Magn Reson Med* 2020;84:3246–55 CrossRef Medline
30. Jang H, Lu X, Carl M, et al. **True phase quantitative susceptibility mapping using continuous single-point imaging: a feasibility study.** *Magn Reson Med* 2019;81:1907–14 CrossRef Medline
31. Latta P, Starcuk Z, Kojan M, et al. **Simple compensation method for improved half-pulse excitation profile with rephrasing gradient.** *Magn Reson Med* 2020;84:1796–1805 CrossRef Medline
32. Ma YJ, Searleman A, Jang H, et al. **Whole-brain myelin mapping using 3D double echo sliding inversion recovery ultrashort echo time (DESIRE UTE) MRI.** *Radiology* 2020;294:362–74 CrossRef Medline
33. Jang H, Wei Z, Wu M, et al. **Improved volumetric myelin imaging in human brain using 3D dual echo inversion recovery-prepared UTE with complex echo subtraction.** *Magn Reson Med* 2020;83:1168–77 CrossRef Medline

Peak Width of Skeletonized Mean Diffusivity as Neuroimaging Biomarker in Cerebral Amyloid Angiopathy

 N. Raposo,  M.C. Zanon Zotin,  D. Schoemaker,  L. Xiong,  P. Fotiadis,  A. Charidimou,  M. Pasi,  G. Boulouis,  K. Schwab,  M.D. Schirmer,  M.R. Etherton,  M.E. Gurol,  S.M. Greenberg,  M. Duering, and  A. Viswanathan



ABSTRACT

BACKGROUND AND PURPOSE: Whole-brain network connectivity has been shown to be a useful biomarker of cerebral amyloid angiopathy and related cognitive impairment. We evaluated an automated DTI-based method, peak width of skeletonized mean diffusivity, in cerebral amyloid angiopathy, together with its association with conventional MRI markers and cognitive functions.

MATERIALS AND METHODS: We included 24 subjects (mean age, 74.7 [SD, 6.0] years) with probable cerebral amyloid angiopathy and mild cognitive impairment and 62 patients with MCI not attributable to cerebral amyloid angiopathy (non-cerebral amyloid angiopathy–mild cognitive impairment). We compared peak width of skeletonized mean diffusivity between subjects with cerebral amyloid angiopathy–mild cognitive impairment and non-cerebral amyloid angiopathy–mild cognitive impairment and explored its associations with cognitive functions and conventional markers of cerebral small-vessel disease, using linear regression models.

RESULTS: Subjects with Cerebral amyloid angiopathy–mild cognitive impairment showed increased peak width of skeletonized mean diffusivity in comparison to those with non-cerebral amyloid angiopathy–mild cognitive impairment ($P < .001$). Peak width of skeletonized mean diffusivity values were correlated with the volume of white matter hyperintensities in both groups. Higher peak width of skeletonized mean diffusivity was associated with worse performance in processing speed among patients with cerebral amyloid angiopathy, after adjusting for other MRI markers of cerebral small vessel disease. The peak width of skeletonized mean diffusivity did not correlate with cognitive functions among those with non-cerebral amyloid angiopathy–mild cognitive impairment.

CONCLUSIONS: Peak width of skeletonized mean diffusivity is altered in cerebral amyloid angiopathy and is associated with performance in processing speed. This DTI-based method may reflect the degree of white matter structural disruption in cerebral amyloid angiopathy and could be a useful biomarker for cognition in this population.

ABBREVIATIONS: CAA = cerebral amyloid angiopathy; CMB = cerebral microbleeds; CSO-PVS = perivascular spaces in the centrum semiovale; cSS = cortical superficial siderosis; cSVD = cerebral small vessel disease; ICH = intracerebral hemorrhage; IQR = interquartile range; MCI = mild cognitive impairment; MD = mean diffusivity; MMSE = Mini-Mental State Examination; PSMD = peak width of skeletonized mean diffusivity; nTBV = normalized total brain volume; nWMHV = normalized white matter hyperintensity volume; WMH = white matter hyperintensities

Sporadic cerebral amyloid angiopathy (CAA) is a highly prevalent cerebral small-vessel disease (cSVD) in the elderly.¹ CAA

is a well-known cause of lobar intracerebral hemorrhage (ICH) and is also increasingly recognized as a major contributor to vascular cognitive impairment and dementia.^{2,3} Although underlying


Received July 17, 2020; accepted after revision November 20.

From the Stroke Research Center (N.R., M.C.Z.Z., D.S., L.X., P.F., A.C., K.S., M.D.S., M.R.E., M.E.G., S.M.G., A.V.), Massachusetts General Hospital, Harvard Medical School, Boston, Massachusetts; Department of Neurology (N.R.), Centre Hospitalier Universitaire de Toulouse, Toulouse, France; Toulouse Neuroimaging Center (N.R.), Université de Toulouse, Institut National de la Santé et de la Recherche Médicale, Toulouse, Université Paul Sabatier, France; Center for Imaging Sciences and Medical Physics (M.C.Z.Z.), Department of Medical Imaging, Hematology and Clinical Oncology, Ribeirão Preto Medical School, University of São Paulo, Ribeirão Preto, São Paulo, Brazil; Department of Neurology (M.P.), Centre Hospitalier Universitaire de Lille, Lille, France; Department of Neuroradiology (G.B.), Centre Hospitalier Sainte-Anne, Université Paris-Descartes, Paris, France; Computer Science and Artificial Intelligence Lab (M.D.S.), Massachusetts Institute of Technology, Boston, Massachusetts; Department of Population Health Sciences (M.D.S.), German Center for Neurodegenerative Diseases, Bonn, Germany; and Medical Image Analysis Center (MIAC) and Quantitative Biomedical Imaging Group (M.D.), Department of Biomedical Engineering, University of Basel, Basel, Switzerland.

N. Raposo and M.C. Zanon Zotin contributed equally to this work.

This study was supported by the following National Institutes of Health grants: R01AG047975, R01AG026484, P50AG005134, K23AG02872605. Nicolas Raposo was supported by a Fulbright Scholarship and received an Arthur Sachs Scholarship from the Harvard University Committee on General Scholarship and a Philippe Foundation research grant. Markus D. Schirmer was supported by the European Union's Horizon 2020 Research and Innovation Program under the Marie Skłodowska-Curie grant agreement No 753896.

Please address correspondence to Nicolas Raposo, MD, PhD, Service de Neurologie, Hôpital Pierre-Paul Riquet, Centre Hospitalier Universitaire de Toulouse, Place Baylac, 31059 Toulouse Cedex 9, France; e-mail: raposo.n@chu-toulouse.fr

 Indicates open access to non-subscribers at www.ajnr.org

 Indicates article with online supplemental data.

<http://dx.doi.org/10.3174/ajnr.A7042>

mechanisms leading to cognitive impairment in CAA remain uncertain, it has been hypothesized that recurrent vascular lesions cause progressive disruption of the brain's structural connectivity, compromising network efficiency.^{4,5} Conventional MR imaging markers of CAA, including lobar cerebral microbleeds (CMB),⁶ cortical superficial siderosis (cSS),⁷ white matter hyperintensities (WMH),⁸ and cortical microinfarcts⁹ have been linked to cognitive functions. However, these associations are mostly weak and inconsistent across studies, suggesting that these markers may reflect only the tip of the iceberg in the whole spectrum of vascular pathology.¹⁰

Accumulating evidence suggests that DTI methods detect loss of microstructural integrity and other abnormalities not captured by structural MRI and tend to show stronger associations with cognition in subjects with cSVD.^{11,12} Yet, the direct application of DTI in routine clinical practice is hampered by highly variable, complex, and time-consuming processing techniques.

Peak width of skeletonized mean diffusivity (PSMD) is a recently developed, fully automated DTI marker based on the skeletonization of white matter tracts and histogram analysis of mean diffusivity (MD).¹³ PSMD has been shown to be particularly sensitive to vascular-related white matter abnormalities, demonstrating consistent associations with processing speed in subjects with cSVD.¹³ However, despite the common nature and high prevalence of CAA in aging populations, potential applications of PSMD in CAA have been scarcely investigated.

In the current study, we tested whether PSMD reflects the burden of underlying cSVD and cognitive dysfunctions in subjects with CAA. Among subjects with mild cognitive impairment (MCI) recruited specifically from a memory clinic setting, we explored the following: 1) whether PSMD is increased in subjects with CAA compared with those with non-CAA, 2) whether it is associated with structural MRI markers of CAA, and 3) whether it is correlated with cognitive functions.

MATERIALS AND METHODS

The data supporting findings of this study are available from the corresponding author on reasonable request.

Participants

We analyzed data from a memory clinic research cohort from the Massachusetts General Hospital between March 2010 and October 2016 and designed a case-control study. Patients underwent clinical examination, neuropsychological evaluation, and research MRI. The Institutional Review Board of Massachusetts General Hospital approved this study, and written informed consent was obtained from all participants or their surrogates.

We included subjects 55 years of age or older meeting Petersen criteria (2004)¹⁴ for MCI based on clinical assessment of functional status, neurologic evaluation, and extensive neuropsychological assessment. On visual examination of research MRIs, patients with MCI were categorized as the following: 1) CAA-MCI if they fulfilled the Modified Boston criteria¹⁵ for probable CAA (55 years of age or older; multiple lobar CMB with or without cSS or a single lobar cerebral microbleed and the presence of cSS), or 2) non-CAA-MCI. In both groups, exclusion criteria were dementia, history of symptomatic or asymptomatic ICH (defined as hemorrhagic focus of > 5

mm in diameter), the presence of deep CMB (suggesting arteriolosclerosis as underlying cSVD), contraindications for MRI, and the presence of excessive motion artifacts on DTI on careful qualitative visual inspection.

Data Collection

We systematically collected demographic information and medical history for each participant. All subjects underwent a standardized neuropsychological test battery, as previously described.⁹ Global cognitive status was assessed with the Mini-Mental State Examination (MMSE).¹⁶ Performance on neuropsychological tests was clustered to create composite scores exploring specific cognitive domains:¹⁷ executive function (Trail-Making Test B¹⁸ and Digit Span Backward¹⁹), processing speed/attention (Trail-Making Test A,²⁰ Digit Span Forward, and the Wechsler Adult Intelligence Scale, Third Edition Digit Symbol Coding¹⁹), memory (Hopkins Verbal Learning Test-Revised²¹ and Wechsler Memory Scale for logical memory,²² immediate recall, and delayed recall), and language function (Boston Naming Test²³ and Animal Naming Test²⁴). Performance on each test was first transformed into sex-, age-, and education-adjusted *z* scores using published normative data.^{16,24-26} Then, the *z* scores were averaged within each composite domain to obtain domain-specific scores for each subject.

MRI Acquisition

Neuroimaging was acquired on a 3T MRI scanner (TIM Trio; Siemens), using a 32-channel head coil. MRI sequences included high-resolution diffusion-weighted imaging (60 directions; TR = 8040 ms; TE = 84 ms; slice thickness = 2 mm; in-plane resolution = 2 × 2 mm; b-value = 700 s/mm²), 3D T1-weighted multiecho (TR = 2300 ms; TE = 2.98 ms; slice thickness = 1 mm; in-plane resolution = 1 × 1 mm), 3D FLAIR (TR = 6000 ms; TE = 455 ms; slice thickness = 1 mm; in-plane resolution = 1 × 1 mm), and SWI (TR = 27 ms; TE = 20 ms; slice thickness = 1.5 mm; in-plane resolution = 0.86 × 0.86 mm).

The median delay between neuropsychological evaluation and MRI was 1.85 months (interquartile range [IQR] = 0.00–3.06 months) and was shorter in subjects with CAA-MCI compared with those with non-CAA-MCI (median, 0 [IQR = 0.0–0.24] months versus 2.1 [1.17–3.30] months; *P* < .001).

DTI and PSMD Processing

PSMD was calculated from unprocessed DTI data using a publicly available script (PSMD Marker, Version 1.0; <http://www.psmd-marker.com>).¹³ This fully automated pipeline relies on the FMRIB Software Library (FSL, Version 6.0.1; <http://www.fmrib.ox.ac.uk/fsl>) for the preprocessing of DTI data (eddy current and motion correction, [eddy_correct <https://fsl.fmrib.ox.ac.uk/fsl/fslwiki/eddy>]), brain extraction (FSL Brain Extraction tool; <http://fsl.fmrib.ox.ac.uk/fsl/fslwiki/BET>), and tensor fitting (dtifit; http://fsl.fmrib.ox.ac.uk/fsl/fsl-4.1.9/fdt/fdt_dtifit.html), followed by skeletonization of preprocessed DTI data, application of a custom mask, and histogram analysis (Fig 1). Precisely, DTI data were skeletonized using the Tract-Based Spatial Statistics procedure (TBSS; <http://fsl.fmrib.ox.ac.uk/fsl/fslwiki/TBSS>), part of the FSL, and the FMRIB 1-mm fractional anisotropy template (FA template; <https://fsl.fmrib.ox.ac.uk/fsl/fslwiki/Atlases>, thresholded at a fractional

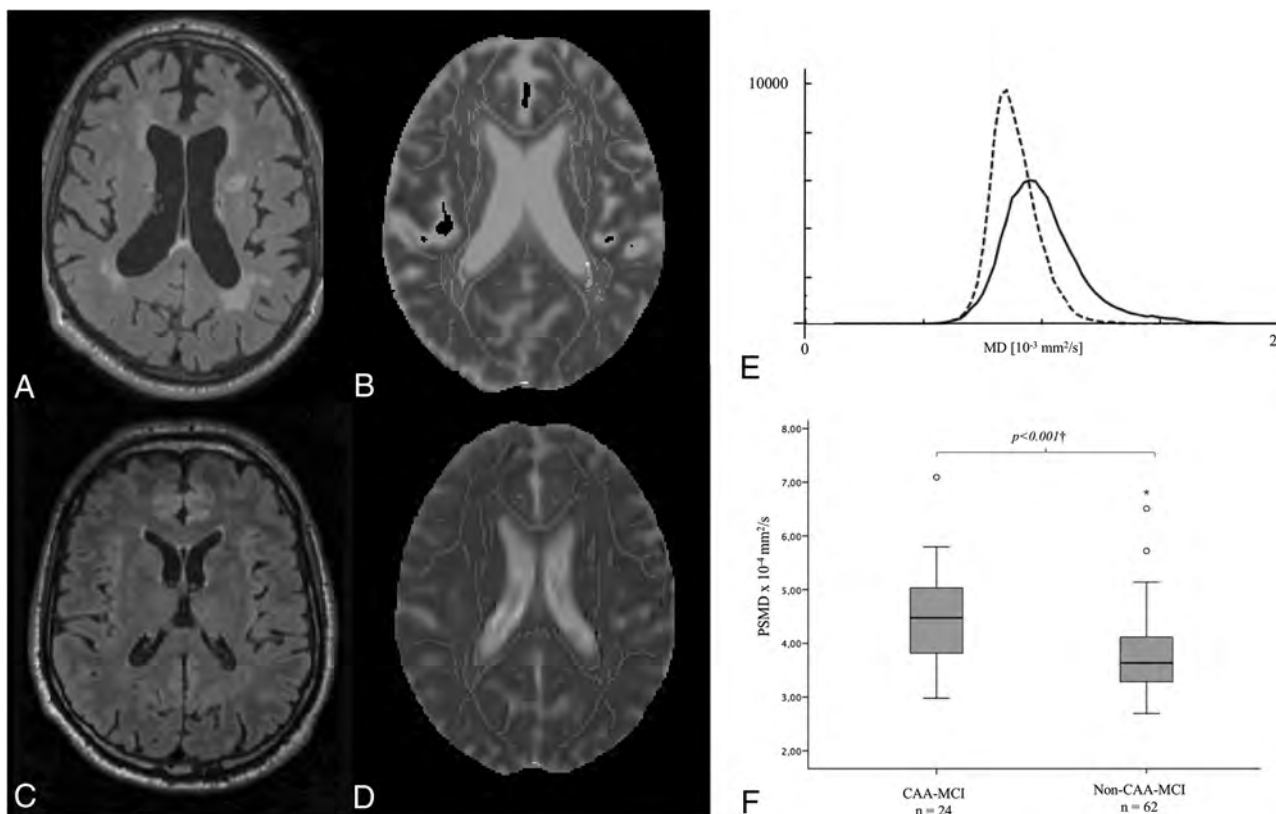


FIG 1. FLAIR images from a subject with CAA-MCI (A) and one with a non-CAA-MCI (B), demonstrating different burdens of WMH. MD maps display the skeletonized WM tracts from the same subjects with CAA-MCI (C) and non-CAA-MCI (D). E, Histograms depict the MD values of the voxels contained in the WM tract skeleton from the same subjects with CAA-MCI (solid line) and non-CAA-MCI (dashed line). F, The boxplot represents group differences in PSMD between CAA-MCI and non-CAA-MCI. The dagger indicates the results derived from ANCOVA, adjusting for age at MRI ($P < .001$).

anisotropy value of 0.2). MD images were projected onto the skeleton, using the fractional anisotropy–derived projection parameters. Next, to avoid contamination of the skeleton through CSF partial volume effects, we further masked the MD skeleton with a standard skeleton thresholded at a fractional anisotropy value of 0.3 and a mask provided with the PSMD pipeline to exclude regions adjacent to the ventricles, such as the fornix. Finally, PSMD was calculated as the difference between the 95th and fifth percentiles of the MD values of voxels contained within the skeleton.¹³ To ensure that results were not driven by outliers, we identified extreme PSMD (values below $1.5 \times \text{IQR}$ from the first quartile or above $1.5 \times \text{IQR}$ from the third quartile) and excluded them from analyses.

Neuroimaging Markers of cSVD

MRI markers of cSVD were quantified by investigators blinded to all clinical data and according to the Standards for Reporting Vascular Changes on Neuroimaging (STRIVE) recommendations.²⁷

The presence, number, and location of CMB were evaluated on the SWI according to the current consensus criteria.^{27,28} They were classified as lobar when located in cortical and corticosubcortical areas. cSS was visually assessed according to recently proposed criteria and transformed into a dichotomous variable (absence versus presence).²⁹ Perivascular spaces in the centrum semiovale (CSO-PVS) were rated on axial T1-weighted MRI, according to a previously developed score,³⁰ and were analyzed as both dichotomous (≤ 2 versus > 2) and ordinal variables. CMB, cSS, and CSO-PVS

were analyzed by 2 experienced raters (N.R. and D.S.) using validated scales, and final ratings were obtained via a consensus.

After visual inspection of MR image quality, WMH volume, total brain volume, and total intracranial volume were calculated using FreeSurfer, Version 5.3 (<http://surfer.nmr.mgh.harvard.edu>), as previously described.³¹ Normalized total brain volume (nTBV) was calculated as the total brain volume/intracranial volume ratio, and normalized WMH volume (nWMHV) was calculated as WMH volume/intracranial volume $\times 100$.

Statistical Analysis

We compared the clinical and imaging characteristics between subjects with MCI with and without CAA using the χ^2 or Fisher test for categorical variables and an independent t test or Mann-Whitney U test for continuous variables, as appropriate. The distribution of continuous variables was tested for normality with the Shapiro-Wilk test.

Log-transformed PSMD values were compared between patients with CAA-MCI and those with non-CAA-MCI using ANOVA, adjusted for age. We further adjusted for log-transformed nWMHV and cognitive status (MMSE).

Receiver operating characteristic curve analyses were used to quantify the performance of PSMD and nWMHV in discriminating subjects with CAA from those with non-CAA.

The association between PSMD and MRI markers of cSVD and PSMD and cognitive performances was evaluated in CAA-

Table 1: Baseline characteristics of subjects with CAA-MCI and those with non-CAA-MCI

	CAA-MCI (<i>n</i> = 24)	non-CAA-MCI (<i>n</i> = 62)	<i>P</i> Value
Demographics			
Age at NPT (mean) [SD] (yr)	74.73 [5.99]	73.25 [8.33]	.36
Female (No.) (%)	7 (29.2)	26 (41.9)	.27
Education (median) (IQR) (yr)	16 (16, 18)	16 (14, 18)	.04 ^a
Vascular risk factors			
Hypertension (No.) (%)	13 (54.2)	40 (64.5)	.38
Diabetes (No.) (%)	1 (4.2)	10 (16.1)	.17
Atrial fibrillation (No.) (%)	4 (16.7)	5 (8.1)	.26
Dyslipidemia (No.) (%)	13 (54.2)	44 (71.0)	.14
Neuropsychological performances			
MMSE (median) (IQR)	25.5 (24–28)	28 (26–29)	.006 ^a
MMSE (<i>z</i> score) (median) (IQR)	−1.88 (−3.28, −0.16)	0 (−1.48–1.11)	.003 ^a
Memory (<i>z</i> score) (median) (IQR)	−1.91 (−2.38, −0.75)	−0.47 (−1.60–0.56)	.005 ^a
Processing speed (<i>z</i> score) (median) (IQR)	−0.24 (−0.62–0.15)	−0.11 (−0.46–0.27)	.34
Language (<i>z</i> score) (median) (IQR)	−0.44 (−0.91–0.36)	−0.36 (−1.17–0.19)	.95
Executive function (<i>z</i> score) (median) (IQR)	−0.59 (−1.89–0.22)	−0.21 (−0.86–0.12)	.20
Imaging			
PSMD ($\times 10^{-4}$ mm ² /s) (median) (IQR)	4.48 (3.81–5.09)	3.63 (3.28–4.13)	<.001 ^a
Lobar CMB count (median) (IQR)	5.5 (3.0–24.50)	0 (0–0)	<.001 ^a
cSS (presence) (No.) (%)	9 (37.5)	0 (0.0)	<.001 ^a
High CSO-PVS score (>2) (No.) (%)	11 (45.8)	3 (4.8)	<.001 ^a
nWMHV (median) (IQR)	0.42 (0.28–1.74)	0.29 (0.14–0.75)	.02 ^a
nTBV (mean) [SD]	0.61 [0.04]	0.64 [0.05]	.004 ^a

Note:—NPT indicates neuropsychological tests.

^aSignificant.

MCI and non-CAA-MCI separately. Linear regression models were used to explore relationships between PSMD and structural MRI markers of cSVD (lobar CMB count, CSO-PVS score, the presence of cSS, nWMHV, and nTBV), adjusting for age. The association between PSMD and cognitive scores in each domain was explored using linear regression models in both groups separately, adjusting for structural MRI markers of cSVD and the time delay between the neuropsychological evaluation and the MRI. Because cognitive scores were already adjusted for age, sex, and education level, these variables were not included in the models.

The statistical significance level was set at .05 for all analyses. We used the Statistical Package for the Social Sciences, Version 24.0 for Windows (IBM) and R (v3.5.3) for statistical analysis.

RESULTS

We identified 134 subjects with cognitive impairment enrolled in this prospective study who underwent a research MRI. Of them, 42 subjects were excluded on the basis of the prespecified criteria: diagnosis of dementia (*n* = 6), possible CAA category (*n* = 10), presence of deep CMB (*n* = 5), lack of neuropsychological tests (*n* = 19), and the presence of excessive motion artifacts on DTI, based on qualitative visual inspection (*n* = 2). Additionally, 3 outliers with extreme PSMD values (all with high values) were identified in each group and were excluded from the analysis. The final cohort consisted of 86 subjects with MCI (mean age, 73.7 [SD, 7.7] years; 38.4% female) without a history of ischemic stroke or ICH, including 24 subjects with probable CAA (CAA-MCI; 27.9%) and 62 without CAA (non-CAA-MCI; 72.1%).

Comparison between Subjects with CAA and Those with Non-CAA

Subjects with CAA-MCI and non-CAA-MCI were similar in age and vascular risk factors (Table 1). MMSE scores were lower in

subjects with CAA-MCI compared with subjects with non-CAA-MCI (*P* = .003). Patients with CAA-MCI had worse performance in memory than subjects with non-CAA-MCI (*P* = .005). The 2 groups had similar scores across all other cognitive domains (*P* > .05, for all). Compared with those with non-CAA-MCI, subjects with CAA-MCI presented with a higher burden of MRI markers of cSVD, including a higher prevalence of cSS (*P* < .001), higher lobar CMB count (*P* < .001), greater nWMHV (*P* = .016), a higher prevalence of high CSO-PVS scores (*P* < .001), and lower nTBV (*P* = .004). PSMD values were significantly higher in CAA-MCI in comparison with non-CAA-MCI (*P* < .001) (Fig 1F), even after adjusting for age (*P* < .001). In a post hoc analysis, we found that PSMD remained significantly higher in subjects with CAA-MCI compared with subjects with non-CAA-MCI when further controlling for nWMHV (*P* = .007) or cognitive status (MMSE *z* scores) (*P* < .001). In receiver operating characteristic analyses, PSMD (area under the curve = 0.755; 95% CI, 0.636–0.873; *P* < .001) was able to significantly discriminate subjects with CAA from those without CAA, and it yielded a greater area under the curve than nWMHV (area under the curve = 0.668; 95% CI, 0.544–0.792; *P* = .016) (Online Supplemental Data).

Associations between PSMD and Markers of cSVD

In linear regression analyses adjusted for age, increased PSMD was associated with greater nWMHV both in CAA-MCI (β = 0.75; *P* < .001) and non-CAA-MCI (β = 0.69; *P* < .001) groups, but not with nTBV, CMB, CSO-PVS, or cSS (Table 2). In multiple regression models including all quantified structural MRI markers of cSVD, only nWMHV remained independently associated with PSMD in subjects with CAA-MCI (β = 0.66; *P* < .001) and non-CAA-MCI (β = 0.71; *P* < .001) (Table 2 and Online Supplemental Data).

Table 2: Association between PSMD and MRI markers of small-vessel disease in subjects with CAA-MCI and non-CAA-MCI^a

	Model 1 ^b				Model 2 ^c			
	Std. β	95% CI		P	Std. β	95% CI		P
CAA-MCI (n = 24)								
Lobar CMB count	0.15	−0.27	0.58	.46	0.15	−0.13	0.42	.28
cSS	0.27	−0.15	0.70	.20	0.12	−0.16	0.40	.38
CSO-PVS score	0.31	−0.09	0.71	.13	0.20	−0.10	0.49	.18
nWMHV	0.75	0.49	1.02	<.001 ^d	0.66	0.37	0.95	<.001 ^d
nTBV	−0.26	−0.79	0.26	.31	−0.17	−0.54	0.20	.34
Non-CAA-MCI (n = 62)								
CSO-PVS	−0.02	−0.24	0.21	.87	0.10	−0.07	0.27	.25
nWMHV	0.69	0.50	0.89	<.001 ^d	0.71	0.51	0.91	<.001 ^d
nTBV	−0.23	−0.51	0.06	.11	−0.14	−0.36	0.08	.20

Note:—Std. β indicates standardized beta coefficient.

^a Linear regression models with PSMD ($\times 10^{-4}$ mm²/s) as the dependent variable.

^b Simple Linear regression analyses adjusted for age.

^c Multiple regression models, including all neuroimaging markers and adjusted for age. In subjects with non-CAA-MCI, the presence of cSS and lobar CMB count was automatically excluded from the models due to the absence of variance within the group.

^d Significant.

Table 3: Association between PSMD and cognitive performance in subjects with CAA-MCI and non-CAA-MCI^a

	Adjusted Model ^b			
	Std. β	95% CI		P Value
CAA-MCI (<i>n</i> = 24)				
Global cognitive status	−0.40	−1.21	0.41	.31
Memory	−0.69	−1.52	0.15	.10
Processing speed/ attention	−1.08	−1.76	−0.40	.004 ^c
Language	−0.47	−1.16	0.21	.16
Executive function	−0.64	−1.37	0.10	.09
non-CAA-MCI (<i>n</i> = 62)				
Global cognitive status	0.30	−0.13	0.72	.17
Memory	0.14	−0.28	0.56	.50
Processing speed/ attention	0.16	−0.27	0.59	.46
Language	0.14	−0.29	0.57	.52
Executive function	0.11	−0.30	0.53	.58

^a Multiple regression models with cognitive performance as the dependent variable.

^b Models include PSMD, nWMHV, nTBV, CSO-PVS score, the presence of cSS and lobar CMB count; adjusting for the time delay between the neuropsychological evaluation and the MRI. In subjects with non-CAA-MCI, the presence of cSS and the lobar CMB count were automatically excluded from the models due to an absence of variance within the group.

^c Significant.

Associations between PSMD and Cognitive Function

In the CAA-MCI group, multiple regression models accounting for lobar CMB count, cSS, CSO-PVS score, nWMHV, and nTBV demonstrated that increased PSMD was independently associated with worse performance in processing speed ($\beta = -1.08$; $P = .004$) (Table 3 and Online Supplemental Data). In the non-CAA-MCI group, multiple regression analyses did not reveal any significant associations between PSMD and scores reflecting each cognitive domain (Table 3 and Online Supplemental Data).

DISCUSSION

Several key findings emerge from this study on PSMD in patients with CAA presenting with MCI in the absence of ICH. First, subjects with MCI with CAA showed increased PSMD values compared with subjects with MCI without CAA, even after adjusting for baseline differences in age, nWMHV, and cognitive status.

Second, we confirmed that PSMD was strongly associated with WMHV in our CAA population, but not with other structural markers of cSVD. Third, we found that PSMD values were associated with worse performance in processing speed among subjects with CAA-MCI after controlling for the presence of other MRI markers of cSVD. In contrast, PSMD was not associated with cognitive function in subjects with non-CAA-MCI.

PSMD studies have, so far, focused mainly on community-dwelling^{13,32,33} and cognitively impaired elderly subjects,^{13,34} as well as those with inherited^{13,35} and sporadic cSVD.^{13,36} To our knowledge, only 1 previous study has investigated the performance of PSMD in sporadic CAA, including subjects with and without ICH recruited from both stroke-prevention and memory clinics.³⁷ Because CAA pathology is highly prevalent and significantly contributes to vascular cognitive impairment in the elderly population,³⁸ further investigating the performance of PSMD in the context of CAA is an important step for the validation of this new neuroimaging biomarker as a surrogate for cognitive dysfunction in cSVD.³⁹

As expected, the PSMD values we obtained in subjects with CAA in a memory clinic were remarkably similar to those found in other sporadic cSVD cohorts,^{13,36} including another CAA cohort,³⁷ corroborating the reproducibility and stability of PSMD across different scanners, sequences, and even clinical samples.^{13,40}

The observed increase in PSMD values among subjects with CAA-MCI supports the hypothesis that whole-brain microstructural integrity is impaired in this population. Our results are in accordance with previous studies showing microstructural abnormalities in CAA when relying on other DTI-based methods.^{11,41} Most important, PSMD offers several advantages in comparison with other DTI methods: It is a fully automated and fast technique; it offers higher interscanner reproducibility; power calculations have shown smaller sample size estimates for PSMD; and it is more strongly associated with performance in processing speed.¹³

Group differences in PSMD remained significant (CAA-MCI versus non-CAA-MCI) even after adjusting for age, nWMHV, and MMSE scores. This finding suggests that PSMD differences are not solely driven by these factors and may indicate that this marker, like other global DTI measures, might capture abnormalities not visible on structural MRI sequences.

In our CAA-MCI sample, PSMD was strongly associated with nWMHV, but not with hemorrhagic markers of CAA (lobar CMBs and cSS), a finding in line with those from a recent study on a different CAA sample,³⁷ and this finding suggests that white matter tract disruption in CAA may be more closely linked to cSVD damage from ischemic rather than hemorrhagic origin.

The encouraging finding that PSMD is independently associated with processing speed in our subjects with CAA-MCI, after adjusting for other conventional MRI markers of cSVD, is in consonance with recently published results from another CAA sample.³⁷ The lack of association between PSMD and cognition in the non-CAA-MCI sample is consistent with findings from other studies in cohorts with low burdens of cSVD.^{13,36} PSMD, like other DTI metrics, appears to be more sensitive to cSVD-related white matter abnormalities than to neurodegenerative pathology.^{13,42} The low burden of cSVD pathology observed in our non-CAA sample might explain the absence of association between PSMD and processing speed.

Our results argue in favor of a strong link between PSMD and processing speed in cSVD populations, as advocated in the original PSMD study.¹³ However, mechanisms underlying these strong associations with cognition are incompletely understood. McCreary et al³⁷ reported that a greater variation in white matter MD could be seen in microarchitectural disruption caused by pathologic processes. Although the histopathologic features specifically associated with increases in PSMD remain unknown, tissue rarefaction and lower myelin density have been related to MD variations in subjects with CAA.⁴³ It is possible that similar microstructural abnormalities underlie changes in PSMD in CAA, reflecting disruption of synaptic transmission, which could affect cognition.

Our study has limitations. The small sample size of our cohort may account for the relatively weak cognitive correlations observed. Hence, our findings should be considered preliminary and require external validation in larger CAA cohorts. By including only subjects with MCI (cognitively healthy and subjects with CAA and dementia were excluded), our study was not designed to assess relationships between PSMD and the full spectrum of cognitive impairment, ranging from MCI to dementia. Still, our significant findings in subjects with mild forms of cognitive impairment argue in favor of the robustness of PSMD as a biomarker for cognitive function in CAA. Additionally, our study included participants with a specific presentation of CAA (ie, mild cognitive symptoms without ICH). We excluded subjects with ICH because this likely represents a different phenotype of the disease.⁴⁴ While we designed our study to examine this specific group of subjects with CAA who frequently present in memory clinic settings, our results cannot be generalized to other CAA populations or phenotypes. Another limitation of our study is the absence of comparisons between PSMD and other previously validated DTI-based markers to assess whether this new method constitutes a superior biomarker.

Nonetheless, this study also has several strengths and expands on previous literature by evaluating the relevance of PSMD in a specific phenotype of CAA and investigating its independent cognitive and neuroimaging associations.

CONCLUSIONS

PSMD values are higher among cognitively impaired subjects with CAA in comparison with those without CAA and are associated with nWMHV and performance in processing speed. Our preliminary results support the relevance of PSMD, a completely automated DTI-based method, in capturing microstructural brain changes in subjects with CAA, even in the absence of ICH. PSMD may serve as a biomarker in future clinical trials involving CAA and other cSVD.

Disclosures: Nicolas Raposo—RELATED: Grant: Fulbright Scholarship, Arthur Sachs Scholarship from the Harvard University Committee on General Scholarship, and a Philippe Foundation research grant; UNRELATED: Travel/Accommodations/Meeting Expenses Unrelated to Activities Listed: Pfizer, Bristol Myers Squibb, Bayer. Maria Clara Zanon Zotin—RELATED: Support for Travel to Meetings for the Study or Other Purposes: Mass General Brigham, Comments: support to travel to a conference. Dorothee Schoemaker—RELATED: Grant: American Heart Association, Comments: postdoctoral fellowship.* Kristin Schwab—UNRELATED: Employment: Massachusetts General Hospital MarkVCID. Markus D. Schirmer—UNRELATED: Grants/Grants Pending: European Research Council.* Mark Etherton—UNRELATED: Grants/Grants Pending: American Academy of Neurology.* Steven Greenberg—RELATED: Grant: National Institutes of Health; UNRELATED: Consultancy: Bayer, Biogen, IQVIA, Roche, Comments: Data Safety Monitoring Boards; Grants/Grants Pending: National Institutes of Health; Royalties: UpToDate. Marco Duering—RELATED: Grant: Else Kröner-Fresenius-Stiftung*; UNRELATED: Payment for Lectures Including Service on Speakers Bureaus: Bayer Vital, Pfizer, Comments: Lecture honoraria paid to individual author. Anand Viswanathan—RELATED: Grant: National Institutes of Health*; UNRELATED: Consultancy: Biogen, Alnylam Pharmaceuticals, Roche. *Money paid to the institution.

REFERENCES

- Charidimou A, Gang Q, Werring DJ. **Sporadic cerebral amyloid angiopathy revisited: recent insights into pathophysiology and clinical spectrum.** *J Neurol Neurosurg Psychiatry* 2012;83:124–37 CrossRef Medline
- Planton M, Saint-Aubert L, Raposo N, et al. **High prevalence of cognitive impairment after intracerebral hemorrhage.** *PLoS One* 2017;12:e0177886 CrossRef Medline
- Boyle PA, Yu L, Nag S, et al. **Cerebral amyloid angiopathy and cognitive outcomes in community-based older persons.** *Neurology* 2015;85:1930–36 CrossRef Medline
- Heinen R, Vlegels N, de Bresser J, et al. **The cumulative effect of small vessel disease lesions is reflected in structural brain networks of memory clinic patients.** *Neuroimage Clin* 2018;19:963–69 CrossRef Medline
- O'Sullivan M, Jones DK, Summers PE, et al. **Evidence for cortical “disconnection” as a mechanism of age-related cognitive decline.** *Neurology* 2001;57:632–38 CrossRef Medline
- Martinez-Ramirez S, Greenberg SM, Viswanathan A. **Cerebral microbleeds: overview and implications in cognitive impairment.** *Alzheimers Res Ther* 2014;6:1–7 CrossRef Medline
- Charidimou A, Ni J, Ramirez Martinez S, et al. **Cortical superficial siderosis in memory clinic patients: further evidence for underlying cerebral amyloid angiopathy.** *Cerebrovasc Dis* 2016;41:156–62 CrossRef Medline
- Smith EE, Gurrol ME, Eng JA, et al. **White matter lesions, cognition, and recurrent hemorrhage in lobar intracerebral hemorrhage.** *Neurology* 2004;63:1606–12 CrossRef Medline
- Xiong L, Van Veluw SJ, Bounemia N, et al. **Cerebral cortical microinfarcts on magnetic resonance imaging and their association with cognition in cerebral amyloid angiopathy.** *Stroke* 2018;49:2330–36 CrossRef Medline
- Charidimou A, Boulouis G, Gurrol ME, et al. **Emerging concepts in sporadic cerebral amyloid angiopathy.** *Brain* 2017;140:1829–50 CrossRef Medline
- Reijmer YD, Fotiadis P, Martinez-Ramirez S, et al. **Structural network alterations and neurological dysfunction in cerebral amyloid angiopathy.** *Brain* 2015;138:179–88 CrossRef Medline

12. Charidimou A, Boulouis G, Haley K, et al. **White matter hyperintensity patterns in cerebral amyloid angiopathy and hypertensive arteriopathy.** *Neurology* 2016;86:505–11 CrossRef Medline
13. Baykara E, Adam R, Tuladhar AM, et al. **A novel imaging marker for small vessel disease based on skeletonization of white matter tracts and diffusion histograms.** *Ann Neurol* 2016;40:581–92 CrossRef Medline
14. Petersen RC. **Mild cognitive impairment as a diagnostic entity.** *J Intern Med* 2004;256:183–94 CrossRef Medline
15. Linn J, Halpin A, Demaerel P, et al. **Prevalence of superficial siderosis in patients with cerebral amyloid angiopathy.** *Neurology* 2010;74:1346–50 CrossRef Medline
16. Crum RM, Anthony JC, Bassett SS, et al. **Population-based norms for the Mini-Mental State Examination by age and educational level.** *JAMA* 1993;269:2386–91 CrossRef Medline
17. Weintraub S, Salmon D, Mercaldo N, et al. **The Alzheimer's Disease Centers' Uniform Data Set (UDS): the neuropsychologic test battery.** *Alzheimer Dis Assoc Disord* 2009;23:91–101 CrossRef Medline
18. Corrigan JD, Hinkley NS. **Relationships between parts A and B of the Trail Making Test.** *J Clin Psychol* 1987;43:402–09 CrossRef Medline
19. Joy S, Kaplan E, Fein D. **Speed and memory in the WAIS-III Digit Symbol-Coding subtest across the adult lifespan.** *Arch Clin Neuropsychol* 2004;19:759–67 CrossRef Medline
20. Sánchez-Cubillo I, Periañez JA, Adrover-Roig D, et al. **Construct validity of the Trail Making Test: role of task-switching, working memory, inhibition/interference control, and visuomotor abilities.** *J Int Neuropsychol Soc.* 2009;15:438–50 CrossRef Medline
21. Brandt J. **The Hopkins Verbal Learning Test: development of a new memory test with six equivalent forms.** *Clin Neuropsychol* 1991;5:125–42 CrossRef
22. Wechsler D. *Wechsler Memory Scale-Revised Manual.* Harcourt Brace Jovanovich; 1987
23. Mack WJ, Freed DM, Williams BW, et al. **Boston Naming Test: shortened versions for use in Alzheimer's disease.** *J Gerontol* 1992;47:P154–58 CrossRef Medline
24. Tombaugh T, Kozak J, Rees L. **Normative data stratified by age and education for two measures of verbal fluency FAS and animal naming.** *Arch Clin Neuropsychol* 1999;14:167–77 Medline
25. Fastenau PS, Denburg NL, Mauer BA. **Parallel short forms for the Boston Naming Test: psychometric properties and norms for older adults.** *J Clin Exp Neuropsychol* 1998;20:828–34 CrossRef Medline
26. Tombaugh T. **Trail Making Test A and B: normative data stratified by age and education.** *Arch Clin Neuropsychol.* 2004;19:203–14 CrossRef Medline
27. Wardlaw JM, Smith EE, Biessels GJ, et al. **Neuroimaging standards for research into small vessel disease and its contribution to ageing and neurodegeneration.** *Lancet Neurol* 2013;12:822–38 CrossRef Medline
28. Greenberg SM, Vernooij MW, Cordonnier C, et al. **Cerebral microbleeds: a field guide to their detection and interpretation.** *Lancet Neurol* 2009;8:165–74 CrossRef Medline
29. Charidimou A, Linn J, Vernooij MW, et al. **Cortical superficial siderosis: detection and clinical significance in cerebral amyloid angiopathy and related conditions.** *Brain* 2015;138:2126–39 CrossRef Medline
30. Potter GM, Chappell FM, Morris Z, et al. **Cerebral perivascular spaces visible on magnetic resonance imaging: development of a qualitative rating scale and its observer reliability.** *Cerebrovasc Dis* 2015;39:224–31 CrossRef Medline
31. Fotiadis P, van Rooden S, van der Grond J, et al. **Cortical atrophy in patients with cerebral amyloid angiopathy: a case-control study.** *Lancet Neurol* 2016;15:811–19 CrossRef Medline
32. Deary IJ, Ritchie SJ, Muñoz Maniega S, et al. **Brain peak width of skeletonized mean diffusivity (PSMD) and cognitive function in later life.** *Front Psychiatry* 2019;10:524 CrossRef Medline
33. Lam BY, Leung KT, Yiu B, et al. **Peak width of skeletonized mean diffusivity and its association with age-related cognitive alterations and vascular risk factors.** *Alzheimers Dement (Amst)* 2019;11:721–29 CrossRef Medline
34. Low A, Mak E, Stefaniak JD, et al. **Peak width of skeletonized mean diffusivity as a marker of diffuse cerebrovascular damage.** *Front Neurosci* 2020;14:238 CrossRef Medline
35. Schouten TM, de Vos F, van Rooden S, et al. **Multiple approaches to diffusion magnetic resonance imaging in hereditary cerebral amyloid angiopathy mutation carriers.** *J Am Heart Assoc* 2019;8:e011288 CrossRef Medline
36. Wei N, Deng Y, Yao L, et al. **A neuroimaging marker based on diffusion tensor imaging and cognitive impairment due to cerebral white matter lesions.** *Front Neurol* 2019;10:1–7 CrossRef Medline
37. McCreary CR, Beaudin AE, Subotic A, et al. **Cross-sectional and longitudinal differences in peak skeletonized white matter mean diffusivity in cerebral amyloid angiopathy.** *Neuroimage Clin* 2020;27:102280 CrossRef Medline
38. Viswanathan A, Greenberg SM. **Cerebral amyloid angiopathy in the elderly.** *Ann Neurol* 2011;70:871–80 CrossRef
39. Smith EE, Biessels GJ, De Guio F, et al. **Harmonizing brain magnetic resonance imaging methods for vascular contributions to neurodegeneration.** *Alzheimers Dement (Amst)* 2019;11:191–204 CrossRef Medline
40. Beaudet G, Tsuchida A, Petit L, et al. **Age-related changes of peak width skeletonized mean diffusivity (PSMD) across the adult lifespan: a multi-cohort study.** *Front Psychiatry* 2020;11:342 CrossRef Medline
41. Salat DH, Smith EE, Tuch DS, et al. **White matter alterations in cerebral amyloid angiopathy measured by diffusion tensor imaging.** *Stroke* 2006;37:1759–64 CrossRef Medline
42. Finsterwalder S, Vlegels N, Gesierich B, et al. **Small vessel disease more than Alzheimer's disease determines diffusion MRI alterations in memory clinic patients.** *Alzheimers Dement* 2020;16:504–14 CrossRef Medline
43. van Veluw SJ, Reijmer YD, van der Kouwe AJ, et al. **Histopathology of diffusion imaging abnormalities in cerebral amyloid angiopathy.** *Neurology* 2019;92:43 CrossRef Medline
44. Charidimou A, Martinez-Ramirez S, Shoamanesh A, et al. **Cerebral amyloid angiopathy with and without hemorrhage: evidence for different disease phenotypes.** *Neurology* 2015;84:1206–12 CrossRef

A Novel Endovascular Therapy for CSF Hypotension Secondary to CSF-Venous Fistulas

W. Brinjikji, L.E. Savastano, J.L.D. Atkinson, I. Garza, R. Farb, and J.K. Cutsforth-Gregory



ABSTRACT

SUMMARY: We report a consecutive case series of patients who underwent transvenous embolization of the paraspinal vein, which was draining the CSF-venous fistula, for treatment of spontaneous intracranial hypotension. These are the first-ever reported cases of this treatment for CSF-venous fistulas. All patients underwent spinal venography following catheterization of the azygous vein and then selective catheterization of the paraspinal vein followed by embolization of the vein with Onyx. All patients had improvement of clinical and radiologic findings with 4 patients having complete resolution of headaches and 1 patient having 50% reduction in headache symptoms. Pachymeningeal enhancement resolved in 4 patients and improved but did not resolve in 1 patient. Brain sag resolved in 4 patients and improved but did not resolve in 1 patient. There were no cases of permanent neurologic complications. All patients were discharged home on the day of the procedure.

ABBREVIATIONS: DSM = digital subtraction myelography; SIH = spontaneous intracranial hypotension

CSF-venous fistulas have been increasingly recognized as a cause of spontaneous intracranial hypotension (SIH).¹ The exact pathogenesis of these lesions is unclear, with potential hypotheses being that these lesions represent aberrant connections between the nerve root sleeve and a paraspinal vein or that these lesions are secondary to increased CSF drainage via spinal arachnoid granulations into adjacent radicular veins. Advanced imaging techniques such as digital subtraction myelography (DSM) and decubitus CT myelography have improved the detection of these occult lesions.²⁻⁵ A number of treatment options have been proposed for CSF-venous fistulas, including surgical ligation, nerve root skeletonization (ie, isolation of the nerve root and surrounding vasculature), and blood/fibrin patching.⁶ Surgical ligation has been shown to be extremely effective in treating CSF-venous fistulas, likely by means of disconnecting the venous outflow pathway of the CSF-venous fistula.

On reviewing the anatomy of the paraspinal venous system in the cervical, thoracic, and lumbar spine, it is apparent that catheter-based navigation of these veins is feasible. In fact, multiple studies dating back to the 1970s and 1980s have documented

techniques for spinal phlebography, which, in those times, were used primarily to diagnose mass effect from disc herniations and spinal masses and have shown that catheter-based venography of the paraspinal venous system is safe.⁷⁻⁹ Given the relatively simple organization of the paraspinal venous system, we considered it feasible to navigate into these veins and close the venous outflow of the CSF-venous fistula using liquid embolic materials such as Onyx (Covidien). Herein, we report the first series of patients undergoing transvenous embolization of paraspinal veins draining CSF-venous fistulas for treatment of SIH.

MATERIALS AND METHODS

Patient Selection

Following institutional review board approval at the Mayo Clinic, we retrospectively reviewed our series of patients with CSF hypotension secondary to definite CSF-venous fistula diagnosed on DSM. All patients had imaging evidence of CSF hypovolemia on MR imaging, including brain sag and pachymeningeal enhancement and no extradural fluid collection on total spine MR imaging, and all patients underwent clinical evaluation by neurology subspecialists in headache and CSF disorders. All included patients were imaged and embolized between July 2020 and August 2020, when all CSF venous fistulas were treated endovascularly only. All images were reviewed on the PACS.

DSM Technique

Our technique for DSM has been previously described.² Briefly, all DSMs were performed with spinal angiography set to 1 frame

Received November 17, 2020; accepted after revision November 30.

From the Departments of Interventional Neuroradiology (W.B., L.E.S.), Neurosurgery (W.B., L.E.S., J.L.D.A.), and Neurology (I.G., J.K.C.-G.), Mayo Clinic, Rochester, Minnesota; and Joint Department of Medical Imaging (R.F.), Toronto Western Hospital, Toronto, Ontario, Canada.

Please address correspondence to Waleed Brinjikji, MD, Interventional Neuroradiology, Mayo Clinic, 200 1st St SW, Rochester, MN 55905; e-mail: Brinjikji.waleed@mayo.edu; @wbrinjikji

<http://dx.doi.org/10.3174/ajnr.A7014>

per 1–2 seconds. A tiltable table was used to adjust spine angling. All DSMs were performed with a single plane. In general, a 20-ga spinal needle was placed at L2–L3 or below and into the thecal sac. Following return of CSF, in general, 10 mL of saline was slowly injected into the thecal sac. Following this, 5–6 mL of iohexol (Omnipaque 300; GE Healthcare) was injected in rapid fashion while the imaging system was centered on the thoracic spine, and angiography was performed. Another 5–6 mL of contrast was then injected in the thoracolumbar region, and angiography was performed. Of note, for the first run in all patients, the first rib was clearly in the FOV to allow us to clearly identify the level of the leak. For the run focusing on the thoracolumbar spine, we clearly had the lowest rib in the FOV so that rib counting could be easily performed. In general, patients were imaged on consecutive days with the left side down being performed on day 1 and right side down performed on day 2.

Patient Imaging Evaluation

All patients included underwent baseline and 2- to 3-month follow-up brain MR imaging with and without IV contrast. MR imaging sequences included precontrast sagittal T1, FLAIR, T2, and gradient recalled-echo as well as postcontrast T1-weighted imaging. MRIs were analyzed according to the methods put forth by Dobrocky et al.¹⁰ For the purpose of this study, we call this the Bern SIH score. We analyzed the following imaging findings: venous sinus distension, pachymeningeal enhancement, the presence of subdural fluid collections, suprasellar cistern effacement (defined as ≤ 4.0 mm), effacement of the prepontine cistern of ≤ 5.0 mm, and mamillopontine distance of ≤ 6.5 mm. Measurements were performed exactly according to the criteria described by Dobrocky et al. Three imaging findings were considered major (2 points each), including pachymeningeal enhancement, venous sinus engorgement, and suprasellar cistern effacement. Three were considered minor (1 point each), including subdural fluid collection, effacement of the prepontine cistern, and mamillopontine distance of ≤ 6.5 mm. Patients were then classified as having a low, intermediate, or high probability of having a CSF leak with total Bern SIH scores of ≤ 2 points, 3–4 points, or ≥ 5 points, respectively, on a scale of 9 points. All imaging was reviewed by a single neurointerventional radiologist with 2.5 years of postfellowship experience who was not blinded to patient health information at the time of MR imaging.

Patient Clinical Evaluation

All patients underwent a comprehensive neurologic evaluation before and after endovascular therapy. For the evaluation, patients were queried regarding position-dependent symptoms, hearing loss, tinnitus, and cognitive disturbance (ie, brain fog).

Endovascular Technique

For embolization of the fistulas, our approach was to selectively catheterize the paraspinal vein that was identified as draining the fistula on the DSM and then embolize the vein using Onyx. For 4 patients, we obtained venous access in the right common femoral vein, and in 1 patient, we obtained venous access in the right internal jugular vein. Following this, we would advance a 5F Vertebral catheter (Merit Medical) in the superior vena cava. To

enter the azygous vein, the catheter was steered to a point in a posterior direction, and with the patient taking a gentle inspiration, we would probe around the origin of the azygous vein with an 0.035-inch Glidewire (Terumo). Once the wire was able to access the azygous vein, we would advance the wire as far distally as possible, in general to the level of T12. Then, we would slowly advance the Vertebral catheter into the azygous vein. When the 0.035-inch wire did not provide enough support, we would use a stiff Glidewire. Following this, we would use a Headway Duo microcatheter (MicroVention) to selectively catheterize the paraspinal vein draining the fistula. To perform this procedure, we would point the tip of the Vertebral catheter in the direction of the paraspinal vein (right posterior for right-sided fistulas, left posterior for left-sided fistulas). Then, we would advance the Headway Duo microcatheter over a gently angled 14-inch wire into the paraspinal vein by probing with the wire. Once the wire was in the proximal paraspinal vein, we would advance the microcatheter.

Once the microcatheter was past the anatomic landmark of the pedicle (ie, in the proximal intercostal vein, roughly 1 cm from the site of fistula), a venogram was performed of the paraspinal vein. Then, we would proceed with embolization, starting with about 0.5 mL of Onyx 34 to build a plug that would not escape into the systemic venous system and then push about 1 mL of Onyx 18 into the network surrounding the nerve root sleeve. Onyx did enter the epidural venous plexus in 1 patient, but it was well tolerated with no resultant symptoms. Entry into the epidural plexus was identified by the flow of Onyx medial to the pedicle. In general, follow-up CT was performed for evaluation of the Onyx cast. For 1 lesion at T4, it was difficult to catheterize the T4 vein from a transfemoral route, given the sharp takeoff angle of the supreme intercostal vein off the apex of the azygous arch, so a transjugular approach was chosen.

Statistical Analysis

Descriptive statistics are reported. To compare the mean Bern SIH scores, we used a paired *t* test to determine whether there was improvement in imaging findings of CSF hypotension.

RESULTS

A summary of the 5 patients reported in this series is shown in the Table. Mean patient age was 60 [SD, 10] years. Four patients were men, and 1 patient was a woman. All patients had position- and Valsalva-dependent headaches. Two patients had hearing loss. Three patients had cognitive disturbances described as brain fog, and 4 patients had tinnitus.

All 5 patients had bilateral DSMs. CSF-venous fistulas were located at the right T4 in 2 patients, the right T7 in 1 patient, the right T8 in 1 patient, and bilateral T9 in 1 patient. The CSF-venous fistulas are shown in Fig 1.

For the embolization procedure, the transfemoral route was used in 4 of 5 patients, and a transjugular approach, in 1 patient. In all cases, the draining paraspinal vein could be selectively catheterized and embolized with Onyx. Two patients who underwent embolization of right T4 CSF-venous fistulas reported back pain in the right T4 dermatome, which resolved after 1 month. There were no cases of permanent radiculitis or radiculopathy,

Patient characteristics and outcomes

Patient No.	Age (yr)/Sex	Symptoms	Fistula Level	Approach	Complications	Bern Score Pre-Tx	Bern Score Post-Tx	Improvement in Symptoms?
1	44/M	Position- and Valsalva-dependent headache	Right T8	Transfemoral	None	8	0	Complete resolution
2	67/F	Position- and Valsalva-dependent headache, tinnitus, brain fog	Right T4	Transfemoral	Pain at right T4, resolved after 1 month	9	0	Complete resolution
3	58/M	Position- and Valsalva-dependent headache, tinnitus, brain fog, hearing loss	Right T7	Transfemoral	None	6	2	50% Improvement in headache and hearing loss, stable tinnitus
4	65/M	Position- and Valsalva-dependent headache, tinnitus, brain fog	Right T4	Transjugular	Pain at right T4, resolved after 1 month	9	0	Complete resolution
5	68/M	Position- and Valsalva-induced headache, tinnitus, hearing loss, vertigo	Bilateral T9	Transfemoral	None	6	1	Complete resolution of headache and hearing loss, persistent tinnitus with SCC dehiscence

Note:—SCC indicates semicircular canal; TX, treatment.

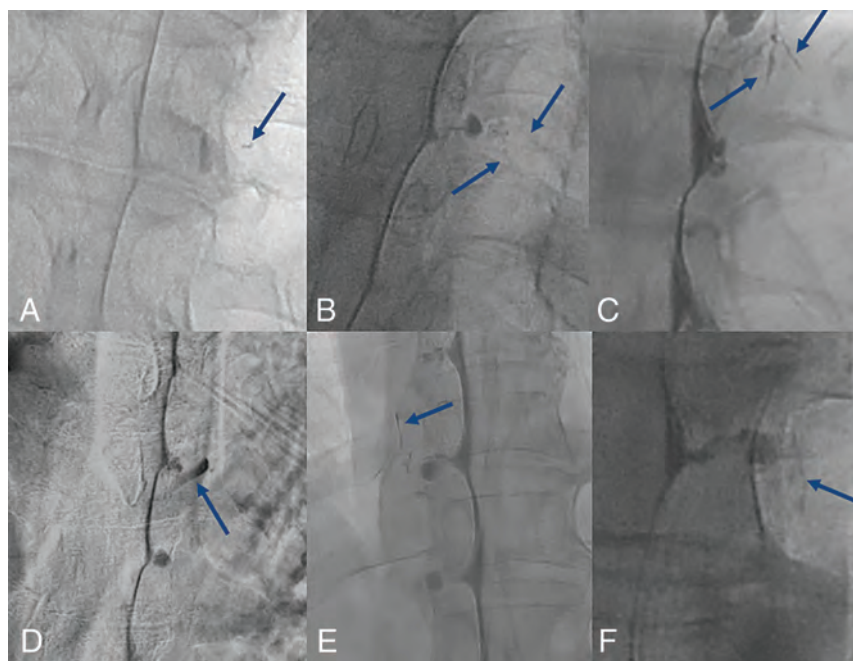


FIG 1. Examples of CSF-venous fistulas from the 5 patients. A, CSF-venous fistula at the right T8 in patient 1 with contrast in the paraspinal vein (blue arrow). B, CSF-venous fistula at the right T4 in patient 2 with contrast in the paraspinal vein (blue arrows). C, CSF-venous fistula at the right T7 in patient 3 with contrast in the paraspinal vein (blue arrows). D, Large CSF-venous fistula in patient 4 with complete opacification of the right T4 paraspinal vein (blue arrow). E and F, Bilateral CSF-venous fistulas at T9 in patient 5 (blue arrows).

no cases of new neurologic deficits after the procedure, and no access-site complications. There were no cases of embolization material entering the subarachnoid space. All patients were discharged home on the day of the procedure. No patients required narcotics for postoperative pain. No patients had rebound hypertension. An example of the steps of the embolization procedure are shown in Fig 2.

On baseline imaging, all patients had MR imaging findings consistent with a high probability of CSF leak with a mean

Bern SIH score of 7.6 [SD, 1.5]. At follow-up (median follow-up of 2 months; range, 1.5–3 months), the mean Bern score was 0.6 [SD, 0.9] ($P = .002$). Three patients had complete resolution of brain sag, subdural fluid collections, and pachymeningeal enhancement with a final Bern score of 0. One patient had persistent effacement of the suprasellar cistern, and 1 patient had persistent-but-subtle pachymeningeal enhancement. Pre- and postimaging findings are shown in Figs 3 and 4.

At last follow-up (median follow-up of 3 months; range, 2–4 months), all patients had documented clinical improvement. Three patients had complete resolution of SIH-related symptoms. One patient had complete resolution of headaches and hearing loss but had persistent tinnitus. However, this patient was found to have a semicircular canal dehiscence, which confounded the evaluation of the tinnitus. One patient, the patient with mild residual pachymeningeal enhancement, had a 50% improvement in headache and hearing loss, but persistent tinnitus.

DISCUSSION

We present the first case series of transvenous catheter-based embolization of CSF-venous fistulas causing SIH. In all cases, the fistulas were localized using DSM, and in all cases, embolization resulted in significant improvement in both imaging findings and

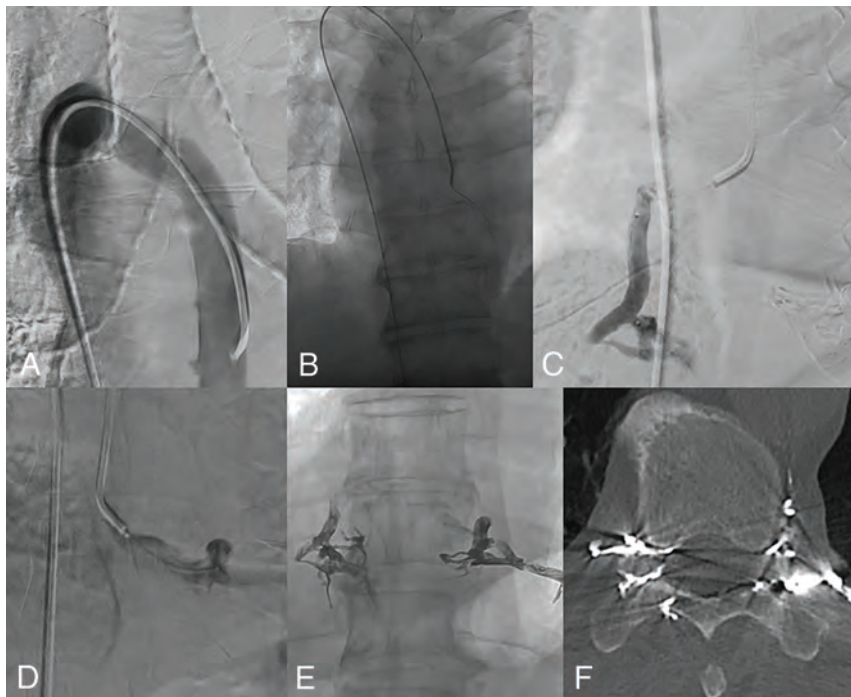


FIG 2. Steps involved in CSF-venous fistula embolization (patient 5). *A*, The azygous vein is selectively catheterized using a 5F Vertebral catheter. The catheter is directed posteriorly to face the azygous vein. In this case, the patient had to take a shallow inspiration to open up the valve between the azygous vein and the superior vena cava. *B*, The catheter is then advanced into the azygous vein over a stiff Glidewire. This support is needed for the catheter to make the 180° turn. *C*, This patient had bilateral CSF-venous fistulas at the right T9. We advanced a Headway Duo microcatheter into the right T9 paraspinal vein, and a venogram was performed. The same procedure was performed for the left T9 paraspinal vein (*D*). *E*, Both veins are embolized with Onyx 34 to build a plug followed by Onyx 18. *F*, Postoperative CT shows excellent filling of the radicular veins at T9 bilaterally, essentially sealing off the CSF-venous fistulas.

clinical symptoms. Pain localized to the site of the embolization was a common minor complication, but in no cases did this require narcotics, and in all cases, the pain subsided in a matter of weeks. All procedures were performed on an outpatient basis, and there were no permanent neurologic deficits. Our findings are important because they suggest that CSF-venous fistulas may be amenable to obliteration via transvenous embolization and may not require surgical intervention.

Currently, surgical intervention that includes laminectomy, facetectomy, and ligation of the nerve root and associated veins has been reported to be most effective in obliterating CSF-venous fistulas.¹¹ This intervention works by completely disconnecting the fistula, including both the CSF-filled nerve root sleeve as well as the draining vein. In a recent series of 42 patients who underwent surgical ligation of fistulas, 49% were headache-free and 27% had at least 50% improvement at 5 months, and 80% had improvement or resolution of MR imaging findings of CSF hypotension.⁶ Other minimally invasive treatment options such as epidural blood patch and fibrin glue injection have been

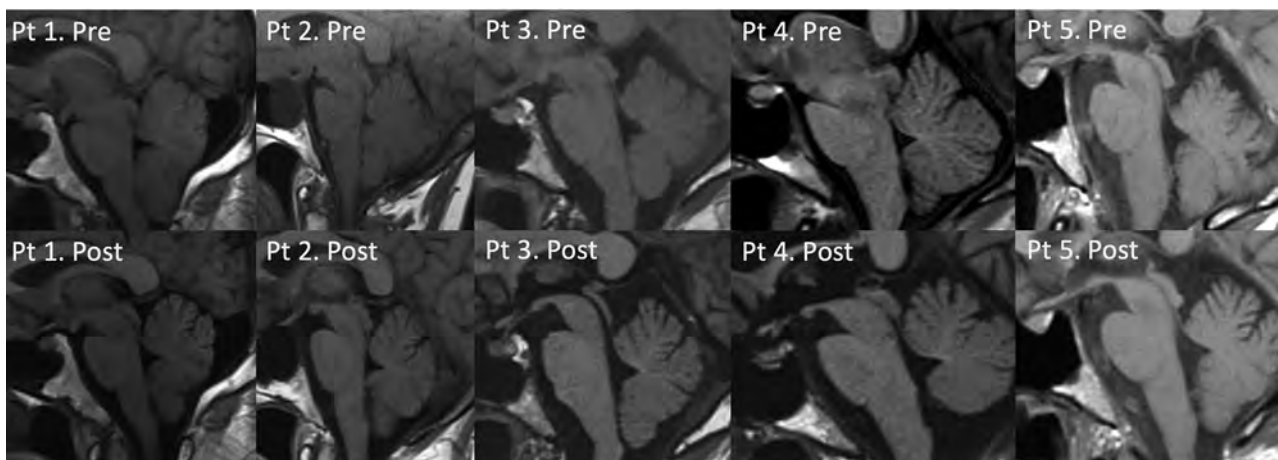


FIG 3. Pre- and posttreatment sagittal T1-weighted MRIs in patients 1–5. Patient 1 had a decreased mamillopontine distance, effacement of the prepontine and suprasellar cistern, tonsillar descent, and engorgement of the pituitary gland. Following embolization, there was normalization of the suprasellar cistern and mamillopontine cistern distances as well as the prepontine cistern and resolution of tonsillar ectopia. Pituitary engorgement improved as well. Patient 2 had prepontine and suprasellar cistern effacement and decreased mamillopontine distance and tonsillar ectopia. Following embolization, these all resolved. Note the incidental pituitary cyst. Patient 3 had decreased mamillopontine distance and effacement of the suprasellar cistern and prepontine cistern, all of which normalized postembolization. Patient 4 had effacement of the suprasellar cistern and prepontine cistern and decreased mamillopontine distance, all of which resolved on follow-up MR imaging. Patient 5 had effacement of the suprasellar cistern and prepontine cistern. There was still suprasellar cistern effacement on posttreatment MR imaging, but the prepontine cistern distance normalized. Pt indicates patient; Pre, pretreatment; Post, posttreatment.

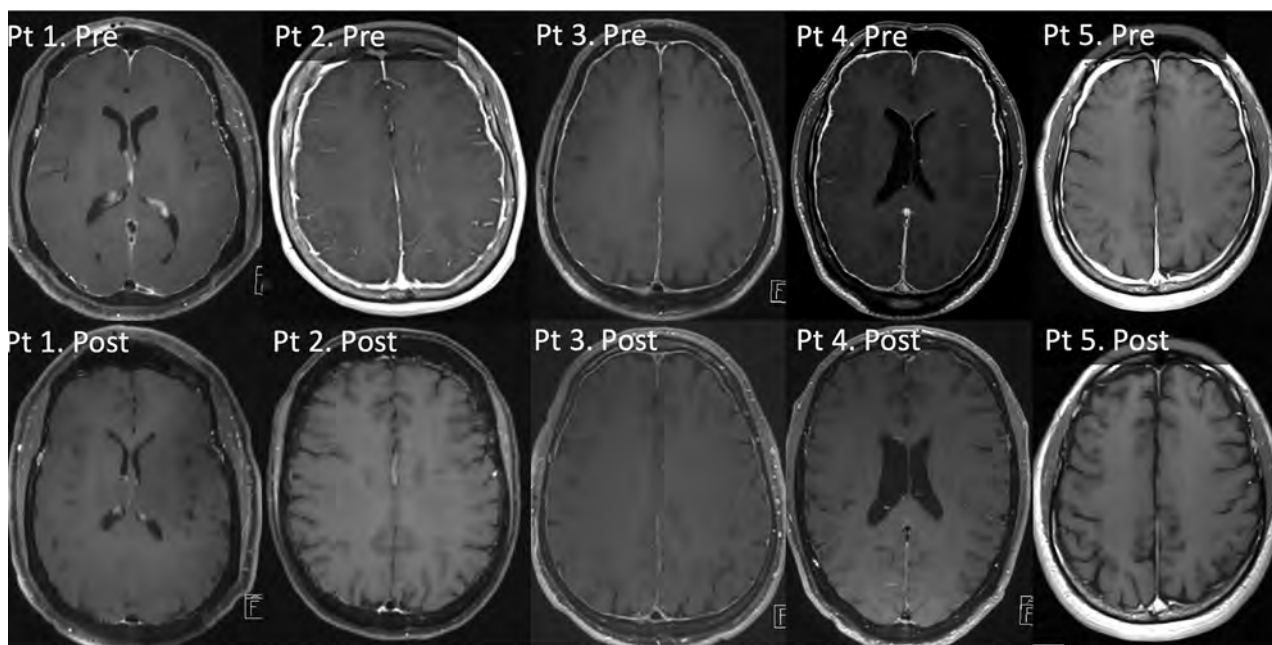


FIG 4. Pre- and posttreatment postcontrast T1-weighted MRIs in patients 1–5. Pretreatment MRIs show diffuse pachymeningeal enhancement in all 5 patients. Posttreatment, there is complete resolution of pachymeningeal enhancement in patients 1, 2, 4, and 5, with subtle pachymeningeal enhancement in patient 3. Pt indicates patient; Pre, pretreatment; Post, posttreatment.

reported as potential treatment options for CSF-venous fistulas and are thought to work by compressing the fistula. However, these have been shown to be effective in a minority of patients.¹²

As demonstrated in this report, occlusion of the CSF draining vein with a liquid embolic agent such as Onyx leads to a reduction in shunting sufficient to result in symptomatic and radiographic cure. This effect could be due to direct occlusion of the fistula by the liquid embolic agent or by creating local venous hypertension that reverses the favorable pressure gradient for CSF to leak into the vein.¹³ Given that the anatomy of the nerve root sleeve has somewhat of a plexus-like organization, we have opted to use Onyx to embolize these fistulas because Onyx can permeate tinier veins and venules, especially in its more dilute formulation (Onyx 18). We build a plug with Onyx 34 because this keeps the Onyx 18 from refluxing into the azygous vein and then into the lung.

Limitations

Our case series has limitations. First, the follow-up duration ranges from 2 to 4 months in these patients. Scoring of the Bern SIH score was performed by a single neurointerventional radiologist, possibly introducing some bias. The long-term effects of this treatment have yet to be elucidated, including the possibility of delayed rebound hypertension. Given that Onyx is a permanent embolic agent and that these fistulas are slow-flow shunts with very small pressure gradients, we have no reason to believe that fistulas would recanalize. We suspect that it is more likely that patients would develop additional fistulas at other levels, which could later be embolized. Second, because patients are referred to us from multiple centers, we do not have uniform pretreatment MR imaging protocols and some MR imaging scans pretreatment were performed at 1.5T. Third, we did not collect

measures such as the Headache Impact Test-6, quality of life, and other standardized questionnaires but will do so in the future. Fourth, while we do not report any technical complications in this series, there are a few complications that could potentially occur with such an embolization. One such example is that reflux of Onyx into the azygous vein could result in Onyx ending up in the lung, causing small pulmonary emboli. We suspect that these emboli would be tolerated similar to how most cement emboli following vertebroplasty are asymptomatic and well-tolerated.

CONCLUSIONS

We report the first case series of transvenous paraspinal vein embolization of a CSF-venous fistula. This novel treatment approach resulted in clinical and radiographic improvement in all patients with no permanent complications. Further studies are needed to confirm our technique and to study the durability of this treatment effect.

Disclosures: Luis Savastano—*UNRELATED: Employment:* VerAvanti; *Stock/Stock Options:* Endovascular Engineering, VerAvanti. Ivan Garza—*UNRELATED: Employment:* Mayo Clinic; *Comments:* I receive a salary for my full-time work as a neurologist at the Mayo Clinic; *Royalties:* UpToDate; *Comments:* I receive royalty payments for my work as an author for UpToDate. Jeremy K. Cutsforth-Gregory—*UNRELATED: Royalties:* Oxford University Press; *Comments:* Mayo Clinic Medical Neurosciences (textbook). Waleed Brinjikji—*UNRELATED: Stock Options:* Marblehead Medical LLC. *Consulting Fee:* Cerenovus, Microvention.*
*Money paid to the institution.

REFERENCES

1. Schievink WI, Moser FG, Maya MM. CSF-venous fistula in spontaneous intracranial hypotension. *Neurology* 2014;83:472–73 CrossRef Medline
2. Kim DK, Brinjikji W, Morris PP, et al. Lateral decubitus digital subtraction myelography: tips, tricks, and pitfalls. *AJNR Am J Neuroradiol* 2020;41:21–28 CrossRef Medline

3. Farb RI, Nicholson PJ, Peng PW, et al. **Spontaneous intracranial hypotension: a systematic imaging approach for CSF leak localization and management based on MRI and digital subtraction myelography.** *AJNR Am J Neuroradiol* 2019;40:745–53 CrossRef Medline
4. Kranz PG, Gray L, Amrhein TJ. **Decubitus CT myelography for detecting subtle CSF leaks in spontaneous intracranial hypotension.** *AJNR Am J Neuroradiol* 2019;40:754–56 CrossRef Medline
5. Amrhein TJ, Gray L, Malinzak MD, et al. **Respiratory phase affects the conspicuity of CSF-venous fistulas in spontaneous intracranial hypotension.** *AJNR Am J Neuroradiol* 2020;41:1754–56 CrossRef Medline
6. Duvall JR, Robertson CE, Cutsforth-Gregory JK, et al. **Headache due to spontaneous spinal cerebrospinal fluid leak secondary to cerebrospinal fluid-venous fistula: case series.** *Cephalalgia* 2019;39:1847–54 CrossRef Medline
7. Djindjian R, Faure C. **Neuro-radiological investigations (arteriography and phlebography) in vascular malformations of the spinal cord** [in French]. *Rontgeneur Radiodiagn Clin Eur* 1963;5:171–95 Medline
8. Tarkkainen E. **Intercostal vein meningoarachidography: a technical, anatomic and clinical study.** *Acta Radiology Diagn (Stockh)* 1967 (Suppl 271):1+ Medline
9. Theron J, Djindjian R. **Cervicovertebral phlebography using catheterization: a preliminary report.** *Radiology* 1973;108:325–31 CrossRef Medline
10. Dobrocky T, Grunder L, Breiding PS, et al. **Assessing spinal cerebrospinal fluid leaks in spontaneous intracranial hypotension with a scoring system based on brain magnetic resonance imaging findings.** *JAMA Neurol* 2019;76:580–87 CrossRef Medline
11. Wang TY, Karikari IO, Amrhein TJ, et al. **Clinical outcomes following surgical ligation of cerebrospinal fluid-venous fistula in patients with spontaneous intracranial hypotension: a prospective case series.** *Oper Neurosurg (Hagerstown)* 2020;18:239–45 CrossRef Medline
12. Kranz PG, Amrhein TJ, Schievink WI, et al. **The “hyperdense paraspinous vein” sign: a marker of CSF-venous fistula.** *AJNR Am J Neuroradiol* 2016;37:1379–81 CrossRef Medline
13. Scapinelli R. **Antireflux mechanisms in veins draining the upper territory of the vertebral column and spinal cord in man.** *Clin Anat* 2000;13:410–15 CrossRef Medline

Distal Transradial Access for Diagnostic Cerebral Angiography and Neurointervention: Systematic Review and Meta-analysis

H. Hoffman, M.S. Jalal, H.E. Masoud, R.B. Pons, I. Rodriguez Caamaño, P. Khandelwal, T. Prakash, and G.C. Gould

ABSTRACT

BACKGROUND: Radial artery access for cerebral angiography is traditionally performed in the wrist. Distal transradial access in the anatomic snuffbox is an alternative with several advantages.

PURPOSE: Our aim was to review the safety and efficacy of distal transradial access for diagnostic cerebral angiography and neurointerventions.

DATA SOURCES: We performed a comprehensive search of the literature using PubMed, Scopus, and EMBASE.

STUDY SELECTION: The study included all case series of at least 10 patients describing outcomes associated with distal transradial access for diagnostic cerebral angiography or a neurointervention.

DATA ANALYSIS: Random-effects models were used to obtain pooled rates of procedural success and complications.

DATA SYNTHESIS: A total of 7 studies comprising 348 (75.8%) diagnostic cerebral angiograms and 111 (24.2%) interventions met the inclusion criteria. The pooled success rate was 95% (95% CI, 91%–98%; $I^2 = 74.33$). The pooled minor complication rate was 2% (95% CI, 1%–4%; $I^2 = 0$). No major complications were reported. For diagnostic procedures, the combined mean fluoroscopy time was 13.53 [SD, 8.82] minutes and the mean contrast dose was 74.9 [SD, 35.6] mL.

LIMITATIONS: A small number of studies met the inclusion criteria, all of them were retrospective, and none compared outcomes with proximal transradial or femoral access.

CONCLUSIONS: Early experience with distal transradial access suggests that it is a safe and effective alternative to proximal radial and femoral access for performing diagnostic cerebral angiography and interventions. Additional studies are needed to establish its efficacy and compare it with other access sites.

ABBREVIATIONS: dTRA = distal transradial access; FT = fluoroscopy time; pTRA = proximal transradial access; RAO = radial artery occlusion; TFA = trans-femoral access; TRA = transradial access; US = ultrasound

Neuroendovascular procedures have traditionally been performed using transfemoral access (TFA). Transradial access (TRA) recently gained popularity due to its lower rate of access site complications, quicker recovery time, and greater patient satisfaction.¹ However, TRA is not without complications, including radial artery occlusion (RAO), hematoma, vasospasm, pseudoaneurysm,

and arteriovenous fistula.² Distal transradial access (dTRA) with puncture of the radial artery in the anatomic snuffbox may be safer than proximal transradial access (pTRA) in the forearm.³ The former is distal to the origin of the superficial palmar arch, lowering the risk of hand ischemia with RAO, and preserves the proximal radial artery for future interventions. It also affords shorter time to achieve hemostasis and improved ergonomics for both the patient and the operator.⁴ The latter may be especially beneficial in left-sided approaches and in patients who have limited supination.

Although numerous reports on the safety and efficacy of dTRA for coronary angiography and percutaneous coronary interventions are available, data regarding this approach for neuroendovascular procedures are sparse and have not been reviewed. The goal of this study was to perform a systematic review and meta-analysis of dTRA for cerebral angiography and

Received September 14, 2020; accepted after revision November 11.

From the Departments of Neurosurgery (H.H., M.S.J., G.C.G.) and Neurology (H.E.M.), State University of New York Upstate Medical University, Syracuse, New York; Department of Interventional Neuroradiology (R.B.P., I.R.C.), Hospital Universitari de Bellvitge, Fundació Institut d'Investigació Biomèdica de Bellvitge, L'Hospitalet de Llobregat, Barcelona, Spain; and Department of Neurosurgery (P.K., T.P.), Rutgers New Jersey Medical School, Newark, New Jersey.

Please address correspondence to Haydn Hoffman, MD, Department of Neurosurgery, State University of New York Upstate Medical University, 750 E Adams St, Syracuse, NY 13210; e-mail: hoffmanh@upstate.edu; @haydnhoffmanmd <http://dx.doi.org/10.3174/ajnr.A7074>

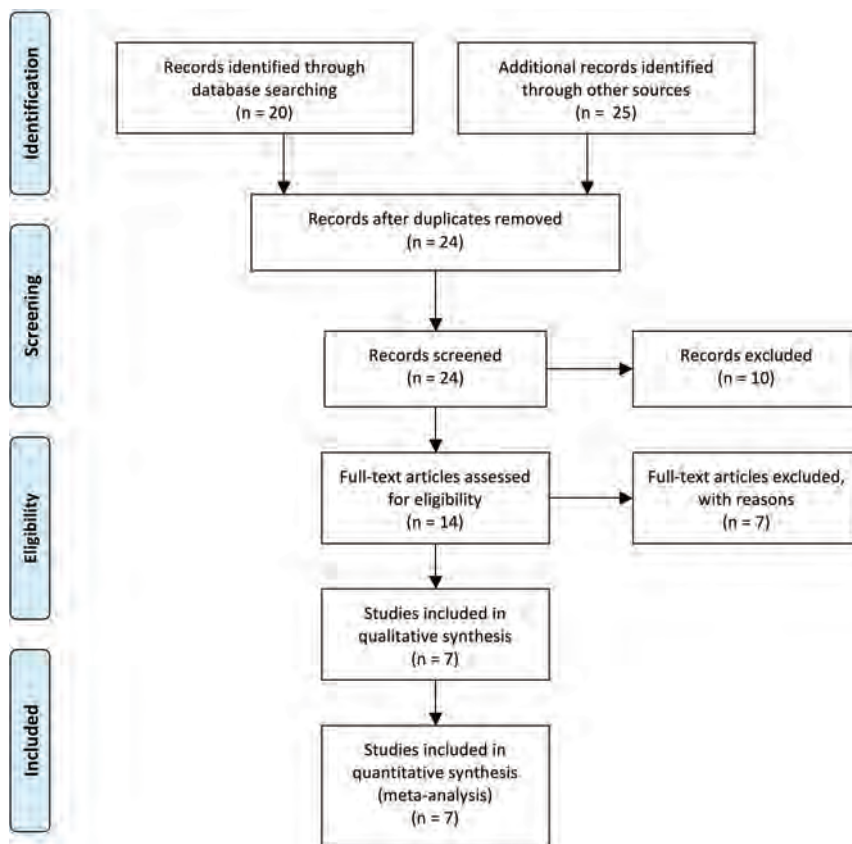


FIG 1. PRISMA flow diagram.

neurointerventions to determine the success and complication rates of this approach.

MATERIALS AND METHODS

This study was performed in accordance with the Preferred Reporting Items for Systematic Reviews and Meta-Analyses (PRISMA) guidelines.⁵

Search Strategy

We performed a comprehensive search of the literature as of August 21, 2020, using PubMed, Scopus, and EMBASE with the following keywords: (“distal radial” OR “distal transradial” OR “snuffbox”) AND (“cerebral” OR “neuroendovascular” OR “neurointervention”).

Selection Criteria

Studies were included if the authors reported original data regarding their outcomes performing distal transradial access for diagnostic cerebral angiography or neurointerventions. Only series of at least 10 patients were considered.

Data Extraction

A standardized form was used to extract the following data from the included studies: 1) number of patients undergoing the dTRA approach, 2) mean age, 3) proportion of diagnostic and interventional procedures, 4) success rate and reasons for failures, 5) complication rate and nature of complications, 6) use of ultrasound (US),

7) use of the Barbeau or Allen test, 8) method for achieving hemostasis, 9) mean radial artery diameter in the snuff-box, 10) sheath used, 11) mean number of vessels catheterized (diagnostic procedures), 12) mean fluoroscopy time (FT) (diagnostic procedures), and 13) contrast dose (diagnostic procedures). Data were extracted in duplicate by 2 authors (M.S.J. and H.H.), and all inconsistencies were resolved with discussion. In cases of missing data, the corresponding authors were contacted for clarification. The authors of 1 study provided details regarding additional cases that met the inclusion criteria, which were included in the quantitative analysis.⁶

Critical Appraisal

The methodologic quality of the studies was assessed using a previously described version of the Newcastle-Ottawa Scale modified for case series.⁷ Studies were evaluated in 4 domains: selection, ascertainment, causality, and reporting. Risk of publication bias across studies was evaluated using a funnel plot.

Statistical Analysis

Pooled estimates for outcomes were calculated using random-effects models and are represented by forest plots. The primary outcome was the proportion of procedural success, which was defined as catheterization of the intended vessels and completion of the angiogram or intervention without conversion to pTRA or common femoral access. Secondary outcomes included complication rates, defined as major or minor. Major complications included symptomatic RAO, pseudoaneurysm or arteriovenous fistula formation, and hematoma requiring transfusion. Minor complications included minor bleeding, asymptomatic RAO, and local pain or numbness extending beyond the duration of the procedure. Heterogeneity was evaluated with the I^2 statistic. Outliers were identified using the Grubb test with a 5% significance level. Meta-regression models were developed to determine the associations between routine use of US and procedural success as well as complications.

RESULTS

Search Results

A total of 7 studies^{6,8-13} met the inclusion criteria and were included in the meta-analysis (Fig 1). All 7 studies were retrospective case series, and none of them compared outcomes associated with dTRA and pTRA or TFA. The methodologic quality of the 7 studies is described in Table 1.

Description of Studies and Procedural Characteristics

The 7 included studies comprised 348 (75.8%) diagnostic cerebral angiograms and 111 (24.2%) interventions. Three studies included

Table 1: Assessment of methodologic quality of the 11 included studies using criteria described by Murad et al⁷

Study	Selection	Ascertainment		Causality		Reporting
	Do the patients represent the whole experience of the investigator? ^a	Was the exposure adequately ascertained?	Was the outcome adequately ascertained? ^b	Were other alternative causes that may explain the observation ruled out?	Was follow-up long enough for outcomes to occur? ^b	Are the cases described with sufficient detail?
Weinberg et al ⁸ 2020	Yes	Yes	Yes	Yes	No	Yes
Pons et al ⁶ 2020	Yes	Yes	Yes	Yes	Yes	Yes
Saito et al ⁹ 2020	Yes	Yes	Yes	Yes	Yes	Yes
Kuhn et al ¹⁰ 2020	Yes	Yes	Yes	Yes	No	Yes
Goland et al ¹¹ 2019	NR	NR	Yes	No	No	No
Patel et al ¹² 2019	Yes	Yes	Yes	Yes	No	Yes
Brunet et al ¹³ 2019	Yes	Yes	Yes	Yes	No	No

Note:—NR indicates not reported.

^a This criterion was met if authors reported consecutive series of patients.

^b Follow-up was considered sufficient if authors reported any delayed follow-up after the procedure in the form of telephone interviews, clinical examinations, or sonography evaluations of the distal radial artery.

Table 2: Details of each study

Study	No.	Mean Age [SD] (yr)	Proportion Women (%)	Proportion of Interventions (%)	Interventions (No.)	Success Rate (%)	Complication Rate (%)	Complication Description (No.)
Weinberg et al ⁸ 2020	120	54.7 [14.7]	55.8	7.5	AVM/dAVF (7) Aneurysm (1) Other (1)	100	1.7	Hematoma (1) Radial artery spasm (1)
Pons et al ⁶ 2020	98	58 [15.6]	44	46.9	Aneurysm (17) Stroke (13) ICAD (4) AVM/dAVF (4) CAS (3) BTO (3) Embolization (2)	96.9	4.1	Hematoma (3) Dissection (1)
Saito et al ⁹ 2020	51	59.4 [13.5]	68.6	0	NA	92.2	2	Numbness (1)
Kuhn et al ¹⁰ 2020	48	64.4	56.3	100	Aneurysm (18) Embolization (8) CAS (6) AVM/dAVF (3) Stroke (3) ICAD (3) Vasospasm (1) Spinal embolization (1) Aneurysm (9)	89.6	2.1	Asymptomatic RAO (1)
Goland et al ¹¹ 2019	19	52 [14.5]	57.9	42.1	NA	20	NR	NA
Patel et al ¹² 2019	38	54.5 [11.5]	50	0	NA	89.5	5.9	Local pain (2)
Brunet et al ¹⁴ 2019	85	53.8 [15]	78.8	0	NA	91.8	NR	NA

Note:—AVM indicates arteriovenous malformation; BTO, balloon test occlusion; CAS, carotid artery stent placement; dAVF, dural arteriovenous fistula; ICAD, intracranial atherosclerotic disease; NA, not applicable; NR, not reported.

only diagnostic angiograms,^{9,12,13} one included only interventions,¹⁰ and 3 combined both.^{6,8,11} Details of the interventions are provided in Table 2. The mean ages in each study ranged between 52 and 64.4 years. There was a slight female predominance (58.8%). The modified Allen test was routinely used in 1 study,⁹ but this did not preclude the authors' use of dTRA. Five studies reported routinely using US to guide arterial puncture,^{6,8,10,12,13} while 1 study used it in approximately 20% of cases⁹ and another did not use US at all.¹¹ The mean diameter of the radial artery in the anatomic snuffbox was reported in 3 studies^{9,10,13} and ranged from 2.19 to 2.4 mm.

Procedural Success

Success rates ranged from 20% to 100%. The 20% success rate reported by Goland et al¹¹ was determined to be a statistically significant ($P < .05$) outlier and was removed from the analysis. As shown in Fig 2, the pooled success rate was 95% (95% CI, 91%–98%), though there was significant heterogeneity ($I^2 = 74.33$, $P < .01$). Routine US use was associated with procedural success (OR = 1.41; 95% CI, 0.98–2.02), though this approached but did not reach statistical significance ($P = .061$). Reasons for conversion to pTRA or TFA included an inability to cannulate the radial artery, vasospasm, the presence of arteria lusoria, the presence of

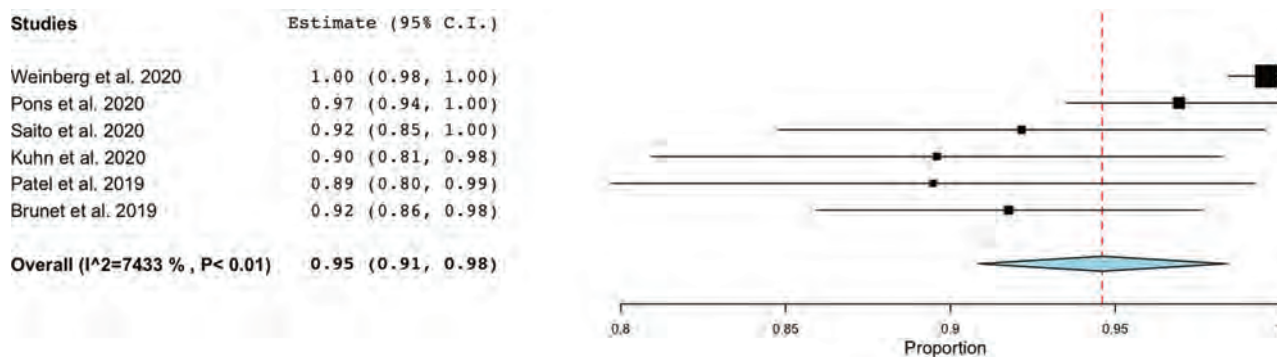


FIG 2. Forest plot demonstrating the pooled procedural success rate.

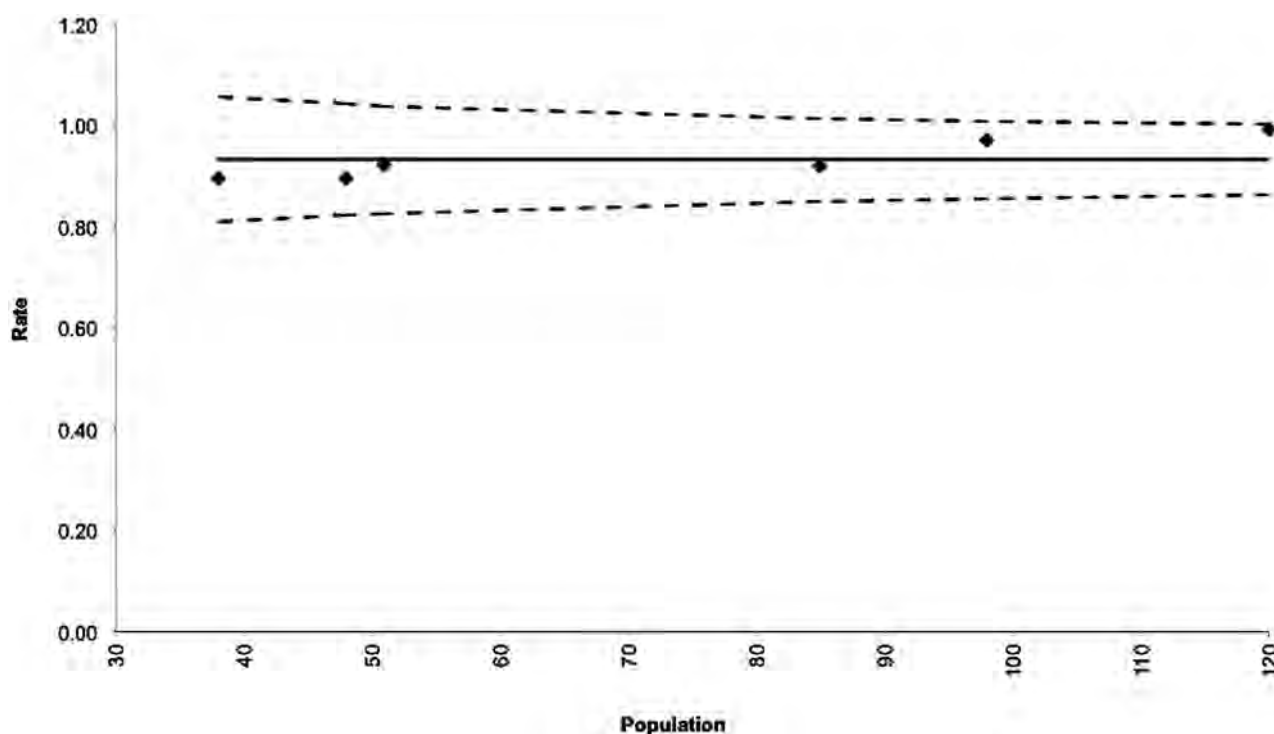


FIG 3. Funnel plot depicting the success rates for the 6 studies included in the pooled rate. The *solid line* represents the pooled success rate, and the *hashed lines* indicate its 95% confidence interval.

a radial artery loop, and lack of catheter support in the aortic arch. All 6 success rates were within the 95% confidence interval of the funnel plot for publication bias (Fig 3).

Successful selective catheterization of specific vessels was described in 2 studies.^{6,9} Pons et al⁶ reported decreasing success rates in selecting the right ICA (97%), left ICA (93.5%), and left vertebral artery (82%). Saito et al⁹ also reported decreased success in catheterizing the left ICA.

Complications

Five studies reported access-related complication rates.^{6,8-10,12} No major complications were experienced in any of the series. The incidence of minor complications ranged from 1.7% to 5.9%. As shown in Fig 4, the pooled complication rate was 2% (95% CI, 1%–4%), and there was low heterogeneity ($I^2 = 0$, $P = .77$).

Routine US use was not associated with access-related complications (OR = 1.00; 95% CI, 0.96–1.05; $P = .829$). Of the 10 complications reported, hematoma was the most common (40%), followed by pain or numbness (30%), radial artery spasm (10%), dissection (10%), and asymptomatic RAO (10%). Only 1 study⁶ reported the rate of procedural complications (6.5%), which were related to aneurysm treatment in 2 patients and carotid stent placement in one.

Procedural Details

Each study that included interventions described the use of 6F sheaths, while 5F sheaths were used for diagnostic cerebral angiograms with the exception of 1 study⁹ in which 4F sheaths were used. The use of Simmons type 1 or 2 catheters was described for diagnostic angiography in 4 studies.^{6,9,11,12} For interventions, long

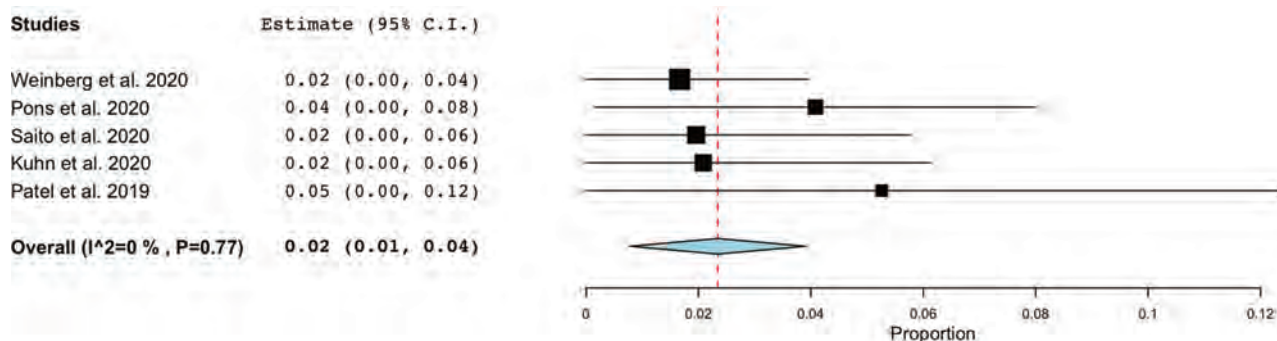


FIG 4. Forest plot demonstrating the pooled rate of minor complications.

sheaths were described in 2 studies^{6,10} and included 6F 9-cm sheaths, including the Shuttle (Cook) and Ballast (Balt), as well as the AXS Infinity LS (Stryker Neurovascular). Kuhn et al¹⁰ also reported the use of Fubuki guide catheters (Asahi Intecc) in a sheathless fashion. Alternatively, 5F or 6F guide or intermediate catheters were placed directly through a short radial sheath.^{6,11} The mean/median number of vessels catheterized ranged from 1.5 to 5. FTs for diagnostic procedures could be combined from 4 studies ($n = 285$),^{8,9,12,13} yielding a mean FT of 13.53 [SD, 8.82] minutes. Contrast doses for diagnostic procedures were available in 3 studies,^{8,9,12} producing a combined mean of 74.9 [SD, 35.6] mL. All 7 studies described their methods for hemostasis. The PreludeSYNC DISTAL Radial Compression Device (Merit Medical) was the most common (4 studies), while the Safeguard Radial Compression Device (Merit Medical), the TR BAND Radial Compression Device (Terumo), and the Stepty P compression bandage (NICHIBAN) were used in 1 study each. One study did not use a hemostatic device.

DISCUSSION

Following the publication of multiple studies in the cardiology literature demonstrating the improved safety of TRA compared with TFA,¹⁴⁻¹⁷ the radial artery is becoming increasingly used for neurointerventional procedures. Multiple authors have reported high procedural success rates using TRA not only for diagnostic angiograms but also for interventions.^{18,19} TRA also affords direct access to the ipsilateral vertebral artery and easier vessel catheterization in type III aortic arches. dTRA has the same benefits as pTRA, with the potential advantages of reduced risk of hand ischemia, improved ergonomics, preservation of the proximal radial artery for future endovascular procedures or bypass, and shorter time to achieve hemostasis. While the safety and efficacy of dTRA have been established for coronary angiography and intervention,²⁰ less evidence supports its use in cerebral angiography and neurointerventions. The latter requires more distal access in increasingly tortuous vessels, meriting its own study. Although success and complication rates associated with pTRA for neurointervention have been reviewed,² dTRA requires a separate investigation due to its unique features. These include the smaller diameter, angled course in the snuffbox, propensity for vasospasm, and greater distance from the supra-aortic vessels of the distal radial artery. We found a high overall rate of procedural success and a low complication rate with dTRA, suggesting that it

may be a useful addition to the neurointerventionalist's armamentarium. The lack of any direct comparison with pTRA in the literature precludes any conclusion regarding the superiority of one approach over the other.

The puncture site for dTRA is in the proximal anatomic snuffbox (Fig 5), which is a triangular depression bounded by the tendons of the abductor pollicis longus and extensor pollicis brevis muscles laterally and the tendon of the extensor pollicis longus medially. The scaphoid and trapezium bones form the floor of the snuffbox. Here, the radial artery courses in a medial-to-lateral direction and continues as the deep palmar arch.

Summary of Evidence

We identified a high pooled success rate of 95% in this study, which is comparable with the rates described in the cardiology literature. It is also similar to the 4.8% rate of crossover to TFA in a meta-analysis of pTRA for coronary interventions.¹⁵ In a meta-analysis of 5 studies with 3209 patients undergoing dTRA, Hamandi et al²⁰ identified a nearly identical success rate of 94.7%. A separate meta-analysis of 4212 patients yielded similar results, demonstrating a 95.4% success rate.²¹ The inability to use dTRA can arise from various causes and steps in the procedure. Failure to cannulate the distal radial artery may occur due to hypoplasia or vasospasm from multiple punctures. A minimum artery diameter of 2 mm has been described, but little empiric evidence is available to support this. All 3 studies reporting the distal radial artery diameter obtained mean measurements of >2 mm, and Brunet et al¹³ did not identify a difference in radial artery diameter between the proximal and distal segments. US guidance may reduce the number of attempts required for arterial cannulation. Although the distal radial artery is usually palpable in the snuffbox, US can help ensure a single-wall puncture and visualize the course of the artery. The radial artery travels from medial to lateral in the snuffbox, requiring a 30°–45° angulation of the needle.²² The Radial Artery Access with Sonography Trial (RAUST) demonstrated a reduced number of attempts and shorter time to access with US guidance, though this was performed for pTRA.²³ Six of the 7 studies in this review described the use of US, and meta-regression demonstrated an association between US and procedural success that neared statistical significance.

Vasospasm may also preclude dTRA, which was a frequently cited reason for access failure in this review. Slow injection of 2.5 mg of verapamil and 200 µg of nitroglycerin is commonly

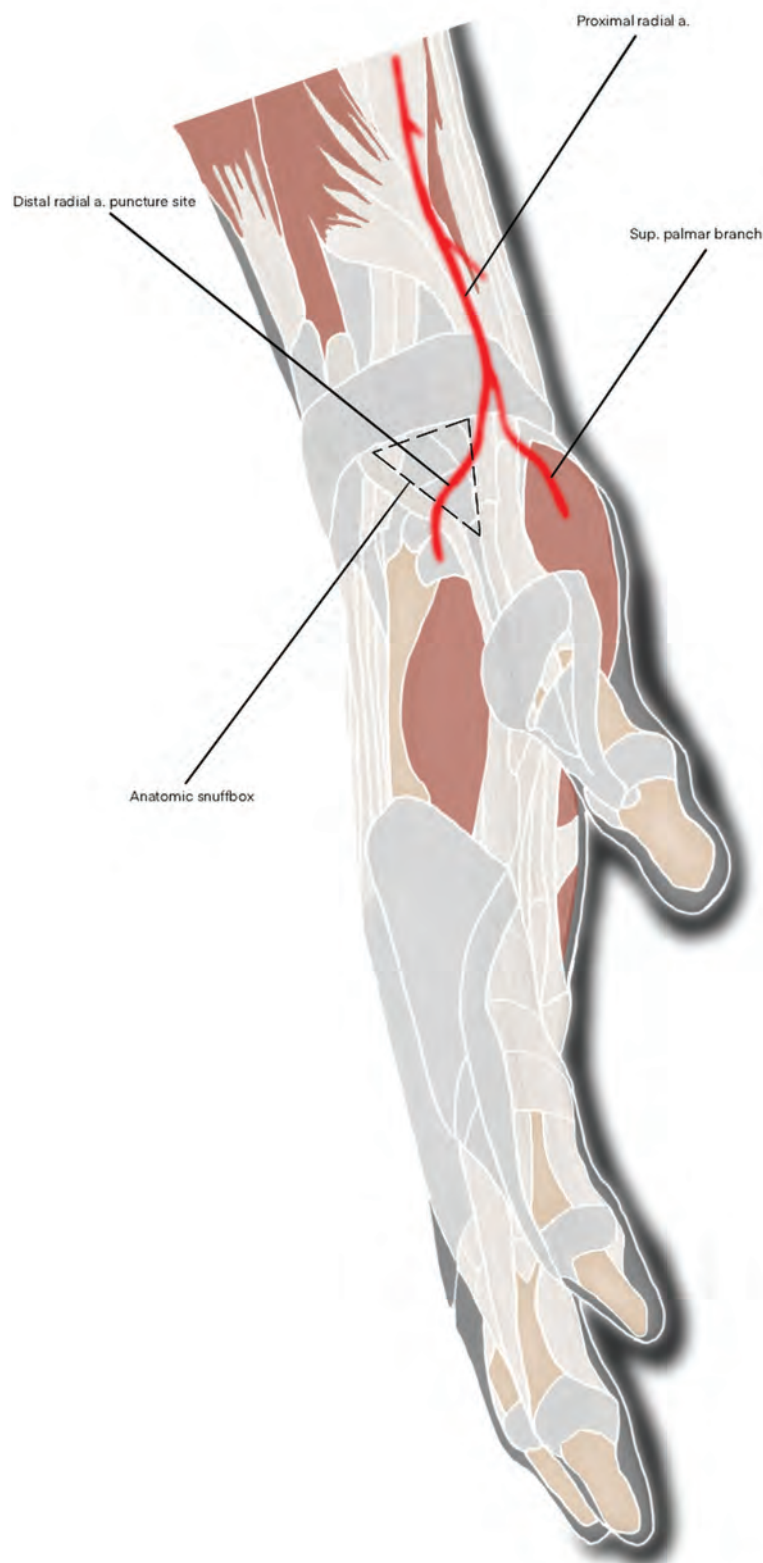


FIG 5. Diagram of the distal radial artery puncture site in the wrist and its proximal course superimposed on the surrounding anatomic structures. a indicates artery; sup, superficial.

performed once access is obtained to avoid vasospasm around the sheath. Longer sheaths can also bypass the proximal radial artery where vasospasm is usually encountered. However, vasospasm may also be encountered on initial cannulation of the artery, especially with multiple punctures. In our experience, this can sometimes be avoided by infiltrating the periarterial tissues with a mixture of 1 mL of lidocaine and 200 μ g of nitroglycerin before puncture. Following successful sheath placement, the remainder of the procedure is performed in a manner similar to pTRA, with potential reasons for conversion to TFA including the presence of a radial artery loop, arteria lusoria configuration, and lack of catheter support in the aortic arch. The latter may be particularly relevant for dTRA because of the approximately 5 cm of extra distance from the puncture site to the target vessel.

Complications were rare, minor, and self-limiting, findings similar to those in prior reports. Hamandi et al²⁰ identified low rates of various complications with dTRA, ranging between 0.11% and 2.3%. In addition, RAO was lower with dTRA compared with pTRA.²⁰ Park et al²⁴ found a 2.2% minor complication rate with noncoronary and noncerebral interventions, which is almost identical to our pooled complication rate of 2%. These rates are lower than those of TFA, which is associated with a 2.8%–5.1% complication rate.²⁵ Furthermore, many of these were major complications such as retroperitoneal hematoma, arteriovenous fistula, and pseudoaneurysm. Our 2% complication rate was similar to the 2.75% minor complication rate associated with pTRA.² However, major complications have been reported with pTRA, including symptomatic RAO following carotid artery stent placement.²⁶ Only 1 case of RAO was reported in this review, which was asymptomatic. This may underestimate the true incidence, however, given that follow-up US or angiography was not routinely performed. Minimizing the volume of air in the compression band needed to achieve hemostasis can reduce the risk of RAO.¹³ This follows

the principles of the patent hemostasis technique, which is associated with lower rates of RAO.²⁷

In our experience with the PreludeSYNC DISTAL, typical volumes range between 5 and 8 mL, which enable rapid hemostasis and discharge following elective diagnostic procedures. The time to achieve hemostasis may be shorter with dTRA than with pTRA.²⁸ Overall, the lack of hand ischemia in any of the patients in this review can be explained by the location of the access site distal to the origin of the superficial palmar arch, which anastomoses with the ulnar artery and the deep palmar arch. Hematomas composed approximately half of the complications, which did not require transfusion. The radial artery in the snuffbox is superficial and easily compressible against the scaphoid bone. Prolonged pain was another minor complication, and both cases were self-limited. Patients may experience puncture site pain during the procedure, which is usually due to vasospasm. Typically, this resolves with conclusion of the procedure and removal of the sheath. US guidance could lower the rate of complications by reducing the number of arterial punctures, but we did not find an association between routine US use and the complication rate, likely due to the low pooled complication rate and relatively small sample size. Overall, the results of this review suggest that dTRA is very safe for both diagnostic procedures and interventions.

Fluoroscopy times for diagnostic angiograms performed with dTRA were slightly longer compared with prior reports using pTRA (6.5–10.3 minutes).^{29,30} However, direct comparison is difficult without adjusting for the number of vessels catheterized and operator experience. As mentioned previously, the additional length to the aortic arch with dTRA theoretically could make the procedure more difficult and increase FTs. Studies directly comparing FT between pTRA and dTRA are warranted.

Limitations

Limitations include the small number of studies, which reflects the relatively late adoption of radial access in the neurointerventional field. All these studies were retrospective, and the decision to perform dTRA could have introduced selection bias. In addition, there were relatively few interventions included ($n = 111$). Success rates are highly dependent on operator experience, and a substantial learning curve for dTRA exists. Therefore, various levels of experience could have introduced variability into the success rate, which we attempted to account for with a random-effects model. This may have contributed to the significant heterogeneity of this outcome. Several studies did not report each variable that we collected, which we tried to address by contacting the original authors. Procedural complications (ie, occurring after obtaining access) were sparsely reported but are important for assessing the overall safety of the approach. Only 2 studies reported their success in selecting specific vessels, which is an important measure of the efficacy of dTRA, given that left ICA and vertebral artery catheterization is more difficult with this approach. An additional limitation is the lack of any comparison with pTRA or TFA.

Future Directions

Additional series regarding the safety and efficacy of dTRA for cerebral angiography and neurointervention are needed because the

current literature comprises a small number of centers with operators who may have had prior experience performing radial access. In 1 study, all operators had performed at least 50 angiograms with pTRA.¹³ Therefore, caution should be used when extrapolating the results of this meta-analysis. To this end, characterization of operators' learning curves transitioning to dTRA may be informative. Studies directly comparing pTRA and dTRA may offer insight regarding any superiority of one approach over the other. The ongoing DISTal Versus CONventional RADIAL Access for Coronary Angiography and Intervention (DISCO) radial trial (clinicaltrials.gov Identifier: NCT04171570) will determine the success and complication rates associated with each radial artery access site for coronary procedures. Similar trials for neurointervention are warranted. As more operators adopt dTRA, the technique will likely be refined and even greater success rates will be realized. The development of catheters specifically designed for transradial neurointervention may also improve the efficacy of the approach.

CONCLUSIONS

dTRA is a safe and effective option for diagnostic cerebral angiography and neurointervention that has distinct advantages compared with pTRA and TFA. However, the literature is mostly limited to small, single-institution case series and diagnostic procedures. Additional studies are required with large sample sizes, greater proportions of interventions, prospective enrollment, and direct comparisons with other approaches.

Disclosures: Priyank Khandelwal—RELATED: Consulting Fee or Honorarium: American Academy of Cardiology, Comments: paid \$2000 honoraria as a speaker; UNRELATED: Grants/Grants Pending: pending, feasibility of the Infinity Catheter for transradial neurology procedures, Comments: submitted, under review. Roger B. Pons—UNRELATED: Payment for Development of Educational Presentations: Merit Medical, Comments: presentations for educational purpose.

REFERENCES

1. Valgimigli M, Gagnor A, Calabró P, et al. MATRIX Investigators. Radial versus femoral access in patients with acute coronary syndromes undergoing invasive management: a randomised multi-centre trial. *Lancet* 2015;385:2465–76 CrossRef Medline
2. Joshi KC, Beer-Furlan A, Crowley RW, et al. Transradial approach for neurointerventions: a systematic review of the literature. *J Neurointerv Surg* 2020;12:886–92 CrossRef Medline
3. McCarthy DJ, Chen SH, Brunet MC, et al. Distal radial artery access in the anatomical snuffbox for neurointerventions: case report. *World Neurosurg* 2019;122:355–59 CrossRef Medline
4. Koutouzis M, Kontopodis E, Tassopoulos A, et al. Distal versus traditional radial approach for coronary angiography. *Cardiovasc Revasc Med* 2019;20:678–80 CrossRef Medline
5. Moher D, Liberati A, Tetzlaff J, et al. PRISMA Group. Preferred reporting items for systematic reviews and meta-analyses: the PRISMA statement. *J Clin Epidemiol* 2009;62:1006–12 CrossRef Medline
6. Pons RB, Caamano IR, Chirife OS, et al. Transradial access for diagnostic angiography and interventional neuroradiology procedures: a four-year single-center experience. *Interv Neuroradiol* 2020;26:506–13 CrossRef Medline
7. Murad MH, Sultan S, Haffar S, et al. Methodological quality and synthesis of case series and case reports. *BMJ Evid Based Med* 2018;23:60–63 CrossRef Medline
8. Weinberg JH, Sweid A, Khanna O, et al. Access through the anatomical snuffbox for neuroendovascular procedures: a single institution series. *Oper Neurosurg* 2020;19:495–501 CrossRef Medline

9. Saito S, Hasegawa H, Ota T, et al. **Safety and feasibility of the distal transradial approach: a novel technique for diagnostic cerebral angiography.** *Interv Neuroradiol* 2020;26:713–18 CrossRef Medline
10. Kuhn AL, Rodrigues KM, Singh J, et al. **Distal radial access in the anatomical snuffbox for neurointerventions: a feasibility, safety, and proof-of-concept study.** *J Neurointerv Surg* 2020;12:798–801 CrossRef Medline
11. Goland J, Domitrovic L, Doroszk G, et al. **Distal radial approach for neurointerventional diagnosis and therapy.** *Surg Neurol Int* 2019;10:211 CrossRef Medline
12. Patel P, Majmundar N, Bach I, et al. **Distal transradial access in the anatomic snuffbox for diagnostic cerebral angiography.** *AJNR Am J Neuroradiol* 2019;40:1526–28 CrossRef Medline
13. Brunet MC, Chen SH, Sur S, et al. **Distal transradial access in the anatomical snuffbox for diagnostic cerebral angiography.** *J Neurointerv Surg* 2019;11:710–13 CrossRef Medline
14. Brueck M, Bandorski D, Kramer W, et al. **A randomized comparison of transradial versus transfemoral approach for coronary angiography and angioplasty.** *JACC Cardiovasc Interv* 2009;2:1047–54 CrossRef Medline
15. Jolly SS, Yusuf S, Cairns J, et al. **Radial versus femoral access for coronary angiography and intervention in patients with acute coronary syndromes (RIVAL): a randomised, parallel group, multicentre trial.** *Lancet* 2011;377:1409–20 CrossRef Medline
16. Hamon M, Rasmussen LH, Manoukian SV, et al. **Choice of arterial access site and outcomes in patients with acute coronary syndromes managed with an early invasive strategy: the ACUTY trial.** *EuroIntervention* 2009;5:115–20 CrossRef Medline
17. Cesaro A, Moscarella E, Gragnano F, et al. **Transradial access versus transfemoral access: a comparison of outcomes and efficacy in reducing hemorrhagic events.** *Expert Rev Cardiovasc Ther* 2019;17:435–47 CrossRef Medline
18. Khanna O, Mouchtouris N, Sweid A, et al. **Transradial approach for acute stroke intervention: technical procedure and clinical outcomes.** *Stroke Vasc Neurol* 2020;5:103–06 CrossRef Medline
19. Chivot C, Bouzerar R, Yzet T. **Transitioning to transradial access for cerebral aneurysm embolization.** *AJNR Am J Neuroradiol* 2019;40:1947–53 CrossRef Medline
20. Hamandi M, Saad M, Hasan R, et al. **Distal versus conventional transradial artery access for coronary angiography and intervention: a meta-analysis.** *Cardiovasc Revasc Med* 2020;21:1209–13 CrossRef Medline
21. Coomes EA, Haghbayan H, Cheema AN. **Distal transradial access for cardiac catheterization: a systematic scoping review.** *Catheter Cardiovasc Interv* 2020;96:1381–89 CrossRef Medline
22. Kiemeneij F. **Left distal transradial access in the anatomical snuffbox for coronary angiography (IdTRA) and interventions (IdTRI).** *EuroIntervention* 2017;13:851–57 CrossRef Medline
23. Seto AH, Roberts JS, Abu-Fadel MS, et al. **Real-time ultrasound guidance facilitates transradial access: RAUST (Radial Artery Access with Ultrasound Trial).** *JACC Cardiovasc Interv* 2015;8:283–91 CrossRef Medline
24. Park SE, Cho SB, Baek HJ, et al. **Clinical experience with distal transradial access for endovascular treatment of various noncoronary interventions in a multicenter study.** *PLoS One* 2020;15:e0237798 CrossRef Medline
25. Oneissi M, Sweid A, Tjoumakaris S, et al. **Access-site complications in transfemoral neuroendovascular procedures: a systematic review of incidence rates and management strategies.** *Oper Neurosurg* 2020;19:353–63 CrossRef Medline
26. Ruzsa Z, Nemes B, Pintér L, et al. **A randomised comparison of transradial and transfemoral approach for carotid artery stenting: RADCAR (Radial Access for Carotid Artery Stenting) study.** *EuroIntervention* 2014;10:381–91 CrossRef Medline
27. Pancholy S, Coppola J, Patel T, et al. **Prevention of Radial Artery Occlusion-Patent Hemostasis Evaluation Trial (PROPHET study): a randomized comparison of traditional versus patency documented hemostasis after transradial catheterization.** *Cathet Cardiovasc Intervent* 2008;72:335–40 CrossRef Medline
28. Aoi S, Htun WW, Freeo S, et al. **Distal transradial artery access in the anatomical snuffbox for coronary angiography as an alternative access site for faster hemostasis.** *Catheter Cardiovasc Interv* 2019;94:651–57 CrossRef Medline
29. Liu Y, Wen X, Bai J, et al. **A single-center, randomized, controlled comparison of the transradial vs transfemoral approach for cerebral angiography: a learning curve analysis.** *J Endovasc Ther* 2019;26:717–24 CrossRef Medline
30. Luo N, Qi W, Tong W, et al. **Efficacy and safety of a novel catheter for transradial cerebral angiography.** *Ann Vasc Surg* 2019;60:236–45 CrossRef Medline

Posterior Circulation Endovascular Thrombectomy for Large-Vessel Occlusion: Predictors of Favorable Clinical Outcome and Analysis of First-Pass Effect

A.M. Alexandre, I. Valente, A. Consoli, M. Piano, L. Renieri, J.D. Gabrieli, R. Russo, A.A. Caragliano, M. Ruggiero, A. Saletti, G.A. Lazzarotti, M. Pileggi, N. Limbucci, M. Cosottini, A. Cervo, F. Viaro, S.L. Vinci, C. Commodaro, F. Pilato, and A. Pedicelli



ABSTRACT

BACKGROUND AND PURPOSE: Successful vessel recanalization in posterior circulation large-vessel occlusion is considered crucial, though the evidence of clinical usefulness, compared with the anterior circulation, is not still determined. The aim of this study was to evaluate predictors of favorable clinical outcome and to analyze the effect of first-pass thrombectomy.

MATERIALS AND METHODS: A retrospective, multicenter, observational study was conducted in 10 high-volume stroke centers in Europe, including the period from January 2016 to July 2019. Only patients with an acute basilar artery occlusion or a single, dominant vertebral artery occlusion (“functional” basilar artery occlusion) who had a 3-month mRS were included. Clinical, procedural, and radiologic data were evaluated, and the association between these parameters and both the functional outcome and the first-pass effect was assessed.

RESULTS: A total of 191 patients were included. A lower baseline NIHSS score (adjusted OR, 0.77; 95% CI, 0.61–0.96; $P = .025$) and higher baseline MR imaging posterior circulation ASPECTS (adjusted OR, 3.01; 95% CI, 1.03–8.76; $P = .043$) were predictors of better outcomes. The use of large-bore catheters (adjusted OR, 2.25; 95% CI, 1.08–4.67; $P = .030$) was a positive predictor of successful reperfusion at first-pass, while the use of a combined technique was a negative predictor (adjusted OR, 0.26; 95% CI, 0.09–0.76; $P = .014$).

CONCLUSIONS: The analysis of our retrospective series demonstrates that a lower baseline NIHSS score and a higher MR imaging posterior circulation ASPECTS were predictors of good clinical outcome. The use of large-bore catheters was a positive predictor of first-pass modified TICI 2b/3; the use of a combined technique was a negative predictor.

ABBREVIATIONS: BAO = basilar artery occlusion; F-P mTICI = first-pass effect mTICI; IQR = interquartile range; mTICI = modified TICI; pc-ASPECTS = posterior circulation ASPECTS; pc-LVO = large-vessel occlusion of the posterior circulation

Posterior circulation stroke accounts for about 20% of all ischemic stroke cases.^{1,2} The etiology is variable (thromboembolic, atherosclerosis, arterial dissection, perforating vessels disease, and so forth), affecting different vascular territories; rarely, this type

of stroke is due to a large-vessel occlusion of the posterior circulation (pc-LVO), representing about 1% of all acute ischemic strokes.^{3,4} Acute pc-LVO carries a high risk of disabling stroke or death. In this context, designing a randomized controlled trial is challenging, and even appropriate patient selection is problematic. Successful vessel recanalization is considered crucial for survival or for improving functional outcome,^{5,6} though the evidence of the clinical usefulness of endovascular

Received August 12, 2020; accepted after revision November 19.

From the Unità Operativa Complessa Radiologia e Neuroradiologia (A.M.A., I.V., A.P.), Dipartimento di Diagnostica per Immagini, Radioterapia Oncologica ed Ematologia, and Unità Operativa Complessa Neurologia (F.P.), Fondazione Policlinico Universitario A. Gemelli, Istituto Di Ricovero e Cura a Carattere Scientifico, Roma, Italy; Diagnostic and Interventional Neuroradiology (A. Consoli, R.R.), Foch Hospital, Suresnes, France; Neuroradiologia (M. Piano, A. Cervo), Azienda Socio Sanitaria Territoriale Grande Ospedale Metropolitano Niguarda, Milano, Italy; UOC Interventistica Neurovascolare (L.R., N.L.), Azienda Ospedaliera Universitaria Careggi, Firenze, Italy; Neuroradiology Unit (J.D.G.) and UOC Neurologia (F.V.), Policlinico Universitario di Padova, Padua, Italy; Neuroradiology Unit, Biomedical Sciences and Morphologic and Functional Images (A.A.C., S.L.V.), Azienda Ospedaliera Universitaria Policlinico G. Martino, Messina, Italy; Neuroradiology Unit (M.R., C.C.), Azienda Unità Sanitaria Locale Romagna, Cesena, Italy; Interventional Neuroradiology (A.S.), S. Anna University Hospital of Ferrara, Ferrara, Italy; Department of Neuroradiology (G.A.L., M.C.), Azienda Ospedaliera Universitaria Pisana, Pisa, Italy; and Department of Neuroradiology (M. Pileggi), Neurocenter of Southern Switzerland, Lugano, Switzerland.

This work is part of a nonprofit study protocol approved by Fondazione Policlinico Universitario A. Gemelli (Istituto di Ricovero e Cura a Carattere Scientifico, Roma) institutional ethics committee: protocol number 6410/20, ID 3004.

Please address correspondence to Andrea M. Alexandre, MD, Unità Operativa Complessa Radiologia e Neuroradiologia, Dipartimento di Diagnostica per Immagini, Radioterapia Oncologica ed Ematologia, Fondazione Policlinico Universitario A. Gemelli Istituto di Ricovero e Cura a Carattere Scientifico, Roma, Italy, Largo A. Gemelli 8, 00168 Roma, Italy; e-mail: andrea.alexandre@policlinicogemelli.it

Indicates article with online supplemental data.
<http://dx.doi.org/10.3174/ajnr.A7023>

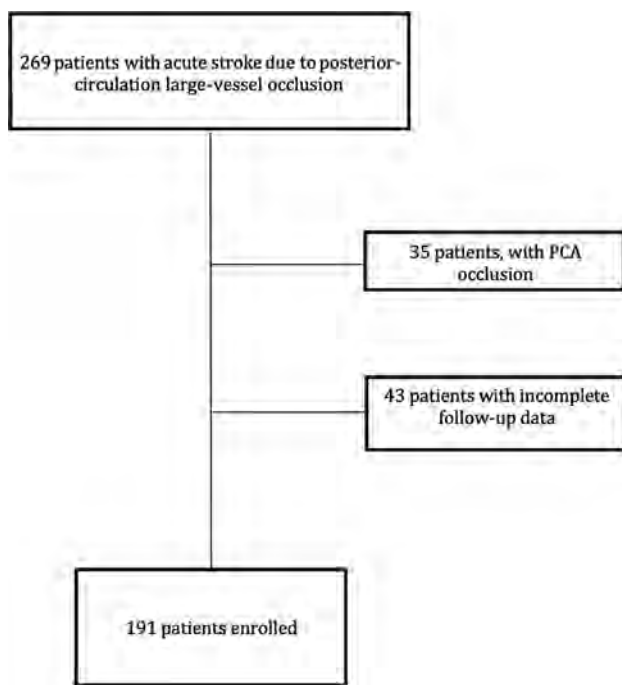


FIG 1. Enrollment flow chart. PCA indicates posterior cerebral artery.

treatment in pc-LVO compared with anterior circulation LVO is still not determined due to a lack of randomized controlled trial data.

In this setting, a recent study supports the safety and efficacy of endovascular treatment for patients with acute ischemic stroke caused by basilar artery occlusion (BAO) who could be treated within 24 hours of the estimated occlusion time.⁷

The aims of our study included the evaluation of the effectiveness of the endovascular treatment for acute BAO or single, dominant vertebral artery occlusion (“functional” BAO), the analysis of predicting factors of favorable outcome, and of first-pass effect.

MATERIALS AND METHODS

Patients and Study Design

This retrospective, multicenter, observational study was conducted in 10 European high-volume stroke centers (≥ 100 thrombectomies performed annually). We included all consecutive patients with acute pc-LVO who underwent a mechanical thrombectomy between January 2016 and July 2019. Only patients with an acute BAO or a single, dominant vertebral artery occlusion (functional BAO) were included. We excluded all patients with incomplete follow-up data (Fig 1). Clinical and radiologic data were retrospectively collected and stored in a specific data base at each center. We collected and reviewed the following data: age, sex, baseline NIHSS score, arterial occlusion site, administration of intravenous thrombolysis, onset-to-groin time, procedural duration, time from onset to reperfusion, first-line thrombectomy technique, procedure-related complications, postprocedural complications, reperfusion grade (assessed using the modified TICI [mTICI] scale⁸), and the 90-day mRS score. The presumed etiology of the stroke has been classified on the angiographic assessment,⁹ according to the literature.

Ethics approval was obtained from the institutional review board of each center. Informed consent for participation in the study was obtained only in patients who were neurologically able to give it; for all the other patients, the informed consent was obtained from a legal representative. All patients underwent baseline imaging (CT and/or MR imaging) according to the acute stroke imaging protocol at each center. According to guidelines,¹⁰ before thrombectomy, intravenous recombinant tissue plasminogen activator was administered to eligible patients who could be treated within 4.5 hours of symptom onset.

Differences in technical performances among the centers involved were analyzed by comparing the percentages of successful reperfusion (mTICI 2b/3).

Endovascular Treatment. All procedures were performed with the patient under general anesthesia or conscious sedation after evaluation by a dedicated anesthesiology team. The thrombectomy devices were chosen at the interventionalist’s discretion, using a stent retriever, aspiration, or a combined technique approach in the first instance, with a possible switch toward another strategy in case of reperfusion failure (mTICI 0/2a).

Periprocedural complications were also recorded. Aspiration catheters with an inner lumen of >0.060 inches were considered large-bore catheters.

Time Assessment

The symptom-to-groin time was defined as the interval between the estimated time of stroke onset (or the time last-seen-well) and the time of arterial puncture. Reperfusion time was defined as the interval between the time of arterial puncture and the final angiogram. The symptom-to-reperfusion time was the time from stroke onset to the final angiogram.

Outcome Assessment

The primary outcome was clinical independence, defined as an mRS score of 0–2 at the 90-day outpatient visit or telephone interview, assessed by stroke neurologists at each center. Reperfusion was assessed according to the mTICI scale;⁸ successful reperfusion was defined as an mTICI of 2b/3 and was considered as the efficacy outcome when comparing techniques. Image analysis was performed by neuroradiologists at each center.

The secondary outcome was the achievement of successful reperfusion (mTICI 2b/3) at first attempt (the so-called first-pass effect^{11,12}).

Statistical Analysis

Demographics and clinical characteristics were compared between subjects with unfavorable (mRS score 3–6) and favorable (mRS score 0–2) outcomes at 90 days and between patients with or without first-pass successful reperfusion (F-P mTICI 2b/3). For continuous measures, mean [SD] and median and interquartile range (IQR) are presented, and *P* values were calculated with a 2-tailed *t* test for Gaussian continuous variables, and the Mann-Whitney *U* or Kruskal-Wallis test for non-Gaussian continuous variables. Normality distribution was tested with the Shapiro-Wilk test. For categoric measures, frequencies and percentages are presented, and *P* values were calculated with a χ^2 or 2-tailed Fisher exact tests as

Table 1: Baseline, clinical, and technical characteristics

Characteristics	Overall	Poor Outcomes at 90-Day mRS (3–6)	Favorable Outcomes at 90-Day mRS (0–2)	P Value
No.	191	118 (61.78%)	73 (38.21%)	
Age (mean)	68.3 [SD, 13.97]	69.94 [SD, 12.83]	65.63 [SD, 15.35]	.037
Women	61 (31.9%)	40/118 (33.9%)	21/73 (28.7%)	.460
Baseline NIHSS (IQR)	12 (7–20)	15 (9–26)	9 (5–15)	<.001
CT	161 (84.2%)	96/118 (81.6%)	65/73 (89.0%)	.156
CTA	130 (68.0%)	77/118 (65.2%)	53/73 (72.6%)	.290
CTP	18 (9.4%)	10/118 (8.4%)	8/73 (10.9%)	.568
MR imaging	80 (41.9%)	53/118 (44.9%)	27/73 (36.9%)	.280
Pc-ASPECTS (CT)	8.16 [SD, 2.76]	8.08 [SD, 2.60]	8.27 [SD, 3.00]	.168
Pc-ASPECTS (MR imaging)	6.63 [SD, 1.64]	6.33 [SD, 1.62]	7.22 [SD, 1.55]	.006
Occlusion site				.611
BA	180 (94.2%)	112/118 (94.9%)	68/73 (93.1%)	
VA	11 (5.3%)	6/118 (5.1%)	5/73 (6.89%)	
Presumed etiology				.001
Atherosclerotic	67 (35.1%)	52/118 (44.1%)	15/73 (20.8%)	
Thromboembolic	124 (64.9%)	66/118 (55.9%)	58/73 (79.4%)	
Thrombolysis	57 (30%)	28/118 (23.7%)	29/73 (40.3%)	.019
Wake-up stroke	13 (6.8%)	8/118 (6.8%)	5/73 (6.8%)	.985
Contact aspiration	110 (57.6%)	58/118 (49.1%)	52/73 (71.2%)	.003
Stent retriever	23 (12.0%)	15/118 (12.7%)	8/73 (10.9%)	.718
Combined	43 (22.5%)	33/118 (27.9%)	10/73 (13.7%)	.022
Use of alternative thrombectomy techniques	11 (5.7%)	8/118 (6.8%)	3/73 (4.10%)	.441
No endovascular access	4 (2.1%)	4/118 (3.4%)	0	
mTICI 2b/3	165 (86.4%)	95/118 (80.5%)	70/73 (95.9%)	.003
mTICI 3	129 (67.5%)	64/118 (54.2%)	65/73 (89.0%)	<.001
First-pass effect mTICI 2b/3	97 (50.8%)	48/118 (40.7%)	49/73 (67.1%)	<.001
First-pass effect mTICI 3	82 (42.9%)	36 (30.5%)	46 (63.0%)	<.001
Large-bore catheters	74 (38.7%)	39/118 (33.0%)	35/73 (47.9%)	.040
Symptom-to-groin (IQR)	290 (201–420)	295 (201–405)	278.9 (201–455)	.941
Reperfusion time (IQR)	50.5 (27–92.5)	60 (30–105)	40.5 (25–77)	.021
Onset-to-reperfusion (IQR)	392.5 (285–570)	392.5 (300–560)	388.5 (275–655)	.747

Note:—VA indicates vertebral artery; BA, basilar artery.

appropriate. Multivariate analysis was performed using a logistic regression model with 90-day favorable outcome and F-P mTICI 2b/3 as dependent variables separately; except for age and sex as confounding factors, only variables with $P < .05$ at univariate analysis were included into the multivariate models. An interaction term between center and technique used was included in both multivariable models to control for the possible effect modification by the center.¹³ All variables (with the exception of confounding factors) included in the multivariate model with a variable-inflating factor of >2.5 were excluded from the analysis due to multicollinearity issues. To improve the interpretability of the results, we used the marginal effects of our independent variables. The efficacy of different techniques was assessed using the multivariate logistic regression model adjusted for prespecified confounding factors (age, sex, occlusion site, and onset-to-groin time); the technique that yielded the worst results was used as reference category. A subgroup analysis on patients with presumed atherosclerotic etiology was performed with 90-day favorable outcome as a dependent variable.

Receiver operating characteristic curve analysis was performed to determine the discriminative power (area under the curve) of 3 models derived from the multivariate logistic regression analysis for 90-day good outcome (mRS 0–2), considering only clinical variables (age, sex, NIHSS), considering only technical variables (thrombectomy techniques, mTICI, F-P mTICI,

large-bore catheters, groin-to-reperfusion time), or considering the whole model.

Statistical analysis has been performed with STATA 15.1 (StataCorp).

RESULTS

The mean age was 68.3 [SD, 13.9] years, and 61 patients (31.9%) were women. The baseline characteristics and main results are summarized in Table 1. The mean number of passages in contact aspiration procedures was 1.43 [SD, 0.79]; in the stent retriever procedures, it was 1.78 [SD, 1.04]; and in combined-technique procedures, it was 2.95 [SD, 1.65]. Favorable outcome (90-day mRS 0–2) was obtained in 73/191 patients (38.2%), whereas an ability to walk unassisted by another person (90-days mRS 0–3) was achieved in 88 patients (46%). The rate of successful reperfusion achieved was 86.3%, respectively, 97.2% in the mRS 0–2 group and 80.5% in the mRS 3–6 group. The distribution of 90-day mRS according to mTICI is summarized in Fig 2. Types of complications are summarized in the Online Supplemental Data.

Univariate analysis showed an association between presumed stroke etiology and outcome ($P < .001$), with a worse outcome for atherosclerotic occlusions (22.3% versus 38.2%; $P = .001$); atherosclerotic occlusions had worse results in technical outcome

considering both mTICI and F-P mTICI and a higher mortality rate compared with the overall population (38.8% versus 29.3%).

Table 2 summarizes the results of multivariate logistic regression analysis for predicting good outcome. The model included

age, sex, baseline NIHSS, MR imaging pc-ASPECTS, aspiration technique, combined technique, large-bore catheters, reperfusion status (mTICI 2b/3, mTICI 3, F-P mTICI 2b/3, and F-P mTICI 3), reperfusion time, intravenous thrombolysis, and presumed

stroke etiology. mTICI 3 and F-P mTICI 3 were excluded from the analysis due to multicollinearity issues. Of the other variables included, statistically significant predictors of better outcomes were lower baseline NIHSS (adjusted OR, 0.77; 95% CI, 0.61–0.96; $P = .025$) and higher baseline MR imaging pc-ASPECTS (adjusted OR, 3.01; 95% CI, 1.03–8.76; $P = .043$) (Fig 3).

Results of univariate and multivariate logistic regression analysis for predictors of first-pass successful reperfusion (mTICI 2b/3) are reported in Table 3 and Table 4. This model included age, sex, presumed stroke etiology, aspiration technique, combined technique, and large-bore catheters. The use of large-bore catheters (adjusted OR, 2.25; 95% CI, 1.08–4.67; $P = .030$) and female sex (adjusted OR, 2.05; 95% CI, 1.02–4.11; $P = .041$) were positive predictors of successful reperfusion at first-pass; the use of a combined technique was a negative predictor of successful reperfusion at first-pass (adjusted OR, 0.26; 95% CI, 0.09–0.76; $P = .014$).

Results of subgroup analysis for the atherosclerotic etiology for predicting good outcome are shown in the Online Supplemental Data. In this subgroup, a lower baseline NIHSS score was associated with better outcome (adjusted OR,

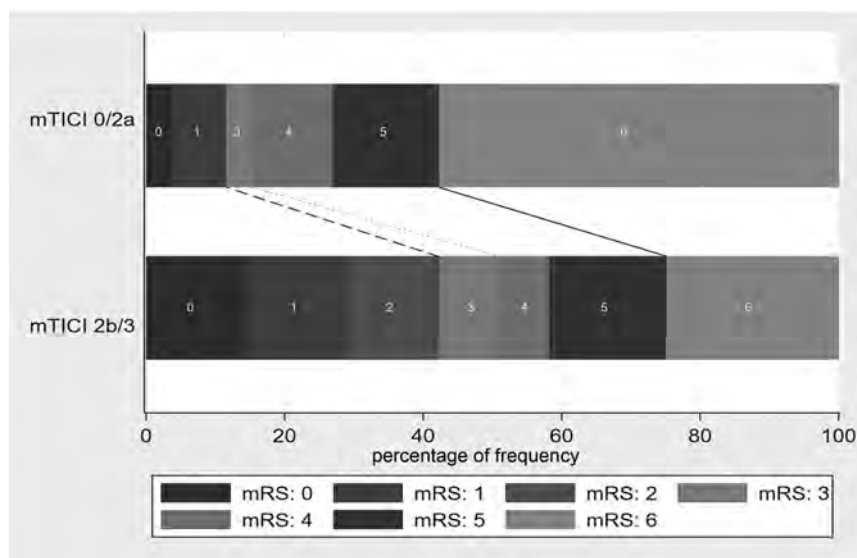


FIG 2. Ninety-day mRS according to mTICI. The *dashed line* indicates mRS 0–2; the *dotted line*, mRS 0–3 mRS; the *continuous line*, mRS 0–5 and mortality.

Table 2: Multivariate logistic regression analysis for 90-day good outcome

Variable	OR	95% CI	P Value
Age	0.91	0.84–1.00	.067
NIHSS baseline	0.77	0.61–0.96	.025
Pc-ASPECTS MR imaging	3.01	1.03–8.76	.043
Contact aspiration	18.06	0.39–833.14	.139
Combined	0.10	0.00–17.07	.383
mTICI 2b/3	0.24	0.00–9.65	.450
Thrombolysis	0.02	0.00–2.19	.106
First-pass effect mTICI 2b/3	3.24	0.11–95.42	.495
Presumed etiology (atherosclerotic)	0.12	0.00–1.88	.133
Large-bore catheters	0.98	0.04–21.89	.991
Reperfusion time	0.99	0.97–1.02	.869

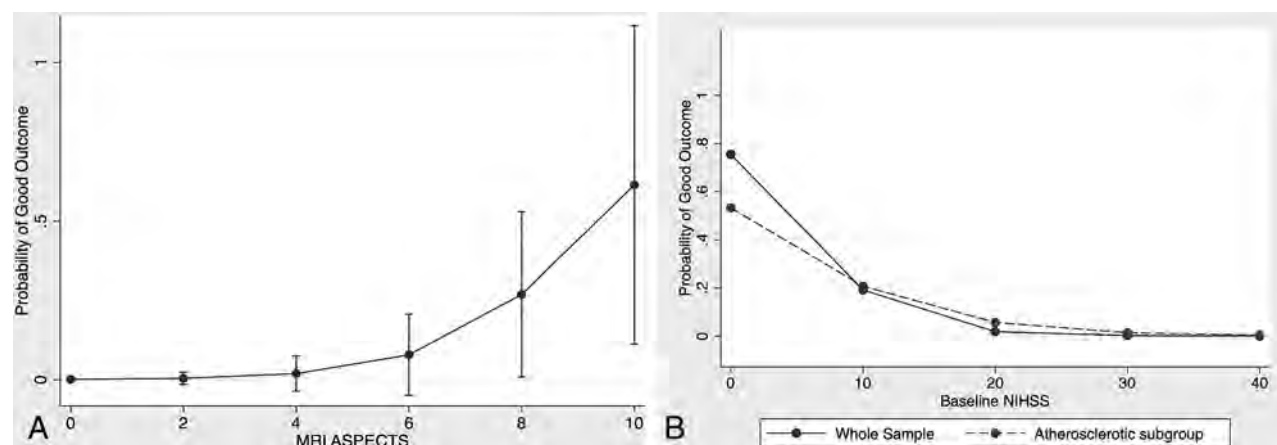


FIG 3. A, Probability of good outcome according to MR imaging pc-ASPECTS. B, Probability of good outcome according to the baseline NIHSS score comparing the whole sample and the atherosclerotic subgroup.

Table 3: Univariate analysis for predictors of first-pass effect

Characteristics	Overall	First-Pass Effect, mTICI 0/2a	First-Pass Effect, mTICI 2b/3	P Value
No.	187	90 (48.13%)	97 (51.87%)	
Age (mean) (yr)	68 [SD, 13.9]	66.2 [SD, 13.30]	69.7 [SD, 14.4]	.085
Women	61 (32.6%)	22/90 (24.4%)	39/97 (40.2%)	.022
CTA	126 (68.1%)	57/90 (63.3%)	69/97 (71.1%)	.256
Occlusion site				.540
BA	176 (94.1%)	86/90 (95.6%)	90/97 (92.8%)	
VA	11 (5.9%)	4/90 (4.4%)	7/97 (7.2%)	
Presumed etiology				.014
Atherosclerotic	66 (35.3%)	40/90 (44.4%)	26/97 (26.80%)	
Thromboembolic	121 (64.7%)	50/90 (55.6%)	71/97 (73.2%)	
Thrombolysis	56 (29.9%)	27/90 (30%)	29/97 (29.9%)	.988
Contact aspiration	110 (58.8%)	39/90 (43.3%)	71/97 (73.2%)	<.001
Stent retriever	23 (12.3%)	12/90 (13.3%)	11/97 (11.3%)	.678
Combined	43 (23.0%)	33/90 (36.7%)	10/97 (10.3%)	<.001
Use of alternative thrombectomy techniques				
Large-bore catheters	74 (39.6%)	24/90 (26.7%)	50/97 (51.5%)	.001
Symptom-to-groin (IQR)	293 (210–420)	287 (201–405)	300.5 (210–432.5)	.086

Note:—VA indicates vertebral artery; BA, basilar artery.

Table 4: Multivariate logistic regression analysis for predictors of first-pass effect

Variable	OR	95% CI	P Value
Age	1.02	0.99–1.04	.091
Female	2.05	1.02–4.11	.041
Presumed etiology (atherosclerotic)	0.68	0.33–1.38	.289
Contact aspiration	1.30	0.50–3.34	.582
Combined	0.26	0.09–0.76	.014
Large-bore catheters	2.25	1.08–4.67	.030

0.86; 95% CI, 0.75–0.98; $P = .027$). In this subgroup, percutaneous transluminal angioplasty of the stenosis was performed in 3 patients; stent placement of the stenosis, in 5 patients; and percutaneous transluminal angioplasty plus stent placement, in 1 patient. Multivariate analysis (adjusted for prespecified confounding factors) comparing the 3 techniques (Table 5) showed no differences, considering neither a successful nor a complete reperfusion, whereas contact aspiration showed better results in both F-P mTICI 2b/3 (adjusted OR, 6.67; 95% CI, 2.65–15.30; $P < .001$) and F-P mTICI3 (adjusted OR, 5.88; 95% CI, 2.38–14.49; $P < .001$).

The analysis of the area under the curve–receiver operating characteristic curves showed that by combining only the 2 classes of variables, we obtained the maximum area under the curve and the accuracy of the model reached its best value (Fig 4).

No differences were found in the rates of successful reperfusion among the centers involved in this study ($P = .925$).

DISCUSSION

A favorable clinical outcome (mRS 0–2) was observed in 38.2%; when we considered patients with 90-day 0–3 mRS, which can be considered an acceptable result if compared with the natural history of this disease, the percentage increased to 46%. These data are higher than those reported by Bouslama et al¹⁴ and by the

BASILAR study investigators;⁷ this result could be due to a lower mean NIHSS score in our cohort.

Our analysis showed that the baseline NIHSS score (OR, 0.77; $P = .025$) and the pc-ASPECTS on MR imaging (OR, 3.01; $P = .043$) are predictors of 90-day good clinical outcome, as previously reported by several studies.^{14–18} The correlation between a lower baseline NIHSS score and the probability of good outcome was first demonstrated by the ENDOSTROKE study group for endovascular therapy,¹⁷ whose results are similar to those we observed and in line with previous studies about thrombolytic treatment in basilar occlusions.¹⁹

The probability of good outcome rapidly decreases at each MR imaging pc-ASPECTS point drop; with an MR imaging pc-ASPECTS of <6, the adjusted probability of good outcome is <10%. Most patients underwent CT and CTA; CTP was performed in only 9.4% of patients, probably because of its limited efficacy in posterior fossa evaluation, whereas MR imaging was used 41.8%, because of the lack of availability in the emergency setting in some of the involved centers. A recent study by Guillaume et al²⁰ had additionally demonstrated that although a rapid recanalization of BAO in patients with pretreatment DWI pc-ASPECTS of <8 was associated with good clinical outcome, a dramatic decrease in good outcome probability was observed with the increase of time to reperfusion, and those patients could be considered “fast progressors.” A further consideration is that CT pc-ASPECTS cannot accurately differentiate patients with ischemia in life-threatening brain regions, such as the pons, mesencephalon, and diencephalon.⁹ We concur that MR imaging becomes essential in those cases in which the potential benefit of endovascular thrombectomy is not clear.

When we adjusted for confounding factors, age was not associated with good clinical outcome, unlike what was reported by Gramegna et al,⁹ who noted an association between younger age and a favorable clinical outcome. This difference is not justified by either the mean age of the 2 subgroups, which was similar (68.3 and 70.9 years) or by the percentage of favorable clinical outcome (38.2% and 36.2%, respectively); this difference could be due to the smaller population of their study compared with ours.

Obtaining a successful reperfusion (mTICI 2b/3) is the main goal for neurointerventionalists; the percentage of successful reperfusion that we achieved was 86.3%, in line with other series.¹⁴ The successful reperfusion (mTICI 2b/3) correlated significantly with the outcome in univariate analysis ($P < .001$), but not in multivariate analysis ($P = .495$). Probably, TICI 2b reperfusion is simply not good enough, and the goal of reperfusion should be TICI 2c/3. Moreover, among patients in whom a successful reperfusion was obtained and who underwent MR imaging, 69.70% of

Table 5: Multivariate logistic analysis of successful reperfusion among aspiration, stent retriever, and other techniques (combined technique was used as a reference category)

Technical Outcome	Aspiration		Stent Retriever		Other Techniques	
	Unadjusted OR (95% CI)	Adjusted OR (95% CI)	Unadjusted OR (95% CI)	Adjusted OR (95% CI)	Unadjusted OR (95% CI)	Adjusted OR (95% CI)
mTICI 2b/3	1.32 (0.46–3.78)	0.79 (0.25–2.55)	1.70 (0.31–9.20)	4.22 (0.40–44.17)	0.72 (0.12–4.23)	1.39 (0.18–10.58)
mTICI 3	1.82 (0.86–3.84)	1.47 (0.66–3.29)	1.22 (0.42–3.51)	2.03 (0.59–6.97)	1.14 (0.29–4.51)	1.40 (0.28–6.82)
First-pass effect mTICI 2b/3	6.00 (2.67–13.48) ^a	5.75 (2.41–13.70) ^a	3.02 (1.02–8.92) ^a	2.04 (0.60–6.96)	2.75 (0.69–10.94)	2.07 (0.37–11.46)
First-pass effect mTICI 3	5.65 (2.40–13.29) ^a	5.18 (2.11–12.72) ^a	2.33 (0.73–7.38)	1.90 (0.52–6.99)	2.49 (0.58–10.64)	1.68 (0.27–10.20)

^a P value < .05.

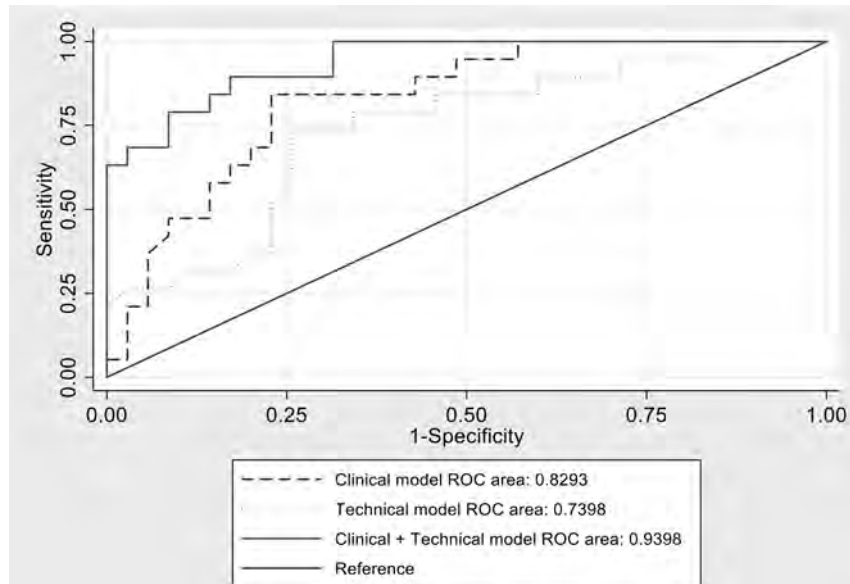


FIG 4. Receiver operating curve (ROC) analysis of different predictive models. The technical model area includes the following: thrombectomy techniques, mTICI, F-P mTICI, large-bore catheters, and groin-to-reperfusion time. The clinical model area includes age, sex, and NIHSS score.

them had a pc-ASPECTS of <8; consequently, the probability of good outcome was low (Online Supplemental Data).

F-P mTICI 2b/3 and the use of large-bore catheters were both associated with good clinical outcome in the univariate analysis (respectively, $P < .001$ and $P = .04$), but none of these technical results were confirmed in the multivariate analysis. This discrepancy between univariate and multivariate analysis could be attributed to the small sample size when we consider specific technical subgroups.

Reperfusion time (in minutes) was significantly lower in the good-outcome group (40.5 versus 60; $P = .021$). However, the impact of reperfusion time on good clinical outcome at 90 days was not consistent in multivariate analysis, unlike in other studies.^{20,21} This finding could be explained because faster procedures are more frequently associated with thromboembolic occlusions ($P < .001$; Online Supplemental Data), which are more likely to be related to a better outcome.

The multivariate analysis for successful reperfusion at first-pass showed that the use of large-bore catheters (OR, 2.25; $P = .030$) and female sex (OR, 2.05; $P = .041$) are positive predictors of successful reperfusion at first-pass, while the use of a

combined technique (OR, 0.26; $P = .014$) is a negative predictor of successful reperfusion at first-pass. The better technical outcome reached in the female sex could be explained by slightly less prevalence of atherosclerotic occlusions in this group (27.9% versus 38.9%). The combined technique had worse results, and this cannot be explained by either the need for the change of strategy or the number of revascularization attempts. Even if predictors of first-pass effects have already been studied by other authors for anterior circulation occlusion,^{22,23} this is the first time that this concept has been applied to posterior circulation stroke.

When we compared the 3 techniques (adjusting for prespecified confounding factors), no difference was found in obtaining either an mTICI 2b/3 or an mTICI 3, especially if there were no differences in better functional outcomes and complication rates. However, aspiration had better results in F-P mTICI 2b/3 (OR, 5.82; $P < .001$) and F-P mTICI3 (OR, 5.27; $P < .001$). These results could be partially explained by the most frequent use of the A Direct Aspiration First Pass Technique in most of the centers involved in the study.

Common guidelines containing specific recommendations with strong levels of evidence for treating posterior circulation stroke are lacking because randomized controlled trial results are missing. The Acute Basilar Artery Occlusion: Endovascular Interventions versus Standard Medical Treatment (BEST)²⁴ trial was terminated prematurely due to a high crossover rate and negative results in the intention-to-treat analysis. The Basilar Artery International Cooperation Study (BASICS)²⁵ recently showed that endovascular therapy administered <6 hours from stroke onset in conjunction with best medical management did not substantially improve functional outcome at 90 days (mRS 0–3) compared with best medical management alone.²⁶ In this trial, 44.2% of the participants randomly assigned to receive endovascular therapy together with best medical management experienced a favorable functional outcome, compared with 37.7% of the control group. This result was mainly due

to a better-than-expected outcome in the control group. Endovascular therapy tended to be more effective in patients older than 70 years than in younger patients, and most interesting, there was a significant difference in outcome favoring endovascular therapy in patients with worse clinical presentation (NIHSS ≥ 10), while there was a trend toward a better outcome after thrombolysis in patients with minor deficits, or NIHSS < 10 . Favorable results (mRS 0–2) were 35.1%, while in our cohort, they were 38.2%; mRS 0–3 was 44.2% in their endovascular group, while in our cohort, it was 46%. Compared with our study, mortality was higher (43.2% versus 29.3%).

Another trial is currently running, the Basilar Artery Occlusion: Chinese Endovascular Trial (BAOCHE; ClinicalTrials.gov identifier: NCT02737189). This trial investigates the benefit of standard medical treatment associated with endovascular treatment in acute BAO versus standard medical treatment alone, but it is facing the challenge of achieving the inclusion target because a growing number of stroke centers are unwilling to randomize patients to standard medical treatment alone after the many positive results of trials for endovascular therapy in patients with anterior circulation stroke.

Using a propensity score-matching analysis, a recent non-randomized cohort study⁷ demonstrated that endovascular therapy administered within 24 hours of the estimated occlusion time is associated with better functional outcomes and reduced mortality. These findings suggest that endovascular thrombectomy might be considered the standard of care for eligible patients with acute BAO, despite the lack of a published randomized controlled trial.

Limitations

This study has several limitations: first, its retrospective and observational design and the consequent use of post hoc hypotheses. Then, mTICI and ASPECTS were assessed by the attending stroke specialist and interventional neuroradiologist without a central core lab; so, bias cannot be excluded. Stroke imaging protocols could differ among the centers involved in the study.

CONCLUSIONS

The analysis of our retrospective series showed that a lower baseline NIHSS score and a higher MR imaging pc-ASPECTS were predictors of good clinical outcome for acute BAO treated with endovascular thrombectomy. A lower baseline NIHSS score was also a predictor of good clinical outcome in the atherosclerotic subgroup. The use of large-bore catheters was a positive predictor of F-P mTICI 2b/3, while the use of a combined technique was a negative predictor of F-P mTICI 2b/3. The aspiration technique achieved better results in F-P mTICI 2b/3 and F-P mTICI 3 compared with other thrombectomy techniques.

Disclosures: Nicola Limbucci—UNRELATED: Consultancy: Cerenovus, Medtronic, Stryker.

REFERENCES

- De Marchis GM, Kohler A, Renz N, et al. **Posterior versus anterior circulation strokes: comparison of clinical, radiological and outcome characteristics.** *J Neurol Neurosurg Psychiatry* 2011;82:33–37 CrossRef Medline
- Markus HS, van der Worp HB, Rothwell PM. **Posterior circulation ischaemic stroke and transient ischaemic attack: diagnosis, investigation, and secondary prevention.** *Lancet Neurol* 2013;12:989–98 CrossRef Medline
- Mattle HP, Arnold M, Lindsberg PJ, et al. **Basilar artery occlusion.** *Lancet Neurol* 2011;10:1002–14 CrossRef Medline
- Greving J, Schonewille W, Wijman C, et al. **BASICS Study Group. Predicting outcome after acute basilar artery occlusion based on admission characteristics.** *Neurology* 2012;78:1058–63 CrossRef Medline
- Kumar G, Shahripour RB, Alexandrov AV. **Recanalization of acute basilar artery occlusion improves outcomes: a meta-analysis.** *J Neurointerv Surg* 2015;7:868–74 CrossRef Medline
- Phan K, Phan S, Huo YR, et al. **Outcomes of endovascular treatment of basilar artery occlusion in the stent retriever era: a systematic review and meta-analysis.** *J Neurointerv Surg* 2016;8:1107–15 CrossRef Medline
- Zi W, Qiu Z, Wu D, et al. **Writing Group for the BASILAR Group. Assessment of endovascular treatment for acute basilar artery occlusion via a nationwide prospective registry.** *JAMA Neurol* 2020;77:561 CrossRef Medline
- Zaidat OO, Yoo AJ, Khatri P, et al. **STIR Thrombolysis in Cerebral Infarction (TICI) Task Force. Recommendations on angiographic revascularization grading standards for acute ischemic stroke: a consensus statement.** *Stroke* 2013;44:2650–63 CrossRef Medline
- Gramegna LL, Requena M, Dinia L, et al. **Predictors of response to endovascular treatment of posterior circulation stroke.** *Eur J Radiol* 2019;116:219–24 CrossRef Medline
- Powers WJ, Rabinstein AA, Ackerson T, et al. **Guidelines for the Early Management of Patients with Acute Ischemic Stroke: 2019 Update to the 2018 Guidelines for the Early Management of Acute Ischemic Stroke: a Guideline for Healthcare Professionals from the American Heart Association/American Stroke Association.** *Stroke* 2019;50:e344–418 CrossRef Medline
- Nikoubashman O, Dekeyser S, Riabikin A, et al. **True first-pass effect: first-pass complete reperfusion improves clinical outcome in thrombectomy stroke patients.** *Stroke* 2019;50:2140–46 CrossRef Medline
- Zaidat OO, Castonguay AC, Linfante I, et al. **First-pass effect: a new measure for stroke thrombectomy devices.** *Stroke* 2018;49:660–66 CrossRef Medline
- Localio AR, Berlin JA, Ten Have TR, et al. **Adjustments for center in multicenter studies: an overview.** *Ann Intern Med* 2001;135:112–23 CrossRef Medline
- Bousslama M, Haussen DC, Aghaebrahim A, et al. **Predictors of good outcome after endovascular therapy for vertebrobasilar occlusion stroke.** *Stroke* 2017;48:3252–57 CrossRef Medline
- Lin SF, Chen CI, Hu HH, et al. **Predicting functional outcomes of posterior circulation acute ischemic stroke in first 36 h of stroke onset.** *J Neurol* 2018;265:926–32 CrossRef Medline
- Tran AT, Nguyen HA, Vu DL, et al. **Basilar artery thrombectomy: assessment of outcome and identification of prognostic factors.** *Acta Neurol Belg* 2020;120:99–105 CrossRef Medline
- Singer OC, Berkefeld J, Nolte CH, et al. **ENDOSTROKE Study Group. Mechanical recanalization in basilar artery occlusion: the ENDOSTROKE study—recanalization in BA occlusion.** *Ann Neurol* 2015;77:415–24 CrossRef Medline
- Khatibi K, Nour M, Tateshima S, et al. **Posterior circulation thrombectomy-pc-ASPECT score applied to preintervention magnetic resonance imaging can accurately predict functional outcome.** *World Neurosurg* 2019;129:e566–71 CrossRef Medline
- Striban D, Sairanen T, Silvennoinen H, et al. **Thrombolysis of basilar artery occlusion: Impact of baseline ischemia and time.** *Ann Neurol* 2013;73:688–94 CrossRef Medline
- Guillaume M, Lapergue B, Gory B, et al. **Rapid successful reperfusion of basilar artery occlusion strokes with pretreatment diffusion-weighted imaging posterior circulation ASPECTS < 8 is associated with good outcome.** *J Am Heart Assoc* 2019;8:e010962 CrossRef Medline
- Vergouwen MD, Algra A, Pfefferkorn T, et al. **Basilar Artery International Cooperation Study (BASICS) Study Group. Time is brain(stem) in basilar artery occlusion.** *Stroke* 2012;43:3003–06 CrossRef Medline

22. Srivatsa S, Duan Y, Sheppard JP, et al. **Cerebral vessel anatomy as a predictor of first-pass effect in mechanical thrombectomy for emergent large-vessel occlusion.** *J Neurosurg* 2020 Jan 24. [Epub ahead of print] CrossRef Medline
23. Di Maria F, Kyheng M, Consoli A, et al. ETIS investigators. **Identifying the predictors of first-pass effect and its influence on clinical outcome in the setting of endovascular thrombectomy for acute ischemic stroke: results from a multicentric prospective registry.** *Int J Stroke* 2021;16:20–28 CrossRef Medline
24. Liu X, Xu G, Liu Y, et al. BEST Trial Investigators. **Acute Basilar Artery Occlusion: Endovascular Interventions versus Standard Medical Treatment (BEST) Trial—design and protocol for a randomized, controlled, multicenter study.** *Int J Stroke* 2017;12:779–85 CrossRef Medline
25. van der Hoeven EJ, Schonewille WJ, Vos J, et al. BASICS Study Group. **The Basilar Artery International Cooperation Study (BASICS): study protocol for a randomised controlled trial.** *Trials* 2013;14:200 CrossRef Medline
26. Schonewille WJ, on behalf of the BASICS study group. **A randomized acute stroke trial of endovascular therapy in acute basilar artery occlusion.** In: *Proceedings of the European Society of Radiology-World Stroke Organization Conference*. May 13, 2020; Virtual.

Early Postmarket Results with EmboTrap II Stent Retriever for Mechanical Thrombectomy: A Multicenter Experience

A. Srivatsan, V.M. Srinivasan, R.M. Starke, E.C. Peterson, D.R. Yavagal, A.E. Hassan, A. Alawieh, A.M. Spiotta, Y. Saleem, K.M. Fargen, S.Q. Wolfe, R.A. de Leacy, I.P. Singh, I.L. Maier, J.N. Johnson, J.-K. Burkhardt, S.R. Chen, and P. Kan



ABSTRACT

BACKGROUND AND PURPOSE: EmboTrap II is a novel stent retriever with a dual-layer design and distal mesh designed for acute ischemic stroke emergent large-vessel occlusions. We present the first postmarket prospective multicenter experience with the EmboTrap II stent retriever.

MATERIALS AND METHODS: A prospective registry of patients treated with EmboTrap II at 7 centers following FDA approval was maintained with baseline patient characteristics, treatment details, and clinical/radiographic follow-up.

RESULTS: Seventy patients were treated with EmboTrap II (mean age, 69.9 years; 48.6% women). Intravenous thrombolysis was given in 34.3%, and emergent large-vessel occlusions were located in the ICA ($n = 18$), M1 ($n = 38$), M2 or M3 ($n = 13$), and basilar artery ($n = 1$). The 5×33 mm device was used in 88% of cases. TICI $\geq 2b$ recanalization was achieved in 95.7% (82.3% in EmboTrap II-only cases), and first-pass efficacy was achieved in 35.7%. The NIHSS score improved from a preoperative average of 16.3 to 12.1 postprocedure and to 10.5 at discharge. An average of 2.5 [SD, 1.8] passes was recorded per treatment, including non-EmboTrap attempts. Definitive treatment was performed with an alternative device (aspiration or stent retriever) in 9 cases (12.9%). Some hemorrhagic conversion was noted in 22.9% of cases, of which 4.3% were symptomatic. There were no device-related complications.

CONCLUSIONS: Initial postmarket results with the EmboTrap II stent retriever are favorable and comparable with those of other commercially available stent retrievers. Compared with EmboTrap II, the first-generation EmboTrap may have a higher first-pass efficacy; however, data are limited by retrospective case analysis, incomplete clinical follow-up, and small sample size, necessitating future trials.

ABBREVIATIONS: AIS = acute ischemic stroke; BGC = balloon-guide catheter; FPE = first-pass efficacy; LKN = last known healthy; sICH = symptomatic intracerebral hemorrhage

Several landmark trials in 2015 established mechanical thrombectomy with stent retriever devices as the treatment of choice for emergent large-vessel occlusion acute ischemic stroke (AIS) in the anterior circulation. The thrombectomy window was further expanded in certain cases on the basis of the recent Endovascular Therapy Following Imaging Evaluation for Ischemic Stroke 3 (DEFUSE 3) and Clinical Mismatch in the

Triage of Wake Up and Late Presenting Strokes Undergoing Neurointervention with Trevo (DAWN) studies.¹⁻⁷ Various stent retrievers are available in the United States, such as the Solitaire (Medtronic) and Trevo (Stryker), each with different configurations, mechanisms, and clinical outcome profiles.

The EmboTrap device (Neuravi/Cerenovus) received FDA approval in May 2018 and is indicated for neurovascular reperfusion within 8 hours of symptom onset in patients experiencing AIS.⁸ The EmboTrap device has a novel dual-layer construct designed to improve clot engagement and a distal mesh designed to reduce distal emboli. The Analysis of Revascularization in Ischemic Stroke

Received August 21, 2020; accepted after revision November 23.

From the Department of Neurosurgery and Neurology (A.S., V.M.S., Y.S., J.N.J., J.-K.B., P.K.), Baylor College of Medicine, Houston, Texas; Department of Neurosurgery (R.M.S., E.C.P., D.R.Y.), University of Miami Miller School of Medicine, Miami, Florida; Department of Neurology and Radiology (A.E.H.), University of Texas Health Science Center San Antonio, San Antonio, Texas; Department of Neurology (A.E.H.), University of Texas Rio Grande Valley, Harlingen, Texas; Department of Neurosurgery (A.A., A.M.S.), Medical University of South Carolina, Charleston, South Carolina; Department of Neurosurgery (K.M.F., S.Q.W.), Wake Forest University School of Medicine, Winston-Salem, North Carolina; Department of Neurosurgery (R.A.d.L., I.P.S.), Mt. Sinai Icahn School of Medicine, New York, New York; Department of Neurology (I.L.M.), University Medical Center Göttingen, Göttingen, Germany; and Department of Interventional Radiology (S.R.C.), MD Anderson Cancer Center, Houston, Texas.

Paper previously presented at: Annual Meeting of the Congress of Neurological Surgeons, October 19–23, 2019; San Francisco, California.

Please address correspondence to Peter Kan, MD, MPH, FAANS, FRCS, University of Texas, Medical Branch, Department of Neurosurgery, 1005 Harborside Dr f5, Galveston, TX 77555; e-mail: ptkan@utmb.edu; @PeterKa80460001

Indicates article with online supplemental data.

<http://dx.doi.org/10.3174/ajnr.A7067>

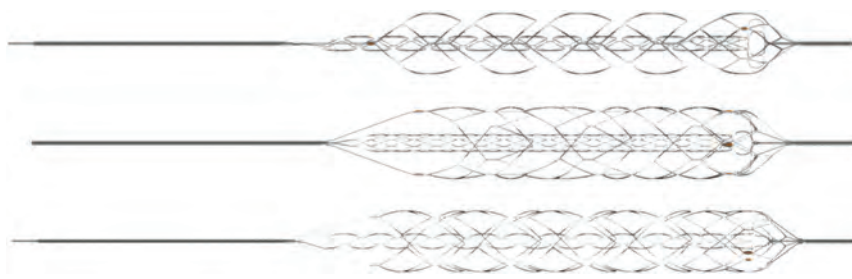


FIG 1. Structure of the EmboTrap II device. Three different angles of the EmboTrap II device (the second is rotated 90° and third is rotated 45° further). Courtesy of Cerenovus, part of DePuy Synthes Products, Inc.

with EmboTrap (ARISE II) was an open-label, single-arm, multicenter, prospective clinical study that evaluated the safety and efficacy of EmboTrap, the first-generation EmboTrap device.⁸ The EmboTrap II stent retriever is a recent iteration that incorporates a few changes, including the following: 1) a double proximal marker to allow a more precise stent placement, and 2) an increase of outer cages from 3 to 5 to potentially improve the ability of the device to capture clots during device retraction (Fig 1).⁹

To date, only 1 single-center study has evaluated EmboTrap II, with a relatively small sample size.⁹ In this study, we present the first prospective multicenter experience with the EmboTrap II stent retriever.

MATERIALS AND METHODS

Study Design

The study was a prospective registry of all patients treated with EmboTrap II at 7 academic neurointerventional centers from May 2018 to October 2019 following FDA approval of the device. These patients were not enrolled in any other studies (eg, the ARISE II trial). All patients older than 18 years of age with emergent large-vessel occlusion AIS who underwent endovascular therapy with at least 1 EmboTrap II deployment (when EmboTrap II was used as the initial device) were included in the study. For each patient, demographic, baseline clinical, procedural, and clinical and radiologic outcome data were collected. Institutional review board approval was obtained for the collection and review of patient data for this study (H-33379).

Procedural Technique

All patients were first evaluated with baseline noncontrast CT of the head and CTA. CTP was performed at the discretion of the treating physicians. Experienced neurologists performed all NIHSS and mRS assessments. Mechanical thrombectomy was performed with the patient under conscious sedation or general anesthesia by experienced fellowship-trained neurointerventionalists. Patients underwent endovascular treatment if they had an ASPECTS of 6–10, moderate-to-good collaterals on CTA, and an ischemic penumbra of >50% of the total hypoperfused area identified by CTP. Each case was evaluated on the basis of clinical history and radiologic imaging. Informed consent was obtained for mechanical thrombectomy for all patients except those whose legally authorized representatives were not available (2-physician consent was used in those cases). Thrombectomy techniques used included a stent retriever with a

balloon guide catheter (BGC), Solumbra, EmboTrap pinning catheter (EPIC), and A Direct Aspiration First Pass Technique (ADAPT) as described below (determined by the individual neurointerventionalist). Balloon-guide catheter use varied depending on the interventionist's preference. There was no limit to the number of passes attempted with the EmboTrap II stent retriever; however, in case of clot-retrieval failure, each interventionist could independently choose an alternate device for treatment continuation. ADAPT was only used as a rescue technique after failure of the EmboTrap II stent retriever.

ADAPT

In ADAPT, a large-bore aspiration catheter is advanced to the proximal aspect of the thrombus and connected to a source of continuous aspiration, and the thrombus is suctioned.

Stent Retriever with Balloon Guide

In stent retriever with balloon guide, a large-bore BGC is first placed in the cervical ICA. Next, a microcatheter is navigated over a microwire across the clot. A stent retriever is then deployed across the occlusion. During the removal of the stent retriever with thrombus, the balloon guide catheter is inflated to occlude the proximal vessel and achieve proximal flow arrest. The balloon-guide catheter is also placed under suction to achieve flow reversal.

Solumbra

In the Solumbra technique, a guide catheter is first placed in the cervical ICA. Next, a large-bore aspiration catheter is then advanced to the proximal portion of the thrombus over a microcatheter. A stent retriever is then deployed across the occlusion. During removal of the stent retriever into the aspiration catheter, the aspiration catheter is connected to a continuous aspiration source.

EPIC

In EPIC, a large-bore BGC is first placed in the cervical ICA. An aspiration catheter is then advanced to the proximal portion of the thrombus over a microcatheter. A stent retriever is deployed across the occlusion. During removal of the stent retriever and the aspiration catheter as a unit, the balloon-guide catheter is inflated, with negative suction applied to achieve proximal occlusion and flow reversal. The aspiration catheter is simultaneously connected to a continuous source of aspiration during its removal with the stent retriever.

Outcomes

The TICI score was used to evaluate immediate angiographic results, and TICI ≥ 2b was defined as successful reperfusion. The NIHSS score was assessed after the procedure, at hospital discharge, and at 90 days after the procedure. MR spectroscopy was assessed at hospital discharge and 90 days after the procedure. Both evaluations were performed by experienced neurologists

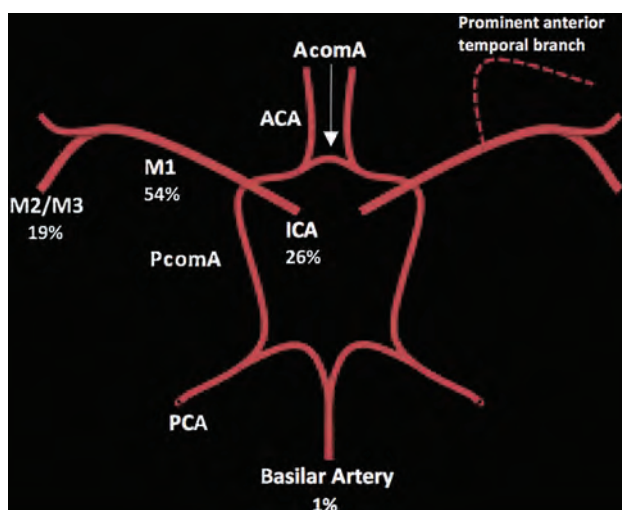


FIG 2. Distribution of sites of vessel occlusion treated. Most occlusions were in M1 (54.3%), followed by the ICA (25.7%), followed by M2 (15.7%) and M3 (2.9%). AcomA indicates anterior communicating artery; PcomA, posterior communicating artery; PCA, posterior cerebral artery; ACA, anterior cerebral artery.

not involved in the procedure. Device-related complications, procedural complications, and instances of hemorrhagic conversion were recorded. Mean and [SD] were used to express continuous variables, while categorical variables were described through frequency distributions. All data analysis was conducted using STATA, Version 15.1 (StataCorp).

RESULTS

A total of 70 patients were treated with the EmboTrap II device, with a mean age of 69.9 years; 48.6% of patients were women. Hypertension was the most common comorbidity (80.3%), followed by atrial fibrillation, hyperlipidemia, diabetes, and prior strokes. The mean preoperative NIHSS score on admission was 16.3 [SD, 6.6] (range, 3–27), the mean preoperative baseline mRS score was 0.4 [SD, 0.9] (range, 0–4), and 94.0% of patients had mRS ≤ 2 at admission. All except 1 case (basilar artery occlusion) were in the anterior circulation, with most occlusions in M1 (54.3%), followed by the ICA (25.7%), M2 (15.7%), and M3 (2.9%) as shown in Fig 2. There were 3 tandem occlusions, and one of the ICA occlusions was in the petrocavernous segment. Intravenous thrombolysis was administered in 34.3% of cases. Baseline patient characteristics are detailed in Table 1.

Most patients had conscious sedation (63.2%), while 36.8% underwent general anesthesia. Last-known healthy (LKN) to puncture time was 444.7 [SD, 310.4] minutes, and the mean procedure time (puncture to reperfusion) was 54.2 [SD, 36.0] minutes. The 5 × 33 mm device was used in 88% of cases, while the 5 × 21 mm device was used in the other 12%. A mean of 2.5 [SD, 1.8] (range, 1–7) passes was made per treatment, including non-EmboTrap II attempts, and a mean of 2.2 [SD, 1.6] (range, 1–7) passes was made per treatment when the EmboTrap II was the definitive treatment. Definitive treatment with an alternative device (aspiration, another stent retriever, intra-arterial tPA, and stent placement) was required in 12.9% of cases. Procedural variables are detailed in Table 2. A

Table 1: Baseline characteristics and demographics

Characteristics	n = 70
Mean age (range) (yr)	69.9 [SD, 16.5] (25–96)
Women (%)	48.6
Race (%)	
White	61.7
Hispanic	28.3
Black	6.7
Other	3.3
Atrial fibrillation (%)	56.9
Hypertension (%)	80.3
Hyperlipidemia (%)	52.4
Diabetes (%)	32.8
Previous ischemic stroke/TIA (%)	20
Mean NIHSS on admission (range)	16.3 [SD, 6.6] (3–27)
Mean premorbid mRS (range)	0.4 [SD, 0.9] (0–4)
Premorbid mRS ≤ 2 (%)	94.0
Location	
ICA (%)	25.7
M1 (%)	54.3
M2 (%)	15.7
M3 (%)	2.9
Basilar (%)	1.4
IV tPA (%)	34.3

Table 2: Procedural variables

Variables	n = 70
Anesthesia type (%)	
Conscious sedation	63.2
General anesthesia	36.8
Balloon-guide catheter used (%)	38.6
Intracranial stent (%)	5.7
Intra-arterial tPA (%)	7.1
Mean No. of passes per treatment (range)	2.5 [SD, 1.8] (1–7)
Mean LKN to puncture time (min)	444.7 [SD, 310.4]
Mean puncture to reperfusion (min)	54.2 [SD, 36.0]
Mean LKN to reperfusion time (min)	480.1 [SD, 320.1]
Mean No. of passes per treatment (range)	2.5 [SD, 1.8] (1–7)
Mean No. of passes per treatment with EmboTrap II as definitive device (%)	2.2 [SD, 1.6] (1–7)
Thrombectomy technique	
SRBG	37 (52.9%)
Solumbra	18 (25.7%)
EPIC	15 (21.4%)
Definitive treatment with alternative device (%)	12.9

Note:—SRBG indicates stent retriever with balloon guide; EPIC, EmboTrap pinning catheter.

balloon-guide catheter was used in 38.6% of cases. As overviewed in Table 3, TICI ≥ 2b recanalization was achieved in 95.7% of patients. TICI ≥ 2b recanalization was achieved in 82.3% of patients for whom the EmboTrap II was used as the definitive device. First-pass efficacy (FPE), defined as TICI ≥ 2b recanalization after a first pass with the device, was achieved in 35.7% of patients.

The NIHSS score improved from a preoperative mean of 16.3 [SD, 6.6] to 12.1 [SD, 7.6] postprocedure, and to 10.5 [SD, 11.2] at discharge (deceased patients were given an NIHSS score of 42). The mean mRS at discharge was 3.2 [SD, 1.7] (range, 0–6), with 43.1% of patients having mRS ≤ 2, and the mean mRS at 90 days was 2.7 [SD, 2.2] (range, 0–6), with 52.9% of patients having mRS ≤ 2. Embolization to distal or a new territory was found in 15.7% of patients, and hemorrhagic conversion of any type was noted in 22.9% of cases, of which 4.3% were symptomatic (Table

4). Mortality at 90 days was 11.4%. There were no device-related complications.

Sample Case

A 72-year-old man with a history of diabetes, hypertension, and hyperlipidemia presented with acute onset of expressive aphasia

Table 3: Clinical and radiographic outcomes

Outcomes	n = 70
Rate of final successful reperfusion (defined as $\text{TICI} \geq 2\text{b}$ reperfusion) (%)	95.7
$\text{TICI} \geq 2\text{b}$ rate with EmboTrap II as definitive device (%)	82.3
FPE (%)	35.7
Mean 24-hour NIHSS (range)	12.1 [SD, 7.6] (0–32)
Mean NIHSS at day 5/7 or at discharge	10.5 [SD, 11.2] (0–42)
Mean mRS at discharge	3.2 [SD, 1.7] (0–6)
mRS 0–2 at discharge (%)	43.1
Mean mRS at 90 days	2.7 [SD, 2.2] (0–6)
mRS 0–2 at 90 days (%)	52.9

Table 4: Adverse events

Adverse Events	
Embolization to distal or a new territory (%)	15.7
Hemorrhagic conversion (%)	22.9
Symptomatic hemorrhagic conversion (%)	4.3
Mortality in follow-up period (%)	11.4

and right-sided weakness. His LKN was at 9:30 PM before he went to bed, and at 2:30 AM, the patient was found on the floor of the restroom, unable to talk and with weakness in his right upper extremity. On initial examination, the patient had an NIHSS score of 17. CTA and angiography showed left M2 occlusion (Fig 3). Mechanical thrombectomy was performed with a 5×33 EmboTrap II and a distal-access catheter using the Solumbra technique. TICI 3 revascularization was achieved after a single pass. On postoperative day 1, the patient was found to have marked improvement on examination with an NIHSS score of 2. The patient was discharged home on postoperative day 5.

DISCUSSION

The results of our study support the safety and efficacy of EmboTrap II, and its procedural success and safety metrics are comparable with those of other commercially available stent retrievers. Table 5 presents a comparison of our study with that of Valente et al,⁹ ARISE II,⁸ Solitaire With the Intention for Thrombectomy as Primary Endovascular Treatment (SWIFT PRIME),⁴ and Thrombectomy Revascularization of Large Vessel Occlusions in Acute Ischemic Stroke (TREVO 2).¹⁰ Valente et al studied EmboTrap II, ARISE II studied the first-generation EmboTrap device, and SWIFT PRIME and TREVO 2 studied the Solitaire and Trevo stent retrievers, respectively, the 2 most commonly used stent retrievers in the United States. Overall, the final

reperfusion rate in EmboTrap II-only cases in our study was 82%, similar to the results in Valente et al. Most interesting, although our FPE was similar to that of Valente et al (36% versus 34%), both our study and Valente et al's had a lower FPE than was reported in ARISE II (52%), in which the original EmboTrap device was used. This finding suggests that the original design may have a higher FPE, especially because the use of the BGC was similar between ARISE II and Valente et al. The rate of good functional outcome (mRS 0–2) at 90 days in this study was similar to that of Valente et al (53% versus 55%), but both our study and that of Valente et al's had worse outcome than reported in ARISE II (67%). This finding may be related to our lower FPE. In addition, ARISE II evaluated only patients treated within 8 hours, whereas our real-world study had many cases beyond the ones with a mean time from LKN to puncture of 7.4 [SD, 5.2] hours. This finding may also explain the slightly worsened results in our study.

The mean procedure time in our study (54.2 minutes) is on the longer side; however, it is likely related to the difficulty of the cases rather than an

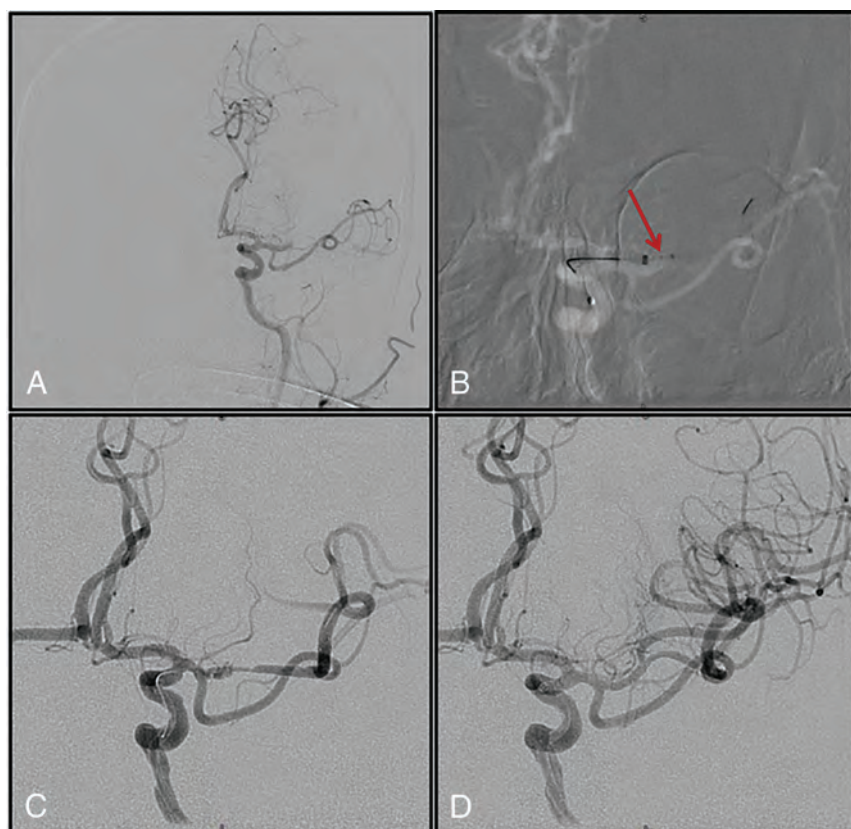


FIG 3. Angiographic runs of a patient case. A, Preoperative angiogram shows M2 occlusion. B, EmboTrap II deployed across the occlusion. C, Angiogram run after EmboTrap II deployment. D, Angiogram run after EmboTrap II removal.

Table 5: Comparison with prior studies

	Present Study (n = 70)	Valente et al ⁹ (n = 29)	ARISE II ⁸ (n = 227)	SWIFT PRIME ⁴ (n = 98)	TREVO 2 ¹⁰ (n = 88)
Stent retriever	EmboTrap II	EmboTrap II	EmboTrap	Solitaire	Trevo
Balloon-guide catheter used	39%	79%	74%	NR	NR
Mean No. of passes without alternate-device rescue treatment	2.2	1.86	NR	NR	2.4
Final reperfusion rate (TICI ≥ 2b) without alternative-device rescue treatment	82%	76%	80%	83%	68%
FPE (TICI ≥ 2b)	36%	34%	52%	NR	NR
90-day mRS ≤ 2	53%	55%	67%	60%	40%
Mean/median baseline NIHSS	16.3	18.5	15.8	17	18.3
Mean/median 24-hour NIHSS	10.5	NR	NR ^a	8.5	12
Mean/median procedure time (min)	54	59	36	24 ^b	48
sICH	4%	0	5%	0	7%
Distal embolization	16%	0	7%	NR	7%

Note:—NR indicates not reported.

^aNeurologic deterioration by ≥4 NIHSS points at 24 hours occurred in 4.5% of patients.

^bMean of 24 minutes from groin puncture to stent deployment.

inherent problem with the stent retriever. Our rate of symptomatic intracerebral hemorrhage (sICH) was similar to that of ARISE II, lower than that of TREVO 2, and higher than that of Valente et al and SWIFT PRIME, which both reported no sICH.

Of note, our rate of distal embolization (15.7%) was higher than that of the other studies. Valente et al⁹ also studied the EmboTrap II device and reported no cases with distal embolization. The mechanical design of the EmboTrap stent retriever with the distal mesh has been shown to reduce distal embolization, thus making our results surprising,¹¹ especially in comparison with the results of Valente et al. A study by Chueh et al¹² examined distal embolization and found that BGC use during thrombectomy led to a lower rate of distal embolization. Our rate of BGC use (39%) is substantially lower than that of Valente et al and ARISE II (79% and 74%). Furthermore, our mean number of passes when EmboTrap II was used as the definitive treatment was slightly higher than that of Valente et al. These 2 reasons in combination could potentially explain the high rate of distal embolization in our study.

With the addition of our multicenter study to the prior single-center series of 29 patients of Valente et al,⁹ we bring the total number of EmboTrap II cases in the literature to 99. Combining both datasets yields the following cumulative literature rates for EmboTrap II: final reperfusion rate (80%), FPE (35%), sICH (3%), 90-day mRS ≤ 2 (54%), mean procedure time (55.6 minutes), and distal embolization (11%). These results are comparable with those in studies of other stent retrievers depicted in Table 5.

Limitations

Our study has several limitations. First, as a multicenter series, there were variations in thrombectomy techniques among different interventionalists, which could affect the results. Second, our study was a single-arm study with no comparison group, making a definitive comparison with other stent retrievers difficult. Third, the results of our study may have low generalizability because most emergent large-vessel occlusions were treated with alternative devices per center (Online Supplemental Data). Fourth, the angiographic results were self-adjudicated, and the analysis was performed in a retrospective manner, thus introducing bias. In contrast, the clinical

follow-up was performed by experienced neurologists unrelated to the study. Last, 90-day follow-up mRS data were limited and were only available in 49% of patients.

CONCLUSIONS

We present the first prospective multicenter experience with the novel EmboTrap II stent retriever. The procedural efficacy and safety profile of the device in our study are favorable and comparable with those of other commercially available stent retrievers. Compared with EmboTrap II, the first generation EmboTrap may have a higher FPE, but this possibility needs to be further examined in future studies comparing the 2 devices. Data on this new device are still limited by retrospective case analysis, incomplete clinical follow-up, and low sample size, necessitating further future trials.

Disclosures: Robert M. Starke—UNRELATED: Consultancy: Medtronic, Penumbra, Cerenovus, Abbott Laboratories Ineurico; Grants/Grants Pending: National Institutes of Health, Bee, Braf, Joe Niekro, Poseydon, and The Aneurysm and AVM Foundation*. Ameer E. Hassan—RELATED: Consulting Fee or Honorarium: Medtronic, Stryker, MicroVention, Cerenovus, Penumbra, Genentech, Balt, Vizai, Scientia Vascular, GE Healthcare, Comments: consulting; Support for Travel to Meetings for the Study or Other Purposes: Medtronic, Stryker, MicroVention, Cerenovus, Penumbra, Genentech, Vizai, GE Healthcare; Fees for Participation in Review Activities such as Data Monitoring Boards, Statistical Analysis, Endpoint Committees, and the Like: Medtronic, Penumbra; UNRELATED: Patents (Planned, Pending or Issued): I have device patents that are not part of this work. Peter Kan—UNRELATED: Consultancy: Consultant for Cerenovus. Reade A. de Leacy—UNRELATED: Consultancy: Cerenovus, Comments: Scientific Advisory Board member. Dileep R. Yavagal—RELATED: Grant: Cerenovus, Comments: Cerenovus funded the EXCELLENCE registry and my institution, University of Miami, was a site for the EXCELLENCE registers*; Consulting Fee or Honorarium: I am a consultant to Cerenovus. I have not had any projects or payments from Cerenovus in the last 18 months; UNRELATED: Consultancy: Medtronic, Cerenovus, Rapid Medical, Neural Analytics, Poseydon; Stock/Stock Options: Rapid medical and Poseydon. None issued to date; OTHER RELATIONSHIPS: Global Chair of Mission Thrombectomy 2020+, a nonprofit public health campaign and alliance. This is a campaign run by the Society of Vascular and Interventional Neurology I, a nonprofit medical society. Alejandro M. Spiotta—UNRELATED: Consultancy: Penumbra, Stryker, Terumo, Siemens, Cerenovus; Grants/Grants Pending: Penumbra, Stryker, Medtronic.* Money paid to the institution.

REFERENCES

1. Berkhemer OA, Fransen PSS, Beumer D, et al. MR CLEAN Investigator. A randomized trial of intraarterial treatment for acute ischemic stroke. *N Engl J Med* 2015;372:11–20 CrossRef Medline

2. Goyal M, Demchuk AM, Menon BK, et al. ESCAPE Trial Investigators. **Randomized assessment of rapid endovascular treatment of ischemic stroke.** *N Engl J Med* 2015;372:1019–30 CrossRef Medline
3. Campbell BCV, Mitchell PJ, Kleinig TJ, et al. EXTEND-IA Investigators. **Endovascular therapy for ischemic stroke with perfusion-imaging selection.** *N Engl J Med* 2015;372:1009–18 CrossRef Medline
4. Saver JL, Goyal M, Bonafe A, et al. SWIFT PRIME Investigators. **Stent-retriever thrombectomy after intravenous t-PA vs. t-PA alone in stroke.** *N Engl J Med* 2015;372:2285–95 CrossRef Medline
5. Jovin TG, Chamorro A, Cobo E, et al. REVASCAT Trial Investigators; **Thrombectomy within 8 hours after symptom onset in ischemic stroke.** *N Engl J Med* 2015;372:2296–2306 CrossRef Medline
6. Albers GW, Marks MP, Kemp S, et al. DEFUSE 3 Investigators. **Thrombectomy for stroke at 6 to 16 hours with selection by perfusion imaging.** *N Engl J Med* 2018;378:708–78 CrossRef Medline
7. Nogueira RG, Jadhav AP, Haussen DC, et al. DAWN Trial Investigators. **Thrombectomy 6 to 24 hours after stroke with a mismatch between deficit and infarct.** *N Engl J Med* 2018;378:11–21 CrossRef Medline
8. Zaidat OO, Bozorgchami H, Ribó M, et al. **Primary results of the multicenter ARISE II study (Analysis of Revascularization in Ischemic Stroke with EmboTrap).** *Stroke* 2018;49:1107–15 CrossRef Medline
9. Valente I, Nappini S, Renieri L, et al. **Initial experience with the novel EmboTrap II clot-retrieving device for the treatment of ischaemic stroke.** *Interv Neuroradiol* 2019;25:271–76 CrossRef Medline
10. Nogueira RG, Lutsep HL, Gupta R, et al. TREVO 2 Trialists. **Trevo versus Merci retrievers for thrombectomy revascularisation of large vessel occlusions in acute ischaemic stroke (TREVO 2): a randomised trial.** *The Lancet* 2012;380:1231–40 CrossRef Medline
11. Chueh J-Y, Marosfoi MG, Brooks OW, et al. **Novel distal emboli protection technology: the EmboTrap.** *Interv Neurol* 2017;6:268–76 CrossRef Medline
12. Chueh JY, Puri AS, Wakhloo AK, et al. **Risk of distal embolization with stent retriever thrombectomy and ADAPT.** *J Neurointerv Surg* 2016;8:197–202 CrossRef Medline

Do Outcomes between Women and Men Differ after Endovascular Thrombectomy? A Meta-analysis

 A.A. Dmytriw,  J.C. Ku,  V.X.D. Yang,  N. Hui,  K. Uchida,  T. Morimoto,  J. Spears,  T.R. Marotta, and  J.D.B. Diestro



ABSTRACT

BACKGROUND: Research on the presence of sex-based differences in the outcomes of patients undergoing endovascular thrombectomy for acute ischemic stroke has reached differing conclusions.

PURPOSE: This review aimed to determine whether sex influences the outcome of patients with large-vessel occlusion stroke undergoing endovascular thrombectomy.

STUDY SELECTION: We performed a systematic review and meta-analysis of endovascular thrombectomy studies with either stratified cohort outcomes according to sex (females versus males) or effect size reported for the consequence of sex versus outcomes. We included 33 articles with 7335 patients.

DATA ANALYSIS: We pooled ORs for the 90-day mRS score, 90-day mortality, symptomatic intracranial hemorrhage, and recanalization.

DATA SYNTHESIS: Pooled 90-day good outcomes ($\text{mRS} \leq 2$) were better for men than women ($\text{OR} = 1.29$; 95% CI, 1.09–1.53; $P = <.001$, $I^2 = 56.95\%$). The odds of the other outcomes, recanalization ($\text{OR} = 0.94$; 95% CI, 0.77–1.15; $P = .38$, $I^2 = 0\%$), 90-day mortality ($\text{OR} = 1.11$; 95% CI, 0.89–1.38; $P = .093$, $I^2 = 0\%$), and symptomatic intracranial hemorrhage ($\text{OR} = 1.40$; 95% CI, 0.99–1.99; $P = .069$, $I^2 = 0\%$) were comparable between men and women.

LIMITATIONS: Moderate heterogeneity was found. Most studies included were retrospective in nature. In addition, the randomized trials included were not specifically designed to compare outcomes between sexes.

CONCLUSIONS: Women undergoing endovascular thrombectomy for large-vessel occlusion have inferior 90-day clinical outcomes. Sex-specific outcomes should be investigated further in future trials as well as pathophysiologic studies.


ABBREVIATIONS: EVT = endovascular thrombectomy; HRT = hormone replacement therapy; RCT = randomized controlled trial; rtPA = recombinant tissue plasminogen activator; sICH = symptomatic intracranial hemorrhage

Differences in the treatment and outcomes between women and men with cardiovascular disease are well-documented

Received October 8, 2020; accepted after revision November 25.

From the Department of Medical Imaging (A.A.D., T.R.M., J.D.B.D.) and Division of Neurosurgery (J.C.K., V.X.D.Y., J.S., T.R.M.), Department of Surgery, University of Toronto, Toronto, Ontario, Canada; NeuroSpine Surgery Research Group (N.H.), The University of New South Wales, Sydney, New South Wales, Australia; Department of Clinical Epidemiology (K.U., T.M.), Hyogo College of Medicine, Nishinomiya, Japan; Division of Diagnostic and Therapeutic Neuroradiology (J.S., T.R.M., J.D.B.D.), Department of Medical Imaging, St. Michael's Hospital, University of Toronto, Toronto, Ontario, Canada; and Neuroradiology and Neurointervention Service (A.A.D.), Brigham and Women's Hospital, Harvard Medical School, Boston, Massachusetts.

Please address correspondence to Adam A. Dmytriw, MD, MPH, MSc, Neuroradiology and Neurointervention Service, Brigham and Women's Hospital, Harvard Medical School, Boston, Massachusetts; e-mail: admytriw@bwh.harvard.edu; @AdamDmytriw; @DanniDiestro

 Indicates article with online supplemental data.

<http://dx.doi.org/10.3174/ajnr.A7075>

in the literature. Women undergoing percutaneous coronary interventions have higher hospital mortality rates and complications compared with men.¹ For stroke, men had a higher incidence, but female patients with stroke were more severely ill.² A large series spanning 10 years found that women were less likely to receive IV recombinant tissue plasminogen activator (rtPA) and were also less likely to be enrolled in a clinical trial.³ More recently, however, a review suggested that the disparity between women and men in the rate of IV rtPA administration was no longer apparent in more modern cohorts.⁴

The advent of endovascular thrombectomy (EVT) ushered in a new era in the treatment of large-vessel ischemic stroke. Sex-specific outcome analysis of the Multicenter Randomized Clinical Trial of Endovascular Treatment for Acute Ischemic Stroke in the Netherlands (MR CLEAN), a randomized controlled trial (RCT) that demonstrated the superiority of endovascular

thrombectomy over best medical management, showed that there were no statistically significant treatment effects of EVT for women in terms of 90-day functional outcomes.⁵ On the other hand, a meta-analysis of all the landmark trials for EVT did not show any differences between women and men in terms of outcomes.⁶ However, the latest evidence on the subject comes from the largest real-world cohort of 2399 patients, which shows that women were less likely to receive EVT and be functionally independent at 90 days.⁷ Our systematic review primarily aimed to determine whether sex influences the 90-day clinical outcomes of patients with large-vessel ischemic stroke undergoing EVT. We also examined symptomatic intracranial hemorrhage (sICH), 90-day mortality, and recanalization rate.

MATERIALS AND METHODS

A systematic review with a meta-analysis was conducted in accordance with the Preferred Reporting Items for Systematic reviews and Meta-Analyses (PRISMA).⁸

Search Strategy, Information Sources, and Study Selection

Electronic searches were performed using Ovid MEDLINE, PubMed, the Cochrane Central Register of Controlled Trials, the Cochrane Database of Systematic Reviews, the American College of Physicians Journal Club, and the Database of Abstracts of Reviews of Effectiveness from their dates of inception to March 21, 2020 (Online Supplemental Data). To achieve maximum sensitivity of the search strategy, we combined the following terms: “stroke,” “thrombectomy,” “endovascular,” “ADAPT,” “sex,” as either keywords or Medical Subject Headings terms. The reference lists of all retrieved articles were reviewed for further identification of potentially relevant studies. Authors of studies with incomplete data were also contacted by e-mail. All identified articles were systematically assessed using the inclusion and exclusion criteria.

Study Eligibility

Eligible studies for the present systematic review and meta-analysis included cohorts of patients with acute ischemic stroke who were treated with an endovascular approach, including stent-retrieval maneuvers or aspiration thrombectomy. Specifically, the studies included in this review must have included either stratified cohort outcomes according to sex (females versus males) or reported an effect size for the consequence of sex versus outcomes reported. If the proportion data were not available, then effect size either in the form of odds ratio, relative risk, or hazard ratio with 95% confidence intervals was collected. Studies must have included data on our desired outcomes: 90-day clinical outcomes according to the mRS score, recanalization rate according to the modified TICI, 90-day mortality, and sICH.

To capture modern thrombectomy results, we excluded studies published before January 1, 2015. When institutions published duplicate studies with accumulating numbers of patients or increased lengths of follow-up, only the most complete reports were included for quantitative assessment at each time interval. All publications were limited to those involving human subjects in the English language. Studies with <10 patients, abstracts, case

reports, conference presentations, editorials, reviews, and expert opinions were excluded.

Risk of Bias

We included 31 observational studies (3 prospective, 28 retrospective), 1 RCT, and 1 meta-analysis⁶ of individual patient data from the landmark RCTs (MR CLEAN, ESCAPE, REVASCAT, EXTEND IA, SWIFT PRIME, THRACE, and PISTE) on EVT. None of the RCTs were randomized according to sex. We used the Newcastle-Ottawa Assessment Scale for Cohort Studies for the observational studies.⁹ The RCTs and the meta-analysis of individual patient data of RCTs were assessed using the Cochrane Collaboration tool for assessing the risk of bias in randomized trials.¹⁰ The 7 RCTs included in the meta-analysis were also assessed individually. All studies had a low-to-moderate degree of bias (Online Supplemental Data).

Data Collection Process

Two physicians (J.C.K. and J.D.B.D.) independently searched and reviewed the selected studies. Data were extracted and documented on a predesigned spreadsheet (Excel for Mac, Version 16.28; Microsoft) with the following variables of interest: first author, title, year of publication, study location, study design, sample size, age, number of women, NIHSS score, use of IV rtPA, TICI 2b–3, recanalization, 90-day mRS, and sICH. Any disagreements with data extraction and article appraisal were settled by a third independent reviewer (A.A.D.). The severity of stroke was classified according to the NIHSS score based on the most common classification system used in the literature: A score of <8 was classified as mild; 8–16, as moderate; and >16, as severe stroke.¹¹

Statistical Analysis

The statistical analysis was performed by 2 of the authors (A.A.D., N.H.). All analyses were conducted in OpenMeta [Analyst] (<http://www.cebm.brown.edu/openmeta/download.html>) and R statistical and computing software, Version 3.5.0 (metafor package 2.0–0; <https://metafor-project.org/doku.php>). Statistical significance was considered with a 2-tailed *P* value ≤ .05. Unadjusted OR risk and 95% confidence intervals were reported to pool the effect of sex on thrombectomy outcomes. Interstudy heterogeneity was estimated using the Higgins *I*²; ≤25% denoted low, 25% to 50% denoted moderate, and >50% denoted high heterogeneity.¹² In cases of high heterogeneity, random-effects models were used. Otherwise, fixed-effect models were used. In light of the high residual heterogeneity, univariate and multivariate meta-regression analyses were performed to identify potential confounders contributing to the heterogeneity. All the variables included in the meta-regression analyses were demographics, study characteristics, or preoperative variables. Specifically, for multivariate meta-regression analyses, only variables with ≥8 included studies were included in the model.¹⁰ To examine potential publication bias, we constructed funnel plots, and Egger and Begg and Mazumdar rank correlation tests were used for each primary outcome.

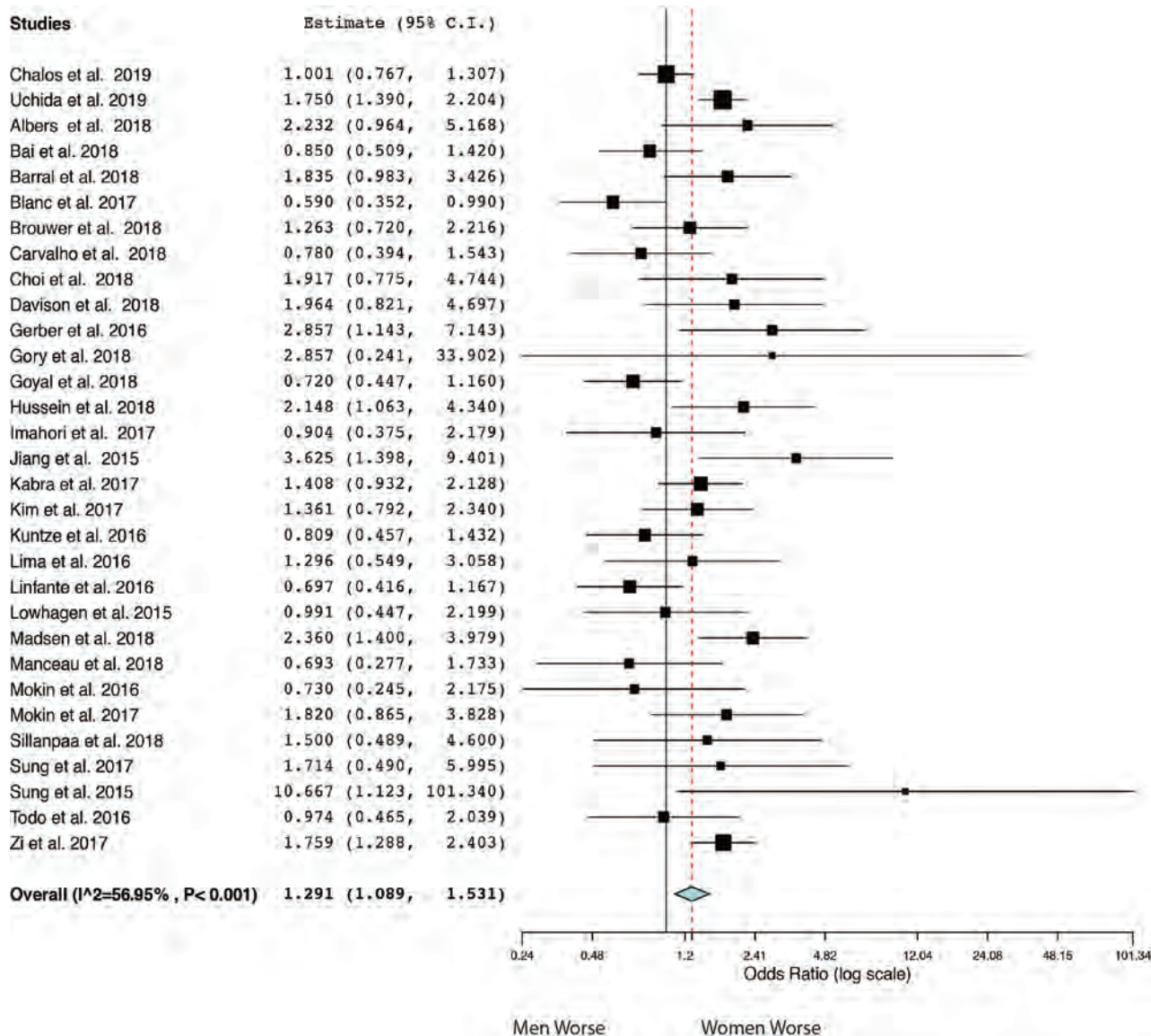


FIG 1. Forest plot of meta-analysis results for good functional outcome ($mRS \leq 2$) at 90 days

RESULTS

After removing duplicates, we identified 2885 studies for screening. Of these, 55 full-text articles were assessed. A total of 33 articles that met our inclusion and exclusion criteria were included in the final analysis (Online Supplemental Data). The PRISMA diagram of the study selection process is presented in the Online Supplemental Data. All the studies had a low-to-moderate degree of risk of bias (Online Supplemental Data).

Among the 7335 included subjects, the average age was 69.3 years (range, 61.5–84.8 years), and 47.4% of the subjects were women (range, 33.6%–67.0%). On the basis of the NIHSS score, 12 studies had moderate-severity stroke at baseline (range, 13–16), while 12 studies had severe stroke (range, 17–21); 50.1% of the subjects had received IV rtPA before thrombectomy (range, 11%–100% of subjects); and 74.8% had a TICI 2b–3 (range, 50%–100% of subjects) post-EVT radiologic outcome.

Primary Outcomes

Pooled 90-day good outcomes were better for men than women ($n = 31$, $OR = 1.29$; 95% CI, 1.09–1.53; $P = <.001$, $I^2 = 56.95\%$) (Fig 1). By contrast, the odds of the other outcomes, recanalization ($n = 10$, $OR = 0.94$; 95% CI, 0.77–1.15; $P = .38$, $I^2 = 0\%$), 90-day mortality ($n = 7$, $OR = 1.11$; 95% CI, 0.89–1.38; $P = .093$, $I^2 = 0\%$), and sICH ($n = 8$, $OR = 1.40$; 95% CI, 0.99–1.99; $P = .069$, $I^2 = 0\%$), were comparable between men and women (Fig 2). Because the heterogeneity tests showed that 90-day mortality ($df = 6$, $I^2 = 44.73\%$, $P = .093$), sICH ($df = 7$, $I^2 = 46.71\%$, $P = .069$), and recanalization ($df = 9$, $I^2 = 6.83\%$, $P = .379$) had low-to-moderate heterogeneity, the fixed-effect model was used in keeping with the Cochrane recommendations for meta-analysis.

Meta-Regression Analysis

In univariate meta-regression analysis, IV rtPA ($n = 5$, $P = .028$) was positively associated with sICH, whereas the NIHSS

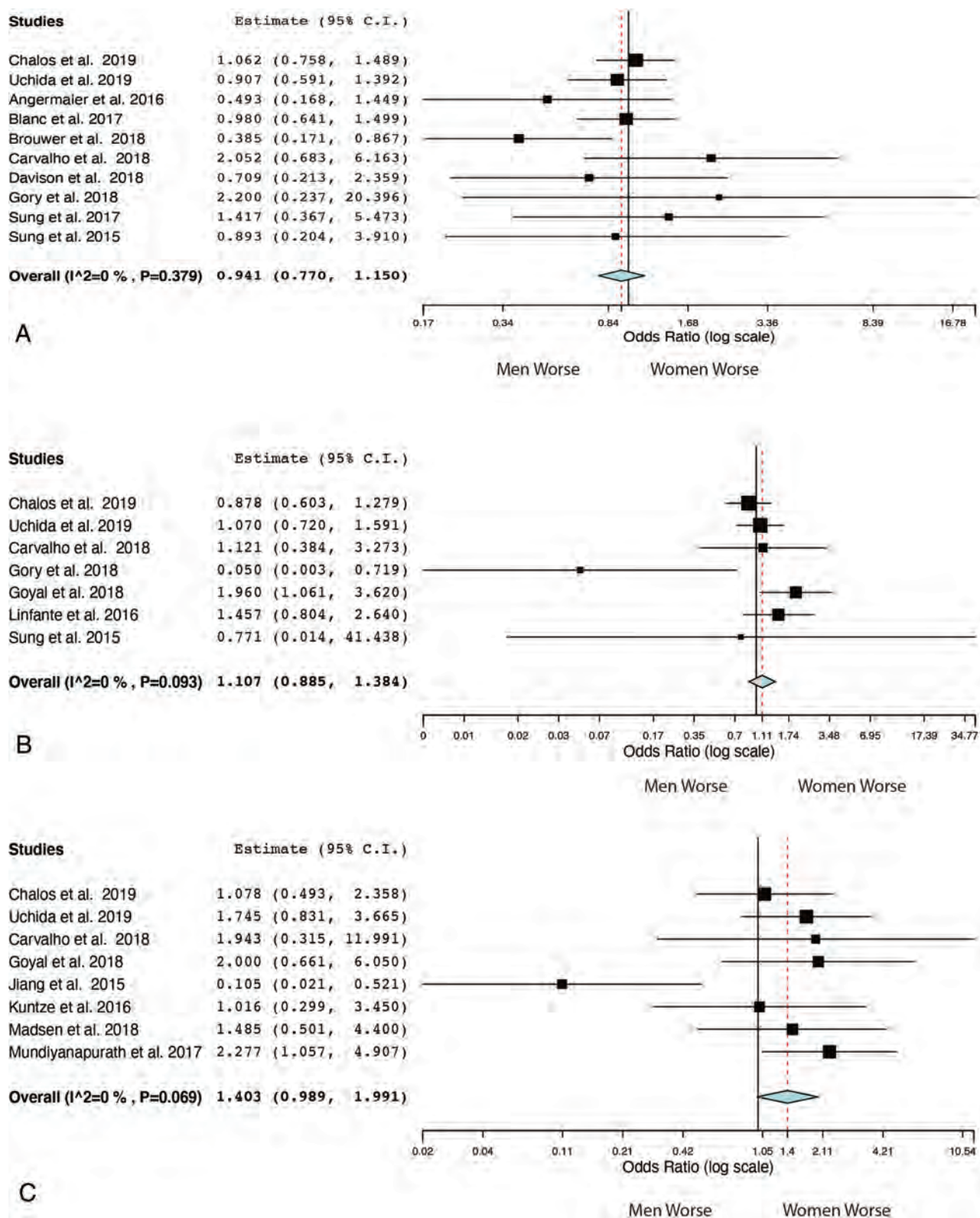


FIG 2. Forest plot for secondary outcomes. A, Recanalization (TICI \geq 2b). B, Mortality at 90 days. C, sICH.

score ($n = 5$, $P = .040$) was inversely associated with sICH. Although no variables had a significant association with good outcome in univariate analysis, age ($P = .003$) and male sex ($P < .001$) were positively associated with good outcome, after

adjusting for IV rtPA and year of publication. When the variable IV rtPA was replaced by TICI 2b–3, age ($P = .045$) and male sex ($P = .0084$) were still positively associated with good outcome.

Publication Bias

Publication bias was assessed by visually inspecting funnel plots. For good outcome, sICH, and recanalization, the plots were symmetric and with minimal extreme values. Publication bias in these outcomes was interrogated by Egger and Begg as well as Mazumdar rank correlation tests, and found to be insignificant. For 90-day mortality, although the funnel plot was asymmetric, both Egger and Begg and Mazumdar rank correlation tests did not suggest potential publication bias (Online Supplemental Data).

DISCUSSION

Our meta-analysis demonstrates that women are less likely to attain good 90-day functional outcomes (mRS 0–2) compared with men. The 2 groups did not vary in terms of sICH and 90-day mortality and recanalization rates.

Women have an overall lower lifetime incidence of stroke compared with men. This has been attributed principally to the cardiovascular protective effects of estrogen and progesterone in younger women.¹³ However, starting at about 45 years of age, the pattern is reversed.¹⁴ Experimental rat models mimicking middle cerebral artery stroke have found consistent results. Aged female rats with lower levels of estrogen had significantly larger infarcts compared with the other groups (aged male rats, young male and female rats).¹⁵ The identification of pathomechanisms underlying this phenomenon may help identify molecular targets for sex-based neuroprotection in the future.

In a pooled, sex-based matched analysis among patients receiving IV rtPA for stroke in randomized controlled trials, no overall difference was seen in the outcome of patients between women and men.¹⁶ However, when inspecting the probability of obtaining a good outcome across age groups in the same cohort, women fared better than men before the age of 45 but had poorer outcomes after that. This finding provides further evidence for the effect of age on sex differences in stroke. A meta-analysis of 60,159 patients on this topic found that women had worse clinical outcomes compared with men after thrombolysis.¹⁷ Higher levels of plasminogen activator inhibitor 1, a known predictor of thrombolysis resistance, in female patients with stroke was theorized to underlie these outcomes.¹⁸

However, differences in baseline characteristics between sexes may also account for inferior functional outcomes in women. The largest cohort included in the analysis also showed poorer outcomes in women. However, women in the study were also older and presented with worse strokes (higher NIHSS scores and lower ASPECTS). Nevertheless, the inferior functional outcomes remained after adjusting for the aforementioned factors.⁷ The use of hormone replacement therapy (HRT) was a risk factor not routinely collected in the studies included in our meta-analysis. The use of HRT has been found to decrease the levels of plasminogen activator 1.¹⁹ Intuitively, HRT should be protective for stroke. However, large randomized trials on the use of HRT for both primary and secondary prevention of cardiovascular disease have revealed that its use likely increases the risk of stroke and stroke-related death.^{20,21} How HRT affects the response of the female brain to recanalization and reperfusion after EVT remains to be elucidated. Thus, HRT use may ultimately be another

important factor worth noting in future studies focused on sex-based differences in EVT for stroke.

This meta-analysis has several limitations. First, moderate heterogeneity was found. Next, there is also bias inherent in the retrospective nature of most studies included. None of the studies including the randomized trials were specifically designed to compare outcomes between sexes. Thus, differences in the baseline characteristics of both groups may have led to poorer functional outcomes in women undergoing EVT. Last, the definition of sICH was not uniform throughout all the studies included.

CONCLUSIONS

This sex-based meta-analysis of patients with stroke undergoing EVT suggests that women have inferior clinical outcomes at 90 days compared with men. Large-scale prospective cohorts with attention to sex and reporting of these outcome data would be instrumental in interrogating this disparity. Studies on the pathophysiology and/or systems-based cause of this phenomenon would also help to create alleviation strategies.

Disclosures: Thomas R. Marotta—UNRELATED: Consultancy: Medtronic, proctor for the Pipeline Endovascular Device; Patents (Planned, Pending or Issued): EVASC, for eCLIPS; principal medical advisor; Stock/Stock Options: EVASC.

REFERENCES

1. Potts J, Sirker A, Martinez SC, et al. **Persistent sex disparities in clinical outcomes with percutaneous coronary intervention: insights from 6.6 million PCI procedures in the United States.** *PLoS One* 2018;13:e0203325 CrossRef Medline
2. Appelros P, Stegmayr B, Terént A. **Sex differences in stroke epidemiology: a systematic review.** *Stroke* 2009;40:1082–90 CrossRef Medline
3. Reid JM, Dai D, Gubitz GJ, et al. **Gender differences in stroke examined in a 10-year cohort of patients admitted to a Canadian teaching hospital.** *Stroke* 2008;39:1090–95 CrossRef Medline
4. Bushnell C, Howard VJ, Lisabeth L, et al. **Sex differences in the evaluation and treatment of acute ischaemic stroke.** *Lancet Neurol* 2018;17:641–60 CrossRef Medline
5. de Ridder IR, Franssen PS, Beumer D, et al. **Is intra-arterial treatment for acute ischemic stroke less effective in women than in men.** *Interv Neurol* 2016;5:174–78 CrossRef Medline
6. Chalos V, de Ridder IR, Lingsma HF, et al. HERMES Collaborators. **Does sex modify the effect of endovascular treatment for ischemic stroke?** *Stroke* 2019;50:2413–19 CrossRef Medline
7. Uchida K, Yoshimura S, Sakai N, et al. RESCUE-Japan Registry 2 Investigators. **Sex differences in management and outcomes of acute ischemic stroke with large vessel occlusion.** *Stroke* 2019; 50:1915–18 CrossRef Medline
8. Moher D, Liberati A, Tetzlaff J, et al. PRISMA Group. **Preferred Reporting Items for Systematic Reviews and Meta-Analyses: the PRISMA Statement.** *PLoS Med* 2009;6:e1000097 CrossRef Medline
9. Wells GA, Shea B, Connell D, et al. **The Newcastle-Ottawa Scale (NOS) for assessing the quality of nonrandomised studies in meta-analyses.** *Scale Vol* 2000. http://www.evidencebasedpublichealth.de/download/Newcastle_Ottawa_Scale_Pope_Bruce.pdf. Accessed October 1, 2020
10. Higgins JP, Altman DG, Gotzsche PC, et al. Cochrane Statistical Methods Group. **The Cochrane Collaboration's tool for assessing risk of bias in randomised trials.** *BMJ* 2011;343:d5928 CrossRef Medline

11. Briggs DE, Felberg RA, Malkoff MD, et al. **Should mild or moderate stroke patients be admitted to an intensive care unit?** *Stroke* 2001;32:871–76 CrossRef Medline
12. Higgins JP, Thompson SG. **Quantifying heterogeneity in a meta-analysis.** *Stat Med* 2002;21:1539–58 CrossRef Medline
13. Liu F, McCullough LD. **Interactions between age, sex, and hormones in experimental ischemic stroke.** *Neurochem Int* 2012; 61:1255–65 CrossRef Medline
14. Towfighi A, Saver JL, Engelhardt R, et al. **A midlife stroke surge among women in the United States.** *Neurology* 2007;69:1898–1904 CrossRef Medline
15. Liu F, Yuan R, Benashski SE, et al. **Changes in experimental stroke outcome across the life span.** *J Cereb Blood Flow Metab* 2009;29: 792–802 CrossRef Medline
16. Hametner C, MacIsaac RL, Kellert L, et al. VISTA Collaborators. **Sex and stroke in thrombolized patients and controls.** *Stroke* 2017;48: 367–74 CrossRef Medline
17. Liu M, Li G, Tang J, et al. **The influence of sex in stroke thrombolysis: a systematic review and meta-analysis.** *J Clin Neurol* 2018;14: 141–52 CrossRef Medline
18. Ribo M, Montaner J, Molina C, et al. **Admission fibrinolytic profile predicts clot lysis resistance in stroke patients treated with tissue plasminogen activator.** *Thromb Haemost* 2004;91:1146–51 CrossRef Medline
19. Shahar E, Folsom AR, Salomaa VV, et al. **Relation of hormone-replacement therapy to measures of plasma fibrinolytic activity.** *Circulation* 1996;93:1970–75 CrossRef Medline
20. Viscoli CM, Brass LM, Kernan WN, et al. **A clinical trial of estrogen-replacement therapy after ischemic stroke.** *N Engl J Med* 2001;345:1243–49 CrossRef Medline
21. Anderson G, Limacher M, Annlouise A, et al. Women's Health Initiative Steering Committee. **Effects of conjugated equine estrogen in postmenopausal women with hysterectomy: the Women's Health Initiative randomized controlled trial.** *JAMA* 2004;291: 1701–12 CrossRef Medline

Middle Meningeal Artery Embolization Using Combined Particle Embolization and *n*-BCA with the Dextrose 5% in Water Push Technique for Chronic Subdural Hematomas: A Prospective Safety and Feasibility Study

F. Al-Mufti, G. Kaur, K. Amuluru, J.B. Cooper, K. Dakay, M. El-Ghanem, J. Pisapia, C. Muh, R. Tyagi, C. Bowers, C. Cole, S. Rosner, J. Santarelli, S. Mayer, and C. Gandhi

ABSTRACT

BACKGROUND AND PURPOSE: Embolization of the middle meningeal artery for treatment of refractory or recurrent chronic subdural hematomas has gained momentum during the past few years. Little has been reported on the use of the *n*-BCA liquid embolic system for middle meningeal artery embolization. We present the technical feasibility of using diluted *n*-BCA for middle meningeal artery embolization.

MATERIALS AND METHODS: We sought to examine the safety and technical feasibility of the diluted *n*-BCA liquid embolic system for middle meningeal artery embolization. Patients with chronic refractory or recurrent subdural hematomas were prospectively enrolled from September 2019 to June 2020. The primary outcome was the safety and technical feasibility of the use of diluted *n*-BCA for embolization of the middle meningeal artery. The secondary end point was the efficacy in reducing hematoma volume.

RESULTS: A total of 16 patients were prospectively enrolled. Concomitant burr-hole craniotomies were performed in 12 of the 16 patients. Two patients required an operation following middle meningeal artery embolization for persistent symptoms. The primary end point was met in 100% of cases in which there were no intra- or postprocedural complications. Distal penetration of the middle meningeal artery branches was achieved in all the enrolled cases. A 7-day post-middle meningeal artery embolization follow-up head CT demonstrated improvement (>50% reduction in subdural hematoma volume) in 9/15 (60%) patients, with 6/15 (40%) showing an unchanged or stable subdural hematoma. At day 21, available CT scans demonstrated substantial further improvement (>75% reduction in subdural hematoma volume).

CONCLUSIONS: Embolization of the middle meningeal artery using diluted *n*-BCA and ethiodized oil (1:6) is safe and feasible from a technical standpoint. The use of a dextrose 5% bolus improves distal penetration of the glue.

ABBREVIATIONS: cSDH = chronic subdural hematoma; D5 = dextrose 5%; D5W = dextrose 5% in water; MMA = middle meningeal artery; PVA = polyvinyl alcohol; SDH = subdural hematoma

Despite traditional treatment with surgical evacuation, chronic subdural hematomas (cSDHs) tend to have an indolent course with frequent recurrences.¹ In recent years, embolization

of the middle meningeal artery (MMA) for treatment of refractory or recurrent cSDH has gained momentum, with recent literature showing a significant reduction in the size of the cSDH as well as lower rates of recurrence.² The primary endovascular techniques used to date have involved the use of polyvinyl alcohol particles (PVA) and Onyx liquid embolic (ethylene-vinyl alcohol dissolved in dimethyl-sulfoxide; Medtronic). Another commonly used liquid embolic agent in the neurointerventional area is *n*-BCA, which is a liquid adhesive that polymerizes rapidly on contact with ionic substances and can be injected to achieve permanent vessel occlusion. The rates of polymerization and flow and the penetration depth can be modified using varying amounts of ethiodized oil as well as concurrent infusion of dextrose 5% in water (D5W) during *n*-BCA (Trufill, Cordis Neurovascular) injection (D5W-push technique).³ Data on the use of *n*-BCA as an embolic agent in cases of cSDH

Received August 31, 2020; accepted after revision November 25.

From the Departments of Neurosurgery (F.A.-M., G.K., J.B.C., K.D., J.P., C.M., R.T., C.C., J.S., C.G.) and Neurocritical Care (S.M.), New York Medical College, Westchester Medical Center, Valhalla, New York; Department of Neurointerventional Radiology (K.A.), Goodman Campbell Brain and Spine, Carmel, Indiana; Department of Neurology (M.E.-G.), University of Arizona-Tucson, Tucson, Arizona; Department of Neurosurgery (C.B.), School of Medicine, University of New Mexico, Albuquerque, New Mexico; and Department of Neurosurgery (S.R.), New York-Presbyterian/Hudson Valley Hospital, Cortlandt Manor, New York.

Please address correspondence to Jared B. Cooper, MD, Department of Neurosurgery, New York Medical College, Westchester Medical Center, 100 Woods Rd, Valhalla, NY 10595; e-mail: jared.cooper@wmchealth.org

Indicates article with online supplemental data.
<http://dx.doi.org/10.3174/ajnr.A7077>

are extremely limited. Herein, we sought to study the safety and technical feasibility of using diluted *n*-BCA for embolization of the MMA for cSDHs.

MATERIALS AND METHODS

Study Population and Patient Selection

Prospective patients with chronic refractory or recurrent subdural hematomas admitted to our quaternary care level 1 trauma center (Westchester Medical Center) were enrolled from September 2019 to June 2020. Informed consent was obtained from patients and/or their families. This study was approved by the institutional review board at our institution. Enrolled patients were older than 18 years of age and had symptomatic cSDH.

We enrolled 3 subgroups of patients in our study. Patients with a previously untreated subdural hematoma (SDH) were offered treatment with MMA embolization if they were clinically symptomatic, had failed conservative management, and did not require urgent surgical evacuation. Patients with a history of SDH (acute or chronic) who underwent surgical evacuation with radiographic evidence of recurrence were offered treatment with MMA embolization if they were clinically symptomatic, had failed conservative management, but did not require urgent surgical re-evacuation. Finally, for patients who underwent surgical evacuation for acutely symptomatic SDHs due to mass effect with evidence of herniation on cranial imaging, MMA embolization was offered in the acute postoperative period as a means of prophylaxis in patients who needed to be on anticoagulation therapy, had platelet dysfunction due to systemic conditions (such as renal failure or alcohol use), or had re-accumulation or incomplete hematoma evacuation, to potentially reduce the risk of recurrence regardless of postoperative symptomatology.

Patients were excluded if the hematoma had an underlying chronic cause such as a vascular lesion, brain tumor, arachnoid cyst, or spontaneous intracranial hypotension. Patients with mixed-density subdural hematomas were excluded if the acute component exceeded 50%. Patients with ophthalmic collaterals from the MMA or other signs of dangerous anastomoses identified during angiography were excluded. Patients were also excluded if they were clinically asymptomatic.

Clinical Management

Clinical management conformed to Brain Trauma Foundation and the Neurocritical Care Society guidelines.^{4,5}

Data Collection

Prospective comprehensive data on each patient were collected, including demographics, medical history, baseline clinical status, imaging results, as well as treatment and complications during hospitalization.

Clinical and Radiologic Variables

The diagnosis of the SDH was established by admission CT based on standard radiographic characteristics. After endovascular treatment, a follow-up CT scan was obtained on day 7, day 21, and at 3 months to assess stability and/or a change in size of the cSDH. Percentage hematoma reduction based on volume was assessed.

Hematoma volume was measured by applying the ABC/2 technique modified for ellipsoid cSDH to noncontrast head CT.⁶

MMA Embolization Procedure

All embolization procedures were performed with the patient under general anesthesia using an arterial line for blood pressure monitoring. Femoral or radial 6F access was obtained. A Benchmark 071 (2.03 mm) Intracranial Access Catheter (Penumbra) was advanced into the common carotid artery ipsilateral to the cSDH, and intracranial angiography was performed to evaluate dangerous external carotid artery–ICA collaterals via the MMA. In case of MMA–ophthalmic artery collaterals, embolization was not performed. Embolization of the frontal and parietal branches of the MMA was performed using a dilute mixture of 1:6 *n*-BCA and ethiodized oil, with dextrose 5% (D5) boluses from the guide catheter to improve the distal penetration of the glue. Visibility was improved using tantalum powder. Cases in which there were ophthalmic collaterals from the MMA or other signs of dangerous anastomoses were excluded. The Prowler Select Plus microcatheter (Codman), 2.8F/2.3F 0.021 inch, was used for all cases.

After we advanced the Benchmark catheter into the internal maxillary artery, a Prowler Select Plus 2.8/2.3F straight-tip microcatheter was advanced into the frontal and parietal branches of the MMA. Initially, particulate embolysate (150–300 μ m) was infused into the distal frontal and parietal branches of the MMA until there was stagnation of anterograde flow. Following PVA embolization, a dilute preparation of *n*-BCA was prepared with ethiodized oil (14%; 1:6 mixture of *n*-BCA/ethiodized oil). The guide catheter was connected to two 60-mL syringes filled with D5W. As the *n*-BCA mixture was injected through the microcatheter into the frontal and parietal branches of the MMA, a second operator simultaneously infused D5W through the guide catheter to enhance distal penetration (D5W-push technique). Depending on the duration of the procedure, some patients were given 25–50 U/kg of heparin to prevent thromboembolic complications. An XperCT Dual Cone Beam CT of the head (Philips Healthcare) was performed on the table immediately after the endovascular procedure.

Outcome Assessment

The primary outcome measure was the safety and technical feasibility of MMA embolization using diluted *n*-BCA, defined as any intra- or postprocedural neurologic or non-neurologic complication. Procedural complications were defined as nontarget embolization or unintentional retention of the catheter. The secondary end point was the efficacy in reducing hematoma volume, defined as >50% reduction in SDH volume. Global outcome was assessed by virtual interview or a telephone structured interview using the 7-point version of the mRS rated from death (6) to symptom-free full recovery (0). Poor outcome was defined as death or moderate-to-severe disability (unable to walk or tend to bodily needs, mRS score of 4–6).

RESULTS

Demographics

A total of 16 patients were prospectively enrolled in our study between September 2019 and June 2020. The mean age was 72 years,

with a male/female ratio of 2:1. A history of trauma was confirmed in 13 of the 16 patients. Of the 16 patients enrolled, 10 patients were on anticoagulation at the time of the SDH identification (Online Supplemental Data).

Indications for MMA Embolization and Surgical Evacuation

Burr-hole craniotomies were performed in 12 of the 16 patients (75%). Of the 12 patients who underwent both surgical evacuation of their subdural hematoma and middle meningeal artery embolization, 9 underwent embolization post-surgical evacuation. Postsurgical MMA embolization was performed in 8 patients within 2 weeks of the operation when there was clear re-accumulation, defined as an increase in hematoma volume of >10%, or incomplete hematoma evacuation on the 7-day follow-up head CT. One patient underwent middle meningeal embolization approximately 8 months following surgical evacuation for persistent symptoms and hematoma expansion related to cerebral hypotension. Three patients underwent MMA embolization preoperatively. Of the patients requiring burr-hole craniotomy following MMA embolization, 2 underwent an operation for persistent symptoms during

their initial hospitalization, while the remaining patient underwent craniotomy after returning to the hospital following a subsequent fall with a head strike and expansion of her subdural hematoma 11 days after undergoing her MMA embolization.

Embolization Results: Technical Feasibility and Safety

Embolization of the MMA was successfully performed in all 16 patients enrolled in the study (Fig 1). A total of 20 patients were screened for the procedure. Consent could not be obtained for 2 patients. Ophthalmic collaterals from the MMA were identified in 1 patient, and the MMA was not visualized, possibly secondary to neurosurgical evacuation, in the remaining patient.

The primary end point was met in 100% of cases; there were no intra- or postprocedural complications in the 16 patients enrolled. Distal penetration of the MMA branches was achieved in all cases. Average fluoroscopy time was 27.9 minutes. The fluoroscopy time attributed to glue embolization added an average of 2.5 minutes to each procedure (range, 1.5–3.5 minutes).

7-Day Follow-up CT Scan

A 7-day postembolization follow-up head CT was available for 15 of 16 patients and demonstrated improvement (>50% reduction in SDH volume) in 9/15 (60%), with 6/15 (40%) showing an unchanged or stable SDH (Fig 2). The remaining patient was discharged before the 7-day follow-up scan and was lost to follow-up.

21-Day and 3-Month Follow-up CT Scan

Day 21 head CTs were available for 11/16 patients, all of whom demonstrated a further >50% decrease in SDH volume (thus a total of >75% reduction in initial SDH volume). Three-month CT was available for 5/16 patients, all showing further >50% decrease in SDH volume. Four patients were lost to follow-up, and the remaining 21-day and 3-month scans are pending at the time of this writing.

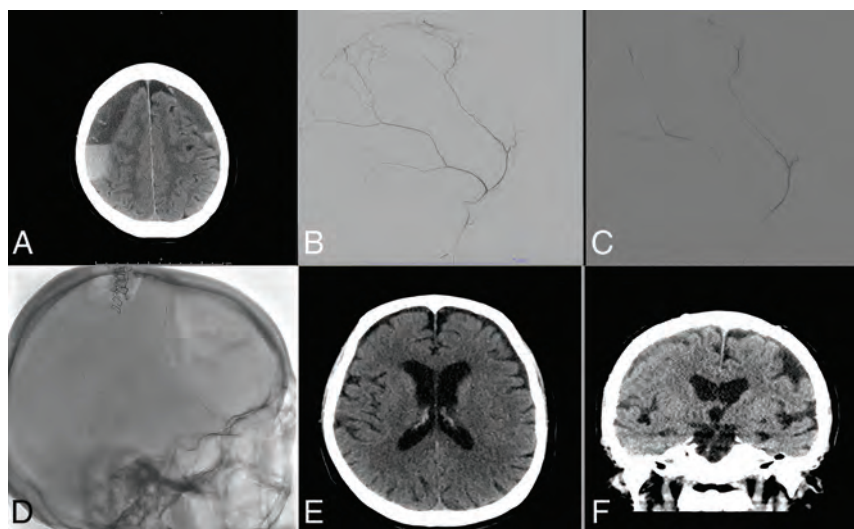


FIG 1. Treatment course of a 77-year-old man with bilateral cSDH. Noncontrast axial head CT reveals bilateral subacute-on-chronic SDHs on admission (A). Diagnostic cerebral angiogram reveals robust filling of the MMA (B). The MMA was then embolized using *n*-BCA diluted with D5W (C). Postprocedural spin sequence reveals the glue cast left in the MMA (D). Noncontrast head CT at 3 months reveals significant resolution of the patient's SDHs (E and F).

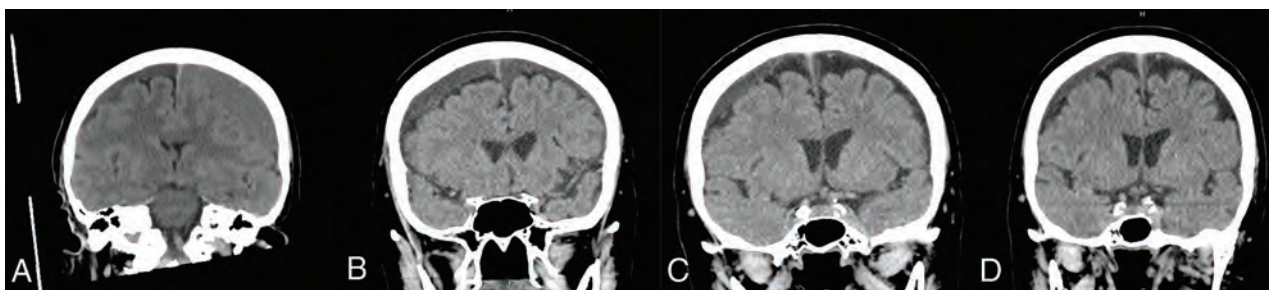


FIG 2. Imaging course of a 75-year-old woman with bilateral cSDHs managed by unilateral burr-hole evacuation followed by bilateral MMA embolization. Noncontrast head CT images were obtained on presentation (A), postoperatively (B), 1 week postembolization (C), and 4 months postembolization (D).

Clinical Outcomes

Overall, 6 patients showed improvement (38%), 8 were unchanged (50%), and 2 (12%) had clinically deteriorated after MMA embolization. Of the 7 patients with at least 3 months of follow-up, 6 (85.7%) had partial-to-complete resolution of clinical symptoms. Of these, 5 of 7 (71.4%) had unchanged mRS scores, while 2 had a 1-point improvement in mRS (Online Supplemental Data). Of the 9 patients who have not yet had long-term follow-up, 4 (44.4%) had improved symptoms at discharge, 3 were unchanged, and 2 patients experienced a 1-point decline in the mRS score. Because the size of the SDH had not increased, we believe that this worsening could be attributed to generalized deconditioning or poor tolerance of procedural anesthesia, given the patients' advanced age; long-term follow-up will be assessed in subsequent reports.

DISCUSSION

cSDH is a public health issue with an estimated 1-year incidence of 5–58/100,000, which is highest in elderly patients.⁷ cSDH presents a challenge to neurosurgeons due to high recurrence rates (2%–37%) and the numerous associated medical comorbidities. Recent results have demonstrated the effectiveness of MMA embolization as an alternative to an operation for the treatment of cSDH. Most data on MMA embolization have been achieved with PVA particle embolization. To the best of our knowledge, this study is one of the first series of patients treated with *n*-BCA embolization of the MMA for cSDH. In this study, 60% of patients achieved a reduction in the maximum width of the SDH of >50% at 7 days, while 31% of patients showed a reduction in volume at the longest follow-up study of 3 months. All cases were technically successful, and there were no procedure-related complications.

Development of cSDH starts with the separation of the dural border cell layer, which triggers an inflammatory response that includes dural border cell proliferation, granulation tissue formation, and macrophage deposition.⁷ A surrounding membrane is formed due to the inflammatory response, which develops neovascularity due to the release of angiogenic factors. The primary pathologic mechanism behind recurrent hemorrhage and growth may involve repeat microvascular hemorrhage within this surrounding membrane.^{8,9} The neovascularity is supplied from distal branches of the MMA; thus, embolizing the MMA could potentially halt this process and allow the collection to be resorbed.²

Surgical approaches for cSDH have traditionally included a twist-drill hole, burr-hole, and craniotomy-based evacuations. While the outcomes with surgical evacuation are favorable, after the initial evacuation, there is a tendency for cSDH to recur, oftentimes with neurologic deterioration and a requirement for an urgent or emergent re-operation.¹⁰ Conservative management leading to spontaneous resolution is rare and can be as low as 5%.¹¹ Medical management strategies such as steroids, platelet activating factor antagonists, and statins have been explored with limited success.¹² In particular, recent evidence suggests a role for atorvastatin alone and/or in combination with corticosteroids in reducing the likelihood of subdural recurrence following surgical

evacuation; however, there is still a paucity of evidence to support this strategy, and several trials are currently underway.^{13,14}

MMA embolization for cSDH aims to devascularize the surrounding subdural membranes to a sufficient extent so that the balance is shifted from the continued leakage and accumulation of blood products toward reabsorption.¹¹ MMA embolization has been used as the sole therapy, as well as a preoperative or postoperative adjunct to surgical evacuation with the intention of reducing postoperative recurrence. A recent study evaluated 27 patients who underwent MMA embolization alone for asymptomatic cSDH and 45 patients who underwent MMA embolization in addition to surgical evacuation for symptomatic cSDH and found significantly lower recurrences in the embolization group (1.4%) compared with historical surgical controls (27.5%, $P = .001$).¹⁵ To date, embolization of the MMA has been most commonly performed with PVA particles. In a small randomized controlled trial with 46 patients undergoing surgical treatment, 21 patients additionally underwent MMA embolization. The addition of MMA embolization to the operation led to an increase in cSDH resorption at 3 months.¹⁵ In a systematic review and case series, the use of Onyx as a liquid embolic for MMA embolization was described with good success.¹⁶ In another review including 177 MMA embolization procedures, the most common embolic material used was PVA (91%, 160/177), occasionally supplemented with coils (4%, 7/161) and *n*-BCA (9%, 16/177).¹⁷

Fiorella and Arthur¹¹ described technical considerations of using liquid embolics-versus-particulate embolysates for MMA embolization. The authors argued that particulates may only penetrate as distally as flow will allow and may be limited by the diminutive size of the meningeal arteries compared with the microcatheter used. The authors also argued that liquid embolics may be advantageous over particulate embolics due to the ability to inject under pressure from a wedged position to achieve a greater casting of the subdural membranes and retrograde reflux of adjacent meningeal branches. Furthermore, increased visualization of liquid embolics may prevent iatrogenic embolization to unintended territory. Finally, liquid agents are permanent compared with the transient nature of particulate embolysates, possibly benefitting patients who have repeat episodes of hemorrhage.

Given the same considerations, we describe a novel approach of a combined technique using PVA particle embolization, followed by diluted *n*-BCA with simultaneous D5 injection through the guide catheter. The use of a D5-push technique improves distal penetration of the *n*-BCA by delaying polymerization within the target vessel. This, in combination with the initial embolization with PVA, capitalizes on the advantages of each embolic material compared with their use in isolation. The initial PVA embolization markedly penetrates the microscopic neovascularity and immature capillaries of the surrounding membrane, while the *n*-BCA embolization provides an easily visualized, long-term solution to a chronic problem. The diluted mixture of *n*-BCA in combination with the D5-push may compensate for the decreased distal penetration of liquid embolics compared with smaller particulate embolysates. Further advantages of this technique include low cost, because both PVA and *n*-BCA are significantly more cost-effective than Onyx.

We report the efficacy of this technique in our small series because we were able to demonstrate substantial improvement in hematoma volume in >60% of patients at the latest follow-up. No procedural complications were encountered after MMA embolization. Seventy-five percent of patients underwent concurrent surgical evacuation of their subdural hematoma; however, most of these patients received MMA embolization following an operation as a means of prophylaxis against recurrent hemorrhage. Three patients required surgical evacuation of their hematoma following MMA embolization. In other words, 13 of the 16 (81.3%) included patients have been able to avoid an additional operation for recurrent subdural hematoma. A recent systematic review suggested that surgically evacuated chronic subdural hematomas have a recurrence rate approaching 35% requiring re-evacuation.¹⁸ Of the 3 patients who required an operation following MMA embolization, 2 underwent craniotomy for persistent altered mental status shortly after embolization. Most interesting, both patients had been taking antiplatelet medications before the discovery of their subdural hematoma. There was no increase in subdural hematoma volume following MMA embolization in either patient.

Limitations of our study include its small size and being a single-center study with certain patient data still pending follow-up. Given the small sample size and unique niche for this procedure, there may have been selection bias as well. Additionally, not all postoperative imaging was performed using 3D reconstructed thin-cut CT, limiting our ability to optimally calculate hematoma volume; however, we believe that we were still able to accurately compare changes in hematoma volume despite these differences in imaging techniques. However, despite these limitations, we were able to demonstrate the safety and technical feasibility of MMA embolization using diluted *n*-BCA and, to a lesser extent, efficacy (secondary end point). These pilot data will be instrumental in the design of any upcoming multicenter trial on the use of dilute *n*-BCA for MMA embolization and any comparison studies that may follow.

CONCLUSIONS

Embolization of the MMA using diluted *n*-BCA is safe and effective for patients with cSDH, with a low risk of recurrence, and may be considered an effective therapeutic intervention to arrest SDH enlargement and promote resolution. The use of a D5-push technique improves distal penetration of the embolic material.

Disclosures: Stephan Mayer—UNRELATED: Consultancy: Biogen, Idorsia, BrainCool; Expert Testimony: occasional work all unrelated to this article; Stock/Stock Options: NeuroOptics.

REFERENCES

1. Yang W, Huang J. **Chronic subdural hematoma: epidemiology and natural history.** *Neurosurg Clin N Am* 2017;28:205–10 CrossRef Medline
2. Haldrup M, Ketharanathan B, Debrabant B, et al. **Embolization of the middle meningeal artery in patients with chronic subdural hematoma—a systematic review and meta-analysis.** *Acta Neurochir (Wien)* 2020;162:777–84 CrossRef Medline
3. Ashour R, Aziz-Sultan A. **Preoperative tumor embolization.** *Neurosurg Clin N Am* 2014;25:607–17 CrossRef Medline
4. Carney N, Totten AM, O'Reilly C, et al. **Guidelines for the Management of Severe Traumatic Brain Injury, Fourth Edition.** *Neurosurgery* 2017;80:6–15 CrossRef Medline
5. Cook AM, Morgan Jones G, Hawryluk GW, et al. **Guidelines for the acute treatment of cerebral edema in neurocritical care patients.** *Neurocrit Care* 2020;32:647–66 CrossRef Medline
6. Kothari RU, Brott T, Broderick JP, et al. **The ABCs of measuring intracerebral hemorrhage volumes.** *Stroke* 1996;27:1304–05 CrossRef Medline
7. Santarius T, Kirkpatrick PJ, Kolias AG, et al. **Working toward rational and evidence-based treatment of chronic subdural hematoma.** *Clin Neurosurg* 2010;57:112–22 Medline
8. Asghar M, Adhiyaman V, Greenway MW, et al. **Chronic subdural haematoma in the elderly: a North Wales experience.** *J R Soc Med* 2002;95:290–92 CrossRef Medline
9. Zhang P, Li Y, Huang J, et al. **Chronic subdural haematoma in antithrombotic cohorts: characteristics, surgical outcomes, and recurrence.** *Br J Neurosurg* 2020;34:408–15 CrossRef Medline
10. Link TW, Boddu S, Paine SM, et al. **Middle meningeal artery embolization for chronic subdural hematoma: a series of 60 cases.** *Neurosurgery* 2019;85:801–07 CrossRef Medline
11. Fiorella D, Arthur AS. **Middle meningeal artery embolization for the management of chronic subdural hematoma.** *J Neurointerv Surg* 2019;11:912–15 CrossRef Medline
12. Gjerris F, Schmidt K. **Chronic subdural hematoma: surgery or mannitol treatment.** *J Neurosurg* 1974;40:639–42 CrossRef Medline
13. He CX, Xu J, Chen L, et al. **Evaluation of the efficacy of atorvastatin in the treatment for chronic subdural hematoma: a meta-analysis.** *Neurosurgical Review* 2020 Jan 17. [Epub ahead of print] CrossRef Medline
14. Wang DG, Gao C, Xu X, et al. **Treatment of chronic subdural hematoma with atorvastatin combined with low-dose dexamethasone: phase II randomized proof-of-concept clinical trial.** *J Neurosurg* 2020 Jan 31. [Epub ahead of print] CrossRef Medline
15. Ng S, Derraz I, Boetto J, et al. **Middle meningeal artery embolization as an adjuvant treatment to surgery for symptomatic chronic subdural hematoma: a pilot study assessing hematoma volume resorption.** *J Neurointerv Surg* 2020;12:695–99 CrossRef Medline
16. Waqas M, Vakhari K, Weimer PV, et al. **Safety and effectiveness of embolization for chronic subdural hematoma: systematic review and case series.** *World Neurosurg* 2019;126:228–36 CrossRef Medline
17. Jumah F, Osama M, Islim AI, et al. **Efficacy and safety of middle meningeal artery embolization in the management of refractory or chronic subdural hematomas: a systematic review and meta-analysis.** *Acta Neurochir (Wien)* 2020;162:499–507 CrossRef Medline
18. Ivamoto HS, Lemos HP, Atallah AN. **Surgical treatments for chronic subdural hematomas: a comprehensive systematic review.** *World Neurosurg* 2016;86:399–418 CrossRef Medline

Postprocedural Antiplatelet Treatment after Emergent Carotid Stenting in Tandem Lesions Stroke: Impact on Stent Patency beyond Day 1

R. Pop, A. Hasiu, P.H. Mangin, F. Severac, D. Mihoc, D. Nistoran, M. Manisor, M. Simu, S. Chibbaro, R. Gheoca, V. Quenardelle, O. Rouyer, V. Wolff, and R. Beaujeux



ABSTRACT

BACKGROUND AND PURPOSE: Postprocedural dual-antiplatelet therapy is frequently withheld after emergent carotid stent placement during stroke thrombectomy. We aimed to assess whether antiplatelet regimen variations increase the risk of stent thrombosis beyond postprocedural day 1.

MATERIALS AND METHODS: Retrospective review was undertaken of all consecutive thrombectomies for acute stroke with tandem lesions in the anterior circulation performed in a single comprehensive stroke center between January 9, 2011 and March 30, 2020. Patients were included if carotid stent patency was confirmed at day 1 postprocedure. The group of patients with continuous dual-antiplatelet therapy from day 1 was compared with the group of patients with absent/discontinued dual-antiplatelet therapy.

RESULTS: Of a total of 109 tandem lesion thrombectomies, 96 patients had patent carotid stents at the end of the procedure. The early postprocedural stent thrombosis rate during the first 24 hours was 14/96 (14.5%). Of 82 patients with patent stents at day 1, in 28 (34.1%), dual-antiplatelet therapy was either not initiated at day 1 or was discontinued thereafter. After exclusion of cases without further controls of stent patency, there was no significant difference in the rate of subacute/late stent thrombosis between the 2 groups: 1/50 (2%) in patients with continuous dual-antiplatelet therapy versus 0/22 (0%) in patients with absent/discontinued dual-antiplatelet therapy ($P=1.000$). In total, we observed 88 patient days without any antiplatelet treatment and 471 patient days with single antiplatelet treatment.

CONCLUSIONS: Discontinuation of dual-antiplatelet therapy was not associated with an increased risk of stent thrombosis beyond postprocedural day 1. Further studies are warranted to better assess the additional benefit and optimal duration of dual-antiplatelet therapy after tandem lesion stroke thrombectomy.

ABBREVIATIONS: DAPT = dual-antiplatelet therapy; ST = stent thrombosis

In around 15% of endovascular procedures for anterior circulation stroke,¹ there is a tight stenosis or occlusion of the cervical carotid artery in addition to the intracranial artery occlusion. The optimal endovascular management of tandem lesions has yet to be defined; however, there is mounting evidence^{2,3} that emergent stent

placement in the carotid artery associated with at least 1 antiplatelet agent could lead to better recanalization rates and improved clinical outcomes. A more definitive answer should be provided by the Thrombectomy In TANdem lesions (TITAN) randomized multicenter trial,⁴ designed to assess the safety and efficacy of emergent internal carotid artery stent placement in tandem lesion thrombectomy. This study recently enrolled the first patient in early 2020.

In patients undergoing emergent carotid stent placement, there is no consensus regarding the optimal periprocedural antiplatelet therapy. Many groups^{5,6} chose to avoid dual-antiplatelet therapy (DAPT) during the first 24 hours in an attempt to reduce the risk of hemorrhagic transformation. Conversely, less aggressive antiplatelet regimens might increase the risk of carotid stent thrombosis.

Stent thrombosis was recently identified as a predictor of unfavorable clinical outcome.^{7,8} To date, available data regarding stent patency rates remain scarce. Most case series of endovascular management for tandem lesions^{5,9-11} do not report postprocedural

Received October 9, 2020; accepted after revision November 10.

From the Departments of Interventional Neuroradiology (R.P., A.H., D.M., D.N., M.M., R.B.), Public Healthcare (F.S.), Neurosurgery (S.C.), and Stroke Unit (R.G., V.Q., O.R., V.W.), Strasbourg University Hospitals, Strasbourg, France; Institut de Chirurgie Minimale Invasive Guidée par l'Image (R.P., R.B.), Strasbourg, France; Institut National de la Santé et de la Recherche Médicale (P.H.M.), University of Strasbourg, l'Établissement français du sang Grand-Est, BPPS UMR-S1255, Fédération de Médecine Translationnelle de Strasbourg, Strasbourg, France; Neurology Department (M.S.), Victor Babes University of Medicine and Pharmacy, Timisoara, Romania.

Please address correspondence to Raoul Pop, MD, PhD, Department of Interventional Neuroradiology, Strasbourg University Hospital, Strasbourg, France, 1 Ave Molière, 67098 Strasbourg, France; e-mail: pop.raoul@gmail.com; @RaoulPop25

 Indicates article with online supplemental data.

<http://dx.doi.org/10.3174/ajnr.A6993>

stent patency, while some publications^{12–15} offer partial data for a subgroup of patients for whom carotid imaging controls were available. Reported rates of stent thrombosis ranged between 1.2% and 22.0%.^{6–8,12–14,16,17}

To date, no study has attempted to differentiate between early (first 24 hours) and subacute/late postprocedural stent thrombosis. During the first 24 hours, protection against stent thrombosis is conferred by antiplatelet agents administered during the procedure (periprocedural antiplatelets). Beyond 24 hours, the recommended antiplatelet regimen is DAPT for 4–12 weeks,^{9,17} but in reality, antiplatelets are often tailored in view of neurological and extra-neurological hemorrhagic events. It is currently unknown whether discontinuation of DAPT is associated with an increased risk of late stent thrombosis.

Thus, we aimed to describe the variations in the postprocedural antiplatelet regimen in a large consecutive cohort of tandem lesion thrombectomies with emergent carotid artery stent placement and to assess whether discontinuation of DAPT was associated with an increased risk of carotid stent thrombosis.

MATERIALS AND METHODS

We performed a retrospective review of a prospectively collected data base of stroke endovascular procedures in a single comprehensive stroke center (Strasbourg University Hospital, France), including all consecutive cases treated by endovascular thrombectomy for acute stroke with tandem lesions in the anterior circulation between January 9, 2011, and March 30, 2020. Tandem lesions were defined as an association of extracranial ICA occlusion or stenosis of $\geq 70\%$ using the NASCET criteria and an intracranial artery occlusion in the anterior circulation. Patients were included in the study if treated by emergent carotid stent placement during thrombectomy and if stent patency was confirmed at day 1 postprocedure. Exclusion criteria were as follows: no carotid stent implanted, failure of recanalization, periprocedural stent thrombosis, imaging study showing an occluded carotid stent at day 1, and absence of further imaging studies for stent patency after day 1 or after antiplatelet treatment discontinuation.

Images stored on the PACS and radiology reports were reviewed to extract technical details of the endovascular procedure, as well as postprocedural imaging. Patient files were reviewed to extract patient demographics, comorbidities, peri- and postprocedural antiplatelet regimens, clinical status at discharge, and clinical follow-up information.

Patient Selection and Preprocedural Imaging

Patients with acute stroke were selected for endovascular procedures using MR imaging, except in case of extreme agitation or absolute contraindications. Patients with favorable profiles for recanalization were selected using clinical-radiologic mismatch (discrepancy between the severity of neurologic deficits and the size of acute ischemic lesion on the diffusion sequence) as well as estimation of leptomeningeal collateral status using FLAIR vascular hyperintensities.¹⁸ Patients with acute infarction in more than two-thirds of the middle cerebral artery territory were generally not considered for treatment. Wake-up strokes and patients with unclear time of onset were considered for treatment if last seen well <12 hours before evaluation, using the same imaging selection criteria.

Endovascular Procedure

All procedures were performed with the patient under general anesthesia. During the studied period, the strategy did not change significantly and consisted, in most cases, of an antegrade approach: stent placement and angioplasty of the proximal occlusion before addressing the intracranial occlusion.

Periprocedural and Postprocedural Antiplatelet Treatment

The periprocedural antiplatelet regimen consisted of an IV loading dose of aspirin (250 mg) with or without a loading dose of clopidogrel (300 mg), depending on operator preferences and case-by-case discussion (estimation of hemorrhagic transformation risk depending on the size of the acute ischemic lesion and concomitant treatment with IV thrombolysis). Periprocedural DAPT was generally avoided in cases with a DWI ASPECTS of <5 . In selected cases, glycoprotein IIb/IIIa inhibitors were administered in the acute phase for treatment of periprocedural stent thrombosis.

Postprocedural antiplatelet treatment was initiated after 24 hours (day 1 postprocedure). If the stent was patent and in the absence of significant hemorrhagic transformation, clopidogrel, 75 mg/day, was administered for 3 months in addition to lifelong aspirin, 75 mg/day. In case of significant hemorrhagic transformation, antiplatelets were suspended or a single antiplatelet was administered (aspirin) until the clinical status was stable and the extent of hemorrhagic transformation was reassessed on repeat cerebral imaging.

Postprocedural Imaging and Clinical Follow-up

All patients underwent cerebral CT at day 1 postprocedure. Hemorrhagic transformation was evaluated using the European Cooperative Acute Stroke Study criteria.¹⁹ In addition, for patients with carotid stents, cervical and transcranial Doppler sonography was performed at day 1 and, if possible, before discharge, to check for stent patency. If a sonographic examination was not feasible at day 1, CT angiography of the carotid arteries was performed along with the CT examination. In addition, whenever possible, patients were recalled for additional clinical and carotid sonography examinations between 3 months and 1 year after the initial event.

Statistical Analysis

Continuous variables were presented as median with interquartile range and compared using the Mann-Whitney test after assessment of the normality of distribution. Categorical variables were presented as numbers and percentages and compared using the Pearson χ^2 test or Fisher exact test, depending on theoretic numbers. Statistical data were analyzed using GraphPad Prism, Version 6.0 (GraphPad Software).

RESULTS

During the study period, we identified 109 thrombectomies for acute strokes with tandem lesions. The Figure illustrates the patient-selection diagram. Among 96 patients with patent carotid stents at the end of the thrombectomy procedure, 14 cases had occluded carotid stents at day 1, accounting for an early postprocedural stent thrombosis rate of 14.5%. Among the 14 patients with occluded carotid stents at 24 hours, the median mRS score

at discharge was 4 (interquartile range, 4–4) and the mortality rate was 1/14 (7.1%). Only 1 patient (7.1%) had mRS \leq 2.

Among 82 patients with patent carotid stents at day 1, in 54 cases (65.8%), DAPT could be initiated at day 1 and continued without interruptions. In the remaining 28 cases (34.1%), DAPT was either not initiated at day 1 or was discontinued thereafter.

After further exclusion of cases without further controls of stent patency beyond day 1 or after DAPT discontinuation, the first group of 50 patients without interruptions in postprocedural DAPT was compared with the second group of 22 patients with absent or discontinued postprocedural DAPT.

A comparison of baseline characteristics, procedural metrics, and outcomes across the 2 groups is detailed in the Online

Supplemental Data. Patients with absent/discontinued DAPT had significantly longer onset-to-femoral puncture times, lower ASPECTSs, more frequent hemorrhagic transformation, and less favorable clinical outcomes. All these differences can be explained by the selection process: The main reason for avoiding DAPT was hemorrhagic transformation. Late time window treatment and lower baseline ASPECTS are known predictors of hemorrhagic transformation, while hemorrhagic transformation itself is a known predictor of worse clinical outcomes.

The Table details antiplatelet regimen variations within the group of 22 cases with absent/discontinued DAPT. Most frequently, DAPT was avoided because of hemorrhagic transformation of ischemic stroke (68.1%), followed by subarachnoid hemorrhage (9.1%) and decompressive craniectomy (13.6%). Nine patients (40.9%) never received DAPT, while for the remaining 13 (59.1%), DAPT was discontinued for varying periods (median, 9 days; interquartile range, 5–12 days). In total, we observed 88 patient days without any antiplatelet treatment and 471 patient days with single-antiplatelet treatment. The median stent patency follow-up duration in this group was 57 days (interquartile range, 35–125 days).

There was no significant difference in the rate of subacute/late stent thrombosis between the 2 groups: 1/50 (2%) in patients with continuous DAPT versus 0/22 (0%) in patients with absent/discontinued DAPT ($P=1.000$).

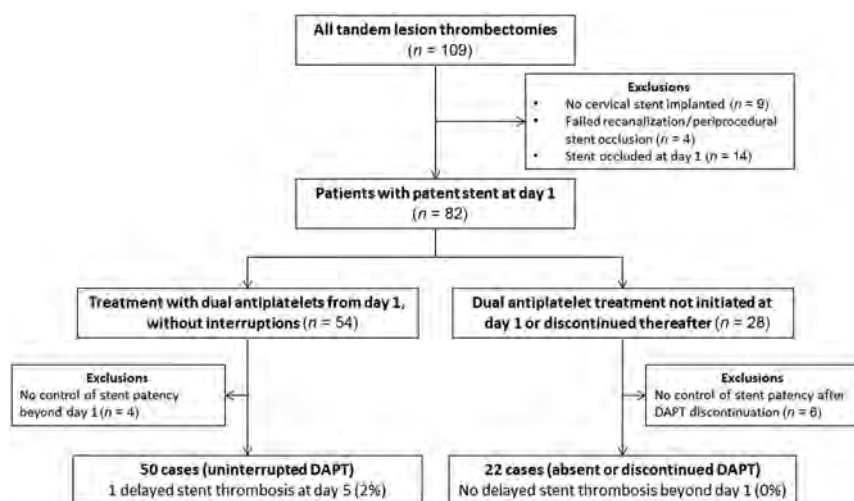


FIGURE. Patient-selection diagram.

Description of patients with absent/discontinued dual-antiplatelet treatment

	DAPT Not Initiated at Day 1 or Discontinued Thereafter (n = 22)
Antiplatelet regimen	
Never received DAPT (No) (%)	9/22 (40.9%)
Patient days without antiplatelet treatment	71
Patient days with single antiplatelet treatment	355
Discontinued DAPT (No) (%)	13/22 (59.1%)
Duration without DAPT (median) (IQR) (day)	9 (5–12)
Patient days without antiplatelet treatment	17
Patient days with single antiplatelet treatment	116
Total	
Patient days without antiplatelet treatment	88
Patient days with single antiplatelet treatment	471
Reason for avoiding DAPT (No) (%)	
Hemorrhagic transformation of ischemic stroke	15 (68.1%)
Subarachnoid hemorrhage	2 (9.1%)
Decompressive craniectomy	3 (13.6%)
Gastrointestinal bleeding ^a	2 (9.1%)
Planned interventional/surgical procedure ^b	2 (9.1%)
Lack of naso-/orogastric access	1 (4.5%)
Duration of stent patency follow-up (median) (IQR) (day)	57 (35–125)
Stent occlusion beyond day 1 (No) (%)	0 (0%)

Note:—IQR indicates interquartile range.

^a One patient had both SAH and gastrointestinal bleeding; the second patient had both hemorrhagic transformation and gastrointestinal bleeding.

^b One patient had both hemorrhagic transformation and a surgical procedure.

DISCUSSION

To the best of our knowledge, this is the first study to specifically assess the risk of subacute/late stent thrombosis beyond postprocedural day 1 in patients treated with emergent carotid stent placement for acute stroke with tandem lesions. The 3 main findings of this work are as follows: 1) Postprocedural DAPT is frequently discontinued in this population; 2) subacute/late stent thrombosis is much less frequent than early stent thrombosis (during the first 24 hours); and 3) discontinuation of postprocedural DAPT does not seem to be associated with an increased risk of stent thrombosis.

In a previous publication,⁷ we analyzed predictors of postprocedural stent thrombosis in 73 patients. We observed 14 cases (19.1%) of stent thrombosis, most of which (13/14,

92.8%) occurred during the first 24 hours. Due to this finding, we hypothesized that the highest risk of stent thrombosis is observed during the first 24 hours. To further assess the real frequency of stent thrombosis in the subacute/late phase (beyond day 1), in the present study, we focused exclusively on patients with a patent stent at day 1. Although a multivariate analysis to identify predictors of late stent thrombosis was planned, this was not feasible due to the very low number of detected events. In the cardiology literature,²⁰ the timing of coronary stent thrombosis (ST) is delineated as follows: early ST (acute ST, between 0 and 24 hours, and subacute ST, 24 hours to 30 days), late ST (between 30 days and 1 year), and very late ST (>1 year). Given the very low rate of stent thrombosis observed beyond the first 24 hours, we chose to simplify the classification of carotid stent thrombosis into 2 categories: early ST (first 24 hours) and subacute/late ST (beyond day 1).

Few published studies have reported stent patency rates for a large proportion of patients in their cohort.^{8,12–14,17} The time point of stent thrombosis (early versus subacute/late) is not listed in most of these studies. Malik et al¹⁶ reported 24-hour imaging follow-up of stent patency for all 77 patients in their cohort, with only 1 (1.2%) thrombosed stent. Long-term stent patency follow-up was available in only 27 patients, with an in-stent restenosis rate of 2/27 (7.4%). Postprocedural antiplatelet regimen variations were not listed. Renú et al⁸ reported a stent occlusion rate of 22% at 24 hours in a cohort of 99 patients; however, they did not record stent patency beyond day 1. Wallocha et al⁶ reported 24-hour Doppler sonography results for all 149 patients with stents in their cohort, with 8 (5.4%) cases of stent thrombosis. Stent patency rates beyond day 1 were not listed. However, the authors did offer details on postprocedural antiplatelet regimen variations; 32.2% of patients received only a single antiplatelet agent, 3.3%, no antiplatelet agent. The duration of DAPT discontinuation was not provided; however, this relatively high proportion of patients who did not receive postprocedural DAPT is concordant with the findings in our study.

That postprocedural DAPT discontinuation was not associated with an increased risk of stent thrombosis is surprising. In the cardiology literature, early antiplatelet therapy discontinuation was identified as a prevalent and consistent, significant predictor of coronary stent thrombosis.²⁰ However, the comparison with our clinical setting is limited by significant differences in vessel size and morphology, types of stents, and local hemodynamic conditions. One possible explanation might be that the overall percentages of late stent thrombosis are very low, either with or without continuous postprocedural DAPT. To detect a small difference between the 2 groups, a very large sample size would be needed; thus, the negative result of the present study could represent a type II error. Nevertheless, the low rate of late stent thrombosis in itself (1/72, 1.3% for our entire cohort) could prove useful for decision-making in the clinical setting. There are no established criteria for withholding DAPT, and often the decisions are based on a subjective evaluation of the extent of hemorrhagic transformation. Given the overall low likelihood of carotid stent thrombosis, clinicians could probably use a low threshold to temporarily withhold DAPT in patients with concomitant hemorrhagic events.

In view of the worse clinical outcomes for patients with discontinued DAPT, an alternative hypothesis is that interruption of

DAPT could cause thromboembolic events short of stent occlusion. In the Safety and Efficacy Study for Reverse Flow Used During Carotid Artery Stenting Procedure (ROADSTER II) trial,²¹ a report on elective transcatheter artery revascularization, the investigators blamed most of their strokes on discontinuation of DAPT. In the current study, because the group with discontinued DAPT did clinically worse mostly because of factors related to the index stroke and complications, it is not feasible to discern this effect.

Of note, the only case of late stent thrombosis observed in our study occurred at day 5 postthrombectomy in a patient treated with continuous DAPT from day 1. A Casper stent (MicroVention) was placed and then subsequently had to be covered with a second stent (Wallstent; Boston Scientific) due to malapposition in the carotid bifurcation. The presence of 3 layers of metal mesh, in addition to the initial stent malapposition, most likely played a principal role in the subsequent stent thrombosis in this case; however, clopidogrel resistance was not tested and might also have been a contributing factor.

Currently, there is no consensus on the optimal duration of postprocedural DAPT; available data in the literature reveal a large variation in practices, ranging from 4 to 12 weeks.^{6,9} If the findings of our current study are confirmed in larger cohorts, in light of the low frequency of subacute/late stent thrombosis and the likely small additional benefit of DAPT versus single antiplatelet agent beyond the first 24 hours, the recommended duration of postprocedural DAPT could potentially be shortened in patients with higher neurologic or systemic hemorrhagic risk.

The present study has 2 main strengths. First, it included all consecutive cases of tandem lesion stroke thrombectomies performed during a long time interval. Second, all patients benefited from stent patency imaging at day 1, and most patients also had further controls during follow-up. This process allowed differentiation between early and subacute/late stent thrombosis. However, several limitations also need to be considered when interpreting the current data: most important, the retrospective study design, all patients being treated in a single center, and the reduced statistical power due to overall cohort size and the relatively small number of cases in the group with discontinued postprocedural DAPT. Moreover, a quarter of the patients with discontinued DAPT were followed for <35 days. Hence, they did not have the usual 1-month follow-up standard for determining stent patency as in carotid stent trials; thus, some cases of subacute stent thrombosis might have gone undetected.

CONCLUSIONS

In this study of consecutive patients treated with emergent carotid stent placement during tandem lesion stroke thrombectomy, stent thrombosis beyond the first 24 hours was rare. Despite postprocedural DAPT being frequently discontinued in this population, this outcome was not associated with an increased risk of stent thrombosis. Further studies are warranted to better assess the additional benefit and the optimal duration of DAPT versus a single-antiplatelet agent beyond the first 24 hours postthrombectomy.

REFERENCES

1. Rubiera M, Ribo M, Delgado-Mederos R, et al. **Tandem internal carotid artery/middle cerebral artery occlusion: an independent predictor of poor outcome after systemic thrombolysis.** *Stroke* 2006;37:2301–05 CrossRef Medline
2. Papanagiotou P, Haussen DC, Turjman F, et al; TITAN Investigators. **Carotid stenting with antithrombotic agents and intracranial thrombectomy leads to the highest recanalization rate in patients with acute stroke with tandem lesions.** *JACC Cardiovasc Interv* 2018;11:1290–99 CrossRef Medline
3. Dufort G, Chen BY, Jacquin G, et al. **Acute carotid stenting in patients undergoing thrombectomy: a systematic review and meta-analysis.** *J Neurointerv Surg* 2020 Jun 12. [Epub ahead of print] CrossRef Medline
4. Zhu F, Hossu G, Soudant M, et al. **Effect of emergent carotid stenting during endovascular therapy for acute anterior circulation stroke patients with tandem occlusion: a multicenter, randomized, clinical trial (TITAN) protocol.** *Int J Stroke* 2020 Jun 9. [Epub ahead of print] CrossRef Medline
5. Fahed R, Redjem H, Blanc R, et al. **Endovascular management of acute ischemic strokes with tandem occlusions.** *Cerebrovasc Dis* 2016;41:298–305 CrossRef Medline
6. Wallocha M, Chapot R, Nordmeyer H, et al. **Treatment methods and early neurologic improvement after endovascular treatment of tandem occlusions in acute ischemic stroke.** *Front Neurol* 2019;10:127 CrossRef Medline
7. Pop R, Zinchenko I, Quenardelle V, et al. **Predictors and clinical impact of delayed stent thrombosis after thrombectomy for acute stroke with tandem lesions.** *AJNR Am J Neuroradiol* 2019;40:533–39 CrossRef Medline
8. Renú A, Blasco J, Laredo C, et al. **Carotid stent occlusion after emergent stenting in acute ischemic stroke: incidence, predictors and clinical relevance.** *Atherosclerosis* 2020;313:8–13 CrossRef Medline
9. Behme D, Mpotsaris A, Zeyen P, et al. **Emergency stenting of the extracranial internal carotid artery in combination with anterior circulation thrombectomy in acute ischemic stroke: a retrospective multicenter study.** *AJNR Am J Neuroradiol* 2015;36:2340–44 CrossRef Medline
10. Maurer CJ, Joachimski F, Berlis A. **Two in one: endovascular treatment of acute tandem occlusions in the anterior circulation.** *Clin Neuroradiol* 2015;25:397–402 CrossRef Medline
11. Grigoryan M, Haussen DC, Hassan AE, et al. **Endovascular treatment of acute ischemic stroke due to tandem occlusions: large multicenter series and systematic review.** *Cerebrovasc Dis* 2016;41:306–12 CrossRef Medline
12. Heck DV, Brown MD. **Carotid stenting and intracranial thrombectomy for treatment of acute stroke due to tandem occlusions with aggressive antiplatelet therapy may be associated with a high incidence of intracranial hemorrhage.** *J Neurointerv Surg* 2015;7:170–75 CrossRef Medline
13. Lockau H, Liebig T, Henning T, et al. **Mechanical thrombectomy in tandem occlusion: procedural considerations and clinical results.** *Neuroradiology* 2015;57:589–98 CrossRef Medline
14. Steglich-Arnholm H, Holtmannspotter M, Kondziella D, et al. **Thrombectomy assisted by carotid stenting in acute ischemic stroke management: benefits and harms.** *J Neurol* 2015;262:2668–75 CrossRef Medline
15. Gory B, Haussen DC, Piotin M, et al; Thrombectomy In TANdem lesions (TITAN) investigators. **Impact of intravenous thrombolysis and emergent carotid stenting on reperfusion and clinical outcomes in acute stroke patients with tandem lesion treated with thrombectomy: a collaborative pooled analysis.** *Eur J Neurol* 2018;25:1115–20 CrossRef Medline
16. Malik AM, Vora NA, Lin R, et al. **Endovascular treatment of tandem extracranial/intracranial anterior circulation occlusions: preliminary single-center experience.** *Stroke* 2011;42:1653–57 CrossRef Medline
17. Neuberger U, Moteva K, Vollherbst DF, et al. **Tandem occlusions in acute ischemic stroke – impact of antithrombotic medication and complementary heparin on clinical outcome and stent patency.** *J Neurointerv Surg* 2020;12:1088–93 CrossRef Medline
18. Legrand L, Tisserand M, Turc G, et al. **Do FLAIR vascular hyperintensities beyond the DWI lesion represent the ischemic penumbra?** *AJNR Am J Neuroradiol* 2015;36:269–74 CrossRef Medline
19. Hacke W, Kaste M, Bluhmki E, et al; ECASS Investigators. **Thrombolysis with alteplase 3 to 4.5 hours after acute ischemic stroke.** *N Engl J Med* 2008;359:1317–29 CrossRef Medline
20. D'Ascenzo F, Bollati M, Clementi F, et al. **Incidence and predictors of coronary stent thrombosis: evidence from an international collaborative meta-analysis including 30 studies, 221,066 patients, and 4276 thromboses.** *Int J Cardiol* 2013;167:575–84 CrossRef Medline
21. Kashyap VS, Schneider PA, Foteh M, et al; ROADSTER 2 Investigators. **Early outcomes in the ROADSTER 2 study of transcarotid artery revascularization in patients with significant carotid artery disease.** *Stroke* 2020;51:2620–29 CrossRef Medline

The Challenge of an Acute Antithrombotic Regimen for Treatment of Tandem Lesions Stroke

In the treatment of tandem stroke, several studies have shown the efficacy and safety of endovascular treatment. However, there are many unanswered questions regarding this treatment strategy including technical aspects as well as peri- and postprocedural antithrombotic management. The extracranial lesion is usually treated by acute stent placement, but balloon angioplasty can be performed as an alternative. Data from the TITAN Registry and German Stroke Registry support that acute stent placement is associated with a better clinical outcome compared with balloon angioplasty in treating extracranial lesions.^{1,2} The main disadvantage of acute stent placement is the potential risk for stent thrombosis with re-occlusion of the internal carotid artery.

In the current issue of *AJNR*, Pop et al³ report 2 important findings regarding acute stent placement in tandem lesions. First, the rate of stent thrombosis was not insignificant, with a frequency of 14.5%. Although data from large registries regarding stent patency are limited, other authors report the thrombosis risk after acute stent placement as up to 45%.⁴ The second important finding was that the highest risk of stent thrombosis was observed during the first 24 hours, and stent thrombosis beyond the first day was rare. Both findings suggest that the current acute antithrombotic regimen is not appropriate for preventing acute stent thrombosis.

The major questions that arise are: 1) Can we avoid acute stent thrombosis? 2) Can the acute antithrombotic regimen be improved? and 3) Can we be more aggressive with the antithrombotic medication in the acute phase? A more aggressive scheme is not without risks, as additional antithrombotic agents may increase the risk of intracerebral hemorrhagic complications, which is the major concern in the endovascular treatment of acute stroke. Therefore, properly calibrating the acute antithrombotic regimen in tandem stroke remains an important challenge.

There are heterogeneous antithrombotic regimens in use by various interventionalists and centers, which limits our complete understanding of this topic. We do not know which agents and what dosing should be applied in the acute setting. What we do know is that an antiplatelet agent is necessary for peri-interventional care to avoid stent occlusion. Platelets are now known to have a pivotal role in thrombosis and inflammation after vessel injury.⁵ Some patients receive antiplatelet agents with their pre-stroke medication. These patients are likely to be at low risk of stent thrombosis, and therefore, an aggressive antiplatelet strategy could be avoided. In the remaining patients, acute peri-

interventional antiplatelet agents should be applied to prevent stent thrombosis. Agents that can be used include intravenous aspirin, clopidogrel, ticagrelor, and glycoprotein IIb/IIIa inhibitors (GPIs), or the new drug, cangrelor. Aspirin and clopidogrel inhibit 2 vital pathways of platelet activation; however, this effect does not occur immediately after usage. In contrast, GPIs directly block the most abundant receptor on the platelet surface and are highly effective. Although, if given at full dosage, a substantially increased risk of bleeding is known to occur with GPIs.⁶

The high rate of acute stent thrombosis in treatment of tandem lesions stroke highlights the challenge of acute antiplatelet therapy. Future studies should focus on establishing an optimal antithrombotic regimen.

REFERENCES

1. Papanagiotou P, Haussen DC, Turjman F, et al. **Carotid stenting with antithrombotic agents and intracranial thrombectomy leads to the highest recanalization rate in patients with acute stroke with tandem lesions.** *JACC Cardiovasc Interv* 2018;11:1290–99 CrossRef Medline
2. Feil K, Herzberg M, Dorn F, et al. **Tandem lesions in anterior circulation stroke: analysis of the German stroke registry-endovascular treatment.** *Stroke* 2021 Feb 21 [Epub ahead of print] CrossRef Medline
3. Pop R, Hasiu A, Mangin PH, et al. **Postprocedural antiplatelet treatment after emergent carotid stenting in tandem lesions stroke: impact on stent patency beyond day 1.** *AJNR Am J Neuroradiol* 2021;42:921–25 CrossRef Medline
4. Yilmaz U, Körner H, Mühl-Benninghaus R, et al. **Acute occlusions of dual-layer carotid stents after endovascular emergency treatment of tandem lesions.** *Stroke* 2017;48:2171–75 CrossRef Medline
5. Prasad A, Herrmann J. **Myocardial infarction due to percutaneous coronary intervention.** *N Engl J Med* 2011;364:453–64 CrossRef Medline
6. Yousuf O, Bhatt DL. **The evolution of antiplatelet therapy in cardiovascular disease.** *Nat Rev Cardiol* 2011;8:547–59 CrossRef Medline

© P. Papanagiotou

Department of Radiology

Areteion University Hospital, National and Kapodistrian University of Athens
Athens, Greece

Department of Diagnostic and Interventional Neuroradiology
Hospital Bremen-Mitte
Bremen, Germany

© B. Gory

Department of Diagnostic and Therapeutic Neuroradiology
Université de Lorraine
Nancy, France

<http://dx.doi.org/10.3174/ajnr.A7122>

Diagnosing Carotid Near-Occlusion with Phase-Contrast MRI

E. Johansson, L. Zarrinkoob, A. Wåhlin, A. Eklund, and J. Malm



ABSTRACT

SUMMARY: Carotid near-occlusion is a frequently overlooked diagnosis when CTA examinations are assessed in routine practice. To evaluate the potential value of phase-contrast MR imaging in identifying near-occlusion, we examined 9 carotid near-occlusions and 20 cases of conventional $\geq 50\%$ carotid stenosis (mean stenosis degree, 65%) with phase-contrast MR imaging. Mean ICA flow was lower in near-occlusions (52 mL/min) than in conventional $\geq 50\%$ stenosis (198 mL/min, $P < .001$). ICA flow of ≤ 110 mL/min was 100% sensitive and specific for near-occlusion. Phase-contrast MR imaging is a promising tool for diagnosing carotid near-occlusion.

ABBREVIATION: PC = phase-contrast

Carotid near-occlusion is a severe carotid stenosis associated with a reduction (collapse) of the extracranial ICA distal to the stenosis.¹⁻⁴ The collapse can be severe (near-occlusion with full collapse; Fig 1A) or subtle (near-occlusion without full collapse; Fig 1B).¹⁻⁴ Separating symptomatic near-occlusions and conventional stenoses is crucial because their recommended treatments often differ.^{5,6}

Near-occlusion is diagnosed by assessing several features on angiography (such as conventional angiography or CTA). Although the feature assessments are reliable among collaborating experts,⁴ implementation in routine practice can be challenging because expertise and feature synthesis likely vary among observers.⁷ Near-occlusion is presumed to be a marker of reduced flow.² Carotid sonography has poor diagnostic performance because there is a nonlinear relationship between the degree of

stenosis and flow velocity in stenosis.^{8,9} Phase-contrast (PC) MR imaging to assess ICA flow might be useful because it is based on flow, but no PC MR imaging study has assessed ICA flow in near-occlusion.

The aim of this study was to compare ICA flow in carotid near-occlusion and conventional $\geq 50\%$ stenosis.

MATERIALS AND METHODS

Patients with symptomatic or asymptomatic $\geq 50\%$ carotid stenosis at the University Hospital of Northern Sweden were included. Clinical exclusion criteria were atrial fibrillation, any previous central nervous system diseases, mRS ≥ 3 , Mini-Mental State Examination score of < 23 , an inability to walk unassisted, severe aphasia, or contraindications for MR imaging. Imaging exclusions were any ICA occlusion, intracranial carotid stenosis, uncertainty about whether the index stenosis was conventional or near-occlusion ($n = 3$), and delay between CTA and MR imaging of > 35 days. The study was approved by the regional ethics board in Umeå. All patients provided informed consent.

CTA

See the Online Supplemental Data for protocol details. All CTAs were evaluated by 1 observer, and a subset ($n = 20$) was also evaluated by a second observer. Both observers had near-occlusion expertise and were blinded to each other and to flow data. Disagreements were resolved by consensus discussion. Near-occlusion was diagnosed when a severe stenosis was associated with reduction in the distal ICA diameter, as presented elsewhere.^{4,10,11} The definition of full collapse and acknowledging circle of Willis variants are presented elsewhere.^{4,10} In cases without near-occlusion, the degree of stenosis was calculated with the

Received September 16, 2020; accepted after revision December 7.

From the Department of Clinical Science (E.J., L.Z., J.M.), Neurosciences; Wallenberg Center for Molecular Medicine (E.J.); Departments of Perioperative Sciences (L.Z.) and Radiation Sciences (A.W., A.E.); and Umeå Center for Functional Brain Imaging (A.W., A.E.), Umeå University, Umeå, Sweden.

The study was funded by the Swedish Research Council, grant Nos. 2015–05616; 2017–04949; the Knut and Alice Wallenberg Foundation; Region Västerbotten, the Swedish Heart and Lung Foundation, grant No. 20140592; the research fund for neurologic research at the University Hospital of Northern Sweden; the Swedish Stroke Fund; the Northern Swedish Stroke Fund; and the Swedish Medical Association.

Paper previously presented at: Annual Meeting of the European Society of Neuroradiology, October 5–9, 2020; Virtual.

Please address correspondence to Elias Johansson, MD, Department of Clinical Science, Neurosciences, Umeå University, 901 87, Umeå, Sweden; e-mail: elias.johansson@umu.se

Indicates open access to non-subscribers at www.ajnr.org

Indicates article with online supplemental data.

<http://dx.doi.org/10.3174/ajnr.A7076>

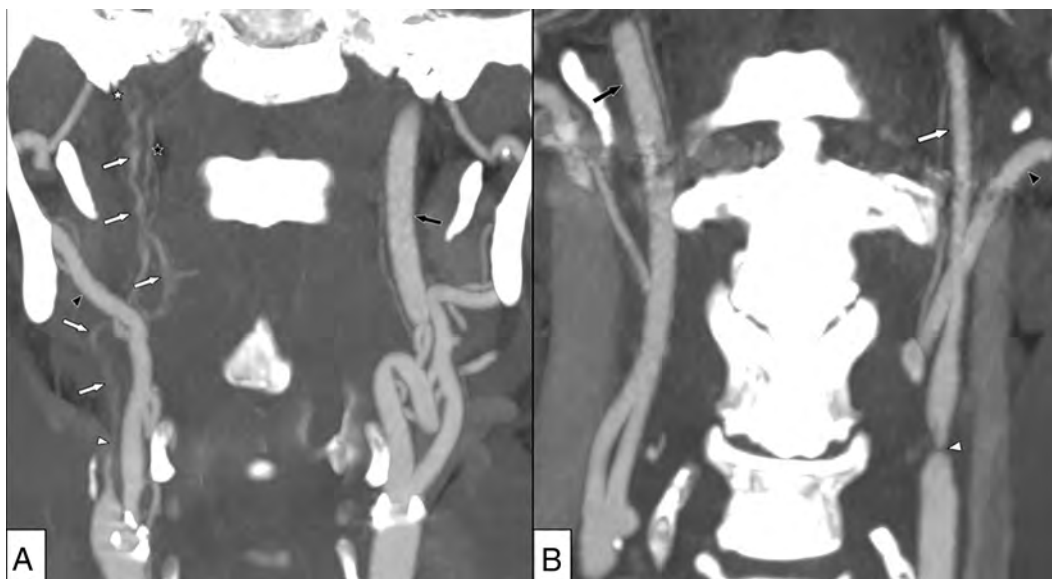


FIG 1. A, Right-sided near-occlusion with full collapse. Coronal view of CTA. Beyond severe stenosis (white arrowhead), distal ICA is difficult to visualize and has a threadlike appearance (white arrows). The distal ICA is clearly smaller than both the contralateral ICA (black arrow) and ipsilateral external carotid artery (black arrowhead) but is similar to the ascending pharyngeal artery (black star). A thrombus just proximal to the skull base is suspected (white star). ICA flow was 6 mL/min on the right side and 267 mL/min on the left side. B, Left-sided near-occlusion without full collapse. Coronal view of CTA. After severe stenosis (white arrowhead), the distal ICA is small but normal-appearing (white arrow), smaller than the contralateral ICA (black arrow), and similar to the ipsilateral external carotid artery (black arrowhead). ICA flow was 37 mL/min on the left side and 259 mL/min on the right side.

NASCET approach, comparing stenosis diameter with distal ICA well beyond the stenosis.

Phase-Contrast MR Imaging

A 3T MR imaging scanner (Discovery MR 750; GE Healthcare) with a 32-channel head coil was used. 4D PC MR images were gathered and analyzed with in-house software similar to a recent study (Online Supplemental Data).^{12,13} Two observers blinded to CTA findings and each other extracted flow data from both extracranial ICAs just below the skull base in all cases. The mean value between the 2 observers was used for main calculations. When the observers differed >20%, consensus measurements were performed. Each observer's measurements were also analyzed.

Analyses

Patients were categorized by CTA into conventional $\geq 50\%$ stenosis and near-occlusion. Flow rates in the ICA were compared between stenosis groups, degrees of stenosis, and CTA measurements. Relative flow and area were calculated as ipsilateral/(ipsilateral + contralateral). We used mean, SD, a 2-sided χ^2 test, a t test, linear regression, a receiver operating characteristic curve, κ analysis, and intraclass correlation. The 95% confidence intervals for correlation (r) were calculated with z scores. $P < .05$ was prespecified as statistically significant. We used SPSS 24.0 (IBM) for all calculations.

RESULTS

In total, we included 29 patients: Twenty (69%) had conventional $\geq 50\%$ stenosis, and 9 (31%) had near-occlusion. Baseline characteristics were similar ($P \geq .13$) in both groups: The mean age was 73 years, 24% were women, the mean delay between examinations was 6 days, and 86% had symptomatic stenosis. Among the

conventional stenoses, the mean stenosis degree was 65%, 8 were $\geq 70\%$, and the remaining degrees were 50%–69%. Two cases of conventional stenoses had asymmetric distal ICAs, best explained by circle of Willis asymmetry. Eight cases had bilateral $\geq 50\%$ stenosis, but there were no cases with bilateral near-occlusion.

The mean ICA flow was lower in near-occlusions (52 mL/min) than in conventional $\geq 50\%$ stenosis (198 mL/min, $P < .001$). The mean relative ICA flow was lower in near-occlusions (16%) than in conventional $\geq 50\%$ stenosis (48%, $P < .001$). Neither parameter had overlap between the groups (Online Supplemental Data). Thus, several thresholds, such as ICA flow ≤ 110 mL/min and relative flow $< 35\%$, were 100% sensitive and specific for near-occlusion. One case had near-occlusion with full collapse, with a 6 mL/min ICA flow.

Among the 20 patients with conventional $\geq 50\%$ stenosis, there was no correlation between percentage degree of stenosis and ICA flow ($r = 0.06$; 95% CI, -0.44 – 0.55 ; $P = .81$). There was no difference in the mean ICA flow between the 12 patients with 50%–69% stenoses (199 mL/min) and the 8 patients with $\geq 70\%$ stenoses (197 mL/min, $P = .90$). However, when analyzing all 29 patients, there was a correlation between stenosis diameter and ICA flow ($r = 0.68$; 95% CI, 0.39 – 0.96 ; $P < .001$). A similar correlation was noted for the ipsilateral distal ICA area and ipsilateral ICA flow ($r = 0.69$; 95% CI, 0.42 – 0.96 ; $P < .001$). Relative distal ICA area and relative ICA flow were even more strongly correlated ($r = 0.90$; 95% CI, 0.74 – 1.00 ; $P < .001$). Please see the Online Supplemental Data for figures of these regression analyses.

Overall agreement between the blinded CTA observers was 96% (1 disagreement over whether there was occlusion), and interrater reliability was $\kappa = 0.78$. The 2 PC MR imaging observers had a consensus discussion over 17 (29%) neck sides but 100% agreement

as to whether ICA flow and relative ICA flow were above or below the proposed diagnostic thresholds (110 mL/min and 35%, respectively), and the intraclass correlation coefficient was 0.96 (Online Supplemental Data).

DISCUSSION

The main findings of this study were that carotid near-occlusions had low ipsilateral ICA flow, whereas conventional $\geq 50\%$ carotid stenoses had no correlation between the degree of stenosis and ICA flow ($r = 0.06$). Flow was correlated with stenosis diameter and distal ICA area, both hallmarks of near-occlusion.

No single feature in CTA is both $>90\%$ sensitive and specific for near-occlusion; thus, several features are used for angiographic diagnosis.^{3,11} Flow measurement seems more accurate, but a larger sample will be needed for a relevant assessment. According to guidelines, patients with symptomatic conventional stenosis should be treated with revascularization.^{5,6} However, patients with symptomatic near-occlusions should not be treated with revascularization⁶ or only treated after careful consideration in cases with recurrent events despite optimal medical therapy.⁵ To separate conventional stenosis and near-occlusion, there might be a role for PC MR imaging in routine carotid stenosis diagnostics after the stenosis has been identified by another technique. See the Online Supplemental Data for details on PC MR imaging literature. The association between near-occlusion and flow might also improve understanding of prognostics^{4,14} and sonography findings^{8,15} in near-occlusion. Other PC MR imaging techniques (2D and 3D) are likely to produce similar results, but they should be evaluated.

The concepts of near-occlusion and conventional stenoses are limited to NASCET grading. If near-occlusions are not recognized, percentage grading with NASCET leads to stenosis underestimation. Stenosis diameter was correlated with flow, as expected from the Spencer curve model.⁹ However, the Spencer model assumes a stable denominator,⁹ which is not the case in NASCET grading. When stenoses were graded with the NASCET method, only near-occlusions affected flow, not the conventional stenoses regardless of percentage grade. The ICA flow of conventional stenoses was rather similar in healthy elderly.¹³

This work has several limitations: The sample size was small. The near-occlusion prevalence (31%) might be perceived to be high but was similar (27%) to that in a recent larger study using the same diagnostic approach.⁴ We excluded cases with contralateral occlusion and those that were unclear as to whether the degree of stenosis was conventional $\geq 50\%$ stenosis or near-occlusion. Thus, although the results are promising, large studies and studies dedicated to the cases now excluded and bilateral near-occlusion are warranted.

CONCLUSIONS

When we used NASCET-grading, only near-occlusions had a reduced ICA flow, while ICA flow was not affected by conventional stenoses. Because near-occlusion has a different clinical management than conventional stenosis and near-occlusion is difficult to diagnose with CTA, there is support for including ICA PC MR imaging in the imaging protocol for patients with ICA stenosis.

ACKNOWLEDGMENTS

We want to thank Dr Allan J. Fox for help with CTA interpretations and assistance with manuscript preparations, including details about NASCET grading methodology.

Disclosures: Elias Johansson—RELATED: Grant: several grants to my institution, listed in funding section*; UNRELATED: Royalties: Studentlitteratur, Comments: 2 book chapters in 2014 in a medical textbook on stroke; generates annual royalties. Anders Eklund—RELATED: Grant: Swedish Research Council.* *Money paid to the institution.

REFERENCES

1. Johansson E, Fox AJ. **Carotid near-occlusion: a comprehensive review, Part 1: definition, terminology, and diagnosis.** *AJNR Am J Neuroradiol* 2016;37:2–10 CrossRef Medline
2. Johansson E, Fox AJ. **Carotid near-occlusion: a comprehensive review, Part 2: prognosis and treatment, pathophysiology, confusions, and areas for improvement.** *AJNR Am J Neuroradiol* 2016;37:200–04 CrossRef Medline
3. Fox AJ, Eliasziw M, Rothwell PM, et al. **Identification, prognosis, and management of patients with carotid artery near occlusion.** *AJNR Am J Neuroradiol* 2005;26:2086–94 Medline
4. Gu T, Aviv RI, Fox AJ, et al. **Symptomatic carotid near-occlusion causes a high risk of recurrent ipsilateral ischemic stroke.** *J Neurol* 2020;267:522–30 CrossRef Medline
5. Naylor AR, Ricco JB, de Borst GJ, et al. **Management of Atherosclerotic Carotid and Vertebral Artery Disease: 2017 Clinical Practice Guidelines of the European Society for Vascular Surgery (ESVS).** *Eur J Vasc Endovasc Surg* 2018;55:3–81 CrossRef Medline
6. Brott TG, Halperin JL, Abbara S, et al. Society for Vascular Surgery. **ASA/ACCF/AHA/AANN/AANS/ACR/ASNR/CNS/SAIP/SCAI/SIR/SNIS/SVM/SVS Guideline on the Management of Patients with Extracranial Carotid and Vertebral Artery Disease.** *Circulation* 2011;124:e54–130 CrossRef Medline
7. Johansson E, Gu T, Aviv RI, et al. **Carotid near-occlusion is often overlooked when CT-angiography is assessed in routine practice.** *Eur Radiol* 2020;30:2543–51 CrossRef Medline
8. Khangure SR, Benhabib H, Machnowska M, et al. **Carotid near-occlusion frequently has high peak systolic velocity on Doppler ultrasound.** *Neuroradiology* 2018;60:17–25 CrossRef Medline
9. Spencer MP, Reid JM. **Quantitation of carotid stenosis with continuous-wave (C-W) Doppler ultrasound.** *Stroke* 1979;10:326–30 CrossRef Medline
10. Johansson E, Aviv RI, Fox AJ. **Atherosclerotic ICA stenosis coincidental with ICA asymmetry associated with circle of Willis variations can mimic near-occlusion.** *Neuroradiology* 2020;62:101–04 CrossRef Medline
11. Bartlett ES, Walters TD, Symons SP, et al. **Diagnosing carotid stenosis near-occlusion by using CT angiography.** *AJNR Am J Neuroradiol* 2006;27:632–37 Medline
12. Zarrinkoob L, Wåhlin A, Ambarki K, et al. **Blood flow lateralization and collateral compensatory mechanisms in patients with carotid artery stenosis.** *Stroke* 2019;50:1081–88 CrossRef Medline
13. Zarrinkoob L, Ambarki K, Wåhlin A, et al. **Blood flow distribution in cerebral arteries.** *J Cereb Blood Flow Metab* 2015;35:648–54 CrossRef Medline
14. Johansson E, Öhman K, Wester P. **Symptomatic carotid near-occlusion with full collapse might cause a very high risk of stroke.** *J Intern Med* 2015;277:615–23 CrossRef Medline
15. Johansson E, Benhabib H, Herod W, et al. **Carotid near-occlusion can be identified with ultrasound by low flow velocity distal to the stenosis.** *Acta Radiol* 2019;60:396–404 CrossRef Medline

Altered Processing of Complex Visual Stimuli in Patients with Postconcussive Visual Motion Sensitivity

 J.W. Allen,  A. Trofimova,  V. Ahluwalia,  J.L. Smith,  S.A. Abidi,  M.A.K. Peters,  S. Rajananda,  J.E. Hurtado, and  R.K. Gore



ABSTRACT

BACKGROUND AND PURPOSE: Vestibular symptoms are common after concussion. Vestibular Ocular Motor Screening identifies vestibular impairment, including postconcussive visual motion sensitivity, though the underlying functional brain alterations are not defined. We hypothesized that alterations in multisensory processing are responsible for postconcussive visual motion sensitivity, are detectable on fMRI, and correlate with symptom severity.

MATERIALS AND METHODS: Twelve patients with subacute postconcussive visual motion sensitivity and 10 healthy control subjects underwent vestibular testing and a novel fMRI visual-vestibular paradigm including 30-second “neutral” or “provocative” videos. The presence of symptoms/intensity was rated immediately after each video. fMRI group-level analysis was performed for a “provocative-neutral” condition. Z-statistic images were nonparametrically thresholded using clusters determined by $Z > 2.3$ and a corrected cluster significance threshold of $P = .05$. Symptoms assessed on Vestibular Ocular Motor Screening were correlated with fMRI mean parameter estimates using Pearson correlation coefficients.

RESULTS: Subjects with postconcussive visual motion sensitivity had significantly more Vestibular Ocular Motor Screening abnormalities and increased symptoms while viewing provocative videos. While robust mean activation in the primary and secondary visual areas, the parietal lobe, parietoinsular vestibular cortex, and cingulate gyrus was seen in both groups, selective increased activation was seen in subjects with postconcussive visual motion sensitivity in the primary vestibular/adjacent cortex and inferior frontal gyrus, which are putative multisensory visual-vestibular processing centers. Moderate-to-strong correlations were found between Vestibular Ocular Motor Screening scores and fMRI activation in the left frontal eye field, left middle temporal visual area, and right posterior hippocampus.

CONCLUSIONS: Increased fMRI brain activation in visual-vestibular multisensory processing regions is selectively seen in patients with postconcussive visual motion sensitivity and is correlated with Vestibular Ocular Motor Screening symptom severity, suggesting that increased visual input weighting into the vestibular network may underlie postconcussive visual motion sensitivity.

ABBREVIATIONS: BESS = Balance Error Scoring System; DHI = Dizziness Handicap Inventory; FEF = frontal eye fields; MT/V5 = middle temporal visual area; PCSS = Post Concussion Symptom Scale; PCVMS = postconcussive visual motion sensitivity; PIVC = parietoinsular vestibular cortex; VOMS = Vestibular Ocular Motor Screening; VVAS = Visual Vertigo Analog Scale

Up to 3.8 million concussions occur annually in the United States, with estimated direct and indirect costs totaling more than \$12 billion.^{1,2} Vestibular symptoms occur in up to 80% of patients in the first few days following injury.³⁻⁵ Persistent dizziness has been reported to occur in up to one-third of postconcussive patients reporting acute vestibular symptoms, and a positive

Vestibular Ocular Motor Screening (VOMS) outcome is associated with protracted recovery.^{3,6,7} The link between visual and vestibular motion-processing is critical for spatial orientation and balance control, and oculomotor dysfunction, balance, and vestibular

Received September 3, 2020; accepted after revision November 16.

From the Departments of Radiology and Imaging Sciences (J.W.A., A.T., J.L.S.) and Neurology (J.W.A.) and School of Medicine (S.A.A.), Emory University, Atlanta, Georgia; Wallace H. Coulter Department of Biomedical Engineering (J.W.A., R.K.G.), Georgia Institute of Technology and Emory University, Atlanta, Georgia; Georgia State University/Georgia Tech Center for Advanced Brain Imaging (V.A.), Atlanta, Georgia; Department of Bioengineering (M.A.K.P., S.R.), University of California, Riverside, Riverside, California; Shepherd Center (J.E.H., R.K.G.), Atlanta, Georgia; and Shepherd Center (J.E.H., R.K.G.), Atlanta, Georgia.

This work was supported by the Georgia State/Georgia Tech Center for Advanced Brain Imaging Neural Engineering Center Seed Grant and the Emory University Department of Radiology and Imaging Sciences Seed Grant.

Paper previously presented, in part, at: Annual Meeting of the American Society of Neuroradiology May 18–23, 2019; Boston, Massachusetts.

Please address correspondence to Jason W. Allen, MD, PhD, 1364 Clifton Rd, NE, Suite BG20, Atlanta, GA 30322; e-mail: jwallen@emory.edu; @jwallen_neuro

 Indicates article with online supplemental data.

<http://dx.doi.org/10.3174/ajnr.A7007>

networks share multisensory integration pathways implicated as the primary deficits in postconcussive dizziness and imbalance.⁸⁻¹¹

Similar to patients with other vestibular disorders, patients with postconcussive vestibular impairment may compensate through an increased reliance on other somatosensory input, leading to the re-weighting of sensory data including visual and vestibular cues.^{5,12-14} We hypothesized that while these changes may be beneficial in the acute phase, persistent overreliance on a specific sensory system may become pathologic and maladaptive during recovery. This may lead to persistent and debilitating dizziness syndromes such as “visual motion sensitivity,” which are characterized by inappropriate responses including disorientation, dizziness, imbalance, and headaches triggered by visual environmental motion.^{5,12}

The alterations in multisensory processing that likely underlie visual motion sensitivity are currently largely theoretic and represent an important knowledge gap in our understanding of these symptoms.¹⁵ We hypothesized that alterations in multisensory processing involving the primary vestibular cortex and associated input are responsible for postconcussive visual motion sensitivity (PCVMS). The purpose of this study was to define functional brain activation in patients with PCVMS compared with control subjects and to correlate these changes with clinical symptom severity. To this end, we have developed a novel visual-vestibular task-based fMRI paradigm, which is presented here for the first time.

MATERIALS AND METHODS

Study Population

This study was approved by the Emory University and Shepherd Center Institutional Review Boards, and all subjects provided informed consent. Twelve subjects with subacute PCVMS and 10 age-matched controls without a history of concussion or vestibular impairment were recruited. Inclusion criteria for subjects with PCVMS were a diagnosis of concussion, as defined by the World Health Organization Collaborating Center for Neurotrauma Task Force¹⁶ 2–12 weeks before enrollment; and clinical evidence of vestibular impairment, defined as a subjective report of dizziness and/or imbalance, clinical visual motion-sensitivity symptoms,¹⁷ and provocation of symptoms during VOMS.¹⁸ Exclusion criteria were being younger than 18 years of age or older than 50 years, a history of moderate or severe head injury, intracranial hemorrhage, seizure disorder, prior neurologic surgery, peripheral neuropathy, musculoskeletal injuries affecting gait and balance, and chronic drug or alcohol use. In addition, subjects with abnormal head impulse testing findings or videonystagmography consistent with peripheral vestibular hypofunction or benign paroxysmal positional vertigo were excluded.

Clinical Testing

Both groups completed the Post Concussion Symptom Scale (PCSS).¹⁹ Self-report and subjective measures included the Dizziness Handicap Inventory (DHI),²⁰ Visual Vertigo Analog Scale (VVAS),²¹ and VOMS.¹⁸ Objective measures included balance assessment with the Balance Error Scoring System (BESS),⁸ drop stick reaction time,²² and videonystagmography.

Video Optic Flow Assessment

Motion optic flow from each neutral and provocative 30-second video (defined below) was estimated using the Farneback algorithm²³ from OpenCV (Open Source Computer Vision Library). Each video was converted into gray-scale, and then a Farneback algorithm (parameters: window size = 3, levels = 1, iterations = 15, pixel neighborhood size = 3, SD of Gaussian-to-smooth derivatives used for a basis for polynomial expansion = 5) was applied. Mean flow between each pair of frames was averaged across the entire video, providing an estimate of flow. A 2 (group: PCVMS versus control) × 2 (video: provocative versus neutral) mixed-design ANOVA was used to evaluate group-level change in symptoms from baseline in response to the videos.

MR Imaging Acquisition

All MR imaging scans were acquired on a 3T Tim Trio scanner (Siemens) with a 12-channel head coil. Sequences included the following: T1-weighted 3D-MPRAGE (FOV = 256 mm, 176 slices, 1-mm³ isotropic voxels, TR = 2250 ms, TE = 3.98 ms, TI = 850 ms, flip angle = 9°), gradient-echo fieldmap (37 slices, TR = 488 ms, TE1 = 4.92 ms, TE2 = 7.38 ms, flip angle = 60°, in-plane resolution = 3 × 3 mm², section-thickness = 3 mm, gap = 0.5 mm), and task-based fMRI (37 slices, TR = 2000 ms, TE = 30 ms, flip angle = 90°, FOV = 204 mm, matrix-size = 68 × 68, in-plane resolution = 3 × 3 mm², section thickness = 3 mm, gap = 0.5 mm, generalized autocalibrating partially parallel acquisition = 2, with 603 volumes).

A novel task-based, block design visual-vestibular fMRI paradigm was developed for this study (Online Supplemental Data). Videos were chosen from our vestibular rehabilitation therapy program, which includes progressive exposure to complex visual stimuli. Provocative videos were defined as those from which patients noted an increase in headache, dizziness, nausea, or fog-giness symptoms while viewing. Subjects randomly viewed 5 provocative videos and 5 neutral videos containing nonprovocative content. Immediately after each 30-second video, subjects rated their predominant symptom followed by the symptom intensity on a 5-point Likert scale. Each question was presented for 7.5 seconds. After the 15-second question period, subjects fixated on a crosshair for 15 seconds. This process was then repeated until each subject had viewed all 10 videos.

MR Imaging Analysis

fMRI data processing was performed with FSL FEAT, Version 6.00 (<https://fsl.fmrib.ox.ac.uk/fsl/wiki/FEAT>). Prestatistics processing was applied including the following: motion correction using MCFLIRT (<https://fsl.fmrib.ox.ac.uk/fsl/wiki/MCFLIRT>);²⁴ distortion correction using Boundary-Based Registration (BBR; https://fsl.fmrib.ox.ac.uk/fsl/wiki/FLIRT_BBR) and FUGUE (<https://fsl.fmrib.ox.ac.uk/fsl/wiki/FUGUE>);^{25,26} nonbrain removal using the FSL Brain Extraction Tool (BET; <https://fsl.fmrib.ox.ac.uk/fsl/wiki/BET>);²⁷ spatial smoothing using a Gaussian kernel of full width at half maximum of 5 mm; grand mean intensity normalization of the entire 4D dataset by a single multiplicative factor; and high-pass temporal filtering (Gaussian-weighted least-squares straight line fitting, with ς = 50.0 seconds). Independent Component Analysis was performed with MELODIC (<https://fsl.fmrib.ox.ac.uk/>

Table 1: Clinical testing in patients with PCVMS and control subjects^a

	Concussed Patients	Control Subjects	P Value ^b
Subjective measurements			
PCSS	37.93 (SD, 26.61)	0.14 (SD, 0.38)	.002
DHI	44 (SD, 17.9)	0 (SD, 0)	<.001
VVAS	24.47 (SD, 28.28)	1.20 (SD, 2.10)	<.001
VOMS domain ^c			
Smooth pursuit	0.52 (SD, 0.92)	0.00 (SD, 0.00)	.003
Horizontal saccade	0.50 (SD, 1.03)	0.03 (SD, 0.16)	.004
Vertical saccade	0.77 (SD, 1.36)	0.00 (SD, 0.00)	<.001
Convergence	2.02 (SD, 2.42)	0.00 (SD, 0.00)	<.001
Horizontal vestibular ocular reflex	1.29 (SD, 1.69)	0.20 (SD, 0.76)	<.001
Vertical vestibular ocular reflex	1.13 (SD, 1.71)	0.08 (SD, 0.35)	<.001
Visual motion sensitivity	1.25 (SD, 1.97)	0.03 (SD, 0.16)	.002
Near point of convergence distance (cm)	7.74 (SD, 7.20)	2.47 (SD, 1.76)	.019
Objective measurements			
BESS	17.9 (SD, 7.35)	13.7 (SD, 4.8)	.170
Drop stick reaction time	215.6 (SD, 18.4)	184.9 (SD, 56.9)	.096

^a Patient and subject values are mean (SD).^b Mann-Whitney *U* nonparametric test or 2-tailed *t* test.^c Mean symptom intensity reported for each VOMS domain.

fsl/fslwiki/MELODIC).²⁸ Components from head motion and physiologic noise were manually identified and filtered out using the FSL_Regfilt script (<http://wikis.la.utexas.edu/imagelab/book/fsl-regfilt.html>). FLIRT (<https://fsl.fmrib.ox.ac.uk/fsl/fslwiki/FLIRT>) was used for registration to high-resolution structural and/or standard space images.^{24,29} Registration from high-resolution structural-to-standard space was further refined using FNIRT (<https://fsl.fmrib.ox.ac.uk/fsl/fslwiki/FNIRT>) nonlinear registration.^{30,31}

Time-series statistical analysis was performed on the preprocessed data using FILM (<https://fsl.fmrib.ox.ac.uk/fsl/fslwiki/FEAT>) with local autocorrelation correction.³² Regressors of interest were generated using stimulus-onset timing for provocative videos, neutral videos, and rating conditions convolved with a double- γ hemodynamic response function. Temporal derivatives of these regressors were included to achieve a better fit to the data. Confound regressors included 6 head-motion parameters and motion-outlier volumes. A contrast was defined as brain areas showing greater response to provocative videos than neutral videos (provocative-neutral). Contrast of parameter estimates from each subject were subsequently used to perform higher-level analyses carried out using FLAME (<https://fsl.fmrib.ox.ac.uk/fsl/fslwiki/FEAT>) stage 1 with automatic outlier detection.³³⁻³⁵ Group mean activation maps were generated for PCVMS and control groups. A 2-sample unpaired *t* test was performed to find differences in activation between the groups for the first-level contrast provocative-neutral. Resultant *Z* (Gaussianised *t*) statistic images were thresholded nonparametrically using clusters determined by $Z > 2.3$ and a corrected cluster significance threshold of $P = .05$.

fMRI ROIs and VOMS-fMRI Correlations

ROIs were selected from areas found to have statistically significant differences in activation between patients with PCVMS and controls as well as those that are hypothesized to be related to visual-vestibular processing.^{36,37} Spheric ROIs of 5-mm radii were created for the

following (Online Supplemental Data): the parietoinsular vestibular cortex, frontal eye fields (FEF), posterior hippocampus, middle temporal visual area (MT/V5), middle frontal gyrus, inferior frontal gyrus, and inferior parietal lobule. fMRI mean parameter estimates within each ROI for provocative-neutral contrast defined above were extracted from each subject.

VOMS testing was performed immediately before the MR imaging session and included assessment of symptoms (headache, dizziness, nausea, and foginess) at rest and after smooth pursuit, horizontal saccades, vertical saccades, near-point convergence, horizontal vestibular-ocular reflex, and visual motion-sensitivity testing. For each subject, the results of the pre-MR imaging VOMS testing were transformed as fol-

lows: 1) sum of domain scores for the initial, nonprovoked results (initial aggregate); 2) sum of domain scores on initial testing subtracted from the sum of all provocation testing conditions (Δ aggregate); 3) sum of domain scores for each individual provocation testing condition; 4) difference between the sum of domain scores on the initial and each individual provocative testing condition (Δ condition); and 5) domain score that demonstrated the highest change between initial and provocative testing (highest condition). Correlation analysis was performed between ROI brain activation and VOMS testing using the Pearson correlation coefficient, with a significance threshold of $P \leq .05$ and reported with 95% CIs.

Statistical Analysis

Unless otherwise noted, differences between groups on demographic, clinical, and video metrics were evaluated using a 2-tailed Student *t* test, χ^2 test, ANOVA, or Mann-Whitney *U* nonparametric test when appropriate. *P* values $\leq .05$ were considered statistically significant.

RESULTS

Demographic and Clinical Data

The PCVMS group consisted of 12 patients (1 male, 11 females; 29.3 [SD, 12.9] years of age with 15.8 [SD, 2.6] years of schooling) who were evaluated for vestibular impairment 2–12 weeks following a concussion (mean, 39.8 days; median, 22 days). The control group consisted of 10 patients (9 men, 1 woman; 27.5 [SD, 4.0] years of age with 19.8 [SD, 0.8] years of schooling). There was no statistically significant difference between age (2-tailed *t* test, $P = .70$) or ethnicity (χ^2 test, $P = .89$) of these 2 groups; however, both sex (2-tailed *t* test, $P < .001$) and years of schooling (2-tailed *t* test, $P < .001$) were significantly different between the groups. All subjects in both groups were right-handed.

None of the control subjects had experienced a concussion in the preceding 6 months. For the PCVMS group, 5 subjects reported a sports-related concussion; 6 subjects, a non-sports-

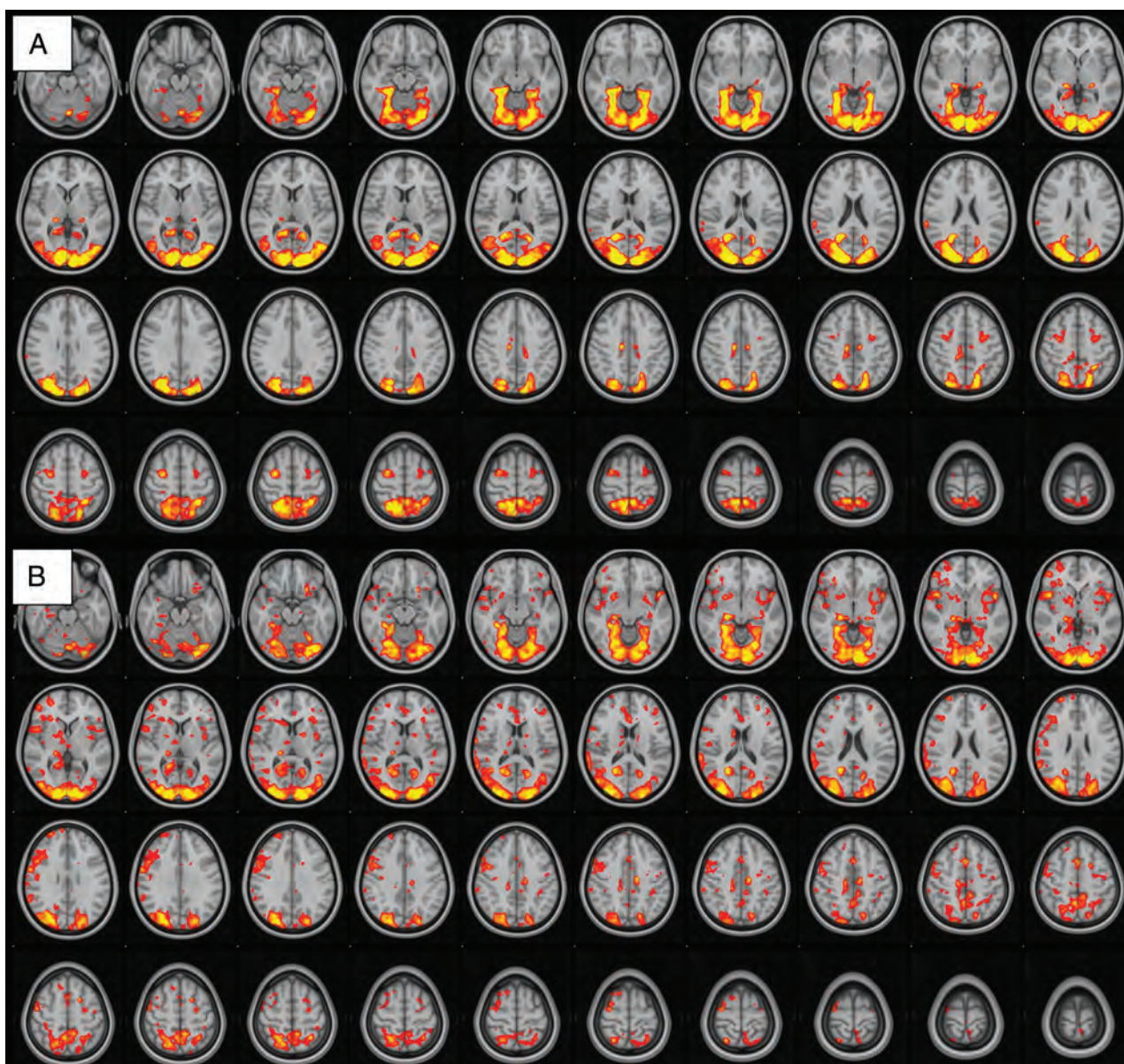


FIG 1. fMRI visual-vestibular paradigm group results. Group mean activation for provocative-neutral contrast in control subjects (A) and patients with PCVMS (B). Widespread activation is seen in the bilateral occipital lobe primary and secondary visual areas, parietal lobes, PIVC, frontal lobes in the region of the FEF, and cingulate gyri.

related concussion; and 1 subject had both. The results of subjective and objective testing are shown in Table 1. The PCVMS group reported significantly more symptoms on the PCSS, the Dizziness Handicap Inventory, and the VVAS, and they were significantly more impaired on all VOMS domains.

Video Optic Flow and Symptom Response

Provocative videos had significantly greater mean and maximum optic flow values in comparison with neutral videos (2-tailed t test, $P < .01$; Online Supplemental Data). In addition, there was significantly greater variance in optic flow in provocative than in neutral videos (2-tailed t test, $P < .01$; Online Supplemental Data).

All subjects rated the type and intensity of subjective symptoms immediately after viewing each video during the fMRI acquisition (Online Supplemental Data). Due to a technical error, the response data from a single subject with PCVMS was not recorded. None of

the control subjects reported symptoms while viewing neutral videos. The mean [SD] symptom-intensity increase over baseline for the control group was 0 [SD, 0] for neutral and 0.12 [SD, 0.48] for provocative videos. The PCVMS group reported significantly increased mean symptom intensity after viewing both neutral videos (0.55 [SD, 2.63]) and provocative videos (2.08 [SD, 2.16]) in comparison with the control group (main effect of group, $F(1, 416) = 16.28$, $P < .001$). The increase in mean symptom intensity between viewing neutral and provocative videos was statistically significant for both the PCVMS (2-tailed t test, $P < .001$) and control (2-tailed t test, $P = .011$) groups.

Visual-Vestibular fMRI

There was robust mean activation in both groups when viewing provocative videos in comparison with neutral videos (provocative-neutral) in several brain regions (Fig 1). Selective

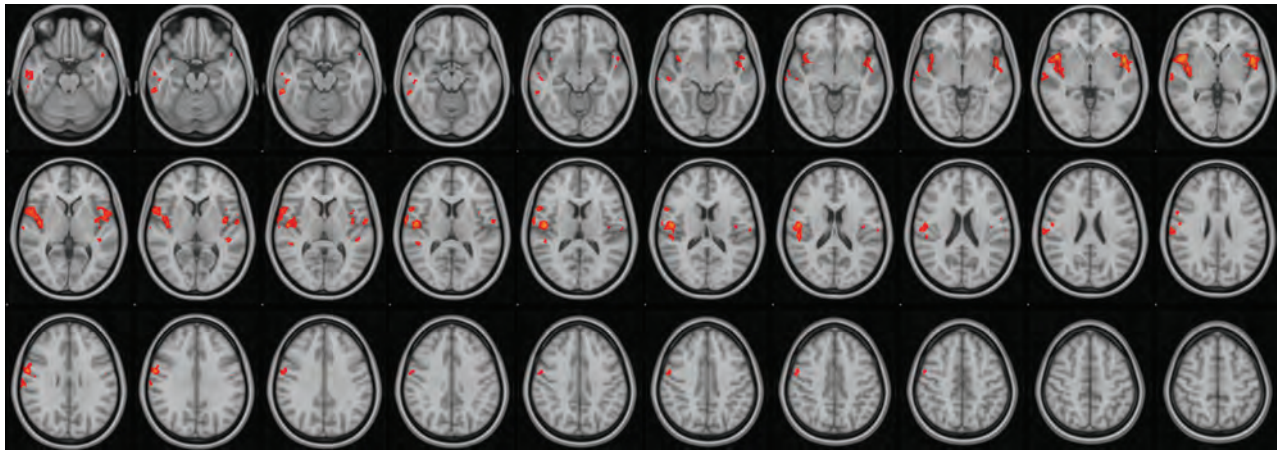


FIG 2. fMRI visual-vestibular paradigm PCVMS results. Selective increased activation was demonstrated in the PCVMS>control group for provocative-neutral contrast in several regions, including the opercular cortex, insular cortex, inferior and middle temporal gyri, precentral gyrus, inferior frontal gyrus, and supramarginal gyrus.

Table 2: Correlation between fMRI brain activation and VOMS testing scores in patients with PCVMS and control subjects

ROI/VOMS Domain	R (10) ^a	95% CI	P Value
Left FEF			
Δ aggregate	0.583	0.014–0.867	.047
Smooth pursuit	0.608	0.052–0.876	.036
Δ smooth pursuit	0.684	0.183–0.904	.014
Horizontal saccade	0.578	0.001–0.865	.049
Δ horizontal saccade	0.722	0.253–0.916	.008
Δ vertical saccade	0.695	0.201–0.907	.012
Vertical vestibular-ocular reflex	0.694	0.200–0.907	.012
Δ vertical vestibular-ocular reflex	0.645	0.113–0.890	.024
Δ horizontal vestibular-ocular reflex	0.584	0.015–0.867	.046
Right posterior hippocampus			
Δ smooth pursuit	0.609	0.054–0.877	.036
Δ horizontal saccade	0.638	0.101–0.887	.026
Δ vertical saccade	0.599	0.038–0.873	.040
Left MT/V5			
Vertical vestibular-ocular reflex	0.723	0.254–0.916	.008

Note:—Δ indicates the difference in scores between the initial and provocative testing portions of VOMS;

Aggregate, the sum of all VOMS symptoms scores.

^a Pearson correlation coefficient.

increased activation was demonstrated in the PCVMS versus control groups (PCVMS>control) for provocative-neutral contrast in several brain regions (Fig 2 and Online Supplemental Data). In particular, activation was seen in the bilateral central opercular and insular cortices and the right inferior frontal and supramarginal gyri. The control>PCVMS group contrast did not reveal any statistically significant activation.

fMRI-VOMS Correlations

Moderate-to-strong statistically significant correlations were found between the transformed VOMS obtained immediately before the MR imaging and activation in several ROIs when viewing provocative videos in comparison with neutral videos (provocative-neutral) in the FEF, posterior hippocampus, and MT/V5 (Table 2). No other statistically significant correlations between the remaining ROIs and VOMS scores were found.

DISCUSSION

Using a novel task-based fMRI visual-vestibular paradigm, we found evidence of altered functional brain activation involved in multisensory processing of visual-vestibular stimuli in patients with PCVMS. Moreover, we have demonstrated that significant correlations exist between regional functional brain activation and clinical symptom severity assessed with VOMS.

Because most adult patients with concussion recover within 2 weeks,³⁸ we chose to focus on patients with subacute vestibular impairment symptoms. As expected, our PCVMS population demonstrated significantly increased PCSS symptoms. Because vestibular impairment was part of our inclusion criteria for this group, it is also not surprising that subjects with PCVMS reported sig-

nificantly greater impairment on the Dizziness Handicap Index, the VVAS, and VOMS. Notably, there was no statistically significant difference between groups on more objective clinical measurements of balance (BESS) and reaction time (drop stick), which is concordant with prior studies demonstrating that balance measures such as the BESS fail to differentiate those with concussions from controls outside of the acute phase.^{39–41} Our results provide some of the first concrete evidence that central mechanisms involving the vestibular network and its input are likely responsible for visual motion sensitivity-related dysfunction, which, to date, has been largely theoretic.¹⁵

Our novel task-based fMRI visual-vestibular paradigm includes a combination of naturalistic videos with either provocative or neutral content for patients with PCVMS. Because head motion is prohibited in the MR imaging environment, this paradigm provides a surrogate for visual-vestibular sensory conflict because participants may experience a subjective sense of motion

induced by these videos, while vestibular sensory input indicates that the participant is stationary. The provocative videos used in the current study demonstrated significantly more objective optic flow and induced more symptoms in patients with PCVMS, indicating that these videos replicate symptom-producing scenarios these patients experience outside the magnet. The current fMRI paradigm provides a novel framework in which to study differential brain activation in patients with PCVMS.

The vestibular network includes the vestibular end organs, brain stem nuclei, thalami, and the parietoinsular vestibular cortex (PIVC).^{36,42,43} In this study, we focused on the central mechanism of vestibular impairment and excluded subjects with peripheral vestibular end organ dysfunction. In addition to the PIVC, prior studies have reported that vestibular stimuli activate the more anterior insula and operculum, FEF, hippocampus, and parahippocampal areas, among others.^{36,43} Similar to language lateralization, PIVC activation occurs asymmetrically with vestibular stimulation, with the primary vestibular cortex localized to the nondominant hemisphere,⁴⁴ concordant with our findings.

A recent fMRI study reported that whereas isolated visual stimulation produces activation in the primary and associative visual cortices and isolated vestibular stimulation activates the PIVC and inferior parietal lobe, bimodal visual/vestibular stimulation produces additional activation of the middle and inferior frontal gyri.³⁷ These regions have been suggested to represent multisensory convergence zones for the vestibular and visual networks, with input from the parietal, occipital, and temporal lobes.³⁷ In addition, Brandt et al⁴⁵ hypothesized the presence of a multisensory orientation area that receives input from the thalamus and visual cortices and co-localizes to the nondominant hemisphere with the PIVC. This region is thought to serve as a primary site of multisensory processing related to higher vestibular spatial orientation. Our results support the importance of these regions in processing complex, provocative visual stimuli. We found selective increased activation in patients with PCVMS in both the hypothesized multisensory orientation area, including the nondominant hemisphere PIVC and adjacent cortex, as well as in the nondominant inferior frontal gyrus, the putative multisensory convergence zone for the vestibular and visual networks.

The posterior hippocampus also provides input to the PIVC and is hypothesized to be involved in spatial memory and contributes to vestibular dysfunction-related visual dependency.⁴³ A prior study by Kontos et al⁴⁶ reported decreased *N*-acetylaspartate/choline ratios, which reflect the ratio of neurons to metabolism in a region, within several hippocampal subdivisions in patients with postconcussive vestibular impairment, which were moderately-to-highly associated with impaired VOMS scores. We found similar positive correlations between VOMS testing and fMRI activation within the nondominant posterior hippocampus as well as correlations with the left FEF and left MT/V5 visual-association area.

While DTI has demonstrated decreased fractional anisotropy in several areas in patients with head injury and vestibular impairment, these have been located in the posterior fossa, medial temporal lobes, inferior occipital lobes, and centrum semiovale.^{47,48} No abnormal DTI metrics were reported in the vestibular-auditory network or in regions known to provide input into the PIVC. In conjunction with our functional results, in

which we found increased (as opposed to decreased) activation, we hypothesized that the primary deficit in PCVMS may be altered multisensory processing, with particular increased weighting of visual-vestibular stimuli, and not primary injury or disruption of the PIVC and associated input.

While increased reliance on visual stimuli may be beneficial acutely in patients with postconcussive vestibular impairment, possibly to compensate for disrupted somatosensory input into the PIVC, persistent overreliance may become pathologic and maladaptive during recovery, manifesting as visual motor sensitivity in the subacute and chronic time periods. This increased visual reliance has clear implications for postconcussion vestibular rehabilitation therapy, which currently focuses on gaze stability and gait and balance exercises.⁴⁹ Based on our fMRI results and preliminary clinical studies, the addition of interventions targeted to visual-vestibular processing may be more efficacious.⁵⁰ We recently reported improved outcomes in patients with PCVMS using a combination rehabilitation intervention of conventional vestibular therapy coupled with a visual desensitization program that included progressively provocative videos similar to those used in the current visual-vestibular task-based fMRI paradigm.⁵¹ This vestibular rehabilitation program may be further improved by incorporating therapies that target the areas of increased brain activation in patients with PCVMS detailed above.

The current study has several limitations. Despite the robust and statistically significant results found in our study, the sample size was relatively small. There were also significant differences between our patient populations, with control subjects having fewer women and a greater mean number of years of schooling than subjects with PCVMS. These differences, unfortunately, arose due to unequal drop-out of enrolled subjects across the 2 groups, which was, in part, related to the multisession study design, which required subjects to undergo both a research MR imaging and vestibular evaluation at different times and locations. Sex differences in response to traumatic brain injury have been reported, with women generally found to have a survival advantage.⁵² Because the postconcussive patients in our current study had more women than men, it may be that a larger effect would have been found if the 2 groups had been sex-matched. However, while it is possible that some of our group-level results may be due to sex and education differences, the correlations between symptom severity and regional fMRI activation are not reliant on matching the 2 group populations.

Furthermore, because the group-level analysis was partly used to identify ROIs for use in the symptom correlational analysis, the group mismatch has minimal consequences as these ROIs were substantiated by the more impactful finding of significant correlations between symptom severity and selective increased activation in patients with PCVMS, providing strong evidence to support the importance of these regions in driving PCVMS symptomatology. Finally, our study compared patients with PCVMS with healthy controls; therefore, our results may reflect general concussion changes as opposed to postconcussive vestibular impairment. However, selective fMRI activation using our visual-vestibular paradigm was again positively correlated with symptom severity, suggesting that our findings reflect PCVMS in particular.

CONCLUSIONS

Using a novel fMRI visual-vestibular paradigm, we found that patients with subacute PCVMS demonstrated increased activation in putative multisensory processing centers involved in visual-vestibular sensory processing. Furthermore, selective regional brain activation on fMRI was positively correlated with symptom severity. These findings suggest that increased weighting of input into the vestibular network may underlie PCVMS.

Disclosures: Jason W. Allen—RELATED: Grant: Georgia State/Georgia Tech Center for Advanced Brain Imaging Neural Engineering Center Seed Grant and Emory University Department of Radiology and Imaging Sciences Seed Grant.* Anna Trofimova—RELATED: Grant: Georgia State/Georgia Tech Center for Advanced Brain Imaging Neural Engineering Center Seed Grant and Emory University Department of Radiology and Imaging Sciences Seed Grant.*; UNRELATED: Grants/Grants Pending: Radiological Society of North America Research and Education Foundation Resident Research Grant.* Jeremy L. Smith—RELATED: Grant: Georgia State/Georgia Tech Center for Advanced Brain Imaging Neural Engineering Center Seed grant and Emory University Department of Radiology and Imaging Sciences Seed Grant.*; UNRELATED: Consultancy: Bold & Stark LC, Comments: rodent data analysis for Albert Einstein College of Medicine. Julia E. Hurtado—UNRELATED: Employment: Shepherd Center. Russell K. Gore—RELATED: Grant: Shepherd Center, Comments: Georgia State/Georgia Tech Center for Advanced Brain Imaging Neural Engineering Center Seed Grant and Emory University Department of Radiology and Imaging Sciences Seed Grant; funding for imaging and subject reimbursement; I was not compensated for the effort.*; UNRELATED: Employment: Shepherd Center, Comments: employed physician; Grants/Grants Pending: Shepherd Center, Comments: Arthur M. Blank Family Foundation Grant.* *Money paid to the institution.

REFERENCES

- Finkelstein EA, Corso PS, Miller TR. *Incidence and Economic Burden of Injuries in the United States*. Oxford University Press; 2006:208
- Faul M, Xu L, Wald MM, et al. National Center for Injury Prevention and Control (U.S.). *Traumatic Brain Injury in the United States: Emergency Department Visits, Hospitalizations and Deaths 2002–2006*. U.S. Department of Health and Human Services, Centers for Disease Control and Prevention, National Center for Injury Prevention and Control; 2010:208
- Maskell F, Chiarelli P, Isles R. **Dizziness after traumatic brain injury: overview and measurement in the clinical setting**. *Brain Inj* 2006;20:293–305 CrossRef Medline
- Hoffer ME, Balaban C, Gottshall K, et al. **Blast exposure: vestibular consequences and associated characteristics**. *Otol Neurotol* 2010;31:232–36 CrossRef Medline
- Bronstein AM, Golding JF, Gresty MA. **Vertigo and dizziness from environmental motion: visual vertigo, motion sickness, and drivers' disorientation**. *Semin Neurol* 2013;33:219–30 CrossRef Medline
- Griffiths MV. **The incidence of auditory and vestibular concussion following minor head injury**. *J Laryngol Otol* 1979;93:253–65 CrossRef Medline
- Anzalone AJ, Blueitt D, Case T, et al. **A Positive Vestibular/Ocular Motor Screening (VOMS) is associated with increased recovery time after sports-related concussion in youth and adolescent athletes**. *Am J Sports Med* 2017;45:474–79 CrossRef Medline
- Guskiewicz KM. **Balance assessment in the management of sport-related concussion**. *Clin Sports Med* 2011;30:89–102 CrossRef Medline
- Franke LM, Walker WC, Cifu DX, et al. **Sensorintegrative dysfunction underlying vestibular disorders after traumatic brain injury: a review**. *J Rehabil Res Dev* 2012;49:985–94 CrossRef Medline
- Fife TD, Giza C. **Posttraumatic vertigo and dizziness**. *Semin Neurol* 2013;33:238–43 CrossRef Medline
- Wright WG, DiZio P, Lackner JR. **Vertical linear self-motion perception during visual and inertial motion: more than weighted summation of sensory inputs**. *J Vestib Res* 2005;15:185–95 Medline
- Cousins S, Cutfield NJ, Kaski D, et al. **Visual dependency and dizziness after vestibular neuritis**. *PLoS One* 2014;9:e105426 CrossRef Medline
- Bronstein AM. **Visual vertigo syndrome: clinical and posturography findings**. *J Neurol Neurosurg Psychiatry* 1995;59:472–76 CrossRef Medline
- Gurley JM, Hujsak BD, Kelly JL. **Vestibular rehabilitation following mild traumatic brain injury**. *Neurorehabilitation* 2013;32:519–58 CrossRef Medline
- Lee JO, Lee ES, Kim JS, et al. **Altered brain function in persistent postural perceptual dizziness: a study on resting state functional connectivity**. *Hum Brain Mapp* 2018;39:3340–53 CrossRef Medline
- Carroll L, Cassidy J, Holm L, et al. WHO Collaborating Centre Task Force on Mild Traumatic Brain Injury. **Methodological issues and research recommendations for mild traumatic brain injury: the WHO Collaborating Centre Task Force on Mild Traumatic Brain Injury**. *J Rehab Med* 2004;(43 Suppl):113–25 CrossRef Medline
- Broglio SP, Collins MW, Williams RM, et al. **Current and emerging rehabilitation for concussion: a review of the evidence**. *Clin Sports Med* 2015;34:213–31 CrossRef Medline
- Mucha A, Collins MW, Elbin RJ, et al. **A Brief Vestibular/Ocular Motor Screening (VOMS) assessment to evaluate concussions: preliminary findings**. *Am J Sports Med* 2014;42:2479–86 CrossRef Medline
- Lovell MR, Iverson GL, Collins MW, et al. **Measurement of symptoms following sports-related concussion: reliability and normative data for the post-concussion scale**. *Appl Neuropsychol* 2006;13:166–74 CrossRef Medline
- Jacobson GP, Newman CW. **The development of the Dizziness Handicap Inventory**. *Arch Otolaryngol Head Neck Surg* 1990;116:424–27 CrossRef Medline
- Dannenburg E, Chilingaryan G, Fung J. **Visual vertigo analogue scale: an assessment questionnaire for visual vertigo**. *J Vestib Res* 2011;21:153–59 CrossRef Medline
- Eckner JT, Whitacre RD, Kirsch NL, et al. **Evaluating a clinical measure of reaction time: an observational study**. *Percept Mot Skills* 2009;108:717–20 CrossRef Medline
- Farneback G. **Two-frame motion estimation based on polynomial expansion**. In: *Proceedings of the Scandinavian Conference on Image Analysis*. Halmstad, Sweden. June 27 to July 2, 2003; 363–70
- Jenkinson M, Bannister P, Brady M, et al. **Improved optimization for the robust and accurate linear registration and motion correction of brain images**. *Neuroimage* 2002;17:825–41 CrossRef Medline
- Greve DN, Fischl B. **Accurate and robust brain image alignment using boundary-based registration**. *Neuroimage* 2009;48:63–72 CrossRef Medline
- Jenkinson M. **Fast, automated, N-dimensional phase-unwrapping algorithm**. *Magn Reson Med* 2003;49:193–97 CrossRef Medline
- Smith SM, Zhang Y, Jenkinson M, et al. **Accurate, robust, and automated longitudinal and cross-sectional brain change analysis**. *Neuroimage* 2002;17:479–89 CrossRef Medline
- Beckmann CF, Smith SM. **Probabilistic independent component analysis for functional magnetic resonance imaging**. *IEEE Trans Med Imaging* 2004;23:137–52 CrossRef Medline
- Jenkinson M, Smith S. **A global optimisation method for robust affine registration of brain images**. *Med Image Anal* 2001;5:143–56 CrossRef Medline
- Andersson JL, Jenkinson M, Smith SM. **Non-linear optimization: FMRIB Technical Report TR07JA1**. 2007. <https://www.fmrib.ox.ac.uk/datasets/techrep/tr07ja1/tr07ja1.pdf>. Accessed November 5, 2020
- Andersson JL, Jenkinson M, Smith SM. **Non-linear registration, aka spatial normalisation: FMRIB Technical Report TR07JA2**. 2007. <https://www.fmrib.ox.ac.uk/datasets/techrep/tr07ja2/tr07ja2.pdf>. Accessed November 5, 2020
- Woolrich MW, Ripley BD, Brady M, et al. **Temporal autocorrelation in univariate linear modeling of FMRI data**. *Neuroimage* 2001;14:1370–86 CrossRef Medline
- Beckmann CF, Jenkinson M, Smith SM. **General multilevel linear modeling for group analysis in FMRI**. *Neuroimage* 2003;20:1052–63 CrossRef Medline

34. Woolrich MW, Behrens TE, Beckmann CF, et al. **Multilevel linear modelling for fMRI group analysis using Bayesian inference.** *Neuroimage* 2004;21:1732–47 CrossRef Medline
35. Woolrich M. **Robust group analysis using outlier inference.** *Neuroimage* 2008;41:286–301 CrossRef Medline
36. zu Eulenburg P, Caspers S, Roski C, et al. **Meta-analytical definition and functional connectivity of the human vestibular cortex.** *Neuroimage* 2012;60:162–69 CrossRef Medline
37. Della-Justina HM, Gamba HR, Lukasova K, et al. **Interaction of brain areas of visual and vestibular simultaneous activity with fMRI.** *Exp Brain Res* 2015;233:237–52 CrossRef Medline
38. McCrory P, Meeuwisse W, Dvorak J, et al. **Consensus statement on concussion in sport—the 5th international conference on concussion in sport held in Berlin, October 2016.** *Br J Sports Med* 2017;51:838–47 CrossRef Medline
39. Bell DR, Guskiewicz KM, Clark MA, et al. **Systematic review of the balance error scoring system.** *Sports Health* 2011;3:287–95 CrossRef Medline
40. Alkathiry AA, Kontos AP, Furman JM, et al. **Vestibulo-ocular reflex function in adolescents with sport-related concussion: preliminary results.** *Sports Health* 2019;11:479–85 CrossRef Medline
41. Hendershot KA, Evans KM, Geary B, et al. **Comparison of clinical assessment tools in patients with dizziness and imbalance post-concussion.** In: *Proceedings of the National Symposium of the Neurotrauma Society*, Lexington, Kentucky. June 26–29, 2016
42. Dieterich M, Brandt T. **The bilateral central vestibular system: its pathways, functions, and disorders.** *Ann N Y Acad Sci* 2015;1343:10–26 CrossRef Medline
43. Alsaman O, Ost J, Vanspauwen R, et al. **The neural correlates of chronic symptoms of vertigo proneness in humans.** *PLoS One* 2016;11:e0152309 CrossRef Medline
44. Kirsch V, Boegle R, Keeser D, et al. **Handedness-dependent functional organizational patterns within the bilateral vestibular cortical network revealed by fMRI connectivity based parcellation.** *Neuroimage* 2018;178:224–37 CrossRef Medline
45. Brandt T, Strupp M, Dieterich M. **Towards a concept of disorders of “higher vestibular function.”** *Front Integr Neurosci* 2014;8:47 CrossRef Medline
46. Kontos AP, Van Cott AC, Roberts J, et al. **Clinical and magnetic resonance spectroscopic imaging findings in veterans with blast mild traumatic brain injury and post-traumatic stress disorder.** *Mil Med* 2017;182:99–104 CrossRef Medline
47. Gattu R, Akin FW, Cacace AT, et al. **Vestibular, balance, microvascular and white matter neuroimaging characteristics of blast injuries and mild traumatic brain injury: four case reports.** *Brain Inj* 2016;30:1501–14 CrossRef Medline
48. Alhilali LM, Yaeger K, Collins M, et al. **Detection of central white matter injury underlying vestibulopathy after mild traumatic brain injury.** *Radiology* 2014;272:224–32 CrossRef Medline
49. Alsalaheen BA, Whitney SL, Mucha A, et al. **Exercise prescription patterns in patients treated with vestibular rehabilitation after concussion.** *Physiother Res Int* 2013;18:100–08 CrossRef Medline
50. Murray DA, Meldrum D, Lennon O. **Can vestibular rehabilitation exercises help patients with concussion? A systematic review of efficacy, prescription and progression patterns.** *Br J Sports Med* 2017;51:442–51 CrossRef Medline
51. Hurtado JE, Heusel-Gillig L, Risk BB, et al. **Technology-enhanced visual desensitization home exercise program for post-concussive visually induced dizziness: a case series.** *Physiother Theory Pract* 2020 Sep 21. [Epub ahead of print] CrossRef Medline
52. Sethuraman KN, Marcolini EG, McCunn M, et al. **Gender-specific issues in traumatic injury and resuscitation: consensus-based recommendations for future research.** *Acad Emerg Med* 2014;21:1386–94 CrossRef Medline

The Pharyngolaryngeal Venous Plexus: A Potential Pitfall in Surveillance Imaging of the Neck

 P.M. Bunch,  R.T. Hughes,  E.P. White,  J.R. Sachs,  B.A. Frizzell, and  C.M. Lack

ABSTRACT

BACKGROUND AND PURPOSE: Among patients undergoing serial neck CTs, we have observed variability in the appearance of the pharyngolaryngeal venous plexus, which comprises the postcricoid and posterior pharyngeal venous plexuses. We hypothesize changes in plexus appearance from therapeutic neck irradiation. The purposes of this study are to describe the CT appearance of the pharyngolaryngeal venous plexus among 2 groups undergoing serial neck CTs—patients with radiation therapy–treated laryngeal cancer and patients with medically treated lymphoma—and to assess for changes in plexus appearance attributable to radiation therapy.

MATERIALS AND METHODS: For this retrospective study of 98 patients (49 in each group), 448 contrast-enhanced neck CTs (222 laryngeal cancer; 226 lymphoma) were assessed. When visible, the plexus anteroposterior diameter was measured, and morphology was categorized.

RESULTS: At least 1 plexus component was identified in 36/49 patients with laryngeal cancer and 37/49 patients with lymphoma. There were no statistically significant differences in plexus visibility between the 2 groups. Median anteroposterior diameter was 2.1 mm for the postcricoid venous plexus and 1.6 mm for the posterior pharyngeal venous plexus. The most common morphology was “bilobed” for the postcricoid venous plexus and “linear” for the posterior pharyngeal venous plexus. The pharyngolaryngeal venous plexus and its components were commonly identifiable only on follow-up imaging.

CONCLUSIONS: Head and neck radiologists should be familiar with the typical location and variable appearance of the pharyngolaryngeal plexus components so as not to mistake them for neoplasm. Observed variability in plexus appearance is not attributable to radiation therapy.

ABBREVIATIONS: AP = anteroposterior; PCVP = postcricoid venous plexus; PLVP = pharyngolaryngeal venous plexus; PPVP = posterior pharyngeal venous plexus; RT = radiation therapy; SI = superior-inferior

Laryngeal and hypopharyngeal venous anatomy has been a subject of interest in the anatomic,^{1–7} otolaryngologic,^{8,9} and radiologic^{10–14} literature. Anatomists have consistently identified a rich plexus of veins in the postcricoid and posterior hypopharynx, which has been termed the “pharyngolaryngeal venous plexus” (PLVP).^{2,8} The PLVP has been described as larger and better developed in fetal and infant dissections than in those performed in older children and adults.^{3,15}

The PLVP can be subdivided (Fig 1) into a ventral portion along the posterior aspect of the cricoid cartilage (termed the

“postcricoid venous plexus” [PCVP]), and a dorsal portion along the posterior pharyngeal wall (termed the “posterior pharyngeal venous plexus” [PPVP]).^{2,4,7,8,16,17} Historically, the PCVP has received more attention in the literature than the PPVP. The PCVP extends cranially to at least the level of the transverse and oblique arytenoid musculature⁵ and drains into the superior laryngeal and lingual veins.^{2,4,5} In the otolaryngologic literature, the PCVP (also referred to as the “postcricoid cushion”^{8,18}) has been documented to cyclically enlarge with Valsalva during the expiratory phase of an infant’s cry.⁸ In keeping with the age-related differences of the PLVP noted in the anatomic literature, the postcricoid cushion has been observed on flexible fiber-optic laryngoscopy to be most prominent among infants and to become less noticeable in older children.⁸ It has been suggested that the increased PCVP prominence in infants may be mechanically beneficial to protect from aspiration,^{4,5} prevent emesis during crying,^{4,8} and minimize aerophagia during crying.⁷

Received July 10, 2020; accepted after revision November 24.

From the Department of Radiology (P.M.B., E.P.W., J.R.S., C.M.L.) and Radiation Oncology (R.T.H., B.A.F.), Wake Forest School of Medicine, Winston Salem, North Carolina.

Please address correspondence to Paul M. Bunch, MD, Department of Radiology, Wake Forest School of Medicine, Medical Center Blvd, Winston Salem, NC 27157; e-mail: paul.m.bunch@gmail.com; @pbunchmd
<http://dx.doi.org/10.3174/ajnr.A7033>

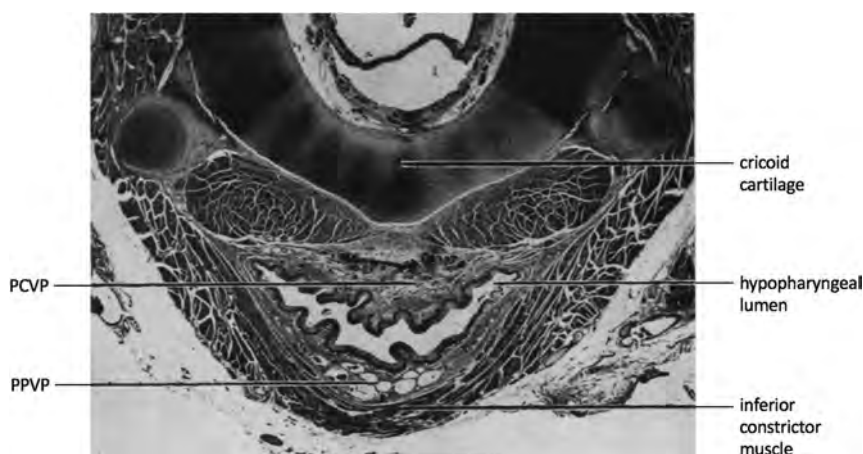


FIG 1. Transverse histopathologic section of the hypopharynx of a full-term fetus at the level of the cricoid cartilage shows the locations of the PCVP and the PPVP. Reproduced from Butler⁵ with permission from BMJ Publishing Group Ltd.

Most prior radiologic studies addressing postcricoid anatomy have focused on fluoroscopy.^{10-12,14} In such fluoroscopic studies, the PCVP has also been referred to as the “postcricoid impression”¹⁰ and has been emphasized to be a normal finding that should not be mistaken for neoplasm.¹¹ Descriptions of the CT appearance of the PCVP are lacking in the published literature.

In the anatomic literature, the PPVP is reported to be associated with the posterior pharyngeal wall,^{2,16,17} lying between the posterior mucosal surface and the inferior constrictor musculature.^{3,5} The PPVP drains into the superficial pharyngeal plexus and subsequently into the internal jugular veins.^{3,5} Some authors report the PPVP to be located inferiorly with respect to the PCVP,^{16,17} though others describe the PCVP and the PPVP being located at the same level.⁵ As is true for the PCVP, descriptions of the CT appearance of the PPVP in the published literature are also lacking.

Head and neck radiologists are accustomed to the typical findings of prior therapeutic neck irradiation, including mucosal hyperenhancement, submucosal edema, and fat reticulation.^{19,20} As such, these well-described treatment-related changes do not represent diagnostic dilemmas on surveillance imaging. In our clinical practice, we have observed the PLVP on neck CT examinations performed for head and neck cancer follow-up and noticed variations in PLVP thickness and in PLVP visibility within the same patient on different neck CT examinations. The reasons for this observed variability are unclear, but radiation therapy (RT)-induced vascular changes may play a role. Acute increases in vascular permeability and treatment-related local inflammation may influence the CT appearance of the PLVP in the early post-RT period, whereas endothelial cell proliferation and perivascular fibrosis may alter the CT appearance of the PLVP on later imaging follow-up.²¹⁻²³

We hypothesize that PLVP visibility on neck CT imaging changes as a result of therapeutic neck irradiation. The purposes of this study are to describe the CT appearance of the PLVP and its components (the PCVP and the PPVP) among 2 groups of patients undergoing serial neck CTs (patients with RT-treated

laryngeal cancer and patients with chemotherapy-treated lymphoma) and to assess for potential RT-associated effects on PLVP visibility through comparison of the 2 groups.

MATERIALS AND METHODS

Subjects

For this retrospective, Health Insurance Portability and Accountability Act-compliant, institutional review board-approved study, an institutional head and neck cancer data base of 266 patients treated with curative intent for laryngeal cancer was first queried for patients satisfying the following criteria: treated with definitive radiation with or without chemotherapy for laryngeal squamous cell carcinoma

(excluded = 111); no other previous therapeutic head and neck irradiation (excluded = 6); no primary or salvage surgical management (excluded = 56); pretreatment baseline neck CT with contrast obtained with images available for review (excluded = 15); and at least 1 post-RT neck CT with contrast obtained with images available for review (excluded = 29). Patients were excluded if diagnostic assessment of the larynx and hypopharynx was precluded by severe artifacts on the pretreatment baseline CT or on all post-RT neck CTs. All potential subjects were treated between 2011 and 2018 with intensity-modulated RT or 3D-conformal RT (in cases of stage I–II glottic cancer). Patient age, patient sex, smoking history, and radiation dose were obtained from the electronic medical record.

After determination of the RT-treated laryngeal cancer cohort meeting all inclusion criteria, an age- and sex-matched cohort of patients with lymphoma with no prior history of therapeutic neck irradiation was selected from a local radiology report data base as a control group who had also undergone serial neck CTs. Patient age, patient sex, and smoking history were obtained from the electronic medical record.

Image Acquisition

Given the retrospective nature of this study, there was variability with respect to CT scanners used to acquire images, as well as specific CT acquisition parameters. However, most neck CT examinations were acquired on a LightSpeed VCT (GE Healthcare) with acquisition parameters of 120 kV(peak), Auto mA (noise index = 6, minimum = 100 mA, maximum = 250 mA), 0.969: 1 pitch, 0.8-second rotation time, 2.5-mm helical section thickness, and 1.25-mm interval. Multiplanar reconstructions were generated, including 2.5-mm axial (20-to 30-cm FOV; “standard” kernel) images. Imaging was performed 90 seconds after the injection of 95 mL of iohexol, 350 mg I/mL (split-bolus technique, 65 mL at 4 mL/s, 30-second pause, 30 mL at 4 mL/s) and spanned the skull base to the thoracic inlet.

Reader Assessment

One fellowship-trained neuroradiologist (with 3 years’ subspecialty experience) reviewed the neck CT examination axial 2.5-mm

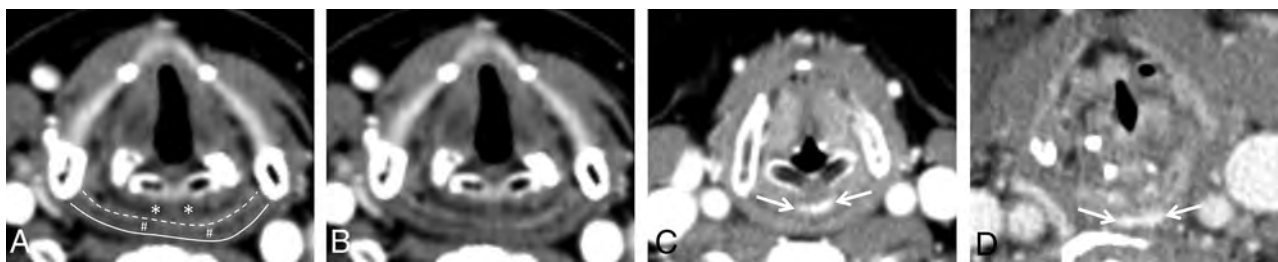


FIG 2. Labeled (A) and unlabeled (B) axial neck CT images with contrast at the level of the cricoarytenoid joints in a patient without visible PLVP demonstrate the expected locations of the PCVP (asterisk, A) between the larynx anteriorly and the hypopharyngeal mucosa (dashed line, A) posteriorly, and the PPVP (pound sign, A) between the hypopharyngeal mucosa anteriorly and the inferior constrictor musculature (solid line, A) posteriorly. Axial neck CT images with contrast in 2 additional patients (C and D) demonstrate visible PCVP (arrows, C) and visible PPVP (arrows, D).

Table 1: Characteristics of the study groups

	Laryngeal Cancer	Lymphoma	P-Value
Sex			
Male	33 (67%)	33 (67%)	1.00
Female	16 (33%)	16 (33%)	
Age (yr)			
Mean [SD]	58.9 [11.0]	58.9 [11.1]	1.00
Minimum	25	25	
Maximum	83	84	
Smoking history			
Yes	47 (96%)	26 (53%)	<.001
No	2 (4%)	23 (47%)	
Radiation dose (Gy)			
Median	70.0	NA	
Minimum	64.0	NA	
Maximum	70.2	NA	
Neck CTs			
Total	222	226	
Per patient (mean) (SD)	4.5 (2.8)	4.6 (2.7)	.88
Minimum	2	2	
Maximum	16	14	
Months of CT follow-up ^a			
Total	1005	1835	
Mean (SD)	20.5 (13.5)	37.4 (31.4)	<.001
Minimum	4	1	
Maximum	59	162	

Note:—NA indicates not applicable.

^aFor patients with laryngeal cancer, follow-up ended when either no more neck CTs were available or the patient underwent salvage laryngectomy.

soft-tissue kernel images to determine the visibility of the PLVP and its components, the PCVP and the PPVP.

The PCVP was defined as “visible” if tubular or curvilinear submucosal enhancement matching the contrast attenuation of adjacent veins was located posterior to the laryngeal mucosa and anterior to the hypopharyngeal mucosa (Fig 2). The PPVP was defined as visible if tubular or curvilinear submucosal enhancement matching the contrast attenuation of adjacent veins was located posterior to the hypopharyngeal mucosa and anterior to the inferior constrictor musculature (Fig 2). The PLVP was defined as visible if either the PCVP or the PPVP was visible.

When visible, the PCVP and PPVP anteroposterior (AP) diameters and superior-inferior (SI) extent were measured in millimeters. The SI level (eg, cricoid cartilage, arytenoid cartilage, supra-arytenoid) at which the PCVP and PPVP appeared thickest was also recorded. When both the PCVP and the PPVP were visible in the same patient, the relative SI position of the PPVP with respect to

the PCVP was documented. In addition, a qualitative, descriptive assessment of PCVP and PPVP morphology on axial CT images was performed with the goal of morphologic categorization.

Statistical Analysis

Descriptive analyses were performed using absolute and relative frequencies for categorical variables and mean or median for normally and non-normally distributed continuous variables, respectively. The Fisher exact test was used to compare proportions, 1-way analysis of variance was used to compare normally distributed continuous variables, and the Wilcoxon rank sum test was used to compare non-normally distributed continuous variables. Analyses were performed with JMP, Version 14 (SAS Institute), and a *P* value < .05 indicated a statistically significant difference.

RESULTS

Subjects

A total of 49 patients with post-RT laryngeal cancer (222 neck CTs) met all inclusion criteria and formed the study cohort for which 49 age- and sex-matched patients with medically-treated lymphoma (226 neck CTs) were selected to serve as controls. Characteristics of the 2 study groups are provided in Table 1.

Reader Assessment

The PLVP was visible on at least 1 neck CT in 36/49 (73%) patients with laryngeal cancer and in 37/49 (76%) patients with lymphoma (*P* = 1.00). The PLVP was identifiable on baseline neck CT in 21/49 (43%) patients with laryngeal cancer and identifiable on initial neck CT in 22/49 (45%) patients with lymphoma (*P* = 1.00). Among patients with laryngeal cancer, the PLVP was visible on at least 1 post-RT neck CT in 34/49 (69%) patients and identifiable on 90/173 (52%) of all post-RT neck CTs. Among patients with lymphoma, the PLVP was visible on at least 1 follow-up neck CT in 36/49 (73%) patients (*P* = .82) and identifiable on 108/177 (61%) of all follow-up neck CTs (*P* = .11).

For both the laryngeal cancer and lymphoma cohorts, PLVP visibility on the baseline examination predicted PLVP visibility on at least 1 follow-up neck CT: Nineteen of 21 (91%) patients with laryngeal cancer with PLVP visible at baseline exhibited PLVP on at least 1 post-RT neck CT compared with 15/28 (54%) patients with no visible PLVP at baseline (*P* = .011), and 21/22 (95%) patients with lymphoma with PLVP visible on initial neck CT exhibited PLVP on at least 1 follow-up neck CT compared

Table 2: Visibility of PLVP within the study groups with respect to patient characteristics

	Laryngeal Cancer			Lymphoma		
	PLVP Visible?					
	Yes	No	P	Yes	No	P
Sex						
Male	23	10	.50	23	10	.29
Female	13	3		14	2	
Age (yr)						
Mean [SD]	58.4 [11.5]	60.3 [10.0]	.60	59.3 [11.6]	57.6 [9.6]	.64
Smoking history						
Yes	34	13	1.00	17	9	.10
No	2	0		20	3	
Radiation dose (Gy)						
Median (range)	70.0 (64.0–70)	70.0 (65.3–70.2)	.26	NA	NA	NA

Note:—NA indicates not applicable.

Table 3: Visibility of PCVP within the study groups with respect to patient characteristics

	Laryngeal Cancer			Lymphoma		
	PCVP Visible?					
	Yes	No	P	Yes	No	P
Sex						
Male	20	13	.36	23	10	.29
Female	12	4		14	2	
Age (yr)						
Mean [SD]	57.3 [10.9]	61.9 [10.8]	.17	59.3 [9.6]	57.6 [11.6]	.64
Smoking history						
Yes	30	17	.54	17	9	.10
No	2	0		20	3	
Radiation dose (Gy)						
Median (range)	70.0 (64.0–70)	70.0 (65.3–70.2)	.57	NA	NA	NA

Note:—NA indicates not applicable.

with 15/27 (56%) patients without visible PLVP on initial imaging ($P = .002$).

Among patients with laryngeal cancer and lymphoma with a visible PLVP, the frequency with which the PLVP was identifiable in each patient ranged from 15% to 100% (median, 67%). Both the PCVP and the PPVP were visible in 34/73 (47%) patients, only the PCVP was visible in 35/73 (48%), and only the PPVP was visible in 4/73 (5%). When both the PCVP and the PPVP were visible in the same patient, the PPVP was located below the level of the PCVP in 30 patients (88%), at the level of the PCVP in 3 patients (9%), and above the level of the PCVP in 1 patient (3%).

There was no statistically significant association between PLVP visibility and any of the studied patient factors (Table 2).

The PCVP was visible on at least 1 neck CT in 32/49 (65%) patients with laryngeal cancer and in 37/49 (76%) patients with lymphoma ($P = .38$). The PCVP was identifiable on baseline neck CT in 18/49 (37%) patients with laryngeal cancer and identifiable on initial neck CT in 20/49 (41%) patients with lymphoma ($P = .84$). Among patients with laryngeal cancer, the PCVP was visible on at least 1 post-RT neck CT in 30/49 (61%) patients and identifiable on 87/173 (50%) post-RT neck CTs. Among patients with lymphoma, the PCVP was visible on at least 1 follow-up neck CT in 36/49 (73%) patients ($P = .28$) and identifiable on 98/177 (55%) of all follow-up neck CTs ($P = .39$).

For both the laryngeal cancer and lymphoma cohorts, PCVP visibility on the baseline examination predicted PCVP visibility

on at least 1 follow-up neck CT: Sixteen of 18 (89%) patients with laryngeal cancer with PCVP visible at baseline exhibited visible PCVP on at least 1 post-RT neck CT compared with 14/31 (45%) patients with no visible PCVP at baseline ($P = .003$), and 19/20 (95%) patients with lymphoma with PCVP visible on initial neck CT exhibited PCVP on at least 1 follow-up neck CT compared with 17/29 (59%) patients without visible PCVP on initial imaging ($P = .007$).

Among patients with laryngeal cancer and lymphoma with visible PCVP, the frequency with which the PCVP was identifiable in each patient ranged from 17% to 100% (median 64%). There was no statistically significant association between PCVP visibility and any of the studied patient factors (Table 3).

When visible, the maximum AP diameter of the PCVP ranged from 0.9 to 5.0 mm (median, 2.1). The PCVP maximum AP diameter increased on at least 1 follow-up neck CT relative to initial imaging in 53/69 (77%) patients, and the PCVP thickness was decreased on all follow-up neck CTs relative to initial imaging in 16/69 (23%) patients. In 1 patient with laryngeal cancer, the prominent post-RT PCVP on follow-up imaging was described by the interpreting radiologist as suspicious for progressive neoplasm (Fig 3); however, the PCVP was confirmed with 22 months of follow-up imaging. The SI extent of PCVP ranged from 2.5 to 26.5 mm (median, 10 mm).

The PCVP appeared thickest at the level of the cricoid cartilage in 14/69 (20%) patients, at the level of the arytenoid cartilage

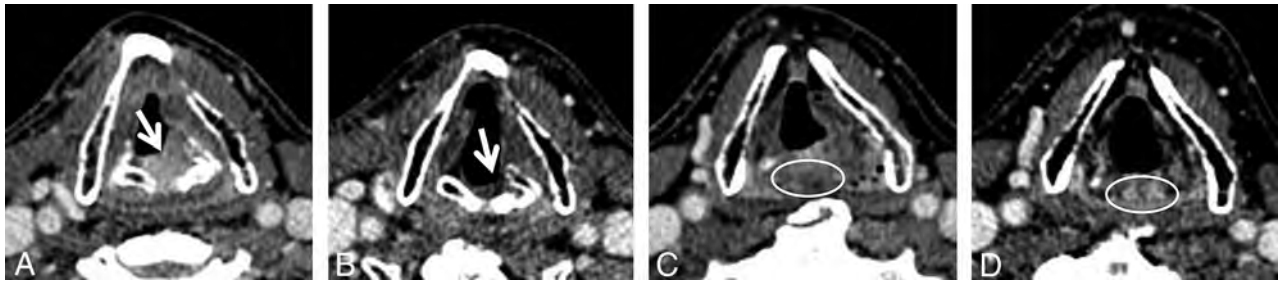


FIG 3. Axial contrast-enhanced neck CT images obtained before (A and C) and after (B and D) definitive radiation therapy for laryngeal squamous cell carcinoma (arrow, A). Posttreatment images demonstrate a substantial decrease in size of the treated tumor (arrow, B) as well as prominent PCVP (circle, D) that was not definitively identifiable on the baseline pretreatment neck CT (circle, C). The prominent PCVP (circle, D) was described as suspicious for progressive neoplasm but confirmed to be vascular after 22 months of imaging follow-up.

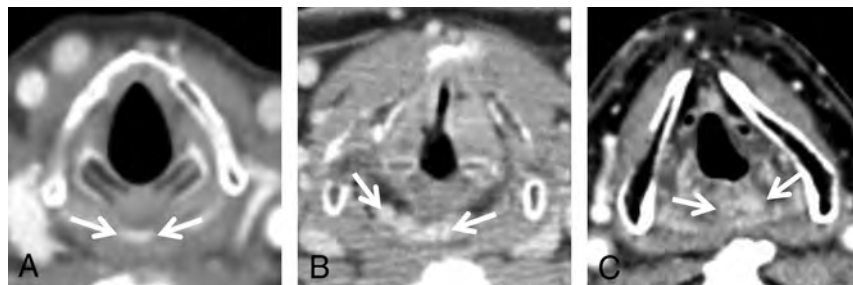


FIG 4. Axial contrast-enhanced neck CT images obtained in 3 different patients demonstrate representative images of the PCVP (arrows, A–C) at the cricoid cartilage level (A), the arytenoid cartilage level (B), and the supra-arytenoid level (C).



FIG 5. Axial contrast-enhanced neck CT images in 3 different patients demonstrate representative examples of bilobed (arrows, A), dot-dash (arrows, B), and linear (arrows, C) PCVP morphology.

in 21/69 (30%) patients, and at a supra-arytenoid level in 34/69 (49%) patients (Fig 4).

Qualitative assessment of the PCVP appearance resulted in the following morphologic categories (Fig 5): bilobed ($n = 31$), linear (thin or thick) ($n = 14$), and dot-dash ($n = 19$). Five patients exhibited a combination of these morphologies depending on the axial section level. No morphologic category changes were observed between initial and follow-up neck CTs.

The PPVP was visible on at least 1 neck CT in 17/49 (35%) patients with laryngeal cancer and in 21/49 (43%) patients with lymphoma ($P = .53$). The PPVP was identifiable on baseline neck CT in 6/49 (12%) patients with laryngeal cancer and identifiable on initial neck CT in 10/49 (20%) patients with lymphoma ($P = .41$). Among patients with laryngeal cancer, the PPVP was visible on at least 1 post-RT neck CT in 17/49 (35%) patients and

identifiable on 42/173 (24%) post-RT neck CTs. Among patients with lymphoma, the PPVP was visible on at least 1 follow-up neck CT in 20/49 (41%) patients ($P = .68$) and identifiable on 53/177 (30%) of all follow-up neck CTs ($P = .28$).

For both the laryngeal cancer and lymphoma cohorts, PPVP visibility on the baseline examination predicted PPVP visibility on at least 1 follow-up neck CT: Six of 6 (100%) patients with laryngeal cancer with PPVP visible at baseline exhibited visible PPVP on at least 1 post-RT neck CT compared with 11/43 (26%) patients with no visible PPVP at baseline ($P < .001$); and 9/10 (90%) patients with lymphoma with PPVP visible on initial neck CT exhibited PPVP on at least 1 follow-up neck CT compared with 10/39 (26%) patients without visible PPVP on initial imaging ($P < .001$).

Among patients with laryngeal cancer and lymphoma with visible PPVP, the frequency with which the PPVP was identifiable in each patient

ranged from 15% to 100% (median, 50%). Among patients with lymphoma, the PPVP was more likely visible among women ($P = .01$). A significant difference was also observed between the mean age of patients with lymphoma with visible PPVP (62.6 years) and the mean age of patients with lymphoma without visible PPVP (56.1 years; $P = .04$). Otherwise, there were no statistically significant associations between PPVP visibility and any of the studied patient factors (Table 4).

When visible, the maximum AP diameter of the PPVP ranged from 0.9 to 4.0 mm (median 1.6). The PPVP maximum AP diameter increased on at least 1 follow-up neck CT relative to baseline imaging in 31/38 (82%) patients, and the PPVP thickness was decreased on all follow-up neck CTs relative to baseline imaging in 7/38 (18%) patients. In no cases were prominent PPVPs on follow-up imaging described by the interpreting radiologist as

Table 4: Visibility of PPVP within the study groups with respect to patient characteristics

	Laryngeal Cancer			Lymphoma		
	PPVP Visible?					
	Yes	No	P	Yes	No	P
Sex						
Male	12	21	1.00	10	23	.01
Female	5	11		11	5	
Age (yr)						
Mean [SD]	59.0 [13.9]	58.8 [9.3]	.96	62.6 [10.9]	56.1 [10.6]	.04
Smoking history						
Yes	16	31	1.00	8	18	.09
No	1	1		13	10	
Smoking history						
Median (range)	70.0 (64.0–70)	70.0 (65.3–70.2)	.06	NA	NA	NA

Note:—NA indicates not applicable.



FIG 6. Axial contrast-enhanced neck CT images in 3 different patients demonstrate representative examples of linear (arrows, A), dot-dash (arrows, B), and bilobed (arrows, C) PPVP morphology.

suspicious for progressive neoplasm. The SI extent of PPVP ranged from 5.0 to 26.3 mm (median, 10.0 mm).

The PPVP appeared thickest at the level of the cricoid cartilage in 31/38 (82%) patients, at the level of the arytenoid cartilage in 6/38 (16%) patients, and at a supra-arytenoid level in 1/38 (3%) patients.

Qualitative assessment of the PPVP appearance resulted in the following morphologic categories: linear (thin or thick) ($n = 31$), dot-dash ($n = 5$), and bilobed ($n = 2$) (Fig 6). No morphologic category changes were observed between initial and follow-up neck CTs.

DISCUSSION

Among patients with laryngeal squamous cell carcinoma treated with definitive RT and patients with lymphoma with no history of therapeutic neck irradiation, at least 1 component of the PLVP is commonly identifiable on contrast-enhanced neck CT, though variable in both visibility and thickness between CT examinations. Importantly, in up to 50% of patients in both cohorts with no visible PLVP on initial imaging, at least 1 component could be identified on serial follow-up neck CT. Moreover, the PCVP and PPVP AP thickness measured greatest on a follow-up neck CT examination for greater than 75% of included patients.

We hypothesized that PLVP visibility on neck CT imaging changes because of therapeutic neck irradiation. The results do not support our hypothesis, as there were no significant differences between visibility of the PLVP or its components between the group

with RT-treated laryngeal cancer and the group with medically treated lymphoma (control). Although unlikely related to RT-induced inflammation, the factors accounting for the observed variability in plexus visibility within both groups remain uncertain. Some possibilities include hydration status on the day of imaging, the presence or absence of Valsalva during image acquisition, and the higher number of follow-up neck CTs ($n = 350$) than baseline neck CTs ($n = 98$) within the 2 cohorts.

Nevertheless, it is important that the radiologist be aware of the existence of such variability as well as of the appearance, location, and common morphologies of the PCVP and PPVP so as not to mistake these normal structures for progressive neoplasm when interpreting surveillance imaging of the neck. As shown in previous anatomic dissections and confirmed in this CT-based study, the PCVP lies in a submucosal location posterior to the laryngeal mucosa and anterior to the hypopharyngeal mucosa between the levels of the supraglottis and the cricoid cartilage. The PPVP lies in a submucosal location posterior to the hypopharyngeal mucosa and anterior to the inferior constrictor muscle, most commonly at the level of the cricoid cartilage but rarely at or above the arytenoid cartilage level.

In our cohort, the most common morphology of the PCVP on axial CT images was bilobed, which is in keeping with earlier anatomic descriptions of the PCVP as 2 longitudinal masses on each side of the midline separated by a gap of 2–6 mm.⁵ The most common morphology of the PPVP on axial CT images was linear. PCVP and PPVP longitudinal extent were variable, more commonly 10 mm or greater, and were therefore seen on multiple sequential axial images, though occasionally more focal. Enhancement matching the enhancement of adjacent veins and a tubular rather than masslike configuration would also favor PLVP over neoplasm in the postcricoid region. Alternatively, the PCVP and PPVP could be mistaken for mucositis, particularly among patients who are RT-treated. In our experience, careful attention to the submucosal location of the PCVP and PPVP, immediately anterior and posterior to the hypopharyngeal mucosa, respectively, typically enables differentiation.

There was no correlation between PLVP or PCVP and any studied patient factors. Among patients with lymphoma, PPVP visibility was significantly associated with age and female sex, and these associations were not observed within the group with laryngeal cancer. Although further study may be warranted, we advise caution in ascribing clinical significance to these findings given the small sample size of 21 patients with lymphoma exhibiting visible PPVP.

There are limitations of this study, including small sample size and retrospective design. A single neuroradiologist reader was used, such that interrater reliability was not assessed. It is possible that other neuroradiologists would characterize the visibility and morphology of the PCVP and PLVP differently than what we report, though we have attempted to provide ample illustrative examples in support of our findings. Finally, there were statistically significant differences between the laryngeal cancer and lymphoma groups with respect to smoking history (likely reflecting risk factors for laryngeal cancer) and months of CT follow-up. Although there was no significant association between plexus visibility and smoking history among patients with laryngeal cancer treated with definitive RT, the very few subjects with negative smoking history may influence the accuracy of the statistical comparison between smokers and nonsmokers.

CONCLUSIONS

At least 1 component of the PLVP was identifiable on contrast-enhanced neck CT in most patients with laryngeal cancer and lymphoma, with variable appearance on follow-up imaging compared with baseline. Although the factors contributing to the variable appearance of the PLVP remain uncertain, there is no evidence to support therapeutic neck irradiation as a contributing factor.

In up to 50% of patients with no visible PLVP on initial imaging, the PLVP was identifiable on at least 1 follow-up neck CT and could therefore possibly be confused for neoplasm. Head and neck radiologists should be familiar with the typical location and variable appearance of the PLVP components so as not to mistake this normal vascular structure for progressive neoplasm.

REFERENCES

- Bourgery J, Jacob N. *Atlas of Human Anatomy and Surgery: The Complete Colored Plates of 1831–1854*. 25th ed. Taschen; 2005
- von Luschka H. *Der Kehlkopf des Menschen*. H. Laupp; 1871: 147
- Bimar L, Lapeyre JM. **Recherches sur les veines du pharynx**. *Comp Rend Acad d Sc* 1887;105:825
- Elze C. **Die venosen Wundernetze der Pars laryngea pharyngis**. *Anat Anz* 1918;51:205–07
- Butler H. **The veins of the oesophagus**. *Thorax* 1951;6:276–96 CrossRef Medline
- Tose D, Rodrigues H, DiDio LJ. **The venous architecture of the human pharyngo-esophageal transition**. *Arch Ital Anat Embriol* 1984;89:157–65 Medline
- Tose D, Rodrigues H, DiDio LJ. **Mucosal and submucosal veins of the human pharyngo-esophageal transition**. *Arch Ital Anat Embriol* 1985;90:9–15 Medline
- Hoff SR, Koltai PJ. **The “postcricoid cushion”: observations on the vascular anatomy of the posterior cricoid region**. *Arch Otolaryngol Head Neck Surg* 2012;138:562–71 CrossRef Medline
- Haugen TW, Wood WE, Helwig C. **Postcricoid vascular abnormalities: hemangiomas, venous malformations, or anatomic variant**. *Int J Pediatr Otorhinolaryngol* 2012;76:805–08 CrossRef Medline
- Pitman RG, Fraser GM. **The post-cricoid impression on the oesophagus**. *Clin Radiol* 1965;16:34–39 CrossRef Medline
- Friedland GW, Filly R. **The postcricoid impression masquerading as an esophageal tumor**. *Am J Dig Dis* 1975;20:287–91 CrossRef Medline
- Dodds WJ, Stewart ET, Logemann JA. **Physiology and radiology of the normal oral and pharyngeal phases of swallowing**. *AJR Am J Roentgenol* 1990;154:953–63 CrossRef Medline
- Schmalfuss IM, Mancuso AA, Tart RP. **Postcricoid region and cervical esophagus: normal appearance at CT and MR imaging**. *Radiol* 2000;214:237–46 CrossRef Medline
- Allen JE, White CJ, Leonard RJ, et al. **Posterior cricoid region fluoroscopic findings: the posterior cricoid plication**. *Dysphagia* 2011;26:272–76 CrossRef Medline
- Ramaekers D, Mebis J, Geboes K, et al. **Vascularization of the pharyngo-esophageal transition zone** [in Dutch]. *Acta Gastroenterol Belg* 1990;53:376–85
- Elze C, Beck K. **Die venosen wundernetze der hypopharynx**. *Z Ohrenheilkunde* 1919;185–97
- Baston O. **Veins of the pharynx**. *Arch Otolaryngol* 1942;36:212–19
- Hron TA, Kavanagh KR, Murray N. **Diagnosis and treatment of benign pediatric lesions**. *Otolaryngol Clin North Am* 2019;52:657–68 CrossRef Medline
- Glastonbury CM, Parker EE, Hoang JK. **The postradiation neck: evaluating response to treatment and recognizing complications**. *AJR Am J Roentgenol* 2010;195:W164–71 CrossRef Medline
- Saito N, Nadgir RN, Nakahira M, et al. **Posttreatment CT and MR imaging in head and neck cancer: what the radiologist needs to know**. *Radiographics* 2012;32:1261–82; discussion 1282–84 CrossRef Medline
- Hopewell JW, Campling D, Calvo W, et al. **Vascular irradiation damage: its cellular basis and likely consequences**. *Br J Cancer Suppl* 1986;7:181–91 Medline
- Girinsky T. **Effects of ionizing radiation on the blood vessel wall** [in French]. *J Mal Vasc* 2000;25:321–24 Medline
- Hall EJ, Giaccia AJ. *Radiobiology for the Radiologist*. 7th ed. Wolters Kluwer Health/Lippincott Williams & Wilkins; 2012

Improved Lesion Conspicuity with Contrast-Enhanced 3D T1 TSE Black-Blood Imaging in Cranial Neuritis: A Comparative Study of Contrast-Enhanced 3D T1 TSE, 3D T1 Fast-Spoiled Gradient Echo, and 3D T2 FLAIR

T.-W. Baek, Y. Kang, and H.-J. Lee



ABSTRACT

BACKGROUND AND PURPOSE: Contrast-enhanced 3D-turbo spin-echo (TSE) black-blood sequence has gained attention, as it suppresses signals from vessels and provides an increased contrast-noise ratio. The purpose was to investigate which among the contrast-enhanced 3D T1 TSE, 3D T1 fast-spoiled gradient echo (FSPGR), and 3D T2 FLAIR sequences can better detect cranial nerve contrast enhancement.

MATERIALS AND METHODS: Patients with cranial neuritis based on clinical findings ($n = 20$) and control participants ($n = 20$) were retrospectively included in this study. All patients underwent 3T MR imaging with contrast-enhanced 3D T1 TSE, 3D T1 FSPGR, and 3D T2 FLAIR. Experienced and inexperienced reviewers independently evaluated the 3 sequences to compare their diagnostic performance and time required to reach the diagnosis. Additionally, tube phantoms containing varying concentrations of gadobutrol solution were scanned using the 3 sequences.

RESULTS: For the inexperienced reader, the 3D T1 TSE sequence showed significantly higher sensitivity (80% versus 50%, $P = .049$; 80% versus 55%, $P = .040$), specificity (100% versus 65%, $P = .004$; 100% versus 60%, $P = .001$), and accuracy (90% versus 57.5%, $P = .001$; 90% versus 57.5%, $P = .001$) than the 3D T1 FSPGR and 3D T2 FLAIR sequences in patients with cranial neuritis. For the experienced reader, the 3D T1-based sequences showed significantly higher sensitivity than the 3D T2 FLAIR sequence (85% versus 30%, $P < .001$; 3D T1 TSE versus 3D T2 FLAIR, 85% versus 30%, $P < .001$; 3D T1 FSPGR versus 3D T2 FLAIR). For both readers, the 3D T1 TSE sequence showed the highest area under the curve (inexperienced reader, 0.91, experienced reader, 0.87), and time to diagnosis was significantly shorter with 3D T1 TSE than with 3D T1 FSPGR.

CONCLUSIONS: The 3D T1 TSE sequence may be clinically useful in evaluating abnormal cranial nerve enhancement, especially for inexperienced readers.

ABBREVIATIONS: FSPGR = fast-spoiled gradient echo; CE = contrast-enhanced; GRE = gradient-echo; CNR = contrast to noise ratio; ROC = receiver operating characteristic; AUC = area under the ROC curve; TSE = turbo spin-echo

Cranial neuropathies can have multiple causes, including infectious, neoplastic, inflammatory, traumatic, and idiopathic pathologies.¹ Such conditions cause disruption of the blood-nerve barrier, which is sustained by the combined actions of tight junctions in the endothelium of the endoneurial capillaries and of the inner layers of the perineurium.² Contrast-enhanced (CE) MR imaging plays an important role in the diagnosis of cranial neuritis

by visualizing nerve enhancement attributed to leakage forcing spillage and accumulation of contrast material surrounded by CSF.³

To date, no standard protocol has been established for evaluating cranial nerve enhancement, whereas several sequences have been proposed for detecting leptomeningeal enhancement. CE 3D T1 gradient-echo (GRE) sequences have been widely used in the clinical setting to detect leptomeningeal pathology.⁴⁻⁷ Furthermore, the CE 3D FLAIR sequence is advantageous because it can sensitively detect low concentrations of gadolinium.^{8,9} Recently, a CE 3D turbo spin-echo (TSE) black-blood sequence has gained attention because it provides an increased contrast to noise ratio (CNR) and suppresses diverting signals from vessels.¹⁰⁻¹³

To the best of our knowledge, no study has explored the value of CE 3D T1 TSE black-blood imaging in the diagnosis of cranial neuritis. Although the CE 3D T1 GRE sequence is generally used for the evaluation of cranial nerve enhancement,^{3,14} its

Received July 25, 2020; accepted after revision November 24.

From the Department of Radiology (T.-W.B., Y.K., H.-J.L.), Haeundae Paik Hospital, Inje University College of Medicine, Busan, Korea.

This work was supported by the 2019 Inje University research grant.

Please address correspondence to Yeonah Kang, MD, Department of Radiology, Haeundae Paik Hospital, Inje University College of Medicine, Busan, Korea; e-mail: bsb2312@gmail.com



Indicates article with online supplemental data.

<http://dx.doi.org/10.3174/ajnr.A7025>

ability to evaluate the cisternal segment of cranial nerves is limited owing to the surrounding prominent vessel enhancement. Moreover, hyperintensities on FLAIR are also associated with various conditions, such as subarachnoid hemorrhage, sluggish collateral vessels, and supplemental oxygen, which may produce misinterpretations of the cranial nerve enhancement.¹⁵ Therefore, the aim of this study was to investigate which sequence among 3D T1 TSE, 3D T1 fast-spoiled gradient echo (FSPGR), and 3D T2 FLAIR can better detect contrast enhancement in patients with cranial neuritis.

Detailed description of the included patients

ID	Age/Sex	Diagnosis
1	70/M	Left trigeminal neuritis
2	70/M	Left abducens neuritis
3	59/M	Left facial neuritis
4	36/F	Right facial neuritis
5	74/M	Right facial neuritis
6	46/F	Right trigeminal neuritis
7	61/M	Bilateral trigeminal neuritis
8	54/M	Right trigeminal neuritis
9	71/M	Left facial neuritis
10	48/M	Left facial neuritis
11	48/F	Right vestibular neuritis
12	60/M	Left oculomotor and right abducens neuritis
13	50/M	Left facial neuritis
14	38/F	Right oculomotor neuritis
15	51/M	Left facial neuritis
16	67/F	Right trigeminal neuritis
17	52/M	Left oculomotor neuritis
18	38/M	Left facial neuritis
19	72/M	Left facial neuritis
20	67/M	Right facial neuritis

MATERIALS AND METHODS

Patients

This retrospective study was approved by the institutional review board of our institution, and the requirement to obtain patients' informed consent was waived. From May 2018 to April 2020, 299 consecutive patients underwent cranial nerve MR imaging for symptoms of cranial nerve disorders at our institution. Among them, 38 met the inclusion criteria and were recruited, ie, patients 1) with a final clinical diagnosis of cranial neuritis based on clinical findings, relief of symptoms after administration of steroids, or electromyography results¹⁶ and 2) who had a clinical diagnosis-correlated enhancing cranial nerve lesion on cranial nerve MR imaging. Of these, 18 were excluded for the following reasons: 1) lack of 3D T1 TSE, 3D T1 FSPGR, or 3D T2 FLAIR ($n = 11$); 2) lesion at the cavernous segment of the oculomotor nerve ($n = 5$); or 3) potential for perineural metastasis owing to underlying disease ($n = 2$). Finally, 20 patients were included in this study, and the mean time interval between cranial nerve MR imaging and final clinical diagnosis was 2.75 ± 3.50 days. The detailed information of the patients is provided in the Table. Additionally, 20 patients who underwent cranial nerve MR imaging under suspicion of neurovascular compression syndrome and had no remarkable finding on MR imaging were included as the control group. A flow diagram of patient selection is shown in Fig 1. There was no significant difference in mean age (56.6 years in the patient group; 55.2 years in the control group; $P = .782$) and sex distribution (5 [25%] women in the patient group; 10 [50%] women in the control group; $P = .102$).

MR Imaging

All scans were acquired using 1 of 2 3T MR imaging units (Achieva; Philips Healthcare or Signa Architect, GE Healthcare). Each patient underwent the following 3 postcontrast sequences: 3D T1 TSE, 3D T1 FSPGR, and 3D T2 FLAIR. Detailed scan parameters are provided in the Online Supplementary Data. After IV injection of gadobutrol (Gadovist, Bayer Schering Pharma) at a dose of 0.1 mmol/kg of body weight, the 3D T1 TSE and 3D T1 FSPGR images were acquired in a randomized order followed by the 3D T2 FLAIR images.

Image Analysis

A total of 120 sequences (3 sequences for each of the 40 patients) were de-identified and randomly distributed in 3 sessions. Each of the 3 sequences (3D T1 TSE, 3D T1 FSPGR, and 3D T2 FLAIR) acquired from each patient was included in a different session. There was a 2-week interval between sessions. Images were provided with a reconstructed section thickness of 1.2 mm and analyzed on a DICOM viewer (RadiAnt DICOM Viewer). An inexperienced reader (T.-W.B., a third-year resident) and an experienced reader (Y.K., a board-certified neuroradiologist with

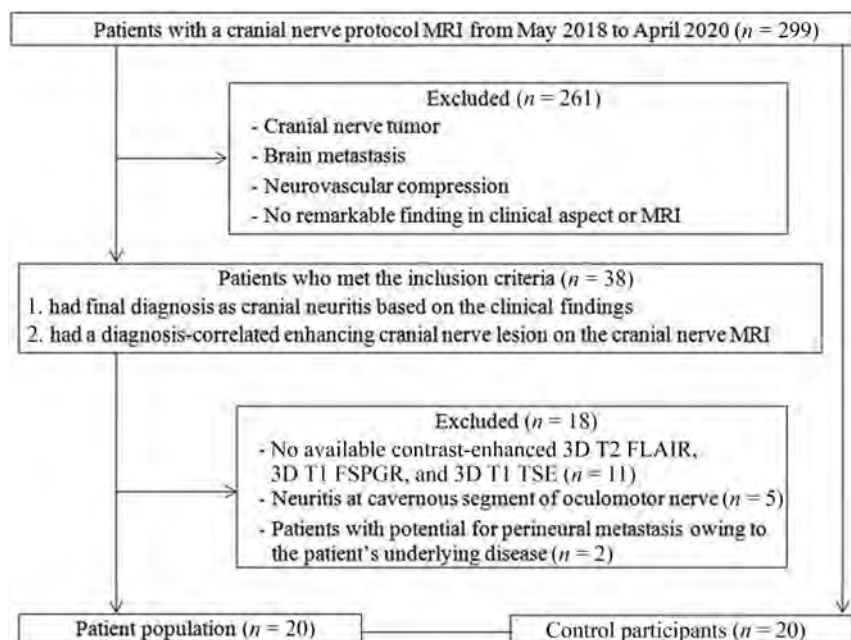


FIG 1. Flowchart algorithm for patient selection.

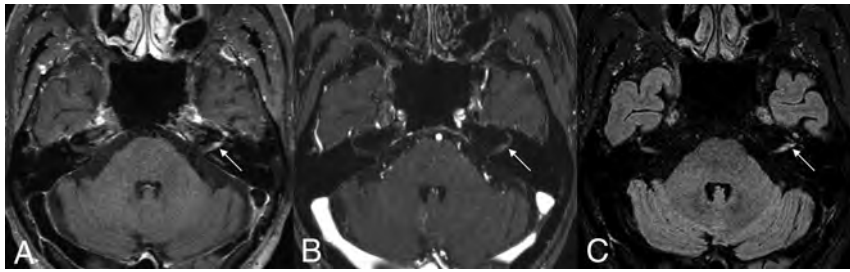


FIG 2. A 71-year-old man with left facial neuritis. Moderate enhancement noted at the left distal meatal segment of the facial nerves on 3D T1 TSE (A), but 3D T1 FSPGR (B) and 3D T2 FLAIR (C) revealed equivocal and mild enhancement, respectively, of the corresponding facial nerve (arrows).



FIG 3. A 60-year-old man with left oculomotor neuritis. On 3D T1 TSE (A), intense enhancement at the distal cisternal portion of left oculomotor nerve was observed, and mild enhancement was observed on 3D T1 FSPGR (B). The 3D T2 FLAIR (C) was negatively interpreted by both reviewers (arrows).

8 years of experience), blinded to patient clinical information, independently reviewed these images. Multiplanar reconstruction and axial images were available on the DICOM viewer.

The reviewers made a diagnosis and rated the contrast enhancement based on a 5-point scoring system, with 1 indicating no enhancement; 2, equivocal enhancement; 3, mild but definite enhancement; 4, moderate enhancement, similar to the signal intensity of the anterior genu of the facial nerve; and 5, intense enhancement, greater than that of the anterior genu of the facial nerve. Finally, they measured the time (in seconds) required to reach the diagnosis.

Statistical Analysis

Sensitivity, specificity, and accuracy were calculated and compared using the McNemar test. A receiver operating characteristic (ROC) analysis was used to evaluate the diagnostic performance of the enhancement grade in each sequence to detect neuritis. Areas under the ROC curve (AUCs) were compared using the Z-test. The Wilcoxon rank sum test was used to compare the time to diagnosis. $P < .05$ was considered statistically significant. All statistical analyses were performed using MedCalc for Windows (version 12.7.1.0) and SPSS Statistics for Windows (version 20.0, IBM).

Clinical Phantom Study

To evaluate the signal intensity according to the contrast agent concentration in the 3D T1 TSE, 3D T1 FSPGR, and 3D T2 FLAIR images, a clinical phantom scan was constructed based on

the data of 1 healthy volunteer. The clinical phantom was constructed as shown in the Online Supplementary Data, containing gadobutrol solutions (Gadovist) of varying concentrations (range, 0.0125–3 mmol/L); the head band was set to the volunteer's head, and the volunteer underwent scanning for the 3 sequences in a 3T MR imaging unit (Signa Architect). We compared the signal intensities of various concentrations of gadobutrol solution, divided by the signal intensity of the brain parenchyma, among 3D T1 TSE, 3D T1 FSPGR, and 3D T2 FLAIR.

RESULTS

Comparison of Diagnostic Accuracy among 3D T1 TSE, 3D T1 FSPGR, and 3D T2 FLAIR

For the inexperienced reader, there was significantly higher sensitivity (80% versus 50%; $P = .049$), specificity (100% versus 65%; $P = .004$), and accuracy (90% versus 57.5%; $P = .001$) with 3D T1 TSE than with 3D T1 FSPGR. Likewise, there was significantly higher sensitivity (80% versus 55%; $P = .040$), specificity (100% versus 60%; $P = .001$), and accuracy (90% versus 57.5%; $P = .001$) with 3D T1 TSE than with 3D T2 FLAIR. There was no significant difference in the sensitivity, specificity, and accuracy between 3D T1 FSPGR and 3D T2 FLAIR (all $P > .05$) (Online Supplementary Data).

For the experienced reader, 3D T1 TSE (85%) and 3D T1 FSPGR (85%) showed the same sensitivity; however, there was a significantly higher sensitivity with the 3D T1-based sequences than with the 3D T2 FLAIR sequences (85% versus 30%, $P < .001$; 3D T1 TSE versus 3D T2 FLAIR, 85% versus 30%, $P < .001$; 3D T1 FSPGR versus 3D T2 FLAIR). The specificity did not significantly differ among the 3 sequences (3D T1 TSE, 90%; 3D T1 FSPGR, 85%; and 3D T2 FLAIR, 90%; all $P > .05$). Meanwhile, there was a significantly higher accuracy with 3D T1 TSE than with 3D T2 FLAIR (87.5% versus 60%; $P = .005$) and with 3D T1 FSPGR, but the difference was not significant (87.5% versus 82.5%; $P = .533$). Representative images are shown in Figs 2–4.

Diagnostic Performance of 3D T1 TSE, 3D T1 FSPGR, and 3D T2 FLAIR Using the AUCs

For the inexperienced reader, the highest AUC was attained with 3D T1 TSE (AUC, 0.91 [95% CI, 0.77–0.97]) with marginal significance compared with 3D T1 FSPGR (AUC, 0.75 [95% CI, 0.58–0.87]; $P = .053$), but a significant difference was noted when compared with 3D T2 FLAIR (AUC, 0.56 [95% CI, 0.39–0.71]; $P < .001$) (Online Supplementary Data and Fig 5).

For the experienced reader, the AUCs for 3D T1 TSE, 3D T1 FSPGR, and 3D T2 FLAIR were as follows: 3D T1 TSE, 0.87 (95% CI, 0.73–0.95); 3D T1 FSPGR, 0.86 (95% CI, 0.72–0.95); and 3D T2 FLAIR, 0.71 (95% CI, 0.54–0.84). The AUC of 3D T1 TSE was significantly higher than that of 3D T2 FLAIR ($P = .049$); however, the difference between 3D T1 TSE and 3D T1 FSPGR was not significant ($P = .891$).

Time to Diagnosis

For both readers, the time to diagnosis was significantly shorter for 3D T1 TSE than for 3D T1 FSPGR (inexperienced reader: 30.75 versus 40.90 seconds, $P = .001$; experienced reader: 23.85 versus 35.55 seconds, $P = .005$).

Clinical Phantom Study

The signal intensity ratios of various concentrations of gadobutrol solution to normal WM on 3D T1 TSE, 3D T1 FSPGR, and 3D T2 FLAIR images were plotted according to the gadobutrol concentration (Online Supplementary Data). The signal intensity ratio of 0.7–2-mmol/L gadobutrol solutions

was higher in 3D T1 TSE than in 3D T1 FSPGR and 3D T2 FLAIR.

DISCUSSION

For the inexperienced reader, the 3D T1 TSE sequence showed higher sensitivity, specificity, and accuracy for the conspicuity of cranial nerve enhancement in patients with cranial neuritis than the 3D T1 FSPGR and 3D T2 FLAIR sequences. For the experienced reader, there was higher sensitivity, specificity, and accuracy with 3D T1 TSE than with 3D T2 FLAIR and 3D T1 FSPGR, but the difference was only significant between 3D T1 TSE and 3D T2 FLAIR. For both readers, the AUCs were higher in 3D T1 TSE than in 3D T1 FSPGR and 3D T2 FLAIR. The 3D T1 TSE sequence may improve lesion conspicuity in cranial neuritis; thus, its inclusion should be considered in the protocol for cranial nerve evaluation in patients with suspected cranial neuritis.

Recently, 3D T1 TSE, which entails variable flip-angle modulation, resulting in blood-flow suppression, has been introduced in brain and leptomeningeal metastasis imaging and proved to improve the diagnostic accuracy compared with 3D T1 GRE.^{10,11,13,17} Oh et al¹³ reported that 3D T1 TSE black-blood sequences had significantly higher sensitivity and higher interobserver agreement than 3D T1 GRE sequences in patients with leptomeningeal metastasis. Similarly, Sommer et al¹¹ demonstrated higher sensitivity and diagnostic confidence regarding leptomeningeal affection when using a 3D T1-weighted modified volumetric isotropic TSE acquisition (T1 mVISTA) sequence than when using a 3D T1-weighted magnetization-prepared rapid

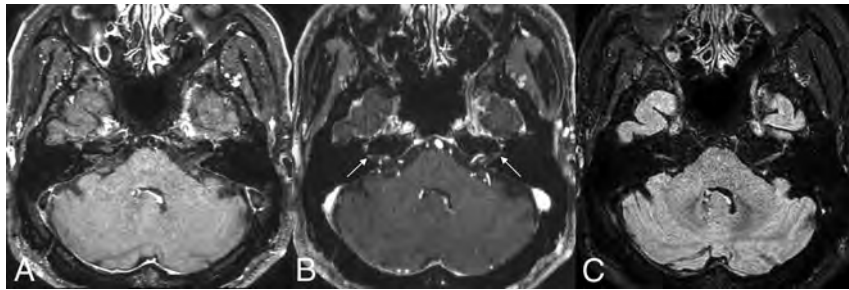


FIG 4. A 65-year-old man in the control group. There is no definite enhancement of the bilateral facial nerves on 3D T1 TSE (A) and 3D T2 FLAIR (C). However, mild enhancement at the distal internal auditory canal (arrows), possibly owing to convergence of dura mater, may lead to misinterpretation as enhancement of the distal meatal segment of the facial nerve on 3D T1 FSPGR (B).

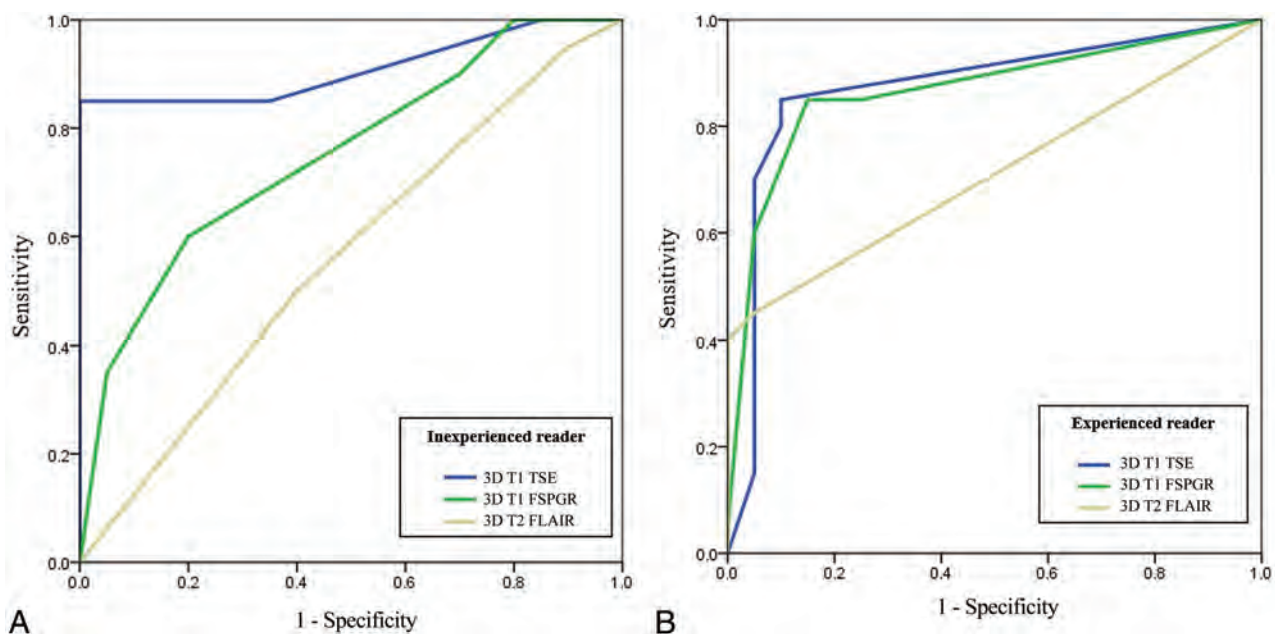


FIG 5. Comparisons of the ROC curves for the inexperienced (A) and experienced (B) readers.

acquisition of gradient echo (T1 MPRAGE) sequence in infectious and neoplastic meningitis. Our findings are in line with the results of these recent studies on leptomeningeal metastases; however, to our knowledge, the diagnostic performance of 3D T1 TSE in cranial neuritis has not been previously compared with that of 3D T1 FSPGR and 3D T2 FLAIR.

In our clinical phantom study, 3D T1 TSE achieved a higher signal intensity than 3D T1 FSPGR at the lower contrast concentration (0.0125–2 mmol/L), which was consistent with previous findings.^{9,18} We speculate that the cisternal segments of the cranial nerves are in a position inevitably affected by active CSF movement, which results in the dilution of contrast material; thus, these might contribute to higher CNR on 3D T1 TSE in cranial neuritis. Our hypothesis is supported by Gil et al's¹⁵ observation that subtle leptomeningeal enhancement was better depicted with 3D T1 sampling perfection with application-optimized contrasts by using different flip angle evolutions (SPACE) than with 2D-T1 GRE and 2D FLAIR. Moreover, we observed that 3D T1 TSE may deter misinterpretation of pseudoenhancement of the distal labyrinthine segments of the facial nerve owing to dural convergence at the distal internal auditory canal; this finding is in line with that of a previous study that revealed more prominent normal dural enhancement with 3D T1 MPRAGE compared with 3D T1 mVISTA.¹¹ We speculate that these advantages contributed toward significantly improved lesion conspicuity with 3D T1 TSE than with 3D T1 FSPGR for the inexperienced reader and significantly shorter time to diagnosis with 3D T1 TSE for both readers. Furthermore, unlike the previous studies of Oh et al¹³ and Gil et al,¹⁵ we randomly shuffled the scan order of 3D T1 TSE and 3D T1 FSPGR; thus, our study may be free from the reported bias that contrast enhancement increases over time.^{19,20}

Our study revealed that there was lower sensitivity, specificity, and accuracy with 3D T2 FLAIR than with 3D T1 TSE for both the inexperienced and experienced readers, with the exception of specificity for the experienced reader. Compared with T1 GRE, T2 FLAIR is considered a more sensitive sequence for the evaluation of meningeal enhancement.^{8,16,21} Meanwhile, controversial results have been reported regarding the comparison of T2 FLAIR with 3D T1 TSE for the detection of leptomeningeal abnormalities.^{9,22} Park et al⁹ revealed that 2D T2 FLAIR could show a greater extent of leptomeningeal metastases than 3D T1 TSE; however, in a subgroup analysis for cranial nerve, there was no significant difference in the ability of detecting cranial nerve enhancement between the 2 sequences. Jeevanandham et al²² concluded that postcontrast 3D T1 SPACE imaging adds significantly more information to postcontrast 3D T2 FLAIR in dural and sulcal space enhancement. At the lower contrast concentration, we observed that the signal intensities were higher with 3D T2 FLAIR than with 3D T1 TSE; however, when dividing the signal intensities by the normal WM, the signal intensity ratio was higher for 3D T1 TSE (from 0.7 mmol/L to 2 mmol/L) than for 3D T2 FLAIR. We speculated that our result (ie, low sensitivity and accuracy demonstrated by 3D T2 FLAIR) may be attributed to its intrinsic high signal intensity for the cranial nerves, which might interfere with the visual assessment of subtle contrast enhancement. According to a previous study involving patients with Bell palsy, a quantitative analysis of the facial nerve on pre-

and postcontrast 3D T2 FLAIR showed an increased diagnostic performance to “visual assessment alone” on postcontrast 3D T2 FLAIR; however, the sensitivity, specificity, and accuracy of postcontrast 3D T2 FLAIR images were lower than those of CE T1 spin-echo images in terms of visual assessment.²³ In respect to clinically efficient scanning time, we also observed that 3D T1 TSE had advantages over 3D T2 FLAIR, which took >5 minutes, when the same parallel imaging factor was applied. By adding the parallel imaging factor to 3D T1 TSE, the scanning time of 3D T1 TSE was equivalent to that of 3D T1 FSPGR (3D T1 TSE versus 3D T1 FSPGR; 3 minutes 43 seconds versus 3 minutes 44 seconds using Achieva; 3 minutes 55 seconds versus 3 minutes 50 seconds using Signa Architect). Thus, we surmise that 3D T1 TSE, a sequence that allows instinctive assessment of abnormal nerve enhancement on postcontrast images alone, may be a practical sequence in daily clinical work.

This study has several limitations. First, the study population was relatively small. However, cranial neuritis is an uncommon disease entity,²⁴ and we believe that our cohort may have been representative of the targeted patient population. Second, we only assessed the cistern segments of the cranial nerves. When the venous plexus in the cavernous sinus shows prominent enhancement but the nerves are best depicted as black structures, contrast enhancement of the nerves is often evaluated as the loss of the boundary with the surroundings.²⁵ Therefore, we inevitably could only study the cistern segments of the cranial nerves to assess the degree of contrast enhancement based solely on the contrast leakage through the blood-nerve barrier. Third, we did not assess the precontrast image as a reference for contrast enhancement, using instead the genu of the facial nerve to this end. However, we believe that a sequence that allows prompt visual assessment of contrast enhancement on a postcontrast enhanced image is appropriate for daily practice.

CONCLUSIONS

3D T1 TSE black-blood imaging showed significantly greater diagnostic performance for cranial neuritis, especially for the inexperienced reader, than T1 FSPGR and 3D T2 FLAIR imaging. Moreover, for the experienced reader, 3D T1 TSE also showed significantly higher sensitivity, specificity, and accuracy than 3D T2 FLAIR. Our results suggest that 3D T1 TSE is a clinically useful sequence for the evaluation of abnormal cranial nerve enhancement, especially for beginners in neuroradiology or general radiologists, because it improves lesion conspicuity.

ACKNOWLEDGMENTS

The authors thank Seonguk Jin, Bayer Schering Pharma, for providing the contrast concentration phantom and Ho-Joon Lee (coauthor) for volunteering to undergo scanning for the clinical phantom study.

Disclosures: Yeonah Kang—RELATED: Grant: Inje University*, Comments: This work was supported by the 2019 Inje University research grant. *Money paid to the individual author.

REFERENCES

1. Khaku A, Patel V, Zacharia T, et al. **Guidelines for radiographic imaging of cranial neuropathies.** *Ear Nose Throat J* 2017;96:E23–39 CrossRef Medline
2. Saremi F, Helmy M, Farzin S, et al. **MRI of cranial nerve enhancement.** *AJR Am J Roentgenol* 2005;185:1487–97 CrossRef Medline
3. Romano N, Federici M, Castaldi A. **Imaging of cranial nerves: a pictorial overview.** *Insights Imaging* 2019;10:33 CrossRef Medline
4. Kakeda S, Korogi Y, Hiai Y, et al. **Detection of brain metastasis at 3T: comparison among SE, IR-FSE and 3D GRE sequences.** *Eur Radiol* 2007;17:2345–51 CrossRef Medline
5. Furutani K, Harada M, Mawlan M, et al. **Difference in enhancement between spin echo and 3-dimensional fast spoiled gradient recalled acquisition in steady state magnetic resonance imaging of brain metastasis at 3-T magnetic resonance imaging.** *J Comput Assist Tomogr* 2008;32:313–19 CrossRef Medline
6. Chamberlain M, Junck L, Brandsma D, et al. **Leptomeningeal metastases: a RANO proposal for response criteria.** *Neuro Oncol* 2016; 9:484–92 CrossRef Medline
7. Le Rhun E, Weller M, Brandsma D, et al. **EANO–ESMO Clinical Practice Guidelines for diagnosis, treatment and follow-up of patients with leptomeningeal metastasis from solid tumours.** *Ann Oncol* 2017;28:iv84–99 CrossRef Medline
8. Fukuoka H, Hirai T, Okuda T, et al. **Comparison of the added value of contrast-enhanced 3D fluid-attenuated inversion recovery and magnetization-prepared rapid acquisition of gradient echo sequences in relation to conventional postcontrast T1-weighted images for the evaluation of leptomeningeal diseases at 3T.** *AJNR Am J Neuroradiol* 2010;31:868–73 CrossRef Medline
9. Park YW, Ahn SJ. **Comparison of contrast-enhanced T2 FLAIR and 3D T1 black-blood fast spin-echo for detection of leptomeningeal metastases.** *Investig Magn Reson Imaging* 2018;22:86 CrossRef
10. Kammer NN, Coppenrath E, Treitl KM, et al. **Comparison of contrast-enhanced modified T1-weighted 3D TSE black-blood and 3D MP-RAGE sequences for the detection of cerebral metastases and brain tumours.** *Eur Radiol* 2015;26:1818–25 CrossRef Medline
11. Sommer NN, Pons Lucas R, Coppenrath E, et al. **Contrast-enhanced modified 3D T1-weighted TSE black-blood imaging can improve detection of infectious and neoplastic meningitis.** *Eur Radiol* 2020;30:866–76 CrossRef Medline
12. Sommer NN, Saam T, Coppenrath E, et al. **Multiple sclerosis: improved detection of active cerebral lesions with 3-dimensional T1 black-blood magnetic resonance imaging compared with conventional 3-dimensional T1 GRE imaging.** *Invest Radiol* 2018;53: 13–19 CrossRef Medline
13. Oh J, Choi SH, Lee E, et al. **Application of 3D fast spin-echo T1 black-blood imaging in the diagnosis and prognostic prediction of patients with leptomeningeal carcinomatosis.** *AJNR Am J Neuroradiol* 2018;39:1453–59 CrossRef Medline
14. Hwang J-Y, Yoon H-K, Lee JH, et al. **Cranial nerve disorders in children: MR imaging findings.** *RadioGraphics* 2016;36:1178–94 CrossRef Medline
15. Gil B, Hwang EJ, Lee S, et al. **Detection of leptomeningeal metastasis by contrast-enhanced 3D T1-SPACE: comparison with 2D FLAIR and contrast-enhanced 2D T1-weighted images.** *PLoS One* 2016;11:e0163081 CrossRef Medline
16. Lim HK, Lee JH, Hyun D, et al. **MR diagnosis of facial neuritis: diagnostic performance of contrast-enhanced 3D FLAIR technique compared with contrast-enhanced 3D T1-fast-field echo with fat suppression.** *AJNR Am J Neuroradiol* 2012;33:779–83 CrossRef Medline
17. Kato Y, Higano S, Tamura H, et al. **Usefulness of contrast-enhanced T1-weighted sampling perfection with application-optimized contrasts by using different flip angle evolutions in detection of small brain metastasis at 3T MR imaging: comparison with magnetization-prepared rapid acquisition of gradient echo imaging.** *AJNR Am J Neuroradiol* 2009;30:923–29 CrossRef Medline
18. Mugler JP, Brookeman JR. **Theoretical analysis of gadopentetate dimeglumine enhancement in T1-weighted imaging of the brain: comparison of two-dimensional spin-echo and three-dimensional gradient-echo sequences.** *J Magn Reson Imaging* 1993;3:761–69 CrossRef Medline
19. Singh SK, Agris JM, Leeds NE, et al. **Intracranial leptomeningeal metastases: comparison of depiction at FLAIR and contrast-enhanced MR imaging.** *Radiology* 2000;217:50–53 CrossRef Medline
20. Uysal E, Erturk SM, Yildirim H, et al. **Sensitivity of immediate and delayed gadolinium-enhanced MRI after injection of 0.5 M and 1.0 M gadolinium chelates for detecting multiple sclerosis lesions.** *AJR Am J Roentgenol* 2007;188:697–702 CrossRef Medline
21. Vaswani AK, Nizamani WM, Ali M, et al. **Diagnostic accuracy of contrast-enhanced FLAIR magnetic resonance imaging in diagnosis of meningitis correlated with CSF analysis.** *ISRN Radiol* 2014; 2014:578986 CrossRef Medline
22. Jeevanandham B, Kalyanpur T, Gupta P, et al. **Comparison of post-contrast 3D-T1-MPRAGE, 3D-T1-SPACE and 3D-T2-FLAIR MR images in evaluation of meningeal abnormalities at 3-T MRI.** *Br J Radiol* 2017;90:20160834 CrossRef Medline
23. Seo JH, You SK, Lee IH, et al. **Quantitative analysis of the facial nerve using contrast-enhanced three dimensional FLAIR-VISTA imaging in pediatric Bell's palsy.** *Investig Magn Reson Imaging* 2015;19:162 CrossRef
24. Zandian A, Osiro S, Hudson R, et al. **The neurologist's dilemma: a comprehensive clinical review of Bell's palsy, with emphasis on current management trends.** *Med Sci Monit* 2014;20:83–90 CrossRef Medline
25. Eisenkraft B, Ortiz AO. **Imaging evaluation of cranial nerves 3, 4, and 6.** *Semin Ultrasound CT MR* 2001;22:488–501 CrossRef Medline

Neuroimaging Offers Low Yield in Children Positive for SARS-CoV-2

G. Orman, N.K. Desai, S.F. Kralik, A. Meoded, V.J. Seghers, A.V. Annapragada, and T.A.G.M. Huisman



ABSTRACT

SUMMARY: The coronavirus disease 2019 (COVID-19) pandemic caused by Severe Acute Respiratory Syndrome coronavirus disease 2 (SARS CoV-2) most commonly presents with respiratory disease, but neurologic complications are being reported. We aimed to investigate the rate of positive neuroimaging findings in children positive for SARS-CoV-2 referred for neuroimaging between March 18 and September 30, 2020. We found that 10% ($n = 2$) had acute findings. Our results may suggest that in children, neurologic involvement in COVID-19 is rare, neuroimaging has a low yield in diagnosis, and acute neuroimaging should involve careful risk-benefit analysis.

ABBREVIATIONS: COVID-19 = coronavirus disease 2019; MIS-C = multisystem inflammatory syndrome in children; SARS-CoV-2 = Severe Acute Respiratory Syndrome coronavirus disease 2

The coronavirus disease 2019 (COVID-19) pandemic is caused by Severe Acute Respiratory Syndrome coronavirus 2 (SARS CoV-2). The most common presentation of SARS-CoV-2 infection is respiratory disease, but associated neurologic complications are increasingly reported in adults.¹

A wide spectrum of neurologic symptoms has been described. Common neurologic manifestations include fatigue, headache, and smell and taste disorders.¹ In addition, the following serious neurologic complications associated with COVID-19 have been reported:² 1) cerebrovascular accidents (ischemic stroke and macro-/microhemorrhages), 2) encephalopathies, 3) infectious-/immune-mediated complications (Guillain-Barre syndrome, acute disseminated encephalomyelitis), 4) meningoencephalitis, 5) seizures, and 6) neuropsychiatric symptoms (psychosis, mood disorders).

Because COVID-19-associated neurologic manifestations or symptoms are less frequent (1.5% versus 36.4%) and usually less severe in children and, in particular, neonates, neuroimaging findings are uncommon relative to adults.³ The goal of this article was to investigate the neuroimaging findings and yield of neuroimaging in children positive for SARS-CoV-2 with suspected neurologic involvement.

MATERIALS AND METHODS

Following institutional review board approval, a master database of all patients who tested positive for SARS-CoV-2 at Texas Children's Hospital between March 18, 2020, and September 30, 2020, was assembled by the Texas Children's Hospital COVID-19 Imaging Taskforce. All imaging studies were extracted from the master database, and the neuroimaging studies were identified for this retrospective study. Data on demographics, new-onset neurologic symptoms, clinical features (comorbidities, respiratory symptoms, multisystem inflammatory syndrome in children [MIS-C]), cardiopulmonary support, intensive care unit or special isolation unit stay, immune-therapy and condition at discharge, and laboratory findings (CSF testing, blood testing, SARS-CoV-2 testing) were reviewed and extracted from the electronic medical records.

New-onset neurologic symptoms that were primary indications for neuroimaging within 1 month of testing positive for SARS-CoV-2 were classified as the following: 1) COVID-19-attributable indications (fever, seizures, status epilepticus, headache, focal neurologic examination findings, impaired consciousness);¹⁻³ and 2) other indications (motor vehicle crash, abusive head trauma, penetrating trauma, history of ventriculoperitoneal shunt, hydrocephalus, global developmental delay, sensorineural hearing loss, primary or metastatic tumor). Only children who met all of the following criteria were included in this study: 1) younger than 18 years, 2) tested positive for SARS-CoV-2 before and within 1 month of neuroimaging, and 3) had neuroimaging studies with COVID-19-attributable indications. The neuroimaging studies were re-evaluated for this study by 2 experienced pediatric neuro-radiologists (S.F.K. and N.K.D. with 9 and 10 years of experience, respectively) in consensus.

Received November 16, 2020; accepted after revision December 14.

From the Edward B. Singleton Department of Radiology, Texas Children's Hospital, Houston, Texas.

Please address correspondence to Gunes Orman, MD, Texas Children's Hospital, Edward B. Singleton Department of Radiology, 6701 Fannin St, Suite 470, Houston, TX 77030; e-mail: gxorman@texaschildrens.org

Indicates open access to non-subscribers at www.ajnr.org

Indicates article with online supplemental data.

<http://dx.doi.org/10.3174/ajnr.A7022>

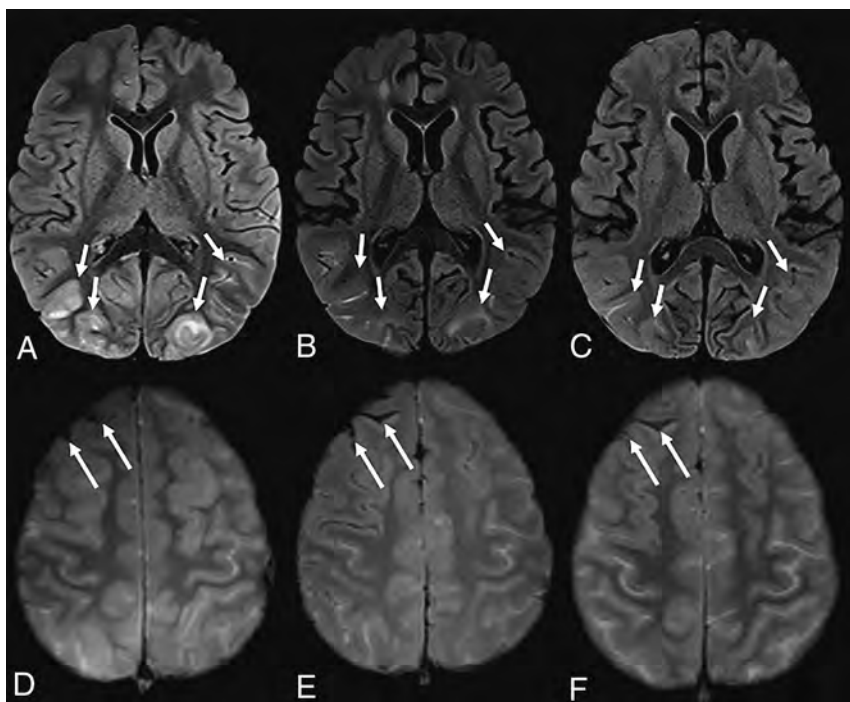


FIG 1. A 7-year-old boy with sickle cell disease who presented with dyspnea and chest pain tested positive for SARS-CoV-2. The patient was unresponsive, having desaturations and being intubated. Brain MR imaging showed T2-FLAIR hyperintensity and cortical edema in the occipital lobes, consistent with posterior reversible encephalopathy syndrome, partially resolving on subsequent imaging (A–C, arrows). Note interval evolution of right frontal subarachnoid hemorrhage (D–F, arrows).

RESULTS

The COVID-19 Imaging Taskforce identified 4351 patients, of whom 3694 were children (0–18 years of age) who tested positive for SARS-CoV-2 by polymerase chain reaction and/or serum antibodies at the Texas Children's Hospital during the study period. There were 3364 imaging studies performed on these patients, of which 217 (6.5%) were neuroimaging studies.

Forty-three neuroimaging studies (17 head CTs, 11 without contrast, 6 with contrast; 26 brain MRIs, 8 stroke protocol, 3 with/without contrast, 6 without contrast, 2 MRVs, and 7 MRAs) of 20 children (male/female, 12:8) met our inclusion criteria. All children had at least 1 neuroimaging study, 8 children had follow-up studies within a 4.47-day interval (range, 0–72 days). The average age at neuroimaging was 8.8 years (range, 0.6–17.8 years). Fifty-five percent of patients ($n = 11$) had no previous medical conditions. The remaining patients had the following pre-existent conditions: epilepsy (patient 3), sickle cell disease (patients 7 and 10), obesity (patients 11 and 13), overweight (patient 17), hemophilia C (patient 14), Sturge-Weber syndrome (patient 18), and autism (patient 20) (Online Supplemental Data).

The patients' neurologic presentation timeline was April ($n = 1$), June ($n = 6$), July ($n = 6$), August ($n = 4$), and September ($n = 3$) of 2020. Ten percent of patients ($n = 2$) had respiratory symptoms, MIS-C was noted in 10% of patients ($n = 2$), and 15% of patients ($n = 3$) had both. Mechanical ventilation was required in 2 patients, and mechanical ventilation with extracorporeal membrane oxygenation was required in 2 additional patients.

Thirty percent of patients ($n = 6$) stayed in our special isolation unit for an average of 5.3 days (range, 1–14 days), and 25% of patients ($n = 5$) stayed in the intensive care unit for an average of 11.2 days (range, 2–25 days). CSF was normal in 3 patients, but no CSF records were available for the remaining 17 patients. Blood testing showed increased inflammatory markers in 55% of patients ($n = 11$), findings were normal in 25% of patients ($n = 5$), and results were not available in 20% of patients ($n = 4$). Thirty percent of patients ($n = 6$) received immune therapy, and 10% ($n = 2$) received antiviral therapy as part of their COVID-19 management (Online Supplemental Data). Two patients (10%) had no follow-up records, and 90% of the patients ($n = 18$) were discharged from the hospital with either an improved (60%) or good (30%) condition (Online Supplemental Data).

The mean time interval between SARS-CoV-2 testing and the initial neuroimaging study was 3.9 days (range, 0–22 days). Neurologic symptoms at neuroimaging included impaired consciousness ($n = 7$), seizures ($n = 4$), status epilepticus ($n = 2$), headache ($n =$

2), focal neurologic findings on examination ($n = 2$), fever with meningeal signs on examination ($n = 1$), transient episode of aphasia ($n = 1$), and fever with headache ($n = 1$). Only 2 patients (10%) had acute findings on their initial MR imaging studies: subarachnoid hemorrhage combined with posterior reversible encephalopathy syndrome in patient 7 (Fig 1) and a right-sided hippocampal T2-hyperintense signal alteration in patient 19 (Fig 2), possibly secondary to seizure activity. Of the 5 children diagnosed with MIS-C, only 1 patient (patient 19) had acute imaging findings (right hippocampal edema).

DISCUSSION

In this limited, preliminary study, we demonstrated systemic and neurologic manifestations and neuroimaging findings in 20 children positive for SARS-CoV-2. We found that 10% of patients ($n = 2$) had acute findings on their neuroimaging studies; in 90% of patients, neuroimaging did not show acute pathology that could be attributed to the SARS-CoV-2 infection.

SARS-CoV-2 neurotropism is still poorly understood, but 4 potential mechanisms have been proposed to explain COVID-19 neurologic involvement: 1) a secondary effect of the systemic inflammatory responses triggered by the viral infection; 2) a secondary effect associated with the vascular and prothrombotic effect of the viral infection on the nervous system vasculature; 3) an immune-mediated parainfectious or postinfectious autoimmune effect in response to the viral infection; and 4) a direct neurotropic or neuroinvasive effect of SARS-CoV-2. Direct viral

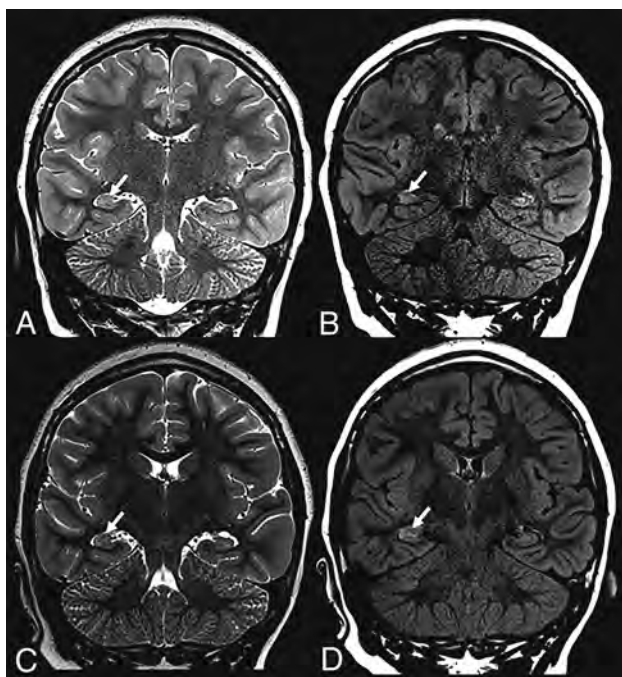


FIG 2. A previously healthy 9-year-old girl who presented with status epilepticus tested positive for SARS-CoV-2. Brain MR imaging showed subtle right hippocampal T2-FLAIR signal alteration with corresponding edema (arrows) on initial (upper row) and follow-up (lower row) imaging.

invasion confirmation would require SARS-CoV-2 sampling in CSF or brain tissue. However, SARS-CoV-2 has not been isolated from CSF or brain samples to date.³ In our patient cohort, only 3 patients had been tested for SARS-CoV-2 in the CSF; all findings were negative.

The most commonly reported neuroimaging finding in children with COVID-19 and MIS-C was reversible splenic lesion syndrome.⁴⁻⁷ Acute disseminated encephalomyelitis, bilateral thalamic cytotoxic lesions, and unilateral focal vasculopathy with acute infarction were other reported neuroimaging findings in pediatric patients with COVID-19.⁸⁻¹¹ We did not see any of these neuroimaging findings in our patient cohort. However, patient 7 with sickle cell disease had imaging findings consistent with posterior reversible encephalopathy syndrome (which was partially resolved on subsequent brain MRI, Fig 1). This patient manifested primarily with respiratory symptoms that required mechanical ventilation. Patient 19, who had no previous history, presented with a status epilepticus and showed a right hippocampus T2-hyperintense signal (Fig 2), possibly secondary to seizure activity. This patient stayed in the intensive care unit for a MIS-C diagnosis. Attributing the positive neuroimaging findings primarily to the positive SARS-CoV-2 findings in these 2 patients with complex medical histories would be highly speculative. We believe that a 10% positivity rate of acute neuroimaging findings in our patient group implies a low yield from acute neuroimaging.

A major strength of our preliminary study is the large number of children positive for SARS-CoV-2 ($n = 3694$) who presented to our hospital. Limitations of this study include the following: 1) due to the retrospective nature of the study, a discrepancy

between the number of neuroimaging studies and children because not each child needed follow-up neuroimaging, 2) single-center evaluation of patients, 3) still emerging data about the SARS-CoV-2 virus and its effects and still developing understanding of its consequences, 4) a positive test for SARS-CoV-2 in a patient with a neurologic symptom not necessarily meaning that the virus caused the symptom, and 5) acute neurologic symptoms being a possible selection bias.

CONCLUSIONS

Our results suggest that neurologic involvement of COVID-19 is rare among children. Only 10% of patients with neurologic manifestations demonstrated acute findings on their initial neuroimaging studies. In addition, a link between the observed imaging findings (posterior reversible encephalopathy syndrome and hippocampal edema) must still be confirmed. Of the 5 children with diagnosed MIS-C, only 1 child had an acute imaging finding (hippocampal edema). In summary, neuroimaging in children may have a low yield in COVID-19 diagnosis; consequently, requests for acute imaging should involve a careful risk-benefit analysis.

ACKNOWLEDGMENTS

The Texas Children's Hospital COVID-19 Imaging Taskforce (Ananth V. Annapragada, Nilesh K. Desai, R. Paul Guillermin, Thierry A.G.M. Huisman, Prakash M. Masand, Gunes Orman, Amir H. Pezeshkmehr, Marla B. Sammer, and Victor J. Seghers).

Disclosures: Ananth Annapragada—UNRELATED: Board Membership: Alzecca Biosciences; Consultancy: Alzecca Biosciences; Employment: Texas Children's Hospital; Grants/Grants Pending: National Institutes of Health, Alzecca Biosciences*; Patents (Planned, Pending or Issued): numerous United States and foreign patent applications; Royalties: University of Texas; Stock/Stock Options: Sensulin, Alzecca Biosciences; Other: Texas Children's Hospital also receives royalties from my inventions.* *Money paid to the institution.

REFERENCES

- Sharifian-Dorche M, Huot P, Oshero M, et al. **Neurological complications of coronavirus infection; a comparative review and lessons learned during the COVID-19 pandemic.** *J Neurol Sci* 2020;417:117085 CrossRef Medline
- Almqvist J, Granberg T, Tzortzakakis A, et al. **Neurological manifestations of coronavirus infection: a systematic review.** *Ann Clin Transl Neurol* 2020;7:2057-71 CrossRef Medline
- Stafstrom CE, Jantzie LL. **COVID-19: neurological considerations in neonates and children.** *Children (Basel)* 2020;7:133 CrossRef Medline
- Abdel-Mannan O, Eyre M, Löbel U, et al. **Neurologic and radiographic findings associated with COVID-19 infection in children.** *JAMA Neurol* 2020;77:1440 CrossRef Medline
- Gaur P, Dixon L, Jones B, et al. **COVID-19-associated cytotoxic lesions of the corpus callosum.** *AJNR Am J Neuroradiol* 2020;41:1905-07 CrossRef Medline
- Lin J, Lawson EC, Verma S, et al. **Cytotoxic lesion of the corpus callosum in an adolescent with multisystem inflammatory syndrome and SARS-CoV-2 infection.** *AJNR Am J Neuroradiol* 2020;41:2017-19 CrossRef Medline
- Bektaş G, Akçay N, Boydağ K, et al. **Reversible splenic lesion syndrome associated with SARS-CoV-2 infection in two children.** *Brain Dev* 2020 Oct 13. [Epub ahead of print] CrossRef Medline

8. de Miranda Henriques-Souza AM, de Melo A, de Aguiar Coelho Silva Madeiro B, et al. **Acute disseminated encephalomyelitis in a COVID-19 pediatric patient.** *Neuroradiology* 2020 Oct 1. [Epub ahead of print] CrossRef Medline
9. Abel D, Shen MY, Abid Z, et al. **Encephalopathy and bilateral thalamic lesions in a child with MIS-C associated with COVID-19.** *Neurology* 2020;95:745–48 CrossRef Medline
10. Mirzaee SMM, Gonçalves FG, Mohammadifard M, et al. **Focal cerebral arteriopathy in a pediatric patient with COVID-19.** *Radiology* 2020;297:E274–75 CrossRef Medline
11. Gulko E, Overby P, Ali S, et al. **Vessel wall enhancement and focal cerebral arteriopathy in a pediatric patient with acute infarct and COVID-19 infection.** *AJNR Am J Neuroradiol* 2020;41:2348–50 CrossRef Medline

Transient Hyperintensity of the Infant Thyroid Gland on T1-Weighted MR Imaging: Correlation with Postnatal Age, Gestational Age, and Signal Intensity of the Pituitary Gland

H. Maki, M. Nakagawa, R. Kagaya, S. Kumazawa, K. Matsumoto, M. Hatano, Y. Miyake, W. Sugihara, and Y. Shibamoto

ABSTRACT

BACKGROUND AND PURPOSE: The signal intensity of the thyroid in neonates is high on T1WI. It is affected by gestational and postnatal ages. However, the extent of the influence of these ages is unknown. This study investigated the relationship of signal intensities of the infant thyroid with postnatal and gestational ages and anterior pituitary using 3D gradient-echo T1WI.

MATERIALS AND METHODS: This retrospective study included 183 T1-weighted images from 181 infants. Using a multiple linear regression analysis, we evaluated the effects of postnatal and gestational ages on the thyroid–muscle signal intensity ratio. The relationship between the thyroid and anterior pituitary signal intensities on T1WI and the age of the infants was evaluated.

RESULTS: Multiple linear regression analysis showed that the thyroid signal intensity was affected negatively by postnatal age at examination and positively by gestational age at birth ($P < .01$ and $P = .04$, respectively). According to the standardized partial regression coefficients, the influence of postnatal age at examination was stronger than that of gestational age at birth (-0.72 and 0.13 , respectively). The thyroid and anterior pituitary signal intensities reached constant values at 12 weeks' postnatal age, and the mean thyroid–anterior pituitary signal intensity ratios were almost 1 throughout the entire period.

CONCLUSIONS: The signal intensity of the infant thyroid on T1WI was more strongly influenced by the postnatal age at examination than the gestational age at birth, and it was almost equal to that of the anterior pituitary.

ABBREVIATIONS: GRE = gradient echo; TSH = thyroid-stimulating hormone

Thyroid hormone is essential for prenatal and neonatal neurologic development.¹ The fetal hypothalamic–pituitary–thyroid axis begins to develop by gestational week 6, and thyroid follicular epithelial cells are able to concentrate iodide and synthesize thyroid hormone by 11 weeks of gestation.^{2,3} After delivery, serum thyroid-stimulating hormone (TSH) demonstrates a transient increase in the first 24 hours, and this TSH surge stimulates a rise in serum levels of thyroxine and triiodothyronine.⁴ A previous study reported that the fetal thyroid gland showed high signal intensity on 3D gradient-echo (GRE) T1WI, and the fetal thyroid–muscle signal intensity ratio did not correlate with gestational age.⁵

In our institution, infants in the neonatal intensive care unit are routinely screened for CNS abnormalities using MR imaging, including 3D GRE T1WI in the head to neck range. Some of these infants display high signal intensity in the thyroid gland on 3D GRE T1WI, especially when the time between birth and the MR examination was short. The anterior pituitary glands of neonates usually show high signal intensity on T1WI, and the relative signal intensity of the anterior pituitary gland to that of the pons was significantly negatively correlated with postnatal age at examination.⁶ A recent study reported that the signal intensity of the infant thyroid and anterior pituitary on 3D GRE T1WI correlated positively with the gestational age at birth and negatively with the postnatal age at examination.⁷ However, the extent of the influence of gestational age at birth and postnatal age at examination on the signal intensities of the infant thyroid and anterior pituitary on T1WI is not known.

It was hypothesized that postnatal age at examination might affect the signal intensity changes of the infant thyroid on 3D GRE T1WI more strongly than the gestational age at birth. The change in signal intensity of the infant thyroid on 3D GRE T1WI was thought to be similar to that of the anterior pituitary. In this

Received September 24, 2020; accepted after revision November 23.

From the Department of Radiology (H.M., M.N., S.K., K.M., W.S., Y.S.), Nagoya City University Graduate School of Medical Sciences, Mizuho-ku, Nagoya, Aichi, Japan; Department of Radiology, Kariya Toyota General Hospital (R.K.), Kariya-shi, Aichi, Japan; Department of Radiology, Nagoya City West Medical Center (M.H.), Nagoya, Japan; and Department of Radiology (Y.M.), Nagoya Daini Red Cross Hospital, Nagoya-shi, Aichi, Japan.

Please address correspondence to Hiroyuki Maki, MD, PhD, Department of Radiology, Nagoya City University Graduate School of Medical Sciences, 1 Kawasumi, Mizuho-cho, Mizuho-ku, Nagoya, Aichi, 467-8601 Japan; e-mail: machikita205@gmail.com
<http://dx.doi.org/10.3174/ajnr.A7024>

study, a multiple linear regression analysis was used to evaluate the effects of postnatal age at examination and gestational age at birth on the thyroid–muscle and anterior pituitary–muscle signal intensity ratios. In addition, the change in signal intensity of the infant thyroid gland on 3D GRE T1WI was assessed to clarify the relationship between signal intensities of the infant thyroid and anterior pituitary.

MATERIALS AND METHODS

Participants

In this retrospective study, subjects included infants with no known thyroid function abnormality who had been referred for screening brain MR examination between July 2016 and April 2019. The institutional review board of Nagoya City University Hospital approved this study and waived the requirement for patient informed consent because of the retrospective nature of the study and the use of anonymized patient data. The inclusion criteria of this study were as follows: 1) brain MR imaging was performed within 4 months of birth, and 2) 3D GRE T1WI was performed. The exclusion criteria were as follows: 1) thyroid function abnormality, 2) unsatisfactory MR images caused by motion artifacts, and 3) infants with severe brain injury. Neonatal thyroid function was tested in neonate screening, which evaluated blood spot TSH, thyroxine, or both.⁸ Among the 223 consecutive neonates who underwent MR imaging, 6 with thyroid function abnormality, 24 with unsatisfactory MR images caused by motion artifacts, and 10 with severe brain injury were excluded. Thus, 183 MR images from 181 infants (96 males and 85 females) formed the final study cohort.

The terms concerning the age of the infant in this study were defined as follows: “gestational age at birth” refers to the age of the infant at birth based on the number of weeks gestation, “gestational age at examination” refers to the age of the infant at the time of the MR imaging examination based on the number of weeks gestation, and “postnatal age at examination” refers to the number of days from birth to the day of the MR imaging examination. In the study cohort, the gestational age at birth, gestational age at examination, and postnatal age at examination ranged from 22 to 41 weeks (mean, 34 weeks), 36 to 50 weeks (mean, 39 weeks), and 0 to 107 days (mean, 32 days), respectively. A total of 117 of the 181 neonates were delivered preterm (birth before 37 weeks of gestation), and 130 of the 181 were delivered by cesarean section. Among the 181 neonates, 178 were admitted to the neonatal intensive care unit after a diagnosis of respiratory distress ($n = 83$); low birth weight ($n = 51$); asphyxia ($n = 18$); congenital cardiac anomaly ($n = 18$); hypoglycemia ($n = 2$); or myelomeningocele, angiomas, diaphragmatic hernia, jaundice, convulsion, or volvulus of the small intestine ($n = 1$ each). The remaining 3 infants underwent MR imaging examination for suspected congenital brain malformations.

MR Imaging Technique

MR imaging was performed using a 1.5T ($n = 53$) or 3T ($n = 130$) scanner (Ingenia; Philips Healthcare), with a 20-channel head coil. T1-weighted sagittal images were obtained using the 3D T1 turbo field echo method. Imaging parameters were as

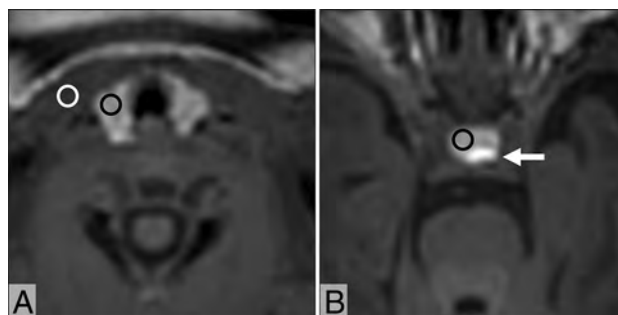


FIG 1. Axial 3D GRE T1-weighted MR images of an infant at postnatal day 6 show the thyroid (A) and pituitary (B). For measurement of the signal intensity, ROIs are placed on the thyroid (black circle, A), sternocleidomastoid muscle (white circle, A), and anterior pituitary (black circle, B). The posterior pituitary is shown (arrow, B).

follows: TR/TE, 9.2–9.5/4.3–4.5 ms; flip angle, 7°; field of view, 224 × 224 mm; section thickness, 1 mm; image matrix, 224 × 224; and parallel imaging (sense factor = 2) for the 1.5T scanner and TR/TE, 6.1–6.7/2.7–3.1 ms; flip angle, 8°; field of view, 256 × 256 mm; section thickness, 1 mm; image matrix, 256 × 256; and parallel imaging (sense factor = 2) for the 3T scanner.

Imaging Analysis

Two experienced radiologists (6 and 17 years of experience in infant MR imaging, respectively) worked together and retrospectively reviewed the 3D GRE T1-weighted MR images. The reviewers were blinded to the clinical details. The mean MR signal intensity from the thyroid, sternocleidomastoid muscle, and anterior pituitary were measured using manually defined circular or oval ROIs ($\sim 5 \text{ mm}^2$). The signal intensities of the thyroid and sternocleidomastoid muscle were measured on reconstructed axial images at the same horizontal level, and the signal intensity of the anterior pituitary was measured on reconstructed axial images, where the maximal diameter of the anterior pituitary was shown (Fig 1). In addition, the thyroid–muscle, anterior pituitary–muscle, and thyroid–anterior pituitary signal intensity ratios were calculated.

Statistical Analysis

The correlation between the thyroid–muscle signal intensity ratio and postnatal age at examination or gestational age at examination were calculated using the Pearson correlation coefficient. A multiple linear regression analysis was used to evaluate the effects of postnatal age at examination and gestational age at birth on the thyroid–muscle and anterior pituitary–muscle signal intensity ratios. Analysis of variance was used to compare the thyroid–pituitary signal intensity ratios with respect to postnatal age at the time of examination. All statistical analyses were performed using Bell-Curve (version 2.11, Social Survey Research Information) for Excel software (Microsoft Office 2019).

RESULTS

Fig 2 shows the thyroid–muscle signal intensity ratio plotted against the corresponding postnatal age at examination or gestational age at examination. There was a negative correlation between the thyroid–muscle signal intensity ratio and postnatal

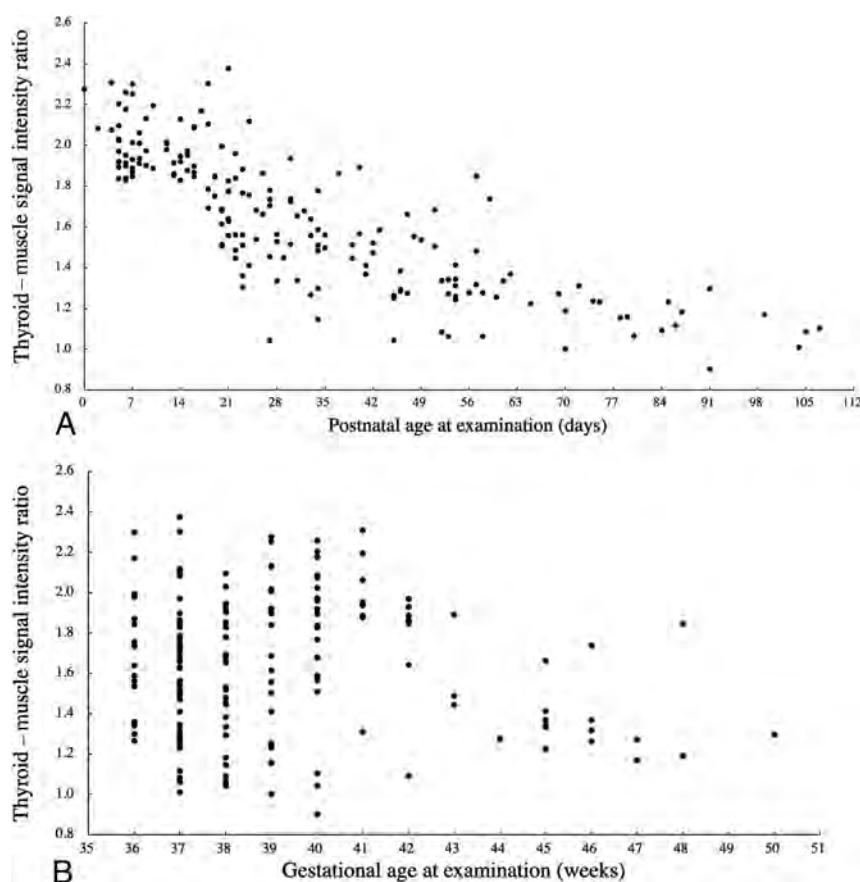


FIG 2. Scatterplots of the thyroid-muscle signal intensity ratio against the corresponding postnatal age at examination (A) and gestational age at examination (B). There is a negative correlation between the thyroid-muscle signal intensity ratio and postnatal age at examination (A). Conversely, there is no distinct relationship between the thyroid-muscle signal intensity ratio and gestational age at examination (B).

age at examination ($r = -0.75$, $P < .01$). Conversely, there was no distinct relationship between the thyroid-muscle signal intensity ratio and gestational age at examination ($r = 0.05$, $P = .18$). Regarding the anterior pituitary and thyroid, there was a negative correlation between the anterior pituitary-muscle signal intensity ratio and postnatal age at examination ($r = -0.67$, $P < .01$), and no distinct relationship between the anterior pituitary-muscle signal intensity ratio and gestational age at examination ($r = 0.10$, $P = .55$).

A multiple linear regression was performed to predict the thyroid-muscle signal intensity ratio based on postnatal age at examination and gestational age at birth. A significant regression equation was found ($F(2, 180) = 177.9$, $P < .01$), with an R^2 of 0.66. The predicted thyroid-muscle signal intensity ratio of participants was equal to $1.6035 - 0.0101$ (postnatal age at examination) + 0.0107 (gestational age at birth), in which the postnatal age at examination was in days and gestational age at birth was in weeks. The standardized partial regression coefficients of postnatal age at examination and gestational age at birth were -0.72 ($P < .01$) and 0.13 ($P = .04$), respectively. A multiple linear regression was also performed to predict the anterior pituitary-muscle signal intensity ratio based on postnatal age at examination and gestational age at birth. A significant regression equation was

found ($F(2, 180) = 120.3$, $P < .01$), with an R^2 of 0.57. Participants' predicted anterior pituitary-muscle signal intensity ratio was equal to $1.2750 - 0.0087$ (postnatal age at examination) + 0.0183 (gestational age at birth) in which postnatal age at examination was in days and gestational age at birth was in weeks. The standardized partial regression coefficients of postnatal age at examination and gestational age at birth were -0.60 ($P < .01$) and 0.21 ($P < .01$), respectively. The thyroid-muscle and anterior pituitary-muscle signal intensity ratios reached a constant value at a postnatal age of 12 weeks (Table). The mean thyroid-anterior pituitary signal intensity ratios were almost 1 throughout the entire period (Table), and there was no statistically significant difference between different postnatal ages per week ($P = .89$).

DISCUSSION

The present study demonstrated that the thyroid usually showed high signal intensity on 3D GRE T1-weighted MR imaging in neonates. However, the hyperintensity diminished in older infants and seemed to be a temporary phenomenon. The disappearance of this hyperintensity correlated well with postnatal age at examination but not with gestational age at examination. From the results of the multiple linear regression analysis, the postnatal age at examination negatively affected the signal intensity in the thyroid, and gestational age at birth positively affected the signal intensity. According to the standardized partial regression coefficients, postnatal age at examination was more effective than gestational age at birth. The same tendency was observed in the signal intensity of the anterior pituitary. The thyroid-muscle and anterior pituitary-muscle signal intensity ratios reached constant values at 12 weeks of postnatal age, and the signal intensity of the thyroid on 3D GRE T1WI was almost equal to that of the anterior pituitary throughout the entire period within the fourth postnatal month (Fig 3).

Because there was lesser effect of gestational age on the signal intensity of the infant thyroid on 3D GRE T1WI, the decreased signal intensity in the neonatal thyroid may be influenced more by changes that occur in the thyroid after birth. The decrease in signal intensity of the infant thyroid may be related to changes in thyroid hormone production, considering the decline in serum thyroid hormone levels after birth.⁹ Furthermore, a previous report showed high signal intensity of the thyroid in the fetal period; hyperintensity of the neonatal thyroid may be related to the immaturity of the thyroid tissue.⁵

Means of thyroid–muscle, anterior pituitary–muscle, and thyroid–anterior pituitary signal intensity ratios against the corresponding postnatal age at examination grouped according to week

Postnatal Age at Examination		Signal Intensity Ratio		
		Thyroid–Muscle	Anterior Pituitary–Muscle	Thyroid–Anterior Pituitary
Day	No	Mean (SD)	Mean (SD)	Mean (SD)
0–6	20	2.03 (0.15)	2.01 (0.30)	1.03 (0.16)
7–13	22	1.99 (0.13)	2.00 (0.23)	1.01 (0.12)
14–20	26	1.88 (0.19)	1.78 (0.29)	1.07 (0.13)
21–27	31	1.67 (0.25)	1.65 (0.17)	1.02 (0.14)
28–34	20	1.54 (0.19)	1.50 (0.19)	1.03 (0.11)
35–41	9	1.57 (0.18)	1.60 (0.27)	1.00 (0.17)
42–48	12	1.38 (0.17)	1.43 (0.20)	0.98 (0.11)
49–55	13	1.34 (0.17)	1.36 (0.21)	1.00 (0.14)
56–62	10	1.40 (0.22)	1.36 (0.18)	1.03 (0.12)
63–69	2	1.25 (0.02)	1.26 (0.18)	1.02 (0.17)
70–76	5	1.19 (0.10)	1.16 (0.10)	1.03 (0.10)
77–83	3	1.13 (0.04)	1.06 (0.02)	1.06 (0.06)
84–90	4	1.16 (0.05)	1.12 (0.04)	1.03 (0.06)
91–97	2	1.10 (0.20)	1.13 (0.03)	0.97 (0.15)
98–104	2	1.09 (0.08)	1.14 (0.12)	0.96 (0.03)
105–111	2	1.10 (0.01)	1.14 (0.11)	0.97 (0.10)
Total	183			

Thyroglobulin and iodine play important roles in the synthesis of thyroid hormones.¹⁰ Thyroglobulin is a glycoprotein synthesized in the thyroid follicular epithelial cells.¹¹ After synthesis, thyroglobulin is transported and stored in the follicular lumen, where the tyrosine residues of thyroglobulin undergo iodination to produce monoiodotyrosine and diiodotyrosine catalyzed by thyroid peroxidase. Subsequent coupling of these iodotyrosines produces thyroxine and triiodothyronine. Relatively large amounts of thyroid hormones are required for normal postnatal development. After delivery, the TSH level surges to approximately 80 mU/L in response to exposure to cold or clamping of the cord.^{2,12} The TSH concentration peaks about 30 minutes after birth and falls rapidly in the first 24 hours and then more slowly to under 10 mU/L after the first week of life.² TSH stimulates a rise in serum thyroxine, which reaches a peak at 24–36 hours followed by a rapid decrease in the third or fourth day and then a slower decrease during the next 4 months, eventually reaching a minimum at about 9–12 months.^{2,9} In the first 24 hours of life, the thyroid shows no or very low colloid content in 60%–80% of neonates, which might be closely related to the low iodine and thyroglobulin contents of the neonatal thyroid.^{13,14} After 24 hours, a progressive filling of the thyroid follicles occurs, and only 6%–7% of thyroids had an absence of colloid at up to 6 days and less than 2% afterward.^{13,14} After 12 days of life, the histologic aspects and iodine and thyroglobulin concentrations tend to match those seen in adults.¹⁴

The storage of thyroglobulin and iodine in the thyroid only occurs around term birth, and these concentrations in the thyroid progressively increase in infants who survive beyond gestational week 42.³ The total iodine concentration in the thyroid of neonates is far lower than that of adults, being

1/10 of the adult concentration up to 42 weeks of gestational age.^{3,15} It is significantly higher in infants who survive longer, reaching 50% of the normal adult value.³ The thyroglobulin concentration is approximately 4% of the adult value in premature neonates and increased 4-fold in term infants.³ It was assumed that the absence of iodine and thyroglobulin storage in the immature thyroid could result either from a limited capacity to synthesize thyroglobulin or a lack of colloid in thyroid follicles.^{3,14,15}

Contrary to the low concentrations of thyroglobulin and iodine in the immature thyroid, the percentage of thyroglobulin iodination and thyroxine to thyroglobulin molar ratio are equal to or higher than adult values for all gestational ages.¹⁶ There is no marked systematic linear correlation in thyroglobulin iodination with duration of life.¹⁷ Coupling efficiency is established in the fetal thyroid, and

the values are comparable to those of adults, even in glands with low relative weight to that of the body.¹⁶ The calculated turnover of the thyroxine pool is very rapid in preterm and term neonates, ranging from 100%–1000% renewal of the pool per day, with lower values in older infants.³ A high percentage of thyroglobulin iodination and coupling efficiency contributes to the active functionality of the fetal thyroid at an early gestational age.¹⁶ If thyroglobulin or iodine concentration in the thyroid or viscosity of colloids in the thyroid follicles is responsible for the signal intensity change of the infant thyroid on 3D GRE T1WI, the signal intensity should increase with gestational age or postnatal age. Therefore, it was speculated that a high percentage of thyroglobulin iodination and ratio of thyroxine to thyroglobulin molar ratio may contribute to T1 shortening. In patients with untreated Graves disease, the thyroid demonstrated a high signal intensity on T1WI, and there was a linear relationship between the thyroid–muscle signal intensity ratio on T1WI and serum thyroxine concentrations.¹⁸ In Grave disease, the percentage of thyroglobulin iodination is higher than that of normal thyroid tissue, and it was demonstrated that the amount of thyroxine per mole of thyroglobulin increases with increasing iodine content.¹⁹ These prior studies also support the hypothesis that the high signal intensity of the fetal and neonatal thyroid on T1WI may be attributed to a higher percentage of thyroglobulin iodination in the immature thyroid.

Several MR studies have revealed that the neonatal anterior pituitary gland usually appears hyperintense on T1-weighted MR images, and the signal intensity of the anterior pituitary gland negatively correlated with postnatal age but not gestational age at birth.^{6,20–22} It was suspected that the mechanisms underlying hyperintensity of the anterior pituitary gland related to hyperplasia

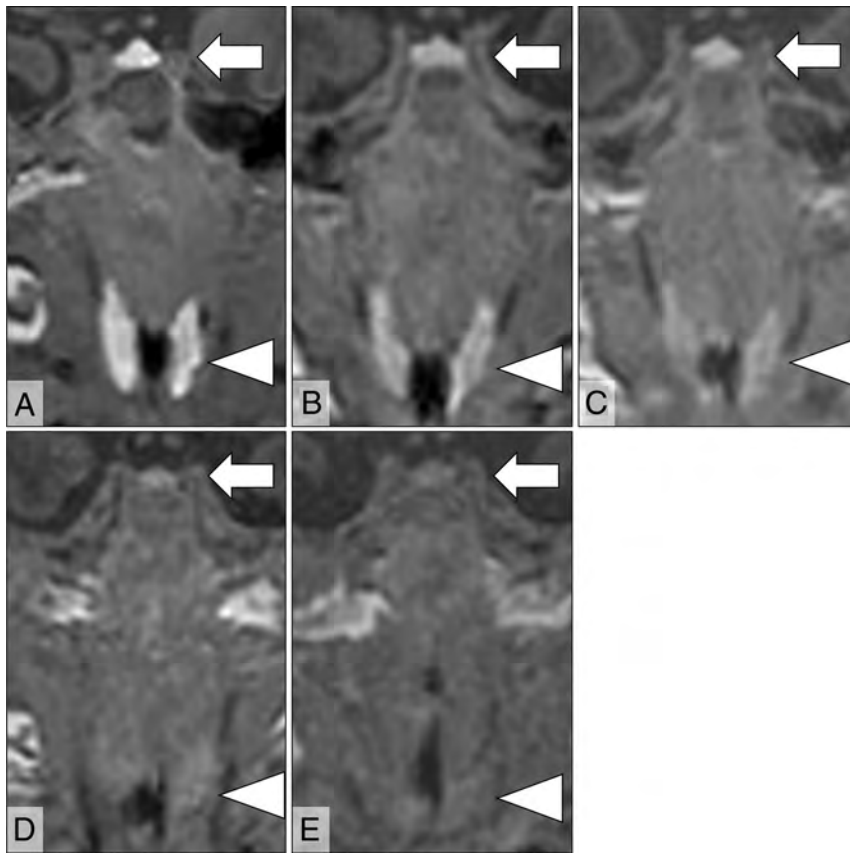


FIG 3. Five different cases showing the thyroid (arrowheads) and anterior pituitary (arrows) on coronal 3D GRE T1-weighted MR images examined at different postnatal ages: 4 days (A), 21 days (B), 33 days (C), 46 days (D), and 70 days (E). These patients' gestational ages at birth are 41, 34, 31, 31, and 29 weeks, respectively. At 4 days of postnatal age, the thyroid and anterior pituitary show extremely high signal intensity (A), and the signal intensity of those glands decreased proportionally to postnatal age (B–E). The signal intensities of the thyroid glands are similar to those of the anterior pituitary glands regardless of postnatal age, and the thyroid–anterior pituitary signal intensity ratios are almost 1 (A = 0.91, B = 1.04, C = 0.83, D = 0.81, E = 0.92).

of prolactin cells in the anterior pituitary, which is caused by estrogen produced by the placenta during pregnancy.⁶ After birth, removal from the effect of placental estrogen may cause a decrease in the number of prolactin cells, resulting in a decline in the signal intensity of the anterior pituitary gland. Although the high signal in the anterior pituitary gland did not reflect TSH production, it was interesting to note that the transition in signal intensity of the anterior pituitary was similar to that of the thyroid.

This study has several limitations. First, although the participant population was confirmed to have normal thyroid function, almost all participants were admitted to the neonate intensive care unit for observation of any perinatal problems leading to potential bias. Second, no histologic specimens of the thyroid were obtained in the current study, and the relationship between T1 signal intensity and thyroid histology was not verified. Third, regarding the signal intensity analysis, the quantification was simply based on the ratio between the signal intensity of the thyroid and that of the muscle or anterior pituitary. The T1 relaxation time could not be measured because this was a retrospective analysis. Finally, in this study, both 1.5T and 3T MR imaging

scanners were used because of the limited availability of MR examination slots. This may have affected the value of the signal intensity ratios.

CONCLUSIONS

The current study revealed that the signal intensity in the thyroid was negatively affected by the postnatal age at examination and positively affected by the gestational age at birth. The disappearance of this hyperintensity was influenced more strongly by the postnatal age at examination than gestational age at birth. The thyroid–muscle and anterior pituitary–muscle signal intensity ratios reached constant values at 12 weeks of postnatal age, and the signal intensity of the thyroid on 3D GRE T1WI was almost equal to that of the anterior pituitary throughout the entire period up to 4 months of postnatal age. The current preliminary data suggest that thyroid signal intensity measurements based on 3D GRE T1WI may provide useful information about hormonal function in infants.

REFERENCES

- Porterfield SP, Hendrich CE. **The role of thyroid hormones in prenatal and neonatal neurological development—current perspectives.** *Endocr Rev* 1993;14:94–106 CrossRef Medline
- LaFranchi S. **Thyroid function in the preterm infant.** *Thyroid* 1999;9:71–78 CrossRef Medline
- van den Hove MF, Beckers C, Devlieger H, et al. **Hormone synthesis and storage in the thyroid of human preterm and term newborns: effect of thyroxine treatment.** *Biochimie* 1999;81:563–70 CrossRef Medline
- Abuid J, Stinson DA, Larsen PR. **Serum triiodothyronine and thyroxine in the neonate and the acute increases in these hormones following delivery.** *J Clin Invest* 1973;52:1195–99 CrossRef Medline
- Fujii S, Nagaishi J, Mukuda N, et al. **Evaluation of fetal thyroid with 3D gradient echo T1-weighted MR imaging.** *Magn Reson Med Sci* 2017;16:203–08. CrossRef Medline
- Kitamura E, Miki Y, Kawai M, et al. **T1 signal intensity and height of the anterior pituitary in neonates: correlation with postnatal time.** *AJNR Am J Neuroradiol* 2008;29:1257–60 CrossRef Medline
- Otani S, Fushimi Y, Iwanaga K, et al. **Signal intensity and volume of pituitary and thyroid glands in preterm and term infants.** *J Magn Reson Imaging* 2020 Oct 16 [Epub ahead of print] CrossRef Medline
- Mass Screening Committee, Japanese Society for Pediatric Endocrinology, Japanese Society for Mass Screening, et al. **Guidelines for Mass Screening of Congenital Hypothyroidism (2014 revision).** *Pediatr Endocrinol* 2015;24:107–33 CrossRef Medline
- O'Halloran MT, Webster HL. **Thyroid function assays in infants.** *J Pediatr* 1972;81:916–19 CrossRef Medline

10. Lamas L, Anderson PC, Fox JW, et al. **Consensus sequences for early iodination and hormonogenesis in human thyroglobulin.** *J Biol Chem* 1989;264:13541–45 Medline
11. van de Graaf SA, Ris-Stalpers C, Pauws E, et al. **Up to date with human thyroglobulin.** *J Endocrinol* 2001;170:307–21 CrossRef Medline
12. Lee SY. **Perinatal factors associated with neonatal thyroid-stimulating hormone in normal newborns.** *Ann Pediatr Endocrinol Metab* 2016;21:206–11 CrossRef Medline
13. Larroche JC. **Histological structure of the thyroid gland in the newborn. With special reference to hypotrophy, hydrops fetalis and cesarean section delivery.** *Biol Neonate* 1976;28:118–24 CrossRef Medline
14. Etling N, Larroche JC. **Histological and biochemical changes in neonatal thyroid tissues.** *Acta Paediatr Scand* 1975;64:315–21 CrossRef Medline
15. Etling N. **Concentration of thyroglobulin, iodine contents of thyroglobulin and of iodoaminoacids in human neonates thyroid glands.** *Acta Paediatr Scand* 1977;66:97–102 CrossRef Medline
16. Costa A, De Filippis V, Panizzo M, et al. **Development of thyroid function between VI-IX month of fetal life in humans.** *J Endocrinol Invest* 1986;9:273–80 CrossRef Medline
17. Savin S, Cvejić D, Nedić O, et al. **Thyroid hormone synthesis and storage in the thyroid gland of human neonates.** *J Pediatr Endocrinol Metab* 2003;16:521–28 CrossRef Medline
18. Charkes ND, Maurer AH, Siegel JA, et al. **MR imaging in thyroid disorders: correlation of signal intensity with Graves disease activity.** *Radiology* 1987;164:491–94 CrossRef Medline
19. Valenta L, Lemarchand-Béraud T. **Thyroglobulin and thyroid acid protease activity in thyroid disease.** *J Clin Endocrinol Metab* 1970;31:422–27 CrossRef Medline
20. Wolpert SM, Osborne M, Anderson M, et al. **The bright pituitary gland—a normal MR appearance in infancy.** *AJNR Am J Neuroradiol* 1988;9:1–3 Medline
21. Dietrich RB, Lis LE, Greensite FS, et al. **Normal MR appearance of the pituitary gland in the first 2 years of life.** *AJNR Am J Neuroradiol* 1995;16:1413–19 Medline
22. Cox TD, Elster AD. **Normal pituitary gland: changes in shape, size, and signal intensity during the 1st year of life at MR imaging.** *Radiology* 1991;179:721–24 CrossRef Medline

A Diagnostic Algorithm for Posterior Fossa Tumors in Children: A Validation Study

C.A.P.F. Alves, U. Löbel, J.S. Martin-Saavedra, S. Toescu, M.H. Tsunemi, S.R. Teixeira, K. Mankad, D. Hargrave, T.S. Jacques, C. da Costa Leite, F.G. Gonçalves, A. Vossough, and F. D'Arco



ABSTRACT

BACKGROUND AND PURPOSE: Primary posterior fossa tumors comprise a large group of neoplasias with variable aggressiveness and short and long-term outcomes. This study aimed to validate the clinical usefulness of a radiologic decision flow chart based on previously published neuroradiologic knowledge for the diagnosis of posterior fossa tumors in children.

MATERIALS AND METHODS: A retrospective study was conducted (from January 2013 to October 2019) at 2 pediatric referral centers, Children's Hospital of Philadelphia, United States, and Great Ormond Street Hospital, United Kingdom. Inclusion criteria were younger than 18 years of age and histologically and molecularly confirmed posterior fossa tumors. Subjects with no available preoperative MR imaging and tumors located primarily in the brain stem were excluded. Imaging characteristics of the tumors were evaluated following a pre-designed, step-by-step flow chart. Agreement between readers was tested with the Cohen κ , and each diagnosis was analyzed for accuracy.

RESULTS: A total of 148 cases were included, with a median age of 3.4 years (interquartile range, 2.1–6.1 years), and a male/female ratio of 1.24. The pre-designed flow chart facilitated identification of pilocytic astrocytoma, ependymoma, and medulloblastoma *sonic hedgehog* tumors with high sensitivity and specificity. On the basis of the results, the flow chart was adjusted so that it would also be able to better discriminate atypical teratoid/rhabdoid tumors and medulloblastoma groups 3 or 4 (sensitivity = 75%–79%; specificity = 92%–99%). Moreover, our adjusted flow chart was useful in ruling out ependymoma, pilocytic astrocytomas, and medulloblastoma *sonic hedgehog* tumors.

CONCLUSIONS: The modified flow chart offers a structured tool to aid in the adjunct diagnosis of pediatric posterior fossa tumors. Our results also establish a useful starting point for prospective clinical studies and for the development of automated algorithms, which may provide precise and adequate diagnostic tools for these tumors in clinical practice.

ABBREVIATIONS: AT/RT = atypical teratoid/rhabdoid tumor; LR = likelihood ratio; NPV = negative predictive value; PA = pilocytic astrocytoma; PPV = positive predictive value; *WNT* = wingless; *SHH* = *sonic hedgehog*

In the past 10 years, there has been an exponential increase in knowledge of the molecular characteristics of pediatric brain tumors, which was only partially incorporated in the 2016 World Health Organization Classification of Tumors of the Central Nervous System.¹ The main update in the 2016

Classification was the introduction of the molecular profile of a tumor as an important factor for predicting different biologic behaviors of entities which, on histology, look very similar or even indistinguishable.² A typical example is the 4 main groups of medulloblastoma: *wingless* (*WNT*), *sonic hedgehog* (*SHH*) with or without the p53 mutation, group 3, and group 4. Although they may appear similar on microscopy, these categories have distinct molecular profiles, epidemiology, prognosis, and embryologic origin.³

Subsequent to the publication of the 2016 World Health Organization Classification, further studies have identified even more molecular subgroups of medulloblastoma with possible prognostic implications⁴ and also at least 3 new molecular subgroups of atypical teratoid/rhabdoid tumor (AT/RT)⁵ and several subgroups of ependymoma.⁶ MR imaging shows promise as a technique for differentiating histologic tumors and their molecular subgroups. This capability relies on not only various imaging characteristics but also the location and spatial extension of the

Received May 22, 2020; accepted after revision November 23.

From the Division of Neuroradiology (C.A.P.F.A., J.S.M.-S., S.R.T., F.G.G., A.V.), Department of Radiology, Children's Hospital of Philadelphia, Philadelphia, Pennsylvania; Departments of Radiology (U.L., K.M., F.D.) and Neurosurgery (S.T.) and Pediatric Oncology Unit (D.H.), University College London Great Ormond Street Hospital for Children, London, UK; Department of Biostatistics (M.H.T.), Instituto de Biociências, São Paulo State University, São Paulo, Brazil; Developmental Biology and Cancer Programme (T.S.J.), University College London Great Ormond Street Institute of Child Health, University College London, London, UK; and Department of Radiology (C.d.C.L.), Hospital das Clínicas, Faculdade de Medicina de São Paulo, São Paulo, Brazil.

Please address correspondence to C.A.P.F. Alves, MD, Division of Neuroradiology, Department of Radiology, Children's Hospital of Philadelphia, 3401 Civic Center Blvd, Philadelphia, PA 19104; e-mail: alvesc@email.chop.edu; @CHOPRadiology; @GOSHneurorad

<http://dx.doi.org/10.3174/ajnr.A7057>

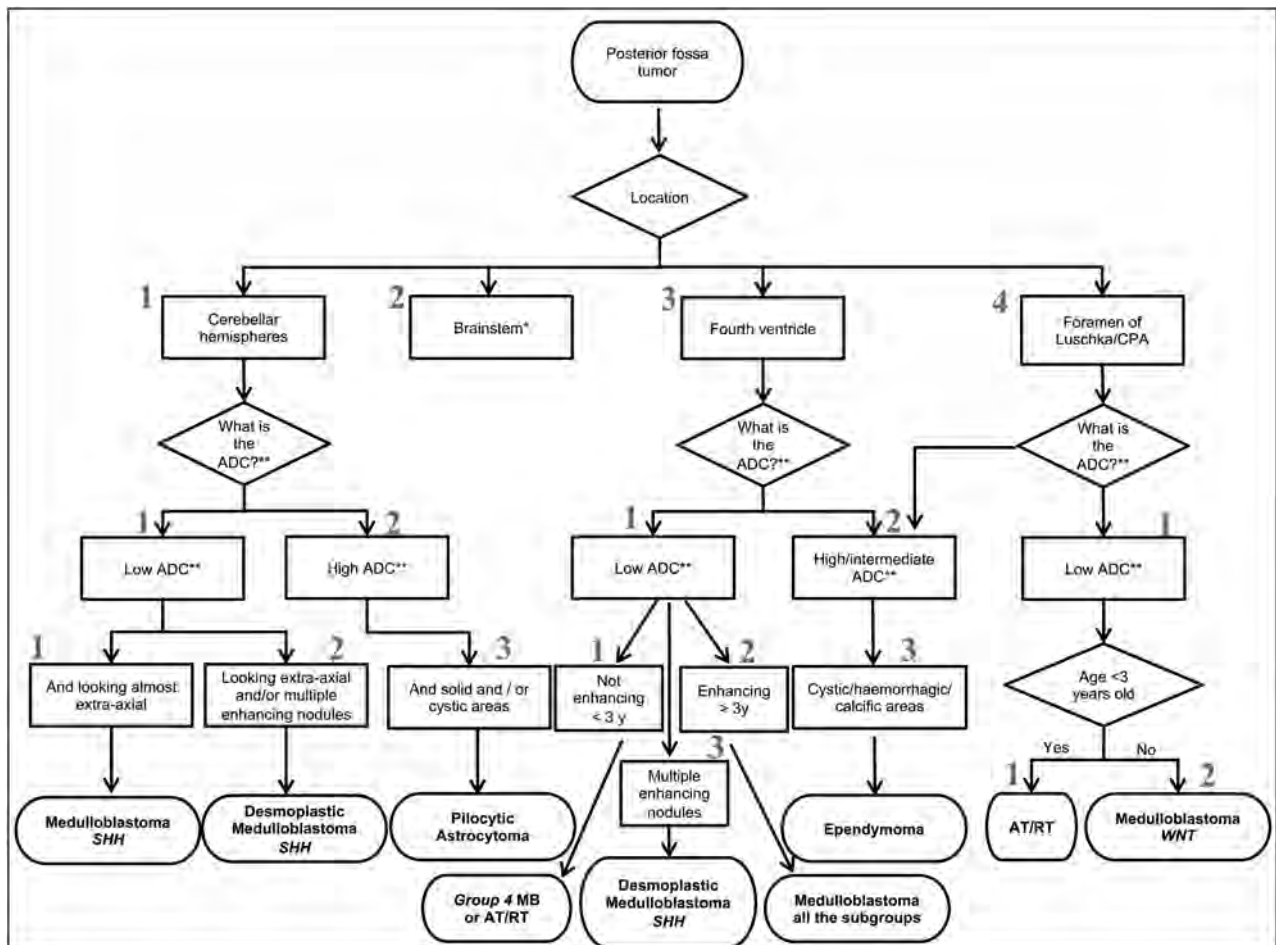


FIG 1. Predesigned radiologic flow chart created according to the literature before diagnostic accuracy analysis. The *asterisk* indicates brain stem tumors excluded from the analysis. *Double asterisks* indicate relative to gray matter. Modified with permission from D'Arco et al.¹¹

tumor, evident on MR imaging, which can be traced to the embryologic origin of the neoplastic cells.^{5,7-10}

One approach to the challenge of identifying imaging characteristics of different tumors in children is to use artificial intelligence. Yet despite this exciting innovation, correctly identifying the location of the mass and its possible use as an element for differential diagnosis still requires the expertise of an experienced radiologist. Previously, D'Arco et al¹¹ proposed a flow chart (Fig 1) for the differential diagnosis of posterior fossa tumors in children based on epidemiologic, imaging signal, and location characteristics of the neoplasm. The aims of the current study were the following: 1) to validate, in a retrospective, large cohort of posterior fossa tumors from 2 separate pediatric tertiary centers, the diagnostic accuracy of that flow chart, which visually represents the neuroradiologist's mental process in making a diagnosis of posterior fossa tumors in children, 2) to describe particular types of posterior fossa lesions that are not correctly diagnosed by the initial flow chart, and 3) to provide an improved, clinically accessible flow chart based on the results.

MATERIALS AND METHODS

Setting and Subjects

A retrospective, cross-sectional study from 2 large tertiary referral pediatric hospitals in 2 countries (Children's Hospital of Philadelphia,

United States, and Great Ormond Street Hospital, London, United Kingdom) was performed on the basis of patient records spanning January 2013 to October 2019 in accordance with the Strengthening the Reporting of Observational Studies in Epidemiology (STROBE) statement.¹² This study was conducted under 2 research protocols (IRB No. 18-015588 and CA Reg No. 2504), approved by the respective institutional review boards at each center.

Subjects were identified by electronic search of brain MR imaging reports and the electronic health record systems. The following terms/diagnoses were used for the search: "brain tumor," "posterior fossa tumor," "brain neoplasia," "posterior fossa neoplasia," "cerebellar tumor," "cerebellar neoplasia," "medulloblastoma," "AT/RT," "atypical teratoid/rhabdoid tumor," "ependymoma," "pilocytic astrocytoma." Results were screened, and subjects younger than 18 years of age with a histologically and genetically confirmed diagnosis of posterior fossa tumor, according to the 2016 World Health Organization classification, were selected.² Subjects with no available preoperative MR imaging study, those with low-quality MR imaging studies, and those without diffusion imaging on their MR imaging study were excluded. Subjects with tumors located primarily in the brain stem were also excluded.

Variables

Age at first MR imaging (before histologic/pathologic confirmation of the tumor), sex, and histologic and genetic/molecular results

were obtained from the electronic medical records. Two experienced pediatric neuroradiologists independently reviewed these initial MR imaging studies at each institution (C.A.P.F.A., A.V., F.D., and U.L.), blinded to the final diagnosis. Imaging characteristics were evaluated following a step-by-step numeric flow chart, with a digit assigned to each level and subsequent branch, providing a flow chart and a 3-digit numeric sequence code for each diagnosis end point to be used in the analysis (Fig 1). The flow chart took into account the following: 1) tumor location, 2) ADC map signal intensity in comparison with gray matter, 3) internal architecture, 4) contrast enhancement, and 5) the patient's age. The flow chart was designed before the initiation of the study; it was based on a review on the topic by D'Arco et al.¹¹ Before starting the blinded analysis of the cohort, one of the readers (C.A.P.F.A.) performed a pilot evaluation using the first 8 cases from each institution (16/148; 10.8%) to confirm the applicability of the flow chart multiple weeks before the formal evaluation.

Statistical Analysis

Visual inspection of the histogram showed non-normal distribution, which was confirmed with the Shapiro-Wilk test ($P < .001$) for all numeric variables. Categorical variables are described with percentage and frequency, and numeric variables, with median and interquartile range. Statistical analysis was performed using R statistical and computing software, Version 3.5.3 for Windows (<http://www.r-project.org/>).

Diagnostic accuracy of the flow chart was verified through a 2×2 contingency table and calculation of sensitivity, specificity, positive predictive values (PPV), and negative predictive value (NPV). To estimate accuracy and effect size, we estimated 95% CIs for sensitivity, specificity, PPV, and NPV. The diagnostic accuracy analysis was performed for each diagnosis, with molecular/histologic diagnosis as the criterion standard comparison. Because flow chart numeric sequences 312 and 311 of the predesigned flow chart would not provide a single unique final tumor molecular diagnosis, we later adjusted the sequences according to the most prevalent diagnosis. The modified flow chart reflects these adjustments. Last, we recalculated diagnostic accuracy tests on the basis of the adjustments for these 2 flow chart modifications. The clinical applicability of findings was further explored with positive and negative likelihood ratios (LR+ and LR–, respectively), and on the basis of changes in probability from the LR described by McGee.¹³ Clinical applicability to rule in diagnosis was considered if the 95% CI of LR+ was above 10. Clinical applicability to rule out diagnosis was considered if the 95% CI of LR– was below 0.5.

RESULTS

Histologic Diagnosis and Demographics

One hundred forty-eight subjects were included. The median age at MR imaging was 3.4 years, (interquartile range = 2.1–6.1 years), and the male/female ratio was 1.24. Fifty-four (36.5%) patients had a histologic diagnosis of medulloblastoma, 56 (37.5%) had pilocytic astrocytoma (PA), 12 (8.1%) had AT/RT, and 19 (12.8%) had ependymoma. Medulloblastomas were also subclassified according to molecular subtypes including 14/54 (26%) *SHH*; 7/54 (13%) *WNT*; 5/54 (9%) group 3; 9/54 (17%) group 4; and 19/54 (35%) group 3 or 4 (separation of groups 3 and 4 was not always

easily possible). Seven cases (5%) had a diagnosis of other tumors not covered by the flow chart (2 low-grade diffuse astrocytomas not otherwise specified, 1 hemangioblastoma, 2 gangliogliomas, 1 case of Langerhans cell histiocytosis, and 1 meningioma). Agreement between readers at each institution was very high ($\kappa = 0.96$ for both institutions, $P < .001$). Because both institutions had almost perfect agreement, we did a pooled analysis without differentiating per institution. The same diagnosis using the predesigned flow chart was reached for 86% of the cohort. In the 14% of cases in which the same diagnosis was not reached by the 2 readers, disagreement was solved through consensus between the readers.

Diagnosis Using the Flowchart

By means of the predesigned flow chart (Fig 1), the most common diagnosis was PA (numeric sequence 123) ($n = 53$, 36%), followed by medulloblastoma all subgroups (numeric sequence 312) ($n = 35$, 24%), ependymoma (numeric sequence 323) ($n = 17$, 11%), medulloblastoma *SHH* (numeric sequence 111) ($n = 10$, 7%), medulloblastoma group 4 or AT/RT (numeric sequence 311) ($n = 5$, 3%), AT/RT (numeric sequence 411) ($n = 7$, 5%), ependymoma (numeric sequence 423) ($n = 7$, 5%), desmoplastic medulloblastoma *SHH* (numeric sequence 112) ($n = 6$, 4%), desmoplastic medulloblastoma *SHH* (numeric sequence 313) ($n = 3$, 2%), and medulloblastoma *WNT* (numeric sequence 412) ($n = 5$, 3%). Figure 2 and Table 1 show the statistical results of the sensitivity, specificity, PPV, and NPV of the flow chart per diagnosis.

In cases that followed sequence 311 (medulloblastoma group 4 or AT/RT), 3/5 (60%) were AT/RT, 1/5 (20%) was an ependymoma, and 1/5 (20%) was a medulloblastoma group 4. This finding suggested that sequence 311 catches more tumors in the AT/RT category than in medulloblastoma group 4, so we recalculated the diagnostic accuracy tests considering both 311 and 411 as AT/RTs. As can be appreciated in Fig 2 and Table 1, diagnostic accuracy for cases of AT/RT improved when combining sequences 311 and 411. Of the 35 cases under sequence 312 (medulloblastoma all subgroups), 26/35 (74%) were confirmed as group 3 or 4 (3 confirmed as group 3, eight confirmed as group 4, and 15, as group 3 or 4). The remaining cases under sequence 312 were 3/35 (9%) *SHH*, 5/35 (14%) *WNT*, and 1/35 (3%) AT/RT. Figure 3 shows the diagnostic accuracy of sequence 312 to identify medulloblastoma *SHH*, *WNT*, and group 3 or 4. For this sequence, the NPV and specificity were higher than the PPV and sensitivity for all other sequences. Table 2 shows the LR analysis per diagnosis and the recommended sequences for the diagnosis. After our analysis and on the basis of Table 1 results, we modified the predesigned flow chart with more precise categorization of the types of tumor. We recommend this new flow chart (Fig 4) for the diagnosis of posterior fossa tumors in children.

Some examples of differentiating posterior fossa tumors from our cohort, diagnosed on the basis of the new flow chart here presented, can be seen in Figs 5 and 6.

DISCUSSION

The 2016 introduction of the new classification of brain tumors based on histologic and molecular characteristics dramatically changed the management of pediatric brain tumors.^{1,2,14,15} Tumors with similar histologic appearance being related to

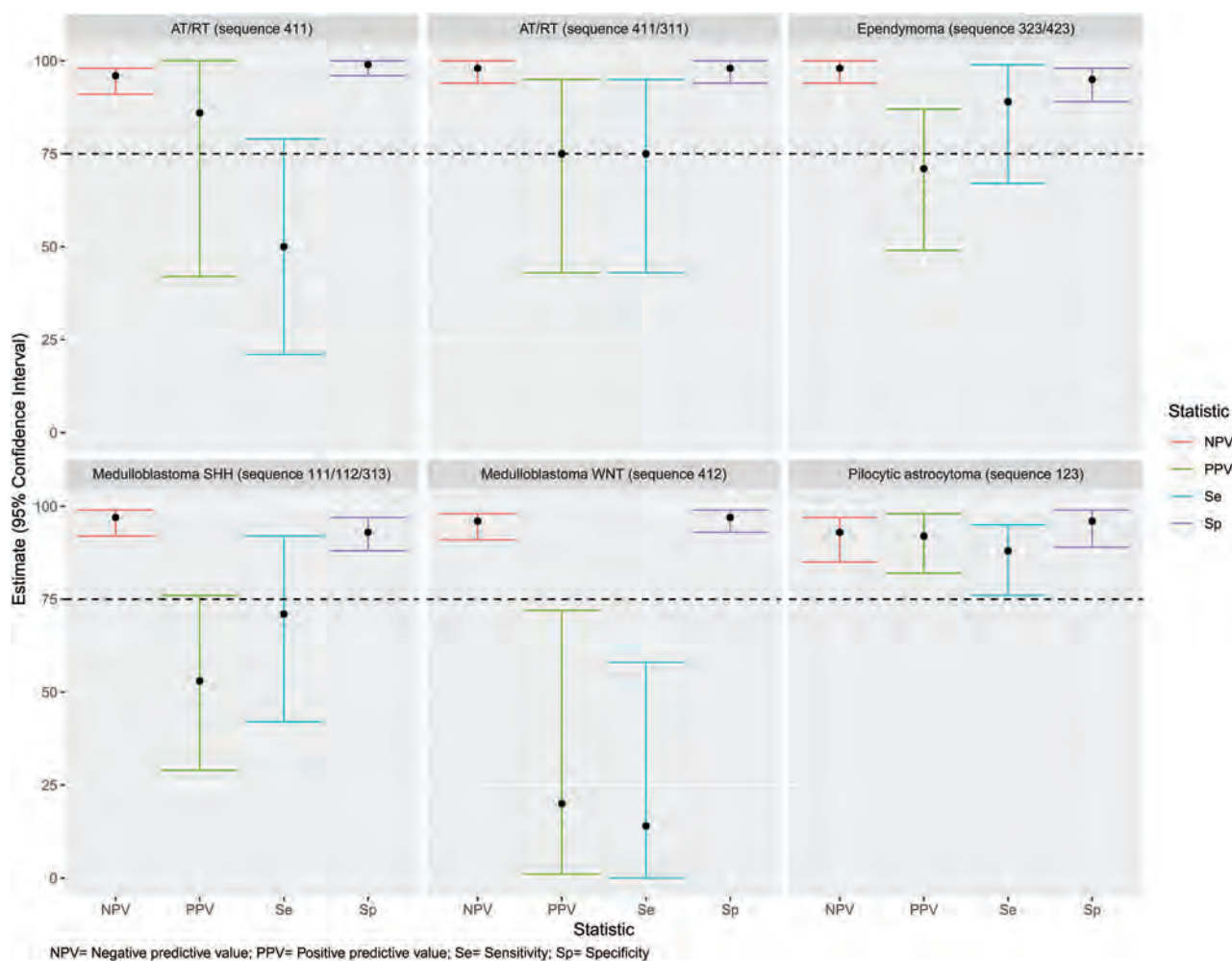


FIG 2. Diagnostic accuracy of a predesigned radiologic flow chart to identify different types of cerebellar tumors.

Table 1: Statistical analysis of the radiologic flow chart to discriminate different types of cerebellar tumors

Diagnosis Equivalent	Flowchart Sequence	Sensitivity (%)	Specificity (%)	PPV (%)	NPV (%)	Accuracy (%)
Ependymoma	323/423	89 (67–99)	95 (89–98)	71 (49–87)	98 (94–100)	94 (89–97)
Pilocytic astrocytoma	123	88 (76–95)	96 (89–99)	92 (82–98)	93 (85–97)	93 (87–96)
AT/RT	411	50 (21–79)	99 (96–100)	86 (42–100)	96 (91–98)	99 (96–100)
AT/RT	411/311	75 (43–95)	98 (94–100)	75 (43–95)	98 (94–100)	91 (96–98)
Medulloblastoma <i>SHH</i>	111/112/313	71 (42–92)	93 (88–97)	53 (29–76)	97 (92–99)	72 (64–79)
Medulloblastoma <i>WNT</i>	412	14 (0–58)	97 (93–99)	20 (1–72)	96 (91–98)	88 (93–97)

completely different cellular populations with different molecular profiles and different embryologic origins implies that they develop along different cellular paths. Thus, tumors that were previously considered as a single group can now be differentiated on imaging by location, age, and/or the patient's signal characteristics, resulting in a more accurate prognosis.^{16–18}

In light of the crucial role of molecular profiling in tumor diagnosis and management, we found that the predesigned flow chart was very useful for categorizing and better understanding pediatric brain tumors. The importance of molecular profiling in the pediatric neuro-oncology clinical practice was first studied in medulloblastomas but is now recognized for ependymomas, low-grade astrocytomas, AT/RTs, and all previously classified primitive neuroectodermal tumors.^{6,18–22}

Yet, since the 2016 classification update, several newly identified radiologic markers have been proposed as surrogates for the molecular diagnosis. The role of these radiologic markers may be limited by the constant evolution of the molecular characterization of brain tumors.^{8,11} However, we believe that a standardized method of evaluating images, such as the proposed flow chart, may facilitate increased diagnostic accuracy.

The initial predesigned diagnostic flow chart has proved reliable and consistently accurate in this validation study, with an almost perfect agreement between 2 blinded neuroradiologists at 2 different institutions. Our results showed high coefficients of specificity and NPV for all diagnoses included in the predesigned flow chart. Sensitivity coefficients were high (>87%) for diagnosing pilocytic astrocytoma and ependymomas, the 2 most common diagnoses in

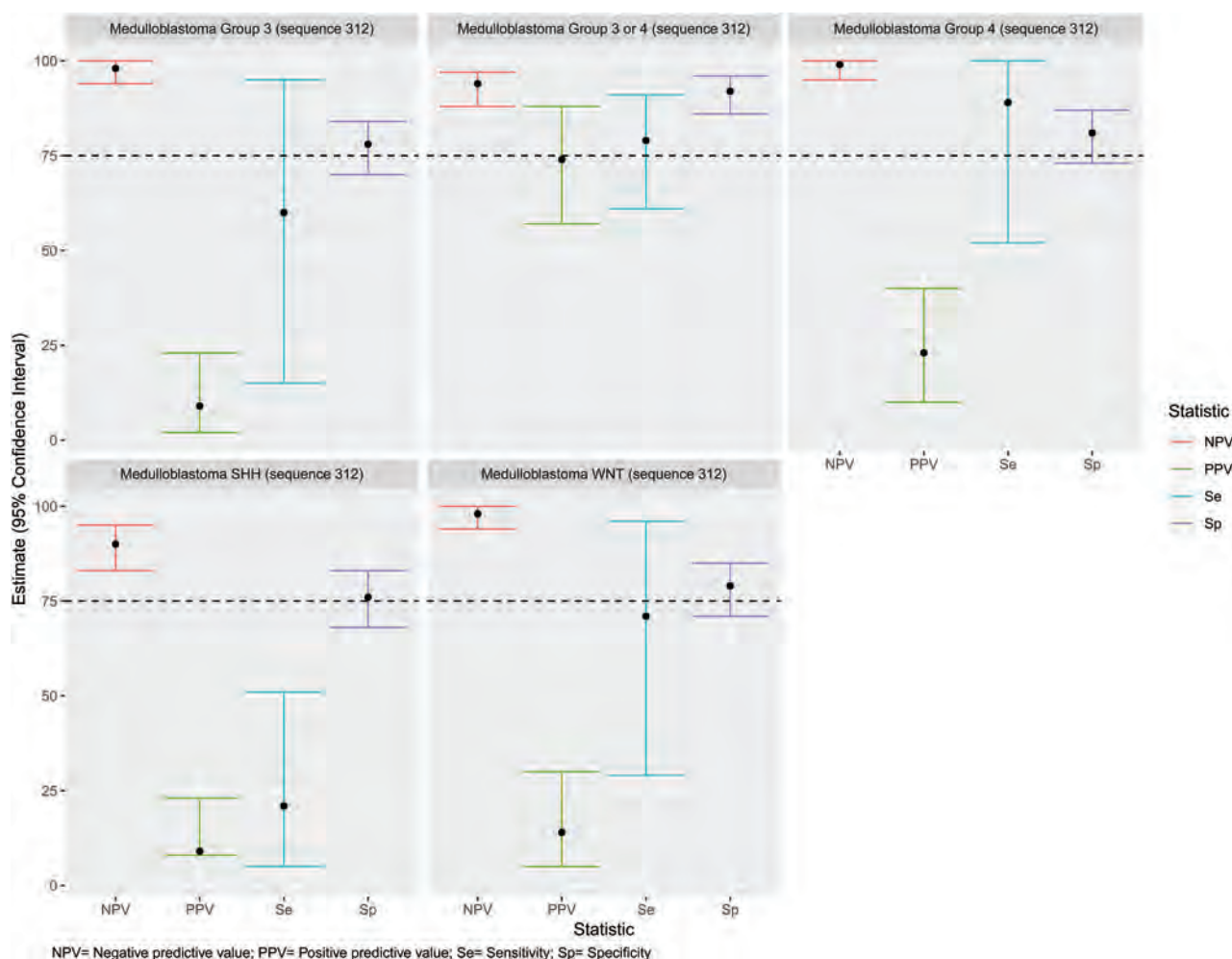


FIG 3. Diagnostic accuracy of sequence 312 (all types of medulloblastomas) of the predesigned radiologic flow chart to identify different types of medulloblastomas.

Table 2: Likelihood ratio analysis of the radiologic flow chart to discriminate different types of cerebellar tumors

Diagnosis	Flow Chart Sequence	LR+ (95% CI)	LR- (95% CI)
AT/RT	411/311	34 (10.6–109) ^a	0.26 (0.1–0.7)
Ependymoma	323/423	16.5 (7.9–35)	0.11 (0.03–0.4) ^a
Medulloblastoma <i>SHH</i>	111/112/313	10.6 (5.2–21.7)	0.3 (0.1–0.7)
Medulloblastoma group 3 or 4	312	10.07 (5.3–19.3)	0.23 (0.12–0.45) ^a
Pilocytic astrocytoma	123	20 (7.7–52.8)	0.13 (0.13–0.26) ^a

^a Clinically applicable confidence intervals.

our cohort. Moreover, PA and ependymoma tumors had the smallest 95% CIs, suggesting reliability in the diagnosis of these 2 types of tumors. This was especially true for PA, in which the lower 95% CI limit for sensitivity was 76%, and for PPV, it was 82%.

After analyzing results from the initial flow chart created on the basis of more recently published literature, we modified it to improve diagnostic accuracy. Our modifications (see Figs 1 and 4 for comparison) successfully improved the sensitivity coefficient for identification of AT/RTs to 75%, but the confidence interval remained wide. The second modification to flow chart sequence 312 made possible the identification of most cases of medulloblastoma

group 3 or 4, with fair-to-good sensitivity (61%–91%) and PPV (57%–88%) and good-to-excellent specificity (86%–96%) and NPV (88%–97%). The modified flow chart (Fig 4) proved to be more clinically relevant. The modified flow chart proved capable of discriminating AT/RTs, ependymomas, medulloblastomas *SHH*, medulloblastoma groups 3 and 4, and PA, which together constitute 90.5% of tumors in our

cohort. Clinically, the flow chart demonstrates great performance in ruling out group 3 or 4 medulloblastomas, PAs, and ependymomas and ruling in AT/RTs.

However, when it came to correctly identifying *WNT* medulloblastoma (numeric sequence 412, Fig 2), diagnostic accuracy was poor. In the predesigned flow chart, the authors designated a tumor in the pontocerebellar angle/foramen of Luschka with high cellularity (ie, low ADC) and patient age older than 3 years as suggestive of *WNT*. The rationale was that the cellular path of embryologic precursors, which can transform into neoplastic *WNT* cells, arises from the fourth ventricle down and laterally into the foramen of

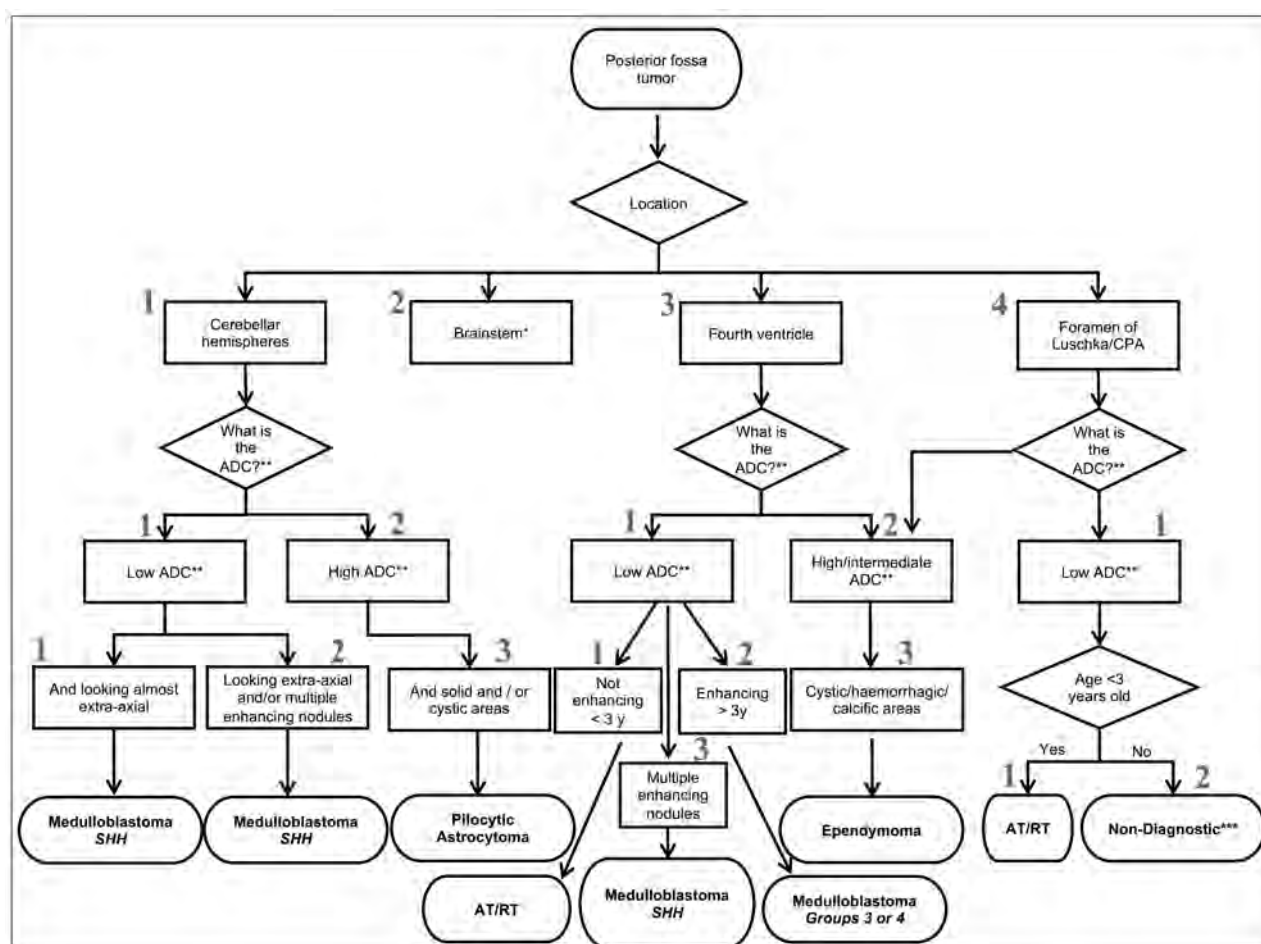


FIG 4. Modified radiologic flow chart (flow chart 2) after diagnostic accuracy analysis. The *asterisk* indicates brain stem tumors excluded from the analysis. *Double asterisks* indicate relative to gray matter. *Triple asterisks* indicates low PPV and sensitivity for any particular molecular/histological group of tumor.

Luschka.⁷ The only other tumor with striking diffusion restriction in the Luschka area is AT/RT, but this is typical of younger children.²³ These results can be explained by several factors: the small number of *WNT* tumors present in our series (10% of all medulloblastomas), most cases in our series being in the fourth ventricle (which is understandable given that the path of the *WNT* cells is thought to start from the fourth ventricle), and the presence of anaplastic ependymomas showing diffusion restriction (therefore simulating *WNT* medulloblastoma on imaging).²⁴ More recently, a study of a larger cohort of *WNT* medulloblastomas has shown that they are not as lateralizing as previously reported in smaller cohorts.²⁵

This study has some limitations, the main one being its retrospective nature. However, we controlled potential biases by doing a blinded review of images by only including cases with images obtained before surgical intervention and creating the baseline flow chart before data collection. Another important limitation is the relatively small number of cases for some types of tumor, which explains the larger confidence intervals for certain tumors. Nevertheless, many pediatric cerebellar tumors are relatively rare, and this is perhaps one of the largest cohorts available in the literature.²⁶ Moreover, we were able to gather a large enough cohort to allow diagnostic accuracy tests for the most common types of pediatric cerebellar tumors, with reliable results for most diagnoses.

Because this was planned as a validation study, we consider it successful in providing results that show that the modified flow chart can be used, is reliable, and has clinical applicability.

More research is still desired, with a larger consistency analysis evaluating results from multiple blinded readers. A larger prospective study would be needed to evaluate the diagnostic efficacy of the modified flow chart with higher precision. Such a study could provide an initial decision model for potential deep learning studies. Artificial intelligence is already being used to predict the molecular profile of brain tumors, most commonly in adult populations, but with recent important studies emerging in pediatric populations.^{27,28} The main limitation for the application of machine learning in posterior fossa tumors may be the identification of tumor location,²⁹ because we know that signal characteristics (which reflect at least partially histologic appearances) can be similar for different molecular groups with similar tissue features. Currently, artificial intelligence is not able to differentiate tumors with the necessary level of precision, though this may be possible in the future.

CONCLUSIONS

A flow chart for the diagnosis of posterior fossa tumors in children has been validated through a retrospective analysis of 148 patients with confirmed diagnoses. On the basis of analysis of these

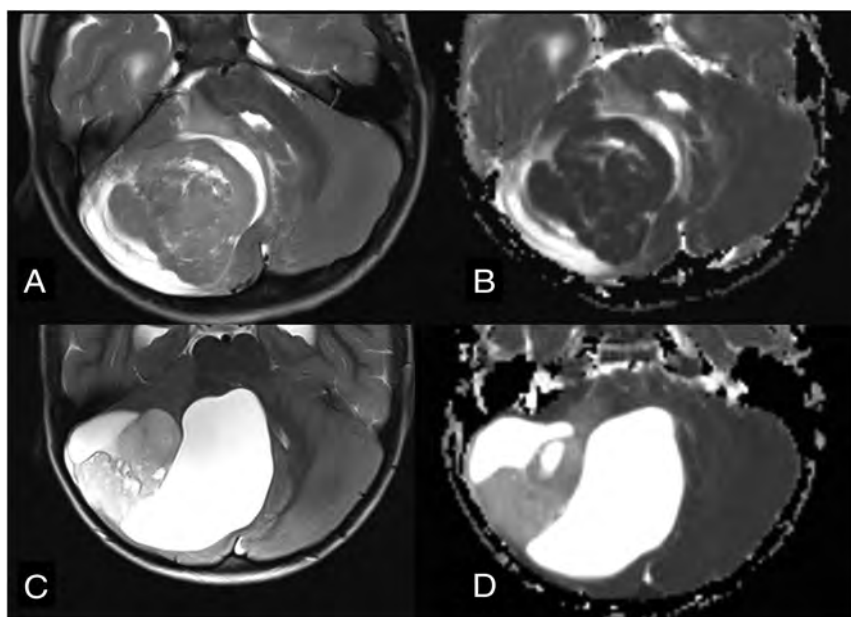


FIG 5. Differential diagnoses in cases of posterior fossa tumors originating from the cerebellar hemisphere. Axial T2WI (A) and axial ADC map (B) show *SHH* medulloblastoma (flow chart 2, number 111) in a typical peripheral location within the cerebellar hemisphere due to its origin from ganglionic cell precursors. Note very low ADC values (ie, diffusion restriction). Axial T2WI (C) and axial ADC map (D) show the typical appearance of a pilocytic astrocytoma (flow chart 2, number 123) originating from the cerebellar hemisphere. Note the typical nodule and appearance of cysts and much higher ADC values in comparison with the medulloblastoma.

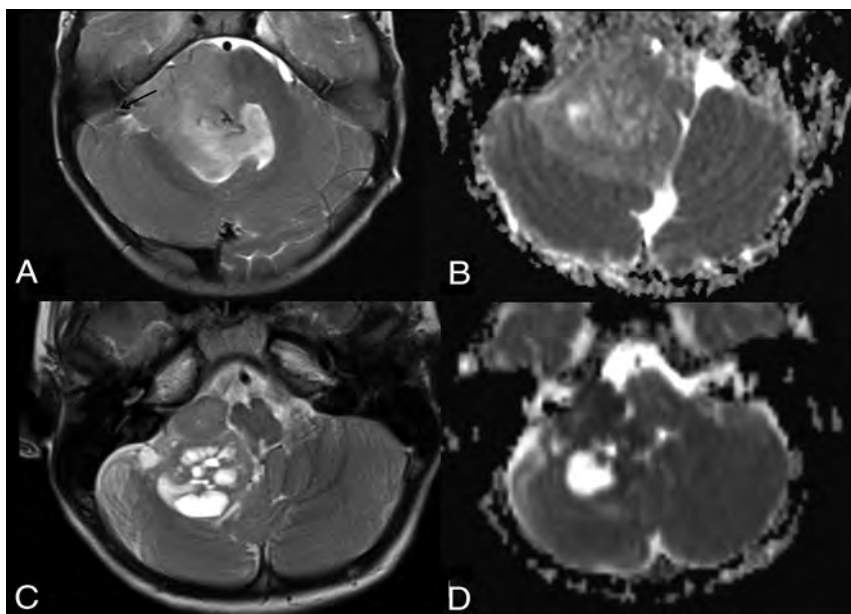


FIG 6. Differential diagnoses in posterior fossa tumors involving the foramen of Luschka and cerebellopontine angle. Axial T2WI (A) and ADC map (B) in a child with ependymoma (flow chart 2, number 423). Note the presence of internal vessels (arrow) and intermediate ADC values. Axial T2 (C) and ADC maps (D) in a 2-year-old boy with a AT/RT (new flow chart number 411). Note very low values of ADC, suggesting an embryonal tumor and peripheral cysts.

results, the predesigned flow chart was accurate in identifying most diagnoses, and with our subsequent modifications, the overall accuracy improved. The modified flow chart showed a good

likelihood ratio for most of the histologic and molecular groups of tumors. Furthermore, it may offer an important starting point for prospective analysis using machine learning techniques. As new molecular subgroups emerge in the classification of pediatric brain tumors, there is the potential for further modifications to the flow chart to aid in diagnosis.

Disclosures: Ulrike Löbel—*UNRELATED: Employment:* Great Ormond Street Hospital; *Travel/Accommodations/Meeting Expenses Unrelated to Activities Listed:* European Course in Pediatric Neuroradiology, money paid to individual author. Juan S. Martin-Saavedra—*UNRELATED: Employment:* The Children's Hospital of Philadelphia, *Comments:* This project was done while I was working as a postdoctoral research fellow. Sebastian S. Toescu—*RELATED: Grant:* Great Ormond Street Hospital Children's Charity, *Comments:* I am funded by the Great Ormond Street Hospital Children's Charity and am an Honorary Research Fellow of the Royal College of Surgeons of England. All research at Great Ormond Street Hospital National Health Service Foundation Trust and the University College London Great Ormond Street Institute of Child Health is made possible by the National Institute of Health Research Great Ormond Street Hospital Biomedical Research Center.* Miriam H. Tsunemi—*UNRELATED: Employment:* Medical School of Botucatu-São Paulo State University. Kshitij Mankad—*UNRELATED: Employment:* Great Ormond Street Hospital, *Comments:* This is my regular place of work. I am salaried; *Expert Testimony:* medicolegal work, *Comments:* I offer expert testimony for cases on an ad hoc basis; *Payment for Lectures Including Service on Speakers Bureaus:* honorarium received from Siemens and Novartis for lecturing. Thomas S. Jacques—*UNRELATED: Board Membership:* Repath Ltd and Neuropath Ltd, *Comments:* I am a director of Repath Ltd and Neuropath Ltd; *Employment:* Repath Ltd, Neuropath Ltd, *Comments:* I am a director of Repath Ltd and Neuropath Ltd; *Expert Testimony:* I undertake expert witness work for Her Majesty's Courts; *Grants/Grants Pending:* The Brain Tumor Charity, Children with Cancer UK, Great Ormond Street Hospital Children's Charity, Olivia Hodson Cancer Fund, Cancer Research UK, and the National Institute of Health Research*; *Payment for Lectures Including Service on Speakers Bureaus:* Bayer, *Comments:* I have been invited to give a lecture organized by Bayer; *Royalties:* Elsevier; *Other:* Wiley, *Comments:* I am editor-in-chief of *Neuropathology* and *Applied Neurobiology*. *Money paid to the institution.

REFERENCES

1. Chhabda S, Carney O, D'Arco F, et al. **The 2016 World Health Organization Classification of Tumours of the Central Nervous System: what the paediatric neuroradiologist needs to know.** *Quant Imaging Med Surg* 2016;6:486–89 CrossRef Medline
2. Louis DN, Perry A, Reifenberger G, et al. **The 2016 World Health Organization Classification of Tumors of the Central Nervous System: a summary.** *Acta Neuropathol* 2016;131:803–20 CrossRef Medline

3. Taylor MD, Northcott PA, Korshunov A, et al. **Molecular subgroups of medulloblastoma: the current consensus.** *Acta Neuropathol* 2012;123:465–72 CrossRef Medline
4. Ramaswamy V, Remke M, Bouffet E, et al. **Risk stratification of childhood medulloblastoma in the molecular era: the current consensus.** *Acta Neuropathol* 2016;131:821–31 CrossRef Medline
5. Nowak J, Nemes K, Hohm A, et al. **Magnetic resonance imaging surrogates of molecular subgroups in atypical teratoid/rhabdoid tumor.** *Neuro Oncol* 2018;20:1672–79 CrossRef Medline
6. Pajtler KW, Witt H, Sill M, et al. **Molecular classification of ependymal tumors across all CNS compartments, histopathological grades, and age groups.** *Cancer Cell* 2015;27:728–43 CrossRef Medline
7. Patay Z, DeSain LA, Hwang SN, et al. **MR imaging characteristics of wingless-type-subgroup pediatric medulloblastoma.** *AJNR Am J Neuroradiol* 2015;36:2386–93 CrossRef Medline
8. Perreault S, Ramaswamy V, Achrol AS, et al. **MRI surrogates for molecular subgroups of medulloblastoma.** *AJNR Am J Neuroradiol* 2014;35:1263–69 CrossRef Medline
9. D'Arco F, Culleton S, De Cockler LJL, et al. **Current concepts in radiologic assessment of pediatric brain tumors during treatment, Part 1.** *Pediatr Radiol* 2018;48:1833–43 CrossRef Medline
10. Tamrazi B, Mankad K, Nelson M, et al. **Current concepts and challenges in the radiologic assessment of brain tumors in children, Part 2.** *Pediatr Radiol* 2018;48:1844–60 CrossRef Medline
11. D'Arco F, Khan F, Mankad K, et al. **Differential diagnosis of posterior fossa tumours in children: new insights.** *Pediatr Radiol* 2018;48:1955–63 CrossRef Medline
12. von Elm E, Altman DG, Egger M, et al. **STROBE Initiative. The Strengthening the Reporting of Observational Studies in Epidemiology (STROBE) statement: guidelines for reporting observational studies.** *Epidemiology* 2007;18:800–04 CrossRef Medline
13. McGee S. **Simplifying likelihood ratios.** *J Gen Intern Med* 2002;17:646–49 CrossRef Medline
14. Srinivasan VM, Ghali MG, North RY, et al. **Modern management of medulloblastoma: molecular classification, outcomes, and the role of surgery.** *Surg Neurol Int* 2016;7:S1135–41 CrossRef Medline
15. Kuzan-Fischer CM, Juraschka K, Taylor MD. **Medulloblastoma in the molecular era.** *J Korean Neurosurg Soc* 2018;61:292–301 CrossRef Medline
16. Raybaud C, Ramaswamy V, Taylor MD, et al. **Posterior fossa tumors in children: developmental anatomy and diagnostic imaging.** *Childs Nerv Syst* 2015;31:1661–76 CrossRef Medline
17. Poretti A, Meoded A, Huisman TA. **Neuroimaging of pediatric posterior fossa tumors including review of the literature.** *J Magn Reson Imaging* 2012;35:32–47 CrossRef Medline
18. Treisman DM, Li Y, Pierce BR, et al. **Sox2+ cells in sonic hedgehog-subtype medulloblastoma resist p53-mediated cell-cycle arrest response and drive therapy-induced recurrence.** *Neurooncol Adv* 2019;11:vdz027 CrossRef Medline
19. Wang J, Garancher A, Ramaswamy V, et al. **Medulloblastoma: from molecular subgroups to molecular targeted therapies.** *Annu Rev Neurosci* 2018;41:207–32 CrossRef Medline
20. Drezner NL, Packer RJ. **The impact of molecular analysis on the survival of children with embryonal tumors.** *Transl Pediatr* 2016;51:5–8 CrossRef Medline
21. Ho B, Johann PD, Grabovska Y, et al. **Molecular subgrouping of atypical teratoid/rhabdoid tumors (ATRT): a reinvestigation and current consensus.** *Neuro Oncol* 2020;22:613–24 CrossRef Medline
22. Venneti S. **Integrating ependymoma molecular subgroups into clinical trials.** *Neuro Oncol* 2019;21:1219–20 CrossRef Medline
23. Meyers SP, Khademian ZP, Biegel JA, et al. **Primary intracranial atypical teratoid/rhabdoid tumors of infancy and childhood: MRI features and patient outcomes.** *AJNR Am J Neuroradiol* 2006;27:962–71 Medline
24. Northcott PA, Dubuc AM, Pfister S, et al. **Molecular subgroups of medulloblastoma.** *Expert Rev Neurother* 2012;12:871–84 CrossRef Medline
25. Stock A, Mynarek M, Pietsch T, et al. **Imaging characteristics of wingless pathway subgroup medulloblastomas: results from the German HIT/SIOP-Trial cohort.** *AJNR Am J Neuroradiol* 2019;40:1811–17 CrossRef Medline
26. Hanzlik E, Woodrome SE, Abdel-Baki M, et al. **A systematic review of neuropsychological outcomes following posterior fossa tumor surgery in children.** *Childs Nerv Syst* 2015;31:1869–75 CrossRef Medline
27. Iv M, Zhou M, Shpanskaya K, et al. **MR imaging-based radiomic signatures of distinct molecular subgroups of medulloblastoma.** *AJNR Am J Neuroradiol* 2019;40:154–61 CrossRef Medline
28. Sotoudeh H, Shafaat O, Bernstock JD, et al. **Artificial intelligence in the management of glioma: era of personalized medicine.** *Front Oncol* 2019;9:768 CrossRef Medline
29. Tang TT, Zawaski JA, Francis KN, et al. **Image-based classification of tumor type and growth rate using machine learning: a preclinical study.** *Sci Rep* 2019;9:12529 CrossRef Medline

Interobserver Reliability of an MR Imaging Scoring System in Infants with Hypoxic-Ischemic Encephalopathy

E. Szakmar, H. Meunier, M. El-Dib, E. Yang, and T.E. Inder



ABSTRACT

BACKGROUND AND PURPOSE: MR imaging has a key role in predicting neurodevelopmental outcomes following neonatal hypoxic-ischemic encephalopathy (HIE). A novel MR imaging scoring system for hypoxic-ischemic brain injury was used in our patient population with the aim of assessing interobserver variability and developing subcategories for the severity of brain injury.

MATERIALS AND METHODS: We evaluated brain MR images of 252 infants who underwent hypothermia for HIE between 2014 and 2019. First, 40 infants were selected randomly to test interobserver variability. Discrepancies were identified during the assessment of the first 20 MR images. The remaining 20 MR images were scored after adjusting the scoring system. Second, we determined cutoff values for the severity of injury that were based on the percentiles of the total scores in the full cohort.

RESULTS: The interobserver reliability showed excellent agreement for the total score both before (intraclass correlation coefficient = 0.96; 95% CI 0.89–0.99) and after the adjustment (intraclass correlation coefficient = 0.96; 95% CI, 0.89–0.98). The average of the differences and the agreement interval between the 2 readers decreased after the adjustment. Subcategories of brain injury were the following: We considered a total score of ≤ 4 ($\leq 75\%$) as normal, 5–10 (76%–90%) as mild, 11–15 (91%–95%) as moderate, and > 15 ($> 95\%$) as severe brain injury. The agreement on the classification of brain injury improved in the second epoch (weighted κ = 0.723 versus 0.887).

CONCLUSIONS: The adjusted scoring system may lead to a higher degree of interrater agreement. The presented cutoff values may be used to determine the severity of brain injury in future clinical studies including infants with mild hypoxia-ischemia.

ABBREVIATIONS: HIE = hypoxic-ischemic encephalopathy; ICC = intraclass correlation coefficient; κ_w = weighted κ ; PLIC = posterior limb of internal capsule; TH = therapeutic hypothermia

Hypoxic-ischemic encephalopathy (HIE) occurs in 2–3 per 1000 live term births in developed countries.¹ To date, therapeutic hypothermia (TH) initiated within the first 6 hours of life and continued for 72 hours with a target central temperature of 33.5°C is the only available treatment to reduce the risk of death and neurodevelopmental impairment.^{2,3}

The ability to predict neurodevelopmental outcomes following HIE allows parents and caregivers to optimize care beyond the neonatal period. MR imaging has a key role in predicting neurologic outcomes.^{4,5} Although many previously reported MR imaging

scoring systems have been related to outcome,^{6–8} they were usually performed with conventional sequences. The widely used scoring system of Barkovich et al⁶ published before the hypothermic era did not originally incorporate diffusion-weighted images, even though DWI has been recognized as the most reliable MR imaging sequence to assess injury during the first week after an hypoxic-ischemic event.^{4,9} Recently, Weeke et al¹⁰ described a novel and more detailed MR imaging scoring system for term infants with HIE, incorporating DWI and ¹H-MR spectroscopy sequences as well patterns of injury to the gray matter, white matter, and cerebellum to improve the predictive value of MR imaging studies in infants with HIE. The gray matter subscore was an independent predictor of adverse outcome at 2 years of age and at school age.¹⁰

Given that our inclusion criteria for infants to undergo TH at Brigham and Women's Hospital had been broadened, offering cooling to milder cases and infants born at > 34 weeks of gestation, we wished to explore the application of this new scoring system in our TH cohort.

We applied the new scoring system to our diverse patient population with the aim of assessing the observer variability

Received May 11, 2020; accepted after revision November 23.

From the Department of Pediatric Newborn Medicine (E.S., H.M., M.E.-D., T.E.I.), Brigham and Women's Hospital, Harvard Medical School, Boston, Massachusetts; First Department of Pediatrics (E.S.), Semmelweis University, Budapest, Hungary; Department of Neonatal Intensive Care Unit, (H.M.), Hôpital Alix de Champagne, Reims, France; and Department of Radiology (E.Y.), Boston Children's Hospital, Harvard Medical School, Boston, Massachusetts.

Please address correspondence to Terrie E. Inder, MBChB, MD, Brigham and Women's Hospital, 5 Francis St, Boston, MA 02215; e-mail: tinder@bwh.harvard.edu

Indicates article with online supplemental data.

<http://dx.doi.org/10.3174/ajnr.A7048>

between 2 experienced readers. We identified discrepancies during the evaluation of the first 20 MR imaging scans and adjusted the scoring system of Weeke et al¹⁰ accordingly.

Second, we also aimed to develop subcategories of severity from the scores of normal brain and, mild, moderate, severe brain injury. Our hypothesis was that the adjusted scoring system can improve interobserver reliability and increase the ease and reliability of the application of this scoring system as a new standard in the documentation of cerebral injury in the setting of hypoxic-ischemic encephalopathy.

MATERIALS AND METHODS

Patients

We have collected data, including imaging data, on 252 infants who underwent TH for neonatal encephalopathy between January 2014 and May 2019. We randomly selected 40 infants to assess the observer variability of the new MR imaging scoring system.¹⁰ This retrospective observational study was conducted at Brigham and Women's Hospital, Department of Pediatric Newborn Medicine, a single, tertiary-level neonatal intensive care unit. Institutional review board approval was obtained with a waiver of consent. The criteria for TH in our center are modified regional center-based criteria in which variables have been broadened from those used in the randomized clinical trials.^{11,12} The adaptations have included the following: 1) decreasing the gestational age criteria to >34 weeks; 2) increasing the inclusion pH from ≤ 7.0 to ≤ 7.1 ; 3) reducing the base excess for inclusion from ≥ 16 mEq/L to ≥ 10 mEq/L; and 4) providing therapeutic hypothermia to infants with mild hypoxic-ischemic encephalopathy on clinical examination, in addition to those with moderate or severe HIE. The stage of HIE was assigned on the basis of the modified Sarnat staging system after combined assessment by clinicians before the initiation of TH.¹³

MR Imaging

All infants underwent at least 1 cerebral MR imaging performed after TH within the first week of life. The second MR imaging was based on the decision of the clinical team caring for the infant. Only the first MR images obtained within the first week of life were analyzed in this study. All scans were performed on a 3T Siemens scanner (Siemens, Erlangen, Germany). The standard clinical imaging protocol included sagittal motion-corrected magnetization-prepared rapid acquisition of gradient echo T1-weighted images (TR = 2800 ms; TE = 2.75, 4.68, 6.54, and 8.4 ms; flip angle = 7°; voxel size = $1 \times 1 \times 1$ mm), axial turbo spin-echo T1-weighted images (TR = 574 ms, TE = 13 ms, flip angle = 140°, voxel size = $0.5 \times 0.5 \times 3$ mm, echo-train length = 2), axial turbo spin-echo T2-weighted images (TR = 9000 ms, TE = 150 ms, flip angle = 120°, voxel size = $0.5 \times 0.5 \times 3$ mm, echo-train length = 19), and coronal turbo spin-echo T2-weighted images (TR = 9210 ms, TE = 187 ms, flip angle = 130°, voxel size = $0.4 \times 0.4 \times 3$ mm, echo-train length = 19). Diffusion-weighted imaging included multidirectional diffusion-weighted measurements (TR = 6200 ms, TE = 92 ms, bandwidth = 1984 Hz/Px, FOV = 140 mm, voxels = $2 \times 2 \times 2$ mm, 30 b-directions with amplitudes ranging from 0 to 1000 s/mm²). ¹H-MR spectroscopy measurements were acquired at TE = 44 and 288 ms in the left thalamus and basal ganglia.

For noncritically ill neonates, we used a “feed and wrap” protocol, which is based on the timing of feeds, induction of natural sleep, and immobilization with wrapping to avoid the need for anesthetic agents.¹⁴ MR imaging scans with motion artifacts were excluded from the interrater analysis.

The pattern of brain injury was evaluated according to the novel grading system.¹⁰

The total score of the grading system is 57, including gray matter (maximum GM subscore = 25), white matter (maximum WM subscore = 21), cerebellum (maximum cerebellum subscore = 8), and an additional subscore (maximum additional subscore = 3). The additional score describes the presence of intraventricular or subdural hemorrhage and sinovenous thrombosis. The score of ¹H-MR spectroscopy was included in the gray matter subscore.¹⁰

The MR images of the first 20 neonates were evaluated on the basis of the description of the original article. We identified discrepancies during the evaluation of the first 20 MR imaging scans and adjusted the scoring system accordingly. A further series of 20 MR images was scored after adjustment of the scoring system.

The adjustments were the following: 1) The gestational age of the infants was taken into consideration when evaluating the myelination of the posterior limb of the internal capsule (PLIC) and the peak of the NAA (Fig 1A, -B); 2) a lesion that had involvement of both WM and the cortex was scored only individually for the principal area injured (Fig 1C); and 3) the extension of signal abnormality (involving 1 lobe or >1 lobe) was scored on the basis of the primary area of injury (Fig 1D). The images were analyzed by a pediatric neuroradiologist (E.Y.) and a dual-board-certified neonatologist and child neurologist (T.E.I.), who were blinded to the stage of neonatal encephalopathy.

Interrater agreement was assessed by total score, subscores, and the severity of brain injury (normal, mild, moderate, and severe) before ($n = 20$) and after the adjustment of the scoring system ($n = 20$).

Statistical Analysis

Interrater reliability was evaluated by calculation of the intraclass correlation coefficient (ICC) with a 2-way random-effects model for total score and WM, GM, cerebellum, and additional subscores. In addition, Bland-Altman plots were performed to assess the absolute limits of interobserver agreement for continuous variables.

The percentiles of the total score in the full cohort ($n = 252$) were calculated to determine the cutoff values for normal brain and mild, moderate, and severe brain injury. Weighted κ (κ_w) tests were used to determine the agreement between the readers for the severity of brain injury as a categorical variable. The McNemar test was run to determine whether there was a difference in the severity of brain injury as categorical variables between the readers. We used SPSS, Version 22 (IBM) and GraphPad Prism, Version 8.1.2 for macOS (GraphPad Software) to analyze and plot the data.

RESULTS

The demographic and prenatal data of the total cohort are presented in Table 1. Fifty-three percent of the infants had mild HIE based on the modified Sarnat staging system, reflecting our

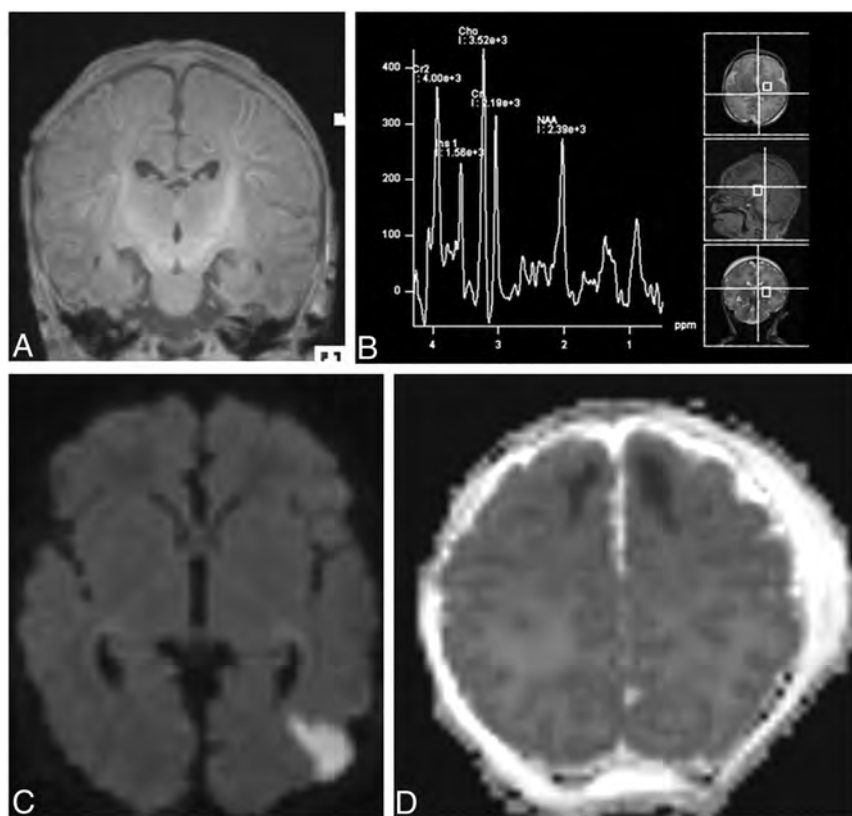


FIG 1. A, The gestational age of the infants considered when evaluating the myelination of the PLIC. In the coronal T1-weighted image, the myelination of the PLIC was considered as age-appropriate for a near-term infant (35 weeks of gestation) and was scored as normal. B, The gestational age of the infants was considered when evaluating the peak of the NAA. In ^1H -MR spectroscopy (TE = 30 ms), the peak NAA was considered as age-appropriate for a near-term infant (35 weeks of gestation) and was scored as normal. C, The lesion that had involvement of both the WM and cortex was scored individually only for the principal area. In axial DWI, the diffusion restriction in the cortex and its location were scored as focal (1 lobe) and unilateral (score of 2). The WM involvement was scored individually as focal and unilateral (score of 2). D, The extension of signal abnormality (involving 1 lobe or >1 lobe) was scored on the basis of the primary area of injury. In axial ADC mapping, the diffusion restriction in the WM was scored as focal (score of 1) because only the frontal lobe was involved and the location was scored as bilateral (score of 2).

institutional policy offering cooling to milder cases. The brain MR imaging scans of the 252 infants were performed at a median of 4.0 (interquartile range = 3.0–4.0) days of life. The randomly selected 40 MR images were evaluated by 2 experienced readers, resulting in a total of 80 reads.

In the first epoch of the study, 20 MR images were scored by 2 readers on the basis of the description of the original article of Weeke et al.¹⁰ There was strong interrater agreement for the total score with an ICC of 0.96 (95% CI, 0.89–0.99). The ICC for subscores also showed an excellent agreement between the raters (Table 2).

In the Bland-Altman analysis, the average of the differences [SD] was 1.80 [3.7] for the total score with –5.5 to 9.1 limits of agreement. Regarding the subscores, there were no mean differences of >2 points (Online Supplemental Data).

The severity of brain injury was classified on the basis of the distribution of total scores in the full cohort including 252 infants. Figure 2 shows the frequency distribution of the total

score in the full cohort. The median of the total score was 2, ranging between 0 and 41 points in the full cohort. Subcategories of brain injury were determined as follows: We considered total score ≤ 4 ($\leq 75\%$) as normal, 5–10 (76–90%) as mild, 11–15 (91–95%) as moderate, and >15 (>95%) as severe brain injury.

The 2 readers agreed that 10/20 (50%) MRI findings were within normal limits, findings of 2/20 (10%) scans were classified as moderate and those of 3/20 (15%) scans were graded as severe brain injury. However, the severity of brain injury in 5 infants (5/20, 25%) was graded differently by the 2 observers. Reader 1 classified findings of 3 MRIs (patients 1, 12, and 19) as moderate, whereas reader 2 rated them as mild (patients 1 and 19) or normal (patient 12). The severity of brain injury was classified differently by the 2 readers in patient 2 (mild versus normal) and in patient 6 (severe versus mild). The κ_w was run to determine whether there was agreement between 2 observers on the severity of brain injury, and it showed a substantial agreement ($\kappa_w = 0.723$) (Fig 3A and Table 3). Figure 3 shows the severity of brain injury based on the total score for each of the subjects.

In the second epoch of the study, 20 MR imaging scans were evaluated by the same readers after the adjustment of the grading system. The adjustments were based on the main discrepancies between the 2 readers in

the first epoch, including the assessment of myelination in the PLIC, the peak of the NAA level, cortical involvement, and the extent of the WM injury.

In the second epoch, the ICC for the total score and subscores also indicated an excellent reliability between the 2 readers, similar to that of the first epoch with the exception of an additional subscore (Table 2). Overall, both the average of the differences (bias) and the limits of agreement improved for the total score and the subscores (Online Supplemental Data).

In addition, only 3 MR images (15%) were classified differently by the 2 observers (Fig 3B). In line with this difference, the κ_w showed a very good agreement between the 2 readers' classifications on the severity of brain injury ($\kappa_w = 0.887$) compared with the substantial agreement in the first epoch ($\kappa_w = 0.723$). The McNemar test determined that the difference of the proportion in each category was not statistically different, similar to the finding in the first epoch (Table 3).

Table 1: Demographics and prenatal data of the full cohort^a

Full Cohort (n = 252)	
Gestational age (wk)	39 (38–40)
Birth weight (g)	3180 (2830–3544)
Sex (% of males)	145 (57.5%)
Inborn	166 (65.9%)
Apgar at 1 min	2 (1–4)
Apgar at 5 min	6 (5–7)
Apgar at 10 min	7 (6–8)
UA pH	7.04 (6.94–7.12)
UA BD (mmol/L)	11.7 (8.5–14.3)
UA lactate (mmol/L)	8.9 (6.4–10.4)
UV pH	7.13 (7.02–7.23)
UV BD (mmol/L)	10.1 (6.9–12.9)
UV lactate (mmol/L)	7.3 (5.6–9.2)
Postnatal pH	7.24 (7.15–7.30)
Postnatal BD (mmol/L)	9.2 (6.2–12.9)
Postnatal lactate (mmol/L)	7.9 (4.9–11.2)
Stage of HIE	
Mild HIE	124/234 (53.0%)
Moderate HIE	105/234 (44.9%)
Severe HIE	5/234 (2.1%)

Note:—BD indicates base deficit; UA, umbilical artery; UV, umbilical vein.

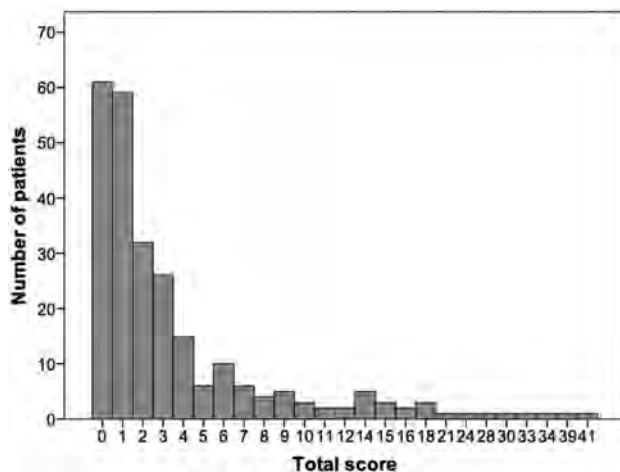
^aNonparametric data are presented as median with interquartile range. The stage of HIE was based on the modified Sarnat stage. The Sarnat stage was available for 234 infants.

Table 2: Interrater reliability for subscores and for total score^a

	Before Adjustment (n = 20)		After Adjustment (n = 20)	
	ICC	95% CI	ICC	95% CI
Gray matter	0.95	0.86–0.98	0.95	0.88–0.98
GM with ¹ H-MR spectroscopy	0.95	0.82–0.98	0.96	0.89–0.98
WM/cortex	0.97	0.91–0.99	0.98	0.96–0.99
Cerebellum	0.95	0.88–0.98	1.00	–
Additional	0.86	0.62–0.94	0.66	0.14–0.87
Total score	0.96	0.89–0.99	0.96	0.89–0.98

Note:—GM indicates Gray Matter; ICC, intraclass correlation coefficient; WM, white matter; –, not applicable (NA).

^aThe ICC with a 2-way random-effects model was calculated to assess the interrater variability between 2 experienced readers.

**FIG 2.** The frequency distribution of the total score in the full cohort.

DISCUSSION

This study has demonstrated the utility of a novel MR imaging scoring system in a cohort of neonates with a wide range of HIE severity. It also showed the potential advantage of adjusting some of its subscores. The interrater reliability showed an excellent level of agreement for the total score between the 2 experienced readers both before and after the adjustment of the scoring system. The Bland-Altman plot revealed, overall, a decreasing bias between the 2 readers and a narrower agreement interval for the subscores after the adjustment. In addition, the agreement between the 2 readers' classifications on the severity of brain injury greatly improved in the second epoch.

The presented cutoff values may be used to determine the severity of brain injury in future clinical studies. However, the cutoff values derived from the percentiles of the total scores in the full cohort may reflect our diverse patient population, including infants with mild HIE. Hence, these cutoff values may not be applicable to centers that provide TH to infants with only moderate and severe HIE.

In recent years, the inclusion criteria for hypothermia have been broadened, and TH has been offered increasingly to near-term infants.^{15,16}

In line with these criteria, the first adjustment related to the gestational age of infants with HIE. Both the metabolic profile and the myelination change as the brain matures. The rate of increase in the NAA peak is related to the maturation process.¹⁷ Likewise, an increase in myelinated WM can be detected between 35 and 41 weeks of gestation.¹⁸ Therefore, in the assessment of the NAA peak and the absence of myelination in the PLIC, the gestational age must be considered. The consistent evaluation of these 2 items is also important because both abnormal signal in the PLIC and NAA concentration have a good predictive value for the neurodevelopmental outcomes.^{19,20}

The second and third adjustment included the involvement of WM and the cortical area. The retrospective study of Rao et al¹⁶ found that the WM injury was the most frequent pattern among near-term infants, followed by GM injury and cortex involvement. Furthermore, isolated WM and cortical abnormalities were associated with communication and behavioral problems, visual impairment, and seizures.²¹ Hence, the consistent evaluation of WM and cortex involvement has a major role in the prediction of long-term outcomes. Moreover, the inconsistent scoring of brain injury can change the category of severity.

The study has several limitations that should be taken into consideration. First, statistical analysis should be interpreted with caution within the context of the small sample size. Second, the 95% limits of agreement in the Bland-Altman plot due the small sample size may be unreliable for estimating larger populations. Another limitation of the study is that we did not validate our cutoff values against long-term neurodevelopmental outcome data.

CONCLUSIONS

The novel grading system developed by Weeke et al¹⁰ provides a detailed evaluation of the neonatal brain with hypoxic-ischemic injury using DWI and ¹H-MR spectroscopy sequences. The modification of the scoring system may help with the correct interpretation

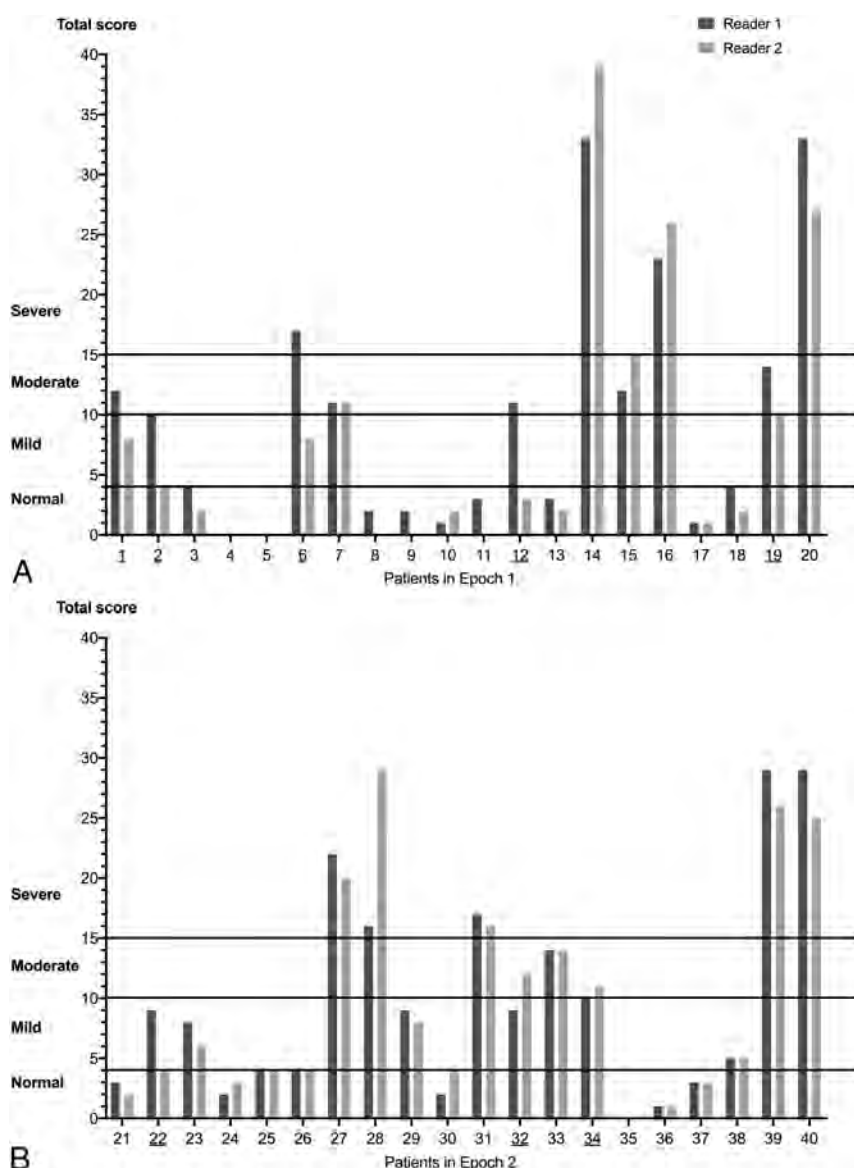


FIG 3. The severity of brain injury based on the total score for each subject in the first (A) and second epochs (B).

Table 3: Severity of injury based on the total scores^a

Severity of Brain Injury	Before Adjustment (n = 20)			After Adjustment (n = 20)		
	Reader 1	Reader 2	P Value	Reader 1	Reader 2	P Value
Normal (≤ 4) (No.) (%)	10 (50%)	12 (60%)	.50	8 (40%)	9 (45%)	1.00
Mild (5–10) (No.) (%)	1 (5%)	3 (15%)	.63	6 (30%)	3 (15%)	.25
Moderate (11–15) (No.) (%)	5 (25%)	2 (10%)	.25	1 (5%)	3 (15%)	.50
Severe (> 15) (No.) (%)	4 (20%)	3 (15%)	1.00	5 (25%)	5 (25%)	1.00

^a A McNemar test was administered to determine whether there was a difference in the proportion of the severity of the brain injury between the 2 readers.

of the selected items and can lead to a higher degree of interrater agreement. The presented cutoff values may be used to determine the severity of brain injury in future clinical studies, including those infants with mild HIE. Clearly, further studies are needed to determine the cutoff values of this novel grading system for the severity of brain injury in relation to neurodevelopmental sequelae.

Disclosures: Edward Yang—UNRELATED: Consultancy: CorticoMetrics, Comments: reviewed brain MRIs for a company developing software to recognize cortical dysplasia, last time in 2017. Terrie E. Inder—UNRELATED: Consultancy: Aspect Imaging, Comments: I am on the Scientific Advisory Board for this novel MR imaging company manufacturing a neonatal MRI system; Expert Testimony: occasional legal services, Comments: occasional medicolegal opinion; Grants/Grants Pending: federal and foundations.* *Money paid to the institution.

REFERENCES

1. Kurinczuk JJ, White-Koning M, Badawi N. **Epidemiology of neonatal encephalopathy and hypoxic-ischaemic encephalopathy.** *Early Hum Dev* 2010;86:329–38 CrossRef Medline
2. Azzopardi D, Strohm B, Marlow N, et al. TOBY Study Group. **Effects of hypothermia for perinatal asphyxia on childhood outcomes.** *N Engl J Med* 2014;371:140–49 CrossRef Medline
3. Jacobs SE, Hunt R, Tarnow-Mordi W, et al. **Cooling for newborns with hypoxic ischaemic encephalopathy.** *Cochrane Database Syst Rev* 2007;CD003311 CrossRef Medline
4. Alderliesten T, de Vries LS, Staats L, et al. **MRI and spectroscopy in (near) term neonates with perinatal asphyxia and therapeutic hypothermia.** *Arch Dis Child Fetal Neonatal Ed* 2017;102:F147–52 CrossRef Medline
5. de Vries LS, Groenendaal F. **Patterns of neonatal hypoxic-ischaemic brain injury.** *Neuroradiology* 2010;52:555–66 CrossRef Medline
6. Barkovich AJ, Hajnal BL, Vigneron D, et al. **Prediction of neuromotor outcome in perinatal asphyxia: evaluation of MR scoring systems.** *AJNR Am J Neuroradiol* 1998;19:143–49 Medline
7. Shankaran S, McDonald SA, Laptook AR, et al. Eunice Kennedy Shriver National Institute of Child Health and Human Development Neonatal Research Network. **Neonatal magnetic resonance imaging pattern of brain injury as a biomarker of childhood outcomes following a trial of hypothermia for neonatal hypoxic-ischemic encephalopathy.** *J Pediatr* 2015;167:987–93 CrossRef Medline
8. Rutherford M, Ramenghi LA, Edwards AD, et al. **Assessment of brain tissue injury after moderate hypothermia in neonates with hypoxic-ischaemic encephalopathy: a nested substudy of a randomised controlled trial.** *Lancet Neurol* 2010;9:39–45 CrossRef Medline
9. Goergen SK, Ang H, Wong F, et al. **Early MRI in term infants with perinatal hypoxic-ischaemic brain injury: interobserver agreement and MRI predictors of outcome at 2 years.** *Clin Radiol* 2014;69:72–81 CrossRef Medline
10. Weeke LC, Groenendaal F, Mudigonda K, et al. **A novel magnetic resonance imaging score predicts neurodevelopmental outcome after perinatal asphyxia and therapeutic hypothermia.** *J Pediatr* 2018;192:33–40 CrossRef Medline

11. Azzopardi DV, Strohm B, Edwards AD, et al. TOBY Study Group. **Moderate hypothermia to treat perinatal asphyxial encephalopathy.** *N Engl J Med* 2009;361:1349–58 CrossRef Medline
12. Gluckman PD, Wyatt JS, Azzopardi D, et al. **Selective head cooling with mild systemic hypothermia after neonatal encephalopathy: multicentre randomised trial.** *Lancet* 2005;365:663–70 CrossRef Medline
13. Shankaran S, Laptook AR, Ehrenkranz RA, et al. National Institute of Child Health and Human Development Neonatal Research Network. **Whole-body hypothermia for neonates with hypoxic-ischemic encephalopathy.** *N Engl J Med* 2005;353:1574–84 CrossRef Medline
14. Mathur AM, Neil JJ, McKinstry RC, et al. **Transport, monitoring, and successful brain MR imaging in unsedated neonates.** *Pediatr Radiol* 2008;38:260–64 CrossRef Medline
15. Jacobs SE, Morley CJ, Inder TE, et al. Infant Cooling Evaluation Collaboration. **Whole-body hypothermia for term and near-term newborns with hypoxic-ischemic encephalopathy: a randomized controlled trial.** *Arch Pediatr Adolesc Med* 2011;165:692–700 CrossRef Medline
16. Rao R, Trivedi S, Vesoulis Z, et al. **Safety and short-term outcomes of therapeutic hypothermia in preterm neonates 34–35 weeks gestational age with hypoxic-ischemic encephalopathy.** *J Pediatr* 2017;183:37–42 CrossRef Medline
17. Xu D, Vigneron D. **Magnetic resonance spectroscopy imaging of the newborn brain: a technical review.** *Semin Perinatol* 2010;34:20–27 CrossRef Medline
18. Dubois J, Dehaene-Lambertz G, Kulikova S, et al. **The early development of brain white matter: a review of imaging studies in fetuses, newborns and infants.** *Neuroscience* 2014;276:48–71 CrossRef Medline
19. Rutherford MA, Pennock JM, Counsell SJ, et al. **Abnormal magnetic resonance signal in the internal capsule predicts poor neurodevelopmental outcome in infants with hypoxic-ischemic encephalopathy.** *Pediatrics* 1998;102:323–28 CrossRef Medline
20. Lally PJ, Montaldo P, Oliveira V, et al. MARBLE consortium. **Magnetic resonance spectroscopy assessment of brain injury after moderate hypothermia in neonatal encephalopathy: a prospective multicentre cohort study.** *Lancet Neurol* 2019;18:35–45 CrossRef Medline
21. Martinez-Biarge M, Bregant T, Wusthoff CJ, et al. **White matter and cortical injury in hypoxic-ischemic encephalopathy: antecedent factors and 2-year outcome.** *J Pediatr* 2012;161:799–807 CrossRef Medline

Widening the Neuroimaging Features of Adenosine Deaminase 2 Deficiency

A.F. Geraldo, R. Caorsi, D. Tortora, C. Gandolfo, R. Ammendola, M. Alessio, G. Conti, A. Insalaco, S. Pastore, S. Martino, I. Ceccherini, S. Signa, M. Gattorno, A. Rossi, and M. Severino



ABSTRACT

SUMMARY: Adenosine deaminase 2 deficiency (OMIM #615688) is an autosomal recessive disorder characterized by a wide clinical spectrum, including small- and medium-sized vessel vasculopathies, but data focusing on the associated neuroimaging features are still scarce in the literature. Here, we describe the clinical neuroimaging features of 12 patients with genetically proven adenosine deaminase 2 deficiency (6 males; median age at disease onset, 1.3 years; median age at genetic diagnosis, 15.5 years). Our findings expand the neuroimaging phenotype of this condition demonstrating, in addition to multiple, recurrent brain lacunar ischemic and/or hemorrhagic strokes, spinal infarcts, and intracranial aneurysms, also cerebral microbleeds and a peculiar, likely inflammatory, perivascular tissue in the basal and peripontine cisterns. Together with early clinical onset, positive family history, inflammatory flares and systemic abnormalities, these findings should raise the suspicion of adenosine deaminase 2 deficiency, thus prompting genetic evaluation and institution of tumor necrosis factor inhibitors, with a potential great impact on neurologic outcome.

ABBREVIATIONS: DADA2 = adenosine deaminase 2 deficiency; TNF = tumor necrosis factor; PAN = polyarteritis nodosa; PRES = posterior reversible encephalopathy syndrome

Adenosine deaminase 2 deficiency (DADA2) is an autosomal recessive disorder (OMIM #615688) usually presenting in the pediatric age group.^{1,2} It is characterized by a wide clinical spectrum, including systemic autoinflammation, polyarteritis nodosa (PAN)-like vasculopathy, noninflammatory medium-

vessel arteriopathy, and pure hematologic disorders without vasculopathy.¹⁻⁵

The *ADA2* gene (previously known as *CECR1*) is located at 22q11.1 and encodes for *ADA2*, a dimeric extracellular enzyme primarily secreted by cells of the myeloid lineage, converting adenosine in inosine.^{1,2} In addition to its catalytic function, *ADA2* presents antiinflammatory and immunomodulatory properties and has a role in maintenance of vascular integrity.²

CNS involvement caused by small- and medium-sized vessel vasculopathy is a well-recognized complication, being present in nearly 50% of cases,⁶ mostly without anomalies detectable on angiographic studies.^{2,6-9} Neurologic events usually occur early in the course of the disease, at a very young age,^{1,2,6,10} frequently associated with inflammatory flares.^{2,10} Affected patients may present with ischemic strokes, distributed in the territory of perforator arteries, or intracranial hemorrhages, often recurrent, leading to clinical manifestations varying from minimal neurologic deficits to fatal outcome.^{1,2,6,8,10-12} Clinically silent brain lesions and TIAs with negative MR imaging findings may also occur,⁷ as well as peripheral neuropathy, acute sensorineural

Received August 22, 2020; accepted after revision November 23.

From the Neuroradiology Unit (A.F.G., D.T., R.A., A.R., M.S.), Center for Autoinflammatory Diseases and Immunodeficiencies (R.C., S.S., M.G.), and Interventional Unit (C.G.), IRCCS Istituto Giannina Gaslini, Genoa, Italy; Diagnostic Neuroradiology Unit, Imaging Department (A.F.G.), Centro Hospitalar Vila Nova de Gaia/Espinho, Vila Nova de Gaia, Portugal; Department of Translational Medical Sciences (M.A.), Federico II University of Naples, Naples, Italy; Pediatric Nephrology and Rheumatology Unit (G.C.), AOU G Martino, Messina, Italy; Division of Rheumatology (A.I.), IRCCS Ospedale Pediatrico Bambino Gesù, Roma, Italy; Department of Pediatrics (S.P.), Institute for Maternal and Child Health - IRCCS "Burlo Garofolo", Trieste, Italy; Division of Pediatric Immunology and Rheumatology, Department of Public Health and Pediatrics (S.M.), Regina Margherita Children Hospital, University of Turin, Turin, Italy; UOSD Genetics and Genomics of Rare Diseases (I.C.), IRCCS Istituto Giannina Gaslini, Genoa, Italy; and Department of Health Sciences (DISSAL) (A.R.), University of Genoa, Genoa, Italy. A.F.Geraldo and R.Caorsi contributed equally to this work.

This work was supported by funds from Ricerca Corrente Disordini Neurologici e Muscolari (Linea 5) of the Italian Ministry of Health and by the Compagnia di San Paolo (Grant ROL 20573).

Paper previously presented as a poster at: 8th International Congress of Familial Mediterranean Fever and Systemic Autoinflammatory Diseases, September 30 to October 3, 2015; Dresden, Germany.

Ethics approval: All procedures performed in studies involving human participants were in accordance with ethical standards of the institutional and/or national research committee and with the 1964 Helsinki declaration and its later amendments or comparable ethical standards.

Informed consent was waived because of the retrospective nature of the study.

Please address correspondence to Domenico Tortora, MD, PhD, Neuroradiology Unit, IRCCS Istituto Giannina Gaslini, Via Gaslini 5, Genova 16148, Italia; e-mail: domenicotortora@gaslini.org; @TortoraDomenico; @DrGeraldFilipa

Indicates open access to non-subscribers at www.ajnr.org

Indicates article with online supplemental data.

<http://dx.doi.org/10.3174/ajnr.A7019>

hearing loss, optic neuritis, and other ophthalmologic abnormalities.^{1,2,6-8,10,11}

Knowledge of DADA2-related neuroimaging patterns is of particular importance because CNS manifestations are considered a marker of severity and may be the presenting form of DADA2.^{4,9,10} Moreover, this may prompt early treatment with tumor necrosis factor (TNF) inhibitors, leading to complete remission and preventing further neurologic events.¹³ However, neuroimaging features associated with this condition are still incompletely elucidated. Indeed, to date, only 1 case series has been published, including neuroimaging data of 12 patients with DADA2, with limited information regarding angiographic features and radiologic follow-up.¹⁴

Recently, we encountered novel neuroimaging findings in patients with DADA2 that could be part of the spectrum of anomalies associated with this syndrome. Therefore, we aimed to provide a detailed description of CNS lesions and their long-term evolution in a series of 12 patients with genetically confirmed diagnosis of DADA2, as well as of the corresponding clinical, laboratory, and genetic data.

CASE SERIES

Twelve patients with DADA2 from 9 different families observed between 2014 and 2019 in 6 Italian hospitals were included in this case series. Institutional review board approval was obtained, waiving parental written informed consent. Demographic information, medical history, laboratory and histopathologic results, and genotypes were retrieved from electronic medical records. Clinical data are summarized in the Table and the Online Supplemental Data.

Details on neuroimaging studies and protocols are presented in the Online Supplemental Data. Images were analyzed by 2 pediatric neuroradiologists in consensus (M.S. and A.F.G., with 10 and 5 years' experience). Neuroimaging features are reported in the Online Supplemental Data.

At first brain MR imaging, 9/12 patients (75%) presented small focal areas of T2/FLAIR signal abnormality with or without restricted diffusion compatible with lacunar infarcts caused by small-vessel occlusions (Online Supplemental Data). Of these, 7 (77.8%) had multiple ischemic lesions, and 1 concomitantly presented with a large chronic hemorrhagic lesion in the left temporal lobe. Both anterior and posterior circulations were involved in 4/9 cases, and either the anterior or the posterior circulation was involved in 3/9 and 2/9 patients, respectively. The nucleocapsular region was the more severely affected region (11 lesions, 5 patients) followed by the midbrain (9 lesions, 5 patients) and the thalamus (6 lesions, 2 patients). One patient exhibited isolated intracranial hemorrhagic lesions, and 2 presented with small foci of susceptibility effect in the parenchyma and another 1 in the interpeduncular cistern (Fig 1). Two additional patients showed clinicoradiologic features compatible with posterior reversible encephalopathy syndrome (PRES) (Online Supplemental Data).

Follow-up MR imaging detected new cerebral infarcts in 5/10 patients (50%), and 1 of them also presented an anterior spinal artery infarct at the cervical level (Online Supplemental Data). All events occurred before institution of anti-TNF or thalidomide except 1 identified shortly after introduction of anti-TNF and another during temporary discontinuation of thalidomide. In

Clinical data of patients with DADA2

Features	Results
Males	6/12
Positive family history	7/11 ^a
Median age (years, range) at:	
Disease onset	1.3 (0.25–7)
Genetic diagnosis	15.5 (5–35)
Neurologic onset	5.5 (0.5–12)
First stroke (n = 10)	6.5 (1.4–12)
Symptoms at presentation	
Fever	5/12
Skin manifestations	4/12
Neurologic problems	4/12
Disease course	
Chronic	11/12
Recurrent	1/12
Manifestations	
Neurologic disorders	12/12
Hypertension	12/12
Elevation of acute phase reactants	12/12
Inflammatory skin lesions	12/12
Musculoskeletal disorders	5/12
Gastrointestinal abnormalities	5/12
Hypogammaglobulinemia	5/12 ^b
Cardiac abnormalities	2/12
Genetics ^c	
Homozygous or compound hemizygous ADA2 variants	11/12
Homozygous tandem 22q.11.1 duplication	1/12
Skin/bowel biopsy	
Polyarteritis nodosa	5/7
Leukocytoclastic vasculitis	2/7
Treatment ^d	
Anti-TNF	9/12
Thalidomide	3/12

^a One adopted patient.

^b No severe infections.

^c Defective ADA2 activity in 10/10 patients.

^d Complete response in all cases.

addition, 3/9 patients (33%) with ischemic strokes developed an abnormal contrast-enhancing soft tissue in the interpeduncular cistern, encasing the midbrain perforating arteries, with associated areas of eccentric arterial wall enhancement and thickening, that completely subsided after anti-TNF treatment (Fig 2, Online Supplemental Data). In addition, 1 patient with PRES presented multiple extraaxial foci of enhancement in the left crural cistern and inner auditory canal (Online Supplemental Data). Arterial spin-labeling studies revealed normal, symmetric cerebral perfusion in 7/7 cases except in the regions corresponding to the infarcts.

Qualitative assessment of the CSF spaces revealed mild diffuse enlargement of the ventricular system, the cortical cerebral sulci, or both in 5/12 (42%) patients at first brain MR imaging. None of the 10 patients with follow-up studies presented signs of progressive atrophy.

Intracranial arterial abnormalities were noted before treatment in 2/12 patients, including small-sized intracranial aneurysms in the superior cerebellar artery and anterior communicating artery, spontaneously thrombosed at follow-up (Fig 3), and transient stenosis of the left posterior communicating artery associated with contrast-enhancing perivascular tissue. Renal Doppler/abdominal CTA and echocardiography were performed in 11/12 and 7/12 patients, respectively, including the patient with intracranial aneurysms, but no visceral aneurysms were found.

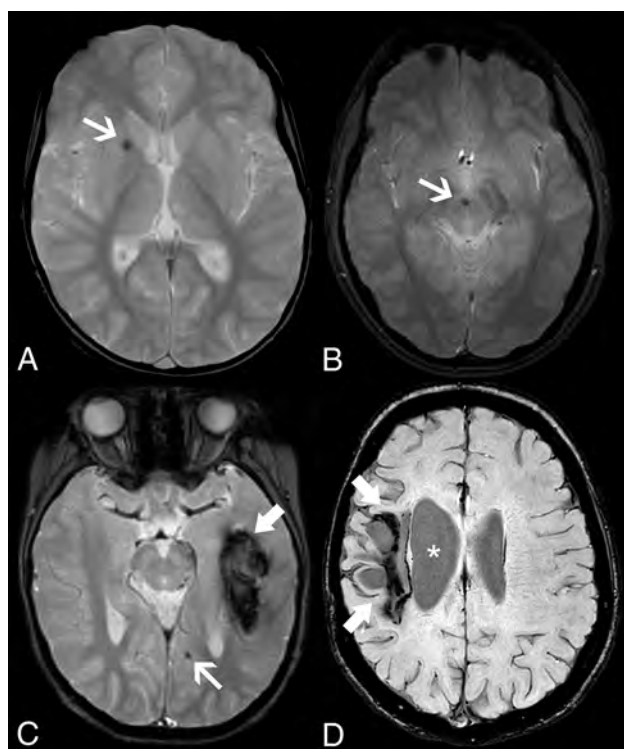


FIG 1. Intracranial hemorrhagic manifestations in adenosine deaminase 2 deficiency. Axial gradient-echo T2-weighted images of patient 4 at 5.8 years of age (A) and patient 11 at 18.3 years of age (B) demonstrate microbleeds in the right lenticular nucleus (arrow) and in the interpeduncular cistern or vessel wall (arrow), respectively. Axial gradient-echo T2-weighted image (C) of patient 1 at 6.1 years of age reveals an acute left temporal hematoma (thick arrow) and a left parameian occipital microbleed (arrow). None of the patients presented with head CT calcifications in the corresponding locations of the microbleeds (not shown). Axial SWI of patient 5 (D) at 16.5 years of age depicts a right frontoparietal hemorrhagic chronic lesion (thick arrows) causing ex vacuo dilation of the lateral ventricle (asterisks).

DISCUSSION

In this series, we identified a wide spectrum of neuroimaging abnormalities associated with DADA2, including 2 novel imaging patterns. All patients presented a vascular phenotype, as expected in most patients harboring missense mutations,⁵ but none had hematologic disorders besides hypogammaglobulinemia. Neurologic involvement at presentation was common (33% of cases). As previously shown,^{2,14} small, multiple ischemic infarcts in the nucleocapsular and mesencephalic or thalamic regions were the most frequent MR imaging abnormality, being present in 75% of our patients and reflecting the prevalent involvement of deep perforators. Before treatment with anti-TNF, thalidomide, or both, new ischemic lesions developed in half of patients at follow-up studies.^{4,7,13,15} Conversely, no new neurologic events or MR imaging lesions were noticed afterward, except for 2 recurrences shortly after introduction of anti-TNF or temporary discontinuation of thalidomide. Of note, the prevalence of ischemic strokes in our cohort was similar to that reported by Bulut et al¹⁴ in patients with DADA2-related vasculopathy and was expectedly higher than that described in a review also including patients with purely hematologic phenotypes (around 40%).⁶ Interestingly, some patients

presented with small lacunar strokes clearly depicted on DWI at clinical onset that were difficult to distinguish from enlarged perivascular spaces in follow-up examinations probably because of their small size and progressive gliotic “healing” changes. This suggests a possible underestimation of these subtle findings if brain MR imaging studies are not performed in the acute stage or with high spatial resolution sequences. As previously identified in a few patients with DADA2,^{14,15} we found an additional small ischemic medullary infarct at the cervical level in 1 patient. Of note, spinal cord involvement in individuals with DADA2 might also be underrated because only a minority of patients underwent a spinal MR imaging in both the current and in Bulut et al’s series.¹⁴

Intracranial hemorrhagic strokes are additional complications of DADA2,^{1,2,6,11,12} involving nearly 12% of cases in a recent review⁶ and 17% in our cohort. These hemorrhages may occur in isolation^{1,12} or in association with ischemic strokes,^{2,12} as seen in our patients. In most published cases, no underlying causes were found. Conversely, 2 intracranial aneurysms were detected in 1 of our patients presenting with diffuse subarachnoid hemorrhage and a history of peripheral intracranial aneurysm and lobar hematoma. Of note, CNS aneurysms have been described only once in a patient with DADA2¹ and in a few patients with PAN who had unknown ADA2 status.^{16–18} These aneurysms are multiple, small (<5 mm), and peripheral, arising in nonbranching sites or rupturing even when small.^{16–18} Additionally, they can cause cranial nerve compression or infarction because of occlusion of the parental vessel.¹⁷ Their management is controversial, with both medical and surgical and interventional treatments proposed.¹⁷ In our case, early follow-up studies demonstrated spontaneous aneurysmal thrombosis with total exclusion from circulation and no new intracranial aneurysms after 5 years. Of note, no visceral aneurysms were found in this patient and in the other investigated patients.

In their series, Bulut et al¹⁴ described brain atrophy in more than 50% of cases, without further information regarding the temporal evolution of this imaging finding. Similarly, we found mild diffuse enlargement of CSF spaces, including the ventricular system, the cortical cerebral sulci, or both, in 42% of patients at first brain MR imaging. However, none of the patients with available follow-up studies presented signs of progressive atrophy.

The first novel finding in this series was the detection of small parenchymal foci of susceptibility effect in 2 patients with DADA2, likely corresponding to brain microhemorrhages. The latter have been shown to correlate with hemosiderin-laden perivascular macrophages and have been associated with progressive aging and multiple neurologic conditions, including small-vessel disease and CNS vasculitis.¹⁹ Another patient presented a similar focal susceptibility effect located in the interpeduncular fossa, likely in a vessel wall, that could have the same origin, considering the absence of intracranial aneurysms and subarachnoid hemorrhage.

Different from Bulut et al,¹⁴ we did not identify any parenchymal area of enhancement after gadolinium injection. However, in one-third of patients, we found another novel feature, which was the presence of irregular, contrast-enhancing tissue in the interpeduncular fossa, crural cistern, and inner auditory canal, surrounding the basilar, posterior cerebral arteries and AICA,

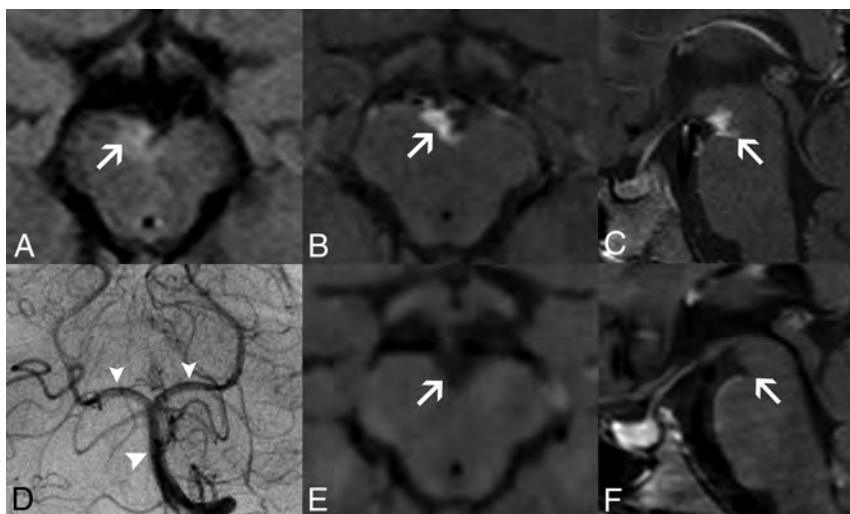


FIG 2. Perivascular enhancing tissue in adenosine deaminase 2 deficiency. Brain MR imaging in patient 1 at 8.5 years of age (A–D) demonstrates a soft tissue component mass in the interpeduncular cistern surrounding the basilar artery and its terminal perforator branches with eccentric vessel wall involvement. The lesion is mildly hyperintense on axial FLAIR (A, arrow), with intense solid enhancement on fat-saturated postgadolinium axial (B) and sagittal (C) T1WI sequences (arrows). DSA (D) reveals normal caliber of the basilar artery and posterior cerebral arteries (arrowheads). Postgadolinium axial (E) and sagittal (F) black-blood T1-weighted images performed at 9.7 years of age, after introduction of anti-TNF treatment, demonstrate a complete resolution of this likely inflammatory perivascular tissue (arrows).

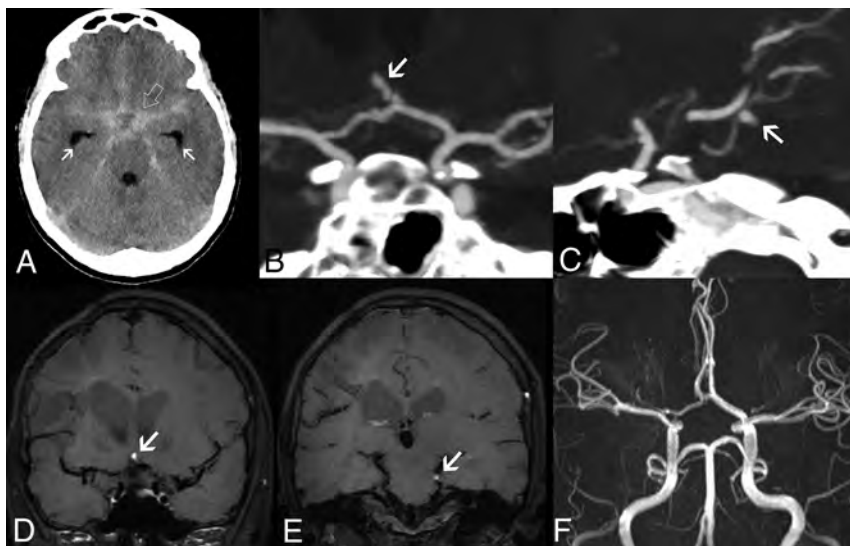


FIG 3. Intracranial aneurysms in adenosine deaminase deficiency. Axial unenhanced head CT scan in patient 5 at 16.4 years of age (A) demonstrates a diffuse subarachnoid acute hemorrhage (SAH) (open arrow) symmetrically distributed in the basal cisterns, horizontal segments of the Sylvian fissures, and anterior interhemispheric fissure, with mild enlargement of the temporal horns in keeping with incipient hydrocephalus (arrows). CTA images (B and C) reveal the presence of small-sized intracranial aneurysms of an anterior communicating artery branch (arrow) and the left superior cerebellar artery (arrow). Note that these 2 aneurysms have a peripheral location and arise in nonbranching sites. Follow-up brain MR imaging performed 23 days after the initial SAH episode, including coronal (D and E) black-blood T1WI, shows signs of intraaneurysmal thrombosis (arrows). TOF-MRA (F) does not depict flow-related signal within the aneurysmal sacs, in keeping with exclusion of the aneurysms from the circulation. These aneurysms remained excluded from circulation at 5-year follow-up.

respectively. Eccentric vessel wall thickening and enhancement were noted in all patients, more pronounced at the origin of brain stem perforators, leading to progressive arterial stenosis in 1 patient. This pattern slightly differs from the concentric smooth arterial wall involvement typically seen in cerebral vasculitis caused by inflammation-related endothelial or vasa vasorum leakage.²⁰ On the other hand, in 2 patients, this new finding was associated with acute ischemic infarcts in the territory of the posterior perforators, reflecting an active disease phase and suggesting an inflammatory origin. Accordingly, after anti-TNF treatment, there was total tissue regression in all patients and normalization in caliber of the stenosed artery at 1-year follow-up. As in the present series, most skin and bowel biopsy specimens of patients with DADA2 either reveal a PAN-like or a leukocytoclastic type of vasculitis.^{1,2,10} However, histologic proof of CNS vasculitis was not obtained so far.² Therefore, the precise mechanism of DADA2-related intracranial vasculopathy remains unknown and awaits further research. Interestingly, most of our patients presented unremarkable angiographic findings. Indeed, abnormalities of intracranial vessels have been only occasionally described in DADA2,^{14,21} probably caused by predominant involvement of medium- and small-sized vessels, frequently beyond the current resolution of lumen-based angiographic studies, including DSA. Accordingly, with the exception of the infarcted tissues, we did not find brain perfusion abnormalities on arterial spin-labeling.

Finally, we identified 2 DADA2-related PRES events in our cohort. PRES has been occasionally reported in patients with DADA2,^{11,14} as well as in patients with PAN with unknown ADA2 status.²² Both our cases occurred during childhood and manifested with seizures associated with typical neuroimaging patterns.²³ These events occurred in the context of arterial hypertension, a complication of DADA2⁶ and a well-known risk factor for PRES²³; none of the patients was under anti-TNF treatment. Of note, ADA2 is an endothelial growth factor.² Therefore,

patients with DADA2 may be intrinsically more prone to endothelial dysfunction, which is the presumed key-role mechanism of PRES.²³

CONCLUSIONS

We expanded the neuroimaging phenotype of DADA2, including (in addition to multiple, recurrent brain lacunar ischemic or hemorrhagic strokes, spinal infarcts, PRES events, and intracranial aneurysms) cerebral microbleeds, and a peculiar, likely inflammatory, perivascular tissue in the basal and prepontine cisterns. Together with early clinical onset, positive family history, inflammatory flares, and systemic abnormalities, these findings should raise the suspicion of DADA2, thus prompting genetic evaluation and institution of TNF inhibitors, with a potentially positive impact on neurologic outcome.

Disclosures: Ana Geraldo—UNRELATED: 12M research fellowship grant; UNRELATED: Payment for Manuscript Preparation: European Society of Neuroradiology, Comments: Money paid to individual author. Roberta Caorsi—UNRELATED: Consultancy: Novartis, SOBI, Eli Lilly; Payment for Lectures Including Service on Speakers Bureaus: SOBI, Novartis. Antonella Insalaco—UNRELATED: Board Membership: Novartis, SOBI, Comments: 1000 euros. Isabella Ceccherini—UNRELATED: Employment: Istituto Giannina Gaslini. Sara Signa—RELATED: Grant: This work was supported by funds from Ricerca Corrente Disordini Neurologici e Muscolari (Linea 5) of the Italian Ministry of Health and by the Compagnia di San Paolo (Grant ROL 20573)*. Marco Gattorno—RELATED: Grant: Novartis, SOBI, Comments: Unrestricted grant to eurofever*; Consulting Fee or Honorarium: Novartis, SOBI; UNRELATED: Board Membership: Novartis, SOBI; Consultancy: Novartis, SOBI; Grants/Grants Pending: Novartis, SOBI, Comments: Unrestricted grant to eurofever*; Payment for lectures including service on speakers bureaus: Novartis, SOBI; Payment for Development of Educational Presentations: Novartis, SOBI. Mariasavina Severino—RELATED: Grant: Ricerca Corrente sui Disordini Neurologici e Muscolari (Linea 5) of the Italian Ministry of Health, Comments: This work was supported by funds from Ricerca Corrente sui Disordini Neurologici e Muscolari (Linea 5) of the Italian Ministry of Health*; UNRELATED: Employment: Neuroradiology consultant, IRCCS Istituto Giannina Gaslini. *Money paid to institution.

REFERENCES

- Navon Elkan P, Pierce SB, Segel R, et al. **Mutant adenosine deaminase 2 in a polyarteritis nodosa vasculopathy.** *N Engl J Med* 2014;370:921–31 CrossRef Medline
- Zhou Q, Yang D, Ombrello AK, et al. **Early-onset stroke and vasculopathy associated with mutations in ADA2.** *N Engl J Med* 2014;370:911–20 CrossRef Medline
- Bras J, Guerreiro R, Santo GC. **Mutant ADA2 in vasculopathies.** *N Engl J Med* 2014;371:478–80 CrossRef Medline
- Van Montfrans JM, Hartman EAR, Braun KPJ, et al. **Phenotypic variability in patients with ADA2 deficiency due to identical homozygous R169Q mutations.** *Rheumatology (Oxford)* 2016;55:902–10 CrossRef Medline
- Lee PY, Kellner ES, Huang Y, et al. **Genotype and functional correlates of disease phenotype in deficiency of adenosine deaminase 2 (DADA2).** *J Allergy Clin Immunol* 2020;145:1664–72.e10 CrossRef Medline
- Fayand A, Sarabay G, Belot A, et al. **Multiple facets of ADA2 deficiency: vasculitis, auto-inflammatory disease and immunodeficiency: a literature review of 135 cases from literature.** *Rev Med Interne* 2018;39:297–306 CrossRef Medline
- Westendorp WF, Nederkoorn PJ, Aksentijevich I, et al. **Unexplained early-onset lacunar stroke and inflammatory skin lesions: consider ADA2 deficiency.** *Neurology* 2015;84:2092–93 CrossRef Medline
- Nanthapaisal S, Murphy C, Omoyinmi E, et al. **Deficiency of adenosine deaminase type 2: a description of phenotype and genotype in fifteen cases.** *Arthritis Rheumatol* 2016;68:2314–22 CrossRef Medline
- Elbracht M, Mull M, Wagner N, et al. **Stroke as initial manifestation of adenosine deaminase 2 deficiency.** *Neuropediatrics* 2017;48:111–14 CrossRef Medline
- Caorsi R, Penco F, Grossi A, et al. **ADA2 deficiency (DADA2) as an unrecognized cause of early onset polyarteritis nodosa and stroke: a multicentre national study.** *Ann Rheum Dis* 2017;76:1648–56 CrossRef Medline
- Özen S, Batu ED, Taşkıran EZ, et al. **A monogenic disease with a variety of phenotypes: deficiency of adenosine deaminase 2.** *J Rheumatol* 2020;47:117–25 CrossRef Medline
- Sahin S, Adrovic A, Barut K, et al. **Clinical, imaging and genotypical features of three deceased and five surviving cases with ADA2 deficiency.** *Rheumatol Int* 2018;38:129–36 CrossRef Medline
- Caorsi R, Omenetti A, Morreale A, et al. **Rapid and sustained effect of anti-TNF treatment in patients with ADA2 deficiency.** *Ped Rheumatol* 2015;13:(Suppl) O80 CrossRef
- Bulut E, Erden A, Karadag O, et al. **Deficiency of adenosine deaminase 2; special focus on central nervous system imaging.** *J Neuroradiol* 2019;46:193–98 CrossRef Medline
- Ganhão S, Loureiro GB, Oliveira DR, et al. **Two cases of ADA2 deficiency presenting as childhood polyarteritis nodosa: novel ADA2 variant, atypical CNS manifestations, and literature review.** *Clin Rheumatol* 2020;39:3853–60 CrossRef Medline
- Toyoda K, Tsutsumi K, Hirao T, et al. **Ruptured intracranial aneurysms in pediatric polyarteritis nodosa.** *Neurol Med Chir (Tokyo)* 2012;52:928–932 CrossRef Medline
- Boukoba M, Dossier A, Laissy JP. **Thrombosed aneurysm of the posterior inferior cerebellar artery and lateral medullary ischemia as the initial presentation of polyarteritis nodosa: case report and literature review.** *J Stroke Cerebrovasc Dis* 2018;27:e168–71 CrossRef Medline
- Smith G, Hoh BL, Albayram MS. **Anterior spinal artery aneurysm presenting with spinal subarachnoid hemorrhage in a case of polyarteritis nodosa.** *Clin Imaging* 2019;56:108–13 CrossRef Medline
- Wardlaw JM, Smith C, Dichgans M. **Mechanisms of sporadic cerebral small vessel disease: insights from neuroimaging.** *Lancet Neurol* 2013;12:483–97 CrossRef Medline
- Mandell DM, Mossa-Basha M, Qiao Y, et al. **Intracranial vessel wall MRI: principles and expert consensus recommendations of the American Society of Neuroradiology.** *AJNR Am J Neuroradiol* 2017;38:218–29 CrossRef Medline
- Garg N, Kasapcopur O, Foster J, et al. **Novel adenosine deaminase 2 mutations in a child with a fatal vasculopathy.** *Eur J Pediatr* 2014;173:827–30 CrossRef Medline
- Navinan MR, Subasinghe CJ, Kandeepan T, et al. **Polyarteritis nodosa complicated by posterior reversible encephalopathy syndrome: a case report.** *BMC Res Notes* 2014;7:89 CrossRef Medline
- Fugate JE, Rabinstein AA. **Posterior reversible encephalopathy syndrome: clinical and radiological manifestations, pathophysiology, and outstanding questions.** *Lancet Neurol* 2015;14:914–25 CrossRef Medline

A Systematic Review of Procedural Complications from Transforaminal Lumbar Puncture for Intrathecal Nusinersen Administration in Patients with Spinal Muscular Atrophy

A. Grayev, M. Schoepp, and A. Kuner

ABSTRACT

BACKGROUND: Spinal muscular atrophy is a progressive neurodegenerative disorder that can be treated with intrathecal antisense oligonucleotide therapy (nusinersen). However, administration is often complicated by posterior spinal fusion and neuromuscular scoliosis, necessitating a transforaminal approach.

PURPOSE: To assess the safety profile of the transforaminal approach for intrathecal access.

DATA SOURCES: Searches of the PubMed, Web of Science, and SCOPUS databases.

STUDY SELECTION: Thirteen articles were selected based on inclusion of transforaminal access and appropriate clinical information about the procedure.

DATA ANALYSIS: Complications were taken from the included articles and aggregated based on Cardiovascular and Interventional Radiological Society of Europe scale adverse event grading.

DATA SYNTHESIS: Total number of complications and grade of complications were analyzed, by year and in total.

LIMITATIONS: Selection bias in publication, small patient population size, and variability of the procedure limits the available data.

CONCLUSIONS: Transforaminal approach is a safe alternative for intrathecal access in patients with spinal muscular atrophy and may be applicable to a larger patient population.

ABBREVIATIONS: CBCT = conebeam CT; CIRSE = Cardiovascular and Interventional Radiological Society of Europe; SMA = spinal muscular atrophy

Spinal muscular atrophy (SMA) is a genetic disease of spinal motor neurons characterized by progressive muscle weakness and hypotonia due to progressive degeneration of motor neurons in the spine and brain stem.^{1,2} It is inherited in an autosomal recessive pattern and roughly 1/10,000 live births have a mutation or deletion of the survival of motor neuron 1, telomeric (*SMN1*) gene, resulting in SMA.^{1,3}

In 2016, nusinersen became the first therapeutic drug approved for the treatment of SMA. The drug must be administered as an intrathecal injection because it is unable to cross

the blood-brain barrier.³ Nusinersen requires intrathecal administration with loading doses on the first, 15th, 30th, and 60th day of treatment, followed by maintenance doses every 4 months for the patient's lifetime. Traditional interlaminar or interspinous lumbar puncture is difficult in this population due to a high prevalence of concomitant neuromuscular scoliosis and spinal deformity correction surgery with long-segment instrumented posterior fusion. Cervical punctures were also initially considered in some patients; however, all were precluded by the complex spinal anatomy. The transforaminal approach to lumbar puncture has emerged as an alternative approach; however, given the small number of patients with SMA in any one center, it is difficult to accurately assess a complication rate.

To assess the safety profile for our institution, we aggregated our own center's experience and compared this with the results of our comprehensive literature review. With our analysis, we hope to establish a broader, more generalizable safety profile for the transforaminal lumbar puncture that has proved to be a

Received October 29, 2020; accepted after revision November 16.

From the School of Medicine and Public Health, University of Wisconsin, Madison, Wisconsin.

Financial support for this work was provided by the University of Wisconsin School of Medicine and Public Health, Herman and Gwendolyn Shapiro Foundation Summer Research Program.

Please address correspondence to Allison Grayev, MD, Department of Radiology, University of Wisconsin School of Medicine and Public Health, EI/334 Clinical Science Center, 600 Highland Ave, Madison, WI 53792-3252; e-mail: agrayev@uwhealth.org; @AGrayev <http://dx.doi.org/10.3174/ajnr.A7009>

Table 1: Search queries as entered for the specific databases

Data Base	PubMed	Web of Science	Scopus
Search query	("transforaminal*[All Fields] OR "foraminal*[All Fields]) AND ("spinal puncture[MeSH Terms] OR ("spinal[All Fields] AND "puncture*[All Fields]) OR ("lumbar[All Fields] AND "puncture*[All Fields]) OR "intrathecal*[All Fields])	TS=(transforaminal* OR foraminal*) AND TS=((spinal AND puncture*) OR (lumbar AND puncture*) OR intrathecal*)	TITLE-ABS-KEY ((transforaminal* OR foraminal*) AND (TITLE-ABS-KEY ((spinal AND puncture*) OR (lumbar AND puncture*) OR intrathecal*)) AND (LIMIT-TO (LANGUAGE, "English"))

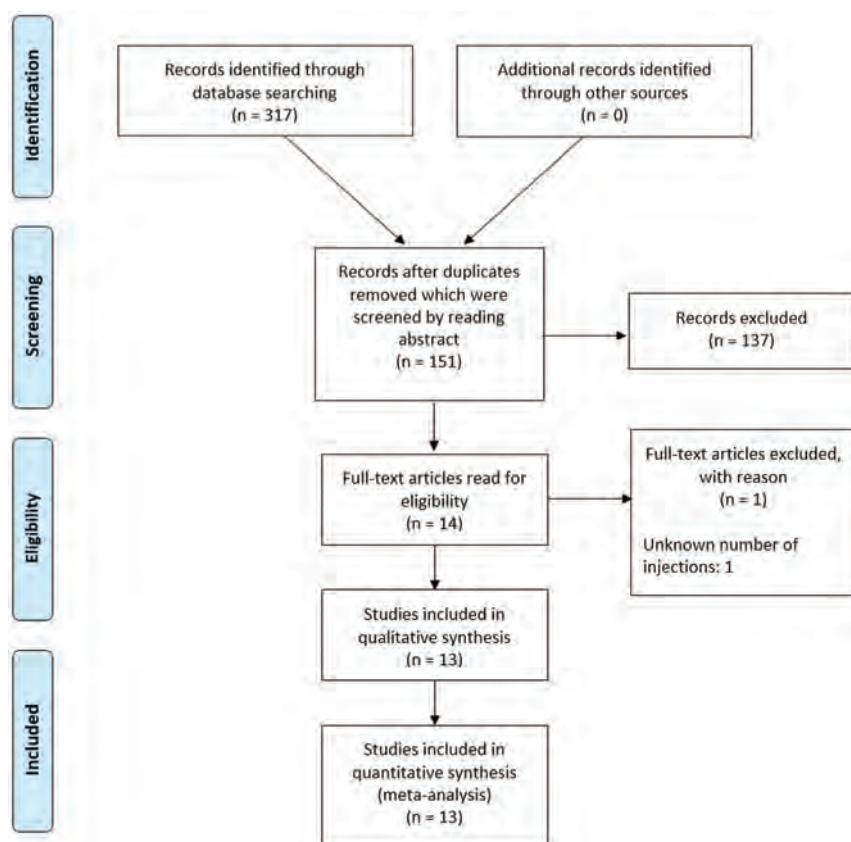


FIGURE. Flowchart demonstrating the identification of eligible articles.

relatively safe and reliable method of intrathecal access as demonstrated in the SMA population.

MATERIALS AND METHODS

This retrospective study was conducted under an institutional review board protocol for Clinical Imaging and Outcomes Research. Funding was provided by the Herman and Gwendolyn Shapiro Foundation through the University of Wisconsin School of Medicine and Public Health.

Following consultation with a health sciences librarian because no review protocol exists, a literature search was performed in PubMed, Web of Science, and SCOPUS by using the keywords “transforaminal,” “foraminal,” “spinal puncture,” “lumbar puncture,” and “intrathecal” on June 24, 2020 (Table 1). Articles were compiled, duplicates were removed, and article abstracts were reviewed for inclusion in the study. Animal research or articles

that did not contain transforaminal access to the intrathecal space were excluded (Figure). Eligible articles were reviewed, and data were extracted as feasible on patient demographics, the number of transforaminal injections, procedure technique, adverse events, and conclusions of the studies. Adverse events were graded based on the Cardiovascular and Interventional Radiological Society of Europe (CIRSE) scale.³ Grade I complications are those that did not require any additional therapy or change from normal post-procedural course. Grade II complications are defined as those requiring a prolonged hospital stay but no additional therapy. Grade III complications require either additional therapy or a prolonged hospital stay (> 2 days), but without long-term sequelae. Given the small number of patients with SMA currently being treated via the transforaminal approach, all studies were included, despite the high risk of selection bias, to increase the overall power of the study.

The SMA data base at our institution was queried for all patients undergoing transforaminal lumbar

punctures for nusinersen administration. All patients underwent a standard procedure planning CT scan at the start of their therapy, followed by limited localization scanning at the time of procedure to minimize patient radiation exposure. All procedures were performed by using 22-ga Quincke tip spinal needles. Needle placement was performed under intermittent visualization with CT fluoroscopy aiming for the Kambin triangle in the inferior-posterior foramen. All procedures were performed in conjunction with the anesthesiology department, which administered appropriate sedation for patient comfort. Routine patient follow-up was performed before patient discharge and at regular intervals after the procedure. The number of patients, number of injections, and adverse events were collated; adverse events were also graded on the basis of the scale.³ Adverse events were collated for each year, as well as an aggregate total based on the available years’ data.

Table 2: Number of injections performed by year in the literature and our data with complications, number, and rate^a

Year	Transforaminal Injections	Patients	CIRSE Grade 1	CIRSE Grade 2	CIRSE Grade 3	Overall Adverse Event Rate
2018	36	16	2	0	0	5.6%
2019	69	16	1	0	0	1.4%
2020	451	74	31	2	3	6.9%
Total	556	106	34	2	3	7%
Adverse event rate			5.8%	0.3%	0.5%	
Institutional experience	42	8	1	0	0	2.4%

^aData include the total adverse event rate categorized by CIRSE grade as well as by year.

RESULTS

A total of 317 articles were identified by searching the 3 data bases, in which there were 151 unique articles after duplicates were reviewed and removed. In addition, 137 records were excluded after reviewing the article abstracts, because they were either animal research studies ($n=9$), did not include a transforaminal approach for intrathecal access ($n=125$), or were not research articles ($n=1$) and articles not available in English ($n=2$). Fourteen full-text articles were then reviewed and 1 additional article was excluded because it did not include the number of injections performed (Figure). Most interesting, despite not including “SMA” in the search terms, no additional articles were identified outside of this patient population. Only 12 articles advocated for the transforaminal approach and 1 article (with the highest complication rate) argued against the safety of this approach, thus further demonstrating the selection bias present in these articles. The included articles are summarized below and in Table 2.

In 2018, Mousa et al⁴ published a review of 26 children, undergoing a total of 104 intrathecal injections. There were 44 injections performed in 11 patients with complex spines, all of which were preceded by a noncontrast lumbar spine CT. There were 19 injections performed via an interspinous approach, 3 via cervical puncture, and 7 patients underwent a total of 22 transforaminal injections. Three of the transforaminal injections were performed by using conebeam CT (CBCT) and 19 by using a biplane fluoroscopy machine. The spinal needles were 22-ga with the length dependent on patient body habitus, but the type of needle was not noted. They report a single adverse event of meningismus and back pain at the injection site, but it is uncertain if this was a patient undergoing a transforaminal approach. For the purposes of this analysis, this was included as a CIRSE grade 1 adverse event. In addition, they note that a transforaminal approach was preferable to a cervical puncture when available.

The same year, Nascene et al⁵ published a review of 26 transforaminal injections in 9 patients during a 21-month period. Two patients did not have SMA (both were complicated postoperative patients requiring myelography) and 1 injection was performed with CT guidance and the other under fluoroscopy. All 7 patients with SMA underwent preprocedural imaging and CT was used for procedural guidance. The review noted that 22-ga Quincke (cutting) needles were used and 24 total injections were performed. Four patients developed self-limited headaches and 1 reported injection site pain, for a total of 5 CIRSE grade 1 adverse events. These data are not included in the 2018 data because they

overlap with an ensuing article from the same group published in 2020.

Finally, the last article from 2018 was published in *Muscle and Nerve* by Geraci et al,⁶ who had a total of 14 injections in 5 patients. This article was slightly different in that patients did not undergo preprocedural imaging and instead had a full diagnostic-quality CT of the lumbar spine at the time of intrathecal injection. CT was also used to guide needle placement and a 22-ga Chiba needle was used for each procedure. A single patient developed postprocedural headache, CIRSE grade 1.

For 2018, there were a total of 36 transforaminal injections published with 2 adverse events reported, both CIRSE grade 1 (adverse event rate 5.6%).

The following year, 2019, there were 2 published studies. Bortolani et al⁷ performed 27 transforaminal injections in 7 patients, all of whom had preprocedural imaging. All procedures were performed under CT guidance, by using a 22-ga spinal needle in 4 patients and a 20-ga Chiba needle in 3 patients. They reported that 1 patient developed a mild headache, CIRSE grade 1. Towbin et al⁸ had a cohort of 9 patients who underwent 42 transforaminal injections. Patients underwent either radiography or CT before the procedure and the procedure was performed under fluoroscopic or CBCT guidance. They used 22-ga Quincke needles for most of the procedures; however, Whitacre needles were used if the patient had a history of prior spinal headache, and a coaxial approach was used with an 18-ga Chiba as a guide if necessitated by body habitus, while still using a 22-ga needle for dural puncture. No complications were reported.

For 2019, there were a total of 69 transforaminal injections published with 1 adverse event reported, CIRSE grade 1 (adverse event rate 1.4%). Combining the articles from the 2 years gives a total of 105 injections with 3 adverse events, again all CIRSE grade 1 (adverse event rate 2.9%).

Most the articles were published in the first half of 2020. Velayudhan et al⁹ published a series of 17 transforaminal injections in 3 patients, all of whom underwent a preprocedural planning CT and they used CT guidance for the procedure. Either a 20-ga or 22-ga Quincke needle was used for the procedure. There were 2 headaches in patients in whom 20-ga needles were used, both of which were self-limited, CIRSE grade 1. In addition, they report 3 episodes of transient radiculopathy in 2 patients, also categorized as CIRSE grade 1.

An additional single report of 1 patient undergoing a single injection was published by Cartwright et al.¹⁰ This patient was transitioned from a fluoroscopically-guided interlaminar lumbar puncture to a CT-guided transforaminal approach secondary to

discomfort during prior 7 interlaminar approach procedures. No complication was reported.

Weaver et al¹¹ published the largest series of transforaminal injections – 200 injections in 28 patients. Preprocedural planning was performed with CT and a 22-ga Quincke needle was used in 199 procedures; a single procedure was performed with a 24-ga Sprotte Spinal needle (Teleflex Medical). There were 187 procedures performed with CBCT and 13 performed under fluoroscopic guidance. Three patients developed transient radiculopathy, 2 patients developed self-limited headache, and 2 patients developed headache that responded to gabapentin for a total of 7 CIRSE grade 1 complications. One patient developed meningitis that was attributed to the nusinersen after CSF tests were negative for bacterial infection (CIRSE grade 2) and 1 patient was admitted for observation and antibiotics after possible traversal of the large bowel during the procedure (CIRSE grade 3).

Another large group of procedures, 85 transforaminal injections in 9 patients, was reported the same year by Shokuhfar et al,¹² including both adult and pediatric patients. All patients underwent preprocedural planning CT and most patients underwent a fluoroscopically-guided procedure (all pediatric patients and 29 of 39 adult patients), with the remainder of procedures performed using CBCT guidance. Whitacre needles were used for all procedures; however, the gauge was not reported. Two complications were reported, but the technique used was not included. A pediatric patient developed constipation and urinary tenesmus, which was successfully treated with polyethylene glycol 3350 (Miralax) (CIRSE grade 1). An adult patient developed bilateral radicular pain after the first injection; no epidural hematoma was visualized on imaging and the pain responded to a single dose of opioid medication (CIRSE grade 1).

A different approach was described by Jacobson et al,¹³ using a coaxial curved-needle technique in 59 procedures performed in 12 patients. Three of the patients had preprocedural CT with the procedures performed under fluoroscopy using a 25-ga coaxial Pakter Curved Needle (Cook). One patient developed a headache that required admission for transforaminal epidural blood patch placement (CIRSE grade 3) and 2 patients had dorsal muscular arterial branch puncture during placement of the 21-ga coaxial needle without complication (CIRSE grade 1).

Özütemiz et al¹⁴ published a series of 65 transforaminal injections in 13 patients; however, there is a 10-month overlap with the previous publication from this group (Nascene et al,⁵ 2018). It is unclear how many of these patients were included in the original analysis. For the purposes of our analysis, we elected to include this cohort of patients in the analysis. All patients underwent preprocedural low-dose CT scanning of the lumbar spine. One patient started the procedure by using fluoroscopic guidance but was transitioned to CT guidance after concern for renal puncture (without adverse outcome – CIRSE grade 1); the remaining procedures were performed under CT guidance from the initiation. The length of the needle was determined by patient body habitus with 64 patients having the procedure performed with a 22-ga Quincke needle and 1 patient with a 25-ga Quincke needle. Eight patients had postprocedural headaches, 1 of which lasted more than a day (CIRSE grade 1). One patient developed hot

flashes, 2 had soreness, and 1 developed self-limited radicular pain (CIRSE grade 1). There was a single CIRSE grade 2 complication of radiculopathy requiring emergency department admission and use of narcotic pain management.

Spiliopoulos et al¹⁵ reported on 20 transforaminal injections performed in 5 patients. All patients underwent lumbar spine CT for procedure planning with limited CT used to evaluate the needle trajectory and advancement. Procedures were performed by using 23-ga Chiba needles. No complications were reported.

Finally, an article was published by Cordts et al¹⁶ detailing their experience performing 4 transforaminal injections in 3 patients. None of the patients underwent preprocedural imaging but CT was used for procedural guidance. Needle type and length were not reported, but the needle gauge was 18–22. Two patients developed self-limited radiculopathy (CIRSE grade 1). One patient developed severe head and back pain for 1 week, necessitating hospitalization; however, the treatment was not reported (CIRSE grade 3). Given the 75% adverse event rate in their patient population, the authors advocate for consideration of laminar drilling to create a posterior approach. However, the needle gauge used in this study was significantly larger than that in any of the other publications, which may have contributed to the higher complication rate.

For 2020, there were 451 transforaminal injections published with a total of 36 adverse events (6.9% adverse event rate). Of the adverse events, 30 were CIRSE grade 1, 2 were grade 2, and 3 were grade 3. In total, this gives an aggregate of 582 injections with an overall adverse event rate of 5.8% (34 total adverse events) as detailed in Table 2. The most common type of complication was headache ($n=19$), followed by radiculopathy ($n=10$) and back pain/soreness ($n=4$). Most of the adverse events were CIRSE grade 1 (34 – 5.8% rate) with 0.3% grade 2 and 0.5% grade 3.

When available, type of needle used in the procedure was evaluated; note that this information was not included in all studies. The number of procedures performed with cutting (Quincke) needles was 216 with 17 CIRSE grade 1 adverse events. Noncutting needle types included Whitacre, Chiba, spinal, and the Pakter Curved Needle with a total of 206 procedures performed with 7 adverse events (6 CIRSE grade 1, 1 CIRSE grade 3). The Pakter Curved Needle system was the only curved system used and had 3 adverse events of which 2 were grade 1 and 1 was grade 3 (5.1% adverse event rate). The overall adverse event rate for cutting needles was 7.9% and for noncutting needles was 3.4% (Table 3).

Procedural guidance varied on the basis of operator preference; granular delineation was not included in all studies. Cross-sectional guidance techniques provide the advantage of direct visualization of other structures that may be encountered along the needle path, with a theoretic decreased risk of traversing the bowel or kidneys with these far lateral needle approaches. Most procedures were performed under CT guidance, but several authors noted transitioning patients to CT or CBCT after unsuccessful fluoroscopic procedures (Table 4). The higher adverse event rate may therefore reflect the more complicated anatomy necessitating CT guidance. The only 2 groups included in the fluoroscopically-guided procedures were the patients reported by

Table 3: Number of adverse events by needle type^a

Needle Type	Transforaminal Injections	Adverse Event Number	CIRSE Grade 1	CIRSE Grade 2	CIRSE Grade 3	Adverse Event Rate
Quincke	216	17	17	0	0	7.9%
Cutting needles						
Sprotte	1	0	0	0	0	
Whitacre	85	2	2	0	0	
Chiba	14	1	1	0	0	
Spinal or Chiba	27	1	1	0	0	3.4%
Pakter	59	3	2	0	1	
Chiba	20	0	0	0	0	
Noncutting needles	206	7	6	0	1	

^a Note that 1 publication reported by using either a spinal or Chiba type needle without delineation of complication rate separately.

Table 4: Number of adverse events by imaging technique

Technique	Transforaminal Injections	Adverse Event Number	CIRSE Grade 1	CIRSE Grade 2	CIRSE Grade 3	Adverse Event Rate
CT	133	19	17	1	1	14.3%
Fluoroscopy	104	4	3	0	1	3.8%
CBCT	39	1	1	0	0	2.6%

Jacobson et al¹³ using the curved needle technique and the pediatric cohort reported by Shokuhfar et al.¹² Towbin et al⁸ did not report the number of each technique used, but did note that CBCT and CT were initially used for guidance before transitioning to fluoroscopy. Nearly all of the studies included preprocedural CT for planning purposes with the following exceptions: Jacobson et al¹³ (curved coaxial technique), Cordts et al¹⁶ (larger needle bore), and Geraci et al⁶ (instead performed full-dose CT for each procedure). Given the additional variables in each of these publications, the decision was made not to separately evaluate for any correlation between performing preprocedural imaging and the adverse event rate.

At our institution, a total of 42 transforaminal injections have been performed in 8 patients. All procedures were performed with 22-ga Quincke type spinal needles with lengths of 3.5, 5, or 7 inches depending on preprocedural images obtained for planning. A single adverse event occurred (2.4% adverse event rate) in 2018, which was deemed to be a CIRSE grade 2 because the patient required inpatient hospitalization for pain management after developing a noncompressive epidural hematoma. The epidural hematoma spontaneously resolved without surgical intervention.

DISCUSSION

The advent of an effective intrathecal treatment for SMA resulting in dramatic clinical improvement has driven the need for the development and use of alternative pathways to access the subarachnoid space.¹⁷ The presence of neuromuscular scoliosis and spinal deformity correction surgery in a large number of these patients complicates the ability to use standard posterior approaches. There are publications supporting the use of cervical puncture by using both fluoroscopic and sonographic guidance,^{18,19} however, this can be precluded given the nonstandard occipitocervical anatomy in this patient population.

Because the transforaminal approach is technically more challenging than a traditional posterior approach – either

interlaminar or interspinous – and has a theoretically potentially higher risk, it is not advocated as a primary approach at our institution. Recently numerous patient series have been published in which transforaminal lumbar puncture was used; however, these publications were limited due to relatively small patient populations. We have aggregated the published multicenter experience with the transforaminal lumbar puncture to assess the safety profile and determine a more generalizable complication rate. Most interesting, there was no clear pattern to the adverse event percentage. It did not parallel the number of transforaminal injections performed, nor the institutional experience (as reported). One study (Cordts et al¹⁶) did report a much higher adverse event rate; however, this may be related to the large needle gauge used in their procedures, because both the needle gauge and the adverse event rate seemed to be outliers. Overall, there was a low rate of significant complication from transforaminal approach lumbar puncture in the patients with SMA after spinal fusion surgery (<1% grade 2 or 3) despite the small number of total procedures (623 procedures total).

During our literature search, we found it interesting that most transforaminal lumbar puncture literature was exclusively focused on the patient population with SMA, without a single publication outside of this patient population even though our search terms were not restricted to this population. Therefore, we must acknowledge that the generalizability of this safety profile is limited to patients with SMA, and additional work would be needed to determine the safety in the general population, despite the 2 successful patients reported by Nascene et al.⁵ The morphology of the foraminal anatomy with a generally exaggerated craniocaudal dimension of the neural foramen may reduce the risk of procedural complications.

Although this literature review addresses the overall safety of the technique, it does not address procedural specifics. The common pathway in all publications is that the neural foramen is traversed by a needle, with a favorable safety profile; however,

there is a large heterogeneity in procedural technique, including imaging guidance (CT versus fluoroscopy) and needle characteristics (needle gauge, type of tip, needle curve, and the use or absence of a guide needle). While most articles focused on CT guidance, there are several institutions that preferentially use either fluoroscopy or CBCT and some that report a combination (starting the procedures with fluoroscopy and transitioning to either CT or CBCT if difficulty was encountered). The determination of the benefits of one technique over the other is beyond the scope of this article and is dependent on multiple factors, including operator preference and experience. An additional procedural component not addressed in this review is the use of general anesthesia or other methods of sedation during the procedures; this was variable between institutions and was not regularly mentioned in the available literature. It is unlikely to affect the complication rate.

A significant limitation of our review is the inability to accurately report complications, because not all complications are likely included in the publication, resulting in significant selection bias. In addition, there is little information regarding how adverse events were reported and what postprocedural follow-up was performed, further limiting the accuracy of the adverse event rate. The published rates (<1% CIRSE grade 2 or higher) are lower than our institutional experience (2.4%); however, we have a small internal patient population with a single adverse event.

There are now both oral (risdiplam) and intravenous (onasemnogene abeparvovec-xioi) treatments for SMA; however, anecdotally, most of our patient population has continued with nusinersen treatment given their previous responses to therapy. Treatment of patients with SMA requires an interdisciplinary team approach for success. Maintaining intrathecal access is of paramount importance to ensure continued delivery of therapy. The published literature supports our anecdotal experience that the transforaminal approach has a favorable safety profile in the SMA population.

CONCLUSIONS

This literature review of all available transforaminal lumbar puncture complication data in the administration of nusinersen demonstrates a favorable safety profile with a low complication rate (<1% CIRSE grades 2 and 3). This is congruent with our own institution experience. Despite a heterogeneous approach to the procedure across institutions, it appears that this is a safe alternative option for intrathecal access in patients with SMA and may have larger applicability in the general population.

Disclosures: Marissa Schoepp—RELATED: Grant: Shapiro Grant, Comments: summer research funding program for medical students at the University of Wisconsin. Anthony Kuner—UNRELATED: Consultancy: Avestis Inc, Comments: Research consultant.

REFERENCES

- Lunn MR, Wang CH. **Spinal muscular atrophy.** *Lancet* 2008;371:2120–33 CrossRef Medline
- Stolte B, Totzeck A, Kizina K, et al. **Feasibility and safety of intrathecal treatment with nusinersen in adult patients with spinal muscular atrophy.** *Ther Adv Neurol Disord* 2018;11:1756286418803246 CrossRef Medline
- Filippidis DK, Binkert C, Pellerin O, et al. **CIRSE quality assurance document and standards for classification of complications: the CIRSE classification system.** *Cardiovasc Intervent Radiol* 2017;40:1141–6 CrossRef Medline
- Mousa MA, Aria DJ, Schaefer CM, et al. **A comprehensive institutional overview of intrathecal nusinersen injections for spinal muscular atrophy.** *Pediatr Radiology* 2018;48:1797–805 CrossRef Medline
- Nascene DR, Ozutemiz C, Estby H, et al. **Transforaminal lumbar puncture: an alternative technique in patients with challenging access.** *AJNR Am J Neuroradiol* 2018;39:986–91 CrossRef Medline
- Geraci AP, Black K, Jin M, et al. **Transforaminal lumbar puncture for intrathecal nusinersen administration.** *Muscle Nerve* 2018 Jan 24 [Epub ahead of print] CrossRef
- Bortolani S, Stura G, Ventili G, et al. **Intrathecal administration of nusinersen in adult and adolescent patients with spinal muscular atrophy and scoliosis: transforaminal versus conventional approach.** *Neuromuscul Disord* 2019;29:742–46 CrossRef Medline
- Towbin R, Schaefer C, Kaye R, et al. **The complex spine in children with spinal muscular atrophy: the transforaminal approach - a transformative technique.** *AJNR Am J Neuroradiol* 2019;40:1422–26 CrossRef Medline
- Velayudhan V, Patel S, Danziger A, et al. **Transforaminal lumbar puncture for intrathecal access: case series with literature review and comparison to other techniques.** *J Clin Neurosci* 2020;72:114–18 CrossRef Medline
- Cartwright MS, Ward ZT, White EP, et al. **Intrathecal delivery of nusinersen in individuals with complicated spines.** *Muscle and Nerve* 2020;62:114–18 CrossRef Medline
- Weaver JJ, Hallam DK, Chick JFB, et al. **Transforaminal intrathecal delivery of nusinersen for older children and adults with spinal muscular atrophy and complex spinal anatomy: an analysis of 200 consecutive injections.** *J Neurointerv Surg* 2021;13:75–78 CrossRef Medline
- Shokuhfar T, Abdalla RN, Hurley MC, et al. **Transforaminal intrathecal access for injection of nusinersen in adult and pediatric patients with spinal muscular atrophy.** *J Pediatr Neurol* 2020;18:88–94 CrossRef
- Jacobson JP, Cristiano BC, Hoss DR. **Simple fluoroscopy-guided transforaminal lumbar puncture: safety and effectiveness of a coaxial curved-needle technique in patients with spinal muscular atrophy and complex spines.** *AJNR Am J Neuroradiol* 2020;41:183–88 CrossRef Medline
- Özütemiz C, Karachunski P, Nascene D.R. **Nusinersen injections in adults and children with spinal muscular atrophy: a single-center experience.** *Diagn Interv Radiol* 2020;26:596–602 CrossRef Medline
- Spiliopoulos S, Reppas L, Zompola C, et al. **Computed-tomography-guided transforaminal intrathecal nusinersen injection in adults with spinal muscular atrophy type 2 and severe spinal deformity: feasibility, safety and radiation exposure considerations.** *Eur J Neurol* 2020;27:1343–49 CrossRef
- Cordts I, Lingor P, Friedrich B, et al. **Intrathecal nusinersen administration in adult spinal muscular atrophy patients with complex spinal anatomy.** *Ther Adv Neurol Disord* 2020;13:1756286419887616 CrossRef Medline
- Claborn MK, Stevens DL, Walker CK, et al. **Nusinersen: a treatment for spinal muscular atrophy.** *Ann Pharmacother* 2019;53:61–69 CrossRef Medline
- Veerapandiyan A, Pal R, D'Ambrosio S, et al. **Cervical puncture to deliver nusinersen in patients with spinal muscular atrophy.** *Neurology* 2018;91:e620–24 CrossRef Medline
- Ortiz CB, Kukreja KU, Lotze TE, et al. **Ultrasound-guided cervical puncture for nusinersen administration in adolescents.** *Pediatr Radiol* 2019;49:136–40 CrossRef Medline

Spinal Compliance Curves: Preliminary Experience with a New Tool for Evaluating Suspected CSF Venous Fistulas on CT Myelography in Patients with Spontaneous Intracranial Hypotension

M.T. Caton Jr, B. Laguna, K.A. Soderlund, W.P. Dillon, and V.N. Shah

ABSTRACT

BACKGROUND AND PURPOSE: Craniospinal space compliance reflects the distensibility of the spinal and intracranial CSF spaces as a system. Craniospinal space compliance has been studied in intracranial pathologies, but data are limited in assessing it in spinal CSF leak. This study describes a method to estimate craniospinal space compliance using saline infusion during CT myelography and explores the use of craniospinal space compliance and pressure-volume curves in patients with suspected cerebrospinal-venous fistula.

MATERIALS AND METHODS: Patients with suspected cerebrospinal-venous fistula underwent dynamic CT myelography. During the procedure, 1- to 5-mL boluses of saline were infused, and incremental changes in CSF pressure were recorded. These data were used to plot craniospinal space compliance curves. We calculated 3 quantitative craniospinal space compliance parameters: overall compliance, compliance at opening pressure, and the pressure volume index. These variables were compared between patients with confirmed cerebrospinal-venous fistula and those with no confirmed source of CSF leak.

RESULTS: Thirty-four CT myelograms in 22 patients were analyzed. Eight of 22 (36.4%) patients had confirmed cerebrospinal-venous fistulas. Bolus infusion was well-tolerated with no complications and transient headache in 2/34 (5.8%). Patients with confirmed cerebrospinal-venous fistulas had higher compliance at opening pressure and overall compliance (2.6 versus 1.8 mL/cm H₂O, $P < .01$). There was no difference in the pressure volume index (77.5 versus 54.3 mL, $P = .13$) between groups.

CONCLUSIONS: A method of deriving craniospinal space compliance curves using saline intrathecal infusion is described. Preliminary analysis of craniospinal space compliance curves provides qualitative and quantitative information about pressure-volume dynamics and may serve as a diagnostic tool in patients with known or suspected cerebrospinal-venous fistulas.

ABBREVIATIONS: C_{op} = compliance at opening pressure; CSC = cerebrospinal space compliance; CTM = CT myelography; CVF = cerebrospinal-venous fistula; PVI = pressure-volume index; SIH = spontaneous intracranial hypotension

Spontaneous intracranial hypotension (SIH) is a debilitating-but-potentially curable syndrome caused by spinal CSF leakage. CSF-venous fistulas (CVFs) are a recently discovered cause of SIH and should be suspected in patients with persistent clinical and brain imaging features of SIH who lack extradural CSF on CT or MR myelography.¹ CVFs are challenging to diagnose and may be position-, volume-, and pressure-dependent; therefore, the true prevalence is likely underestimated.²⁻⁴ Dynamic CT myelography (CTM) and digital subtraction fluoroscopy can facilitate diagnosis,

but the sensitivity of these techniques remains modest.⁵ The pathophysiology of CVF remains poorly understood but is closely tied to the pressure-volume dynamics of the craniospinal axis.² Knowledge of patient-specific CSF pressure-volume dynamics may, therefore, aid in CVF diagnosis and improve our understanding of CVF pathogenesis.

Craniospinal space compliance (CSC) reflects the distensibility of the CSF system as a change in volume relative to a change in pressure.⁶ Building on the Monro-Kellie doctrine, work by Shapiro et al⁷ showed that CSC forms an exponential rather than linear curve. They defined the pressure-volume index (PVI) as a reproducible measure of CSC accounting for this nonlinear relationship, mathematically representing the infusion volume necessary to raise CSF pressure by an order of magnitude.⁷

Later work showed that the PVI can be reliably calculated using bolus-response measurements as opposed to steady-state infusion, more easily performed during routine myelography.⁸

Received August 24, 2020; accepted after revision November 19.

From the Department of Radiology and Biomedical Imaging, Neuroradiology Section, University of California San Francisco, San Francisco, California.

Paper previously presented as a digital poster at: Annual Meeting of the American Society of Neuroradiology, May 30 to June 4, 2020; Virtual.

Please address correspondence to M. Travis Caton, Jr, MD, 505 Parnassus Ave, Room L349, San Francisco, CA 94143; e-mail: michael.caton2@ucsf.edu; @traviscaton
<http://dx.doi.org/10.3174/ajnr.A7018>

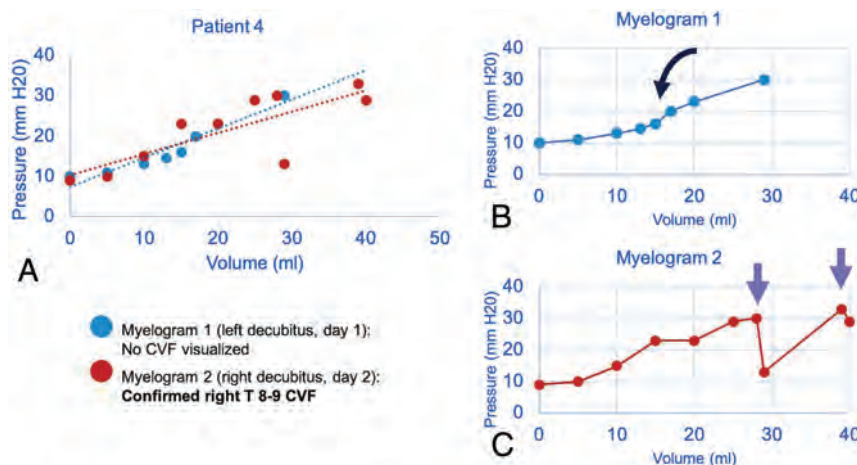


FIG 1. Sample craniospinal compliance curves in a 51-year-old man confirmed to have CVF at operation. Combined plot of 2 CTMs with *dashed lines* showing a linear approximation of compliance (A). Initial nondiagnostic CTM (B) shows a roughly sigmoid pattern with an inflection point seen after a ~15-mL normal saline bolus was administered (*black curved arrow*). Repeat CTM with more aggressive positive-pressure augmentation shows an abrupt loss of pressure (*purple arrows*) after infusion volume of 27 mL of normal saline (C). The CVF became apparent only after pressure was increased beyond this threshold point.

Recent work and our experience indicate that CVF detection is improved with CSF pressure augmentation, which can be achieved with patient positioning, respiratory phase variation, or fluid infusion to the thecal sac.^{3,9-11} Building on prior studies of CSF pressure-volume dynamics using intrathecal CSF infusion in healthy subjects^{12,13} and in pathologic states such as normal-pressure hydrocephalus,¹⁴ we aimed to present our preliminary experience in estimating CSF compliance and PVI using bolus CSF pressure augmentation in patients with SIH suspected of having a CVF.

MATERIALS AND METHODS

In this retrospective case series, we reviewed clinical and imaging records of adult patients with clinical and brain imaging features of SIH suspected of having a CVF from 2015 to 2019 at a single, tertiary referral center. Inclusion criteria were as follows: 1) All patients underwent an initial work-up comprising brain MR imaging and either spine MR imaging or conventional myelography, 2) all patients met the International Classification of Headache Disorders-3 criteria for SIH, and 3) each patient had at least 2 pressure-volume point recordings. Patients with SIH who did not meet these criteria or had confirmation of a non-CVF cause of SIH were excluded. Our institutional CSF leak spine imaging protocol comprises fat-saturated, T2-weighted images of the whole spine in sagittal and coronal planes. In each case, there were findings of SIH on brain MR imaging and no extradural collection on spine MR imaging or conventional myelography. These patients underwent dynamic decubitus, positive-pressure CTM. Patients were classified as having either confirmed CVF (imaging and/or surgical diagnosis) or no definite etiology diagnosed for CSF leak.

CT Myelography Technique

All CTMs were performed by 2 experienced spinal neuroradiologists. A 22-ga Quincke spinal needle (BD) was placed under

intermittent CT fluoroscopy (Discovery CT 750; GE Healthcare) with the patient in the decubitus position. Intrathecal position was confirmed with a test dose of 0.5–1 mL of iohexol contrast (Omnipaque 300 mg; GE Healthcare). Opening CSF pressure was recorded using Glass-Tube (CareFusion) or a digital manometer (Compass; Centurion), allowing equilibration through several respiratory and cardiac cycles, typically 10–15 seconds (this approach was used both pre- and post-bolus infusion). Intrathecal pressure was recorded following serial infusions of normal saline in 1- to 5-mL boluses. When an inflection in CSF pressure (ie, a greater-than-expected change in pressure per bolus, shown in Fig 1) was observed, typically after 10–15 mL of infusion or positive-pressure augmentation was otherwise deemed adequate by the operator, CSF pressure was again recorded, and 8–10 mL of Omnipaque 300 mg was then instilled. Saline bolus infusion was also stopped if patients developed symptoms or peak CSF pressure approached 25–30 cm H₂O to avoid headache and acute visual changes, on the basis of empiric experience of an experienced spine neuroradiologist (unpublished data, W.P.D., May, 2020) and in consultation with a spine neurosurgeon. If the initial CTM was nondiagnostic, a subsequent CTM was performed with the patient in the opposite decubitus position on the following day. At our institution, decubitus dynamic CTM is performed using the HoverMatt device (HoverTech International), which allows rapid transient Trendelenburg positioning for approximately 10 seconds, which is then immediately reversed. Following this maneuver, diagnostic-dose CT is performed with the patient in the decubitus position (typically with 140 kV[peak] and 240 mA) in a dynamic caudal-cranial followed by cranial-caudal fashion, to optimally visualize signs of CVF.

CSF Compliance Analysis and Parameter Calculation

Serial CSF pressure and infusion volume recordings were plotted to generate CSC curves (Fig 1). The PVI was calculated for each patient according to the method of Marmarou et al.¹⁵ This method uses log-transformation of the exponential CSF compliance curve to simplify the calculation (Equation 1):

$$PVI = \frac{\Delta V}{\log \frac{P_p}{P_o}}$$

In this formula, ΔV is the incremental change in volume, equal to the normal saline bolus. P_p is the final (peak) pressure, and P_o is the initial pressure. The PVI value can then be used to estimate CSF-space compliance using an experimentally derived constant function for a given pressure.⁷ To estimate the compliance of the system in equilibrium, we calculated the compliance

Table 1: Demographic and CSF pressure-volume parameters for patients with clinical and imaging features of SIH, all of whom were suspected of having CVF^a

	Total (n = 22)	Definite or Probable CVF (n = 8)	No CVF Identified (n = 14)	P Value
Age (yr)	57.3	60.0	55.8	.5
Sex	59.1% F	37.5% F	71.4% F	.12
Increase in relative pressure during normal saline infusion (cm H ₂ O)	146.7% (SD, 17.3%)	148.5% (SD, 17.9%)	145.4% (SD, 27.0%)	.93
Total volume infusion (mL)	20.7 (SD, 1.8)	27.6 (SD, 2.9)	15.9 (SD, 4.1)	<.001
CSC curves with abrupt pressure loss	11/34 (32.4%)	4/14 (28.6%)	7/20 (35.0%)	.69
Opening pressure (cm H ₂ O)	11.6 (SD, 3.8)	9.8 (SD, 0.9)	12.8 (SD, 0.8)	.02
PVI ^b (mL H ₂ O)	63.9 (SD, 7.5)	77.5 (SD, 10.3)	54.3 (SD, 10.1)	.13
C _{op} ^c (mL/cm H ₂ O)	2.6 (SD, 0.3) mL/cm H ₂ O	3.8 (SD, 0.5) mL/cm H ₂ O	1.8 (SD, 0.3) mL/cm H ₂ O	<.001
Overall compliance (linear slope of CSC curve) (mL/cm H ₂ O)	2.0 (SD, 0.3)	3.1 (SD, 0.6)	1.3 (SD, 0.3)	.005

^aEight patients had definite or probable CVF diagnosed on CTM, and the remaining cases (14/22) remain unconfirmed. All *P* values represent comparison of diagnosed-versus-undiagnosed groups. Data represent either proportions or mean values with standard deviation (SD).

^bEquation 1.

^cEquation 2.

at opening pressure using the following equation, assigning the value of *Pressure* as the measured opening pressure (Equation 2):

$$\text{Compliance} = \frac{0.4343 \times \text{PVI}}{\text{Pressure}}.$$

CSF-space compliance was also estimated as slope⁻¹ of the line of best fit estimated using linear regression of the pressure-volume curves (Fig 1A).¹⁶ Whereas Equation 2 defines the compliance at a particular pressure, the linear regression approximates the compliance over the range of pressures interrogated during saline infusion.

Statistical comparison of continuous variables between groups was assessed with Student *t* tests or the Mann-Whitney *U* test as appropriate. Frequency data were compared using the Pearson χ^2 test. *P* values < .05 were considered statistically significant. Statistical analyses were performed using R statistical and computing software (Version 3.6.2; <http://www.r-project.org/>).

RESULTS

Patient Characteristics

A total of 34 CTMs performed in 22 patients were included in the analysis (14 patients had a single CTM, 5 had 2 CTMs, 2 patients had 3 CTMs, and 1 patient had 4 CTMs). Patient demographic characteristics and a summary of CSC parameters by group are shown in Table 1. The mean age was 57.3 [SD, 13.7] years, and 59.1% of patients were women. Eight patients (36.4%) were diagnosed with confirmed CVF (4 by imaging and surgery, 4 by imaging alone), and the remaining 14 remained undiagnosed. There were no immediate postprocedural complications; however, 2 patients developed mild headaches during the injection (2/34 procedures, 5.8%), which resolved promptly during postprocedural observation.

The mean total normal saline bolus infusion volume was 20.7 [SD, 1.8] mL; range, 4–41 mL with significantly higher infusion volume in the confirmed CVF compared with the unconfirmed CVF group (*P* < .001). Mean opening pressure was lower in the confirmed CVF group (9.8 [SD, 0.9] versus 12.8 [SD, 0.8] cm

H₂O, *P* = .02). The average relative increase in CSF pressure from opening pressure baseline was 146.7% [SD, 17.3%] with no difference between the confirmed/unconfirmed CVF groups (148.5% [SD, 17.9%] versus 145.4% [SD, 27.0%], *P* = .93). The average peak CSF pressure after bolus augmentation was 26.3 [SD, 1.3] cm H₂O (interquartile range 16.3–36.3 cm H₂O). Peak CSF pressures were lower in the group with confirmed CVF, but the mean difference was not statistically significant (23.2 [SD, 2.1] versus 28.4 [SD, 1.6] cm H₂O, *P* = .06).

Craniospinal Compliance Parameters

The mean CSC parameters are summarized in Table 1. The mean PVI for all patients was 63.9 [SD, 7.5] mL. The mean PVI was higher in patients with confirmed CVF, but this difference was not statistically significant (PVI = 77.5 [SD, 10.3] versus 54.3 [SD, 10.1] mL/cm H₂O, *P* = .13). Patients with confirmed CVF had significantly higher compliance at opening pressure (C_{op}) (mean = 3.8 [SD, 0.5] mL/cm H₂O) than the unconfirmed CVF group (mean = 1.8 [SD, 0.3] mL/cm H₂O, *P* ≤ .001). The patient group with confirmed CVF also had higher overall compliance across the range of CSF pressure values compared with patients with unconfirmed CVF (mean = 3.1 [SD, 0.6] versus 1.3 [SD, 0.3] mL/cm H₂O, *P* = .005). Sex-related differences are shown in Table 2. No significant differences were observed between men and women for opening pressure, PVI, C_{op}, or overall compliance (*P* > .05, all cases).

CSC-Curve Morphology

We observed a spectrum of CSC curve shapes, including curves that were roughly linear, sigmoid, and exponential. We also found 2 distinct patterns that may have particular clinical relevance. A sudden drop in measured pressure during positive-pressure augmentation was observed in 11/34 (32.4%) patients (Fig 1). No difference in the frequency of this curve morphology was seen between the confirmed and unconfirmed CVF groups (28.6% versus 35.0%, *P* = .69). Continued administration of normal saline boluses after the pressure drop resulted in

Table 2: CSC parameter differences by sex^a

	Women	Men	P Value
Opening pressure (cm H ₂ O)	11.5 [SD, 0.8]	11.7 [SD, 1.0]	.86 ^b
PVI (mL H ₂ O)	57.5 [SD, 9.1]	74.1 [SD, 7.0]	.29 ^b
Compliance at opening pressure (mL/cm H ₂ O)	2.5 [SD, -0.5]	2.9 [SD, 0.4]	.06 ^c
Overall compliance (mL/cm H ₂ O)	1.7 [SD, 0.4]	2.5 [SD, 0.6]	.06 ^b

^a Data are mean values with standard deviation (SD).

^b Student *t* test.

^c Mann-Whitney *U* test.

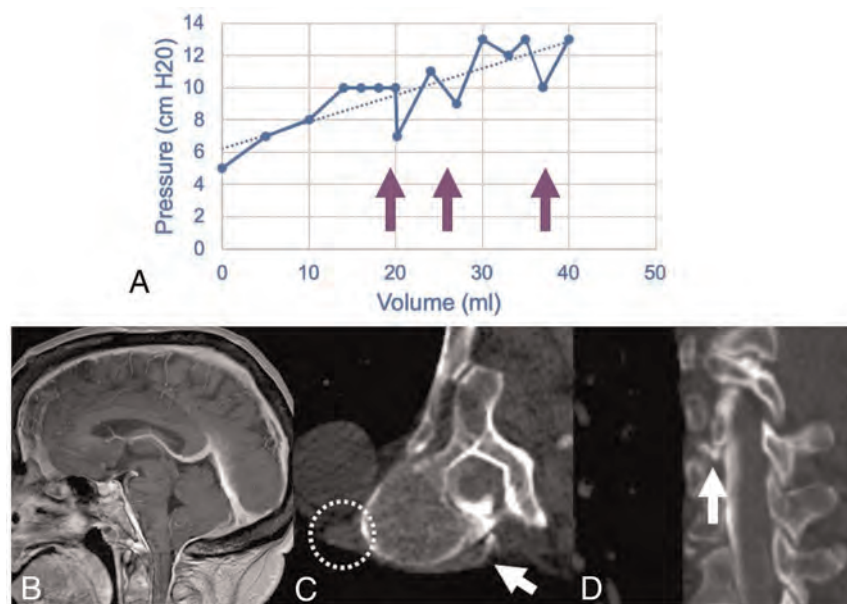


FIG 2. A craniospinal compliance curve in a 70-year-old woman with confirmed CVF (A) shows high compliance (ie, smaller change in pressure per increase in volume) with multiple abrupt pressure drops (arrows) above 10 cm H₂O. Recent brain MR imaging shows characteristic features of SIH (B), including reduced mamillopontine distance, low cerebellar tonsils, and pachymeningeal enhancement. A right T7–8 CVF was identified on decubitus CT myelography (C and D). Hyperdensity of the paraspinal vein and azygous vein (dashed circle) aids in identification of the fistula (white arrows). The patient was treated with percutaneous fibrin glue injection.

reconstitution of the CSC slope in each case, though multiple/recurrent drops were observed in some instances (Fig 2).

DISCUSSION

We report a method of generating craniospinal compliance curves derived from CT myelography and characterize these curves in a preliminary analysis of patients with SIH and suspected CVF. Compliance measurements (C_{op} , overall CSC compliance) in patients with confirmed CVFs were statistically different from those in patients with SIH in whom a final etiology of CSF leak could not be identified. Using a hand-bolus injection as a simple and reproducible alternative to continuous infusion techniques, we show how patient-specific models of pressure-volume dynamics can be reconstructed and the PVI can be estimated.

Although these findings are preliminary, we propose several potential uses of CSC curves in patients with SIH who undergo CTM: First, a drop in CSF pressure observed on the CSC curve may help identify patients with dural leaks or fistulas. Second, there

are probably pressure-dependent CVFs, that otherwise remain occult without adequate pressure augmentation (Fig 1). Finally, the documentation of CSF compliance may also define a patient-specific baseline, allowing quantification of treatment response, as we show with the epidural blood patch (Fig 3). For example, baseline patient-specific CSC parameters could be used in patients who undergo surgical fistula ligation as a means of confirming successful or unsuccessful CVF exclusion.

The theoretic basis for CSC curve analysis in patients with CSF leak warrants additional discussion. Abnormal profiles of PVI and the resistance to CSF outflow have been described in patients with intracranial pathology, including normal-pressure hydrocephalus, subarachnoid hemorrhage, and traumatic brain injury.^{17–19} However, contemporary models of CSF-space compliance treat the cranial and spinal spaces as communicating compartments of the same system.⁶ In these models, the CSC is analogized to an electrical circuit with systemic compliance determined by the additive effects of cranial and spinal compartments.^{16,13,20} Abnormal dural compliance in the spinal compartment should, therefore, influence the entire craniospinal system. CVF, like all spinal CSF leaks, should, in theory, increase compliance, but the pressure-volume relationship is likely dictated by the dynamic equilibrium of CSF pressure and venous pressure. Our

observation that in some patients, a sudden collapse of pressure occurred during saline infusion may indicate that we had reached a CSF-venous pressure equilibrium point. A further increase in CSF pressure could conceivably open the leak and provides one explanation for the inflection in compliance observed in this study (Fig 4). While unproven, this mechanism could provide a physiologic explanation for why CVFs are often occult in the supine position but manifest when the patient is upright or in the decubitus position or provocation maneuvers are performed. Our observation is also concordant with work from Amrhein et al,¹¹ which showed increased conspicuity of the CVF with inspiration, which augments the CSF-venous pressure gradient increasing venous return to the right atrium. It has been postulated that such maneuvers open the leak, which could be detected as a sudden increase in compliance of the craniospinal system.^{5,9,21} A similar mechanism was postulated by Kumar et al,²² who reported indirect treatment of CVFs by reduction of the CSF-venous gradient using an inferior vena cava stent.

The hand-injection bolus pressure augmentation method is easily reproducible and does not require additional equipment,

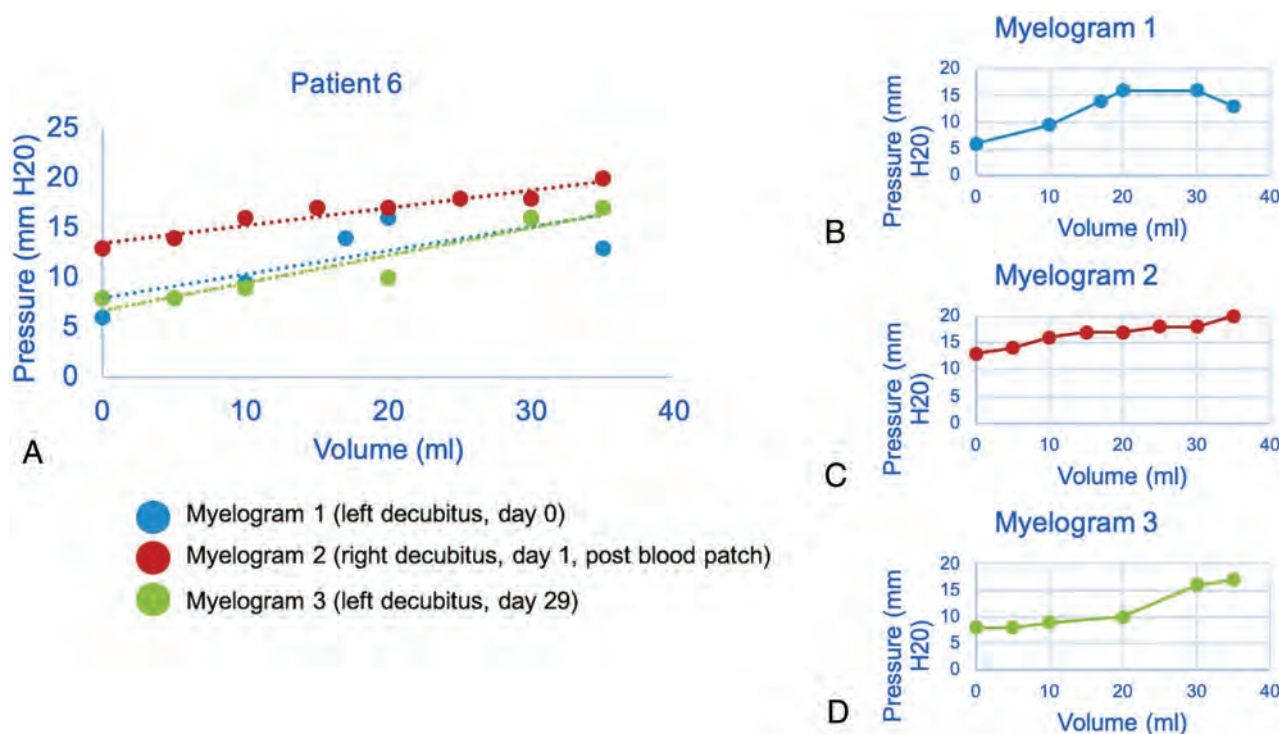


FIG 3. Craniospinal compliance curve in a 63-year-old woman suspected but not radiographically confirmed to have CVF. Estimated linear compliance for each CTM is shown as a *dashed line*, approximating the shape of the pressure-volume curve (A). The second CTM was performed after the blood patch showed an increase in opening pressure (B and C). The effect of the blood patch is diminished on delayed repeat CTM (D), in which the left side of the curve, including opening pressure, more closely matches the prepatch curve.

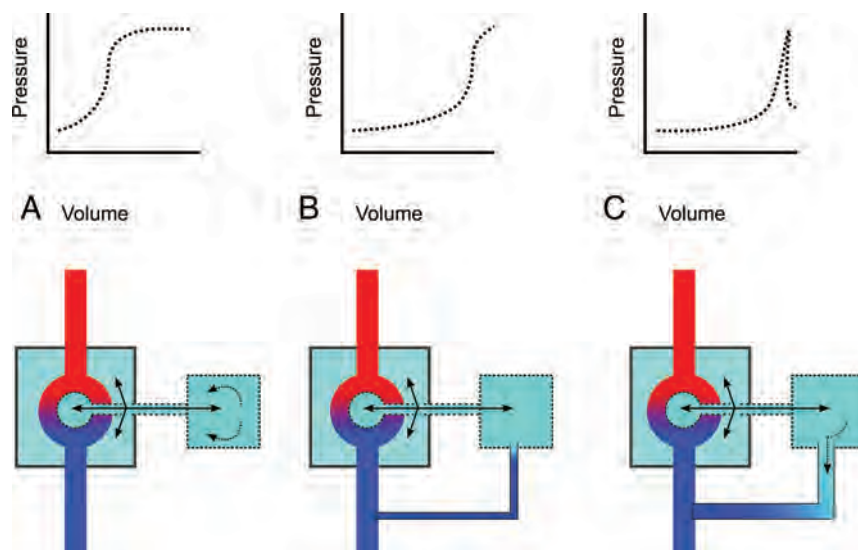


FIG 4. Schematic of the components of craniospinal compliance and hypothesized physiology of CVF (CSF = green, arterial blood = red, venous blood = blue). A normal CSC encompasses both intraventricular and subarachnoid CSF and is defined by cranial and spinal compartments (*larger and smaller boxes*, respectively) as well as the arteriovenous vascular bed (A). In dural tear CSF leak or CVF at low pressure, an equilibrium state (B) may exist in which the leak is occult by CTM. With special maneuvers (dynamic CTM, respiratory-phase variation, jugular pressure, and bolus-pressure augmentation), pressure gradients may open the leak, allowing detection on CTM (C).

described by Griffith et al²⁵ as a means of estimating compliance and PVI. This approach is based in mathematic and empiric observations showing that the PVI can be accurately measured using bolus (rather than steady/continuous) infusion.⁸ Although only a single bolus injection is needed to estimate PVI, multiple measurements, as used in our study, may be advantageous to identify zones in which the pressure-volume relationship changes more quickly due to autoregulatory mechanisms.²⁶ While dynamic CTM is the preferred technique at our institution, the bolus-pressure augmentation method could be performed with conventional or dynamic fluoroscopy. In this preliminary experience, we observed no peri-procedural complications and only 2 instances (5.8%) of transient headache during bolus infusion. These findings suggest that this technique has a reasonable safety profile when pressures and symptoms are closely monitored.

The interpretation of CSC curves has several important technical and theoretic limitations. First, because we did not investigate CSC parameters in controls without SIH, it is difficult to estimate the diagnostic value of CSC curves in

unlike previously described methods using steady-state infusion.^{20,23,24} The hand-bolus technique is more appropriate for patients with SIH than serial CSF withdrawal, which was

routine practice. A corollary limitation is that comparisons between confirmed and unconfirmed (suspected) CVFs are inherently limited and should be interpreted conservatively. Another important limitation is that CSC has been shown to vary with posture, largely due to shifts and redistribution of venous outflow through the jugular veins.²⁷ While our data suggest that a rapid drop in CSF pressure during pressure augmentation may reflect opening of a pressure-dependent CVF, this effect could plausibly be due to other physiologic effects such as respiratory phase variation and the cardiac cycle.¹¹ Definitive correlation could be established if the bolus-pressure augmentation technique were performed during digital subtraction myelography to allow real-time visualization of the CVF; we would expect that the leak would become visible or more conspicuous as CSF pressure is increased with serial intrathecal boluses, controlling for respiratory phase and cardiac cycle variations.

Another important limitation of our study is that the population included in this analysis comprised patients with suspected CVF who remained undiagnosed after conventional diagnostic and interventional studies (eg, MR myelography, conventional CTM). Accordingly, patients with other, non-CVF leaks are not represented, and the relatively low rate of confirmatory diagnosis (8/22, 36.4%) in this cohort reflects the diagnostic challenge of CVF relative to other forms of CSF leak.² Some of these patients may have leaks in locations that are more difficult to visualize (eg, sacrum) or simply CVFs that were not visible at that time. An additional important limitation of our study is that we did not assess control patients, and as a result, we did not define discriminatory threshold values of PVI and compliance in healthy patients. Nonetheless, the mean PVI values in our study (63.9 [SD, 7.5] mL) are higher than those in control patients reported in the literature, for example by Shapiro et al⁷ (PVI = 25.9 [SD, 3.7] mL) and by Wahlin et al¹³ (PVI mean = 9.8 [SD, 2.7 mL]), though methodologic differences may affect comparison. This finding is consistent with the proposed pathophysiology of CVF as a high-compliance state. A final limitation is that we did not use a standardized approach to positive-pressure augmentation because each operator selected the bolus number and volume before imaging.

This work is a preliminary exploration of a novel technique in a dynamic disease process; while these results are promising, investigation of CSC curves and correlation of steady-state and bolus-infusion methods should also be performed in the CSF leak population to confirm the validity of this approach. Future studies should also establish the boundaries of normal physiology in control patients.

CONCLUSIONS

This study describes a method of estimating craniospinal compliance during dynamic CT myelography and presents our preliminary experience in applying this technique in patients with suspected CVF. This method could be applied prospectively to evaluate compliance parameters and pressure-volume curve morphology as tools for the diagnosis of CVF and could inform the practice of spine interventionists treating these patients.

Disclosures: Benjamin Laguna—OTHER RELATIONSHIPS: Cofounder of a pre-revenue company called Sira Medical (augmented reality).

REFERENCES

1. Schievink WI, Moser FG, Maya MM. CSF-venous fistula in spontaneous intracranial hypotension. *Neurology* 2014;83:472–73 CrossRef Medline
2. Kranz PG, Amrhein TJ, Gray L. CSF venous fistulas in spontaneous intracranial hypotension: imaging characteristics on dynamic and CT myelography. *AJR Am J Roentgenol* 2017;209:1360–66 CrossRef Medline
3. Schievink WI. Spontaneous spinal cerebrospinal fluid leaks and intracranial hypotension. *JAMA* 2006;295:2286–96 CrossRef Medline
4. Hunderfund ANL, Mokri B. Orthostatic headache without CSF leak. *Neurology* 2008;71:1902–06 CrossRef Medline
5. Dobrocky T, Mosimann PJ, Zibold F, et al. Cryptogenic cerebrospinal fluid leaks in spontaneous intracranial hypotension: role of dynamic CT myelography. *Radiology* 2018;289:766–72 CrossRef Medline
6. Burman R, Alperin N, Lee SH, et al. Patient-specific cranio-spinal compliance distribution using lumped-parameter model: its relation with ICP over a wide age range. *Fluids Barriers CNS* 2018;15:29 CrossRef Medline
7. Shapiro K, Marmarou A, Shulman K. Characterization of clinical CSF dynamics and neural axis compliance using the pressure-volume index, I: the normal pressure-volume index. *Ann Neurol* 1980;7:508–14 CrossRef Medline
8. Tans JT, Poortvliet DC. CSF outflow resistance and pressure-volume index determined by steady-state and bolus infusions. *Clin Neurol Neurosurg* 1985;87:159–65 CrossRef Medline
9. Griffin AS, Lu L, Peacock S, et al. CSF volume provocation maneuvers during lumbar puncture as a possible predictive tool for diagnosing spontaneous intracranial hypotension. *Clin Neurol Neurosurg* 2019;186:105552 CrossRef Medline
10. Kranz PG, Luetmer PH, Diehn FE, et al. Myelographic techniques for the detection of spinal CSF leaks in spontaneous intracranial hypotension. *AJR Am J Roentgenol* 2016;206:8–19 CrossRef Medline
11. Amrhein TJ, Gray L, Malinzak MD, et al. Respiratory phase affects the conspicuity of CSF-venous fistulas in spontaneous intracranial hypotension. *AJNR Am J Neuroradiol* 2020;41:1754–56 CrossRef Medline
12. Miller JD, Garibi J, Pickard JD. Induced changes of cerebrospinal fluid volume: effects during continuous monitoring of ventricular fluid pressure. *Arch Neurol* 1973;28:265–69 CrossRef Medline
13. Wählin A, Ambarki K, Birgander R, et al. Assessment of craniospinal pressure-volume indices. *AJNR Am J Neuroradiol* 2010;31:1645–50 CrossRef Medline
14. Qvarlander S, Lundkvist B, Koskinen L-OD, et al. Pulsatility in CSF dynamics: pathophysiology of idiopathic normal pressure hydrocephalus. *J Neurol Neurosurg Psychiatry* 2013;84:735–41 CrossRef Medline
15. Marmarou A, Shulman K, LaMorgese J. Compartmental analysis of compliance and outflow resistance of the cerebrospinal fluid system. *J Neurosurg* 1975;43:523–34 CrossRef Medline
16. Löfgren J, von EC, Zwetnow NN. The pressure-volume curve of the cerebrospinal fluid space in dogs. *Acta Neurol Scand* 1973;49:557–74 CrossRef Medline
17. Pomschar A, Koerte I, Lee S, et al. MRI evidence for altered venous drainage and intracranial compliance in mild traumatic brain injury. *PLoS One* 2013;8:e55447 CrossRef Medline
18. Eklund A, Smielewski P, Chambers I, et al. Assessment of cerebrospinal fluid outflow resistance. *Med Biol Eng Comput* 2007;45:719–35 CrossRef Medline
19. Heinsoo M, Eelmäe J, Kuklane M, et al. The possible role of CSF hydrodynamic parameters following in management of SAH patients. In: Marmarou A, Bullock R, Avezaat C, et al, eds. *Intracranial Pressure and Neuromonitoring in Brain Injury*. Springer-Verlag; 1998:13–15
20. Tain RW, Bagci AM, Lam BL, et al. Determination of cranio-spinal canal compliance distribution by MRI: methodology and early application in idiopathic intracranial hypertension. *J Magn Reson Imaging* 2011;34:1397–404 CrossRef Medline

21. Kranz PG, Gray L, Amrhein TJ. **Decubitus CT myelography for detecting subtle CSF leaks in spontaneous intracranial hypotension.** *AJNR Am J Neuroradiol* 2019;40:754–56 CrossRef Medline
22. Kumar N, Neidert NB, Diehn FE, et al. **A novel etiology for craniospinal hypovolemia: a case of inferior vena cava obstruction.** *J Neurosurg Spine* 2018;29:452–55 CrossRef Medline
23. Beck J, Fung C, Ulrich CT, et al. **Cerebrospinal fluid outflow resistance as a diagnostic marker of spontaneous cerebrospinal fluid leakage.** *J Neurosurg Spine* 2017;27:227–34 CrossRef Medline
24. Weerakkody RA, Czosnyka M, Schuhmann MU, et al. **Clinical assessment of cerebrospinal fluid dynamics in hydrocephalus: guide to interpretation based on observational study.** *Acta Neurol Scand* 2011;124:85–98 CrossRef Medline
25. Griffith B, Capobres T, Patel SC, et al. **CSF pressure change in relation to opening pressure and CSF volume removed.** *AJNR Am J Neuroradiol* 2018;39:1185–90 CrossRef Medline
26. Avezaat CJ, Eijndhoven JH, van Wyper DJ. **Cerebrospinal fluid pulse pressure and intracranial volume-pressure relationships.** *J Neurol Neurosurg Psychiatry* 1979;42:687–700 CrossRef Medline
27. Alperin N, Lee SH, Sivaramakrishnan A, et al. **Quantifying the effect of posture on intracranial physiology in humans by MRI flow studies.** *J Magn Reson Imaging* 2005;22:591–96 CrossRef Medline

Celebrating 35 Years of the AJNR

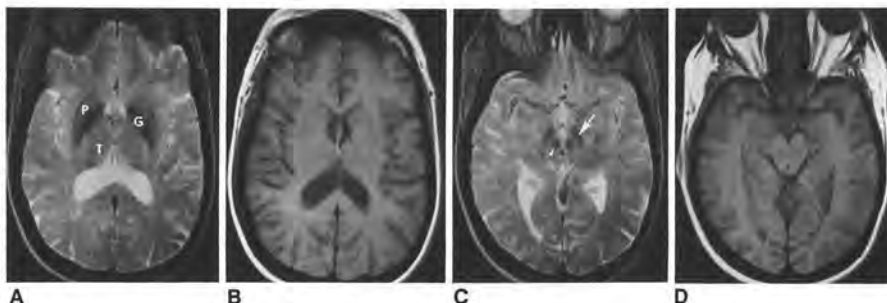
May 1986 edition

Magnetic Resonance Imaging of Brain Iron

Burton Drayer^{1,2}
Peter Burger³
Robert Darwin⁴
Stephen Riedner⁵
Robert Hartkens⁶
G. Allan Johnson⁷

A prominently decreased signal in the substantia nigra, red nucleus, and dentate nuclei on T2-weighted images (SE). This MRI finding correlated closely and the sites of preferential accumulation of iron on normal postmortem brains. T2 thus provides an accurate in vivo and MRI studies in normal brains: the striatum, and still lower levels matter, iron concentration in the capsule and optic radiations. It is prominent in the subcortical "U" in the brain at birth; it increases of brain iron should assist in clarifying neurodegenerative, demyelinating.

It has been suggested that exquisite anatomic images, not brain function. Early attempts have been promising but time-consuming proton MRI imaging have but they have been disappointing. When using a high field strength in every patient studied on a finding consisted of decreased specific brain locales, including the globus pallidum, reticular substantia nigra, red nucleus, dentate nucleus, and putamen [1]. This paper gives an account of our studies to determine the origin of this biochemical effect.



This article appears in the May/June 1986 issue of AJNR and the July 1986 issue of AJR.

Received October 25, 1985; accepted after revision January 3, 1986.

Presented in part at the annual meeting of the American Society of Neuroradiology, New Orleans, February 1986.

¹Department of Radiology, Duke University Medical Center, Durham, NC 27710. Address reprint requests to B. P. Drayer, Department of Radiology, Box 3853, Duke University Medical Center, Durham, NC 27710.

²Department of Medicine (Neurology), Duke University Medical Center, Durham, NC 27710.

³Department of Pathology, Duke University Medical Center, Durham, NC 27710.

⁴Department of Radiology, University of North Carolina at Chapel Hill, Chapel Hill, NC 27514.

⁵Department of Radiology, University of North Carolina at Chapel Hill, Chapel Hill, NC 27514.

⁶Department of Radiology, University of North Carolina at Chapel Hill, Chapel Hill, NC 27514.

⁷Department of Radiology, University of North Carolina at Chapel Hill, Chapel Hill, NC 27514.

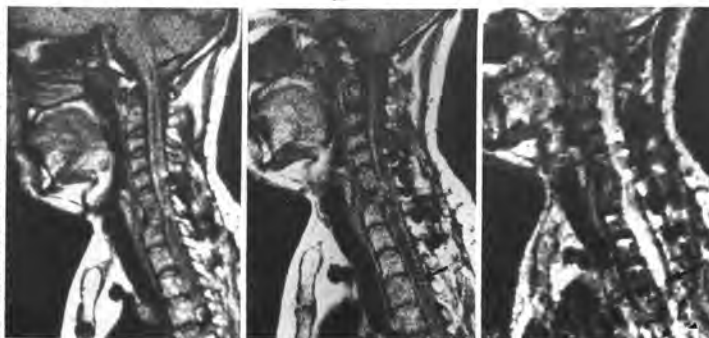
Magnetic Resonance Imaging of the Chronically Injured Cervical Spinal Cord

Robert M. Quencer¹
Jerome J. Sheldahl²
M. Judith Donovan-Pond³
Rovendo D. Diaz⁴
Berta M. Montalvo⁵
Barth A. Green⁶
Frank J. Eismont⁷

Thirteen patients evaluated with MRI because of the role to rule out our residual were compared with in vivo of those the injured spinal cord. It was found that MRI accurately depicted myelomalacia frequently difficult to detect with long.

Over the years, spinal cord has a percutaneous or computed tomography (CT) accurate, because media within the spinal cord cyst [1] associated with a chronically injured sonography. Spec either myelomalacia, therefore, to have patients with shunt but noncystic spinal cord. Although a number of MRI in chronic injured spinal cords. In this paper we report the use of MRI in 13 patients with prior cervical cord trauma, 10 of whom were also studied with delayed metrizamide CT and five of whom had surgery. It is our objective to compare the results of MRI with those of delayed metrizamide CT in order to determine which is the most accurate method of preoperatively evaluating the chronically damaged spinal cord. Further, we correlate these imaging modalities with the patients' clinical presentations and the findings at surgery as determined by intraoperative spinal sonography.

Materials and Methods
Thirteen patients who had suffered severe cervical spinal cord trauma six months to 11 years prior to their present hospitalization were evaluated clinically and examined radiographically.



This article appears in the May/June 1986 issue of AJNR and the July 1986 issue of AJR.

Received August 1, 1985; accepted after revision December 26, 1985.

Presented in part at the annual meeting of the American Society of Neuroradiology, New Orleans, February 1986.

¹Department of Radiology, University of Miami Jackson Memorial Medical Center, Miami, FL. Address reprint requests to R. M. Quencer, Department of Radiology (R-135), University of Miami School of Medicine, P.O. Box 61950, Miami, FL 33101.

²Department of Radiology, Mt. Sinai Medical Center, Miami Beach, FL.

³Department of Neurological Surgery, University of Miami Jackson Memorial Medical Center, Miami, FL.

⁴Department of Orthopaedic Surgery, University of Miami Jackson Memorial Medical Center, Miami, FL.

⁵Department of Radiology, University of Miami Jackson Memorial Medical Center, Miami, FL.

⁶Department of Radiology, University of Miami Jackson Memorial Medical Center, Miami, FL.

⁷Department of Radiology, University of Miami Jackson Memorial Medical Center, Miami, FL.